

Roger LeB. Hooke

Principles of Glacier Mechanics

Second Edition

CAMBRIDGE

CAMBRIDGE

more information - www.cambridge.org/9780521836098

This page intentionally left blank

Principles of Glacier Mechanics

Second Edition

This book provides students and practicing glaciologists with the tools they need to understand modern glaciology. Relatively simple concepts are introduced first, followed by mathematically more sophisticated chapters. A knowledge of basic calculus is assumed, but important equations describing physical processes are developed from elementary principles. Emphasis is placed on connections between modern research in glaciology and the origin of features of glacial landscapes. Student exercises are included. This new edition builds on the successful first edition: it has been completely updated, and important new sections and whole chapters have been added. *Principles of Glacier Mechanics* is designed to be used as a primary textbook in upper division and graduate courses in glaciology, and can be used as either a primary or supplementary text in courses in glacial geology. Practicing glacial geologists and glaciologists will also find it useful as a reference book.

ROGER LEB. HOOKE is Research Professor in the Department of Earth Sciences and the Climate Change Institute, University of Maine. He has been involved in glaciological research for over 30 years, focusing on processes relevant to the origin of glacial landforms. In addition to the first edition of *Principles of Glacier Mechanics*, he has published over 80 refereed research papers in journals such as the *Geological Society of America Bulletin*, *Geology*, the *Journal of Glaciology*, *Quaternary Research*, and the *Journal of Geology*.

Principles of Glacier Mechanics

Second Edition

Roger LeB. Hooke

Research Professor

Department of Earth Sciences

and Climate Change Institute

University of Maine, Orono



CAMBRIDGE
UNIVERSITY PRESS

CAMBRIDGE UNIVERSITY PRESS

Cambridge, New York, Melbourne, Madrid, Cape Town, Singapore, São Paulo

Cambridge University Press

The Edinburgh Building, Cambridge CB2 2RU, UK

Published in the United States of America by Cambridge University Press, New York

www.cambridge.org

Information on this title: www.cambridge.org/9780521836098

© in the Second edition R. LeB. Hooke 2005

This book is in copyright. Subject to statutory exception and to the provision of relevant collective licensing agreements, no reproduction of any part may take place without the written permission of Cambridge University Press.

First published in print format 2005

ISBN-13 978-0-511-08174-3 eBook (EBL)

ISBN-10 0-511-08174-X eBook (EBL)

ISBN-13 978-0-521-83609-8 hardback

ISBN-10 0-521-83609-3 hardback

ISBN-13 978-0-521-54416-0 paperback

ISBN-10 0-521-54416-5 paperback

Cambridge University Press has no responsibility for the persistence or accuracy of URLs for external or third-party internet websites referred to in this book, and does not guarantee that any content on such websites is, or will remain, accurate or appropriate.

First edition © 1998 by Prentice Hall Simon and Schuster / A Viacom Company
Upper Saddle River, New Jersey 07458

It is with a deep sense of gratitude that I dedicate this book to those who, at various times through the formative stages of my life, guided me into the most exciting and rewarding career I can imagine: the study of our Earth.

To my parents, who opened many doors for me;
to my older brother, Richard, who led me through a door leading to
the wilderness;
to John Muir who opened my eyes to the spirituality in wilderness;
to my wife, Ann, who introduced me to Geology;
to John P. Miller who focused my attention on processes at the Earth's
surface; and
to Robert P. Sharp who taught me that basic physical principles could
be used to understand these processes.

Contents

Preface to the first edition	<i>page</i>	xii
Preface to the second edition		xiii
Physical constants relevant to ice		xiv
Derived SI units and conversion factors		xvii
1 Why study glaciers?		1
2 Some basic concepts		5
A note on units and coordinate axes		5
Glacier size, shape, and temperature		6
The condition of incompressibility		9
Stresses, strains, and strain rates		10
3 Mass balance		17
The transformation of snow to ice		18
Snow stratigraphy		20
Mass balance principles		23
Climatic causes of mass balance fluctuations		26
The budget gradient		29
Other modes of ice loss from valley glaciers		31
Mass balance of polar ice sheets		34
Effect of atmospheric circulation patterns on mass balance		37
Global mass balance		40
Summary		41
4 Flow and fracture of a crystalline material		43
Crystal structure of ice		43
Dislocations		44
Rate-limiting processes		48
Internal stresses		53
Recrystallization		54
Deformation mechanism maps		63

	A flow law for glacier ice	66
	Fracture	70
	Summary	74
5	The velocity field in a glacier	76
	Measurement of velocity	77
	Balance velocity	78
	Shear stress distribution	79
	Horizontal velocity at depth in an ice sheet	81
	Horizontal velocity in a valley glacier	83
	Mean horizontal velocity and ice flux	87
	Vertical velocity	88
	Submergence and emergence velocities	91
	Flow field	92
	Transverse profiles of surface elevation on a valley glacier	94
	Radar stratigraphy	96
	Effect of drifting snow on the velocity field	98
	Ice streams	105
	Summary	110
6	Temperature distribution in polar ice sheets	112
	Energy balance in an ice sheet	112
	Dependence of K on temperature	117
	The steady-state temperature profile at the center of an ice sheet	117
	Temperature profiles in the ablation zone	127
	Temperature profiles near the surface of an ice sheet	127
	Temperature distributions far from a divide	131
	Englacial and basal temperatures along a flow line calculated using the Column model	135
	Basal temperatures in Antarctica – comparison of solutions using the Column model and a numerical model	138
	Geomorphic implications	142
	Summary	144
7	The coupling between a glacier and its bed	147
	Sliding	148
	Deformation of subglacial till	168
	Stability of ice streams	190

Effect of a frozen bed	193
Summary	194
8 Water flow in and under glaciers: geomorphic implications	197
The upper part of the englacial hydraulic system	197
Equipotential surfaces in a glacier	201
Melt rates in conduits	205
Water pressures in subglacial conduits on hard beds	208
Types of subglacial drainage system	215
Surges	230
Subglacial drainage paths and the formation of eskers	232
Tunnel valleys	241
Water pressure and glacier quarrying	244
Origin of cirques and overdeepenings	248
Summary	250
9 Stress and deformation	252
Stress	252
Momentum balance	261
Deformation	262
Condition that principal axes of stress and strain rate coincide	267
Summary	269
10 Stress and velocity distribution in an idealized glacier	271
Solutions for stresses and velocities in plane strain	271
Comparison with real glaciers	286
Summary	287
11 Numerical modeling	288
Goals of modeling	289
Numerical integration	289
Finite-difference models	291
Finite-element models	298
Initial conditions and forcing	299
Validation	301

Intercomparison of models	301
Sensitivity testing and tuning	302
Coupling thermal and mechanical models	303
Examples	304
Summary	313
12 Applications of stress and deformation principles to classical problems	315
Collapse of a cylindrical hole	315
Calculating basal shear stresses using a force balance	326
Creep of floating ice shelves	333
Analysis of borehole-deformation data	338
Summary	348
13 Finite strain and the origin of foliation	349
The strain ellipse	349
Simple and pure shear	351
Parameters describing cumulative deformation	352
Calculating cumulative strain	353
Components of foliation	356
Summary	364
14 Response of glaciers to changes in mass balance	365
Positive feedback processes	366
Response of a temperate glacier	367
Elementary kinematic wave theory	368
Analysis of the effect of a small change in mass balance using a perturbation approach	371
Effect of diffusion	375
The problem at the terminus	376
Further study of the response time	376
Numerical modeling of glacier responses	381
Comparison with observation	383
Summary	390
Appendix Problems	391
References	399
Index	421

Preface to the first edition

One might well ask why one should write a book about so specialized a subject as glacier mechanics when there are already other good books on this subject written by eminent glaciologists. This book is an outgrowth of a course that I teach to students who, in many cases, do not have any background in continuum mechanics. Consequently, it was necessary to start at a level considerably less advanced than that at which other similar books begin, and to develop the theoretical principles one step at a time. Thus, unlike other books on the subject and the general scientific literature, in which space is at a premium, the steps leading from one equation to another are, in most cases, easily seen. In addition, qualitative interpretations of the equations are often provided to clarify the physics behind the mathematics. Capable students with a solid background in basic physics and in differential and integral calculus, and with some modest exposure to differential equations, will have little difficulty understanding the concepts and derivations presented.

My goal in writing this book was not to produce a comprehensive treatise on glacier mechanics, but rather to develop the basic foundation upon which the modern literature on this subject rests. Thus, many topics are not covered, or are treated in less detail than some readers might wish. However, students who have a full appreciation for the concepts in this book will have the background they need to understand most of the current literature.

Beginning students in glaciology will find that this book will save them many long hours of searching through the background literature to clarify basic concepts. Glacial geologists and geomorphologists will also find much of value, including applications of glacier physics to the origin of some glacial landforms. Structural geologists and others with interest in stress and deformation will likewise discover that glaciers are, in fact, monomineralic rock masses that are deforming at the Earth's surface where they can be observed in detail. The book is, thus, appropriate for upper division and graduate level courses in glaciology, and as a supplementary text for courses in glacial geology and in structural geology.

In the preliminary pages, readers will find a compilation of physical constants relevant to ice, and a list of SI units and conversion factors. A series of problems keyed to individual chapters is also included.

The encouragement I have received in this undertaking from many present and former students, as well as from other glaciologists, has been a major stimulus in bringing it to completion. I trust the final product is worthy of their confidence. The book has benefited from the critical comments of R. W. Baker at the University of Wisconsin, River Falls; C. R. Bentley at the University of Wisconsin, Madison; G. K. C. Clarke at the University of British Columbia; E. M. Grace, and B. Hanson at the University of Delaware; N. R. Iverson at the University of Minnesota; T. Jóhannesson at the Icelandic Meteorological Office; M. Kuhn at the University of Innsbruck, Austria; M. F. Meier at the University of Colorado; J. F. Nye at the University of Bristol, England; C. F. Raymond at the University of Washington; R. L. Shreve at the University of California, Los Angeles; J. Weertman at Northwestern University, and especially I. Whillans at Ohio State University.

June 25, 1996

Preface to the second edition

When I wrote the preface to the first edition of this book seven years ago, nothing was further from my mind than a second edition. The first edition was well received, however, and on numerous occasions colleagues have lamented the fact that it was no longer available. When Cambridge University Press agreed that a new edition was desirable, little did I realize what I had gotten into.

When I told Matt Lloyd (my editor at Cambridge) that my goal was to have the text ready by a certain time, he graciously gave me a target date that was nearly double that time. I told him that his time schedule was fine, but that I did not want to be held too strictly to it. As it happens, I had an unrealistic view of the volume of new material that needed to be sifted through, absorbed, and translated into language appropriate for the upper-division undergraduate and graduate-level students for whom this book is written. As with the first edition, my goal is not to provide an encyclopedia of research in glaciology, as other books do that well, but rather to give students the basic background they will need to understand the modern literature. At the same time, the book has proven to be a useful reference for professionals who don't keep all of the equations and conversion factors stored for instant recall. I myself use it for that purpose frequently.

I am indebted to many who have encouraged me in this undertaking, and especially to those who have generously given their time to review new sections or entire chapters, who have resurrected archived computer files to provide images or data files from which new figures were produced, or who have made new calculations especially for this volume. The following have assisted me in this effort: Richard Alley, Bob Bindschadler, Ginny Catania, Chris Clark, Lee Clayton, Paul Cutler, Gordon Hamilton, Brian Hanson, Bruce Hooke, Peter Hudleston, Kolumbian Hutter, Philippe Huybrechts, Neal Iverson, Peter Jansson, Susan Kaspari, Katie Leonard, Paul Mayewski, Shawn Marshall, Howard Mooers, Nadine Nereson, Felix Ng, Charlie Raymond, Vandy Spikes, Slawek Tulaczyk, and Joe Walder.

Physical constants relevant to ice

Symbol	Parameter	Value
g	Acceleration of gravity	9.81 m s ⁻²
ρ	Density of bubble-free ice	916 kg m ⁻³
ρ	Density of water at 0 °C	999.84 kg m ⁻³
θ_m	Melting point at atmospheric pressure	0.0 °C 273.15 K
C	Heat capacity (For temperatures above ~ -0.5 °C the effective heat capacity increases owing to the presence of a liquid phase, the amount of which depends upon the concentration of chemical impurities.)	2093 J kg ⁻¹ K ⁻¹
C_w	Heat capacity of air-free water at constant pressure	256.9 J kg ⁻¹ K ⁻¹
\mathbf{C}	Depression of the melting point due to pressure Pure ice and air-free water Pure ice and air-saturated water (Harrison, 1972)	0.074 K MPa ⁻¹ 0.098 K MPa ⁻¹
ζ	Depression of the melting point due to solutes	1.86 °C kg mol ⁻¹
L	Heat of fusion	3.34×10^5 J kg ⁻¹
K	Thermal conductivity at -1 °C K varies with temperature, thus: $K = 7.10 \times 10^7 - 1.96 \times 10^5 \theta = 3.63 \times 10^3 \theta^2$ where θ is in degrees Celsius (a negative number) (Ratcliffe, 1962)	7.1×10^7 J m ⁻¹ a ⁻¹ K ⁻¹

Symbol	Parameter	Value
κ	Thermal diffusivity at $-1\text{ }^{\circ}\text{C}$ (Below $-0.5\text{ }^{\circ}\text{C}$, κ varies with temperature owing to the variation in K (see above). Above $-0.5\text{ }^{\circ}\text{C}$, κ decreases owing to the increase in effective C (see above). Paterson (1971) estimates that at $-0.1\text{ }^{\circ}\text{C}$ κ is half its value for pure ice, and at $-0.01\text{ }^{\circ}\text{C}$ it is 1% of the value for pure ice. These estimates assume a salinity of 10^{-6} .)	$37.2\text{ m}^2\text{ a}^{-1}$
R	Gas constant	$8.31\text{ J mol}^{-1}\text{ K}^{-1}$ $462\text{ J kg}^{-1}\text{ K}^{-1}$
Q	Activation energy for creep below $-10\text{ }^{\circ}\text{C}$ (Barnes <i>et al.</i> , 1971) (Above $-10\text{ }^{\circ}\text{C}$, Q is presumably the same but the $\dot{\epsilon}$ vs $1/\theta$ curve steepens, probably owing to the presence of a liquid phase.)	78.8 kJ mol^{-1}
ν	Poisson's ratio for polycrystalline ice (Gold, 1958) (The ratio of the transverse strain (contraction) to the axial strain (extension) of a bar in a uniaxial tensile test.)	0.31^*
μ	Shear modulus (at $-5\text{ }^{\circ}\text{C}$) (Gold, 1958) (The ratio of shear stress to elastic shear strain in a test in simple shear.)	$3.8 \times 10^3\text{ MPa}^*$
K	Bulk modulus (at $-5\text{ }^{\circ}\text{C}$) (Gold, 1958) (The ratio of applied pressure to fractional change in volume.)	$8.7 \times 10^3\text{ MPa}^*$
E	Young's modulus (Gold, 1958) (The ratio of axial stress to elastic axial strain in a test in uniaxial tension. $E = 2\mu(1 + \nu)$.)	$8.3 \times 10^3\text{ MPa}^*$
a	Coefficient of linear thermal expansion of ordinary water at $0\text{ }^{\circ}\text{C}$ (Kell, 1967) ice at $\sim -10\text{ }^{\circ}\text{C}$	$-22.3 \times 10^{-6}\text{ K}^{-1}$ $51.6 \times 10^{-6}\text{ K}^{-1}$
\mathbf{b}	Burgers vector	$4.5 \times 10^{-10}\text{ m}$

Symbol	Parameter	Value
γ_{SL}	Specific surface energy of liquid–solid interface (Ketcham and Hobbs, 1969)	0.034 J m^{-2}
γ_{gb}	Specific surface energy of grain boundary	0.065 J m^{-2}
β	Dihedral angle ($\cos \beta = \gamma_{\text{gb}}/2\gamma_{\text{SL}}$) (Nye and Mae, 1972)	$2\beta = 32 \pm 3^\circ$
P_{TP}	Triple point pressure	600 Pa
θ_{TP}	Triple point temperature	$+0.0098 \text{ }^\circ\text{C}$
S_{cr}	Crushing strength of ice formed from natural snow. The strength increases substantially with decreasing temperature. Hobbs (1974, p. 331) gives a graph from Butkovitch (1954) that can be approximated by:	1.8 MPa at $0 \text{ }^\circ\text{C}$
	$S_{\text{cr}} = 1.8 - 0.266\theta - 0.0202\theta^2 - 7.72 \times 10^{-4}\theta^3 - 1.39 \times 10^{-5}\theta^4 - 9.37 \times 10^{-8}\theta^5$	
	where θ is the temperature in degrees Celsius (a negative number). There is considerable variability depending on the type of ice tested and its orientation.	
K_{Ic}	Fracture toughness (Rist <i>et al.</i> , 1999)	$0.05\text{--}0.15 \text{ MPa m}^{1/2}$

* Values given are based on the work of Gold (1958) as reported by Hobbs (1974, pp. 255–258). Hobbs also reports other values based on the work of other (earlier) investigators.

Derived SI units and conversion factors

$1 \text{ N} = 1 \text{ kg m s}^{-2}$	Force (mass \cdot acceleration)
$1 \text{ Pa} = 1 \text{ N m}^{-2} = 1 \text{ kg m}^{-1} \text{ s}^{-2}$	Stress
$1 \text{ J} = 1 \text{ N m} = 1 \text{ kg m}^2 \text{ s}^{-2}$	Work or energy
$1 \text{ W} = 1 \text{ J s}^{-1} = \text{N m s}^{-1}$	Power
$1 \text{ bar} = 0.1 \text{ MN m}^{-2} = 0.1 \text{ MPa} = 0.9868 \text{ atm}$	
$1 \text{ cal} = 4.18 \text{ J}$	
$1 \text{ a} = 3.155\,69 \times 10^7 \text{ s}$	
$0^\circ\text{C} = 273.15 \text{ K}$	

Chapter 1

Why study glaciers?

Before delving into the mathematical intricacies with which much of this book is concerned, one might well ask why we are pursuing this topic – glacier mechanics? For many who would like to understand how glaciers move, how they sculpt the landscape, how they respond to climatic change, mathematics does not come easily. I assure you that all of us have to think carefully about the meaning of the expressions that seem so simple to write out but so difficult to understand. Only then do they become part of our vocabulary, and only then can we make use of the added precision which mathematical analysis, properly formulated, is able to bring. Is it worth the effort? That depends upon your objectives; on why you chose to study glaciers.

There are many reasons, of course. Some are personal, some academic, and some socially significant. To me, the personal reasons are among the most important: glaciers occur in spectacular areas, often remote, that have not been scarred by human activities. Through glaciology, I have had the opportunity to live in these areas; to drift silently in a kayak on an ice-dammed lake in front of our camp as sunset gradually merges with sunrise on an August evening; to marvel at the northern lights while out on a short ski tour before bedtime on a December night; and to reflect on the meaning of life and of our place in nature. Maybe some of you will share these needs, and will choose to study glaciers for this reason. I have found that many glaciologists do share them, and this leads to a comradeship which is rewarding in itself.

Academic reasons for studying glaciers are perhaps difficult to separate from socially significant ones. However, in three academic disciplines, the application of glaciology to immediate social problems is

2 Why study glaciers?

at least one step removed from the initial research. The first of these is glacial geology. Glaciers once covered 30% of the land area of the Earth, and left deposits of diverse shape and composition. How were these deposits formed, and what can they tell us about the glaciers that made them? The second discipline is structural geology; glacier ice is a metamorphic rock that can be observed in the process of deformation at temperatures close to the melting point. From the study of this deformation, both in the laboratory and in the field, much can be learned about the origin of metamorphic structures in other crystalline rocks that were deformed deep within the Earth. The final discipline is paleoclimatology. Glaciers record climatic fluctuations in two ways: the deposits left during successive advances and retreats provide a coarse record of climatic change which, with careful study, a little luck, and a good deal of skill, can be placed in correct chronological order and dated. A more detailed record is contained in ice cores from polar glaciers such as the Antarctic and Greenland ice sheets. Isotopic and chemical variations in these cores reflect present atmospheric circulation patterns and past changes in the temperature and composition of the atmosphere. Changes during the past several centuries to several millennia can be rather precisely dated by using core stratigraphy. Changes further back in time are dated with less certainty using flow models.

Relatively recent changes in climate and in concentrations of certain anthropogenic substances in the atmosphere are attracting increasing attention as humans struggle with problems of maintaining a healthy living environment in the face of overpopulation and the resulting demands on natural resources. Studies of ice cores and other dated ice samples provide a baseline from which to measure these anthropogenic changes. For example, levels of lead in the Greenland ice sheet increased about four-fold when Greeks and Romans began extracting silver from lead sulphides (Hong *et al.*, 1994). Then, after dropping slightly in the first millennium AD, they increased to \sim 80 times natural levels during the industrial revolution and to \sim 200 times natural levels when lead additives became common in gasoline (Murozumi *et al.*, 1969). These studies are largely responsible for the fact that lead is no longer used in gasoline. Similarly, measurements of CO₂ and CH₄ in ice cores have documented levels of these greenhouse gases in pre-industrial times.

Other applications of glaciology are not hard to find. An increasing number of people in northern and mountainous lands live so close to glaciers that their lives would be severely altered by ice advances comparable in magnitude to the retreats that have taken place during the past century in many parts of the world. Tales of glacier advances gobbling up farms and farm buildings and of ice falls smashing barns and houses are common from the seventeenth and eighteenth centuries,

a period of ice advance as the world entered the Little Ice Age. Records tell of buildings being crushed into small pieces and mixed with “soil, grit, and great rocks” (Grove, 1988, p. 72). The Mer de Glace in France presented a particular problem during this time period, and several times during the seventeenth century exorcists were sent out to deal with the “spirits” responsible for its advance. They appeared to have been successful, as the glaciers there were then near their Little Ice Age maxima and beginning to retreat.

Other people live in proximity to streams draining lakes dammed by glaciers. Some of the biggest floods known from the geologic record resulted from failure of such ice dams, and smaller floods of the same origin have devastated communities in the Alps and Himalayas.

Somewhat further from human living environments, one finds glaciers astride economically valuable deposits, or discharging icebergs into the shipping lanes through which such deposits are moved. What complications would be encountered, for example, if mining engineers were to make an open pit mine through the edge of the Greenland Ice Sheet to tap an iron deposit? What is the possibility that the present rapid retreat of Columbia Glacier in Alaska will increase perhaps ten-fold, perhaps one hundred-fold, the flux of icebergs into shipping lanes leading to the port of Valdez, at the southern end of the trans-Alaska pipeline? Were shipping to be halted there for an extended period so that the oil flow through the pipeline had to be stopped, oil would congeal in the pipe, making what one glaciologist referred to as the world’s longest candle.

Glacier ice itself is an economically valuable deposit; glaciers contain 60% of the world’s fresh water, and peoples in arid lands have seriously studied the possibility of towing icebergs from Antarctica to serve as a source of water. People in mountainous countries use the water not only for drinking, but also as a source of hydroelectric power. By tunneling through the rock under a glacier and thence up to the ice–rock interface, they trap water at a higher elevation than would be possible otherwise, and thus increase the energy yield. Glaciologists provided advice on where to find streams beneath the glaciers.

With the threat of global warming hanging over the world, the large volume of water locked up in glaciers and ice sheets represents a potential hazard for human activities in coastal areas. Collapse of the West Antarctic Ice Sheet could lead to a worldwide rise in sea level of 7 m in, perhaps, less than a century. Were this to be followed by melting of the East Antarctic Ice Sheet, sea level could rise an additional 50 m or so. Concern over these prospects has stimulated a great deal of research in the past two decades.

Lastly, we should mention a proposal to dispose of radioactive waste by letting it melt its way to the base of the Antarctic Ice Sheet. How long

4 Why study glaciers?

would such waste remain isolated from the biologic environment? How would the heat released affect the flow of the ice sheet? Might it cause a surge, with thousands of cubic kilometers of ice dumped into the oceans over a period of a few decades? This would raise sea level several tens of meters, with, again, interesting consequences! To accommodate these concerns, later versions of the proposal called for suspending the waste canisters on wires anchored at the glacier surface. The whole project was later abandoned, however, but not on glaciological grounds. Rather, there seemed to be no risk-free way to transport the waste to the Antarctic.

A good quantitative understanding of the physics of glaciers is essential for rigorous treatment of a number of these problems of academic interest, as well as for accurate analysis of various engineering and environmental problems of concern to humans. The fundamental principles upon which this understanding is based are those of physics and, to a lesser extent, chemistry. Application of these principles to glacier dynamics is initially straightforward but, as with many problems, the better we seek to understand the behavior of glaciers the more involved, and in many respects the more interesting, the applications become.

So we have answered our first question; we study glaciers for the same reasons that we study many other features of the natural landscape, but also for a special reason which I will try to impart to you, wordlessly, if you will stand with me looking over a glacier covered with a thick blanket of fresh powder snow to distant peaks, bathed in alpine glow, breathless from a quick climb up a steep slope after a day of work, but with skis ready for the telemark run back to camp. “Mäktig,” my companion said – powerful.

Chapter 2

Some basic concepts

In this chapter, we will introduce a few basic concepts that will be used frequently throughout this book. First, we review some commonly used classifications of glaciers by shape and thermal characteristics. Then we consider the mathematical formulation of the concept of conservation of mass and, associated with it, the condition of incompressibility. This will appear again in Chapters 6 and 9. Finally, we discuss stress and strain rate, and lay the foundation for understanding the most commonly used flow laws for ice. Although a complete consideration of these latter concepts is deferred to Chapter 9, a modest understanding of them is essential for a fuller appreciation of some fundamental concepts presented in Chapters 4–8.

A note on units and coordinate axes

SI (Système International) units are used in this book. The basic units of length, mass, and time are the meter (m), kilogram (kg), and second (s) (MKS). Temperatures are measured in Kelvins (K) or in the derived unit, degrees Celsius ($^{\circ}\text{C}$). Some other derived units and useful conversion factors are given on p. xvii.

In comparison with the earlier glaciological literature, one of the most significant changes introduced by use of SI units is that from bars to pascals as the principal unit of stress. The bar ($= 0.1 \text{ MPa} \approx 1 \text{ atmosphere}$) was a convenient unit because stresses in glaciers are typically $\sim 1 \text{ bar}$.

In most discussions herein we use a rectangular coordinate system with the x -axis horizontal or subhorizontal and in the direction of flow,

the y -axis horizontal and transverse, and the z -axis normal to the other two and thus vertical or slightly inclined to the vertical. Some derivations are easier to approach with the z -axis directed upward, while in others it is simpler to have the z -axis directed downward.

Glacier size, shape, and temperature

As humans, one way in which we try to organize knowledge and enhance communication is by classifying objects into neat compartments, each with its own label. The natural world persistently upsets these schemes by presenting us with particular items that fit neither in one such pigeonhole nor the next, but rather have characteristics of both, for continua are the rule rather than the exception. This is as true of glaciers as it is of other natural systems.

One way of classifying glaciers is by shape. Herein, we will be concerned with only two basic shapes. Glaciers that are long and comparatively narrow, and that flow in basically one direction, down a valley, are called *valley glaciers*. When a valley glacier reaches the coast and interacts with the sea, it is called a *tidewater glacier*. (I suppose this name is appropriate even in circumstances in which the tides are negligible, although with luck no one will ever find a valley glacier encroaching on such a tideless marine environment.) Valley glaciers that are very short, occupying perhaps only a small basin in the mountains, are called *cirque glaciers*. In contrast to these forms are glaciers that spread out in all directions from a central dome. These are called either *ice caps*, or, if they are large enough, *ice sheets*.

There is, of course, a continuum between valley glaciers and ice caps or ice sheets. For example, Jostedalsbreen in Norway and some ice caps on islands in the Canadian arctic feed *outlet glaciers*, which are basically valley glaciers flowing outward from an ice cap or ice sheet. However, the end members, valley glaciers and ice sheets, typically differ in other significant ways (see, for example, Figure 3.1). Thus, a classification focusing on these two end members is useful.

Glaciers are also classified by their thermal characteristics, although once again a continuum exists between the end members. We normally think of water as freezing at $0\text{ }^{\circ}\text{C}$, but may overlook the fact that once all the water in a space is frozen, the temperature of the resulting ice can be lowered below $0\text{ }^{\circ}\text{C}$ as long as heat can be removed from it. Thus, the temperature of ice in glaciers in especially cold climates can be well below $0\text{ }^{\circ}\text{C}$. We call such glaciers *polar glaciers*. More specifically, polar glaciers are glaciers in which the temperature is below the melting temperature of ice everywhere, except possibly at the bed. Because the presence of meltwater at the base of a polar glacier has dramatic

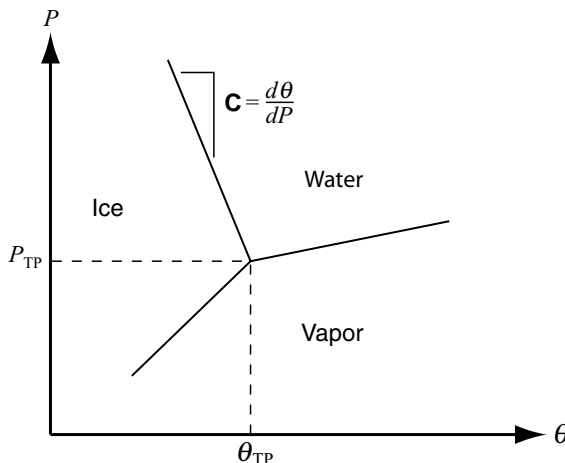


Figure 2.1. Schematic phase diagram for H_2O near the triple point, TP. At the triple point, liquid, solid, and vapor phases are in equilibrium. As long as all three phases are present, neither the pressure nor the temperature can depart from their triple-point values.

consequences for both glacier kinematics and landform development, it will be convenient to refer to such glaciers as *Type II* polar glaciers and to those that are frozen to their beds as *Type I* polar glaciers. In Chapter 6, we will investigate the temperature distribution in such glaciers in some detail.

Glaciers that are not polar are either *polythermal* or *temperate*. Polythermal glaciers, which are sometimes called *subpolar* glaciers, contain large volumes of ice that are cold, but also large volumes that are at the melting temperature. Most commonly, the cold ice is present as a surface layer, tens of meters in thickness, on the lower part of the glacier (the ablation area).

In simplest terms, a temperate glacier is one that is at the melting temperature throughout. However, the melting temperature, θ_m , is not easily defined. As the temperature of an ice mass is increased towards the melting point, veins of water form along the lines where three ice crystals meet (Figure 8.1). At the wall of such a vein:

$$\theta_m = \theta_{\text{TP}} - \mathbf{C}P - \frac{\theta_{\text{mK}}\gamma_{\text{SL}}}{L\rho_i r_p} - \zeta \frac{s}{W} \quad (2.1)$$

(Raymond and Harrison, 1975; Lliboutry, 1976). Here, θ_{TP} is the triple point temperature, 0.0098°C (Figure 2.1); \mathbf{C} is the depression of the melting point with increased pressure, P (Figure 2.1); θ_{mK} is the melting point temperature in Kelvin, 273.15 K ; γ_{SL} is the liquid–solid surface energy, 0.034 J m^{-2} ; L is the latent heat of fusion, $3.34 \times 10^5\text{ J kg}^{-1}$; ρ_i is the density of ice; r_p is the radius of curvature of liquid–solid interfaces; s is the solute content of the ice in mols kg^{-1} , W is the fractional water content of the ice by weight (kg kg^{-1}), and ζ is the depression of the melting point resulting from solutes in the ice,

$1.86 \text{ } ^\circ\text{C kg mol}^{-1}$. The third term on the right in Equation (2.1) represents a change in melting temperature in the immediate vicinity of veins. \mathbf{C} is the Clausius–Clapeyron slope, given by:

$$\mathbf{C} = \frac{d\theta}{dP} = \left(\frac{1}{\rho_i} - \frac{1}{\rho_w} \right) \frac{\theta_{\text{TPK}}}{L} \quad (2.2)$$

Here, ρ_w is the density of water and θ_{TPK} is the triple point temperature in Kelvins. \mathbf{C} is $0.0742 \text{ K MPa}^{-1}$ in pure water, but rises to 0.098 K MPa^{-1} in air-saturated water. As glacier ice normally contains air bubbles, the water is likely to contain air even if it is not saturated with air. Thus, under most circumstances it is probably appropriate to use a value higher than $0.0742 \text{ K MPa}^{-1}$ (Lliboutry, 1976).

Clearly, the melting temperature varies on many length scales in a glacier (Equation (2.1)). On the smallest scales, it varies within the veins that occur along crystal boundaries. On a slightly larger scale, it varies from the interiors of crystals to the boundaries because solutes become concentrated on the boundaries during crystal growth. On the largest scale, it varies with depth owing to the change in hydrostatic pressure.

As a result of these variations, small amounts of liquid are apparently present on grain boundaries at temperatures as low as about $-10 \text{ } ^\circ\text{C}$, and the amount of liquid increases as the temperature increases. This led Harrison (1972) to propose a more rigorous definition of a temperate glacier. He suggested that a glacier be considered temperate if its heat capacity is greater than twice the heat capacity of pure ice. In other words, this is when the temperature and liquid content of the ice are such that only half of any energy put into the ice is used to warm the ice (and existing liquid), while the other half is used to melt ice in places where the local melting temperature is depressed.

Harrison's definition, while offering the benefit of rigor, is not easily applied in the field. However, as we shall see in Chapter 4, relatively small variations in the liquid content of ice can have a major influence on its viscosity and crystal structure, among other things. Thus, this discussion serves to emphasize that the class of glaciers that we loosely refer to as temperate may include ice masses with a range of physical properties that are as wide as, or wider than, those of glaciers that we refer to as polar.

Ice caps and ice sheets are commonly polar, while valley glaciers are more often temperate. However, there is nothing in the respective classification schemes that requires this. In fact, many valley glaciers in high Arctic areas and in Antarctica are at least polythermal, and some are undoubtedly polar. However, none of the major ice caps or ice sheets that exist today is temperate.

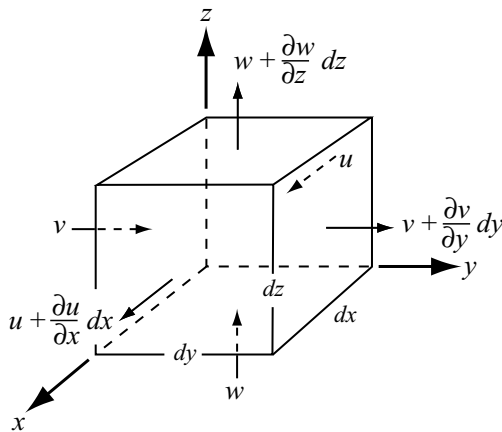


Figure 2.2. Derivation of the condition of incompressibility.

The condition of incompressibility

Let us next examine the consequences of the requirement that mass be conserved in a glacier. In Figure 2.2 a control volume of size $dx \cdot dy \cdot dz$ is shown. The velocities into the volume in the x -, y -, and z -directions are u , v , and w respectively. The velocity out in the x -direction is:

$$u + \frac{\partial u}{\partial x} dx$$

Here $\partial u / \partial x$ is the velocity gradient through the volume, which, when multiplied by the length of the volume, dx , gives the change in velocity through the volume in the x -direction. The mass fluxes into and out of the volume in the x -direction are:

$$\rho u dy dz \quad \text{and} \quad \left(\rho u + \frac{\partial \rho u}{\partial x} dx \right) dy dz$$

$$\frac{\text{kg}}{\text{m}^3} \frac{\text{m}}{\text{a}} \text{m} \quad \text{m} = \frac{\text{kg}}{\text{a}}$$

Here, ρ is the density of ice. (The dimensions of the various parameters are shown beneath the left-hand term to clarify the physics. This is a procedure that we will use frequently in this book, and that the reader is likely to find useful, as errors in equations can often be detected in this way.) Similar relations may be written for the mass fluxes into and out of the volume in the y - and z -directions. Summing these fluxes, we find that the change in mass with time, $\partial m / \partial t$, in the control volume is:

$$\begin{aligned} \frac{\partial m}{\partial t} &= \rho u dy dz - \left(\rho u + \frac{\partial \rho u}{\partial x} dx \right) dy dz + \rho v dx dz - \left(\rho v + \frac{\partial \rho v}{\partial y} dy \right) dx dz \\ &\quad + \rho w dx dy - \left(\rho w + \frac{\partial \rho w}{\partial z} dz \right) dx dy \end{aligned}$$

Note that each term on the right-hand side has the dimensions $M \cdot T^{-1}$, or, in the units which we will use most commonly herein, kg a^{-1} .

Simplifying by canceling like terms of opposite sign and dividing by $dx \cdot dy \cdot dz$ yields:

$$-\frac{1}{dx dy dz} \frac{\partial m}{\partial t} = \frac{\partial \rho u}{\partial x} + \frac{\partial \rho v}{\partial y} + \frac{\partial \rho w}{\partial z} \quad (2.3)$$

Ice is normally considered to be incompressible, which means that ρ is constant. This is not true near the surface of a glacier where snow and firn are undergoing compaction, but to a good approximation it is valid throughout the bulk of most ice masses. In this case, Equation (2.3) becomes:

$$-\frac{1}{\rho dx dy dz} \frac{\partial m}{\partial t} = \frac{\partial u}{\partial x} + \frac{\partial v}{\partial y} + \frac{\partial w}{\partial z} \quad (2.4)$$

The mass of ice in the control volume can change if the control volume is not full initially. When it is full of incompressible ice, however, $\partial m / \partial t = 0$, and Equation (2.4) becomes:

$$\frac{\partial u}{\partial x} + \frac{\partial v}{\partial y} + \frac{\partial w}{\partial z} = 0 \quad (2.5)$$

This is the condition of incompressibility; it describes the condition that mass and density are not changing.

Stresses, strains, and strain rates

A stress is a force per unit area, and has the dimensions N m⁻², or Pa. Stresses are vector quantities in that they have a magnitude and direction. Stresses that are directed normal to the surface on which they are acting are called normal stresses, while those that are parallel to the surface are shear stresses.

Notation

Referring to Figure 2.3, σ_{xz} is the shear stress in the z -direction on the plane normal to the x -axis. Thus, the first subscript in a pair identifies the plane on which the stress acts, and the second gives the direction of the stress.

The sign convention used in such situations is as follows. Let \hat{n} be the outwardly directed normal to a surface; \hat{n} is positive if it is directed in the positive direction and conversely. If a normal stress is in the positive direction and \hat{n} is also positive on this face, the normal stress is defined as positive, and conversely if one is positive and the other negative, the stress is negative. Thus in Figure 2.3, σ_{zz} is positive on both of the faces normal to the z -axis and σ_{xx} is negative on both of the faces normal to the x -axis. In other words, *tension is positive and compression is negative*.

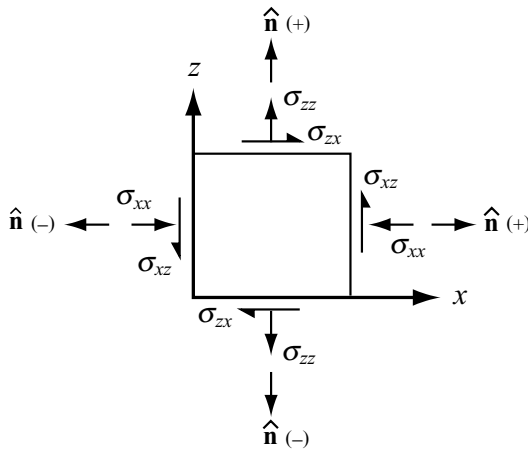


Figure 2.3. Sign convention for stresses in plane strain.

Similarly, if a shear stress, σ_{zx} , is in the positive x -direction on a plane on which $\hat{\mathbf{n}}$ is positive, that shear stress is considered to be positive and conversely. By this definition both shear stresses σ_{xz} and σ_{zx} in the diagram are positive.

As an example, consider the variation of u with depth in a glacier (Figure 2.4). As depicted by the arrows around the box in Figure 2.4, the shear stress, σ_{zx} , is negative in the coordinate system shown. The velocity derivative, du/dz , is also negative (u decreases with increasing z). Thus the negative shear stress results in a negative strain rate, as one would expect.

Tensors

The three-dimensional diagram in Figure 2.5 shows stress vectors on three faces of a cube. Similar stresses occur on the concealed faces, but they are in the opposite directions. The cube is considered to be infinitesimal, representing, say, a point in the glacier. Thus, stresses on any given face can be regarded as uniformly distributed and constant.

To completely describe the state of stress at this point, we need nine stress components; thus:

$$\begin{array}{lll} \sigma_{xx} & \sigma_{xy} & \sigma_{xz} \\ \sigma_{yx} & \sigma_{yy} & \sigma_{yz} \\ \sigma_{zx} & \sigma_{zy} & \sigma_{zz} \end{array}$$

This assemblage of stress vectors is called a *second-rank tensor*. For comparison, to describe a first-rank tensor, a vector, we need its components along three coordinate axes.

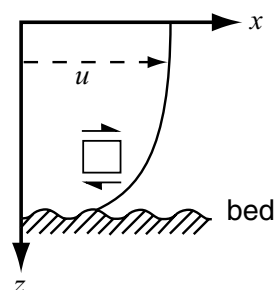
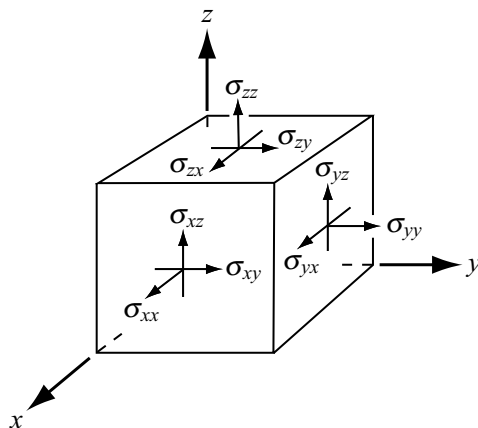


Figure 2.4. Vertical profile of horizontal velocity, u . Sense of shear stress, σ_{zx} , is shown by arrows above and below box.

Figure 2.5. Stresses on a cube.



For steady (non-accelerating) uniform motion, forces must be balanced. Thus, to ensure that there is no tendency for the cube in Figure 2.5 to rotate, it is necessary that $\sigma_{xy} = \sigma_{yx}$, $\sigma_{xz} = \sigma_{zx}$, and $\sigma_{yz} = \sigma_{zy}$. Such tensors are called *symmetric*.

When a tensor is symmetric, it is common to see, for example, xy used where, rigorously, yx might be more correct. In another common abbreviation often encountered, σ_x is written for σ_{xx} .

Strains and strain rates

In a deformable medium, stresses induce deformation or strain. Strain is defined as the change, $\Delta\ell$, in length of a line divided by the initial length of that line, ℓ_0 , thus: $\Delta\ell/\ell_0$. The symbol ε is commonly used to denote strain. The rate at which strain occurs, or the strain rate, is denoted by $\dot{\varepsilon}$. The dot superscript is commonly used to denote a time derivative, making it a rate. As nine separate stress vectors are needed to describe fully the state of stress at a point, so also are nine strains or strain rates needed to describe the state of straining at that point. Thus, these assemblages of strains and strain rates are also second-rank tensors, the strain and strain-rate tensors. As was the case with the stress tensor, these tensors, too, are symmetric, so $\varepsilon_{xy} = \varepsilon_{yx}$, $\dot{\varepsilon}_{xz} = \dot{\varepsilon}_{zx}$, and so forth.

In Chapter 9, we will show that:

$$\dot{\varepsilon}_{xy} = \frac{1}{2} \left(\frac{\partial u}{\partial y} + \frac{\partial v}{\partial x} \right) \quad (2.6a)$$

and similarly for the other shear strain rates. When $x = y$, this becomes:

$$\dot{\varepsilon}_{xx} = \frac{\partial u}{\partial x} \quad (2.6b)$$

and so forth. Note that in terms of expressions like Equation (2.6b), the incompressibility condition, Equation (2.5), becomes:

$$\dot{\varepsilon}_{xx} + \dot{\varepsilon}_{yy} + \dot{\varepsilon}_{zz} = 0 \quad (2.7)$$

Equations (2.6a) and (2.6b) define strain rates in terms of differences in velocity between points that are an infinitesimal distance (for example, dx) apart. However, when measuring strains or strain rates in the laboratory or field, it is technically impossible to resolve differences in velocity over “infinitesimal” distances. Thus, we make measurements over longer distances and use what is called *logarithmic strain*. The quantity measured is the change in the distance between two points over a time interval, Δt . If the initial distance is ℓ_0 and the final distance is ℓ , then $\dot{\varepsilon}$ is defined as:

$$\dot{\varepsilon} = \frac{1}{\Delta t} \ln \frac{\ell}{\ell_0}$$

This relation will be derived in Chapter 9.

Yield stress

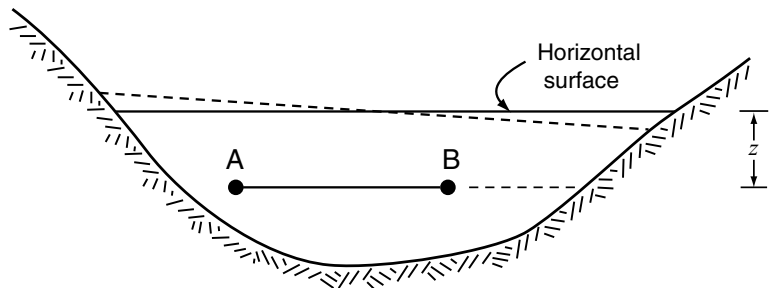
In some materials there is no deformation at stresses below a certain stress, called the *yield stress*. The yield stress is a property of that particular material. In other materials, deformation rates are so low at low stresses that theoretical models *sometimes* assume the existence of a yield stress even though there may not actually be one. Ice is such a material.

Deviatoric stresses

Ice does not deform in response to hydrostatic pressure alone. In other words, in a topographic depression containing ice (Figure 2.6), the hydrostatic (or cryostatic) pressure would increase linearly with depth, z , at a rate $\rho g z$, where g is the acceleration due to gravity. As a rule of thumb, the pressure increases at a rate of 0.1 MPa for every 11 m of depth. Thus, it becomes quite high at large depths. However, if the surface of the ice in the depression is horizontal, as in a lake, the only deformation that would occur would be a relatively insignificant elastic compression.

On the other hand, if the ice surface slopes gently (Figure 2.6, dashed line), and if points **A** and **B** are on a horizontal plane, then the pressure at **A** would be greater than the pressure at **B**. This pressure difference would result in a compressive strain between **A** and **B**. The strain rate would depend upon the small pressure difference and not, in any significant way, on the much larger hydrostatic pressure at depth z .

Figure 2.6. Sketch to illustrate non-hydrostatic pressure.



Because straining in glaciers is related to such stress differences, it is convenient to define a stress, called the *deviatoric stress* or *stress deviator*, which reflects this principle. The deviatoric normal stress in the x -direction is:

$$\sigma'_{xx} = \sigma_{xx} - P \quad (2.8)$$

where P is the mean normal stress:

$$P = \frac{1}{3}(\sigma_{xx} + \sigma_{yy} + \sigma_{zz}) \quad (2.9)$$

P is close to, but not necessarily equal to, the hydrostatic pressure. As P is a normal stress, it contributes only to the normal stresses, and not to the shear stresses in Figure 2.5. In other words, the deviatoric shear stresses are the same as their non-deviatoric or total counterparts, but the deviatoric normal stresses are very different from the total normal stresses, especially at depth.

Effective and octahedral shear stresses and strain rates

Theoretical studies and a limited amount of experimental data suggest that the strain rate in a given direction in ice depends not only on the stress in that direction, but also on all of the other stresses acting on the medium. To take this into account, we define the *effective shear stress*, σ_e , and the *effective strain rate*, $\dot{\epsilon}_e$, by:

$$\sigma_e = \frac{1}{\sqrt{2}} (\sigma'^2_{xx} + \sigma'^2_{yy} + \sigma'^2_{zz} + \sigma^2_{xy} + \sigma^2_{yx} + \sigma^2_{xz} + \sigma^2_{zx} + \sigma^2_{yz} + \sigma^2_{zy})^{1/2} \quad (2.10)$$

and

$$\dot{\epsilon}_e = \frac{1}{\sqrt{2}} (\dot{\epsilon}_{xx}^2 + \dot{\epsilon}_{yy}^2 + \dot{\epsilon}_{zz}^2 + \dot{\epsilon}_{xy}^2 + \dot{\epsilon}_{yx}^2 + \dot{\epsilon}_{xz}^2 + \dot{\epsilon}_{zx}^2 + \dot{\epsilon}_{yz}^2 + \dot{\epsilon}_{zy}^2)^{1/2} \quad (2.11)$$

Alternatively, some glaciologists use the *octahedral shear stress*, σ_o , and *octahedral shear strain rate*, $\dot{\epsilon}_o$, defined by:

$$\sigma_o = \frac{1}{\sqrt{3}} (\sigma'^2_{xx} + \sigma'^2_{yy} + \sigma'^2_{zz} + \sigma^2_{xy} + \sigma^2_{yx} + \sigma^2_{xz} + \sigma^2_{zx} + \sigma^2_{yz} + \sigma^2_{zy})^{1/2} \quad (2.12)$$

and

$$\dot{\varepsilon}_o = \frac{1}{\sqrt{3}} (\dot{\varepsilon}_{xx}^2 + \dot{\varepsilon}_{yy}^2 + \dot{\varepsilon}_{zz}^2 + \dot{\varepsilon}_{xy}^2 + \dot{\varepsilon}_{yx}^2 + \dot{\varepsilon}_{xz}^2 + \dot{\varepsilon}_{zx}^2 + \dot{\varepsilon}_{yz}^2 + \dot{\varepsilon}_{zy}^2)^{1/2} \quad (2.13)$$

respectively.

Principal stresses and strain rates

In Chapter 9, we will show that, at any point in a medium, it is always possible to orient a rectangular coordinate system in such a way that shear stresses vanish. Equation (2.12) then becomes:

$$\sigma_o = \left(\frac{\sigma'_{xx}^2 + \sigma'_{yy}^2 + \sigma'_{zz}^2}{3} \right)^{1/2} \quad (2.14)$$

We give the name *principal stresses* to the remaining normal stresses, and the axes in this coordinate system are called the *principal axes of stress*. Similarly, if the coordinate system is oriented such that shear strain rates vanish, the remaining strain rates are called the *principal strain rates* and the axes are the *principal axes of strain rate*.

Equation (2.14) shows that the octahedral shear stress is the root-mean-square of the principal stress deviators. When the coordinate axes are aligned parallel to the principal stresses, the octahedral shear stress is the resolved shear stress on the octahedral plane, a plane that intersects the three axes at points equidistant from the origin (Figure 2.7). Hence the name: octahedral shear stress.

The flow law

The most commonly used flow law for ice is Glen's flow law, named after John W. Glen upon whose experiments it is based (Glen, 1955). We will normally write Glen's flow law in the form he originally used:

$$\dot{\varepsilon}_e = \left(\frac{\sigma_e}{B} \right)^n \quad (2.15)$$

where B is a viscosity parameter that increases as the ice becomes stiffer, and n is an empirically determined constant. Most studies have found that $n \approx 3$. At very low stresses, however, there is some evidence that $n \rightarrow 1$. An alternative form of the flow law that is commonly used is:

$$\dot{\varepsilon}_e = A \sigma_e^n \quad (2.16)$$

Here, B is normally given in MPa $a^{1/n}$, while A is in MPa $^{-n}$ a^{-1} or kPa $^{-n}$ s^{-1} . If the octahedral shear stress and strain rate are used, the numerical values of B and A must be adjusted accordingly, but the units stay the same.

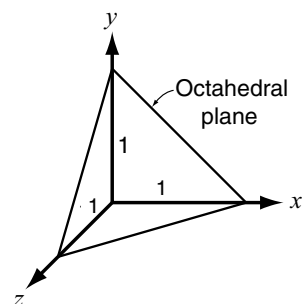


Figure 2.7. A plane that intersects the x -, y -, and z -axes at points equidistant from the origin, in this case a unit distance, is called the octahedral plane. If similar planes are drawn involving the negative directions along the axes, the solid figure formed is a regular octahedron.

Both forms of the flow law have their advantages, and as $A = (1/B)^n$ it is easy to convert between the two forms as long as n is known. The form $\dot{\varepsilon}_e = A\sigma_e^n$ resembles conventional constitutive relations in rheology, and is also easier to generalize if greater precision is needed in situations involving complicated stress configurations (Glen, 1958). For example, some materials, when subjected to a shear stress, swell or contract perpendicular to the plane of shear. In other words, deformation occurs in directions in which the stress is zero. Such rheologies require an extra term in the flow law, and this is more readily accommodated with a flow law of the form $\dot{\varepsilon}_e = A\sigma_e^n$. So far, however, the forms presented in Equations (2.16) and (2.17) seem adequate to represent phenomena observed in studies of ice deformation, both in the laboratory and on glaciers, so the additional term is not needed.

The form $\dot{\varepsilon}_e = (\sigma_e/B)^n$ is similar to that used in fluid mechanics with the viscosity, η , defined by:

$$\tau = \eta \frac{du}{dz} \quad (2.17)$$

Here τ is the shear stress. Thus B , like η , is a ratio of stress to strain rate. An increase in B results in a decrease in strain rate. Scientists interested in geomorphological applications of glaciological principles are more likely to be familiar with principles of fluid mechanics than with those of rheology, so the form $\dot{\varepsilon}_e = (\sigma_e/B)^n$ is used throughout this book.

In Chapter 9, we will show that if the principle axes of stress and strain rate coincide, as is normally the case, the flow law can be written as:

$$\dot{\varepsilon}_{ij} = \frac{\sigma_e^{n-1}}{B^n} \sigma'_{ij} \quad (2.18)$$

where i and j can represent x or y or z . Eliminating σ_e from Equations (2.15) and (2.18) yields:

$$\dot{\varepsilon}_{ij} = \frac{\dot{\varepsilon}_e^{\frac{n-1}{n}}}{B} \sigma'_{ij} \quad (2.19)$$

Equation (2.18) re-emphasizes a fundamental tenet of Glen's flow law mentioned above: namely that *the strain rate in a given direction is a function not only of the stress in that direction, but also of all of the other stresses acting on the medium*. Equation (2.19) shows that we can express this concept in terms of strain rates, which are generally easier to measure than stresses.

In the next several chapters we will be dealing with situations in which it is feasible to assume that one stress so dominates all of the others that the others can be neglected. However, the reader should be aware of the implications of this assumption.

Chapter 3

Mass balance

Glaciers exist because there are areas, generally at high elevations or in polar latitudes, where snow fall during the winter exceeds melt (and other losses) during the summer. This results in net accumulation, and this part of the glacier is thus called the *accumulation area* (Figure 3.1). As each snow layer is buried, the pressure of the overlying snow causes compaction, and movement of molecules in the liquid and vapor phases results in snow metamorphism. Snow that is more than a year old, and has thus been altered by these processes, is called *firn*. The end result of the firnification process, normally after several years, is solid ice.

Where there are lower elevations to which this ice can move, gravitational forces drive it toward these areas. This eventually brings the ice into places where the annual melt exceeds snow fall. Here, all of the winter snow and some of the underlying ice melts during the summer. This is called the *ablation area*. The line separating the accumulation and the ablation areas at the end of a melt season is called the *equilibrium line*. Along the equilibrium line, melt during the just-completed summer exactly equaled net snow accumulation during the previous winter.

In this chapter, we first discuss the transformation of snow to ice, and show how the processes involved result in a physical and chemical stratigraphy that, under the right circumstances, can be used to date ice that is thousands of years old. We then explore the climatic factors that result in changes in the altitude of the equilibrium line, and hence in advance and retreat of glaciers.

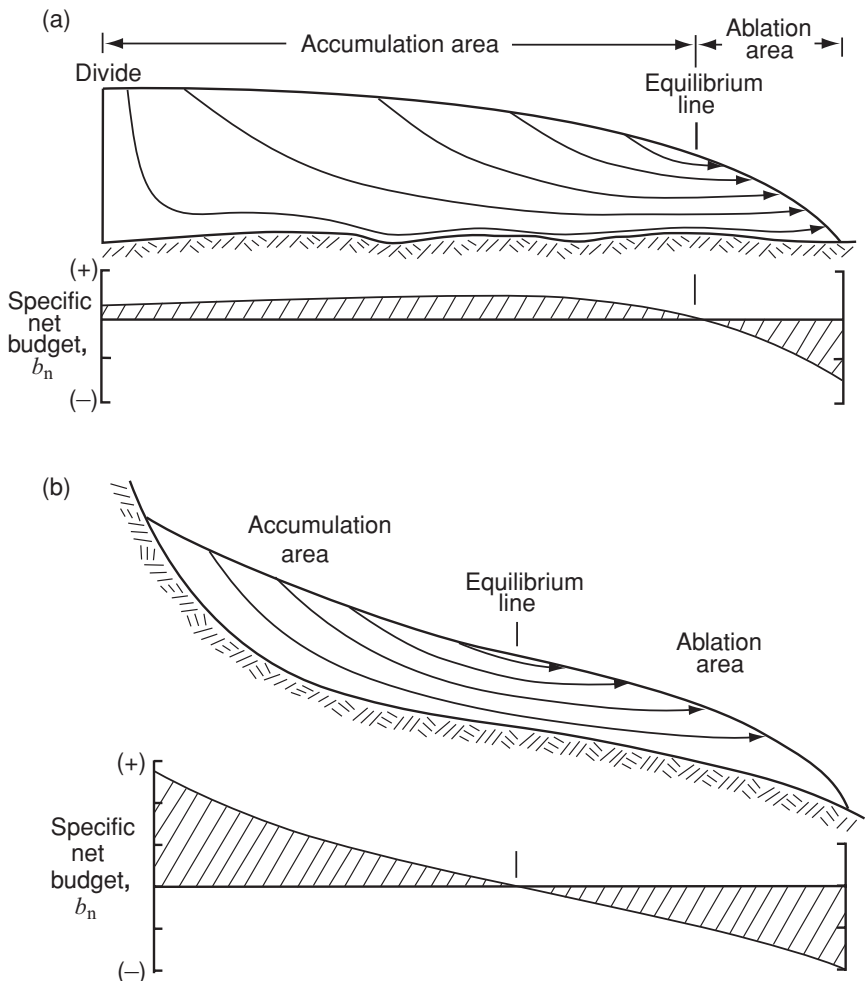


Figure 3.1. Cross sections of: (a) a typical polar ice cap or ice sheet, and (b) a typical valley glacier, showing the relation between equilibrium line and flow lines. Sketches are schematic, but relative proportions are realistic.

The transformation of snow to ice

The first phase of the transformation of snow into ice involves diffusion of water molecules from the points of snow flakes toward their centers; the flakes thus tend to become rounded, or spherical (Figure 3.2a), reducing their surface area and consequently their free energy. This is an example of an important thermodynamic principle, namely that the free energy of a system tends toward a minimum. Such rounding occurs more rapidly at higher temperatures.

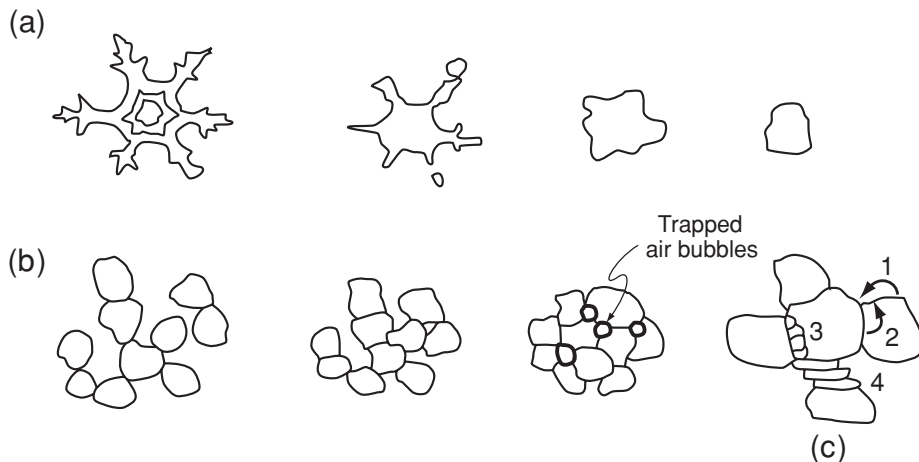


Figure 3.2. Transformation of snow to ice. (a) Modification of snow flakes to a subspherical form. (b) Sintering. (c) Processes during sintering: 1 = sublimation, 2 = molecular diffusion within grains, 3 = nucleation and growth of new grains, and 4 = internal deformation of grains. (Based on Sommerfeld and LaChapelle, 1970, Figures 2, 16, and 17; and on Kinoshita, 1962, as reported by Lliboutry, 1964, Figure 1.14.)

The closest possible packing of spherical particles would be one with a porosity of about 26%, the so-called rhombohedral packing. However, in natural aggregates of spheres of uniform diameter, the pore space is usually closer to 40%. In the case of firn, this corresponds to a density of $\sim 550 \text{ kg m}^{-3}$.

Further densification involves a process called *sintering* (Figure 3.2b), which involves transfer of material by sublimation and by molecular diffusion within grains, nucleation and growth of new grains, and internal deformation of the grains (Figure 3.2c). Sublimation is more important early in the transformation process when pore spaces are still large. Internal deformation increases in importance as the snow is buried deeper and pressures increase. In warm areas, the densification process is accelerated, both because grains may be drawn together by surface tension when water films form around them, and because percolating melt water may fill air spaces and refreeze.

An important transition in the transformation process occurs at a density of $\sim 830 \text{ kg m}^{-3}$. At about this density, pores become closed, preventing further air movement through the ice. Studies of the air thus trapped provide information on the composition of the atmosphere at the time of close off (see, for example, Raynaud *et al.*, 1993). Measurements of the volume of such air per unit mass of ice yield estimates (albeit fairly crude, given present technology) of the altitude of the pores at the time

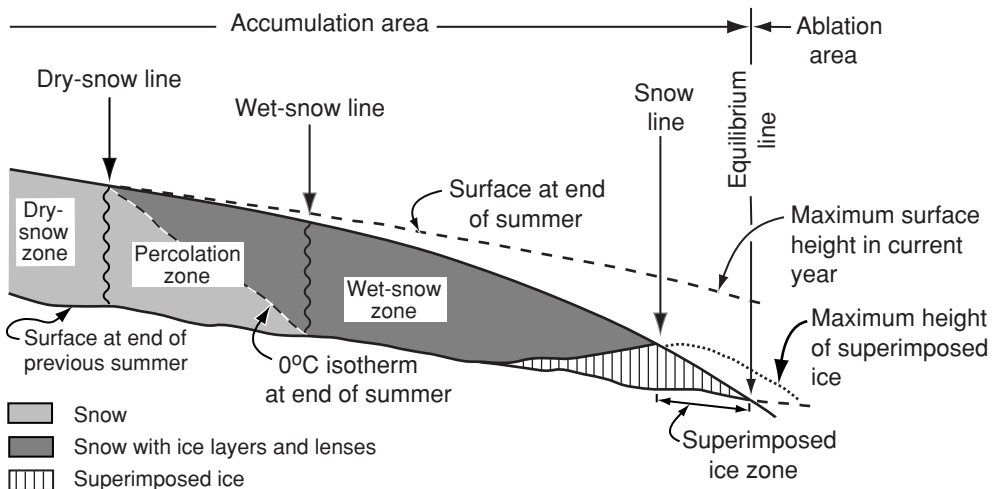


Figure 3.3. Variation in snow facies with altitude. (After Benson, 1962.)

Horizontal distance from equilibrium line to dry-snow line is tens to hundreds of kilometers.

of close off (Martinerie *et al.*, 1992). Knowing the depth in the glacier at which this occurs then permits an estimate of the elevation of the ice surface at that time. Pore close off can occur at depths of tens to over a hundred meters, depending on temperature (Paterson, 1994, Table 2.2).

Snow stratigraphy

At high elevations on polar glaciers, such as the Antarctic or Greenland ice sheets, there are areas where no melting occurs during the summer. At somewhat lower elevations, some melting does occur, and the meltwater thus formed percolates downward into the cold snow where it refreezes, forming lenses or gland-like structures. The higher of these two zones is called the *dry-snow zone* and the lower is the *percolation zone* (Figure 3.3) (Benson, 1961; Müller, 1962). In keeping with stratigraphic terminology in geology, parts of the annual snow pack on an ice sheet that have distinctive properties are referred to as *facies* – in this case the *dry-snow facies* and the *percolation facies*, respectively. The boundary between these two zones or facies, the *dry-snow line*, lies approximately at the elevation where the mean temperature of the warmest month is -6°C (Benson, 1962, cited by Loewe, 1970, p. 263).

At lower elevations, summer melting is sufficient to wet the entire snow pack. This is called the *wet-snow zone* (Figure 3.3). When this snow refreezes, a firm porous layer is formed. In downglacier parts of this zone, the basal layers of the snow pack may become saturated with water. If the

underlying ice is cold, this water-saturated snow may refreeze, forming ice that is called *superimposed ice*. As long as it is still undeformed, superimposed ice is readily recognized by its air bubbles, which are large and often highly irregular in shape.

At still lower elevations, only superimposed ice is present at the end of the melt season, and this is thus called the *superimposed ice zone*. The lower boundary of the superimposed ice zone at the end of the melt season is the equilibrium line.

On typical alpine glaciers, the first water percolating into cold snow at the beginning of the melt season may refreeze to form glands and lenses as on polar ice sheets. However, by the end of the melt season, the entire snow pack will have been warmed to the melting point. Thus, neither the dry-snow nor the percolation facies are present on these glaciers. Furthermore, on a temperate glacier, heat conduction downward into the glacier beneath the snow pack is minimal, so little superimposed ice is formed.

Most of the warming of alpine snow packs is a result of the release of latent heat during refreezing of the first water to infiltrate. Freezing of 1 kg of water can warm 160 kg of snow 1 °C. Conduction of heat from the surface is insignificant by comparison.

In addition to the zonation in snow stratigraphy with altitude (or temperature), particularly on polar glaciers, there is also a distinct vertical zonation at any given point on a glacier. Because the autumn snow in an annual layer is warmer than the overlying winter snow, the former has a higher vapor pressure. Thus, a vapor-pressure gradient exists, resulting in diffusion of molecules from the autumn to the winter snow. The autumn snow thus becomes coarser, and its density may decrease. These layers of coarse autumn snow are called *depth hoar*. Tabular crystals are the norm in depth hoar, but in extreme cases, large prism-shaped, pyramidal, or hollow hexagonal crystals develop.

Dating ice using preserved snow stratigraphy

Depth hoar layers are important because they can be recognized at depth in snow pits and ice cores. Using such stratigraphic markers, glaciologists have been able to determine accumulation rates, averaged over several years or decades, in many areas of Antarctica and Greenland, and in some cases over millennia in deep cores from these ice sheets.

In one of the most remarkable examples of the use of such physical stratigraphy, Alley *et al.* (1993) found that the accumulation rate high on the Greenland Ice Sheet increased by approximately a factor of two at the end of the Pleistocene, and that the change took place in a time span of only three or four years! The increase in the accumulation rate

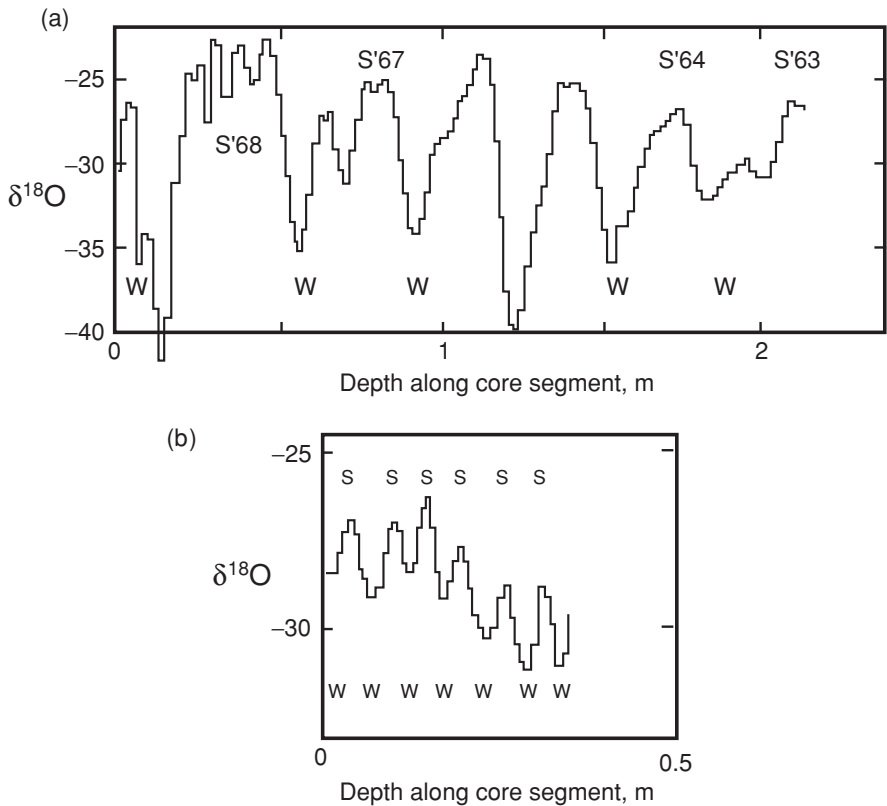


Figure 3.4. Variations of $\delta^{18}\text{O}$ in the Camp Century, Greenland, ice core. (a) Ice from 1963 to 1968. (b) Ice that is approximately 8300 years old, and in which seasonal variations can still be detected. (Adapted from Johnsen *et al.*, 1972. Reproduced with permission of the authors and *Nature*.)

was attributed to a warming of the climate, and it was this warming that caused retreat of the ice sheets.

Dating of ice can also be accomplished by detailed laboratory studies of cores or of samples from pit walls. The most commonly used technique for this purpose involves measuring $\delta^{18}\text{O}$ variations. Because the air is colder during the winter, $\delta^{18}\text{O}$ values in winter snow are more negative (the snow contains less of the heavier isotope of oxygen, ^{18}O) than in summer snow. Thus, a series of samples taken from a single annual layer will show a roughly sinusoidal variation in $\delta^{18}\text{O}$ (Figure 3.4). A prodigious number of samples must be analyzed when this technique is used to date very old ice. However, annual layers, much compressed but still recognizable by their isotopic variations, have been identified in ice more than 8000 years old (Figure 3.4). Thus, the potential is there, and techniques for making the analyses rapidly have been developed.

The electrical conductivity of ice and the concentration of microparticles in ice also vary seasonally. The former is a consequence of seasonal variations in the aerosol content of the snow. The seasonality in microparticle concentration is the result of entrainment of dust by wind during the summer when outwash plains and similar surfaces are free of snow (see, for example, Thompson *et al.*, 1986). Both these variations are used for dating.

When such techniques are used to date relatively old ice, errors accumulate because some annual layers either lack a variation of the parameter being used, or on occasion have two cycles of variation. However, volcanic ash layers are frequently found in cores, and when ash chemistry permits attribution of a layer to an eruption of known age, an absolute date can be assigned to the ice containing the ash. In this way, the age of ice that is thousands of years old has been established quite accurately.

Mass balance principles

A number of terms are used to describe different aspects of the mass balance on a glacier. The *winter balance* is the amount of snow that accumulates during the winter months. Conversely, the *summer balance*, a negative quantity, is the amount of snow and ice lost by melt. Over the course of a balance year, which is commonly taken to extend from the end of one melt season to the end of the next, the sum of the winter and summer balances is the *net balance*. Normally, these balances are expressed in terms of the thickness of a layer of water, or in water equivalents. When referred to a specific place on the glacier, they are expressed in m a^{-1} , or $\text{kg a}^{-1}\text{m}^{-2}$, and are called *specific* balances. Sometimes the word *budget* is used instead of balance, particularly when referring to the net balance.

Significant amounts of accumulation may occur during the summer in the accumulation areas of polar glaciers, and conversely melt may occur throughout the winter in the ablation areas of some temperate glaciers. The terms summer and winter balance are applied with some poetic license in these instances. The most extreme example of this is on tropical glaciers where accumulation and melt may alternate on a time scale of hours to days. Despite these complications, the basic principles are still applicable.

There are a number of ways of measuring mass balance, and we will not go into them all here. Perhaps the most common method, and the one that is easiest to visualize, is to measure the height of the snow or ice surface on stakes that are placed in the glacier in holes drilled for the purpose. The measurements are made first at the end of one melt season, then at the end of the following winter to obtain the winter balance, and

finally at the end of the next melt season to obtain both the summer and the net balances. Snow density measurements must also be made in order to convert the winter accumulation and summer snow melt to water equivalents.

We define $b_s(x,y,z)$ as the specific summer balance, $b_w(x,y,z)$ as the specific winter balance, and $b_n(x,y,z)$ as the specific net balance. Clearly,

$$b_n = b_s + b_w \quad (3.1)$$

and the overall state of health of the glacier can be evaluated from:

$$B_n = \int_A (b_s + b_w) dA \quad (3.2)$$

where A is the area of the glacier and B_n is the net balance. B_n is often normalized to the area of the glacier, thus: $\bar{b}_n = B_n/A$. When B_n or \bar{b}_n are positive, the glacier is said to have a positive mass balance; if this condition persists for some years, the glacier will advance, and conversely. Thus B_n is an important parameter to measure and to understand, and to this end we now consider meteorological factors influencing its components, b_s and b_w .

It is convenient to restrict our discussion to variations in b_s and b_w with elevation, z . This is not normally valid in practice because of the effects of drifting and shading, which result in lateral variations in both accumulation and melt.

It is common to plot $b_n(z)$ as a function of elevation; this is illustrated with data from a valley glacier in the Austrian Alps, Hintereisferner, in Figure 3.5a. The curve labeled “o” in this figure represents the situation during a year in which the mass budget is balanced, or $B_n = 0$. (Despite the low values of b_n at higher elevations, $\int_A b_n dA = 0$ in this instance because, as is true of most valley glaciers, the width of Hintereisferner increases with elevation.) Curves labeled “+” and “-” represent years of exceptionally positive or negative mass balance, respectively. Note that melting normally increases nearly linearly with decreasing elevation, so the lower parts of the curves in Figure 3.5a are relatively straight. However, at higher elevations in this particular case, snow fall decreases with elevation, resulting in curvature in the upper parts of the plot.

The differences between the “o” curve and the “-” and “+” curves are shown in Figures 3.5b and c, respectively. These differences are referred to as the *budget imbalance*, b_i (Meier, 1962). In years of exceptionally negative b_n (Figure 3.5b), b_i typically increases with decreasing elevation; this means that such years are normally a consequence of unusually high summer melt. Conversely, unusually positive budget years commonly result from exceptionally high winter accumulations

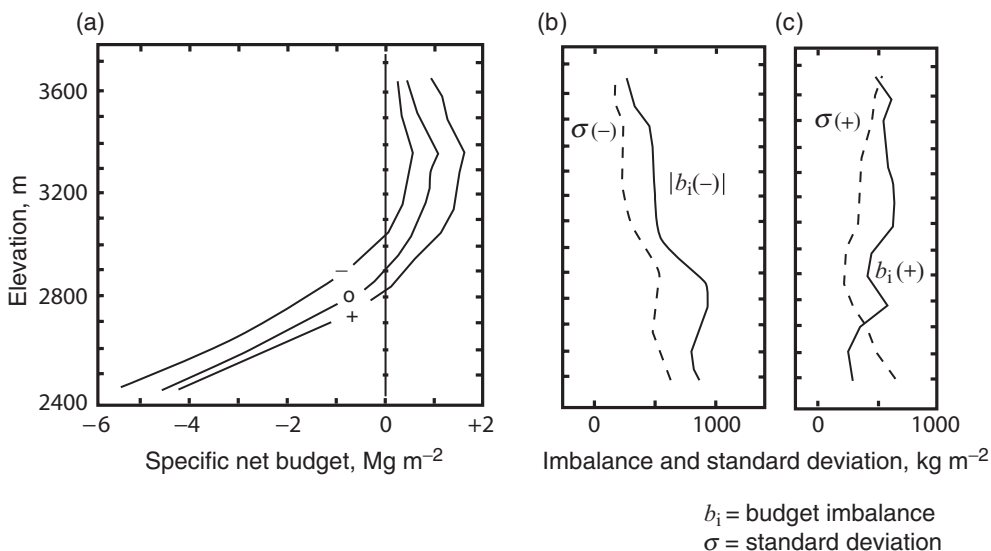


Figure 3.5. (a) Specific net budget, b_n , plotted against elevation for Hintereisferner. Curve “o” is for a year of balanced mass budget, while curves “–” and “+” are for years of exceptionally negative or positive budget, respectively. (b) and (c) Difference between curve “o” and curves “–” and “+”, respectively. (After Kuhn, 1981, Figure 1. Reproduced with permission of the author and the International Association of Hydrological Sciences.)

(Figure 3.5c). Budget years that are only moderately positive or negative can result from deviations of either accumulation or melt from their values in years when the budget is balanced.

Programs of mass balance measurements normally continue for several years. Cumulative mass balances can then be calculated by summing the annual values of B_n . There are two ways of doing this, however. In the *conventional* approach, A in Equation (3.2) should be adjusted annually to reflect expansion or shrinkage of the glacier. (In practice, new maps of the glacier are not prepared every year, and as A varies slowly it is more common to use the same value of A for several years and then adjust it when a new map is made.) In the *reference-surface* approach (Elsberg *et al.*, 2001), on the other hand, A is the area of the glacier surface at a particular time, such as the time of the first mass balance survey if a good map exists for that time, and is not changed during the course of the program. Furthermore, the annual measurements are then adjusted to the level of the reference surface with the use of measured or estimated values of dB_n/dz . The conventional approach is better for hydrological forecasting and other applications when the actual change in glacier volume is desired. However, for studies of climate, the reference-surface

approach is more useful because it provides a measure of climate change at a fixed reference elevation.

Climatic causes of mass balance fluctuations

Let us assume that b_w is composed of precipitation and drifting alone, thus ignoring mass additions by condensation and avalanching. Likewise, we take b_s to be a function only of surface melt, ignoring mass losses by evaporation, calving, bottom melting, and so forth. Although we assume that mass additions and losses by condensation and evaporation, respectively, are negligible, the energy involved in these phase change processes is taken into consideration in the following analysis.

Surface melting is controlled by the available energy:

$$\sum Q = R + H + V \quad (3.3)$$

where Q is the energy in $\text{kJ m}^{-2}\text{d}^{-1}$; R is the net radiation; H is the sensible heat input; and V is the latent heat input due to condensation, or loss due to evaporation (Kuhn, 1981). Then, neglecting any summer snow fall:

$$-b_s = \frac{T}{L} \sum Q \quad (3.4)$$

where T is the length of the melt season and L is the latent heat of fusion, 334 kJ kg^{-1} . (In the remainder of this discussion it will be convenient to use $\text{kg m}^{-2}\text{a}^{-1}$ for the units of mass balance.)

Assume further that the transfer of sensible and latent heat to the glacier surface is proportional to the temperature difference between the air and the glacier surface, thus:

$$H + V = \gamma(T_a - T_s) \quad (3.5)$$

where T_a and T_s are the temperatures of the air and the glacier surface, respectively, and γ is a constant of proportionality. Kuhn (1989) suggests that γ lies between 0.5 and $2.7 \text{ MJ m}^{-2}\text{d}^{-1}\text{K}^{-1}$; a value frequently found for firn is $1.0 \text{ MJ m}^{-2}\text{d}^{-1}\text{K}^{-1}$, while a reasonable mean value for glacier ice is $\sim 1.7 \text{ MJ m}^{-2}\text{d}^{-1}\text{K}^{-1}$. The range of values reflects the fact that the actual heat transfer is strongly influenced by such factors as the wind speed and the roughness of the glacier surface.

Combining Equations (3.1), (3.3), (3.4), and (3.5), rearranging terms, and writing all of the parameters as functions of elevation, z , yields:

$$b_w(z) = \frac{T}{L} [R(z) + \gamma(T_a(z) - T_s)] + b_n(z) \quad (3.6)$$

As we are dealing with melting conditions, $T_s = 0$, and does not vary with z .

Our objective now is to study quantitatively how changes in winter precipitation, summer temperature, and radiation balance affect a glacier's mass balance. Curves “–”, “o”, and “+” in Figure 3.5a are nearly parallel to one another, suggesting that one may be “derived” from another simply by a lateral translation. Such a translation, however, results in a change in the equilibrium line altitude (ELA), represented in Figure 3.5a by the point where the curves cross the 0 specific net balance line. This suggests that changes in equilibrium line altitude may be a fairly good measure of the impact of climate variations. The effects of changes in the principal measures of climate, namely precipitation and temperature, on the ELA are best studied with the use of perturbation theory, a technique used by Kuhn (1981), whose approach we adopt herein.

At the equilibrium line, $b_n(z) = 0$ by definition. Thus if h is the elevation of the equilibrium line and h_o is its elevation in a year of balanced mass budget, Equation (3.6) can be rewritten as:

$$b_w(h_o) = \frac{T}{L} [R(h_o) + \gamma(T_a(h_o) - T_s)] \quad (3.7)$$

The standard approach in perturbation theory is to rewrite Equation (3.7) for a situation in which the equilibrium line is at an elevation, h , which is slightly higher or lower than in the “o” state, and then to subtract this new relation from Equation (3.7), which we now proceed to do. Let primed values represent the perturbed state, thus:

$$b'_w(h) = \frac{T}{L} [R'(h) + \gamma(T'_a(h) - T_s)] \quad (3.8)$$

Subtracting:

$$b'_w(h) - b_w(h_o) = \frac{T}{L} [R'(h) - R(h_o) + \gamma(T'_a(h) - T_a(h_o))] \quad (3.9)$$

Any of the primed parameters in Equation (3.9) that vary with z can be represented by perturbation equations of the form, using T_a as an example:

$$T'_a(h) = T_a(h_o) + \frac{\partial T_a}{\partial z} \Delta h + \delta T_a \quad (3.10)$$

Here, Δh may be an observed change in altitude of the equilibrium line, so $(\partial T_a / \partial z) \Delta h$ represents the change in temperature that would be expected simply because the ELA changed. However, a change in mean summer air temperature may have been partially responsible for the change in ELA, and this part of the change in T_a is represented by δT_a . Figure 3.6 is a graphical representation of Equation (3.10). Writing equations similar to (3.10) for b_w and R , rearranging them, and substituting

Table 3.1. Possible causes of a 100 m increase in ELA

$\delta b_w = -400 \text{ kg m}^{-2}$	if $\delta T_a = \delta R = 0$
$\delta R = +1.35 \text{ MJ m}^{-2}\text{d}^{-1}$	if $\delta b_w = \delta T_a = 0$
$\delta T_a = +0.8 \text{ }^{\circ}\text{C}$	if $\delta b_w = \delta R = 0$

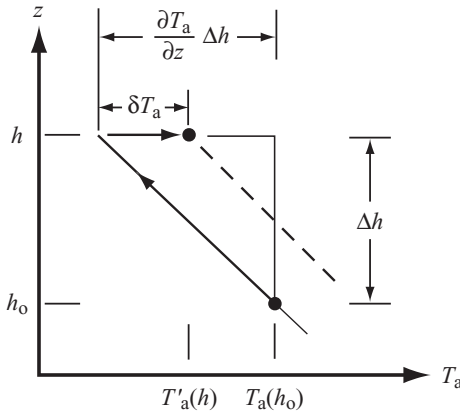


Figure 3.6. Sketch illustrating parameters in Equation (3.10). Consider a year during which the equilibrium line is at elevation h , Δh m above its elevation, h_0 , in years when the mass budget is balanced. The lapse rate during a year of balanced mass budget and during the year in question are represented by the slopes of the slanting solid and dashed lines, respectively. To obtain the mean air temperature, T'_a , at elevation h during this warm summer, start with $T_a(h_0)$, add $(\partial T_a / \partial z) \Delta h$ keeping in mind that $\partial T_a / \partial z$ is negative so this is a negative number, and add δT_a , following the arrows in the figure. Note that δT_a is the amount by which the temperature at elevation h exceeds the temperature at this elevation during a year of balanced mass budget.

into Equation (3.9) yields:

$$\frac{\partial b_w}{\partial z} \Delta h + \delta b_w = \frac{T}{L} \left[\frac{\partial R}{\partial z} \Delta h + \delta R + \gamma \left(\frac{\partial T_a}{\partial z} \Delta h + \delta T_a \right) \right] \quad (3.11)$$

The significance of this relation can be elucidated with the use of a numerical example. Suppose $\partial b_w / \partial z = 1 \text{ kg m}^{-2}\text{m}^{-1}$, $T = 100 \text{ d}$, $\gamma = 1.7 \text{ MJ m}^{-2}\text{d}^{-1}\text{K}^{-1}$, and the lapse rate, $\partial T_a / \partial z$, is -0.006 K m^{-1} . Suppose further, for the purposes of this example, that $\partial R / \partial z = 0$, as the radiation input does not vary significantly with elevation. Now consider an increase in the ELA of 100 m ($= \Delta h$) in a particular year. Calculate the changes δb_w , δR , and δT_a that would be sufficient, if they occurred alone, to cause this change in ELA. The reader is encouraged to carry out this calculation in order to gain familiarity with the relation. The answers are given in Table 3.1.

To place the results of this calculation in perspective, at 3050 m on Hintereisferner in the Austrian Alps, an elevation that is slightly above the normal position of the equilibrium line, the mean winter snow fall is 1620 kg m^{-2} and its standard deviation is 540 kg m^{-2} . Likewise, the mean summer temperature is $+0.4^\circ\text{C}$, and its standard deviation is 0.8°C . Comparing these standard deviations with the values of δb_w and δT_a in Table 3.1, it is clear that a 100 m change in the ELA could result, with nearly equal likelihood, either from a change in b_w or from a change in T_a . Similarly, the total radiation input is $\sim 46 \text{ MJ m}^{-2}\text{d}^{-1}$, while the loss is $\sim 40 \text{ MJ m}^{-2}\text{d}^{-1}$, leaving a mean radiation balance, R , of $\sim 6 \text{ MJ m}^{-2}\text{d}^{-1}$. Changes of $1.35 \text{ MJ m}^{-2}\text{d}^{-1}$, owing to changes in cloud cover for example, are small compared with the total radiation budget, and thus are not unreasonable.

For comparison, the mean winter balance on Barnes Ice Cap on Baffin Island is $\sim 400 \text{ kg m}^{-2}$ (Hooke *et al.*, 1987). Here, a δb_w of -400 kg m^{-2} is highly improbable, as this would mean virtually no accumulation. Thus in this case, a 100 m change in the ELA would most likely be a result of a change in T_a .

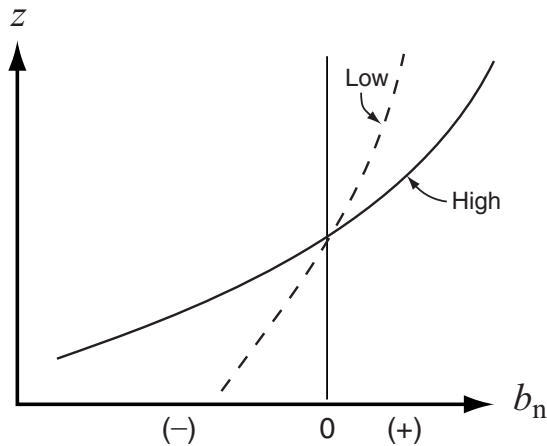
This comparison illustrates a fundamental difference between glaciers in relatively dry but cold areas, areas that we refer to as having a *continental* climate, and glaciers in warmer wetter *maritime* climates. Glaciers in continental settings owe their existence to low temperatures, and fluctuations in their mass budgets are strongly (inversely) correlated with mean summer temperature. Conversely, glaciers in maritime settings form in response to high winter snow fall; on such glaciers, the mass balance is less well correlated with T_a alone, and correlations can be improved significantly by adding winter precipitation to the regression. In fact, on some maritime glaciers the correlation of net balance with b_w alone is quite good (Walters and Meier, 1989, p. 371).

In the above analysis, T_a and R have been treated as independent variables. This is not strictly correct because an increase in T_a of 1°C increases R by about $0.3 \text{ MJ m}^{-2}\text{d}^{-1}$ (Kuhn, 1981). This is a result of the increase in “black body” radiation, which varies as T^4 . Incorporating this effect into the above calculation (Table 3.1) reduces δT_a to $+0.7^\circ\text{C}$.

The budget gradient

Recall that curve “o” in Figure 3.5a represents the distribution of b_n in a year in which the mass budget is balanced. The slope of this curve at the elevation of the equilibrium line in a year of balanced budget, $(\partial b_{no}/\partial z)_{h_o}$, is known as the *budget gradient*. High budget gradients represent situations in which there is a lot of accumulation above the equilibrium line and a lot of ablation below the equilibrium line, and

Figure 3.7. Sketch illustrating difference between low and high budget gradients.



conversely (Figure 3.7). High budget gradients are thus indicative of high flow rates, as a lot of ice must be transferred from the accumulation area to the ablation area in order to maintain a steady state profile. For this reason, Shumskii (1964, p. 442) referred to $\partial b_{no}/\partial z$ as the energy of glaciation and Meier (1961) called it the activity index. (For simplicity we will omit the subscript h_o in this discussion, but all derivatives should be understood as being evaluated at the elevation of the equilibrium line during a year of balanced budget.) High subglacial erosion rates are likely to be associated with high budget gradients.

The budget gradient tends to be high on glaciers in maritime settings and low in continental settings. Typical values might be $10 \text{ kg m}^{-2}\text{m}^{-1}\text{a}^{-1}$ in the former and $3 \text{ kg m}^{-2}\text{m}^{-1}\text{a}^{-1}$ in the latter (Haefeli, 1962).

To explore factors controlling $(\partial b_{no}/\partial z)$, rearrange Equation (3.6) and take its derivative, noting again that $T_s = 0$ on a melting glacier surface:

$$\frac{\partial b_{no}}{\partial z} = \frac{\partial b_w}{\partial z} - \frac{\mathbf{T}}{L} \left[\frac{\partial R}{\partial z} + \gamma \frac{\partial T_a}{\partial z} \right] \quad (3.12)$$

Thus $\partial b_{no}/\partial z$ depends upon $\partial b_w/\partial z$, $(\mathbf{T}/L)(\partial R/\partial z)$, and $(\mathbf{T}\gamma/L) \times (\partial T_a/\partial z)$.

On valley glaciers, the precipitation gradient, $\partial b_w/\partial z$, is commonly almost negligible. It may become significant if snow drift is important at higher elevations, and is also larger in areas where a significant amount of the summer precipitation occurs as snow at high elevations and rain at low elevations. In the Alps, where this is commonly the case, Kuhn (1981) suggests that a value of $0.5 \text{ kg m}^{-2}\text{m}^{-1}\text{a}^{-1}$ is reasonable.

The net radiation gradient, $\partial R/\partial z$, is small as long as snow covers the ablation area. However, once ice is exposed, particularly if it has a thin

dirt cover, the albedo drops and there is a significant change in R across the firn edge, or boundary between firn and ice. The first ice to become exposed is normally near the snout of the glacier or the margin of an ice cap, and the firn edge rises as the melt season progresses. Taking this into consideration, $(T/L)(\partial R/\partial z)$ may be as high as $\sim 7 \text{ kg m}^{-2}\text{m}^{-1}$ over a 120-d melt season (Kuhn, 1981).

The lapse rate, $\partial T_a/\partial z$, is limited by the dry adiabatic rate, $\sim 0.010 \text{ }^\circ\text{C m}^{-1}$, but a more realistic free air lapse rate along a glacier surface is $\sim 0.007 \text{ }^\circ\text{C m}^{-1}$. Thus, for a 120-d melt season, $(T\gamma/L)(\partial T_a/\partial z)$ is $\sim 4.3 \text{ kg m}^{-2}\text{m}^{-1}$.

So to explain the differences in $\partial b_{no}/\partial z$ between maritime and continental climates, the dominant terms are those involving the lapse rate and, below the equilibrium line, the radiation balance. As $\partial T_a/\partial z$ is likely to be comparable in maritime and continental settings, we have to appeal largely to differences in the length of the melt season, T , and in $\partial R/\partial z$. Melt seasons in high arctic continental settings may be a half to a third as long as those in, say, the Alps. Similarly, glaciers in continental settings also tend to be cleaner, thus reducing the albedo contrast across the firn edge, and hence the effective $\partial R/\partial z$. Differences in $\partial b_w/\partial z$ may contribute some, as summer rain is less likely to be a factor in arctic continental areas.

During a year of balanced mass budget, the ratio of the area of the accumulation zone to that of the entire glacier, the *accumulation-area ratio*, is typically ~ 0.7 (Glen, 1963). Using terminal and recessional moraines, one can use this ratio to estimate the change in size of an accumulation area, and hence the change in ELA, during a glacier retreat. Then it is clear that the imbalance in b_n is:

$$b_{ni}(h) = - \left(\frac{\partial b_{no}}{\partial z} \right)_{h_0} \Delta h \quad (3.13)$$

(see Figure 3.5). Thus, if moraines suggest that an equilibrium line rose by an amount Δh , and if $(\partial b_{no}/\partial z)_{h_0}$ can be estimated, $b_{ni}(h)$ can be calculated. To a good approximation, $b_{ni}(h)$ is equal to the average of $b_{ni}(z)$ over the glacier. In this way, one can estimate the change in climate that produced an observed change in glacier area.

Other modes of ice loss from valley glaciers

Calving

Cliffs form at the snouts of tidewater glaciers and of valley glaciers that end in lakes. Blocks of ice, ranging in size from single ice crystals to hundreds of cubic meters, break off these cliffs and float away to melt in more distant places. This process is called *calving*. The cliffs typically

Table 3.2. *Mass balance of the Greenland and Antarctic ice sheets and of smaller glaciers and ice caps^a*

Location	Accumulation, Gt ^b a ⁻¹	Runoff, Gt a ⁻¹	Calving, Gt a ⁻¹	Bottom melting, Gt a ⁻¹	Net balance, Gt a ⁻¹	Equivalent sea-level rise, ^c mm a ⁻¹
Greenland	520 ± 26	297 ± 32	235 ± 33	32 ± 3	-44 ± 53	0.05 ± 0.05
Antarctica	2246 ± 86	10 ± 10	2072 ± 304	540 ± 26	-376 ± 384	-0.1 ± 0.1
Glaciers and ice caps	688 ± 109 ^d	778 ± 114 ^d			-91 ± 36	0.3 ± 0.1

^a Data from Houghton *et al.* (2001, p. 648–651 and Table 11.10).

^b 1 Gt = 10¹² kg or a billion metric tons.

^c Values are for period 1910–1990, and are based, in part, on models and thus may not agree with figures in previous column.

^d Values calculated from data given in Houghton *et al.* (2001, Tables 11.3 and 11.4).

stand 60–80 m above the water level, and may extend to depths of a few hundred meters below the water level (Brown *et al.*, 1982). Most of these glaciers are grounded. The termini of some outlet glaciers in Greenland and Antarctica, however, are afloat.

For the most part, the following discussion applies equally to tidewater glaciers and to valley glaciers ending in freshwater lakes. Thus, we will use the term “tidewater” to refer to both, and will understand “submarine” to include sub-lacustrine. In addition, the reader should keep in mind that most tidewater glaciers are in valleys or, once they reach sea level, in fjords.

Although only a fraction of the world’s glaciers end in water, calving is an important, if not the dominant, mode of mass loss on these glaciers. It is estimated, for example, that nearly 50% of the ice loss from Greenland is through calving from outlet glaciers that end in fjords (Table 3.2).

The characteristics of ice in the snouts of tidewater glaciers control the size of the ice blocks shed from them and the subaerial height of the faces. The ice is normally temperate; thus water is present along crystal boundaries and this weakens the ice. In addition, the snouts are typically heavily crevassed. These two factors limit the size of ice blocks discharged from such glaciers. The crushing strength of a free-standing column of temperate ice with appreciable intergranular water may be reached at depths as shallow as 60–80 m, and this may limit the height of the calving face.

Ice blocks also become detached below the water level and float upward to the surface, creating dramatic disturbances in the process.

Careful observations of calving events on San Rafael Glacier in Chile suggest, however, that the volume of ice released by these submarine events is not sufficient to account for the observed rate of retreat of the subaerial part of the terminus (Warren *et al.*, 1995). This suggests that melting below the water surface may be an important part of the process we call calving. This suspicion is reinforced by the observation that calving rates are highest in October (Meier *et al.*, 1985), when the water is warmest (Matthews, 1981; Walters *et al.*, 1988).

The calving rate, \bar{u}_c , is usually determined by measuring the width-averaged rate of ice flow toward the calving face and the mean position of the calving face at two different times, usually a year apart, to obtain an annual average. If the glacier retreats during this time interval, \bar{u}_c is greater than the ice speed, and conversely. It turns out that \bar{u}_c is proportional to the mean water depth, \bar{h}_w , thus:

$$\bar{u}_c = c\bar{h}_w \quad (3.14)$$

(Brown *et al.*, 1982). The physics behind this relation are poorly understood and hotly disputed (Van der Veen, 1996, 2002), but the relation seems to be robust. In Alaskan marine environments, $c \approx 27 \text{ a}^{-1}$, whereas in freshwater $c \approx 2 \text{ a}^{-1}$ (Funk and Röhlisberger, 1989). This difference is probably a consequence of the greater density difference, in marine environments, between water immediately adjacent to the calving face and that further away. The water against any calving face is diluted by melting. In marine environments, the resulting density contrast is large, resulting in strong free convection and thus enhancing heat transfer to the face. Thus, the observation that c is larger in marine environments further supports the inference, above, that melting is an important part of the calving process.

The dependence of \bar{u}_c on water depth results in an unusual cycle of advance and retreat of tidewater glaciers. As is the case with normal valley glaciers, tidewater glaciers advance during periods when the climate is cool and accumulation exceeds surface melting. During the advance, however, they build a submerged moraine and slowly push it down the fjord (Figure 3.8). This process can take hundreds of years, so the climate may become warm again long before the terminus reaches a stable position. Once the mass balance finally turns sufficiently negative to halt the advance and initiate retreat, the terminus withdraws from its moraine bank, and backs into deeper water. The calving rate thus increases. This increases the budget imbalance, and the retreat accelerates. The retreat usually continues until the terminus reaches shallow water near the head of the fjord. Since the end of the Little Ice Age, all glaciers in coastal Alaska have retreated dramatically in this way. However, the retreats have not been synchronous and have not been in response to

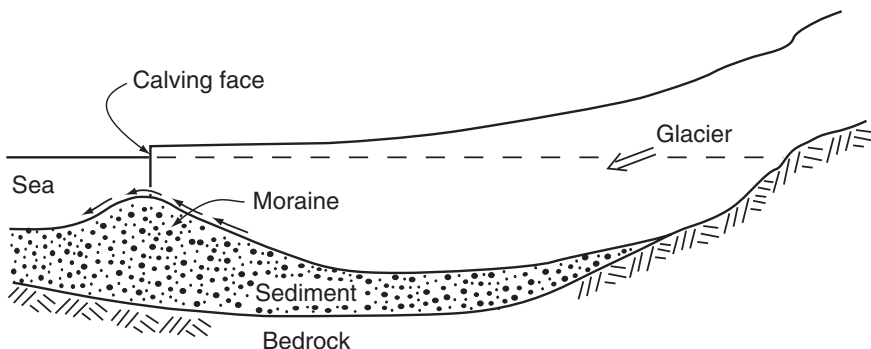


Figure 3.8. Schematic diagram showing how calving tidewater glaciers advance by rolling over their moraines. Arrows show how sediment is washed and dragged up proximal slope of moraine and slumps down distal slope, resulting in migration of the moraine.

identifiable climatic changes. Some glaciers reached their maximum extent and began to retreat in the late 1700s, but Columbia Glacier, the last of these glaciers to begin retreating, did not back off its moraine until the mid 1980s.

Bottom melting

If the base of a glacier is at the pressure melting point and the glacier is sliding over its bed, frictional heating associated with the sliding and with deformation in the basal ice can melt significant quantities of ice. For example, on the lower part of Columbia Glacier, the specific net balance at an elevation of ~ 400 m is $\sim -4.5 \text{ m a}^{-1}$ (Rasmussen and Meier, 1982). The glacier is ~ 600 m thick at this elevation, its surface slope is ~ 0.032 , and the depth-averaged velocity is $\sim 1.3 \text{ km a}^{-1}$ (Meier *et al.*, 1994). Thus, a column of ice of unit cross sectional area would drop ~ 40 m in a year, releasing $\sim 2.2 \times 10^8 \text{ J}$ of potential energy, which is sufficient to melt ~ 0.7 m of ice. Some of this melting will be internal, but much of it will occur near or at the bed. Thus, bottom melting may be as much as $\sim 14\%$ of the total ice loss at this elevation. On most glaciers, however, the amount of such melting is a much smaller fraction of the total, and can be neglected in mass balance studies.

Mass balance of polar ice sheets

On polar ice sheets, owing to their scale, the accumulation pattern reflects elevation and degree of continentality. If there is significant melting near the margin of a continental ice sheet, as is the case in Greenland

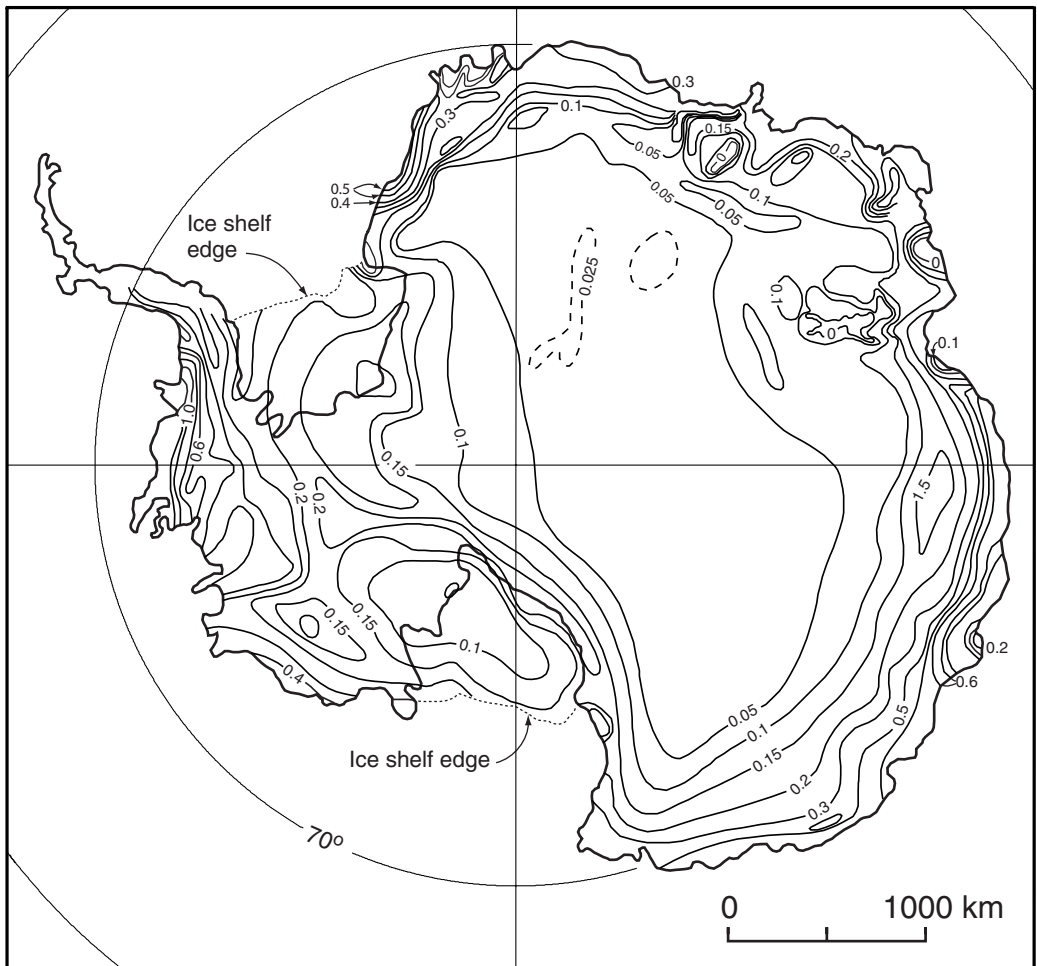


Figure 3.9. Mass balance pattern in Antarctica. Contours at 0.025 (dashed), 0.05, 0.1, 0.15, 0.2, 0.3, 0.4, 0.5, 0.6, 0.8, 1.0, and 1.2 m a⁻¹ (water equivalent). (After Giovinetto and Zwally, 2000. Reproduced with permission of the authors and the International Glaciological Society.)

but not Antarctica, b_n increases with elevation because the temperature decreases and the melt season becomes shorter. However, owing to orographic effects storms also lose much of their moisture within a few hundred kilometers of the coast. Thus, in the interior of the Greenland and Antarctic ice sheets, b_n decreases with distance from the moisture source (which also means that it decreases with increasing elevation). For example, in Antarctica accumulation rates are typically 0.3–0.6 m a⁻¹ (water equivalent) around the perimeter of the continent, but decrease to <0.1 m a⁻¹ at the South Pole (Figure 3.9) (Giovinetto and Zwally, 2000).

Thus, along the margins of ice sheets, accumulation patterns resemble those of maritime glaciers while between the margins and the interiors the pattern reflects the change from a maritime to a continental environment.

Calving of ice shelves

Over 90% of the ice loss from Antarctica is through calving, and most of this is from ice shelves. The blocks of ice released by such calving are commonly much larger than those from tidewater glaciers. This is probably because ice shelves are stronger. Their colder temperatures and less-extensive crevassing would increase their strength. Reeh (1968) has shown that under such conditions the width of an iceberg, measured normal to the calving face, is likely to be comparable to the thickness of the shelf. Many icebergs, however, are much larger than this. Iceberg B-15, which broke off from the Ross Ice Shelf in Antarctica in April 2000, measured 37×290 km and was ~ 430 m thick (WISC, 2003). Processes producing bergs of this size are still poorly understood.

We have recently found that polar ice shelves can break up exceedingly rapidly. The 1600 km^2 Larsen A ice shelf disintegrated in 39 d in 1995, and then in February 2002, in only 41 d, the 3250 km^2 Larsen B shelf collapsed. It appears that climate warming resulted in extensive melting on the shelf surface. Water percolated into crevasses, and because water is denser than ice, high stresses were generated at the tips of the crevasses (Weertman, 1973). As a result, the crevasses apparently propagated through the shelf, resulting in the collapse (Scambos *et al.*, 2000).

During the Wisconsinan glaciation, calving periodically produced armadas of icebergs that spread out across the North Atlantic Ocean, dropping coarse sand as they drifted along. The resulting sand layers were first identified by Hartmut Heinrich, and now bear his name (Heinrich, 1988). These ice-age calving events are widely believed to have been associated with rapid discharges of ice through Hudson Strait and partial collapse of the Laurentide Ice Sheet over Hudson Bay. Whether they were initiated by collapse of a buttressing ice shelf in the Labrador Sea or were entirely a consequence of a tidewater-glacier type of retreat is a matter of speculation.

Bottom melting

Ocean currents penetrate beneath floating ice shelves, and the saline water mixes with fresh water draining subglacially from the interior of the ice sheet. At the base of the ice shelf, either melting or freezing can

take place, depending on the temperature and salinity of the mixture, the pressure, and the temperature gradient in the basal ice. Indeed, melting can occur in one place and freezing in another. In Antarctica, bottom melting beneath ice shelves may account for as much as 20% of the mass loss (Table 3.2).

Effect of atmospheric circulation patterns on mass balance

There are at least two spatial scales of variation in coherence of glacier mass balance patterns. On the one hand, there are world-wide climatic changes such as those that resulted in the major ice advances of the Pleistocene and the minor advances of the Little Ice Age. These are both well-known and poorly understood, except that variations in the Earth's orbit that affected the timing and amount of solar radiation received at higher latitudes appear to have modulated the longer cycles (Hays *et al.*, 1976).

On a smaller scale there are regional variations in weather that may cause glaciers only a few hundred kilometers apart to behave differently. Let us consider some examples of these regional-scale variations.

Between the mid 1960s and the late 1980s, the net balances of maritime glaciers in Alaska were generally out of phase with those of glaciers in southwestern Canada and adjacent areas in the United States. When glaciers in one area had a relatively good year, those in the other normally had a bad year (Walters and Meier, 1989; Hodge *et al.*, 1998). Walters and Meier found that when the atmospheric low pressure region that lies off the Aleutian Islands, the *Aleutian Low* (Figure 3.10), is normal in the fall and winter, storms are deflected into Alaska, resulting in high winter balances there. However, when this low is not as deep as it usually is, storm tracks remain further south and accumulation rates are high in Washington and British Columbia. This pattern began to break down in the mid 1980s. Since then, winter balances on Wolverine and South Cascade glaciers have still been out of phase, but a dramatic increase in ablation has resulted in negative net balances on both, so net balances are in phase (Hodges *et al.*, 1998).

Summer balances in western North America are likewise affected by the summer low along the west coast. When this low is relatively deep and there is a corresponding high over British Columbia, conditions tend to be hot and dry, leading to large negative summer balances.

Asynchrony of mass balances can also result from the scale of pressure patterns. In the winter, small-scale low-pressure disturbances, identified by variations in the height of the 500 mbar surface (the surface

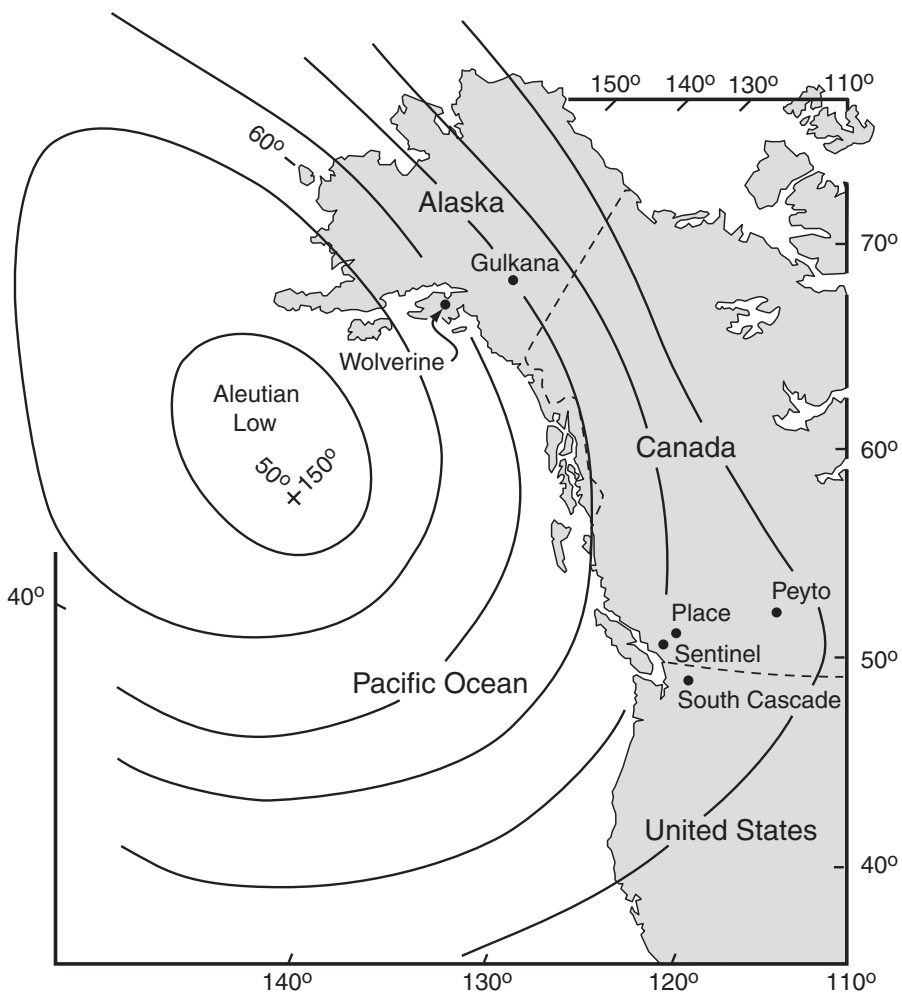


Figure 3.10. Map of the west coast of North America showing the Aleutian Low and locations of some glaciers for which there are good mass balance records. (Based on Walters and Meier, 1989, Figures 1 and 9.)

on which the atmospheric pressure is 500 mbar or about half the pressure at Earth's surface), result in cyclonic storms characterized by counterclockwise winds. Such storms, related to migratory perturbations embedded in larger-scale air flows, increase the winter balance on Sentinel Glacier in British Columbia. Conversely, frequent high-pressure disturbances resulting in anticyclonic patterns and thus accompanied by clockwise winds, inhibit accumulation in winter and increase melt in summer. In contrast, Peyto Glacier, which lies about 500 km east of Sentinel Glacier (Figure 3.10), is affected only by larger disturbances

related to long-wave patterns over the North Pacific. Storms from smaller disturbances do not penetrate that far inland (Yarnal, 1984).

ENSO and Decadal Oscillations

At a larger scale, we are beginning to find that patterns of the type just described are linked to hemispheric and even global patterns. One of the most important of these is the El Niño–Southern Oscillation, or ENSO. Under “normal” conditions winds blow westward in the equatorial Pacific. This drives a westerly surface current in the ocean, resulting in an increase in elevation of the sea surface in the western Pacific relative to that off Peru. This surface current and the resulting super-elevation propel an eastward return current at depth, leading to upwelling of cold water off Peru. At intervals of between 2 and 6 or 7 years, the westerly air flow weakens, the upwelling is damped, and the ocean and hence the air off Peru become warmer. This is an El Niño. The warmer air decreases the pressure gradient between Peru and the western Pacific, thus further weakening the westerly air flow. Consequently, a region of heavy rainfall that is normally located in the western Pacific shifts eastward. This, in turn, shifts the position of the jet stream, and hence weakens the Aleutian Low, causing storms to enter North America hundreds of kilometers south of their normal entry points (Rasmussen, 1984). Eventually, El Niño conditions weaken and normal or even slightly cooler than normal (La Niña) conditions return.

We do not know how El Niños are initiated, but the consequences are far reaching, affecting not only glaciers along the northwest coast but weather patterns around the Pacific, throughout North America, and even globally. Even in Antarctica, accumulation was consistently higher in parts of West Antarctica, and there is a hint that it was lower at the South Pole, during El Niño years (Kaspari *et al.*, 2004). The pattern in West Antarctica persisted during much of the twentieth century; a low-pressure cell in the Admundsen Sea shifted clockwise during El Niño events, and this increased accumulation in the eastern part of West Antarctica and decreased it in the western part (Cullather *et al.*, 1996). This pattern, however, appears to have broken down after 1990.

Although global in its effect, ENSO is generated by ocean–atmosphere interactions that are internal to the tropical Pacific and overlying atmosphere (Houghton *et al.*, 2001, p. 454). Recently, we have become aware of other similar oscillations in the atmosphere and ocean. One is the Pacific Decadal Oscillation, or PDO. During the warm phase of the PDO, sea-surface temperatures in the eastern equatorial Pacific are somewhat warmer than normal, while in the northwest Pacific, they are significantly cooler. The PDO seems to have two dominant periodicities,

15–25 years and 50–70 years (Mantua and Hare, 2002). The transitions between the warm and cool phases are abrupt: a warm phase began in 1977, and appears to have ended in 1998. El Niños tend to be strengthened during the warm phase of the PDO, and moderated during the cool phase (Maxwell, 2002).

Another recently discovered oscillation occurs in the north Atlantic. During the positive phase of this oscillation, there is a strong low-pressure region over southern Greenland and Iceland during the winter, and the jet stream is further north. Northern Europe is thus warmer and wetter than normal, while north Africa is drier (NOAA, 2003). This could affect glacier mass balance in Scandinavia and the Alps. Cook *et al.* (1998) have identified periodicities in the north Atlantic oscillation of 2, 8, 24, and 70 years.

On a still broader scale, temperature and accumulation patterns in Antarctica appear to reflect processes in the upper levels of the atmosphere. Warming of the troposphere, the layer of air between the Earth's surface and $\sim 11\,000$ m, prevents heat from reaching the higher stratosphere. Consequently, the stratosphere cools and becomes denser, strengthening downwelling over the South Pole. Thus, when the periphery of the continent is warmed by a warm troposphere, the interior is cooled by increased downwelling from the stratosphere, and conversely. As cool air contains less moisture, this results in a similar oscillation in accumulation (P. Mayewski, personal communication, 2003).

Clearly, atmospheric circulation patterns that we are just beginning to understand result in regional variations in mass balance on a variety of spatial and temporal scales. The data base necessary for identifying and studying these circulation patterns is expanding rapidly, and much will be learned as glaciologists and meteorologists begin to extend and exploit it. Particularly intriguing are the remarkable teleconnections between oceanic and atmospheric circulation that are beginning to appear. Beyond this, however, is the question of what controls variations in atmospheric and oceanic circulation on time scales of decades to centuries.

Global mass balance

Of considerable interest currently is the question of whether global warming is responsible for melting enough ice to account for the observed world-wide rise in sea level. The best estimates of this rise presently lie between 1 and 2 mm a^{-1} (Houghton *et al.*, 2001, p. 665). Because any estimate of the change in mass of a glacier or ice sheet involves calculating a small difference between two large numbers, namely the total accumulation and total loss, uncertainties are large (Table 3.2). Indeed, even with the best figures available we are still unable to say whether the Greenland and Antarctic ice sheets are growing or

shrinking. The uncertainties for smaller glaciers and ice caps are lower, however, and suggest that melting of these ice masses may be responsible for 15% to 25% of the sea-level rise. (In fact, Arendt *et al.* (2002) estimate that in the late 1990s the mass loss from Alaskan glaciers alone was $-96 \pm 35 \text{ km}^3 \text{ a}^{-1}$, which is more than the estimate in Table 3.2 for all valley glaciers and ice caps.) Other contributions to sea level are thermal expansion of the oceans ($0.5 \pm 0.2 \text{ mm a}^{-1}$), melting of permafrost ($0.025 \pm 0.025 \text{ mm a}^{-1}$), sedimentation in the oceans ($0.025 \pm 0.025 \text{ mm a}^{-1}$), and terrestrial storage in lakes and groundwater reservoirs ($-0.35 \pm 0.75 \text{ mm a}^{-1}$).

Although the mass balance data for Greenland are ambiguous, yielding a net balance of $-44 \pm 53 \text{ Gt a}^{-1}$, the pattern is suggestive. The observational data show that the ice sheet is growing thicker in the interior, at least locally, as warmer air transports more moisture inland. However, it is thinning along the margins where the increased temperature results in more melting (Krabill *et al.*, 2000; Thomas *et al.*, 2000). As mentioned earlier, this is precisely the pattern inferred from Greenland ice cores for the end of the Younger Dryas (Alley *et al.*, 1993).

Summary

In this chapter we discussed snow accumulation and the transformation of snow to ice. We found that in polar environments where there is little if any melting, the physical and chemical stratigraphy in an annual layer of snow persists for many thousands of years and can be used to date the ice.

We then defined some terms used to discuss mass balance, particularly summer, winter, and net balance, and used a perturbation approach to study the influence of winter balance, temperature, and radiation on net balance. By comparing observed variations in these parameters with calculated values, it became clear that the net balance of glaciers in continental environments was sensitive, primarily, to summer temperature, while that of glaciers in maritime areas was sensitive to both winter balance and summer temperature. Radiation balance, principally resulting from differences in cloud cover, could play a role in either environment. The lower budget gradient, and consequently the more sluggish behavior of polar glaciers compared with their temperate counterparts, turned out to be largely related to the shorter melt season in polar environments. On ice sheets, we also noted that accumulation decreases with distance from the moisture source.

We then discussed the importance of calving and bottom melting in mass balance, and discovered that on tidewater glaciers calving can lead to retreats that are, at best, only weakly related to climate. On ice sheets, calving turns out to be a dominant process of mass loss. Bottom melting

is an important component of mass balance on some fast-moving valley glaciers and beneath ice shelves.

Finally, we found that variations in intermediate and large scale weather patterns that we are just beginning to understand can result in asynchronous mass balance patterns on glaciers only a few hundred kilometers apart.

Chapter 4

Flow and fracture of a crystalline material

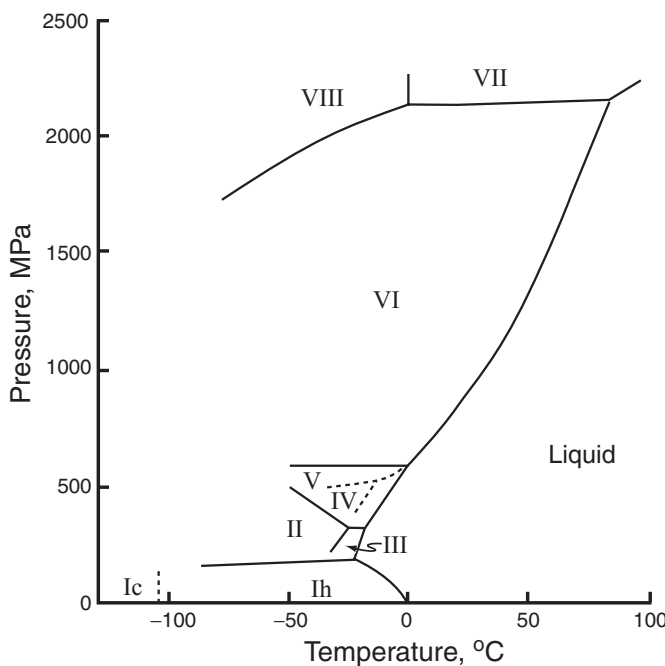
Before proceeding to a more theoretical discussion of the dynamics of glaciers, it will be useful to present a brief introduction to the voluminous literature on deformation or *creep* of ice. We will begin by looking at deformation processes on an atomic scale and then introduce empirical and semi-empirical relations that provide a macroscopic description of the deformation. Finally, we will show how principles of linear fracture mechanics can be used to predict crevasse depth.

Crystal structure of ice

There are nine known crystalline forms of ice, but seven of them are stable only at pressures in excess of about 200 MPa, and the eighth, a cubic form, ice Ic, is stable only at temperatures below about -100°C (Figure 4.1). As the highest pressures and lowest temperatures in glaciers on Earth are about 40 MPa and -60°C , respectively, these eight forms need not concern us. We thus restrict our attention to the common form of terrestrial ice, ice Ih.

The structure of ice Ih is shown, in stereoscopic view, in Figure 4.2a. It is a hexagonal mineral (hence the “h”) with a rather open structure in which every oxygen atom, represented by the large circles in Figure 4.2a, is bonded to four additional oxygen atoms at the corners of a tetrahedron. The tetrahedra are joined together in such a way that the oxygens form hexagonal rings with the O=O bonds zigzagging lightly up and down as one progresses around the ring (Figure 4.2b); three of the oxygens thus lie 0.09 nm above the other three. The plane of these rings is called the *basal plane* of the crystal structure.

Figure 4.1. Part of the phase diagram of water. (After Kamb, 1965, Figure 1.) The various polymorphs of ice are designated by Roman numerals. Ice IV is a metastable phase, unstable everywhere with respect to ice V. Ice Ic is also metastable with respect to ice Ih.



The fourth oxygen atom in the tetrahedron is ~ 0.28 nm above or below that in the center of the tetrahedron. A line parallel to this bond, and hence normal to the basal plane is called the *c-axis*.

It is evident from Figure 4.2b that there are many more O=O bonds within a basal plane than there are between basal planes. Thus, bonding between basal planes is much weaker than that within the basal plane.

Around each oxygen atom there are, of course, two hydrogen atoms. The hydrogen atoms, represented by the small circles in Figure 4.2a, lie on the bonds between the oxygen atoms. They are situated close to the oxygen to which they are bonded. As each oxygen atom is bonded to four other oxygens, only two of these hydrogen sites, selected at random, are occupied.

There are two hydrogen sites along each O=O bond. Normally only one of these is occupied. Situations in which neither site is occupied are called *Bjerrum L defects*, and situations in which both sites are occupied are called *Bjerrum D defects*, or just L and D defects, respectively.

Dislocations

Another type of defect in a crystal is the *dislocation*. Dislocations are places where the crystal structure is discontinuous or offset in some way. The two basic types of dislocation, the *edge dislocation* and the

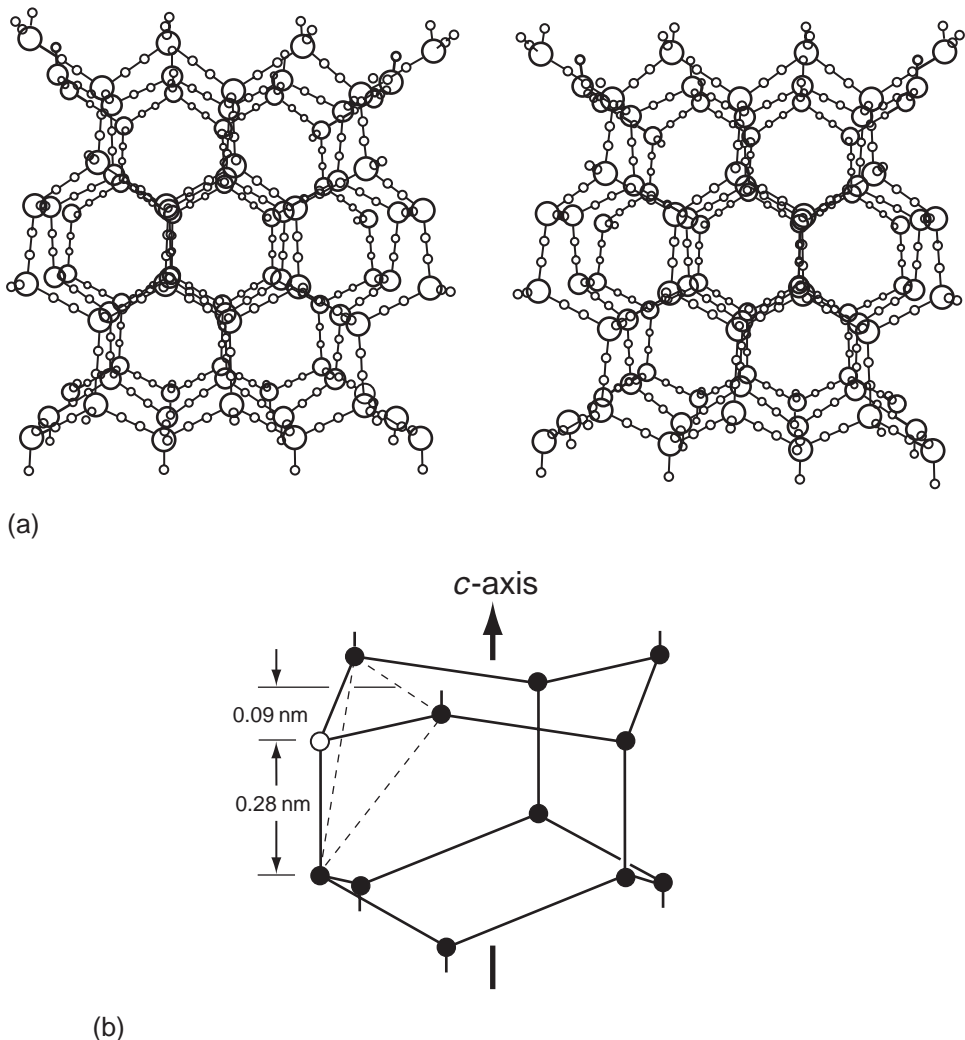


Figure 4.2. (a) Stereographic view of the structure of ice Ih, viewed down the *c*-axis. Only half of the possible hydrogen sites, indicated by small circles, are occupied. (After Hamilton and Ibers, 1968.) (b) Structure of ice Ih viewed normal to the *c*-axis. Two of the hexagonal rings are shown. Short lines leading upward and downward from these rings are bonds to rings above and below. The oxygen shown with an open circle is the center of a tetrahedron, part of which is shown by the light dashed lines. (Modified from Hobbs, 1974, Figure 1.7.)

screw dislocation, are illustrated in Figure 4.3. Virtually all crystalline materials contain dislocations.

Dislocations play a vital role in the deformation or creep of crystalline materials. If one tried to deform the perfect crystal in Figure 4.3a by shearing the top three layers of atoms over the bottom two, the stress

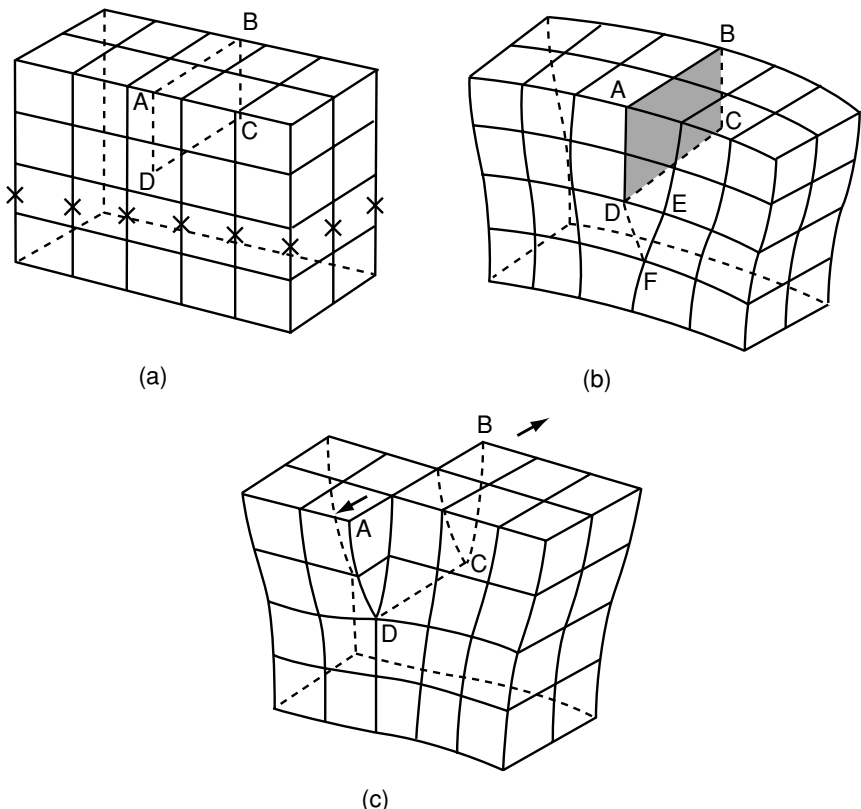


Figure 4.3. (a) A perfect crystal. (b) An edge dislocation. (c) A screw dislocation. (Modified from Hull, 1969, p. 17.)

required would be enormous as every one of the bonds indicated by an “ \times ” would have to be broken *simultaneously*. In contrast, the crystal in Figure 4.3b would deform much more easily because the bonds could be broken sequentially, one at a time. For instance, the bond between E and F could be broken and a new bond formed between D and F. Calculations show that, in the absence of dislocations, crystalline materials could not possibly deform under the stresses at which they are observed to deform. In fact, it was through such theoretical studies that the existence of dislocations was first inferred.

Upon application of a stress, the number of dislocations in a crystal increases. Some of these new dislocations are generated at *Frank-Reed sources*. A Frank-Reed source consists of a dislocation lying between two points at which the dislocation is fixed, called *pinning points* (Figure 4.4). Impurities or immobile tangles of dislocations may serve as pinning points. When a stress is applied, this dislocation is bowed

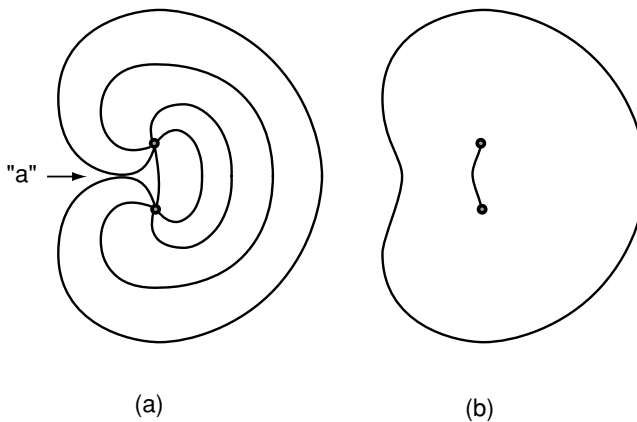


Figure 4.4. Generation of dislocations at a Frank–Reed source. Each line in (a) represents a successive position of a dislocation as it is bowed out between two pinning points. (b) shows the final stage with the new dislocation expanding outward and another dislocation between the pinning points.

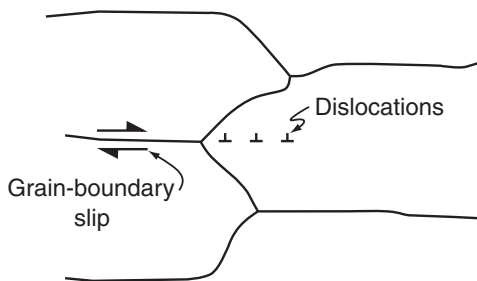


Figure 4.5. Generation of dislocations at a three-grain intersection due to grain-boundary slip.

out until it meets itself at “a”. At this point, dislocations coming from opposite directions are of opposite sign, and the dislocation is locally annihilated, leaving a ring and a new dislocation between the pinning points (Figure 4.4b). This new dislocation can then repeat the process, so there is a continuous source of dislocations. The dislocation is of the edge type ahead of and behind the source, of the screw type at the sides, and of mixed type at intermediate positions. Some dislocations generated by a Frank–Reed source never complete a full cycle but rather multiply by spreading to neighboring planes, a process called *multiple cross glide* (Hull, 1969, pp. 165–7).

Dislocations also form at points of stress concentration on grain boundaries. For example, shear along a discrete atomic plane in one crystal can result in an offset of the crystal boundary. To accommodate this offset, the neighboring crystal must also yield, so dislocations are formed at the boundary and move into this crystal.

Slip along grain boundaries is believed to occur at temperatures above -10°C . This, too, results in stress concentrations in neighboring crystals, and hence in generation of dislocations in these crystals (Figure 4.5).

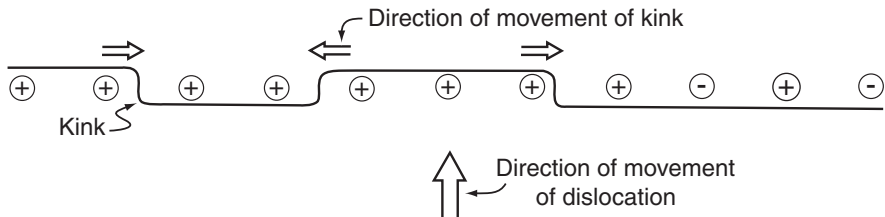


Figure 4.6. Lateral movement of kinks causing forward movement of a dislocation. The symbol $(+)$ represents situations in which a normal bond would form by passage of a kink. The symbol $(-)$ represents situations in which a Bjerrum defect would be formed.

Dislocations move by formation of kink pairs (Figure 4.6), followed by lateral movement of the kinks. As long as the bond formed by movement of a kink is a normal bond, with only one hydrogen between two oxygens, the kink can move readily. However, if the movement would result in a Bjerrum defect the energy required for movement would be much higher. It is presumed that in such situations, movement of the kink is delayed until diffusion or rearrangement of the hydrogen atoms (proton rearrangement) results in a geometry such that the kink can migrate without formation of a Bjerrum defect. As shown in Figure 4.6, there may be a number of kinks along a dislocation line. Two kinks moving toward one another will annihilate each other when they meet, resulting in advance of the dislocation line.

Rate-limiting processes

The rate of deformation of a crystal or of a polycrystalline aggregate depends on how rapidly dislocations can move. This, in turn, may depend upon factors such as the effectiveness of the mechanisms resisting motion, the ability of a dislocation to move from one atomic plane to another, and the orientation of the atomic plane in which the dislocation is moving. Usually, one process is significantly more important than the others, principally because it is more effective than the others in retarding dislocation motion. This process is called the *rate-controlling* or *rate-limiting* process.

It is, in general, not easy to identify the rate-limiting process. This is because it is different in different materials, and within any one material it changes with temperature and stress, and possibly also impurity content. Furthermore, the rate-limiting process may be different in single crystals and in polycrystalline aggregates.

In the next few paragraphs, we describe some possible rate-limiting processes in ice and present evidence for them.

Drag as the rate-limiting process

At the moderate stress levels normally found in glaciers, dislocations moving in a crystallographic plane are restrained in their motion by a number of drag mechanisms. The velocity of such a dislocation is given by:

$$v = c\sigma \mathbf{b}^3 e^{-\frac{Q}{R\theta_K}} \quad (4.1)$$

where c is a constant of proportionality that depends, in part, on Boltzman's constant; σ is the applied stress; \mathbf{b} is the Burgers vector of the dislocations (a measure of the distortion of a crystal produced by a dislocation, and approximately equal to the atomic spacing in the crystal (Hull, 1969, pp. 19)); R is the gas constant; θ_K is the temperature in Kelvins; and Q is the activation energy for the rate-limiting deformation mechanism (Weertman, 1983). Derivation of this equation, as well as some others in this chapter, is beyond the scope of this book. Noteworthy, however, is the dependence on very fundamental physical parameters.

A brief comment on activation energy is in order. The activation energy is the magnitude of an energy barrier that must be overcome for a kinematic process to occur. Each kinematic process has its own activation energy, so there is an activation energy for self-diffusion of hydrogen and oxygen in ice ($\approx 60 \text{ kJ mol}^{-1}$), an activation energy for creep of ice ($\approx 79 \text{ kJ mol}^{-1}$), and so forth.

The creep rate, $\dot{\epsilon}$, resulting from movement of dislocations in a crystallographic plane is:

$$\dot{\epsilon} = \alpha \mathbf{b} \rho_d v \quad (4.2)$$

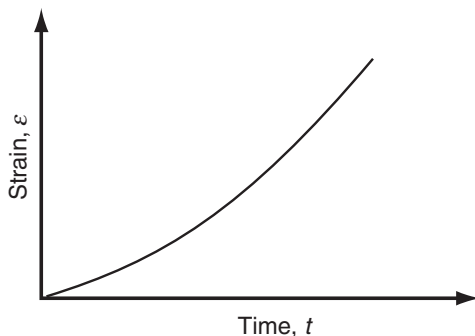
(Weertman, 1983), where α is a constant with dimensions of length and ρ_d is the dislocation density (m^{-2}); α depends on the orientation of the slip planes, but is $\sim 4.5 \times 10^{-10} \text{ m}$. Of interest is the fact that the steady-state dislocation density, which reflects a balance between the applied stress and the internal stress from dislocations, is given by:

$$\rho_d \approx \left(\frac{\sigma}{\mu \mathbf{b}} \right)^2 \quad (4.3)$$

(Weertman, 1983; Alley, 1992), where μ is the shear modulus. (The table on p. xiv gives definitions of parameters such as μ and values appropriate for ice.) Thus, combining Equations (4.1), (4.2), and (4.3) leads to:

$$\dot{\epsilon} \propto \sigma^3 \quad (4.4)$$

Figure 4.7. Variation of total strain with time during deformation of a single crystal oriented so that glide occurs on the basal plane (easy glide).



at constant temperature. In other words, the velocity of dislocations varies with σ , and their density varies with σ^2 , leading to a cubic dependence of $\dot{\varepsilon}$ on σ .

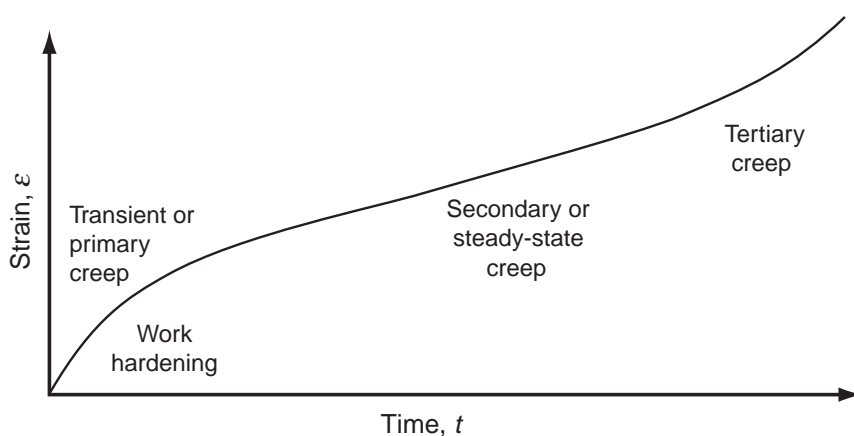
A large volume of experimental data on ice deformed in the laboratory and on natural ice in glaciers and ice shelves yields such a cubic dependence, particularly for stresses above 0.1 MPa. This suggests that the theoretical model presented above is fundamentally sound, and thus that drag mechanisms which determine the velocities of dislocations may be the rate limiting factors.

When a single crystal of ice is stressed in such a way that there is an appreciable component of the stress on the basal (0001) plane, the deformation rate increases with time (Figure 4.7). This can be explained by the fact that the dislocation density is normally low in unstressed crystals, and increases gradually to its steady-state value, given by Equation (4.3), after the stress is applied. This further supports the suggestion that drag is the rate limiting process.

Climb as the rate-limiting process

There is, however, an additional dislocation process that must be considered. As dislocations multiply, they commonly begin to interfere with one another, resulting in gridlock. These dislocation tangles inhibit deformation. Under such conditions, application of a stress to a previously unstrained sample results in a deformation rate that initially decreases with time, a process called *work hardening* (Figure 4.8a). At sufficiently low temperatures this decreasing creep rate may continue indefinitely, but at higher temperatures *recovery processes* come into play. One such process involves diffusion of atoms away from (or vacancies toward) dislocations resulting in movement of the dislocation from one crystallographic plane to another. For example, if the atom at D in Figure 4.3b diffused away, the dislocation would move upward. This is called

(a)



(b)

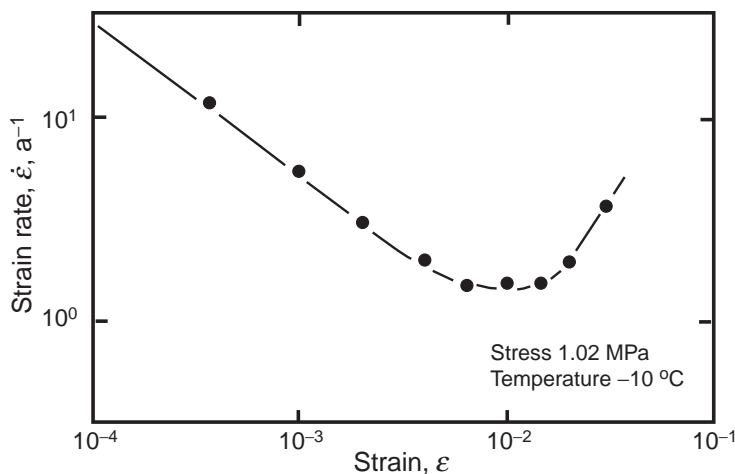


Figure 4.8. (a) A typical strain–time curve for a sample of polycrystalline ice loaded in uniaxial compression. In early experiments, plots like this were used to identify the time span over which steady-state creep appeared to prevail. (b) As laboratory precision improved, it became possible to plot cumulative strain against strain rate, and thus more accurately identify the minimum strain rate. Note the increase in strain rate after about 1% strain. (Plot (b) is adapted with permission from Duval *et al.*, 1983, Figure 6. Copyright 1983 American Chemical Society.)

dislocation climb if the dislocations are of the edge type, and *cross slip* if they are of the screw type. Both processes relieve tangles and, after an initial transient period, allow deformation to continue at a more-or-less steady rate (central part of curve in Figure 4.8a). As climb is the recovery process requiring more energy, it would be rate controlling.

Another recovery process, believed to be active particularly at low stresses, involves movement of grain boundaries as some crystals grow at the expense of their neighbors. The ice behind the moving boundary is unstressed, and thus relatively free of dislocations; ρ_d is thus decreased by grain-boundary migration.

It is noteworthy that samples of polycrystalline ice deformed in compression invariably go through a transient phase of decelerating creep and then a period of nearly constant creep rate. (If the test is continued long enough, the creep rate normally increases again in what is called tertiary creep (Figure 4.8a); this is attributed to recrystallization, which is discussed further below.) This supports the suggestion that recovery processes are rate limiting. Furthermore, it may be significant that the activation energy for creep (79 kJ mol^{-1}) is close to that for self-diffusion (60 kJ mol^{-1}), again suggesting that climb (which is a result of diffusion) is the rate-limiting process. However, the difference between these two activation energies seems to be larger than can be explained by experimental error so other processes may also be involved.

Slip on other crystallographic planes

Deformation of one crystal in a polycrystalline aggregate necessitates deformation of neighboring crystals to preserve continuity of the medium. Thus, all crystals must take part in the deformation. Most crystals will be oriented so that the applied stress on that crystal will have a component parallel to the basal plane. However, a few crystals will not be so oriented, and these must therefore deform in some direction that is not parallel to the basal plane.

Slip on either the prismatic or pyramidal planes (Figure 4.9) is a possibility. However, on the prismatic planes the slip would probably be parallel to the basal plane (Figure 4.9), and so would not accommodate stresses normal to that plane. Thus, slip on pyramidal planes may be necessary, and because such slip is likely to be much harder than that on other planes, it could be rate limiting.

Inhomogeneous strain

The above considerations are based on the assumption of homogeneous strain. However, in polycrystalline ice, the stress on any single crystal is

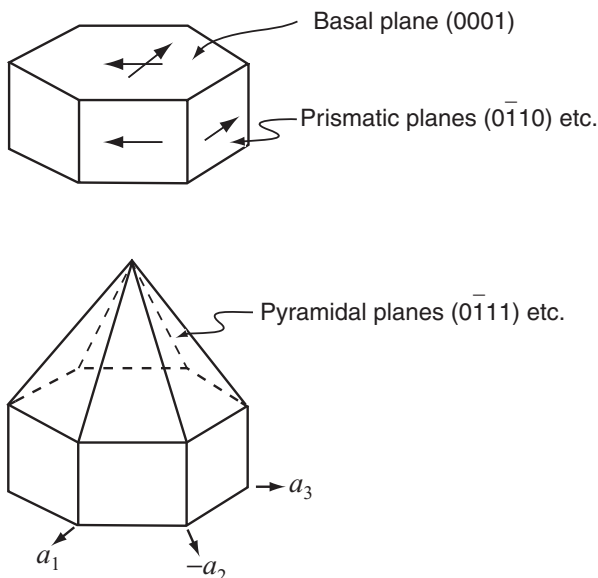


Figure 4.9. Crystallographic planes in a hexagonal crystal.

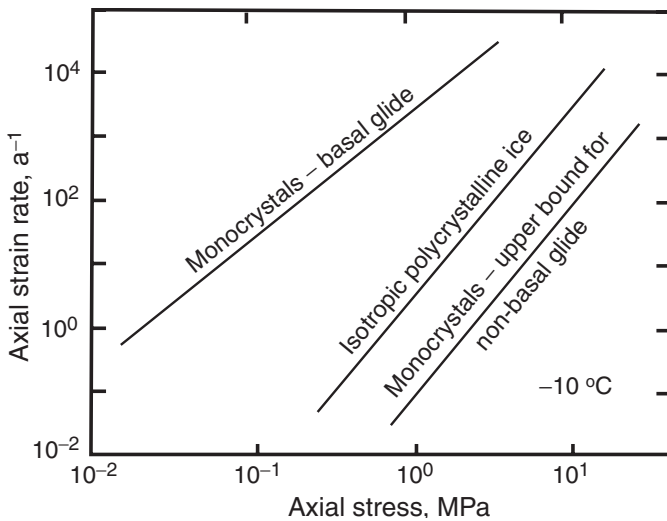
not equal to the stress on the bulk sample, as crystals that slip easily in one direction but not in others will transmit the stress nonuniformly (Duval *et al.*, 1983). If it is assumed, instead, that the strain is inhomogeneous, plastic strain is possible without slip on either prismatic or pyramidal planes. This is because processes such as climb of dislocations normal to the basal plane, grain-boundary migration, and grain translation and rotation can accommodate stresses normal to this plane and facilitate adjustments between crystals (Alley *et al.*, 1997).

Internal stresses

The inhomogeneity of internal stresses in a polycrystalline sample merits further discussion. When an ice sample is loaded, it first deforms elastically. Then, grains that are favorably oriented begin to deform by slip on the basal plane. The load is thus transferred to grains less favorably oriented, and high stresses can develop in such grains. As deformation continues the inhomogeneity of the stress distribution becomes more pronounced, with peak stresses in individual grains that may be many times the mean stress in the sample (Duval *et al.*, 1983).

It has been found experimentally that the resistance to shear on basal planes in monocrystals (single crystals) is much less than the resistance to shear on other crystallographic planes. This is because of the paucity of bonds between basal planes mentioned earlier (Figure 4.2b). For example, to produce a strain rate of 1.0 a^{-1} at -10°C requires a stress

Figure 4.10. Stress-strain rate data for ice at -10°C . (Adapted with permission from Duval *et al.*, 1983, Figure 2. Copyright 1983 American Chemical Society.)



of about 0.03 MPa in a monocrystal oriented for easy glide, and a stress of about 3 MPa in a monocrystal oriented for hard glide (Figure 4.10). Thus, within a sample of polycrystalline ice the local stress may vary over two orders of magnitude. Not surprisingly, the bulk strain rate of the polycrystalline sample lies between the values for the monocrystal in the easy-glide and hard-glide orientations.

A consequence of this inhomogeneous internal stress distribution is that grains that are not favorably oriented for basal glide may accommodate some of the plastic deformation in adjacent crystals by deforming elastically. These crystals, therefore, have stored elastic strain energy. Upon release of the load, this elastic energy exerts a “back stress” on the crystals that previously deformed plastically, and a small amount of reverse creep results (Duval, 1978) (Figure 4.11). This reverse creep is not instantaneous, as would be the case in a purely elastic medium, because the grains favorably oriented for basal glide under the original loading must now creep “backwards” to relieve the stored elastic energy.

Recrystallization

Crystals of glacier ice vary in size and also in the degree to which they are interlocked. If there were no bonding across grain boundaries, for example, some polycrystalline ice samples would fall apart into a pile of roughly equant grains, up to a few millimeters in maximum dimension, while others would hang together like a three-dimensional jigsaw puzzle. We will use the term *texture* to refer to these characteristics of crystal size

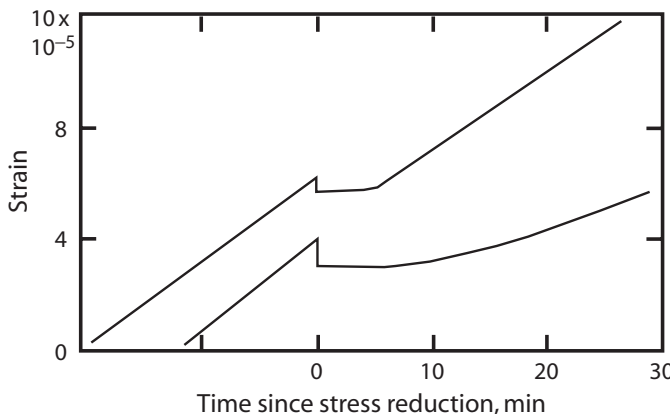


Figure 4.11. Reverse creep due to release of stored elastic strain energy upon unloading of a sample. The original loading of the sample was 1 MPa. At time 0, the stress was reduced by 0.06 MPa (upper curve) and by 0.13 MPa (lower curve), respectively. Horizontal parts of the curves reflect a balance between further creep under the reduced stress and delayed release of elastic strain energy. (Adapted with permission from Duval *et al.*, 1983, Figure 5. Copyright 1983 American Chemical Society.)

and shape. In addition, under prolonged strain the *c*-axes of the crystals develop a variety of preferred orientations, or *fabrics*. Both texture and fabric affect the rheology of ice.

In order to study these processes, glaciologists, like petrologists, use thin sections. The thin sections are typically somewhat less than a millimeter thick and 60–80 mm across. When polarized light is passed through a thin section and then observed through another polarizing filter oriented at right angles to the first, the individual crystals can be seen because the crystal structure rotates the light as it passes through the crystal, and the amount of rotation depends on the orientation of the crystal. When thus viewed, the different crystals have different colors (or grayscale tones in a black and white image – Figure 4.12). With the use of a universal stage on which the thin section can be both rotated around a vertical axis and tilted about either of two mutually perpendicular horizontal axes, crystals can be oriented so their *c*-axes are vertical. In this orientation, the crystal remains black as the stage is rotated around its vertical axis. The orientation of the crystal is then noted and plotted on an equal-area net (Figure 4.13). To interpret such a plot, visualize a hemisphere with its convex side down and with a crystal in its center. The *c*-axis of the crystal intersects the hemisphere. A point on a fabric diagram like those in Figure 4.13 is the projection of this point of intersection onto the flat surface. Thus, a vertical *c*-axis plots at the center

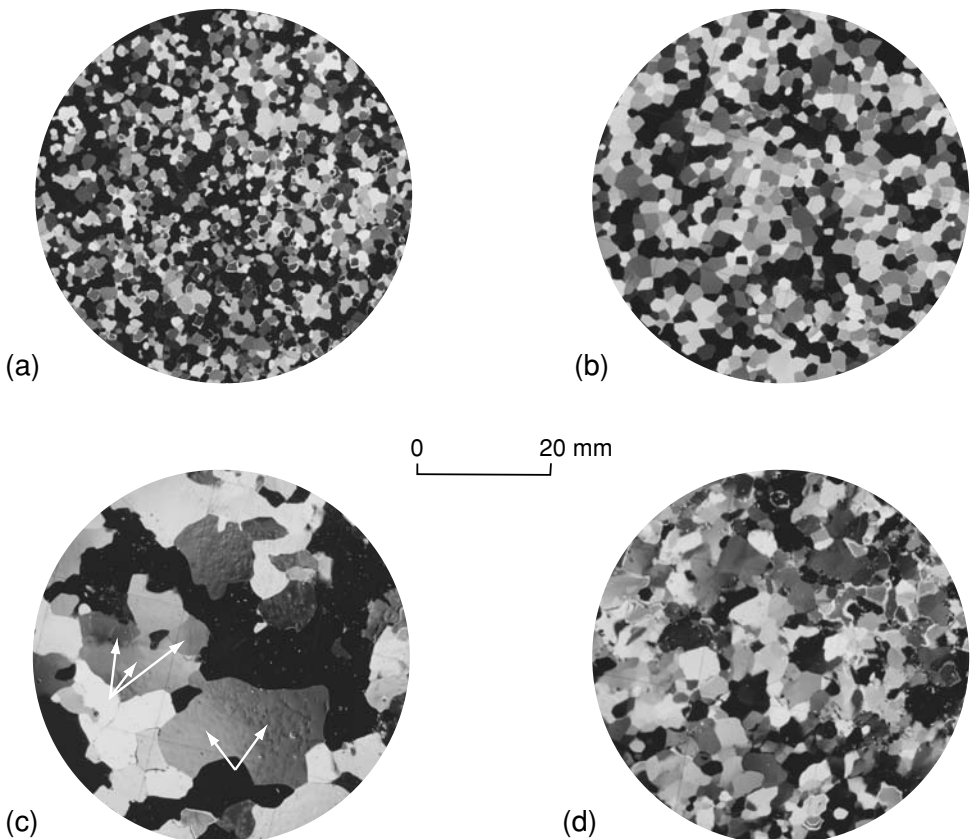


Figure 4.12. Photographs of thin sections of ice from the Greenland ice sheet near Thule. Photographs were taken under crossed polarizers. The different grayscale tones of the grains reflect different orientations of the c -axes. (a) Initial texture formed by compaction of snow with addition of small amounts of melt water. The c -axes have a weak preferred orientation, with a preference for vertical orientations. (b) Texture resulting from grain growth with little or no deformation. The c -axes still have a weak vertical preferred orientation. (c) Texture resulting from polygonization. Adjacent grains with nearly the same grayscale tone (arrows) have c -axes that are nearly parallel to one another. The grain in the lower center is bent; in the one to left of center, distinct boundaries have formed between parts with slightly different orientations. (d) Texture following significant deformation. Grains are interlocked, and c -axes have a strong preferred orientation. (From Hooke, 1970.)

of the circle, and a c -axis dipping “south” plots between the center and the bottom of the circle. The points are normally plotted on a *Schmidt equal-area* net; this net is designed so that a unit area on the hemisphere plots into a unit area on the net. Consequently, a c -axis dipping at 45° actually plots about 55% of the distance from the center of the net to the boundary.

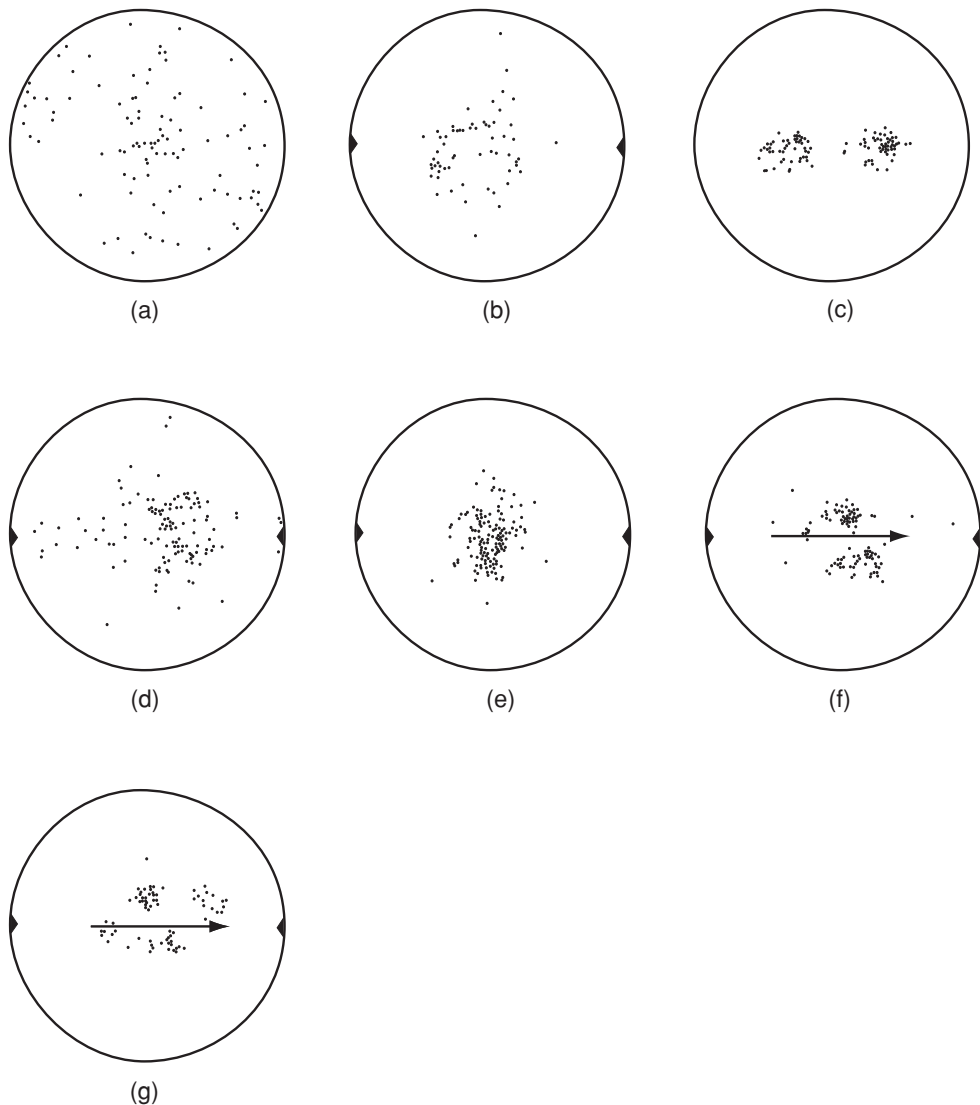


Figure 4.13. Examples of crystallographic fabrics observed in ice. Plots are projections on lower hemisphere of an equal-area net. Triangles on edges show direction of bubble elongation. In fabrics produced by simple shear, direction of shear, shown by arrows, is presumed to be parallel to bubble elongation. All fabrics except (c) were measured on cores from boreholes in Barnes Ice Cap (Figure 4.15); (c) is schematic. (a) Fabric with weak preferred orientation of c-axes in superimposed ice. (b) Fabric resulting from uniaxial compression normal to the plane of the diagram. (c) Schematic fabric formed in pure shear. (d) Broad single-maximum fabric. (e, f, g) Fabrics resulting from simple shear in plane of diagram. ((a) and (d)–(g) from Hooke and Hudleston, 1980; (b) from Hooke and Hudleston, 1981.)

Ice that forms from compaction of snow, perhaps with some addition of percolating meltwater, usually consists of crystals that are 2–4 mm in diameter (Figure 4.12a). Through a series of processes that we will refer to, collectively, as *dynamic recrystallization*, the texture and fabric of this ice are altered during deformation. Dynamic recrystallization, or simply recrystallization, is a consequence of the high local internal stresses mentioned above, and the resulting widely differing internal energies in adjacent grains.

One or more of three processes may be involved in recrystallization. In order of increasing energy difference between adjacent grains, these are *grain growth*, *polygonization*, and *nucleation of new grains* (Duval and Castelnau, 1995). (Note that the terminology for these processes differs among authors.) Grain growth results from relatively slow migration of grain boundaries. This migration is driven by the decrease in free energy that accompanies the reduction in total area of grain boundaries (Montagnat and Duval, 2000). Typical rates range from $\sim 10^{-3}$ mm a $^{-1}$ at -30°C and 1 kPa (local driving stress) to ~ 10 mm a $^{-1}$ at -10°C and 300 kPa (Duval *et al.*, 1983). The migration is driven by the curvature of the grain boundaries. Higher pressures occur on the concave sides of such boundaries, which is commonly the side of the smaller grain, and molecules tend to move from the high-pressure side to the low-pressure side of the boundary (Alley, 1992). Thus, smaller crystals disappear. The result is a characteristic texture with equant crystals of relatively uniform size (Figure 4.12b). Because temperatures in the accumulation zones of polar ice sheets are relatively constant to depths of a few hundred meters (see Figure 6.6a), grain boundary migration occurs at relatively constant rates and grain size thus increases nearly linearly with depth. At greater depths, grain size becomes approximately constant because polygonization, which decreases grain size, balances grain growth (Alley *et al.*, 1995).

Polygonization (also called *rotation recrystallization*) involves the alignment of dislocations to form a new grain boundary within a bent crystal. The crystal is thus divided into two grains with nearly the same orientation (Figure 4.12c, arrows). Under relatively high strain rates, polygonization begins at strains of $\sim 1\%$ (Duval and Castelnau, 1995), but at the much lower strain rates found in the central regions of continental ice sheets, cumulative strains can approach 100% without causing polygonization (Alley, 1992). Thus, polygonization occurs at relatively shallow depths in temperate glaciers, but is normally found only at depths greater than a few hundred meters in polar ice sheets.

Nucleation of new grains entails the appearance of small grains that are oriented for easy glide, with their basal planes parallel to the maximum resolved shear stress. When they first appear, such grains

are relatively unstrained in comparison with adjacent older deformed grains. As the free energy of the system can be lowered by migration of boundaries of the new grains into the adjacent ones, the new grains grow at the expense of the older ones (Alley, 1992). This is probably partly responsible for the interlocking textures seen in highly deformed ice (Figure 4.12d).

Such nucleation and grain growth (also called *migration recrystallization*) occurs at relatively high strain rates and predominantly at temperatures above ~ -10 °C. It is thus characteristic of basal ice in temperate glaciers and of ice in the lowermost few hundred meters of polar ice sheets.

Development of fabrics with preferred orientations of *c*-axes

As just noted, newly nucleated unstrained crystals tend to grow at the expense of older deformed ones. However, as they grow, the continued straining gradually rotates them into orientations that are no longer optimal, and they begin to accumulate strain energy. Consequently they, in turn, are eventually consumed by even newer grains. It is the resulting preference for orientations with basal planes parallel to the maximum resolved shear stress that results in the increase in creep rate, in laboratory experiments, after about 1% strain (Figure 4.8b). Preferred orientations of *c*-axes are the manifestation of this preference (Figure 4.13). Thus two basic processes are involved in the development of these *c*-axis fabrics: recrystallization and grain rotation.

Let us illustrate these processes by tracing the development of such fabrics, starting with ice near the surface in the accumulation area (Figure 4.12a). The *c*-axes of the crystals are either uniformly distributed or have a weak preference for vertical orientations (Figure 4.13a). The latter probably results from the orientation of snowflakes that have thin disk-like shapes, and thus, like a pile of poker chips, tend to lie flat as they accumulate. In addition, the vertical temperature gradient may have had some influence during sintering.

As the ice becomes buried, it is compressed vertically and stretched longitudinally and sometimes also laterally. Where longitudinal and lateral strain rates are comparable in magnitude, the stress field is referred to as *uniaxial compression* (Figure 4.14a), whereas if lateral strain rates are negligible it is *pure shear* (Figure 4.14b). In such stress configurations, slip occurs most readily on the basal planes of crystals whose *c*-axes are inclined at $\sim 45^\circ$ to the compression axis (Figure 4.14d). Thus crystals are nucleated in this orientation, and these crystals grow at the expense of adjacent more highly stressed ones, leading to a conical

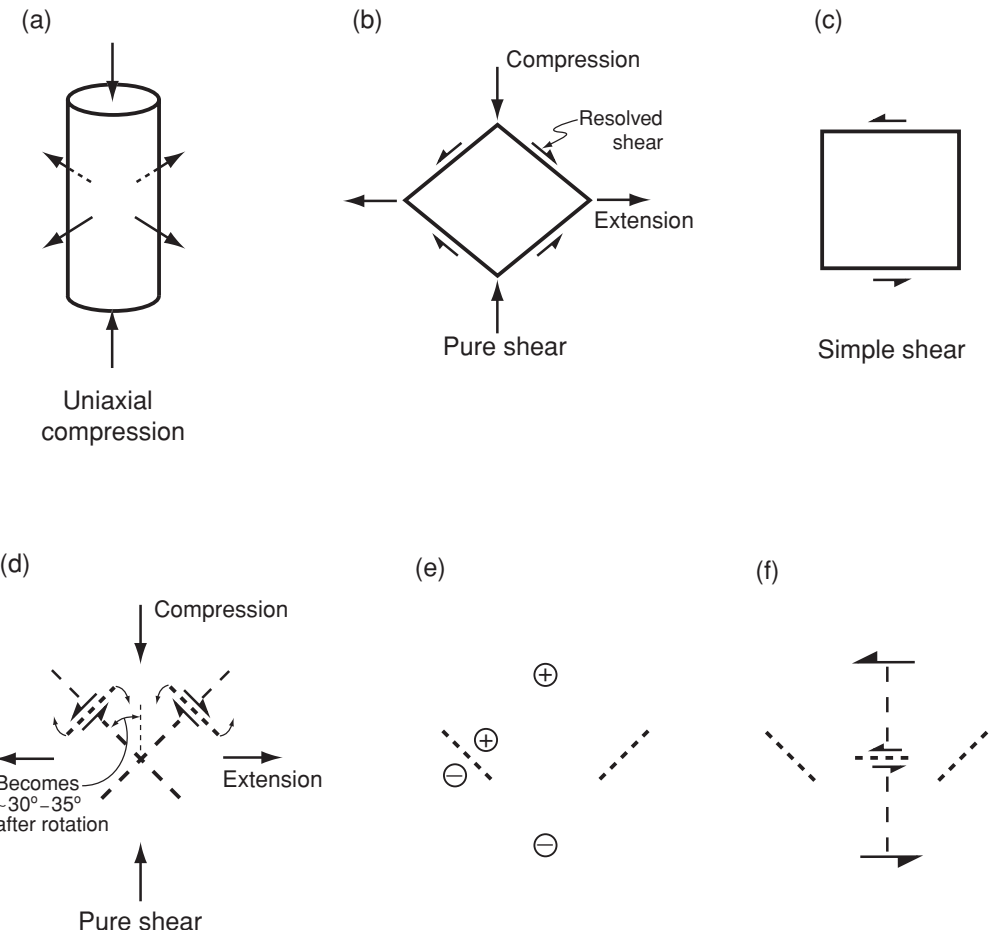


Figure 4.14. Stress configurations and their relation to orientations of c -axes. (a) Uniaxial compression. (b) Pure shear. There is no strain normal to the plane of the diagram. (c) Simple shear. (d) The c -axes and basal planes in a newly nucleated crystal in uniaxial compression or pure shear. With continued compression, the c -axes rotate toward the axis of compression. (e) Simple shear viewed parallel to the shear direction with basal planes also parallel to the shear direction as in the fabric of Figure 4.13f. The symbols \oplus and \ominus signify stress vectors directed into and out of page, respectively. (f) Simple shear viewed normal to the shear direction with basal planes inclined to the shear direction as in the fabric of Figure 4.13g. In (d)–(f) short-dashed lines show orientations of basal planes.

distribution of c -axes in uniaxial compression (a *small-circle* fabric: Figure 4.13b.) and to two maxima aligned in the direction of extension in pure shear (Figure 4.13c). (Small-circle fabrics are also commonly referred to as *girdle* fabrics, although “girdle” implies a great circle.) The vertical compression and lateral extension, however, have the effect

of rotating basal planes clockwise on the left and counterclockwise on the right in Figure 4.14d. Thus, as the crystals grow, the *c*-axes rotate toward the compression axis (Alley, 1992), with the result that the mean angle between the compression axis and the *c*-axes is typically only $\sim 30^\circ\text{--}35^\circ$, not 45° (Kamb, 1972; Hooke and Hudleston, 1980). Crystals that have been rotated too far, and thus become highly stressed, are resorbed, while nucleation develops new crystals in more favorable orientations.

If the ice at this depth is close enough to the bed, drag exerted by the bed results in a stress configuration approximating *simple shear* parallel to the bed (Figure 4.14c). Crystals with vertical *c*-axes are then preferred. The resulting fabrics, which are common in ice sheets (Gow and Williamson, 1976; Hooke and Hudleston, 1980), have single maxima that range from relatively broad (Figure 4.13d) to quite tight (Figure 4.13e).

The fabrics in Figures 4.13b,c,d all seem to form under roughly equivalent cumulative strain. The differences among them are primarily caused by stress configuration. As a class, we will refer to them as *broad single-maximum* fabrics.

Although the increase in creep rate associated with recrystallization usually begins at effective strains, ε_e (see Equation (2.11)) of ~ 0.01 in the laboratory (Figure 4.8b), broad single-maximum (and equivalent) fabrics are not particularly evident until $\varepsilon_e \cong 0.04$ and only become well developed at $\varepsilon_e = 0.4$ (Kamb, 1972; Jacka and Maccagnan, 1984). In the field, Hooke and Hudleston (1980) found that such fabrics first appeared at $\varepsilon_e \cong 0.7\text{--}0.8$. For reference, circles that have been deformed into ellipses by strains of these magnitudes have axial ratios of 1.02, 1.08, 2.22, and ~ 4.5 , respectively. Thus, creep rates increase long before a detectable preferred *c*-axis orientation develops.

In simple shear at cold temperatures or high strain rates (or high cumulative strains), the single-maximum fabric strengthens (Figure 4.13e). However, at lower strain rates and temperatures above -10°C , an unexpected fabric appears. First, the single maximum splits in two, with a maximum on either side of the shear direction (Figure 4.13f). The basal planes corresponding to these *c*-axis orientations are still parallel to the shear direction, but do not have optimal orientations (Figure 4.14e). Then, with increased cumulative strain, strain rate, or temperature, first one and then a second maximum appears inclined to the direction of shear (Figures 4.13g and 4.14f). These planes are definitely not well oriented for glide, and thus must stiffen the ice, at least slightly. These multiple-maximum fabrics appear at $\varepsilon_e \cong 1.3$ (Hooke and Hudleston, 1980). The corresponding axial ratio of the strain ellipse is ~ 15 .

The origin of these multiple-maximum fabrics is not understood. They have been attributed to annealing under conditions of near stagnation (Budd and Jacka, 1989) and have been reproduced in the laboratory

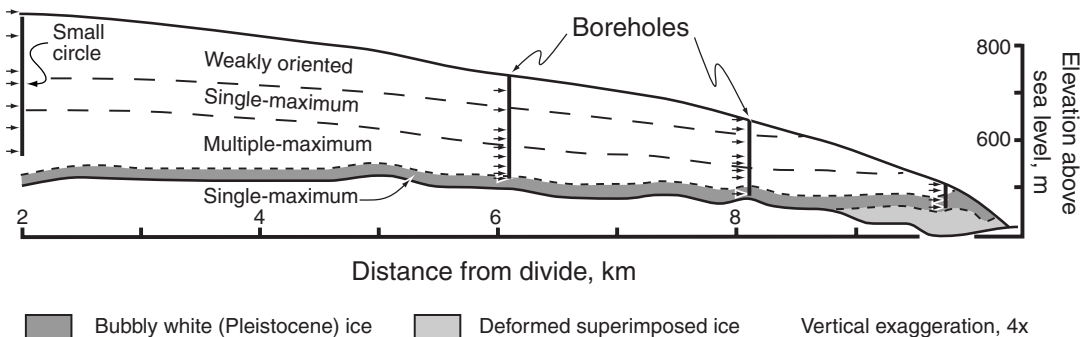


Figure 4.15. Vertical cross section along a flow line on Barnes Ice Cap showing zones characterized by particular fabrics. Arrows show locations of cores used to determine fabric type. (After Hooke and Hudleston, 1980.)

by repeatedly compressing a sample and then annealing it (Huang *et al.*, 1985). However, these processes are not consistent with the occurrence of such fabrics in ice that is actively deforming, as in Barnes Ice Cap (Figure 4.15) (Hooke and Hudleston, 1980).

Matsuda and Wakahama (1978) measured the orientations of *a*-axes as well as *c*-axes in ice with multiple-maximum fabrics. They did this by observing etch pits in the thin sections. In ice with four-maximum fabrics, they found that the *a*-axes of adjacent crystals were systematically aligned in a way that suggested mechanical twinning. Noting that strong shear deformation under high temperatures is required to produce such fabrics, they suggested that the large amount of plastic strain energy thus produced can be absorbed by propagation of twin boundaries without changing the relative structural relation between crystals or the crystal-boundary structure, and without resulting in strong bubble elongation.

Because the various fabrics appear to form under fairly specific conditions of cumulative strain, strain rate, and temperature, and because these parameters all tend to increase systematically with depth in the accumulation area of a glacier, fabric type also varies with depth. For example, in Barnes Ice Cap transitions from weakly oriented to broad single-maximum (or equivalent) fabrics occur at depths of 80–140 m, and the broad single maximum gives way to multiple-maximum fabrics at 140–200 m (Figure 4.15). At Byrd Station in Antarctica, the transition to broad single maximum fabrics (small circle variety) occurs at a depth of ~350 m. Then, a strong single-maximum fabric appears at ~1200 m and multiple-maximum fabrics show up at ~1830 m. Differences in temperature are probably largely responsible for the difference in depths to the transitions, although cumulative strain may also play a role; Barnes

Ice Cap is near or above -10°C throughout, whereas at Byrd Station the temperature exceeds -10°C only below 1900 m. In Barnes Ice Cap, as the various layers are advected outward they become exposed at the surface in the ablation area (Figure 4.15).

Summary

Given these various processes of recrystallization and crystal deformation, one may well ask how we should visualize the deformation of polycrystalline ice on an intergranular scale. Available evidence suggests that stresses are heterogeneous, that intracrystalline glide takes place on basal planes within individual grains, that this glide results in internal rotation of the crystal structure, and that nucleation of grains with basal planes parallel to the maximum resolved shear stress and resorption of grains that have rotated out of this orientation results in the development of fabrics with preferred orientations. Mismatches between adjacent grains resulting from unequal slip at grain boundaries are accommodated by grain-boundary migration and by rotation and translation of grains. These grain-boundary processes are thus likely to be rate limiting. Computer models incorporating these principles successfully simulate many characteristics of fabric evolution in ice sheets (Etchecopar, 1977; Van der Veen and Whillans, 1994).

Deformation mechanism maps

Our discussion so far has focused on the type of creep most commonly observed in glaciers, called power-law creep because the creep rate is proportional to the stress raised to some power >1 (Equation (4.4)). The dominant processes in power-law creep are dislocation glide and climb. For completeness, some other types of creep should be mentioned.

In recent years, scientists working on ice deformation mechanisms have found it useful to plot “maps” showing the deformation mechanisms operating at different temperatures and stresses (Figure 4.16). The temperature is usually normalized by dividing by the melting temperature in Kelvin, θ_{Km} . This is called the *homologous temperature*. Similarly, the stress is normalized by dividing by Young’s modulus. In Figure 4.16 the stress used is $\sqrt{3}\sigma_e$. Note that the equivalent octahedral stress is shown on the right ordinate.

The heavy lines in Figure 4.16 divide the diagram into fields in which a single deformation mechanism is dominant. Power-law creep occupies much of the right side of the diagram. Below and to the left of the power-law creep field is the field of diffusional flow. In this type of flow, atoms move from crystal boundaries that are under compression to ones that are

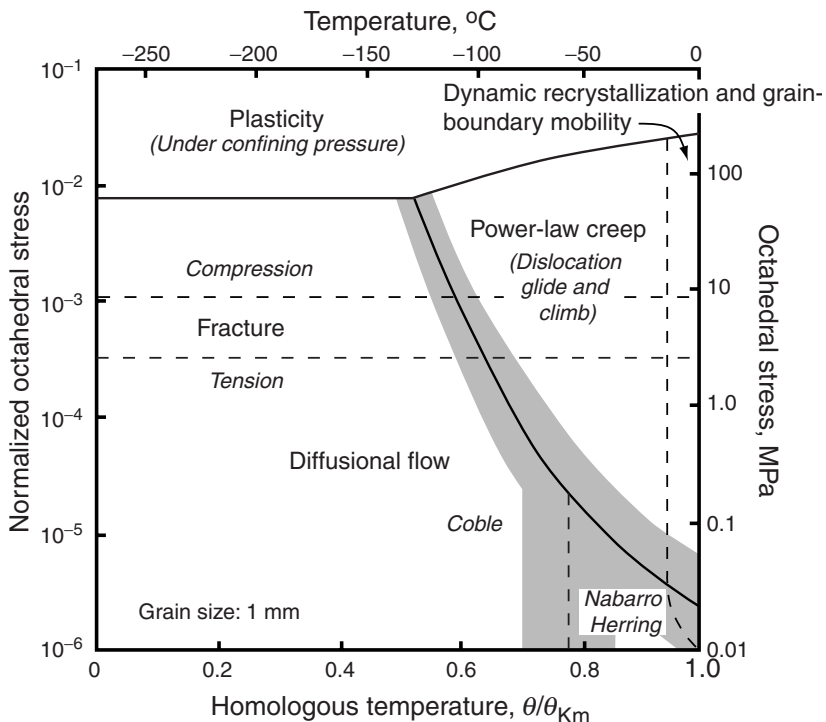


Figure 4.16. Deformation mechanism map for ice with a grain size of 1 mm. (Adapted with permission from Duval *et al.*, 1983, Figure 1. Copyright 1983 American Chemical Society.)

under tension. At low temperatures, atoms are believed to move along grain boundaries (grain-boundary or *Coble* creep) whereas at higher temperatures they probably move through the crystal lattice (lattice diffusion or *Nabarro–Herring* creep). These two diffusional creep fields are separated by a vertical dashed line at about $0.8\theta/\theta_{Km}$. The shading along the heavy lines separating these two diffusional creep fields from each other and from the power-law field represents the zone of overlap of the fields. On the right edge of the shaded zone, power-law creep contributes 90% of the deformation and on the left edge, diffusional creep contributes 90%.

At octahedral stresses between 2 and 10 MPa, fracture also contributes to the deformation. The onset of fracturing occurs at lower stresses in tension than in compression, so this field has an appreciable width. Under sufficiently large confining pressures, fracture is suppressed, and the upper part of the diagram is then accessible.

Another field shown on the diagram is that labeled “dynamic recrystallization and grain-boundary mobility”. At temperatures above about -10°C , the increase in creep rate with temperature is more rapid

than predicted by an activation energy of 79 kJ mol⁻¹. In addition, there is a rapid increase in the electrical conductivity of ice (Mellor and Testa, 1969), and a less striking but still significant increase in the heat capacity (Harrison, 1972). Finally, multiple-maximum fabrics are common in glacier ice deformed at temperatures above -10 °C, but rare or absent in ice below -10 °C (Hooke and Hudleston, 1980). The first three of these phenomena can be explained if grain-boundary melting begins at about -10 °C. Grain-boundary melting involves the formation of a widened zone with a liquidlike structure at grain boundaries and particularly at multiple grain junctions (Duval *et al.*, 1983; de La Chapelle *et al.*, 1995). This liquidlike layer is, in part, a consequence of impurities that become concentrated at grain boundaries, lowering the melting point (Equation (2.1)). In addition, molecules on such a surface are not well bonded to adjacent molecules on all sides, and thus form a liquidlike layer even in the absence of impurities. This layer can explain the increase in creep rate (as the liquid phase reduces grain interactions and thus attenuates the internal stress field), the increase in electrical conductivity (as impure water has a much higher conductivity than pure ice), and the increase in heat capacity (as some heat is absorbed by melting). Whether it can explain the development of multiple-maximum fabrics is uncertain, but attempts to develop a theory explaining these fabrics should take it into consideration.

In glaciers, stresses rarely exceed 0.2 MPa, and temperatures are rarely below -50 °C, so for our purposes only the lower right-hand corner of the deformation mechanism map is of interest. It appears from this part of the diagram that both diffusional and power-law creep should occur, as long as the grain size of the ice is about 1 mm. However, this is actually a lower limit for the grain size in glacier ice. Grain sizes of 10–30 mm are common in polar and polythermal glaciers (Figure 4.12), and much larger crystals can be found deep in polar glaciers and in temperate glaciers. As grain size increases, the power-law creep field increases at the expense of the diffusional creep field. This is intuitively reasonable as larger grain sizes imply longer diffusion paths.

In diffusional creep, the strain rate is linearly proportional to stress, in contrast to the situation with power-law creep. At present, there seems to be no unequivocal field evidence suggesting that pure diffusional creep is important in glaciers. However, Alley (1992) and Montagnat and Duval (2000) have suggested that during grain growth (p. 58), migration of grain boundaries can annihilate dislocations and thus reduce the dislocation density below that predicted by Equation (4.3). In this case, n is likely to be less than 3. Thus, diffusive processes associated with grain-boundary migration may be important, in combination with dislocation glide, to depths of a few hundred meters in colder parts of the Antarctic

and Greenland ice sheets. On the other hand, in a study of floating ice shelves bordering the Antarctic ice sheet, Thomas (1973b) and Jezek *et al.* (1985) found that power-law creep with $n \approx 3$ seemed to prevail at temperatures of ~ -15 °C and stresses of only 0.04–0.06 MPa.

A flow law for glacier ice

In the preceding sections of this chapter we have looked at details of the deformation process, and have found some uncertainty, particularly in attempts to identify the rate-limiting process. In the remainder of this book, we will frequently need a simple yet reasonably accurate expression relating stress and strain rate in ice. In general, we will use the expression:

$$\dot{\varepsilon}_e = \left(\frac{\sigma_e}{B} \right)^n \quad (4.5)$$

which, as mentioned briefly in Chapter 2, is often referred to as Glen's flow law, as it was first suggested by John Glen (1955) on the basis of his early uniaxial compression experiments on ice.

As noted, the exponent, n , depends on the creep mechanism operating. A substantial body of experimental data on laboratory ice and on natural glacier ice supports adopting a value of 3 for this exponent (Hooke, 1981), and this seems to be consistent with theoretical expectations (Equation (4.4)). Older experimental data suggesting a lower value at low stresses are often questionable because tests were not continued long enough to be sure that the transient phase of creep (Figure 4.8) was complete. However, recent experiments by Pimienta and Duval (1987) and studies by Alley (1992) and Montagnat and Duval (2000) again raise the possibility of values between 1 and 2 for deformation at low stresses, temperatures, and cumulative strains. As noted, they argue that grain-boundary migration is particularly efficient under these conditions so internal strain energy is small, and the density of dislocations therefore does not increase as rapidly with stress as suggested by Equation (4.3). Healing of dislocations by diffusional processes may also limit the density (Alley, 1992).

B is a measure of the viscosity of the ice. The viscosity depends upon a number of factors; we have already mentioned the importance of temperature and fabric, and have hinted at the role of water content, particularly along grain boundaries. Other factors of possible significance are pressure, texture, and other molecular or macro-scale structural features such as dislocation density or grain-boundary structure. Thus, Equation (4.5) with a constant value of B is useful only in situations in which an average value of B can be chosen that is reasonably representative of the viscosity of the ice mass as a whole. In the remainder of this

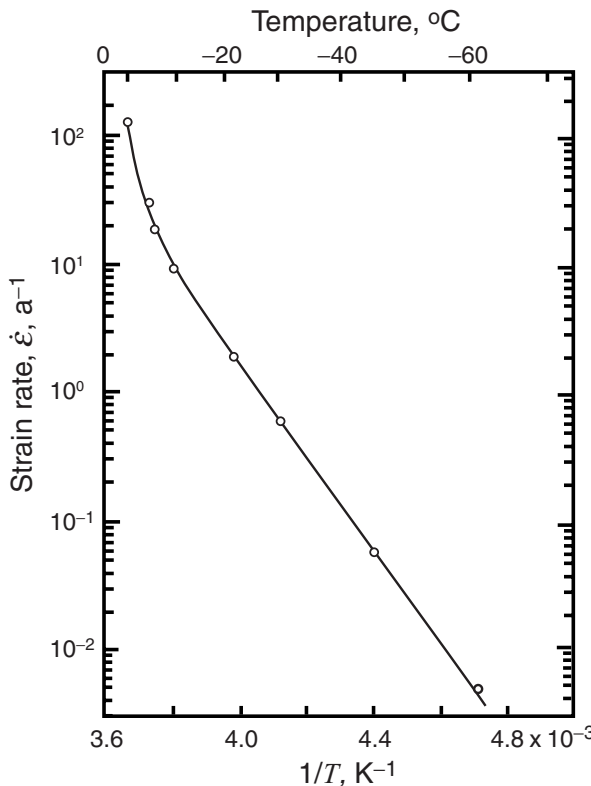


Figure 4.17. Results of a laboratory experiment on the variation of strain rate with temperature. All experiments were run at the same stress. The slope of the straight part of the curve is proportional to the activation energy. (After Mellor and Testa, 1969, Figure 3. Reproduced with permission of the International Glaciological Society.)

section, we will explore modifications of Equation (4.5) that incorporate some of these variables.

The easiest variable to incorporate is temperature, thus:

$$\dot{\epsilon}_e = \left(\frac{\sigma_e}{B_0} \right)^n e^{-\frac{Q}{R\theta_K}} \quad (4.6)$$

where, as before, Q is the activation energy for creep. B_0 is now a reference parameter; literally, it is the viscosity at $\theta_K = \infty$, but this is physically meaningless. B_0 is still a function of the other parameters listed above, such as fabric, texture, microstructure, and so forth.

The activation energy for a process can be determined by running a series of tests at constant stress but varying temperature. In the case of the activation energy for power-law creep, the parameter measured is the strain rate, $\dot{\epsilon}$, and Q is determined from:

$$\frac{\dot{\epsilon}_1}{\dot{\epsilon}_2} = e^{\frac{Q}{R}(\frac{1}{\theta_{K2}} - \frac{1}{\theta_{K1}})} \quad (4.7)$$

where the subscripts 1 and 2 refer to data from two tests at the same σ_e but different temperatures, θ_K . Equation (4.7) is readily derived from Equation (4.6). Figure 4.17 shows a plot of $\ln \dot{\epsilon}$ vs $1/T$ in such a series

of tests. The data points at lower temperatures fall on a straight line with slope Q/R . However, at temperatures above $-10\text{ }^{\circ}\text{C}$, the points deviate from a straight line in a direction implying a higher activation energy. In other words, the increase in creep rate with temperature is greater than expected. This is because the grain-boundary processes discussed above begin to influence the creep rate. In particular, the decrease in grain boundary interactions with increasing water content probably allows the creep rate to increase faster than is the case at lower temperatures.

For some applications, the temperature effect can be represented by:

$$\dot{\varepsilon} = \dot{\varepsilon}_0 e^{k\theta_n} \quad (4.8)$$

where k is a “constant” that is typically between 0.1 and 0.25 $\text{ }^{\circ}\text{C}^{-1}$, θ_n is the temperature in Celsius degrees (hence a negative number), and $\dot{\varepsilon}_0$ is a reference strain rate. This relation has the benefit of mathematical simplicity, and it is a reasonable approximation in situations in which the temperature varies within a restricted range. However, k varies slowly with temperature and with Q , so the approximation becomes increasingly imperfect as the temperature range increases.

The next parameter we will incorporate is hydrostatic pressure, P , thus:

$$\dot{\varepsilon}_e = \left(\frac{\sigma_e}{B_0} \right)^n e^{-\frac{Q+PV}{R\theta_K}} \quad (4.9)$$

where V is the activation volume for self-diffusion, and the quantity $(Q + PV)$ is the *activation enthalpy*. In ice, it turns out that V is very low, and it is not clear whether it is positive or negative. Rigsby (1958) conducted some experiments at constant temperature that suggested a slight increase in creep rate with P , implying a negative V . However, when he varied the temperature in such a way that the difference between the experimental temperature and the melting-point temperature remained constant, the creep rate was essentially independent of pressure. In other words, V was 0. Later experiments have suggested that it might be slightly positive. In any case, it is small enough to be neglected in most if not all applications.

Some experiments have been interpreted as indicating that $\dot{\varepsilon}$ increases with increasing grain size (Baker, 1978). As grain size is believed to influence the creep rate in metals, this was not unexpected. However, subsequent experiments failed to find a dependence on grain size (see, for example, Jones and Chew, 1983; Jacka, 1984). It was thus suggested that Baker’s samples were too small, and that samples with larger crystals may have been able to creep faster because too much of the strain was occurring in single crystals, favorably oriented for basal glide, that were not buttressed by surrounding crystals with unfavorable

orientations. In later experiments, however, Baker (1981, 1982) used larger samples, deformed in simple shear, and still found a clear dependence of $\dot{\epsilon}$ on crystal size.

It is true that crystal size varies directly with temperature and inversely with strain rate. Crystals in rapidly deforming cold ice may be in the millimeter to submillimeter size range, while those in slowly deforming temperate ice may exceed a decimeter. The key question is whether these variations in size are merely a consequence of the temperature and strain rate, or alternatively whether they actually influence the strain rate.

The effect of crystal orientation on the strain rate is normally included in the flow law by multiplying the right-hand side by a factor, E , called the *enhancement factor*, thus:

$$\dot{\epsilon}_e = E \left(\frac{\sigma_e}{B_o} \right)^n e^{-\frac{Q}{R\theta_K}} \quad (4.10)$$

Rigorously, however, Glen's flow law is based on the assumption that the material is isotropic (see Chapter 9). Thus, adding an enhancement factor in this way to accommodate anisotropy is tacit admission of the failure of this assumption.

We do not yet have enough understanding of the recrystallization process to write an empirical relationship between E and the factors such as temperature, strain rate, and cumulative strain on which it depends (Hooke and Hudleston, 1980). Therefore, selection of the appropriate values of E to use in any given situation is largely subjective.

Laboratory experiments provide some basis for estimating E . Russell-Head and Budd (1979) and Baker (1981, 1982) studied natural ice with a single-maximum fabric. When deformed in simple shear in the laboratory, with the sample oriented so that the c -axes were approximately perpendicular to the shear plane, this ice deformed about four times faster than comparable samples with random c -axis orientations. Russell-Head and Budd also found that a section of a borehole in Law Dome, Antarctica, that passed through ice with a single-maximum fabric deformed about four times faster than it would have in ice without such a fabric. More recently, Budd and Jacka (1989) and Jacka and Maccagnan (1984) have suggested that enhancement factors of ~ 3 are reasonable for ice in uniaxial compression once a small-circle fabric has developed, and that factors of 8–10 may be appropriate for ice in simple shear. Borehole deformation experiments in Barnes Ice Cap suggest that, relative to ice with a broad single-maximum fabric (Figure 4.13d), ice with a two-maximum fabric (Figure 4.13f) deforms about 10% faster while that with a three- or four-maximum fabric (Figure 4.13g) deforms about 40% slower (Hooke and Hudleston, 1980). The former is reasonable, but

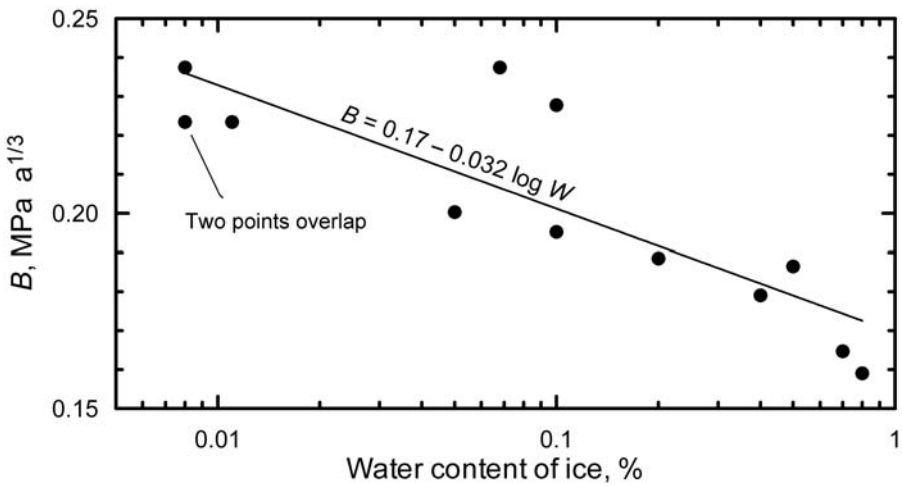


Figure 4.18. Variation in B with water content of the ice. (Data reported by Duval, 1977.)

the latter, while in the expected direction, is probably unreasonable in magnitude.

Finally, we return to the effect of the water content on the creep rate. This was studied by Duval (1977) in a pioneering set of sophisticated experiments. His results, expressed in terms of the decrease in B with increasing water content, are shown in Figure 4.18. With an increase in water content from 0.01% to 0.8%, B decreases from ~ 0.24 to ~ 0.16 MPa $a^{1/3}$. Lliboutry (1983) reports that the water content of basal ice of temperate glaciers typically varies between 0.6% and 0.95%. Based on the line in Figure 4.18, this corresponds to a variation in B from 0.177 to 0.170, and hence in $\dot{\epsilon}$ of $\sim 12\%$. The individual data points in Figure 4.18 suggest an even greater sensitivity. Lower water contents, and hence higher values of B , are likely in temperate ice of polythermal glaciers.

Fracture

At sufficiently high stresses, ice fractures (Figure 4.16). Crevassing, resulting from high tensile stresses, is the type of fracturing with which people are most familiar. However, fracturing near the base of the sub-aerial part of a calving face may be largely a consequence of crushing (compression).

Owing to the importance of fracture in design of structures ranging from buildings to airplanes, the study of *linear elastic fracture mechanics* is well developed, and we will only skim the surface of this field. Basically, flaws or microcracks exist in most if not all crystalline

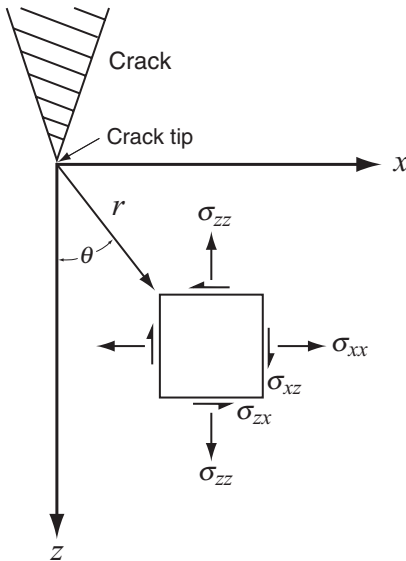


Figure 4.19. Stress field on an infinitesimal element located a distance r from a crack tip. (Modified from Kenneally, 2003.)

materials, and any far-field stresses on the material are amplified at the tips of these cracks. Thus, cracks may propagate at stresses far below the strength of an unflawed specimen of the material.

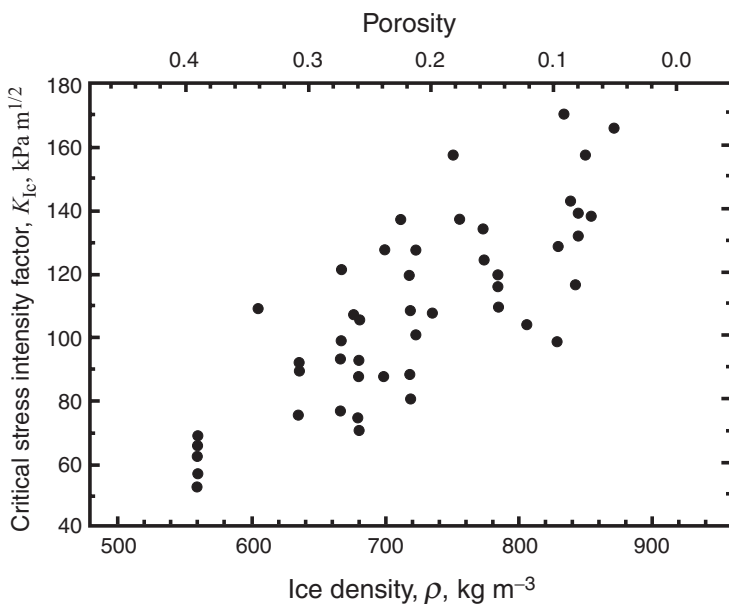
The elastic stress field around the tip of a vertical crack in the surface of a solid of infinite horizontal extent, subjected to a far-field tensile stress, σ , that is normal to the crack, is given by:

$$\begin{aligned}\sigma_x &= \frac{K_I}{\sqrt{2\pi}r} \cos \frac{\theta}{2} \left(1 + \sin \frac{\theta}{2} \sin \frac{3\theta}{2} \right) \\ \sigma_z &= \frac{K_I}{\sqrt{2\pi}r} \cos \frac{\theta}{2} \left(1 - \sin \frac{\theta}{2} \sin \frac{3\theta}{2} \right) \\ \sigma_{xz} &= \frac{K_I}{\sqrt{2\pi}r} \sin \frac{\theta}{2} \cos \frac{\theta}{2} \cos \frac{3\theta}{2}\end{aligned}\quad (4.11)$$

(see, for example, Lawn, 1993, p. 25). Here, r is the distance from the crack tip measured along a line making an angle θ with the crack axis (Figure 4.19), and K_I is a parameter known as the *stress intensity factor*. In general, $K_I = \beta\sigma\sqrt{a}$, where a is the crack length. Thus, K_I increases as either the far-field stress or crack length increase. The β is a geometrical parameter that, in our case, depends upon factors such as the spacing of crevasses, the ice thickness, and the far field stress. Thus, K_I , and particularly β , describe how the far-field stresses are amplified or intensified around a crack tip.

Clearly, high values of K_I translate into high stresses around the crack tip and, if the stresses become high enough, the crack will propagate. Rather than express this critical value in terms of the stresses themselves,

Figure 4.20. Variation of K_{lc} with density. Based on laboratory measurements. (After Rist *et al.*, 1999. Reproduced with permission of the authors and the American Geophysical Union.)



the standard procedure is to express it in terms of a value of K called the fracture toughness, K_{lc} . K_{lc} is a material property of the medium. If K_l exceeds K_{lc} , the fracture will propagate unstably. Rist *et al.* (1999) have summarized their own measurements of K_{lc} on ice cores from Antarctica and other workers' measurements on other types of samples and find that it increases approximately linearly with density (Figure 4.20). The scatter in the data is large, however.

Stress intensity factors are complicated and often tedious to derive, but they can be obtained from handbooks such as Sih (1973). Conveniently, they obey the principle of superposition; thus, in problems with a complex stress configuration, if one can obtain stress intensity factors for each of the stresses separately, they can be added to obtain the stress intensity factor for the whole problem (Kanninen and Popelar, 1985, p. 27). We will illustrate this below.

The alert reader may have noticed that the stresses in Equations (4.11) become infinite as $r \rightarrow 0$. However, deformation in a region immediately around the crack tip is plastic, and this keeps the stresses finite. To estimate the radius, r_p , of this plastic region, take $\theta = 0$ in the first or second of Equations (4.11), assume that plastic behavior will occur once the stress exceeds 0.1 MPa (a commonly cited plastic "yield strength" for ice), adopt a value for K_{lc} of 0.16 MPa $\text{m}^{-1/2}$, and solve for r_p . The result is $r_p \approx 0.4$ m. The principles of linear elastic fracture mechanics only apply if r_p is small compared with a . As we are concerned principally

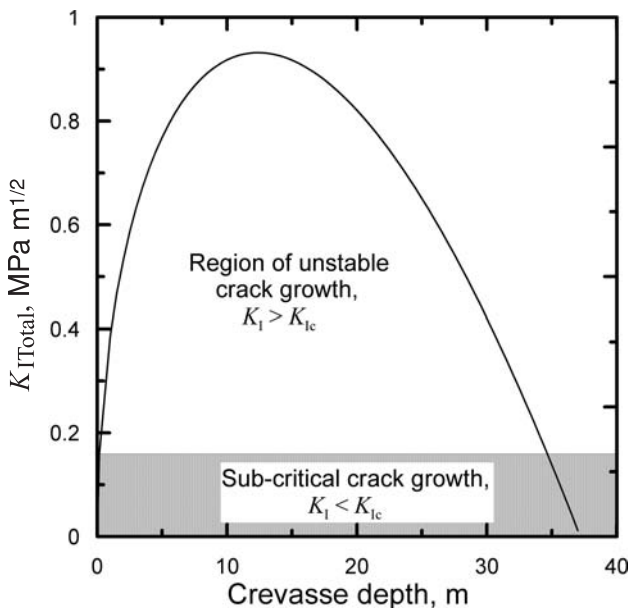


Figure 4.21. Variation in stress intensity factor with crevasse depth for an air-filled crevasse formed by a tensile stress of 0.2 MPa. (Modified from Kenneally, 2003.)

with crevasses, and as most crevasses reach depths of at least 10–20 m, this condition is satisfied.

Let us consider the case of a single crevasse in a glacier of infinite horizontal extent subjected to a tensile stress, σ . Two stresses are involved: the tensile stress that tends to open the crack and the weight of the overlying ice that tends to squeeze it closed. We need a stress intensity factor for both. For the case of a crack of depth d in a medium of thickness $H \gg d$ subjected to a tensile stress, σ , $K_{It} = 1.12\sigma\sqrt{\pi d}$ (Kanninen and Popelar, 1985, p. 31). The subscript “t” signifies tension. The hydrostatic stress from the weight of the ice is $-\rho_i g z$, where ρ_i is the density of ice, g is the acceleration of gravity, and z is the depth below the surface. The negative sign indicates that the stress is compressive. For a crack of depth d with a load varying from 0 at the surface to $-\rho_i g d$ at the crack tip, $K_{Io} = -0.683\rho_i g d \sqrt{\pi d}$ (Kenneally, 2003). Here, the subscript “o” is used for overburden. Vaughan (1993) found that tensile stresses between 0.09 and 0.32 MPa were necessary to open crevasses. (These are considerably lower than the stresses bounding the fracture field in Figure 4.16, probably because glacier ice has more and deeper surface flaws that can develop into crevasses.) For purposes of illustration, let us assume $\sigma = 0.2$ MPa. $K_{ITotal} = K_{It} + K_{Io}$ then varies with crevasse depth as shown in Figure 4.21.

From Figure 4.21, we see that once a crack ~ 0.16 m long is formed, K_{ITotal} exceeds K_{lc} and the crack will propagate unstably to a depth

of ~ 35 m. The depth, of course, depends on σ , but this is a realistic depth for crevasses.

Of considerable interest in view of the recent collapse of the Larsen B Ice Shelf mentioned in Chapter 3, is the effect of water on crevasse depth. By analogy with the K_{Ic} above, the stress intensity factor for stresses induced by water pressure in a crevasse that is filled with water is $K_{Iw} = 0.683\rho_w gd\sqrt{\pi d}$, where ρ_w is the density of water. K_{Iw} is positive because the water pressure tends to open the crevasse. Because $\rho_w > \rho_i$, K_{ITotal} , which now includes K_{Iw} , increases continuously with depth. Thus, once it exceeds K_{Ic} , it never drops below K_{Ic} again, and the crevasse will penetrate to the bed.

Three additional factors that influence crevasse depth are: (1) the presence of low-density firn at the surface, (2) the water level in the crevasse if it is not filled, and (3) the effect of other crevasses. In all three cases, the consequences of taking these factors into consideration are fairly obvious. Low-density firn reduces K_{Ic} so crevasses penetrate deeper; if there is not enough water in the crevasse, K_{Iw} will not exceed K_{Ic} and the crevasse may not penetrate to the bed; and if there is a field of crevasses, the tensile stress will be relieved by adjacent crevasses and no one crevasse will penetrate as deeply as would a single crevasse. Stress intensity factors can be obtained for these three situations (Van der Veen, 1998), but the algebra, while straightforward, becomes considerably more complicated and is beyond the scope of this book.

Summary

In this chapter we first reviewed the crystal structure of ice, and noted that there are imperfections in this structure, called dislocations, that allow ice (and other crystalline materials) to deform under stresses that are low compared with the strength of individual molecular bonds. Processes that may limit the rate of deformation are those which (1) inhibit motion of a dislocation in a single crystallographic plane (drag), (2) prevent dislocations from climbing from one crystallographic plane to another to get around tangles, (3) impede motion on certain crystallographic planes, and (4) inhibit adjustments of boundaries between crystals.

Experimental data do not, at present, provide a basis for choosing between these possible rate-limiting processes. However, the drag mechanism does provide a theoretical basis for the commonly observed value of the exponent, n , in the flow law (see Equation 4.4). Perhaps equally important, however, are the mechanisms that allow adjustment of grain boundaries.

Because some crystals in a polycrystalline aggregate are not oriented for easy glide, stress concentrations develop. These result in

recrystallization by three distinct processes: grain growth, polygonization, and nucleation of new grains. Recrystallization leads to preferred orientations of c -axes, and hence to more rapid deformation. The principal processes involved in the development of these fabrics appear to be nucleation of new grains and rotation of grains as slip occurs on their basal planes.

To place the creep processes in ice in a more general framework, we introduced a deformation mechanism map in which we displayed the range of temperatures and stresses under which different deformation processes occur. Within the temperature and stress ranges normally found in glaciers, power-law creep is likely to be the dominant process although diffusional creep may occur in some low stress situations.

Next, we introduced Glen's flow law, and related the exponent, n , in the flow law to the creep mechanisms discussed earlier. Then we considered how temperature, pressure, texture, fabric, and water content affect the viscosity parameter, B . Temperature and pressure effects may be incorporated into the flow law by rigorous, physically based modifications, whereas *ad hoc* procedures based on empirical evidence are used to incorporate the other effects.

Finally, we introduced principles of linear elastic fracture mechanics and demonstrated that these principles can be used to estimate crevasse depths.

Chapter 5

The velocity field in a glacier

Many problems in glaciology require an understanding of the flow field in a glacier. For example, the way in which flow redistributes mass determines the shape of a glacier, and also the rapidity with which glaciers respond to climatic change. Flow also redistributes energy and thus affects the temperature distribution. This, in turn, has important implications for the nature of the coupling with the glacier bed. Spatial variations in speed, or strain rates, are of concern to structural geologists using glaciers as analogs for deformation of rocks. From a geomorphic perspective, the entrainment of debris and the character of moraines constructed from this debris are dependent upon the flow field. In short, understanding the flow field is fundamental to the analysis of many problems in glacier mechanics.

For a full description of the flow field in a glacier, we need the horizontal and vertical components of the velocity at every point. By making several assumptions, we can obtain approximate solutions to this problem that will give insights into certain characteristics of glaciers and the landforms they produce. Initially, we will limit the analysis to two dimensions and also assume a steady state.

We will begin by studying the distribution of horizontal velocity. Given the pattern of accumulation and ablation over a glacier, we can use conservation of mass to determine the mean (depth-averaged) horizontal velocity. Then, by using conservation of momentum and a simplified version of the flow law (Equation (4.5)), we will consider the variation in horizontal velocity with depth in an ice sheet and in a valley glacier. Differences between these solutions and measured velocity distributions reveal inadequacies of the theory, and draw attention to the need for a

better understanding of the basal boundary condition. Finally, by integrating the velocity over depth, we calculate the mass flux, and also obtain an expression for the mean velocity in terms of the glacier thickness.

The vertical velocity field is treated next. Again we will use the steady-state assumption and the pattern of mass balance (conservation of mass) to determine the vertical velocity at the surface. We then use the longitudinal strain rate, or rate of stretching in the longitudinal direction, at the surface to estimate its variation with depth, and thus calculate the variation in vertical velocity with depth. This yields an approximation to the full velocity field.

Next, we discuss the role of drifting on the flow field, and show that drifting patterns at the surface of an ice sheet can be traced at depth using radio echo sounding techniques. Drifting also affects the topography of a glacier surface, and plays an important role in the formation of certain types of moraine. Finally, we will explore inhomogeneous flow in ice sheets, as manifested by ice streams.

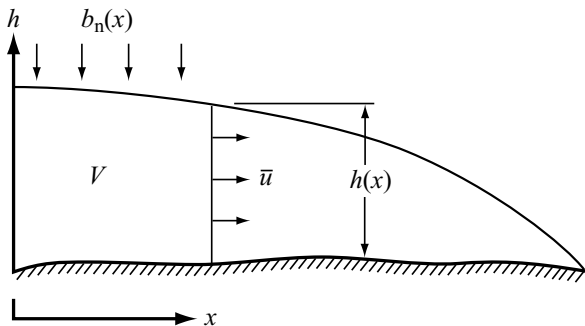
Measurement of velocity

Before describing the velocity field, a brief overview of measurement techniques may be helpful. In the early days of glaciology, velocity measurements were commonly made by triangulation from fixed points on stable surfaces off of the glacier. I have spent many hours peering through a theodolite at stakes drilled into a glacier. In the 1970s, electronic theodolites with laser distance-ranging capabilities greatly reduced the effort needed to make a measurement. Because the distance can be measured directly with such an instrument, a stake location can be determined by occupying only one fixed point rather than two, and electronic display of angles saves hours of adjusting a vernier. Later technological developments have resulted in computer-driven systems that can activate the theodolite and track the stakes. Thus, measurements can be made automatically as often as desired.

Velocity measurements far from stable fixed points are next to impossible with theodolite-based techniques. The advent of geographical positioning systems (GPS) technology solved that problem. GPS units measure the distance to a fleet of satellites with orbits that are known very accurately. With the most precise GPS units, the location of a point can be determined to within a couple of centimeters. Such units are now used to measure rates of continental drift.

An exciting development that is quickly leading to a much better understanding of flow fields in large ice sheets is the use of satellite images taken at, say, intervals of days to a year or so, to determine the velocity field. The images are coregistered based on the assumption that

Figure 5.1. Schematic diagram illustrating dependence of \bar{u} on b_n on an ice sheet.



certain features are stationary or moving only slowly compared with others. Then, cross-correlation techniques are used to compare crevasse patterns or other recognizable moving features on the two images and to determine how far they have moved between the dates of the respective images (Bindschadler and Scambos, 1991; Whillans and Tseng, 1995). High-speed digital computers are used to make these comparisons. In this way, a detailed quantitative map of the flow field can be produced. This technique, called satellite interferometry, is revolutionizing the measurement of velocities that, a scant 35 years ago, could be obtained only by tedious precision surveying with a theodolite.

Balance velocity

The general pattern of flow in a glacier is determined by the net budget. Consider an idealized glacier which, over a period of years, is in a steady state so its thickness (or surface profile) does not change. Then, at some distance, x , from the divide, the mean horizontal velocity averaged over depth is:

$$\bar{u} = \frac{1}{h(x)} \int_0^x b_n(x) dx \quad (5.1)$$

where $h(x)$ is the glacier thickness, and for convenience, the units of b_n are taken to be meters of ice per year (Figure 5.1). This equation is an expression of the principle of *conservation of mass* in an incompressible medium. As much mass must be moved out of the control volume, V , by flow, $\bar{u} h(x)$, as enters it by accumulation on the surface, $\int b_n(x) dx$. The velocity \bar{u} is called the *balance velocity*.

Balance velocities on the Antarctic ice sheet are shown in Figure 5.2. To calculate these velocities, Huybrechts *et al.* (2000) used detailed maps of the surface and bed elevations to obtain ice thicknesses at nearly

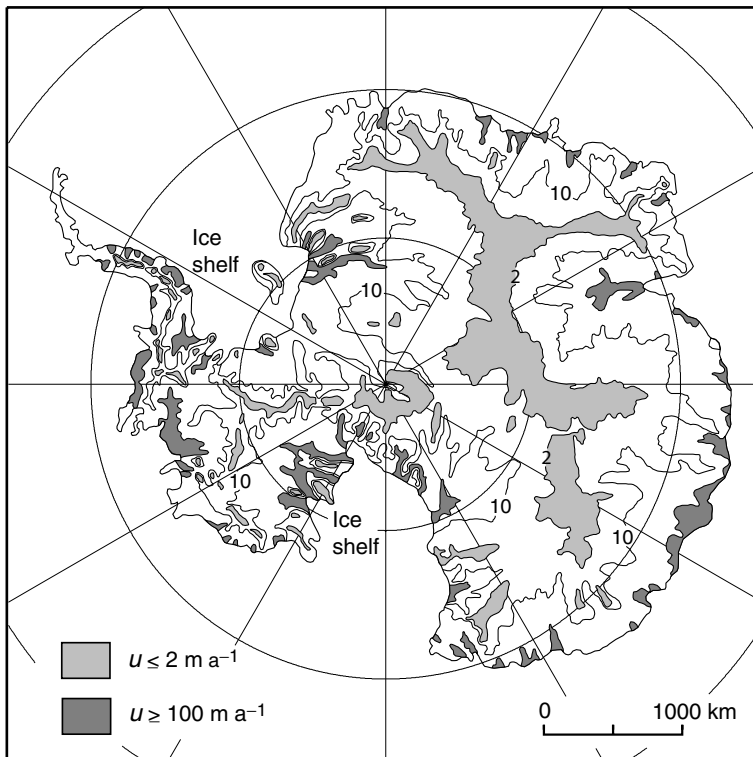


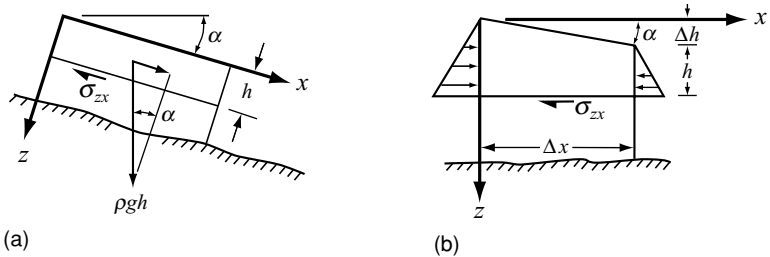
Figure 5.2. Balance velocities on the Antarctic ice sheet. (Modified from Huybrechts *et al.*, 2000, Figure 4. Reproduced with permission of the author and the International Glaciological Society.)

80 000 points of a grid. They then used the surface elevations to calculate surface slopes, and hence directions of ice flow. This allowed the calculation of balance velocities, using a two-dimensional form of Equation (5.1) to take convergence and divergence of flow into consideration. Ice divides show up well on the map as regions of essentially zero velocity. Note also the general increase in velocity toward the coast, and the focusing of flow into relatively narrow zones near the coast. Because most of the ice loss from Antarctica is by calving, there is no decrease in velocity near the coast as there would be if ice were lost by melting in an ablation zone of appreciable width.

Shear stress distribution

To determine the velocity distribution at depth in a glacier, we will find, below, that we need an expression for σ_{zx} as a function of z . Thus, we digress briefly from the principal objectives of this chapter to derive two similar expressions for σ_{zx} that are commonly used in the literature. The derivations differ only in the orientation of the axes and of the plane on which σ_{zx} operates.

Figure 5.3. Derivations of two alternative expressions for the shear stress, σ_{zx} , on a plane at depth h .



Consider, first, the situation in Figure 5.3a. The origin is at the surface. The x -axis is taken parallel to the surface, which slopes at an angle α . The z -axis points downward, normal to the surface. We want the shear stress on a plane at depth h . The column of ice is taken to be 1 m on a side. Therefore, the weight of the column is ρgh , where ρ is the density of ice and g is the acceleration due to gravity. The component of that weight parallel to the plane of interest is, thus, $\rho gh \sin \alpha$. For static equilibrium, this must be balanced by a shear stress on the plane, so:

$$\sigma_{zx} = -\rho gh \sin \alpha. \quad (5.2a)$$

The shear stress is negative because it acts in the negative x -direction on a plane with an outwardly directed normal in the positive z -direction (see p. 5 and Figure 2.3).

Next, consider the situation in Figure 5.3b. The x -axis is now horizontal and the z -axis is vertical. Again, the origin is on the surface and the column is of unit cross-sectional area. On the right side of the column, the plane of interest is at depth h below the surface. To a good approximation, the hydrostatic (or lithostatic) pressure at this depth is ρgh and the pressure varies linearly with depth. Thus, the mean pressure is $\frac{1}{2}\rho gh$, and the force on this side is $\frac{1}{2}\rho gh h$, where the second h represents the area of the face. Similarly, on the left side, the force is $\frac{1}{2}\rho g(h + \Delta h)^2$. The force on the plane of interest is $-\sigma_{zx} \Delta x$. Summing forces on the column yields:

$$\frac{1}{2}\rho g(h + \Delta h)^2 - \frac{1}{2}\rho gh^2 - (-\sigma_{zx} \Delta x) = 0$$

Expanding the first term, neglecting the term in Δh^2 , noting that $\tan \alpha = \Delta h / \Delta x$, and rearranging terms leads to:

$$\sigma_{zx} = -\rho gh \tan \alpha \quad (5.2b)$$

This equation is appropriate for a situation in which both the x -axis and the plane of interest are horizontal, but the glacier surface is sloping.

Because glacier-surface slopes are normally small, $\sin \alpha \approx \tan \alpha \approx \alpha$. Thus, Equations (5.2a) and (5.2b) are nearly interchangeable, and for small slopes we commonly write:

$$\sigma_{zx} = -\rho g h \alpha \quad (5.2c)$$

Note that in a coordinate system in which the z -axis is directed upward, σ_{zx} would be positive.

Local stresses may be augmented or reduced by gradients in longitudinal stress, σ_{xx} . Thus, Equations (5.2) provide only an estimate of σ_{zx} , and they cannot be used to calculate changes in σ_{zx} over short distances. As a rule of thumb, the values of h and α that are used in Equations (5.2) should be averages over horizontal distances that are several times the ice thickness.

Horizontal velocity at depth in an ice sheet

Demorest (1941, 1942) argued that the horizontal velocity in a glacier should increase with depth. He thought that the pressure of the overlying ice would soften the deeper ice, making it flow faster. Nye (1952a), however, pointed out that this concept was physically unsound because the faster-moving deeper ice would exert a shear stress on the overlying ice, and there would be no corresponding resisting forces to oppose this shear stress. Therefore, the overlying ice must move at least as fast as that below. We now know from numerous borehole deformation experiments that Nye's analysis was basically correct.

To pursue Nye's reasoning quantitatively, we start with the flow law, Equation (4.5), and assume that strain rates other than $\dot{\epsilon}_{xz}$ and $\dot{\epsilon}_{zx}$ and stresses other than σ_{xz} and σ_{zx} are negligible. Then, using Equations (2.10) and (2.11), and making use of the symmetry of the tensor so that $\dot{\epsilon}_{xz} = \dot{\epsilon}_{zx}$ and $\sigma_{xz} = \sigma_{zx}$ we obtain:

$$\dot{\epsilon}_{zx} = \left(\frac{\sigma_{zx}}{B} \right)^n \quad (5.3)$$

By using an equation analogous to (2.6a) and assuming that all of the shear takes place in the plane normal to z so $\partial w / \partial x = 0$, the mode of deformation that we identified as simple shear in Chapter 4 (see Figure 4.14c), this becomes:

$$\frac{du}{dz} = 2 \left(\frac{\sigma_{zx}}{B} \right)^n \quad (5.4)$$

To integrate this, σ_{zx} must be expressed as a function of z . We will use the coordinate system of Figure 5.3a and Equation (5.2a), and will

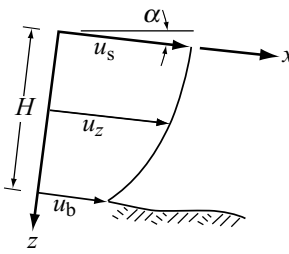


Figure 5.4. Parameters involved in integrating Equation (5.4).

integrate from the surface down to depth z (Figure 5.4), thus:

$$\int_{u_s}^{u(z)} du = -2 \left(\frac{\rho g \sin \alpha}{B} \right)^n \int_0^z z^n dz \quad (5.5)$$

Carrying out the integration and rearranging terms yields:

$$u(z) = u_s - \frac{2}{n+1} \left(\frac{\rho g \sin \alpha}{B} \right)^n z^{n+1} \quad (5.6)$$

This is the desired solution for the velocity profile. It was first obtained by Nye (1952b). Knowing u_s , B , and α , we can calculate the velocity as a function of depth, $u(z)$. If the total thickness, H , is known, we can solve Equation (5.6) for the velocity at the bed, u_b , thus:

$$u_b = u_s - \frac{2}{n+1} \left(\frac{\rho g \sin \alpha}{B} \right)^n H^{n+1} \quad (5.7)$$

Because $n \geq 3$, the velocity at the bed is quite sensitive to the values of α , B , and H .

This derivation is rigorously correct only for a glacier that is in the form of a slab of infinite extent on a uniform slope. If the glacier is bounded laterally, drag on the sides must be considered in calculating σ_{zx} . We will take this up in the [next section](#). If the thickness is not uniform in the longitudinal direction, there are likely to be gradients in the longitudinal stresses that either augment or diminish σ_{zx} relative to the values calculated from any of Equations (5.2). Normally, these gradients are sufficiently small that this source of error is not of major concern in comparison with some others. This is discussed further below and in Chapter 10.

A velocity profile for an ice sheet 300 m thick with a surface slope of 2.2° , $n = 3$, and $B = 0.2 \text{ MPa } a^{1/n}$, calculated from Equation (5.6), is shown in Figure 5.5. The profile has a distinctive form; the velocity is nearly independent of depth in the upper part of the glacier, and then decreases rapidly near the bed. For comparison, the dashed line shows the profile for a linearly viscous ($n = 1$) material, with the value of B adjusted to give the same velocity at the bed. The distinctive form of the $n = 3$ profile is a consequence of the “high” value of n .

Note also in Figure 5.5 that the velocity at the bed, u_b , is composed of two components. If the glacier is at the pressure melting point at the bed, it can slide over its substrate (with speed u_{sl}), whether that substrate be hard bedrock or unconsolidated material. If the substrate is unconsolidated material such as glacial till, this substrate may also deform. This adds a speed u_d to the total. These contributions to the speed of a glacier are discussed in detail in Chapter 7.

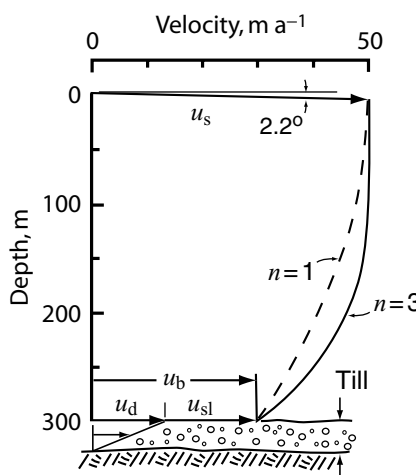


Figure 5.5. Velocity profile for an ice sheet with a surface slope of 2.2° and $B = 0.2 \text{ MPa a}^{1/n}$. A profile for a linearly viscous material is shown for comparison. The thickness of the till layer at the base is greatly exaggerated.

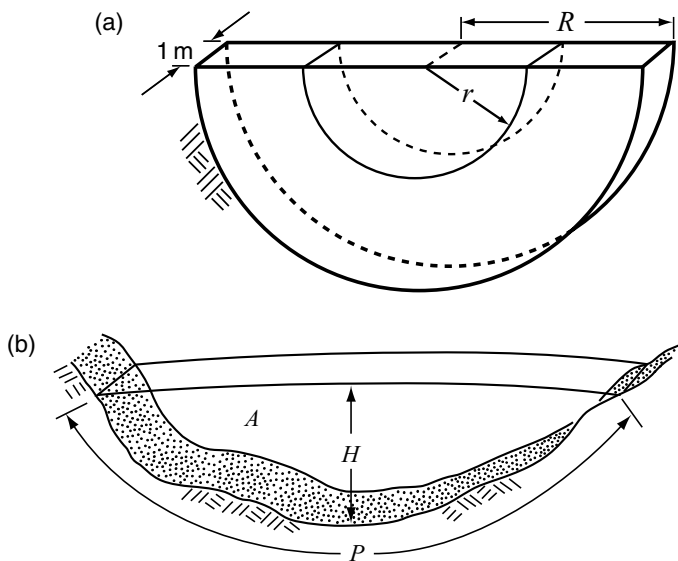


Figure 5.6. (a) Cross section of a glacier in a semicircular valley. (b) Cross section of a realistic valley glacier.

Horizontal velocity in a valley glacier

In a valley glacier, some of the resistance to flow, or drag, is provided by valley sides. To see how this alters the situation, consider first a glacier in a semicircular valley of radius R (Figure 5.6a) and slope α . Balancing forces on a cylindrical surface of radius r and of unit length parallel to the flow gives:

$$\sigma_{rx} \pi r = -\rho g \frac{\pi r^2}{2} \sin \alpha \quad (5.8)$$

Here, πr is the area of the surface and $\rho\pi r^2/2$ is the mass of ice inside the surface. The latter, multiplied by $g \sin \alpha$, is the total force parallel to the surface that must be resisted by a shear stress, σ_{rx} , on the surface. Thus, now:

$$\sigma_{rx} = -\frac{1}{2}\rho gr \sin \alpha \quad (5.9)$$

Inserting this in Equation (5.4) with r in place of z as the depth dimension and integrating as before yields:

$$u(r) = u_{sc} - \frac{2}{n+1} \left(\frac{\rho g \sin \alpha}{2B} \right)^n r^{n+1} \quad (5.10)$$

where u_{sc} is the velocity at the surface on the centerline. But for the change to a cylindrical coordinate system, this result differs from that of Equation (5.6) only in the factor of 2 in the denominator of the term in brackets. However, as $n \approx 3$, the difference in velocity between the surface and a given depth is a factor of 8 less in the valley glacier. This represents the effect of drag on the valley sides.

Semicircular cross sections are not common in nature, so let us consider a more realistic shape (Figure 5.6b). By analogy with Equation (5.8) we write:

$$\bar{\tau}_b P = -\rho g A \sin \alpha \quad (5.11)$$

Here, $\bar{\tau}_b$ is the drag exerted on the glacier by the bed, averaged over the length of the ice–bed interface, P , and A is the cross-sectional area of the glacier. Although τ_b is a force per unit area and is often called the basal shear stress, it is confined to a plane and is thus a vector, not a tensor quantity. Therefore, we will use the term *drag* and the symbol τ for it. Dividing by P and multiplying the top and bottom of the right-hand side by the thickness of the glacier at the centerline, H , yields:

$$\bar{\tau}_b = -\rho g \frac{A}{PH} H \sin \alpha = -S_f \rho g H \sin \alpha \quad (5.12)$$

Here, we have defined $A/PH = S_f$. S_f is known as the shape factor. The reader will readily see that S_f is 1 for an infinitely wide glacier and $\frac{1}{2}$ for a semicircular glacier.

We now make the assumptions:

$$\tau_{b,\text{t}} = \bar{\tau}_b \quad (5.13)$$

and

$$\sigma_{zx} = \frac{z}{H} \tau_{b,\text{t}} = \frac{z}{H} \bar{\tau}_b \quad (5.14)$$

In these equations, the subscript “t” stands for centerline. Assumption (5.13) says that the basal drag at the centerline is equal to the average over the cross section, and assumption (5.14) says that the shear stress at the centerline varies linearly with depth and approaches τ_b at the bed



Figure 5.7. Trimlines above an Alaskan glacier. Photo by B. G. Hooke.

without any discontinuity. With these assumptions, Equation (5.12) can be rewritten as:

$$\sigma_{zx} = -S_f \rho g z \sin \alpha \quad (5.15)$$

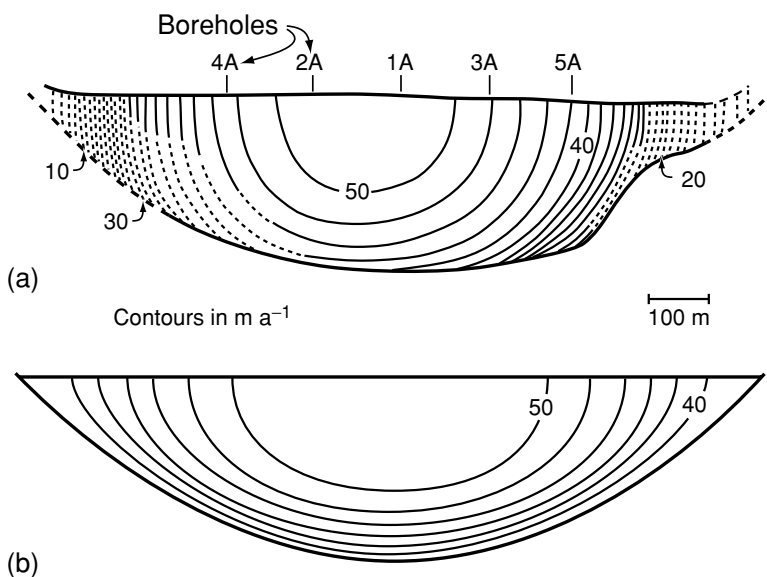
Inserting this in Equation (5.4) and integrating as before yields:

$$u(z) = u_s - \frac{2}{n+1} \left(\frac{S_f \rho g \sin \alpha}{B} \right)^n z^{n+1} \quad (5.16)$$

If one knows u_s and can make reasonable estimates of H , B and S_f , Equations (5.15) and (5.16) can be used to calculate the basal drag and speed, respectively. With such calculations, Nye (1952b) demonstrated that a large fraction of the movement of temperate valley glaciers was due to sliding (or till deformation) at the bed, and that despite a large variation in thickness and surface slope, basal drags fell within a relatively narrow range: $0.05 < \tau_b < 0.15$ MPa. In practice, however, values of u_b thus calculated are not very reliable because small errors in τ_b are amplified when it is raised to the n th power (Equation (5.16)).

The narrow range in τ_b is a consequence of the nonlinearity of the flow law. Small increases in H result in comparatively large increases in u_s , and hence in the rate at which mass is transferred from the accumulation area to the ablation area. Thus, positive net balances may lead to

Figure 5.8. (a) Contours of longitudinal velocity in a transverse cross section of Athabasca Glacier. Contours are based on measurements in boreholes shown. All boreholes reached the bed except 4A, which was only 100 m deep. Dashed contours are extrapolated. (b) Theoretical distribution of longitudinal velocity in a parabolic channel, scaled to cover approximately the observed range of velocities in (a). (After Raymond, 1971, Figure 10. Reproduced with permission of the author and the International Glaciological Society.)



significant increases in speed, and hence to advances of glaciers, with only modest increases in thickness, and conversely. Following retreat of a glacier, evidence for this effect is commonly seen in vegetation boundaries, called *trimlines*, that reflect the former position of the ice surface (see Figure 5.7). Near the terminus, such trimlines are typically high above the present glacier surface, and they meet the valley bottom well down-valley from the terminus. However, when traced up-valley, they become quite close to the level of the present surface.

Comparison with measurements

It is revealing to compare the velocity distribution measured in a temperate glacier with one calculated on the basis of arguments similar to those leading to Equation (5.16). The measurements in Figure 5.8a were made by Raymond (1971) on Athabasca Glacier in the Canadian Rocky Mountains and are compared with calculations (Figure 5.8b) made by Nye (1965a) for a glacier in a cylindrical parabolic channel with a similar aspect ratio. Nye assumed that basal sliding was uniform over the cross section.

There are some interesting discrepancies between the observed and calculated distributions. First, the basal velocity is 80% to 90% of the surface velocity over the central section of Athabasca Glacier, and then decreases rapidly towards the valley sides. These large lateral gradients in u_b conflict with Nye's assumption. The gradients are attributed to lateral variations in water pressure at the ice–rock contact. The role of

water pressure in sliding and till deformation will be discussed further in Chapters 7 and 8.

Secondly, in the field measurements, $\partial u / \partial y > \partial u / \partial z$ (where the y -axis is transverse), whereas in the theoretical model the reverse is true. Unless the ice is quite anisotropic, the contrast in strain rates indicates a similar contrast in stress. The higher shear strain rates near the margin of Athabasca Glacier indicate that the glacier is supported by drag on the margin more than by drag on the bed.

Thirdly, although σ_{zx} increases approximately linearly with depth as in the theory, $\tau_{b,t} < \bar{\tau}_b$, contrary to our assumption (Equation (5.13)). In other words, if S_f is calculated from its definition, A/PH , and if this is then used to calculate σ_{zx} at the centerline, the value of σ_{zx} will be too high. Put differently, to calculate $u(z)$ and τ_b at the centerline of a valley glacier, one should use a value of S_f that is less than A/PH . The fact that the velocity contours are nearly semicircular in shape, which is quite different from the shape of the margin, suggests that $S_f = \frac{1}{2}$ would give a better estimate of τ_b . Furthermore, in some situations, the variation of σ_{zx} with depth may not be linear. Calculations with a numerical model have shown that σ_{zx} depends on the basal water pressure, and that at high water pressures it may actually decrease near the bed (Truffer *et al.*, 2001).

Mean horizontal velocity and ice flux

The ice flux per unit width, q , is readily obtained by integrating the velocity profile (Equations (5.6), (5.10), or (5.16)) over depth. We will illustrate this with Equation (5.16), thus:

$$\begin{aligned} q_t &= \int_0^H u(z) dz = \int_0^H \left[u_s - \frac{2}{n+1} \left(\frac{S_f \rho g \sin \alpha}{B} \right)^n z^{n+1} \right] dz \\ &= u_s H - \frac{2}{(n+1)(n+2)} \left(\frac{S_f \rho g \sin \alpha}{B} \right)^n H^{n+2} \end{aligned} \quad (5.17)$$

Possibly of greater use is the mean velocity over depth, $\bar{u} = q_t / H$:

$$\bar{u} = u_s - \frac{2}{(n+1)(n+2)} \left(\frac{S_f \rho g \sin \alpha}{B} \right)^n H^{n+1} \quad (5.18)$$

Combining this with Equation (5.16) and simplifying the result leads to:

$$\begin{aligned} \bar{u} &= u_b + \frac{2}{(n+2)} \left(\frac{S_f \rho g \sin \alpha}{B} \right)^n H^{n+1} \\ &= u_b + \frac{n+1}{n+2} (u_s - u_b) \\ &= \frac{4}{5} u_s + \frac{1}{5} u_b \end{aligned} \quad (5.19)$$

where the numerical values are calculated assuming $n = 3$. This relation will be of use in Chapter 14.

Vertical velocity

Let us now consider the variation in vertical velocity with depth. Because we are dealing with a two-dimensional situation, the incompressibility condition (Equation (2.5)) becomes:

$$\frac{\partial u}{\partial x} + \frac{\partial w}{\partial z} = 0 \quad (5.20)$$

We will ignore the compressibility of firn near the surface, and also, initially, assume that the longitudinal strain rate, $\partial u / \partial x$, is independent of depth. Thus $\partial u / \partial x = -c$, where c is a constant. Equation (5.20) then reduces to $\partial w / \partial z = c$. Finally, continuing to use the coordinate system of Figure 5.4, we assume that $w = 0$ on the bed where $z = H$, thus ignoring any contribution from the normally small rates of melting or refreezing. Then:

$$\int_0^w dw = c \int_H^z dz$$

or

$$w = c(z - H)$$

At the surface, $z = 0$, we have $w = w_s$ so $c = -w_s/H$. Therefore,

$$w = \frac{H - z}{H} w_s \quad (5.21)$$

In other words, the vertical velocity decreases linearly with depth.

The key assumption in this derivation is that $\partial u / \partial x$ is independent of depth. Because u is nearly independent of depth in the upper part of a glacier (Figure 5.5), the upper parts of two deformation profiles in locations some distance apart in the longitudinal direction will be nearly parallel. Thus, the assumption that $\partial u / \partial x$ is independent of depth seems like a reasonable first approximation. This argument is stronger in polar glaciers because the ice near the surface is colder, and hence more viscous (higher B). The shear strain rate, $\dot{\varepsilon}_{zx}$, is thus lower, so u is nearly constant over a greater fraction of the ice thickness. In view of these rationalizations and the simplicity of Equation (5.21), this approximation is widely used in calculations, as we shall see in Chapter 6 and elsewhere.

However, it is clear that if the ice is frozen to the bed, $\partial u / \partial x = 0$ at the bed. Thus, if it is non-zero higher in the glacier, it must decrease (in absolute value) with depth. We can incorporate this effect in the

following way. Setting $u_b = 0$ in Equation (5.7) and using the resulting expression for u_s in Equation (5.6) leads to:

$$u(z) = u_s \left[1 - \left(\frac{z}{H} \right)^{n+1} \right]$$

whence, ignoring small terms involving $\partial H / \partial x$:

$$\frac{\partial u}{\partial x} = \frac{\partial u_s}{\partial x} \left[1 - \left(\frac{z}{H} \right)^{n+1} \right]$$

Substituting this into Equation (5.20) and integrating upward from the bed where $w = 0$, $z = H$:

$$\int_0^w dw = - \frac{\partial u_s}{\partial x} \int_H^z \left[1 - \left(\frac{z}{H} \right)^{n+1} \right] dz$$

leads to:

$$w = - \frac{\partial u_s}{\partial x} \left[z - \frac{z^{n+2}}{(n+2)H^{n+1}} - H + \frac{H^{n+2}}{(n+2)H^{n+1}} \right] \quad (5.22)$$

At the surface, $z = 0$, this yields:

$$w_s = \frac{\partial u_s}{\partial x} H \left[1 - \frac{1}{n+2} \right] \quad (5.23)$$

Combining Equations (5.22) and (5.23) gives:

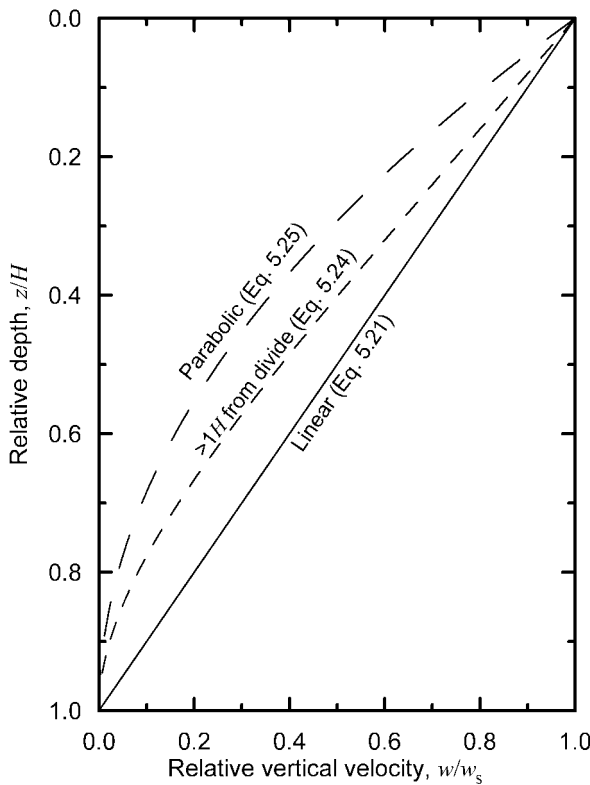
$$w = w_s \left\{ 1 - \frac{z}{H} \left[\frac{n+2}{n+1} - \frac{1}{n+1} \left(\frac{z}{H} \right)^{n+1} \right] \right\} \quad (5.24)$$

a result first obtained by Raymond (1983). Equations (5.21) and (5.24) are plotted in Figure 5.9. The difference between them does not appear large, but we will find that it has important consequences.

Let us follow this line of inquiry somewhat further, giving special attention to conditions at an idealized divide on an ice sheet. We will assume there is no flow parallel to the divide, so $v = 0$ and $\dot{\epsilon}_{yy}$, $\dot{\epsilon}_{xy}$, $\dot{\epsilon}_{yx}$, $\dot{\epsilon}_{zy}$, and $\dot{\epsilon}_{yz}$ are all 0. Ice on either side of the divide flows symmetrically away from it. Therefore, u is 0 at (and everywhere beneath) a divide, and so, therefore, is $\partial u / \partial z$. Finally, if the accumulation rate is symmetrical across the divide, $\partial w / \partial x = 0$. Thus $\dot{\epsilon}_{xz}$ and $\dot{\epsilon}_{zx}$ are 0 (see Equation (2.6a)), and $\dot{\epsilon}_e = (1/\sqrt{2})(\dot{\epsilon}_{xx} + \dot{\epsilon}_{zz})^{1/2}$. Now if $|\partial u / \partial x|$ decreases with depth as just suggested, $|\partial w / \partial z|$ must also decrease (Equation (5.20)). Thus, $\dot{\epsilon}_e$ decreases. But from Equation (2.19), a decrease in $\dot{\epsilon}_e$ stiffens the ice, effectively increasing the viscosity. This reduces $|\partial u / \partial x|$ and $|\partial w / \partial z|$ still further, in a positive feedback.

If $|\partial w / \partial z|$ is higher at the surface than it is at depth, a plot of w against depth must be convex upward like the curve obtained from Equation (5.24) in Figure 5.9. We cannot derive the actual shape of the curve analytically because of the positive feedback effects and because the stresses are not known well enough. Raymond (1983), however, has studied the

Figure 5.9. Variation in vertical velocity, w , with depth. The parabolic relation is a good approximation beneath a divide. Equation (5.24) is appropriate at distances greater than one ice thickness from a divide. The linear approximation is often used for simplicity.



flow field by using a numerical computer model. Under isothermal conditions, he finds that directly beneath the divide the vertical variation of w is closely approximated by a parabolic curve:

$$w = \left(\frac{H - z}{H} \right)^2 w_s \quad (5.25)$$

(Figure 5.9). Outward from the divide, the convexity decreases, so that at a distance of one ice thickness from the divide, the variation of w with depth given by the numerical model is very similar to that given by Equation (5.24) (Raymond, 1983, Figure 3).

In reality, the stiffening resulting from the decrease in $\dot{\varepsilon}_c$ is likely to be partially offset by warming of the ice, with a consequent decrease in B (Equation (2.19)). Raymond studied this effect, and found that the convexity of the profile, although diminished, was still present even when the temperature difference between the surface and the bed was nearly 40°C .

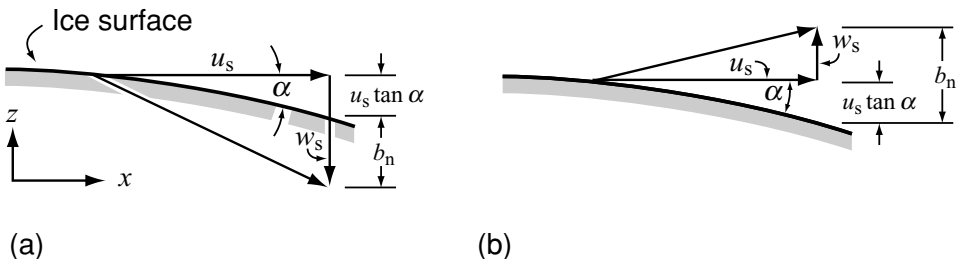


Figure 5.10. Diagrams illustrating (a) submergence, and (b) emergence velocities.

Submergence and emergence velocities

Earlier (Equation (5.1)), we gained insight into the magnitude of the horizontal velocity by considering a glacier in a steady state, such that its surface profile remained unchanged. Let us now use this idealization to study vertical velocities. In such a steady state, the surface in the accumulation area must everywhere be sinking at a rate that balances accumulation, and conversely in the ablation area. Thus, the vertical velocity at the surface, w_s , is clearly related to the net balance rate, b_n . Remembering that a point on the surface is also moving with a horizontal velocity, u_s , and that the surface has a slope, α , we find that the appropriate relation is (Figure 5.10):

$$b_n = -w_s + u_s \tan \alpha \quad (5.26)$$

Here, we have taken the x -axis as horizontal and positive in the downglacier direction, and the z -axis as positive upward. Thus, in the accumulation area, both w_s and α are negative and, owing to the relative magnitude of the two terms on the right-hand side of the equation (see Figure 5.10a), the minus sign in the equation makes the right-hand side positive. In the accumulation area, the right-hand side is called the *submergence velocity*.

Equation (5.26) also applies in the ablation area (Figure 5.10b), except that here w_s is positive so both terms on the right-hand side take on negative values. Thus b_n is negative, reflecting ablation. Here, the right-hand side is called the *emergence velocity*.

Clearly, the submergence and emergence velocities are defined for any point on a glacier surface. However, they equal b_n only in the idealized steady-state situation that we have specified. This is because b_n varies from year to year, and because, even averaged over several years, glaciers are rarely in a steady state. Put differently, if the accumulation rate consistently exceeds the submergence velocity and the ablation rate

consistently falls short of the emergence velocity, the glacier is becoming thicker and will advance, and conversely.

Other possibilities can also be visualized. For example, if the equality in Equation (5.26) holds everywhere except in the lower part of the ablation area where the ablation rate exceeds the emergence velocity, the glacier may be in the final stages of adjustment to a climatic warming. The implication of such a situation would be that the accumulation area has essentially adjusted to the warming, but the glacier is still retreating slightly.

We have shown that on a glacier that is in a steady state and that has a balanced mass budget, the velocity field at the surface is related to b_n . It is instructive to consider in greater detail the physical mechanisms behind this relation. In this case, b_n is the independent variable, and the velocity field is the dependent variable. (In a larger system involving glacier–climate interactions, b_n would be dependent upon the climate.) The physical mechanism by which b_n and the velocity field are related is viscous flow, in which the flow rate increases with the driving stress, $\rho g h \alpha$. If the velocities are, say, too low (in absolute value), the submergence velocity will be less than the accumulation rate so the glacier will become *thicker* in the accumulation area (Figure 5.10a). Similarly, the emergence velocity will be less than the ablation rate, so the glacier will become *thinner* in the ablation area (Figure 5.10b). The slope of the glacier surface thus increases. The increase in slope, coupled with the increase in thickness in the accumulation area, increases the driving stress and hence u_s . Because $u = 0$ at the head of the glacier and at the terminus, an increase in u_s in the middle makes $\partial u / \partial x$ more extending in the accumulation area and more compressive in the ablation area. Thus, by the arguments leading to Equation (5.26), $|w_s|$ increases. The increases in both u_s and $|w_s|$ tend to restore the steady state.

Flow field

We now have the tools needed to make a first-order estimate of the flow field in a glacier, given $b_n(x)$. In a steady-state situation, Equation (5.1) gives the depth-averaged horizontal velocity, $u(x)$, which is probably sufficient for most applications. However, various levels of sophistication could be added; Equations (5.16) (with $z = H$) and (5.19) could be solved simultaneously for u_s and u_b , and Equation (5.16) could then be used to estimate the variation in u with depth. This would give $u(x,z)$. Then, Equations (5.24) and (5.26) provide a reasonable first estimate of $w(x,z)$. Thus, one could plot vectors u and w at a large number of points in a glacier cross section and sketch flowlines based on these vectors. The result would be flowlines much like those in Figure 3.1.

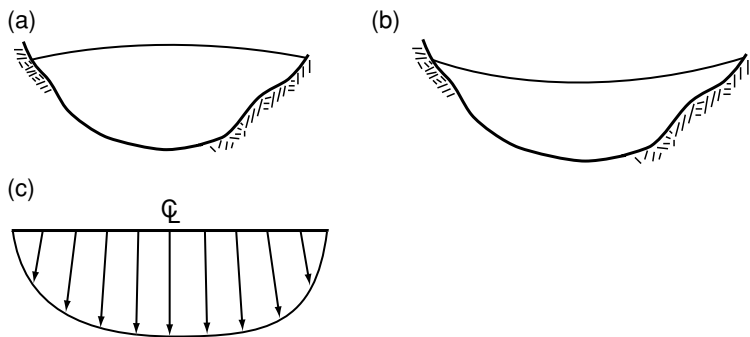
It may be worthwhile studying Figure 3.1 in connection with the above equations to develop an intuitive sense of why the flowlines appear as they do. From Equation (5.26) and Figure 5.10, it is clear that the vertical velocity must be downward in the accumulation area and upward in the ablation area. Owing to the slope of the glacier surface, the location where $w_s = 0$ is not at, but rather slightly downglacier from, the equilibrium line (Equation (5.26)). From Equation (5.1) it is obvious that u increases outward from the divide, reaching a maximum again not at, but rather slightly downglacier from, the equilibrium line. Because the variation in w_s is small compared with that in u_s , the resultant velocity vectors plunge most steeply near the divide and ascend most steeply near the margin, as u_s is low in these locations. In fact, at the divide on a polar ice sheet, $u_s = 0$ so the vector points directly downward. Near the bed, w_s is low so the vectors approach parallelism with the bed.

In summary, flowlines tend to be downward in the accumulation area and upward in the ablation area. At the bed they are parallel to the bed and at the equilibrium line (of our idealized steady-state glacier) they are parallel to the surface. The flowline starting at the divide on an ice sheet will go straight downward until it reaches the bed, and then will follow the bed, remaining strictly parallel to the bed in the absence of melting or refreezing, until it emerges at the margin.

In the steady state, the volume of ice moving between two adjacent flowlines remains constant along the full length of these two flowlines. This is true by definition; material cannot cross a flowline, so all material that starts between two flowlines must remain between them. A consequence of this is that the velocity will be highest where the flowlines are closest together, as the ice is assumed to be incompressible. Thus the highest velocities will be near the equilibrium line, as is evident from Equation (5.1).

Steady-state conditions are, of course, a theoretical abstraction, rarely if ever actually realized in nature. The annually averaged velocity field of a retreating or advancing glacier should not, however, differ too significantly from that described above. On the other hand, seasonal and spatial variations in the velocity field, particularly on valley glaciers, can be appreciable. A number of studies have shown that when water from the surface is able to reach the glacier bed, glaciers speed up in the summer (see Figure 12.10). This is because water pressures increase, thus increasing the sliding speed. There are even diurnal variations in surface speed (see Figures 7.8 and 7.23). Because sliding speeds are highest beneath the centerline of the glacier (Figure 5.8), seasonal accelerations are highest here. These accelerations result in measurable changes in the magnitude and direction of velocity vectors, both at the surface and at depth (Hooke *et al.*, 1992). In contrast, Harper *et al.* (2001), in a study

Figure 5.11. Schematic cross sections of a valley glacier in (a) the ablation area, and (b) the accumulation area; and (c) a plan view of the glacier showing the transverse variation in u_s in the ablation area.



utilizing 31 boreholes in the central part of Worthington Glacier, Alaska, did not find seasonal variations. They did, however, find significant spatial variations at a length scale of tens of meters. In a transverse cross section of the glacier, there were variations in horizontal speed of as much as 5% that did not seem to be related to side drag, but may have been caused by longitudinal stresses originating in an ice fall higher on the glacier.

Transverse profiles of surface elevation on a valley glacier

In the ablation area of a valley glacier, transverse profiles of surface elevation are commonly convex upward (Figure 5.11a), whereas in the accumulation area they are concave upward (Figure 5.11b). This can be understood by considering the emergence and submergence velocities. In a steady-state situation, w_s cannot be zero along the margins of a glacier in either the accumulation area or the ablation area because there is accumulation or ablation, respectively, in these locations. However, the ice thickness goes to zero at the margin. Thus to provide a downward w_s near the margin in the accumulation area, ice must be drawn away from the valley sides, and conversely in the ablation area. The transverse surface slopes, towards the center of the glacier in the accumulation area and away from the center in the ablation area, provide the forcing for this flow.

Consideration of transverse variations in the emergence and submergence velocities provides insight into lateral variations in w_s and into the mechanism of adjustment of transverse profiles. Let us start with the ablation area. Horizontal velocities are normally highest near the center of a glacier and decrease towards the margins owing to drag on the valley sides (Figure 5.11c), in much the same way that velocities decrease with depth owing to drag on the bed. The ablation rate, however, is normally

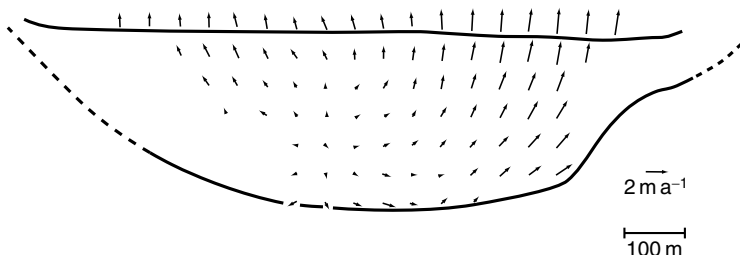


Figure 5.12. Transverse velocity field measured in a cross section of Athabasca Glacier by Raymond (1971, Figure 12). (Reproduced with permission of the author and the International Glaciological Society.)

approximately constant across the glacier. It may, in fact, be somewhat higher near the margins as a result of heat radiated or advected from dark rocks of the valley walls. The longitudinal surface slope, α , will also be approximately constant across the glacier. Thus, from Equation (5.26) or Figure 5.10b, it is clear that w_s must be higher near the margins than along the centerline, as illustrated in Figure 5.12.

The process by which the transverse profile in the ablation area is adjusted is easy to understand. Consider what would happen if the profile were flat and w_s were constant along this profile. Suppose the ablation rate equals the emergence velocity at the centerline. Along the margins where u_s is lower, b_n would exceed the emergence velocity, so the glacier surface would decrease in elevation, leading to the convexity that is commonly observed. The resulting transverse surface slope would force a transverse component to the flow. Because the valley walls inhibit such flow, a transverse compression develops, thus increasing the rate of vertical extension near the sides of the glacier (assuming no compensating change in the longitudinal strain rate). The magnitude of the transverse slope would continue to increase, thus increasing w_s , until the emergence velocity equaled the ablation rate. Of potential interest in trying to understand landforms produced by glacial erosion is the fact that the transverse component of the flow is apparently greatest near the bed, according to measurements made by Raymond (1971) on Athabasca Glacier (Figure 5.12).

In the accumulation area, the situation is reversed. As in the ablation area, u_s is lower near the margin, so if the longitudinal component of α is approximately constant across the glacier, $u_s \tan \alpha$ will be less negative near the margin than on the centerline. In addition, b_n is likely to be higher along the margin owing to drifting and avalanching. The flow field thus has to develop in such a way that w_s is more negative (downward) near the margins than near the centerline (Equation (5.26) or Figure 5.10a). However, the ice is thinner near the margin so the longitudinal stretching rate is likely to be lower, thus contributing less to a negative w_s . Somehow, w_s must become more negative. The concave cross-valley profiles (Figure 5.11b) that are typical of accumulation areas accomplish this.

To visualize the physical processes involved in this adjustment, consider again a hypothetical case in which the transverse profile is initially flat, rather than concave upward. In this case, there would be no transverse component to the surface slope, and hence little or no transverse component to the flow. Flowlines would be parallel to the glacier margin, and longitudinal strain rates along flowlines near the margin would be too low to provide the negative w_s needed to balance the accumulation. In other words, the left-hand side of Equation (5.26) would be larger than the right-hand side, and the glacier would become thicker in this area. This thickening along the margins would continue as long as the imbalance persisted, thus establishing the characteristic concave-upward transverse profile. The transverse surface slope would result in a transverse component of flow toward the center of the glacier, and because glaciers normally increase in thickness rapidly away from the margins, stretching rates are high along flowlines that diverge from the margin. The resulting transverse stretching provides the more negative w_s required near the margins.

If transverse profiles are generally convex upward in the ablation area and concave upward in the accumulation area, it is interesting to consider exactly where the transition between the two types of profile should occur. Let us return to our idealized steady-state glacier with a balanced mass budget. At the equilibrium line on this glacier, $b_n = 0$, so from Equation (5.26) $w_s = u_s \tan \alpha$. As $\alpha < 0$ and $u_s > 0$, w_s must still be somewhat negative (downward), as mentioned previously. The place where $w_s = 0$ is somewhat downglacier from the equilibrium line, where $b_n = u_s \tan \alpha$. It is approximately at this point that one might expect the transition to occur. Leonard and Fountain (2003), in a study of 40 glaciers, found that this indeed was the case. For reasons that are not obvious, the difference in elevation between the transition and the equilibrium line increased systematically with elevation of the equilibrium line. The location of the transition relative to the equilibrium line depends on b_n , u_s , and α , so it will vary from glacier to glacier.

Radar stratigraphy

Prior to World War II, pilots flying over Greenland and Antarctica found that their radar altimeters were giving unreliable data. Upon investigation, it was discovered that the radar waves were passing through the ice sheet and reflecting from the bed (Waite and Schmidt, 1961). Thus was born the tool of radio echo-sounding of glaciers (Gogineni *et al.*, 1998). Initially, the primary objective was to determine the thickness of the ice, as previously gravity measurements, seismic profiling, and drilling were the only techniques available to glaciologists for this purpose. However,

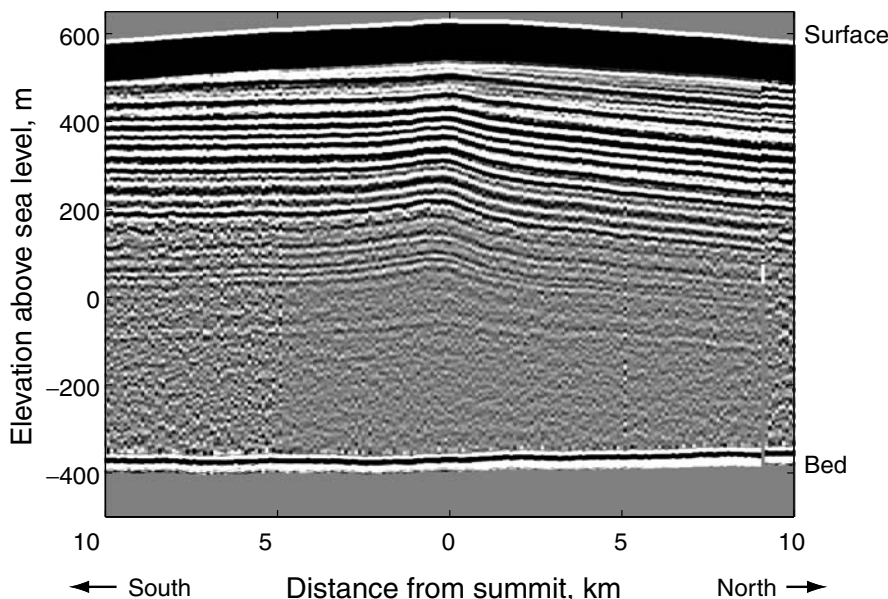


Figure 5.13. A 20 km radar profile across the divide of Siple Dome, Antarctica, showing internal layering. The black band at the top is caused by interference from radio waves passing directly through the air. (From Nereson *et al.*, 1998, Figure 2. Reproduced with permission of the International Glaciological Society.)

it was soon discovered that internal layering of glaciers and ice sheets was also being imaged. By adjusting the frequency of the radio waves and imposing sophisticated filtering on the return signals, remarkably sharp images of this layering are now being obtained routinely (Figure 5.13). Reflections are caused by subtle contrasts in the dielectric constant. Those from shallower layers probably result from differences in density; those from deeper layers are attributed to acidic fallout from volcanic eruptions or to changes in impurity concentration associated with climatic transitions (Morse *et al.*, 1998). Accordingly, such layers are commonly assumed to be stratigraphic horizons, representing isochrones, and they thus can be used to study the flow field and changes in it over time.

A radar profile (Figure 5.13) across the divide of Siple Dome, an elongate high area in West Antarctica (see Figure 5.20), provides one example of a feature that merited study. A bump is clearly visible in the internal layering. The amplitude of this bump increases with depth, reaching a maximum of ~ 50 m. The bump suggests a change in the vertical velocity outward from the divide. There are two possible explanations for such a change (Nereson *et al.*, 1998). As we discovered above, ϵ_r decreases with depth beneath a divide, so the deeper ice

is stiffer than that at the surface. Consequently, the vertical velocity generally decreases more rapidly beneath the divide than it does on the flanks (Figure 5.9), so as layers form at the surface and are buried by subsequent accumulation, they are draped over the stiffer plug. Because this explanation is based on Raymond's (1983) analysis of the vertical velocity field (Equations (5.24) and (5.25)), the resulting distortion of the internal layering has become known as the *Raymond bump*. Alternatively, drifting or wind scouring may reduce the accumulation over the divide, in which case the flow field would have to adjust so that w_s was lower there. Thus, again, isochronous surfaces would be buried less rapidly beneath the divide than on the flanks.

Nereson *et al.* (1998) analyzed the layer shapes with the use of a numerical flow model. The modeling was complicated by the fact that accumulation gradients are likely to exist across the divide even if drifting has not resulted in a local low in b_n . Unfortunately, the true accumulation pattern is not known so these gradients had to be free parameters in the modeling. In addition, the bump is offset to the north with increasing height above the bed (Figure 5.13), suggesting migration of the divide. The divide migration rate thus becomes another free parameter. With this many free parameters it was possible to model the bump rather well, but the relative contributions of a decrease in $\dot{\epsilon}_e$ and drifting could not be evaluated. It seems likely that both are involved. The estimated migration rate, based on the modeling, is $\sim 0.3 \pm 0.2 \text{ m a}^{-1}$ over the past several thousand years.

In another example, Morse *et al.* (1998) found that beneath the divide on Taylor Dome, Antarctica, shallower layers thickened southward while deeper layers thickened northward. Isotopic and chemical variations in a core were used to establish an age/depth time scale; it turned out that the northward-thickening layers were deposited during the Late Glacial Maximum (LGM). By using a numerical model of ice flow, they also found that the accumulation rate was much lower during the LGM. The change in thickness gradient in the radar layering was then attributed to a change in storm tracks during the LGM, with storms coming from the north rather than from the south as at present. Such studies are important in trying to unravel the climatic changes that resulted in the ice ages.

Effect of drifting snow on the velocity field

Glaciers flow over irregular beds, and thus have undulating surface profiles. Furthermore, their transverse flow patterns may be influenced by nunataks or irregular valley walls. Patterns of both accumulation and ablation thus can be uneven owing to drifting and to shading from the

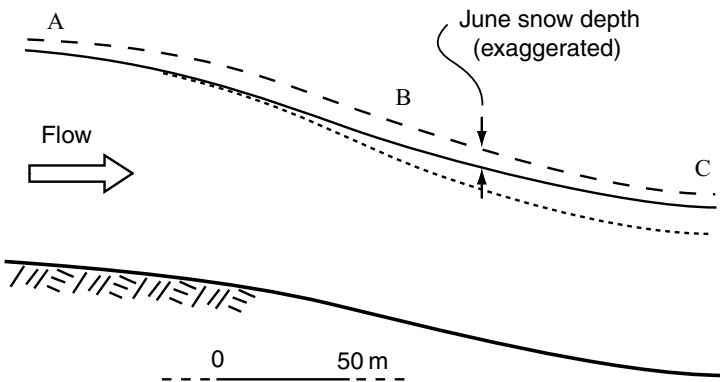


Figure 5.14. Effect of drifting snow on the surface profile of a glacier. Owing to the additional accumulation in the lee of the surface convexity at A, w_s does not need to be as high at B as otherwise would be the case.

sun during the melt season. We have just discussed one example of this from Siple Dome. Let us now consider some other examples.

To understand how drifting influences the flow field and surface profile, consider the hypothetical situation shown in Figure 5.14 in which a glacier flows over a convexity in the bed, resulting in a similar convexity in the surface. Owing to drifting in the lee of the surface convexity, the normal June snow depth at B is, say, 2 m, while that at A it is only 1 m. During a normal melt year, suppose that at A all of the snow and 0.5 m of the underlying ice melts, whereas at B, melting removes only the snow cover. Thus, the emergence velocity at A must be 0.5 m a^{-1} , whereas at B it is 0. In the absence of the extra accumulation at B, the glacier would probably be thinner here as shown schematically by the dotted line in Figure 5.14. The greater surface slope between A and C would then provide the increased longitudinal compression needed to develop a positive emergence velocity at B.

The situation shown in Figure 5.14 occurs on a large scale on the surface of the Antarctic ice sheet above the western edge of Lake Vostok, a subglacial lake under 4 km of ice in central East Antarctica (see Figure 6.13). The increase and then decrease in surface slope reflects flow of ice over a steep slope down into the lake and then an abrupt decrease in basal drag as the ice moves out over the lake. As this is an accumulation area, the thicker accumulation (as at B) is advected downglacier and buried. Because flow rates are relatively low, ice moving over the lake experiences this excess accumulation for about 30 000 years. The excess shows up in radio echo profiles as an increase in the vertical distance between reflectors, and in an ice core from a borehole on the east side of the lake as a zone of high accumulation rate between ~ 800 and ~ 1100 m depth (Leonard *et al.*, 2003).

Thule–Baffin moraines (Figure 5.15), first studied in detail by Goldthwait (1951), provide another geomorphologically significant



Figure 5.15. Thule–Baffin moraines (on skyline) in one of the type areas, Thule (Qânâq), Greenland. Note folding in foliation (sedimentary stratification) in superimposed ice in center of photograph. (From Hooke, 1970, Figure 8. Reproduced with permission of the International Glaciological Society.)

example of the importance of drifting snow. The casual observer will commonly be surprised to learn that although the crest of the moraine in Figure 5.15 is several tens of meters above the margin, the till is usually no more than a meter or so thick. Beneath the till is dirty ice with quite variable debris concentrations. The dirt in the ice is typically segregated into laminae or folia, millimeters in thickness, that dip steeply upglacier (Figure 5.16b). The sediment content of the dirt-bearing folia is normally only a few percent. Layers of clast-supported frozen till, sometimes exceeding 1 m in thickness, are also present. The wedge of ice downglacier from the moraine is clean. It is too thin to flow at an appreciable rate, and is frozen to its bed, preventing sliding. The low flow rate, in conjunction with the observed dip of the foliation, led to the mistaken impression that the foliation planes were shear planes, and that the dirty ice was actively shearing over the wedge of clean ice in such a way that debris, entrained at the bed, was carried to the surface on these planes.

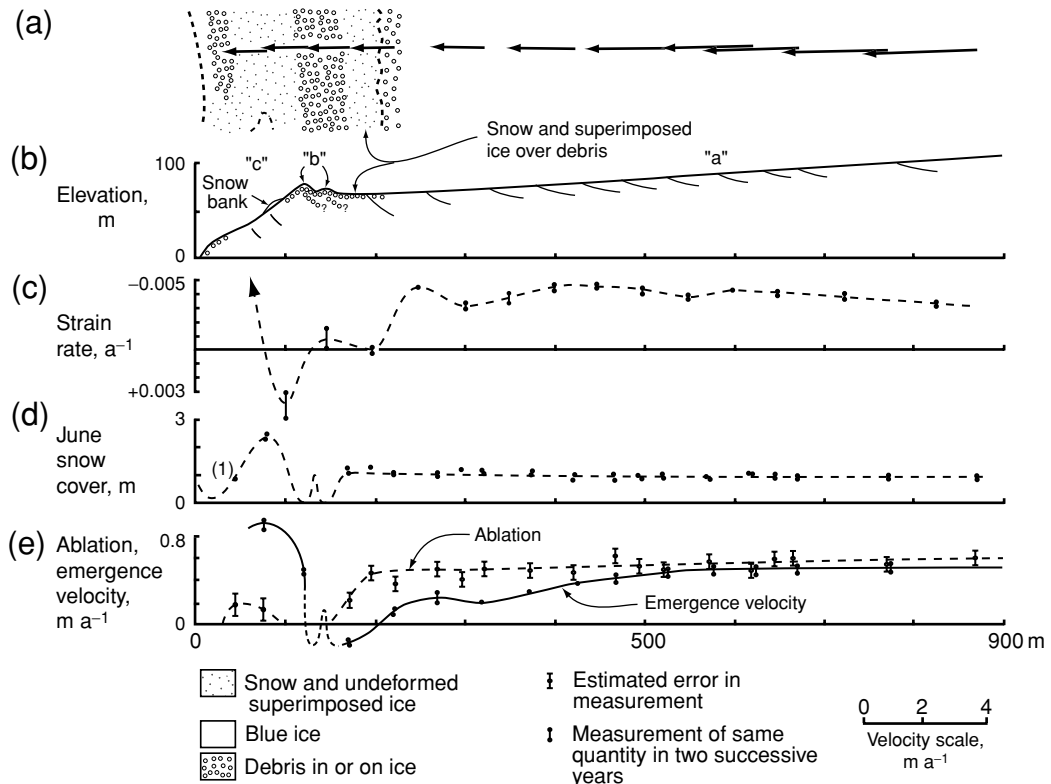


Figure 5.16. Data from a Thule–Baffin moraine on Barnes Ice Cap, Baffin Island. (a) Map showing moraine and line of stakes used for velocity and mass balance measurements. Velocities are shown by arrows. (b) Surface profile along stake line, showing dip of foliation at surface and inferred dip beneath surface. (c) Strain rates. (d) June snow depth. (e) Net balance and emergence velocity along stake line. (Modified from Hooke, 1973a, Figure 3D. Reproduced with permission of the Geological Society of America.)

The geometry of this type of glacier margin can be understood in terms of the concepts we have been discussing. At “a” in Figure 5.16b, the mean June snow cover was about 1 m thick in the 1970s (Figure 5.16d). During an average 1970s summer, this snow and ~ 0.55 m of the underlying ice melted. Longitudinal compression here (Figure 5.16c) resulted in a positive (upward) w_s , and the emergence velocity was $\sim 0.50 \text{ m a}^{-1}$ (Figure 5.16e). This was slightly less than the net balance, but high enough that a slight cooling could have brought about a steady state with Equation (5.26) satisfied.

At “b” in Figure 5.16b, the snow cover was 0, but so was the ablation rate as the till layer insulated the ice. On ridges like these, it is difficult to know what is meant by “emergence velocity”, as a ridge has both

up- and downglacier slopes. However, because there was still some longitudinal compression, the ridges were gradually increasing in height. This is a non-steady-state process: as the height of such a ridge increases, it becomes steeper until, eventually, till slumps off of it, exposing the underlying ice. This ice then melts rapidly owing to the lack of snow cover and to the thin covering of dirt that remains on it, decreasing its albedo. However, a new ridge begins to develop under the slumped till.

At “c” the June snow cover was nearly 2.5 m thick. During an average 1970s summer, this snow melted, but essentially no ice was lost: $b_n \approx 0$. Thus, this sloping margin could exist despite the fact that the emergence velocity in it was negligible.

Thus, during a period of balanced mass budget along a glacier margin like this, till-covered ridges would go through cycles of growth and decay while the ice surface upglacier and the wedge of deformed superimposed ice downglacier remained unchanged. The primary change would be an increase in dirt cover as more debris melted out of dirty ice exposed by slumping from the ridges.

During a series of cool summers the sloping margin downglacier from the moraines becomes a local accumulation area at the edge of the glacier. If cool climatic conditions persist long enough, the glacier will advance, overriding and deforming this accumulation of superimposed ice, as shown in Figure 5.17. Recognition of this process provided an alternative to the shearing mechanism proposed by Goldthwait.

Three lines of evidence support the origin of Thule–Baffin moraines shown in Figure 5.17. Firstly, the less-deformed superimposed ice is fine grained (1–2 mm) and lacks any development of a deformation fabric such as would be present in highly deformed basal ice. Secondly, oxygen isotope ratios show that the deformed superimposed ice accumulated under conditions broadly similar to those prevailing today, yet it, in part (Figure 5.17), underlies ice with isotopic ratios characteristic of Pleistocene ice. Thirdly, folding of the downglacier dipping layers of superimposed ice occasionally can be observed in ice cliffs with the proper orientation (Figures 5.15 and 5.18). Further discussion of this process and the evidence for it is presented by Hooke (1970, 1973a, 1976) and Hooke and Clausen (1982).

Moraines are formed by the process illustrated in Figure 5.17 only under relatively cold climatic conditions. For example, in the Kangerlussuaq area of Greenland, a few hundred kilometers south of Thule (now Qâñâq), summer temperatures are warm enough to melt all of the snow at the margin, even though drifting can result in a rather thick June snow cover there. Thus, there is no marginal zone of superimposed ice. However, the process illustrated in Figure 5.17 was probably important in northern Wisconsin, Minnesota, North Dakota, Alberta, and

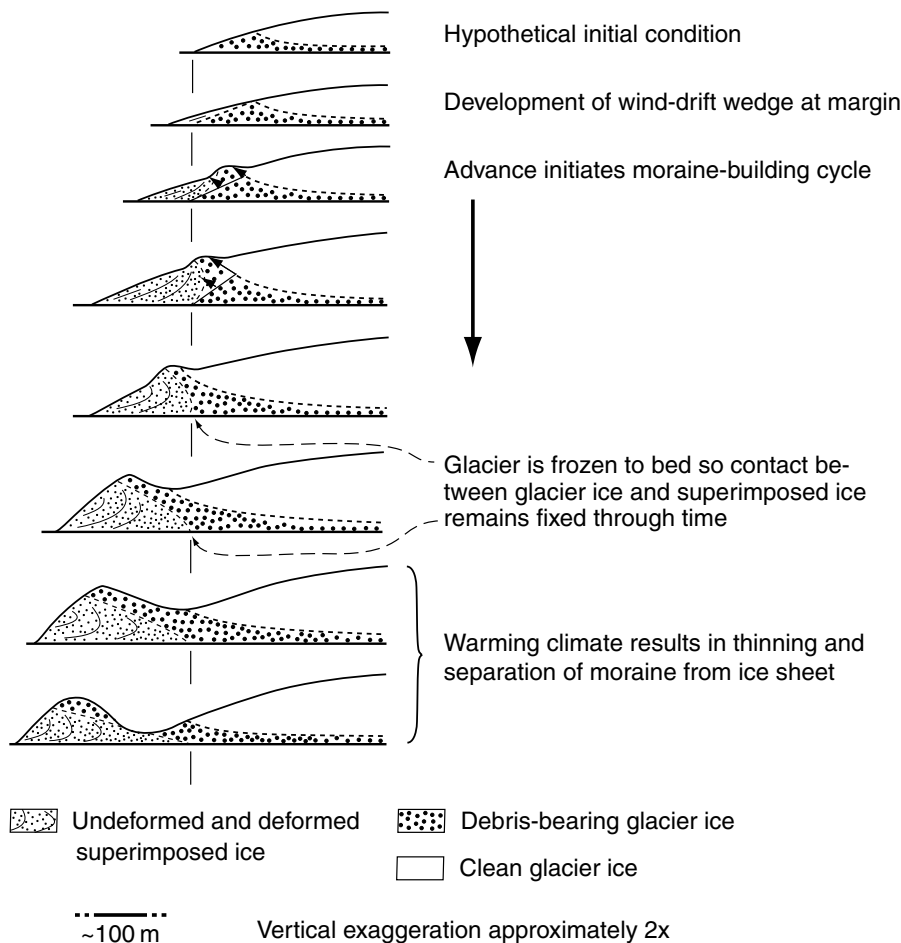


Figure 5.17. Sequential cross sections showing schematically the processes by which superimposed ice is overridden during an advance of a glacier that is frozen to its bed at the margin. Light lines in superimposed ice show deformation of sedimentary layering. Last cross section shows how moraine becomes separated from glacier during subsequent retreat. (Modified from Hooke, 1973a, Figure 1. Reproduced with permission of the Geological Society of America.)

Saskatchewan where, over time spans of millennia as the ice advanced in the late Wisconsinan, geomorphic features indicate that huge quantities of till accumulated on the glacier surface (Attig *et al.*, 1989; Moran *et al.*, 1980) despite the lack of nunataks projecting above the surface. Ice wedge casts and other evidence indicate that the ice advanced over permafrost in these areas.

Disintegration ridges (Gravenor and Kupsch, 1959) are one of the primary geomorphic features suggestive of such a thick till cover.



Figure 5.18. Ice cliff near Thule, Greenland. Sedimentary bedding on the left is wrinkled and overturned by ice advancing from the right. The boundary between the active and the less rapidly deforming superimposed ice is marked by a dirt band (arrows) which can be traced into a Thule–Baffin moraine. (Person in white circle for scale.)

Disintegration ridges are believed to form through a series of topographic reversals such as those just described as occurring on Thule–Baffin moraines (Clayton and Freers, 1967). As the ice sheet stagnated and began to melt down, it is suggested that ridges grew under areas of thicker debris and then melted when the debris slumped, only to be replaced by new ridges that developed under the slumped debris (Figure 5.19a). The only difference between this process and that which forms Thule–Baffin moraines is that in stagnating ice there is no significant longitudinal (or transverse) compression to generate upward flow, so the surface is continually lowered. Thus, the final slumping event deposits the debris directly on the bed. Relatively linear ridges are commonly formed by this process, although hills and circular ridges, informally called *doughnuts* (Gravenor, 1955), are also found. These features can be several meters high. Linear ridges can be hundreds of meters or kilometers in length, and may have most any orientation with respect to the

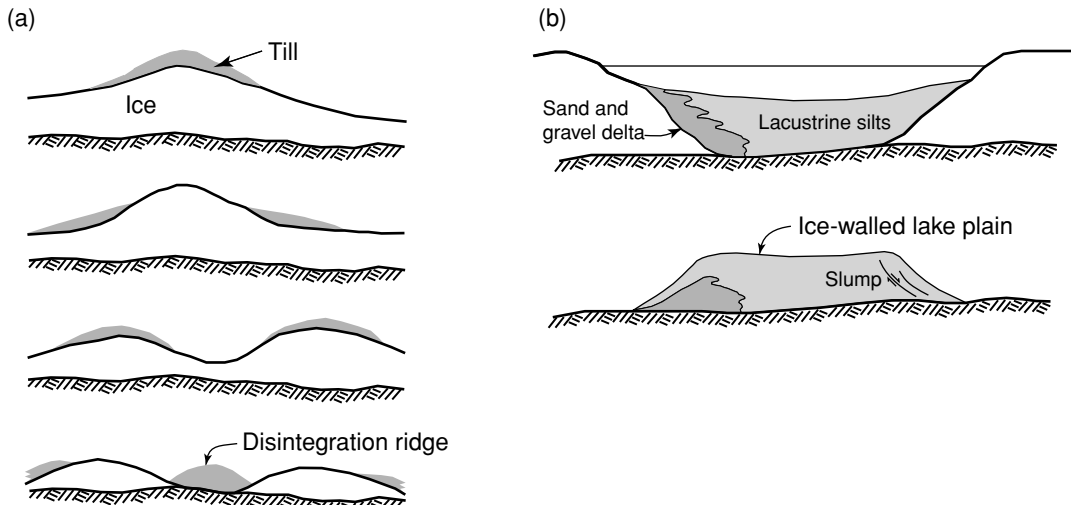


Figure 5.19. Schematic sketches showing origin of (a) a disintegration ridge, and (b) an ice-walled lake plain. (Based on Clayton and Freers, 1967.)

ice margin, depending on whether they formed from morainal accumulations like those illustrated in Figures 5.16 and 5.17 or alternatively from accumulations of debris in crevasses or superglacial stream channels.

Ice-walled lake plains are another geomorphic feature formed during disintegration of debris-covered ice masses and commonly found in the upper midwest of the United States and adjacent areas of Canada (Clayton and Cherry, 1967). The lakes would have first formed when differential melting resulted in depressions in the ice surface. Because water is densest at +4 °C, surface water that warms to this temperature sinks. The resulting convection would have circulated +4 °C water to the bottoms of the lakes, where it could melt ice if the ice was not too cold and the sediment layer in the bottom of the lake not too thick. The lakes thus would have deepened. Field evidence shows that some eventually penetrated all the way to the bed. Superglacial streams then brought sediment to the lakes, forming typical lacustrine deposits with sand and gravel deltas near stream mouths and lacustrine silts and clays further from shore. When the surrounding ice melted, these deposits were left as flat-topped hills on the landscape (Figure 5.19b).

Ice streams

In the mid 1980s, glaciologists became aware that the flow field in large ice sheets was not as homogeneous as previously believed. In particular, several linear zones of accelerated flow were found in an area of West

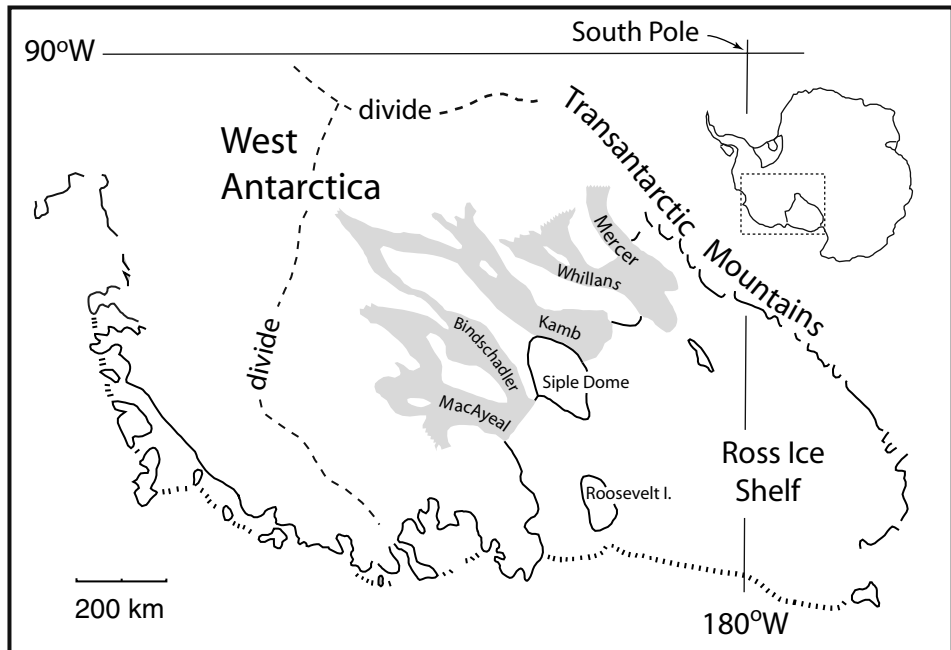


Figure 5.20. Map of West Antarctica showing the Ross Ice Shelf and the ice streams of the Siple Coast. Compiled from Jacobel *et al.* (1996), Joughin *et al.*, (1999), and Hulbe *et al.* (2000). (Reproduced with permission of AGU and the International Glaciological Society.)

Antarctica, known as the Siple Coast, which drains to the Ross Ice Shelf (Figure 5.20). These features, called *ice streams*, are tens of kilometers wide and hundreds of kilometers long. Recently, it has been discovered that they also have long tributaries, albeit with lower flow rates (Figure 5.20) (Joughin *et al.*, 1999; Hulbe *et al.*, 2000). In some cases, tributaries to different ice streams drain a common source area.

The surfaces of the faster-moving parts of ice streams are marked by longitudinal ridges that show up spectacularly on satellite imagery (Figure 5.21). Ice stream margins are delineated by en echelon crevasses in linear zones that can be up to 5 km wide. While some ice streams occupy distinct bedrock valleys, the channels beneath those on the Siple Coast are shallow and poorly defined, and their sides do not always coincide with the edges of the ice streams (Shabtaie and Bentley, 1988; Retzlaff *et al.*, 1993). However, geophysical measurements suggest that, in at least one case, streaming flow begins in a linear trough underlain by a thick sequence of sedimentary rock (Bell *et al.*, 1998; Anandakrishnan *et al.*, 1998).

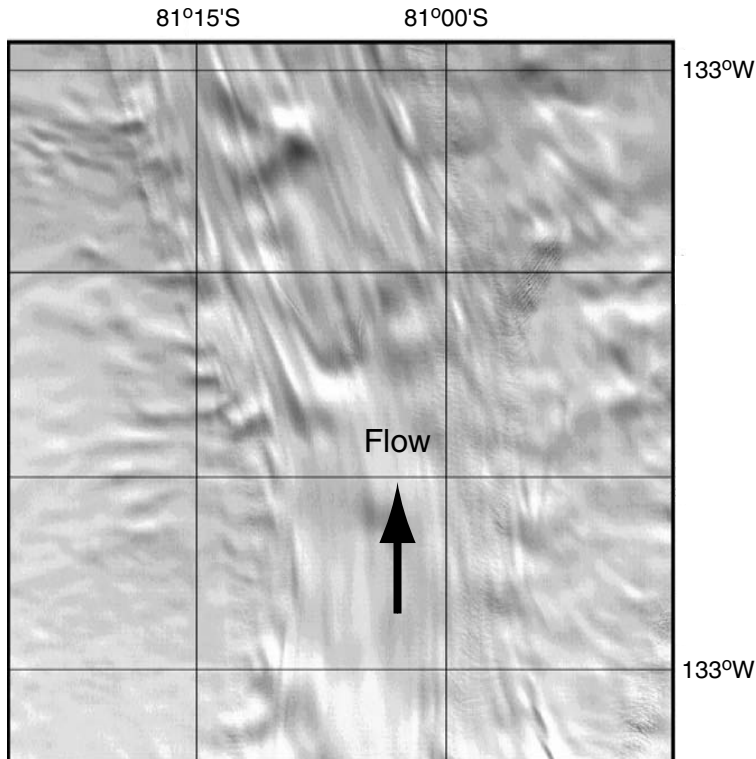


Figure 5.21. Landsat image of Bindschadler Ice Stream showing prominent lineation produced by ridges that parallel ice flow. Figure is a portion of an ASTER satellite image acquired on December 9, 2001 (scene ID is AST_L1B_003_12092001140802_1219002202735 NASA/ERSDAC). (Courtesy of Gordon Hamilton.)

The best studied ice stream, Whillans Ice Stream¹, has a maximum speed of about 825 m a^{-1} while ice on either side of it typically moves only $10\text{--}20 \text{ m a}^{-1}$ (Whillans and Van der Veen, 1993). The high velocity gradients across the lateral boundaries are responsible for the intensely crevassed shear zones that border the ice streams. In fact, it was recognition of these shear zones that, in part, led to the discovery of the ice streams.

Despite thicknesses approaching 1000 m, surface slopes of ice streams on the Siple Coast are so low that driving stresses, $\rho gh\alpha$, are only 10–20 kPa. These driving stresses do not differ appreciably from those in intervening areas. Thus, differences in driving stress cannot account for the great difference in speed. Rather, conditions at the bed are inferred to be responsible. Experiments utilizing boreholes through Whillans Ice Stream show that it is underlain by till with a high clay content, and that water pressures at the ice–till interface are very close

¹ Mercer, Whillans, Kamb, Bindschadler, and MacAyeal Ice Streams were formerly known as Ice Streams A, B, C, D, and E, respectively.

to the overburden pressure (Engelhardt *et al.*, 1990). The high water pressures either decouple the ice from the bed, allowing it to slide rapidly, or weaken the till allowing it to deform, or both. It turns out that drag provided by the bed is actually less than half of the driving stress in most cases; the rest of the resistance comes from drag in the lateral shear zones (Raymond *et al.*, 2001). The role of fine-grained till in the rapid flow of ice streams is reinforced by the finding that sedimentary rocks, which are likely to produce such till, underlie the onset zones.

Kamb Ice Stream (Figure 5.20) is also bounded by shear zones, but in this case the crevasses, recognized only on radar images, are buried beneath several meters of snow. The shear zones indicate that Kamb Ice Stream must once have been active, but velocity measurements show that the lower part of it is now nearly stagnant. Based on the thickness of the snow cover over the crevasses and the accumulation rate, it is estimated that the lower 250 km has been inactive for about 130 years (Retzlaff and Bentley, 1993). Further upstream, the crevasses are less deeply buried, and the ice stream seems to have been inactive for only ~ 30 years, and tributaries to it are still flowing at 50 m a^{-1} . This suggests that a wave of stagnation propagated upstream from the Ross Ice Shelf.

Comparable non-steady-state changes also occurred earlier on Kamb Ice Stream and recently on Whillans Ice Stream. On the former, high-resolution imaging from satellites and internal layer stratigraphy from radio echo profiles suggest that a branch of the ice stream, or perhaps the entire ice stream, once flowed north of Siple Dome (Jacobel *et al.*, 1996). Then, about 1300 years ago, this branch slowed and the branch south of Siple Dome expanded northward. Similarly, satellite images of the area where Whillans Ice Stream merges with the Ross Ice Shelf indicate that its speed decreased $\sim 50\%$ between 1963 and 1992 (Bindschadler and Vornberger, 1998). The reasons for these temporal changes constitute one of the great mysteries of ice stream behavior; currently it is thought that they are a consequence of changes in water pressure at the bed as the basal drainage system changed (Retzlaff and Bentley, 1993).

Ice stream shear margins can also migrate, resulting in changes in width, W . In their study of Whillans Ice Stream, for example, Bindschadler and Vornberger (1998) found that the northern shear margin had migrated outward at a rate of $\sim 140 \text{ m a}^{-1}$ between 1963 and 1992. If only one margin is moving, the rate of migration can be described, kinematically, by:

$$\frac{\partial W}{\partial t} = v_e - v \quad (5.27)$$

where v is the speed with which ice outside the ice stream is moving toward the shear margin and v_e is the rate at which this ice is entrained

into the ice stream (Raymond *et al.*, 2001). Along the south margin of Whillans Ice Stream, GPS measurements yield $v \approx 1 \text{ m a}^{-1}$. Estimates of v_e range from 5 to 28 m a^{-1} , suggesting an outward migration rate of order 10^1 m a^{-1} . If the strength of the substrate remains constant, an increase in width increases the force that must be resisted by the shear margins, and thus is likely to increase the speed of the ice stream.

As noted above, networks of tributaries with elevated speeds have been detected recently, extending upstream from the onset regions of some ice streams (Figure 5.20) (Joughin *et al.*, 1999). These tributaries, discovered with satellite interferometry, are typically 10–20 km wide and, unlike the main ice streams, they *do* occupy distinct valleys in the subglacial topography. Driving stresses in the tributaries are higher, and speeds lower ($<\sim 100 \text{ m a}^{-1}$), than in the main ice streams, so they are not considered to be part of the actual streams (Hulbe *et al.*, 2000). Furthermore, they do not have crevassed shear margins.

Understanding ice streams has taken on new urgency because rising sea levels, induced by global warming, could destabilize the Ross Ice Shelf causing it to break up. Should this occur, ice streams that are currently buttressed by the ice shelf might accelerate, causing a rapid draw down of the West Antarctic Ice Sheet and a further rise in sea level, perhaps amounting to several meters over the next century.

Streaming of ice is apparently not a new phenomenon. Parts of Antarctica seem to have been drained by ice streams during the last glacial maximum, $\sim 20 \text{ ka}$. Imagery of the ocean floor off the northern end of the Antarctic Peninsula, using swath bathymetry, has revealed a set of subparallel ridges and grooves, 100 km long and up to 20 km wide, that extends most of the way across the continental shelf (Canals *et al.*, 2000). The structure is attributed to molding of viscous till by fast-flowing ice, probably in an ice stream.

Similar megalineations (Figure 5.22) bear testimony to the likely presence of ice streams in the Laurentide Ice Sheet that covered the northern part of North America during the Wisconsin glaciation. The number of such ice streams is not known, but based on topography Hughes (1987) has suggested that there may have been as many as 10 major ones and more than a dozen minor ones. Among these are several in the southern part of the ice sheet. In particular, geomorphic features in central Canada suggest the possibility of streaming flow feeding the Des Moines lobe of Minnesota and Iowa (Patterson, 1997). Such ice streams would be unusual in that the bottoms of most known ice streams are well below sea level. Also widely discussed is the possibility that the Laurentide Ice Sheet was drawn down rapidly and repeatedly by a major ice stream discharging through Hudson Strait. The layers of ice rafted detritus that have been identified in cores from the North Atlantic Ocean

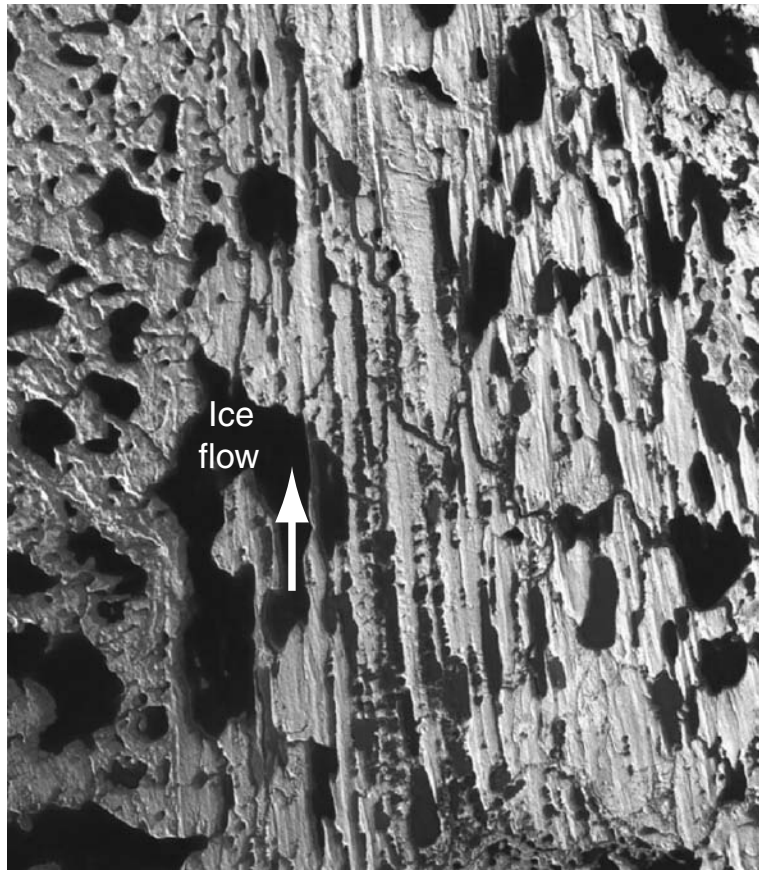


Figure 5.22. Landsat TM image of the boundary of M'Clintock Channel paleo ice stream on Victoria Island, arctic Canada. The western (left) side of the image shows topography formed beneath slow moving ice bounding the ice stream. (See Clark and Stokes (2001) for further details. Image courtesy of C. D. Clark.)

by Heinrich (1988, see also p. 36) are inferred to have been deposited by icebergs that originated in such relatively catastrophic discharges. Broecker (1994) summarizes the evidence for these events, and gives a number of references.

Summary

In this chapter we first developed a broad picture of the flow field in a glacier or ice sheet using a conservation of mass approach based on the distribution of income from accumulation and loss from ablation over the surface. We found that this leads to a flow field in which vertical velocities are downward in the accumulation area and upward in the ablation area,

and in which horizontal velocities increase with distance from the head of the glacier, reaching a maximum just below the equilibrium line, and then decrease again. In developing this model, we assumed a steady state. Steady-state conditions are rarely if ever strictly achieved in nature, but deviations from a steady state are usually sufficiently small that gross patterns of flow are approximated well by this model.

We then used conservation of momentum principles to make more precise calculations of the distribution of both horizontal and vertical velocity with depth. The calculation depends upon being able to choose a viscosity parameter, B , that is reasonably representative for the entire thickness of the glacier (or being able to specify a variation with depth), and also assumes that all deformation takes place as simple shear. Complications resulting from the presence of valley sides and a non-uniform basal boundary condition were discussed.

Next we explored the effects of drifting snow, and found that this could lead to significant differences in the flow field near the terminus in polar and temperate environments. In polar environments, such snow accumulation can lead to the development of ice-cored moraines some distance upglacier from the margin. In addition, variations in layer thickness resulting from local differences in accumulation rate can be traced at depth, using radio-echo sounding techniques. This has led to the detection of changes in the flow field over millennial time scales.

Finally, we noted that inhomogeneous bed conditions can lead to streaming flow within ice sheets. This is a topic of considerable current interest.

Chapter 6

Temperature distribution in polar ice sheets

In this chapter, we will derive the energy balance equation for a polar ice sheet. Solutions to this equation yield the temperature distribution in an ice sheet and the rate of melting or refreezing at its base. We will study some analytical solutions of the equation for certain relatively simple situations. A solution of the full equation is possible, however, only with numerical models. This is because: (1) ice sheets have irregular top and bottom surfaces; (2) the boundary conditions – that is, the temperature or temperature gradient at every place along the boundaries – vary in space and time; (3) longitudinal transport (or *advection*) of heat by ice flow cannot be handled well with the analytical solutions; and (4) there may be extension or compression transverse to the flowline, which makes the problem three dimensional. Furthermore, because the temperature distribution is governed, in part, by ice flow, and conversely, because the flow rate is strongly temperature dependent, a full solution requires coupling of the energy and flow (momentum) equations.

The thermal conditions in and at the base of an ice sheet are of interest not only to the glacier modeler, concerned with flow rates and the possibility of sliding, but also to the glacial geologist with interest in the erosive potential of the ice and processes of subglacial deposition.

Energy balance in an ice sheet

Advection

Consider a control volume of length dx , width dy , and height dz , as shown in Figure 6.1. This volume represents an element of space within an ice

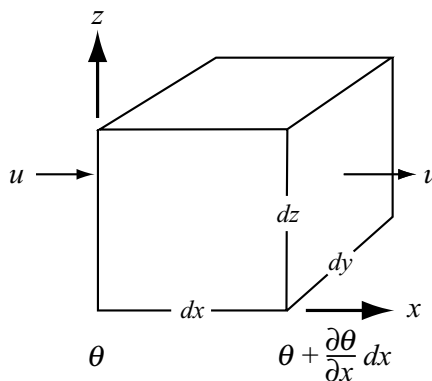


Figure 6.1. Parameters used in derivation of the advection term in the energy balance equation.

sheet. Ice flows into the volume from the left with a velocity u , and out on the right with the same velocity. The temperature of the ice flowing into the volume is θ , and that of the ice flowing out is $\theta + (\partial\theta/\partial x) dx$. The rate of energy transfer into the control volume, measured in joules per year, is:

$$(u \ dy \ dz) \ \rho \ \frac{C}{\text{m}^3 \ \text{kg}} \ \frac{\text{J}}{\text{kgK}} \ \theta = \frac{\text{J}}{\text{a}}$$

where ρ is the density of ice and C is the heat capacity or specific heat. Here, as in some of the equations in earlier chapters and in some to follow, the dimensions of the terms are written beneath the equation to clarify the physics. A similar expression can be written for the rate of energy transfer out of the volume at temperature $\theta + (\partial\theta/\partial x) dx$. The change in energy within the volume per unit time, $\partial q/\partial t$, is the difference between these two expressions, or:

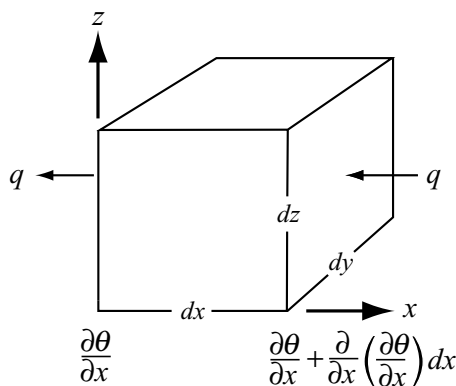
$$\begin{aligned} \frac{\partial q}{\partial t} &= u \ dy \ dz \ \rho C \left[\theta - \left(\theta + \frac{\partial\theta}{\partial x} dx \right) \right] \\ &= -u \ dx \ dy \ dz \ \rho C \frac{\partial\theta}{\partial x} \end{aligned}$$

To obtain the change of temperature in the volume per unit time, it is clear from the dimensions of the terms that it is necessary to divide by $\rho C dx dy dz$, thus:

$$\begin{aligned} \frac{\partial\theta}{\partial t} &= \frac{1}{\rho C dx dy dz} \quad \frac{\partial q}{\partial t} = -u \frac{\partial\theta}{\partial x} \\ \frac{1}{\text{kg} \ \frac{\text{J}}{\text{kgK}} \ \text{m}^3} &\quad \frac{\text{J}}{\text{a}} = \frac{\text{K}}{\text{a}} \end{aligned} \tag{6.1}$$

Here, $\partial\theta/\partial t$ is the rate of change of temperature in the volume as a result of the fact that ice is being advected into the volume at a temperature that

Figure 6.2. Parameters used in derivation of the conduction term in the energy balance equation.



is different from that of ice leaving it. Similar equations may be written for the y - and z -directions, and the results summed to obtain the total change in temperature per unit time in the control volume.

Note that we have been careful to emphasize changes in a particular element of space, the control volume, as distinct from those in an element of ice moving through space. This is because we are using an Eulerian coordinate system, with the coordinate axes fixed in space. Sometimes it is more convenient to use a Lagrangian coordinate system in which an element of ice is followed as it moves through space.

Conduction

The energy content of the control volume may also change as a result of conduction of heat. Consider the situation depicted in Figure 6.2 in which the temperature gradient across the left-hand face, $dy dz$, is $\partial\theta/\partial x$, and that across the corresponding right-hand face is:

$$\frac{\partial\theta}{\partial x} + \frac{\partial}{\partial x}\left(\frac{\partial\theta}{\partial x}\right)dx.$$

The heat flux is proportional to the temperature gradient. The constant of proportionality is K , the thermal conductivity of ice. Thus, on the left-hand face there is a heat flux:

$$q = K \frac{\partial\theta}{\partial x} dy dz \quad (6.2)$$

$$\frac{J}{m \cdot K} \frac{K}{m} m \cdot m = \frac{J}{a}$$

Heat flows from warm areas to cold areas, which means that for positive $\partial\theta/\partial x$, the heat flux is to the left, or out of the left-hand side of the control volume in Figure 6.2.

As before, we write a similar expression for the heat flux into the control volume, and subtract the flux out from the flux in, thus:

$$\begin{aligned}\frac{\partial q}{\partial t} &= \left[K \frac{\partial \theta}{\partial x} + \frac{\partial}{\partial x} \left(K \frac{\partial \theta}{\partial x} \right) dx - K \frac{\partial \theta}{\partial x} \right] dy dz \\ &= \frac{\partial}{\partial x} \left(K \frac{\partial \theta}{\partial x} \right) dx dy dz \\ &= \left(K \frac{\partial^2 \theta}{\partial x^2} + \frac{\partial K}{\partial x} \frac{\partial \theta}{\partial x} \right) dx dy dz\end{aligned}$$

The change in temperature in the control volume is then:

$$\frac{\partial \theta}{\partial t} = \frac{K}{\rho C} \frac{\partial^2 \theta}{\partial x^2} + \frac{1}{\rho C} \frac{\partial K}{\partial x} \frac{\partial \theta}{\partial x} \quad (6.3)$$

$K/\rho C$ is called the thermal diffusivity, κ , so Equation (6.3) becomes:

$$\frac{\partial \theta}{\partial t} = \kappa \frac{\partial^2 \theta}{\partial x^2} + \frac{1}{\rho C} \frac{\partial K}{\partial x} \frac{\partial \theta}{\partial x} \quad (6.4)$$

Thus, the change in temperature with time in the control volume due to conduction is related to the changes, as one moves from one side of the volume to the other, in the temperature gradient, $\partial \theta / \partial x$, and in K . Again, similar equations may be written in the y - and z -directions.

Strain heating

Finally, a certain amount of heat is generated within the control volume owing to straining of the ice. During deformation, the energy expenditure is the work done divided by the time required to do the work, and work is force times distance, thus:

$$\frac{\text{work}}{\text{time}} = \frac{\text{force} \times \text{distance}}{\text{time}} \quad (6.5)$$

In simple shear (Figure 6.3), the average distance moved in a unit time is one-half of the displacement of the top of the control volume with respect to the bottom, or $\frac{1}{2}(\partial u / \partial z) dz$, and the force exerted is $\sigma_{zx} dx dy$. In Chapter 2 (Equation (2.6a)) we noted that strain rates may be defined in terms of velocity derivatives, thus:

$$\dot{\epsilon}_{zx} = \frac{1}{2} \left(\frac{\partial u}{\partial z} + \frac{\partial w}{\partial x} \right)$$

As $\partial w / \partial x = 0$ in simple shear, $\frac{1}{2} \partial u / \partial z = \dot{\epsilon}_{zx}$ and Equation (6.5) becomes:

$$\begin{aligned}\frac{\text{work}}{\text{time}} &= \sigma_{zx} dx dy \dot{\epsilon}_{zx} dz \\ \frac{\text{N}}{\text{m}^2} \text{ m} \text{ m} \frac{1}{\text{a}} \text{ m} &= \frac{\text{N} - \text{m}}{\text{a}} = \frac{\text{J}}{\text{a}}\end{aligned}$$

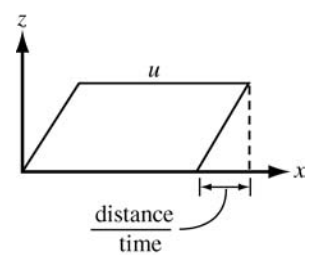


Figure 6.3. Work done in simple shear.

Dimensionally, this is seen to be a rate of energy expenditure, so again we divide by $\rho C dx dy dz$ to obtain the rate of change of temperature per unit volume:

$$\frac{\partial \theta}{\partial t} = \frac{\sigma_{zx} \dot{\varepsilon}_{zx}}{\rho C} \quad (6.6)$$

Equation (6.6) was derived for a situation in which deformation was restricted to simple shear in the $x-z$ plane. In the general case, other components of the stress tensor will be different from 0, so other deformations will be occurring. With a little more background, it is relatively easy to show that the general form of Equation (6.6) is:

$$\frac{\partial \theta}{\partial t} = \frac{\sigma_e \dot{\varepsilon}_e}{\rho C} \quad (6.7)$$

but we will not do this here. For convenience, Q is commonly used to represent the heat production instead of $\sigma_e \dot{\varepsilon}_e$ or $\sigma_{zx} \dot{\varepsilon}_{zx}$, thus:

$$\frac{\partial \theta}{\partial t} = \frac{Q}{\rho C} \quad (6.8)$$

If deformation is restricted to simple shear, we can approximate σ_{zx} by $\rho g d\alpha$ and $\dot{\varepsilon}_{zx}$ by $(\sigma_{zx}/B_o)^n e^{k\theta}$ (see Equations (4.6)–(4.8)). Then:

$$\frac{Q}{\rho C} = \frac{(\rho g d\alpha)^{n+1} e^{k\theta}}{\rho C B_o^n} \quad (6.9)$$

The generalized energy balance equation

The rate of change of temperature in the control volume is the sum of the changes represented by Equations (6.1), (6.4), and (6.8), plus changes resulting from heat advection and conduction in the y - and z -directions, thus:

$$\begin{aligned} \frac{\partial \theta}{\partial t} &= \kappa \left[\frac{\partial^2 \theta}{\partial x^2} + \frac{\partial^2 \theta}{\partial y^2} + \frac{\partial^2 \theta}{\partial z^2} \right] + \frac{1}{\rho C} \left[\frac{\partial K}{\partial x} \frac{\partial \theta}{\partial x} + \frac{\partial K}{\partial y} \frac{\partial \theta}{\partial y} + \frac{\partial K}{\partial z} \frac{\partial \theta}{\partial z} \right] \\ &\quad - u \frac{\partial \theta}{\partial x} - v \frac{\partial \theta}{\partial y} - w \frac{\partial \theta}{\partial z} + \frac{Q}{\rho C} \end{aligned} \quad (6.10)$$

As Equation (6.10) is rather cumbersome, it is often convenient to simplify it by using the del operator, defined by:

$$\nabla = \frac{\partial}{\partial x} \hat{\mathbf{i}} + \frac{\partial}{\partial y} \hat{\mathbf{j}} + \frac{\partial}{\partial z} \hat{\mathbf{k}} \quad (6.11)$$

where $\hat{\mathbf{i}}$, $\hat{\mathbf{j}}$, and $\hat{\mathbf{k}}$ are unit vectors in the x -, y -, and z -directions, respectively. When applied to scalar quantities such as either κ or θ , the del operator gives a gradient, which is a vector quantity. Accordingly, the fourth to sixth terms and the seventh to ninth terms, respectively, in

Equation (6.10) become scalar or dot products of two vectors, thus:

$$\frac{\partial \theta}{\partial t} = \kappa \nabla^2 \theta + \frac{1}{\rho C} \nabla K \cdot \nabla \theta - \vec{u} \cdot \nabla \theta + \frac{Q}{\rho C} \quad (6.12a)$$

Here, \vec{u} is the vector velocity. The first term on the right in Equation (6.12a) also represents a scalar product: $\nabla \cdot \nabla \theta$.

It is sometimes convenient to define:

$$\frac{D\theta}{Dt} = \frac{\partial \theta}{\partial t} + \vec{u} \cdot \nabla \theta$$

in which case, Equation (6.12a) becomes:

$$\frac{D\theta}{Dt} = \kappa \nabla^2 \theta + \frac{1}{\rho C} \nabla K \cdot \nabla \theta + \frac{Q}{\rho C} \quad (6.12b)$$

Equation (6.12a) is the Eulerian form of the equation, in which the coordinates are fixed in space, whereas Equation (6.12b) is the Lagrangian form in which the coordinate system is moving with the ice. $D\theta/Dt$ is known as the substantial or Lagrangian derivative.

Dependence of K on temperature

The thermal conductivity of ice is $\sim 66 \text{ MJ m}^{-1}\text{a}^{-1}\text{K}^{-1}$ at 0°C and $\sim 83 \text{ MJ m}^{-1}\text{a}^{-1}\text{K}^{-1}$ at -60°C . Thus, to the extent that the temperature varies in any of the coordinate directions, K also varies. This effect is normally neglected, except in relatively sophisticated numerical models, and we will follow this custom. Equation (6.10) thus becomes:

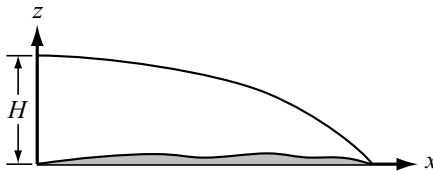
$$\frac{\partial \theta}{\partial t} = \kappa \left[\frac{\partial^2 \theta}{\partial x^2} + \frac{\partial^2 \theta}{\partial y^2} + \frac{\partial^2 \theta}{\partial z^2} \right] - u \frac{\partial \theta}{\partial x} - v \frac{\partial \theta}{\partial y} - w \frac{\partial \theta}{\partial z} + \frac{Q}{\rho C} \quad (6.13)$$

Neglecting the temperature dependence of K is reasonable because the effect is relatively small which, in combination with small temperature gradients, makes these terms negligible in comparison with the others in Equation (6.10).

The steady-state temperature profile at the center of an ice sheet

Our next task is to solve Equation (6.13) for some relatively simple situations. The first is that at an ice divide, at the center of an ice sheet, a problem first investigated by Robin (1955). The following development follows his closely. The coordinate system we will use is shown in Figure 6.4: x is horizontal and directed down glacier, and z is vertical and positive upward; $z = 0$ is at the bed.

Figure 6.4. Coordinate system used in calculating the steady-state temperature profile at the center of an ice sheet.



Simplifying assumptions

At an ice divide, there is no flow in the horizontal directions, and the temperature field is assumed to be symmetrical about the divide. Thus, u and v are zero, as are any derivatives in the x and y directions. We further assume that strain rates are small, so strain heating can be neglected. Finally, we seek a steady state solution so $\partial\theta/\partial t = 0$. Equation (6.13) now becomes:

$$0 = \kappa \frac{d^2\theta}{dz^2} - w \frac{d\theta}{dz} \quad (6.14)$$

As θ is now a function of z alone, this is an ordinary differential equation.

In order to integrate this, w must be expressed as a function of z . To do this we assume that ice is incompressible, that $w = 0$ on the bed, and, initially, that the longitudinal strain rate is independent of depth. These are the conditions used to derive Equation (5.21). In our present coordinate system with the origin on the bed and the z -axis positive upward, Equation (5.21) is:

$$w = \frac{z}{H} w_s \quad (6.15)$$

We have not yet specified either the sign or the magnitude of w_s . At an ice divide, the vertical velocity is downward (Figure 3.1a), so the sign of w_s is negative in the coordinate system of Figure 6.4, and in the steady state $|w_s| = b_n$, the accumulation rate. Thus replacing w_s with $-b_n$ in Equation (6.15), combining it with (6.14), and rearranging, we obtain:

$$0 = \frac{d^2\theta}{dz^2} + \frac{b_n z}{\kappa H} \frac{d\theta}{dz} \quad (6.16)$$

To calculate the temperature distribution, this equation must be integrated twice.

The first integration

For the first integration, let $2\zeta^2 = b_n/\kappa H$ and $\beta = d\theta/dz$. Equation (6.16) then becomes:

$$0 = \frac{d\beta}{dz} + 2\zeta^2 z \beta \quad (6.17)$$

Separating variables, we obtain:

$$\int \frac{d\beta}{\beta} = -2\zeta^2 \int zdz$$

which may be integrated to yield:

$$\ln \beta = -\zeta^2 z^2 + c$$

or:

$$\beta = e^c e^{-\zeta^2 z^2} \quad (6.18)$$

The next task is to evaluate the constant of integration, e^c .

The basal boundary condition

The constant of integration may be evaluated by using the boundary condition $\beta = \beta_o$ on $z = 0$. In other words, we presume that the temperature gradient at the bed, β_o , is known or can be estimated. Making these substitutions in Equation (6.18) yields $e^c = \beta_o$. Thus, replacing e^c with β_o and β with $d\theta/dz$ in Equation (6.18) yields:

$$\frac{d\theta}{dz} = \beta_o e^{-\zeta^2 z^2} \quad (6.19)$$

This is a solution for the temperature gradient as a function of elevation above the bed.

The requirement that the temperature gradient in the basal ice be known is fundamentally unavoidable. However, this is not as serious a problem as one might, at first, expect. In the steady state, β_o is adjusted so that all of the heat coming from within the Earth, the geothermal flux, can be conducted upward into the ice. Thus, if the geothermal flux can be estimated, β_o can be calculated because the constant of proportionality between the two, the thermal conductivity of ice, K , is known.

To clarify the physical processes by which β_o is adjusted, consider a non-steady-state situation in which β_o is too low. Some of the geothermal heat would then remain at the ice–rock interface where it would warm the ice. Because the temperature decreases upward in the glacier, the ice being colder than the Earth’s interior, such warming would increase β_o until all of the heat could be conducted upward into the ice, thus tending to re-establish the steady state. (For the moment, we neglect basal melting.)

Geothermal heat is produced by radioactive decay in the crustal rocks as well as by residual cooling of the mantle and core. Numerous measurements of the geothermal flux have been made, so we have a fair idea of its magnitude in different geological terranes. Geophysicists use the *heat flow unit*, or HFU, to describe this flux: 1 HFU is

Table 6.1. *Geothermal fluxes in some geological terranes in which glaciers are or were found*

Locality	Heat flux		Basal gradient K m^{-1}	Reference
	HFU	mW m^{-2}		
Canadian Shield	0.8	33	0.0151	
World average	1.2	50	0.0226	
East Antarctica	1.2 ¹	50	0.0226	Budd <i>et al.</i> , 1971
Baffin Bay	1.35	56	0.0255	
West Antarctica	1.4 ¹	59	0.0264	Budd <i>et al.</i> , 1971

¹ Estimated.

$1 \mu\text{cal cm}^{-2} \text{s}^{-1}$. In glaciology, however, it is more common to use W m^{-2} . The world-wide average geothermal flux is 1.2 HFU or 50 mW m^{-2} . This corresponds to a temperature gradient in basal ice of 0.0226 K m^{-1} . The gradient in the underlying rock will normally be somewhat different as the thermal conductivity of the rock will not be the same as that of the ice. In general, geothermal fluxes are highest in volcanic terranes, high in geologically young terranes, and lowest in geologically ancient terranes. A few examples of geothermal fluxes in glaciated areas are given in Table 6.1.

In the discussion above, we asserted that knowledge of β_0 was “fundamentally unavoidable”. It is true, of course, that a boundary value problem such as this could be solved with some other basal boundary condition, such as the basal temperature. (This will be left as an exercise for the reader.) However, as the basal temperature is one of the quantities that we are particularly eager to determine, and as basal temperatures are much harder to estimate from existing data than are basal temperature gradients, choosing β_0 as the basal boundary condition is the only logical choice in most situations.

The second integration

To obtain the actual temperature distribution, it is necessary to integrate Equation (6.19). Separating variables as before yields:

$$\int_{\theta(h)}^{\theta_s} d\theta = \beta_0 \int_h^H e^{-\zeta^2 z^2} dz \quad (6.20)$$

Here, the integration is from some level, $z = h$, in the glacier, where the temperature is $\theta(h)$, to the surface at $z = H$ where the temperature

is θ_s . (Note that in this case, rather than solve Equation (6.19) as an indefinite integral and then evaluate a constant of integration by applying a boundary condition, it is more convenient to express the integrals as definite integrals. Thus the boundary condition, $\theta = \theta_s$ on $z = H$, is incorporated into the limits of integration. Further discussion of this boundary condition is deferred for the moment.)

The integral on the right-hand side of Equation (6.20) does not have a solution in closed form. However, it occurs frequently, and thus has been tabulated. In addition, many computer statistical packages have solutions. The challenge is to express it in the terms used in these tables.

We first express the integral on the right-hand side as the difference between integrals over the range $0 \rightarrow H$ and $0 \rightarrow h$, thus:

$$\theta_s - \theta(h) = \beta_o \left[\int_0^H e^{-\zeta^2 z^2} dz - \int_0^h e^{-\zeta^2 z^2} dz \right] \quad (6.21)$$

and then make the substitution: $\zeta z = t$, whence $dz = dt/\zeta$, and $t = \zeta h$ on $z = h$. We also multiply and divide by $\sqrt{\pi}/2$, thus:

$$\theta_s - \theta(h) = \frac{\sqrt{\pi}}{2} \frac{\beta_o}{\zeta} \left[\frac{2}{\sqrt{\pi}} \int_0^{\zeta H} e^{-t^2} dt - \frac{2}{\sqrt{\pi}} \int_0^{\zeta h} e^{-t^2} dt \right] \quad (6.22)$$

By definition:

$$erf(x) = \frac{2}{\sqrt{\pi}} \int_0^x e^{-t^2} dt \quad (6.23a)$$

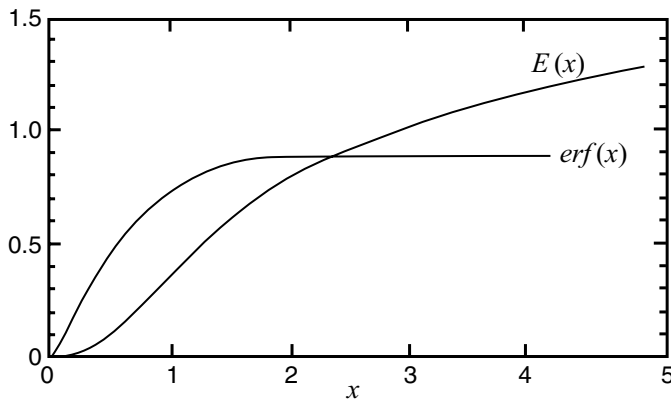
where $erf(x)$ is called the error function of x . Thus, our final solution for the temperature, $\theta(h)$, at depth h is:

$$\theta(h) = \theta_s - \frac{\sqrt{\pi}}{2} \frac{\beta_o}{\zeta} [erf(\zeta H) - erf(\zeta h)] \quad (6.24)$$

As noted, $erf(x)$ has been tabulated, so values of it can be looked up, much as can values of a sine or cosine. Caution is required, however, as some tables define $erf(x)$ slightly differently than we have in Equation (6.23a), and thus require a different set of substitutions in Equation (6.21). A common alternative definition is:

$$erf(x) = \frac{1}{\sqrt{2\pi}} \int_0^x e^{-\frac{t^2}{2}} dt \quad (6.23b)$$

Figure 6.5. Values of the error function, $\text{erf}(x)$, as defined by Equation (6.23c), and of Dawson's integral, $E(x)$, for a typical range of values of $x = \zeta H$. (Modified from Budd, 1969, Figure 4.10. Reproduced with permission of the Australian Antarctic Division.)



which requires the substitution: $\zeta z = t/\sqrt{2}$. This leads to other changes in Equations (6.22) and (6.24). Budd (1969) uses a less common definition, namely:

$$\text{erf}(x) = \int_0^x e^{-t^2} dt \quad (6.23c)$$

and has plotted this (Figure 6.5) along with another function that arises in calculations of temperature distributions in ice sheets. With this definition, Equation (6.22) can be written:

$$\theta(h) = \theta_s - \frac{\beta_o}{\zeta} [\text{erf}(\zeta H) - \text{erf}(\zeta h)] \quad (6.25)$$

In applying Equation (6.24) or (6.25), note that β_o is negative in the coordinate system of Figure 6.4.

The boundary condition at the surface

As noted, the boundary condition at the surface, $z = H$, is the ice temperature, θ_s , and this must be known in order to calculate a temperature profile from Equations (6.24) or (6.25). Below, we will show that the temperature at a depth of about 10 m in a glacier is very close to the mean annual atmospheric temperature, θ_a , so it is normally assumed that $\theta_s = \theta_a$. However, it may be well to note some situations in which this approximation is not very good.

Temperatures in the ablation zones of some glaciers may be somewhat warmer than the mean annual temperature. This is because snow insulates the ice during the winter, preventing cooling. In addition, percolating meltwater reaches the snow/ice interface soon after melting starts in the spring, thus warming the ice faster than would be the case with conduction alone. On Barnes Ice Cap, these two effects result in

near-surface ice temperatures that are about 2 °C above the mean annual temperature (Hooke *et al.*, 1983).

Somewhat higher on a glacier, near and above the equilibrium line, percolating meltwater can penetrate into the firn of prior years. When this water refreezes the heat of fusion is released at a significant depth in the glacier, not just at the snow/ice interface. The warming effect is thus much enhanced, and ice temperatures in this zone may be several degrees warmer than the mean annual temperature.

At high latitudes and altitudes on polar ice sheets, the ice temperature may be slightly below the mean annual temperature because radiative cooling during the clear winter night is more effective than heating during the summer day.

Further discussion of these effects and additional references may be found in Hooke *et al.* (1983).

Melting and freezing at the bed

In our analysis so far, we have tacitly assumed that the temperature at the base of the glacier is below the melting point. However, this assumption has not been incorporated into Equation (6.24) or (6.25). To be specific, if the bed is at the pressure melting point and melting is occurring there, some of the geothermal heat is clearly being used for that purpose and is not being conducted upward into the ice. Thus, our estimate of β_o is likely to be too high. If we inadvertently insert such a value of β_o into Equation (6.24) or (6.25), the calculated temperature at the bed, θ_o , will turn out to be greater than the pressure melting temperature which is clearly impossible.

To obtain a correct solution for the temperature profile in this case, β_o must be adjusted downward. The procedure is straightforward. Because $\text{erf}(0) = 0$ and $\theta(0) = \theta_{\text{pmp}}$, then at the pressure melting point temperature, Equation (6.24) can be solved for β_o , thus:

$$\beta_o = \frac{2\zeta}{\sqrt{\pi}} \frac{(\theta_s - \theta_{\text{pmp}})}{\text{erf}(\zeta H)} \quad (6.26)$$

The melting point is depressed approximately 0.098 K MPa⁻¹ (if the water produced is saturated with air) so, for example, θ_{pmp} under 500 m of ice would be ~ -0.4 °C. Inserting the value of β_o obtained from Equation (6.26) into Equation (6.24) and solving for temperatures at other depths in the glacier will give the desired temperature profile. (Note that this approach is equivalent to solving Equation (6.17) with a temperature boundary condition at the bed.)

The basal melt rate, dm/dt , can also be calculated. The heat available for melting is the difference between the geothermal heat flux and the

heat flux into the ice, or $K(\beta_G - \beta_o)$, where β_G is the gradient that would be required to conduct the geothermal flux upward into the ice. Thus, we obtain:

$$\frac{dm}{dt} = K \frac{(\beta_G - \beta_o)}{L} \cong 220(\beta_G - \beta_o) \text{ mm a}^{-1} \quad (6.27)$$

where L is the latent heat of fusion, and the result is in mm a^{-1} if the gradients are in K m^{-1} .

It is also possible that water formed by basal melting at some distant locality has moved along the bed to the site at which the temperature profile is to be calculated. Until all such water is refrozen, perhaps incorporating sediment into the ice in the process, it will keep the basal temperature at the pressure melting point. Again, Equation (6.24) does not know about this water, so the intelligent scientist must intervene. Presumably, he or she has calculated basal melt and freeze rates further upglacier, and has kept track of how much of the water produced has not refrozen. In any case, the procedure is similar to that above, except that now the value of β_o calculated from Equation (6.26) will be greater than that necessary to conduct the geothermal heat upward into the ice, and dm/dt in Equation (6.27) will be negative, indicating freezing.

Character of the temperature profile

Several temperature profiles calculated from Equation (6.24) are shown in Figure 6.6a. For the conditions assumed, the ice is nearly isothermal in the upper few hundred meters and then warms rapidly near the bed. Higher vertical velocities, resulting from higher accumulation rates at the surface, increase the thickness of the isothermal zone and decrease the basal temperature.

In essence, cold ice is advected downward from the surface, and the upward-moving geothermal heat warms this descending ice. With higher rates of advection (higher vertical velocities), the heat supplied can warm a smaller fraction of the descending ice, so the ice column as a whole is colder.

The shape of the temperature profile can be understood qualitatively in the following way. Consider the three elements of ice labeled A, B, and C in Figure 6.7. All three are moving downward, but because w decreases with depth (Equation (6.15)), element A will be moving fastest and element C slowest. As element C moves down, it must warm up and this requires heat. Thus, the heat flux out of the top of this element will be less than that into the bottom, and the temperature gradient required to conduct this heat will be less at the top of the element than at the bottom. However, w is small in this part of the glacier, so despite the

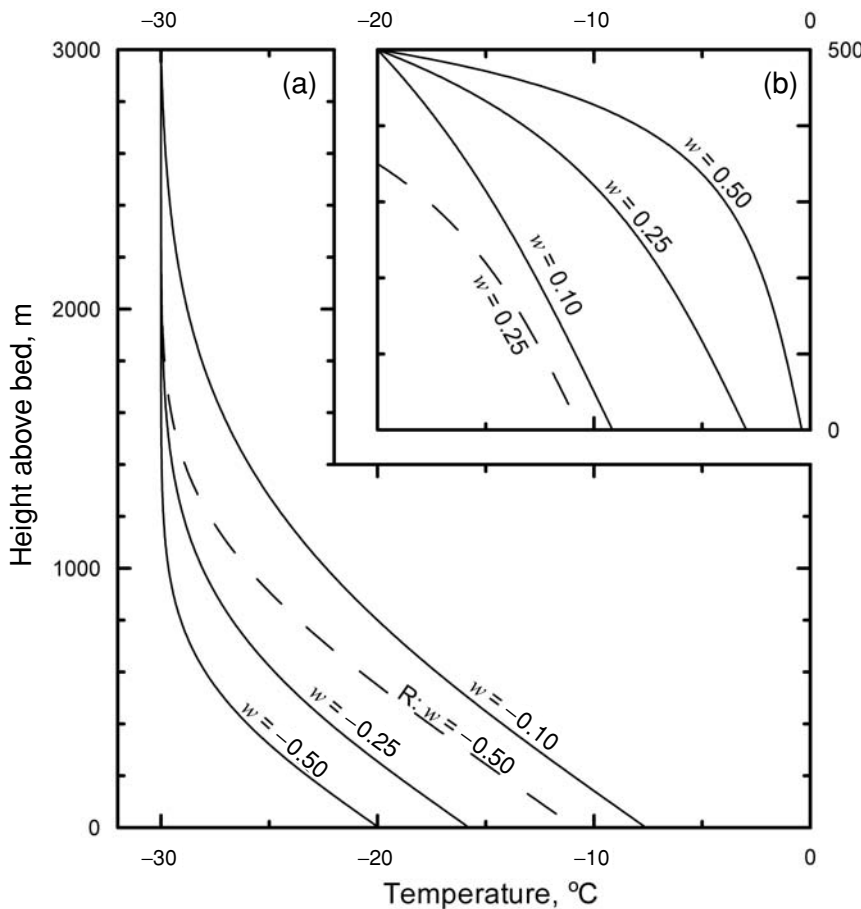
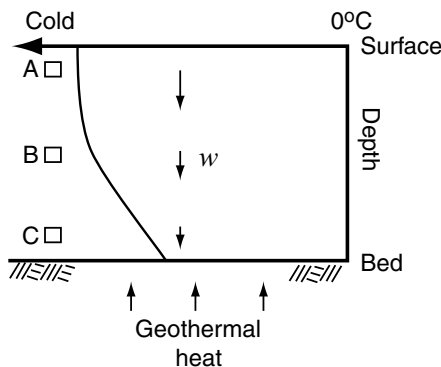


Figure 6.6. Calculated temperature profiles in polar ice sheets.

(a) Accumulation zone. Vertical velocity is negative or downward. Parameters, other than w , are the same for all curves. Dashed profile labeled “R: $w = -0.50$ ” is calculated from Equation (5.25) for w . (b) Ablation zone. Vertical component of velocity is positive or upward. (Modified from Hooke (1977), Figure 3. Reproduced with permission of The University of Washington.)

comparatively high temperature gradient here, this element does not have to warm up very much and the change in temperature gradient through it is small, as shown. Element B has a higher velocity, and the temperature gradient is still comparatively high here, at mid-depth in the glacier, so this element must warm up a lot. Thus, here the change in temperature gradient through the element is rather large. Element A has the highest vertical velocity, but at this level in the glacier nearly all of the heat introduced at the base has been consumed in warming deeper ice. Thus, the temperature gradient here is quite low, and despite

Figure 6.7. Qualitative illustration of effect of downward vertical velocity on a temperature profile.



its high velocity, element A does not have to warm up very much. Thus, again, the change in temperature gradient through the element is small, as shown.

Later we will examine temperature profiles in the ablation area, where the vertical velocity is upward. However, the reader may find it both challenging and instructive to try to deduce the character of the profile there, using the logic just presented.

Error introduced by the assumed vertical velocity distribution

One of the most tenuous assumptions we made in deriving Equation (6.24) was that the longitudinal strain rate, $\partial u / \partial x$, was independent of depth. This led to the use of a linear decrease in w with depth (Equation (6.15)) in Equation (6.16). As discussed in Chapter 5, we know that $\partial u / \partial x$ decreases with depth under most conditions. Early attempts to use a more realistic relation for w were made by Philberth and Federer (1971) and Budd *et al.* (1971), but they relied on *ad hoc* relations without good theoretical basis.

It would be convenient if we could simply use either Equation (5.24) or Equation (5.25) for w , but this leads to solutions for β that cannot be integrated a second time. Thus, a numerical integration is necessary.

To illustrate the importance of this effect, let us use Equation (5.25) in place of Equation (5.21) for w . The solution for the temperature gradient is then:

$$\frac{d\theta}{dz} = \beta_0 e^{-\xi z^3} \quad (6.28)$$

where $\xi = b_n / 3\kappa H^2$. Integrating this numerically with $w = b_n = -0.5 \text{ m a}^{-1}$ yields the dashed curve in Figure 6.6a. Thus, using this

more realistic expression for w leads to basal temperatures that are nearly 10 °C warmer than given by Equation (6.24) for otherwise similar conditions!

Temperature profiles in the ablation zone

In the ablation area, except very near the equilibrium line, w is positive, or upward. In this case, the solution for the temperature gradient becomes:

$$\frac{d\theta}{dz} = \beta_o e^{\zeta^2 z^2} \quad (6.29)$$

Again, this equation cannot be integrated in closed form, and the integral has not been tabulated. Examples of profiles obtained by a numerical integration are shown in Figure 6.6b. Of particular interest is the exponential increase in gradient near the surface, a result that is apparent from Equation (6.29). A consequence of this behavior is that basal temperatures must commonly reach the melting point in the ablation zone, even with modest ice thicknesses and vertical velocities. Furthermore, when basal temperatures do reach the melting point, β_o becomes small, so most of the geothermal heat is trapped at the bed resulting in high basal melt rates.

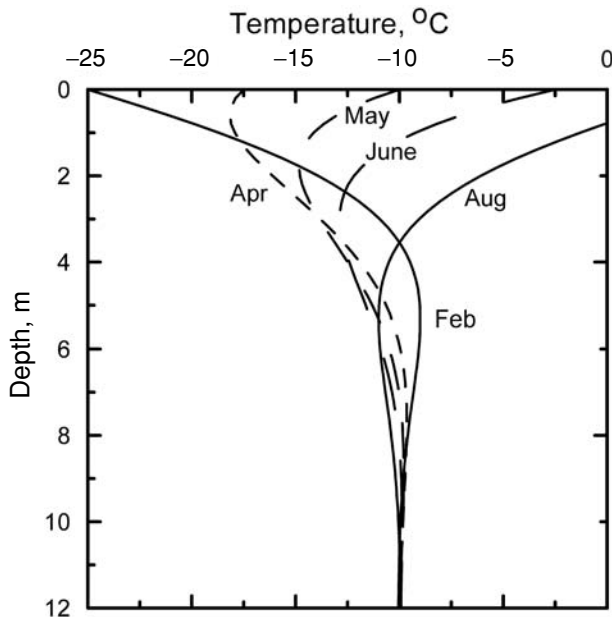
Temperature profiles near the surface of an ice sheet

Earlier (p. 122) we noted that although the temperature at the surface, θ_s , varies seasonally, the temperature at a depth of ~ 10 m is very close to the mean annual temperature. Let us now verify this. We adopt a coordinate system with $z = 0$ at the surface and the z -axis pointing downward. At the surface we assume that the seasonal variation can be described by $\theta(z = 0, t) = \frac{1}{2}\theta_r \sin(\omega t)$, where θ_r is the annual temperature range (twice the amplitude). Beneath the surface, we expect the oscillations to be damped. Let the annual temperature range at depth be denoted by $\Delta(z) = \theta_{\max}(z) - \theta_{\min}(z)$. Our goal is to calculate the depth at which Δ decreases to an acceptably small value. Then, we can measure the temperature at this depth and use it as our boundary condition at the surface.

Ignoring horizontal gradients, strain heating, and vertical advection (so there is no accumulation, ablation, or compaction), Equation (6.13) simplifies to:

$$\frac{\partial\theta(z, t)}{\partial t} = \kappa \frac{\partial^2\theta(z, t)}{\partial z^2} \quad (6.30)$$

Figure 6.8. Seasonal variation in near-surface temperature profiles in the dry-snow zone of an ice sheet.



The solution to this is:

$$\theta(z, t) = \frac{1}{2} \theta_r e^{-z\sqrt{\frac{\omega}{2\kappa}}} \sin\left(\omega t - z\sqrt{\frac{\omega}{2\kappa}}\right) \quad (6.31)$$

where ω is the period of the variation (in this case, 2π radians per year) (Carslaw and Jaeger, 1959, p. 65). If the seasonal variation in temperature at the surface is sinusoidal, the temperature profile at any given time during the year can be calculated from Equation (6.31). Some profiles for representative times are shown in Figure 6.8.

Now at any given depth, $\theta_{\max}(z, t)$ and $\theta_{\min}(z, t)$ occur when $\omega t - z\sqrt{\omega/2\kappa} = \pm\pi/2$, respectively. Thus, using Equation (6.31) to obtain $\theta(z, t)$ at these two times, and solving for z yields:

$$z = \left(\frac{2\kappa}{\omega}\right)^{\frac{1}{2}} \ln \frac{\theta_r}{\Delta} \quad (6.32)$$

From this we find that $z = 10$ m if $\kappa = 16 \text{ m}^2\text{a}^{-1}$, a value appropriate for unpacked snow, and Δ is 1.2% of θ_r . In ice, with $\kappa = 37.2 \text{ m}^2\text{a}^{-1}$, $z = 15.2$ m. Thus, temperatures measured at a depth of 10 m in snow and firn or 15 m in ice should closely approximate the mean annual temperature.

The most serious assumption in this calculation is that accumulation and ablation can be ignored. In the accumulation area, accumulating snow insulates the surface, reducing θ_r . This is probably not too serious a problem. However, in the ablation area, as noted earlier, there is not

only the insulating effect of snow during the fall and winter, but also warming by percolating meltwater in the late spring or early summer and then lowering of the ice surface later in the summer. Combined, these processes result in 15 m temperatures that are likely to be warmer than the mean annual temperature, as noted.

Equation (6.32) can also be used to calculate effects of temperature oscillations over longer time spans. For example, oxygen isotope variations in ice cores have revealed temperature cycles during the Pleistocene that have a range ~ 5 °C and a period of ~ 2000 years. These cycles were discovered by Dansgaard and Oeschger (1989) and are called Dansgaard–Oeschger cycles (see also Dansgaard *et al.*, 1993). Their cause is not yet understood. With $\kappa = 38 \text{ m}^2 \text{a}^{-1}$, a value appropriate for ice at -10 °C, and a more liberal Δ of $0.05\theta_r$, $z = 466$ m. Thus, such cycles would affect basal temperatures significantly only near the margin where the ice was less than ~ 500 m thick.

The speed, \hat{w} , of propagation of a temperature maximum or minimum resulting from such a sinusoidal cycle of temperature is $(2\omega\kappa)^{1/2}$, and the time lag between the maximum at the surface and the maximum at some depth, z , is thus, z/\hat{w} . In the case of the Dansgaard–Oeschger cycles, the speed would be about 0.49 m a^{-1} , and the signal would reach a depth of 466 m after about 950 years.

Let us now consider the temperature profile in the firn area some distance from an ice divide, a problem studied by Robin (1970). We will restrict the problem to two dimensions; assume that strain heating is negligible; and ignore conduction as K is low in firn, while the advective terms are significant. Equation (6.13) then becomes:

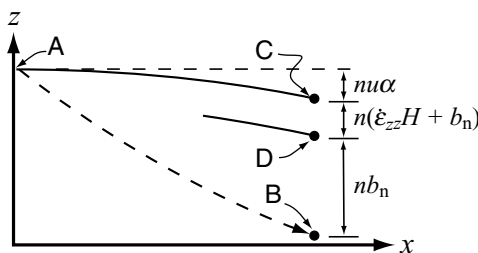
$$\frac{\partial\theta}{\partial t} = -u\frac{\partial\theta}{\partial x} - w\frac{\partial\theta}{\partial z} \quad (6.33)$$

$\partial\theta/\partial t$ may be thought of as being composed of two parts, a thickening or thinning of the ice sheet with time, and climatic change, thus:

$$\frac{\partial\theta}{\partial t} = \lambda(\dot{\varepsilon}_{zz}H + b_n) + \frac{\partial\theta_0}{\partial t}$$

Here, $\dot{\varepsilon}_{zz}H$ represents the change in thickness of the ice sheet by flow (or vertical strain), b_n represents thickening by accumulation, and the difference between them is the net change in surface elevation. Multiplication by the lapse rate, λ , or rate of decrease in temperature with increasing elevation yields the resulting change in temperature at the glacier surface. (As $\dot{\varepsilon}_{zz}$ is normally compressive, or negative, in an accumulation zone, $\dot{\varepsilon}_{zz}H$ will be a negative number; b_n is positive. If $(\dot{\varepsilon}_{zz}H + b_n)$ turns out to be negative, representing net thinning, multiplication by the negative lapse rate yields a positive $\partial\theta/\partial t$.) To this is added any change in temperature due to secular climatic change, $\partial\theta_0/\partial t$.

Figure 6.9. Interpretation of terms in Equation (6.34).



The expression $u \cdot \partial\theta/\partial x$ represents the change in temperature at the glacier surface as the ice flows to lower elevations; $\partial\theta/\partial x$ can thus be replaced with $\alpha\lambda$, where α is the surface slope of the glacier. Finally, w is equated with the accumulation rate, b_n . Making these substitutions in Equation (6.33) yields:

$$\lambda(\dot{\varepsilon}_{zz}H + b_n) + \frac{\partial\theta_o}{\partial t} = -u\alpha\lambda - b_n \frac{\partial\theta}{\partial z} \quad (6.34)$$

The meaning of the terms in Equation (6.34) can be clarified by reference to Figure 6.9. A particle of snow deposited at A has moved to B after n years, and is buried under nb_n meters of new accumulation. In the absence of conduction, it is still at the temperature at which it was deposited at A. The surface above B was at C when the snow was deposited at A and, owing to the lapse rate, snow then accumulating at C was $nu\alpha\lambda$ degrees warmer than that which was accumulating at A. In addition, the ice sheet has thinned by an amount $n(\dot{\varepsilon}_{zz}H + b_n)$ over the intervening years, and the surface is now at D, which is $n(\dot{\varepsilon}_{zz}H + b_n)\lambda$ degrees warmer than C. Finally, there may have been secular climatic warming at a rate $\partial\theta_o/\partial t$, so snow at D is $n \partial\theta_o/\partial t$ warmer than it would be otherwise. Thus the surface at D is:

$$nu\alpha\lambda + n(\dot{\varepsilon}_{zz}H + b_n)\lambda + n \frac{\partial\theta_o}{\partial t}$$

warmer than the firn at B. To obtain the temperature gradient from B to D, divide by nb_n and cancel the ns , thus:

$$\frac{\partial\theta}{\partial z} = \frac{u\alpha\lambda + (\dot{\varepsilon}_{zz}H + b_n)\lambda + (\partial\theta_o/\partial t)}{b_n} \quad (6.35)$$

which, with minor manipulation, can be shown to be the same as Equation (6.34).

When one is far from the edge of an ice sheet, it is very difficult to determine whether the ice sheet is thickening or thinning; that is, whether $(\dot{\varepsilon}_{zz}H + b_n)$ is positive or negative. One can measure b_n in snow pits; the problem is to measure $\dot{\varepsilon}_{zz}$ without a stationary base upon which to establish a survey point. Furthermore, such observations would span

Table 6.2. Values of parameters in Equation (6.34) for Site 2 in Greenland and Byrd Station in Antarctica

	Site 2	Byrd Station
α	-0.004 27	-0.001 61
u_s , m a ⁻¹	17	15
λ , K m ⁻¹	-0.011	-0.008
b_n , m a ⁻¹	0.4	0.2
$\partial\theta/\partial z$, K m ⁻¹	0.001 15	0.000 24
$(\dot{\varepsilon}_{zz}H + b_n)$, m a ⁻¹	0.031	-0.018

Note that $\partial\theta/\partial z$ is measured below 150 m depth.

only a short time interval. However, suppose we can measure u , α , λ , b_n , and $\partial\theta/\partial z$ and have reason to believe that $\partial\theta_0/\partial t$ is negligible. Then, Equations (6.34) or (6.35) can be solved for $(\dot{\varepsilon}_{zz}H + b_n)$. Two examples are shown in Table 6.2. The results, a 0.031 m a⁻¹ thickening rate at Site 2 in Greenland and a 0.018 m a⁻¹ thinning rate at Byrd Station in Antarctica, are surprisingly reasonable.

While potentially providing a sensitive measure of the state of health of an ice sheet, this technique is probably not especially useful because moderately deep boreholes are needed to obtain $\partial\theta/\partial z$, and $\partial\theta_0/\partial t$ is not known well enough. However, the derivation of Equations (6.34) and (6.35) serves to emphasize that, in general, as one moves away from the divide, temperature gradients near the surface of an ice sheet become positive; that is, the temperature decreases with depth (decreasing z). We now turn our attention to a more sophisticated model that enables us to investigate such temperature distributions deep in the ice and far from a divide.

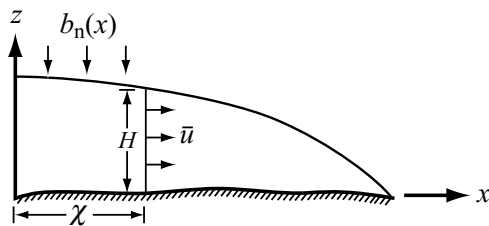
Temperature distributions far from a divide

The Column model

Budd *et al.* (1971) solved Equation (6.13) in a more general form than those we have considered so far. Calculations using their model, which they refer to as the *Column model*, can be done by hand.

The coordinate system they use is shown in Figure 6.10. The temperature profile is to be calculated at a point a distance χ from the divide. Starting again with Equation (6.13), we restrict the model to two dimensions, thus eliminating derivatives in the y -direction; we assume that temperature gradients in the x -direction are sufficiently small that

Figure 6.10. Coordinate system and parameters involved in Column model calculations.



their derivative is negligible; and we assume a steady state. With these assumptions, Equation (6.13) becomes:

$$0 = \kappa \frac{\partial^2 \theta}{\partial z^2} - u \frac{\partial \theta}{\partial x} - w \frac{\partial \theta}{\partial z} + \frac{Q}{\rho C} \quad (6.36)$$

Let us now consider the strain heating term, $Q/\rho C$. From Equation (6.9) it will be seen that this term increases approximately as d^4 , where d is the depth below the surface. In other words, because the strain rate increases rapidly near the bed, most of the strain heating occurs in the basal few meters of ice. (The student may find it interesting to study this effect by solving Equation (6.13) with the assumption that all advection terms and the horizontal conduction terms are negligible, and that a steady state exists. Equation (6.9) is used for $Q/\rho C$. The problem is most easily tackled by using a coordinate system in which the z -axis points vertically downward.) Recognizing that significant strain heating occurs only *near* the bed, Budd (1969) assumed that it occurs only *at* the bed, and that this heat could thus be added to the geothermal flux. The basal boundary condition, β_b , thus becomes:

$$\beta_o = \beta_G + \frac{\tau_b \bar{u}}{K} \quad (6.37)$$

$$\frac{K}{m} \frac{K}{m} \frac{\frac{N}{m^2} \frac{m}{a}}{\frac{J}{maK}} = \frac{K}{m} \quad 1 \text{ Nm} = 1 \text{ J}$$

and $Q/\rho C$ is set to zero. Here, as before, β_G is the gradient required to conduct the geothermal flux upward into the ice; τ_b is the basal drag, approximated by $\rho g d \alpha$; and \bar{u} is the mean horizontal velocity. For \bar{u} at χ we use the balance velocity:

$$\bar{u} = \frac{1}{H} \int_0^\chi b_n(x) dx \quad (6.38)$$

(Equation (5.1)). In calculations, care must be taken to ensure that the sign of the $(\tau_b \bar{u})/K$ term is the same as that of β_G ; this sign is determined by the choice of coordinate axes.

We turn now to the term $u \cdot \partial\theta/\partial x$ in Equation (6.36). In Equation (6.34) we set $\partial\theta/\partial x = \alpha\lambda$, as this is the rate at which the atmospheric temperature increases as one moves to lower elevations along the ice surface. This is, therefore, the rate at which near-surface ice must warm as a result of horizontal advection. If the glacier surface slope is sufficiently low, the deeper ice will warm at the same rate, with negligible lag. This led Budd (1969) to suggest that, to a reasonable first approximation, $u \cdot \partial\theta/\partial x$ can be replaced with $u\alpha\lambda$ in Equation (6.36). The consequences of this assumption are discussed below.

With the additional substitution of $(w_s - w_b)z/H$ for w , Equation (6.36) becomes:

$$\kappa \frac{d^2\theta}{dz^2} - (w_s - w_b) \frac{z}{H} \frac{d\theta}{dz} = u\alpha\lambda \quad (6.39)$$

which is to be solved by using the boundary condition of Equation (6.37). Here, w_s and w_b are the vertical velocities at the surface and bed respectively; w_s can be calculated from the submergence velocity (Equation (5.26)) when b_n , u_s , and α are known. If the velocity at the bed is assumed to be parallel to the bed, w_b can be estimated from knowledge of u_b and the bed slope. Assuming that $u_b = \bar{u} = u_s$ is probably a reasonable approximation in this calculation, but knowing \bar{u} , one could also calculate u_s and u_b from Equations (5.18) and (5.19).

The solution to Equation (6.39) is (Budd, 1969; Budd *et al.*, 1971):

$$\theta(h) = \theta_s - \frac{\beta_b}{\zeta} [erf(\zeta H) - erf(\zeta h)] - \frac{2\bar{u}\alpha\lambda H}{(w_s - w_b)} [E(\zeta H) - E(\zeta h)] \quad (6.40)$$

where:

$$erf(x) = \int_0^x e^{-t^2} dt$$

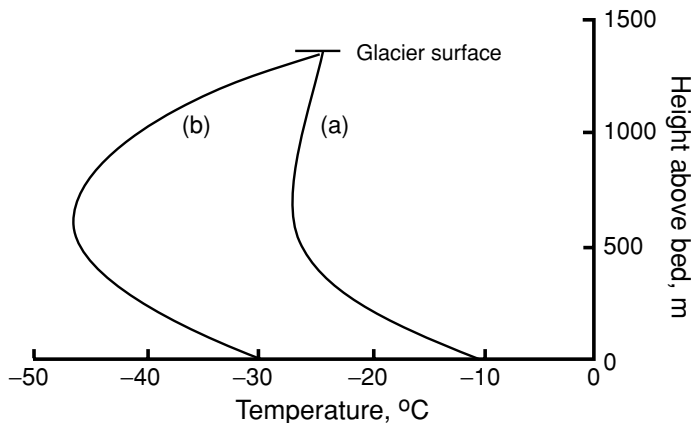
$$E(x) = \int_0^x \left[e^{-y^2} \int_0^y e^{t^2} dt \right] dy$$

$$\zeta = \left[\frac{w_s - w_b}{2H\kappa} \right]^{1/2}$$

Note that this solution uses Budd's definition of the error function, $erf(x)$. $E(x)$ is the integral of a function known as Dawson's integral (the quantity in square brackets), and it too has been tabulated. A plot of it for a reasonable range of ζ is shown in Figure 6.5.

Temperature profiles can be calculated readily by using Equation (6.40) and Figure 6.5. A typical one is shown in Figure 6.11 (profile (a)).

Figure 6.11. Temperature profiles calculated from (a) Equation (6.40) and (b) Equation (6.41). The following values of the parameters, approximately appropriate for Camp Century, Greenland, were used in the calculations: $\alpha = -0.01$, $u = 15 \text{ m a}^{-1}$, $\lambda = -0.01 \text{ K m}^{-1}$, $\kappa = 37.2 \text{ m}^2 \text{ a}^{-1}$, $H = 1368 \text{ m}$, $\theta_H = -24^\circ\text{C}$, and $\beta_b = -0.0508 \text{ K m}^{-1}$.



The minimum temperature occurs at some depth below the glacier surface. This represents, as in Figure 6.9, cold ice that is advected downward and laterally from some point further upglacier where the surface is at a higher elevation and hence colder. However, the Column model does not include this longitudinal advection rigorously, but simply specifies a warming rate. Thus the temperature at depth is only an approximation that becomes better as the warming rate decreases. This approximation is best, therefore, where surface slopes (α) and lapse rates (λ) are lowest.

Both the magnitude and the curvature of the positive temperature gradient near the surface are adjusted so that heat conducted downward from the surface, in combination with heat advected downward, is sufficient to warm the ice everywhere above the point of minimum temperature at the rate $u\alpha\lambda$. Ice below this point is warmed at this rate by heat from the bed – both geothermal and frictional. When the warming rate at depth that is specified (by representing it by $u\alpha\lambda$) is larger than that in the natural situation being modeled, the positive temperature gradient at the surface becomes too high, and the temperatures at depth, thus, too cold.

Further insight into the mathematical properties of the solution can be gained by comparing the profile calculated from Equation (6.40) with one calculated from:

$$\kappa \frac{\partial^2 \theta}{\partial x^2} = u\alpha\lambda \quad (6.41)$$

together, again, with the boundary condition of Equation (6.37). (The integration of Equation (6.41) is left as an exercise for the reader.) This is profile (b) in Figure 6.11. Equations (6.39) and (6.41) differ in that the vertical advection term is omitted in Equation (6.41). By analogy with our discussion of Equation (6.24) and Figure 6.7, one might think that

because vertical advection moves cold ice downward from the surface, omission of this term would make profile (b) warmer than profile (a) at depth. However, in this case the ice at depth is colder than that at the surface, and because the vertical advection term operates on ice at the surface at the point where the profile is being calculated, not at some point upglacier therefrom, the ice advected downward is warmer than the ice at depth. As a result of this downward advection of heat, included in Equation (6.40), the $u\alpha\lambda$ warming rate does not need to be satisfied entirely by conduction from the surface in profile (a).

Englacial and basal temperatures along a flowline calculated using the Column model

Let us now consider the temperature distribution along a flowline calculated with the use of the Column model (Figure 6.12). The original objective of the modeling shown in Figure 6.12 was to investigate the possibility that, along the margin of the Laurentide Ice Sheet in North Dakota, there could have been a ~ 2 km-wide zone in which the ice was frozen to the bed. Such a temperature distribution is implied by glacial landforms, as discussed further below (Moran *et al.*, 1980). Thus, the flowline modeled was assumed to extend from Hudson Bay to North Dakota.

In the model, the accumulation rate was assumed to be 0.20 m a^{-1} 65 km upglacier from the equilibrium line, and to decrease linearly to 0.05 m a^{-1} at the divide, and to 0 at the equilibrium line. The decrease in b_n toward the divide is consistent with the present accumulation pattern in Antarctica (Figure 3.9) and northern Greenland, although not southern Greenland (Zwally and Giovinetto, 2000). In the ablation area, the ablation rate increased linearly downglacier from the equilibrium line, and the rate of increase was adjusted to provide a balanced mass budget. The horizontal velocity was approximated by the balance velocity (Equation (5.1) modified to allow for divergence of the flowlines). The ice sheet profile was adjusted to provide the shear stress necessary to yield this horizontal velocity, using a relation similar to the first of Equations (5.19) with a sliding law to estimate u_b . Isostatic depression of the earth's crust was included. The vertical velocity was calculated from the submergence or emergence velocity relation (Equation (5.26)), and was assumed to decrease linearly with depth (Equation 6.15). The temperature at the margin was -7.5°C . The temperature along the surface was calculated assuming a lapse rate of -0.01 K m^{-1} , and making an empirical correction for warming effects of percolating melt water. The geothermal fluxes used were appropriate to the geologic terrane

along the flowline. To circumvent certain problems, discussed later, it was assumed that the warming rate was $\frac{1}{2}u\alpha\lambda$ instead of $u\alpha\lambda$.

Several features of the temperature distribution in Figure 6.12 merit comment.

- The downward and outward advection of cold ice is represented by the reversal in slope of the -20°C and -25°C isotherms ~ 900 km from the divide.
- The progressive compression of the isotherms near the bed downglacier from the divide reflects the outward increase in basal temperature gradient as strain heating increases.
- Basal melting occurs over the first 250 km of the flowline because the accumulation rate here is low, and downward advection of cold ice is, thus, less important than it is further downglacier. A more realistic vertical velocity distribution would lead to more melting here, while a higher accumulation rate would lead to less melting.
- Between ~ 250 and ~ 420 km from the divide, half of the meltwater formed in the first 250 km is refrozen to the base. This keeps the bed at the pressure melting temperature. The rest of the water was assumed to have drained away into the bedrock. (Had it been assumed, instead, that more of the meltwater stayed at the ice/bed interface, the zone of subfreezing temperatures between ~ 420 and ~ 840 km from the divide would be smaller or absent.)
- The zone of subfreezing basal temperatures between ~ 420 and ~ 840 km owes its existence to increased downward advection of cold ice as the accumulation rate increases outward.
- Basal melting resumes downglacier from ~ 840 km as strain heating warms the basal ice. It becomes particularly important in the ablation area where upward vertical velocities decrease the basal temperature gradient, thus trapping more heat at the bed.
- The basal frozen zone at the margin, barely visible at the scale of the figure, is a result of cold atmospheric temperatures at the margin and decreasing vertical velocity as the margin is approached. The vertical velocity decreases because, as the surface slope steepens, a greater fraction of the ablation rate is balanced by the $u_s \tan \alpha$ term in the emergence velocity. In addition, it is assumed that the meltwater formed in the outer ~ 500 km of the glacier leaves the system as groundwater or by way of localized subglacial conduits.

Even though the Column model is relatively crude in comparison with numerical models being used today, it does reproduce what are probably the essential features of the temperature distribution at the base of a continental-scale ice sheet with an ablation zone of significant width,

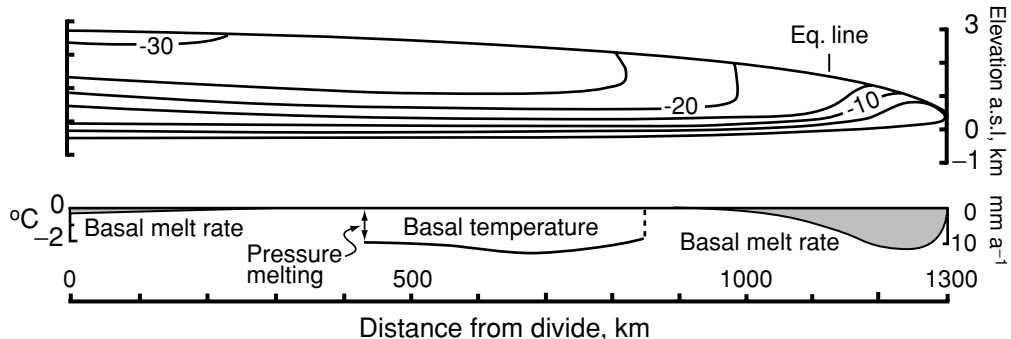


Figure 6.12. Temperature distribution along a flowline calculated with the use of the Column model. The bed is at the pressure melting temperature except in the section labeled "Basal temperature". (From Moran *et al.*, 1980, Figure 6. Reproduced with permission of the International Glaciological Society.)

namely: (1) melting beneath the divide if the accumulation rate is sufficiently low and freezing otherwise; (2) in the former case, a zone of freeze-on in the lower part of the accumulation area followed by a possible zone in which the ice is frozen to the bed; (3) melting beneath the ablation area; and (4) a possible frozen toe in areas where marginal temperatures were relatively cold. The distribution of these zones depends on b_n , β_G , and θ_s . Temporal changes in b_n and θ_s due to climate change will alter the basal temperature distribution, but there will be a lag of order 10^3 years between any change in climate and a response at the bed.

The fact that water from melting basal ice flows downglacier along the bed and refreezes is consistent with observations of layers of dirty ice, several meters thick, that were encountered at the bottoms of both the Byrd Station, Antarctica, and the Camp Century, Greenland, ice cores. In both cases, the dirt was dispersed throughout the ice, and the dirty ice had fewer air bubbles than the overlying clean ice. In the Camp Century core, the oxygen isotope ratios indicated that the basal dirty ice was formed from water that originally condensed at lower temperatures than the overlying ice. All of these observations are consistent with melting of ice that originally formed at a higher altitude than the overlying ice, downglacier flow of that water along the bed, and refreezing of the water incorporating dispersed dirt in the process. It is difficult to account for meters-thick layers of basal ice with dispersed dirt in any other way, although regelation of ice downward into till is a possible way of entraining layers of dirt with higher debris content (Iverson, 1993).

A problem with high $u\alpha\lambda$ warming rates in the Column model

As the warming rate required by the $u\alpha\lambda$ term in the Column model increases, the curvature of the temperature profile increases, and the minimum and basal temperatures decrease (see Figure 6.11 and discussion on p. 134). Near the equilibrium line, the downglacier warming rate is high because meltwater percolating into the firn raises near-surface temperatures. (In the modeling for Figure 6.12 this effect was included by using an effective value of λ that is higher than the atmospheric lapse rate.) If the ice at depth is assumed to be warming at the same rate, calculated minimum temperatures in profiles near the equilibrium line are often lower than the minima in profiles just upglacier. In plots such as Figure 6.12, this appears as a pocket of cold ice beneath the equilibrium line that is surrounded by warmer ice (Hooke, 1977, Figure 4c). Such a temperature distribution is physically impossible; to have cooled off, this ice would have had to have lost heat to colder ice, yet it is surrounded by warmer ice.

To circumvent this problem, as noted, a warming rate of $\frac{1}{2}u\alpha\lambda$ was used.

Basal temperatures in Antarctica – comparison of solutions using the Column model and a numerical model

The reliability and weaknesses of the Column model can be illustrated further by comparing basal temperatures in Antarctica calculated using it (Budd *et al.*, 1971) with those calculated using a state-of-the-art numerical model (Huybrechts, 1990). First, however, it is instructive to discuss some general characteristics of the Antarctic ice sheet that affect the temperature distribution.

A digital elevation model (DEM) of the ice sheet is shown in Figure 6.13 (Liu *et al.*, 1999). By constructing this image with considerable vertical exaggeration, Liu *et al.* have emphasized intricate details of the surface topography, many of which would be difficult to discern were one standing on the surface of the ice sheet. Noteworthy is the apparent roughness of parts of the surface. This is caused by undulations with wavelengths of 4–10 km and amplitudes of only 5–10 m that result from flow over topography on the bed. Also of interest is the remarkably flat area labeled “Lake Vostok”. As discussed previously (p. 99), this area is over a subglacial lake. Lake Vostok is the largest of many subglacial lakes that have been detected through radio-echo sounding.

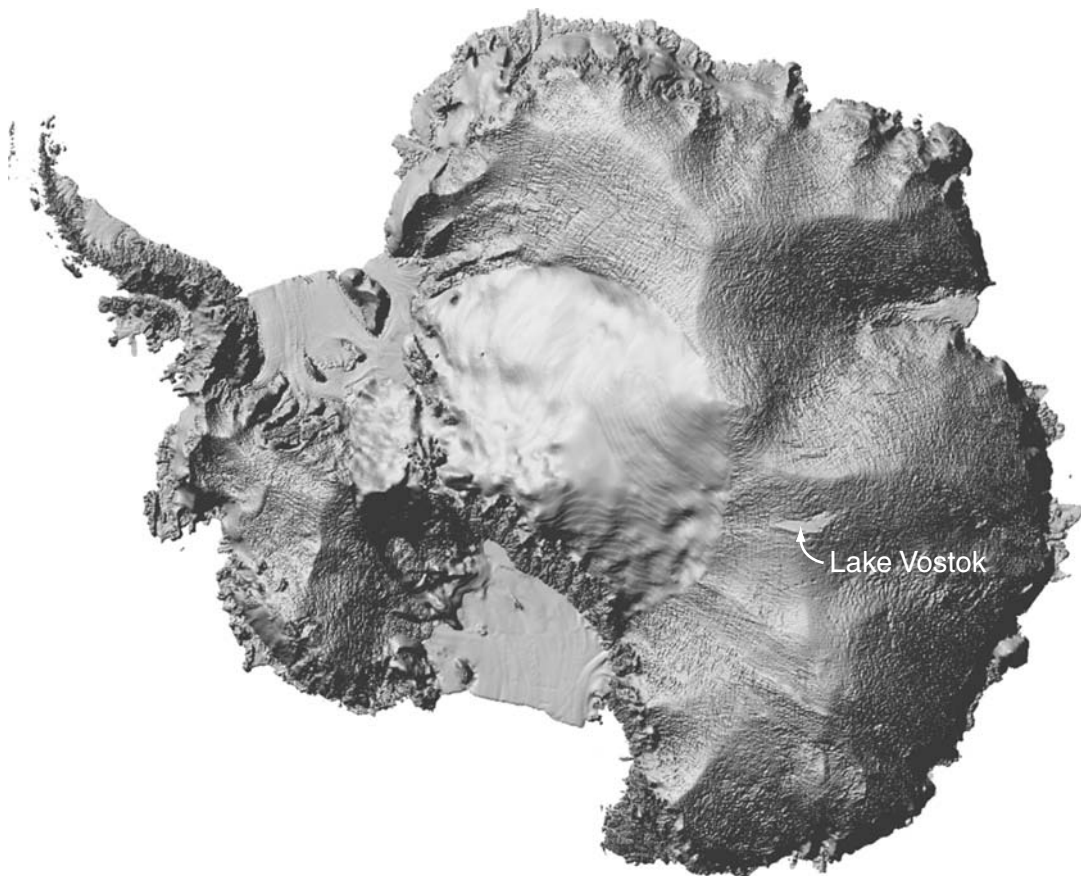


Figure 6.13. Digital elevation model of Antarctica. From Liu *et al.*, 1999.
(Courtesy of G. Hamilton.)

The basal drag in Antarctica, calculated from the surface profile and ice thicknesses, is shown in Figure 6.14. In contrast to the situation on valley glaciers, where τ_b is typically between 0.05 and 0.15 MPa (p. 85), the basal drag is below 0.05 MPa over most of Antarctica. Note also that τ_b decreases inland. The low accumulation rates near the center of the ice sheet result in low balance velocities. Thus, the driving stresses required to provide those balance velocities are also low. Because both τ_b and \bar{u} (Figure 5.2) increase toward the coast, the basal temperature gradient, β_0 , also increases (Equation (6.37)). The geothermal gradient, β_G , is estimated to be only about 0.02 K m^{-1} in East Antarctica, whereas, owing to strain heating, β_b is nearly five times that near the coast.

Basal temperatures calculated with the use of the Column model and by Huybrechts (1990) are shown in Figures 6.15a and 6.15b,

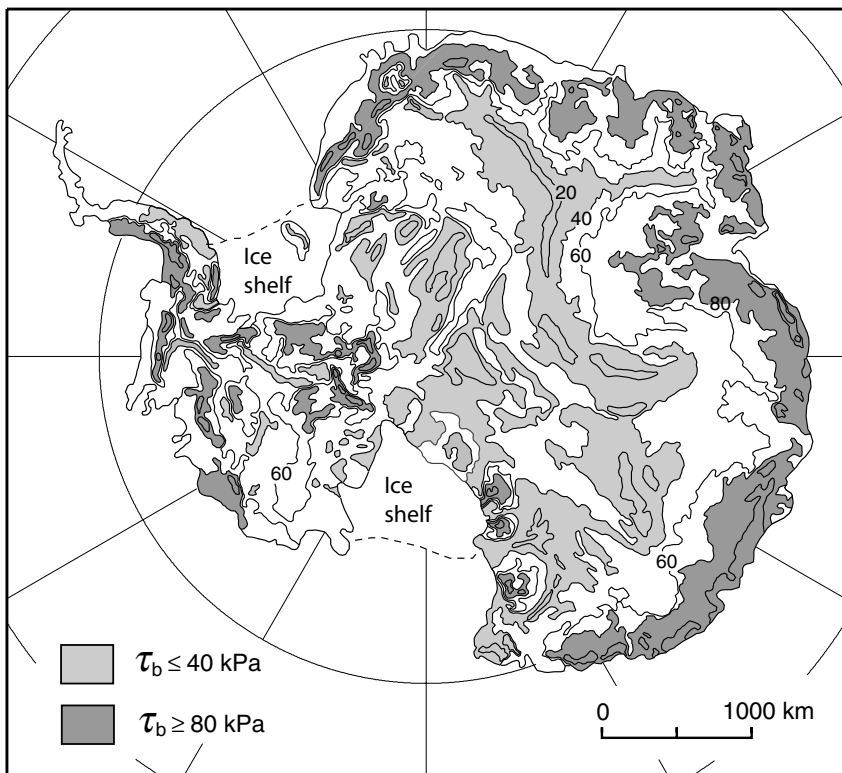


Figure 6.14. Basal drag in Antarctica calculated by Ph. Huybrechts, especially for this book, using the model described in Huybrechts (2002).

respectively. In both maps one of the coldest spots is in central East Antarctica, over a mountain range where the ice is only 1.5–2 km thick. In nearby areas it is over 4 km thick. Both also predict basal melting in the same areas in West Antarctica. However, there are important systematic differences between the maps. Most obvious is the large area of basal melting in East Antarctica in Huybrecht's map. This is, in part, attributable to the fact that Huybrechts used a geothermal flux of 54 mW m^{-2} , while Budd *et al.* used 50 mW m^{-2} . This, however, cannot account for so large a difference. Possible explanations for the remaining difference are the use of an unrealistic linear decrease in w with depth in the Column model and requiring that the warming rate at depth equal that at the surface. As we have seen, the former can lead to basal temperatures that are too cold (Figure 6.6), and the latter can result in temperature gradients at the surface that are too high (Figure 6.11), thus also making deeper temperatures too cold. In contrast, Huybrecht's model predicts colder temperatures in Queen Maud Land. This appears to be because

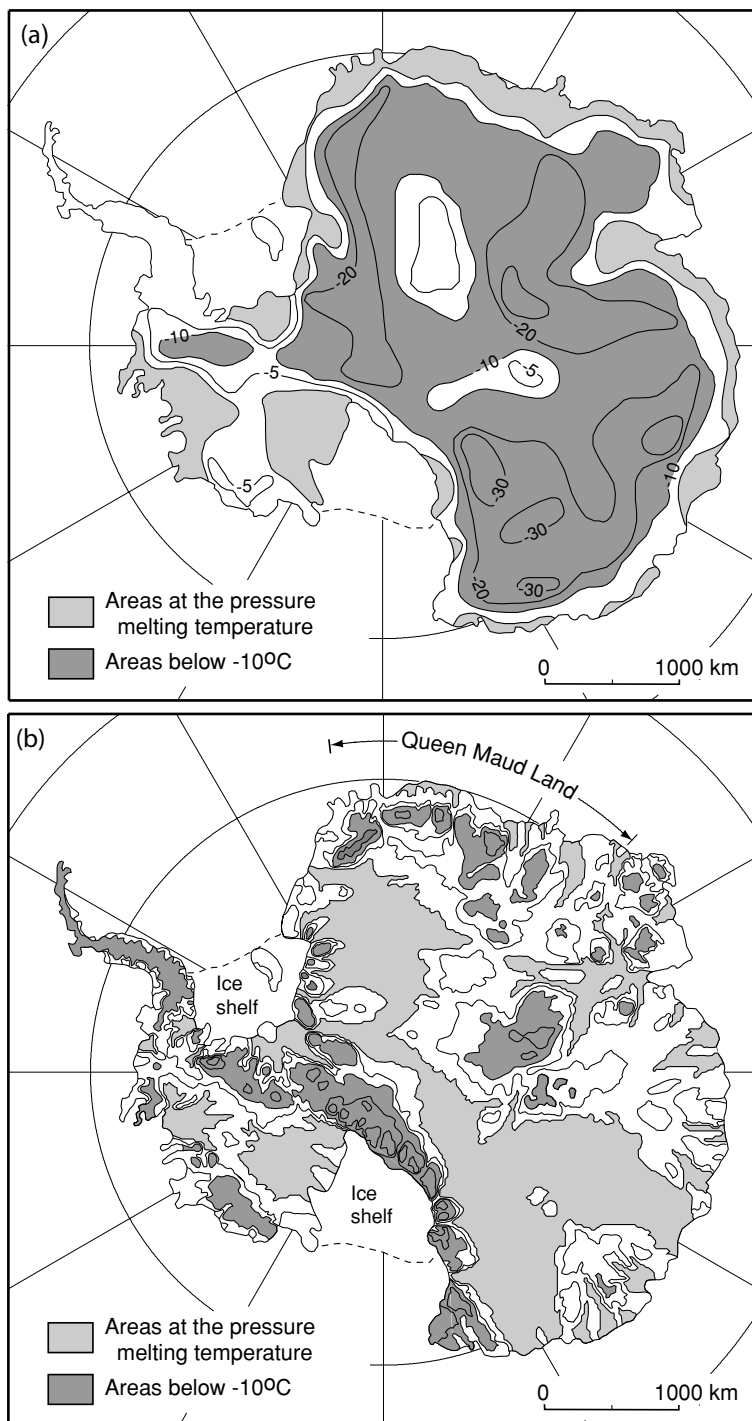


Figure 6.15. (a) Basal temperatures, $^{\circ}\text{C}$, from the Column model; (b) basal temperatures, $^{\circ}\text{C}$, calculated by Ph. Huybrechts, especially for this book, using the model described in Huybrechts (2002). ((a) Modified from Budd *et al.*, 1971. Reproduced with permission of the Australian Antarctic Division.)

Budd *et al.* were using balance velocities that were an order of magnitude higher than Huybrechts in this sector, thus overemphasizing strain heating.

The differences between the temperature distributions in Figure 6.15 emphasize the need for caution in using the Column model. However, the Column model does illustrate the basic physical factors affecting the temperature distribution in ice sheets, and can be used to obtain reasonable estimates of the temperature distribution with only a calculator or spreadsheet. For geomorphologists wishing to test ideas on the origin of certain landforms, for example, the errors introduced by the simplifying assumptions made in the Column model are probably no greater than the uncertainties in the ice age values of parameters like b_n , H , β_b and \bar{u} that are used in it.

Geomorphic implications

Temperature distributions such as that in Figure 6.12 have implications for glacial erosion and deposition and the origin of some glacial landforms. Erosion rates are likely to be highest where basal melt rates are low, and particularly where meltwater is refreezing to the glacier sole. Thus, we might expect to find that erosion was most intense some distance from the divide. Conversely, the formation of lodgment till by subglacial melting should be most prevalent beneath the ablation zone. Both are consistent with observation.

The calculations shown in Figure 6.12 also suggest that zones of frozen bed, a couple of kilometers wide, should develop along ice sheet margins in regions where mean annual temperatures are sufficiently low. This, indeed, seems to have been the case in North Dakota and adjacent areas of Alberta and Saskatchewan. Here, blocks of bedrock, tens to hundreds of meters on a side, became frozen to the base of the glacier and were moved outward a kilometer or so (Figure 6.16). Detachment may have been facilitated by high pore-water pressures in the unfrozen rock beneath the frozen zone. Upon deposition, these blocks formed hills. When the ice eventually receded, the basins from which the blocks were plucked became lakes (Moran *et al.*, 1980).

In some places, subglacial frozen bed conditions persisted throughout the last glacial period. The best studied such areas are in western Sweden, in the divide region of the Weichselian ice sheet. These cold zones were probably a consequence of a combination of high accumulation rates, cold temperatures, and thin ice in the topographically high divide region. Relict periglacial landforms like patterned ground (Kleman and Borgström, 1994) and weathering features such as tors (Kleman and Hättestrand, 1999) are found in these areas. These features

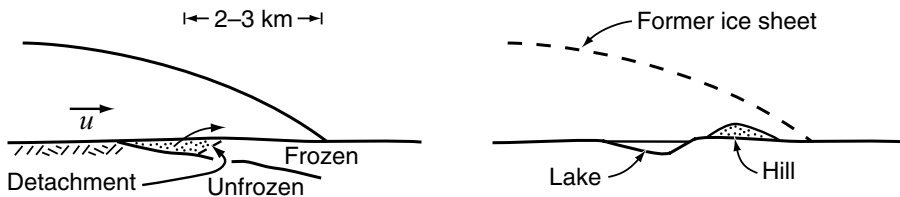


Figure 6.16. Hill–lake pair formed by thrusting at a frozen margin.

developed under ice-free conditions during the last interstadial. Around the edges of these zones of relict landscape, frozen bed conditions persisted on higher ground while lower areas were at the pressure melting point. Kleman and Borgström (1994) have described a distinctive set of landforms in such situations (Figure 6.17). Up- and downglacier from the higher areas the ice was sliding, whereas it remained frozen to the substrate over the hill itself. This led to longitudinal compression on the stoss side of the hill, and longitudinal extension on the lee side. Till dragged by the ice thus became stacked in transverse moraines on the stoss side. On the lee side it was pulled away, forming an abrupt scarp (Figure 6.17). Along the lateral boundaries, there is a narrow transition separating the relict surface from an area of glacially modified topography.

Ribbed moraine is another distinctive landform that is commonly present around the edges of areas where frozen bed conditions either persisted throughout a glaciation or perhaps developed during deglaciation (Hättestrand and Kleman, 1999). Ribbed moraines are anastomosing, somewhat sinuous ridges oriented transverse to ice flow (Figure 6.18a). The ridges typically consist of glacial drift similar to that in adjacent areas without ridges. The drift is usually till but may be glaciofluvial sediment or a combination of the two. In troughs between ridges, seismic investigations and limited exposures suggest that the drift sheet is generally thin or missing (Figure 6.18c). If one could decouple the ridges from the substrate and slide them together, they would fit remarkably well (Figure 6.18b). These characteristics suggest that the ridges were formed by pull-apart of a once-continuous drift sheet at the boundary between zones of thawed and frozen bed (Figure 6.18d). Hättestrand and Kleman have argued convincingly that this is the case. They have shown that ribbed moraine is confined almost exclusively to the core areas of late Pleistocene ice sheets. They find that the ridges are transverse to ice flow directions during deglaciation and not to flow directions during the Late Glacial Maximum, suggesting that they formed during deglaciation.

As our understanding of the origin and distribution of features such as hill–hole pairs, relict surfaces, and ribbed moraine improves, they will become increasingly valuable in constraining numerical models

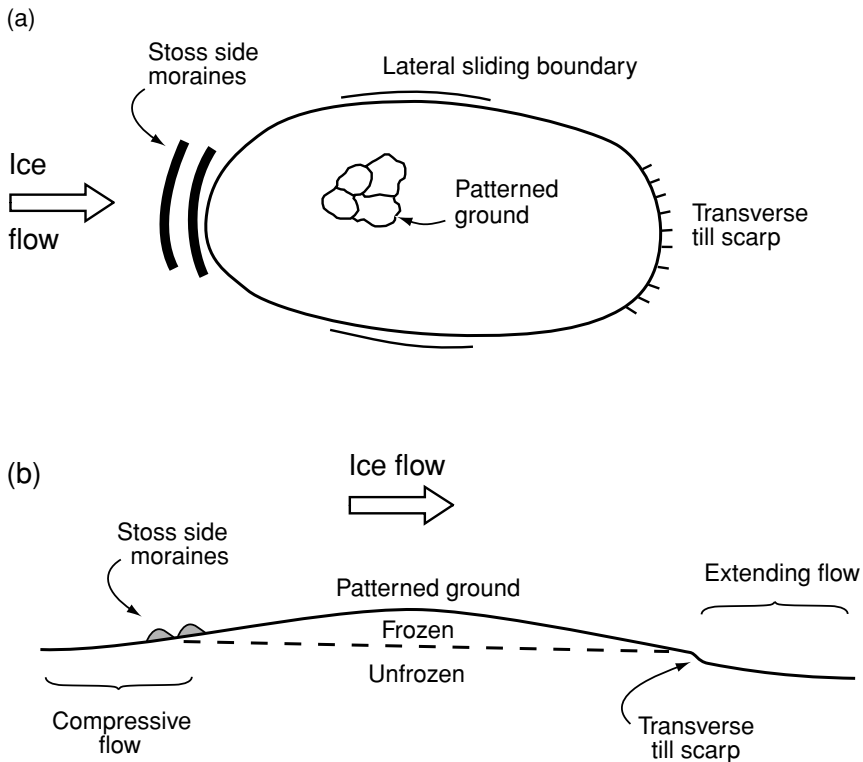


Figure 6.17. Schematic map (a) and cross section (b) through a low hill that remained frozen throughout a glacial advance and on which periglacial landforms are thus preserved. Stoss side moraines were formed in the zone of compressive ice flow on the stoss side of the hill, and transverse till scarps were formed on the lee side.

of Pleistocene ice sheets. Some modeling studies have already used the distribution of these features for this purpose (see, for example, Fastook and Holmlund, 1994; Moran *et al.*, 1980) but much remains to be done.

Summary

We began this chapter by deriving the energy balance equation. Given boundary conditions appropriate for a polar ice sheet, solutions to this equation yield the temperature distribution in the ice sheet. The boundary conditions most commonly used are: (1) the temperature at the surface, which is approximated by the mean annual temperature, perhaps with a correction for heating by percolating melt water; and (2) the temperature gradient at the bed. The latter is based on estimates of the geothermal

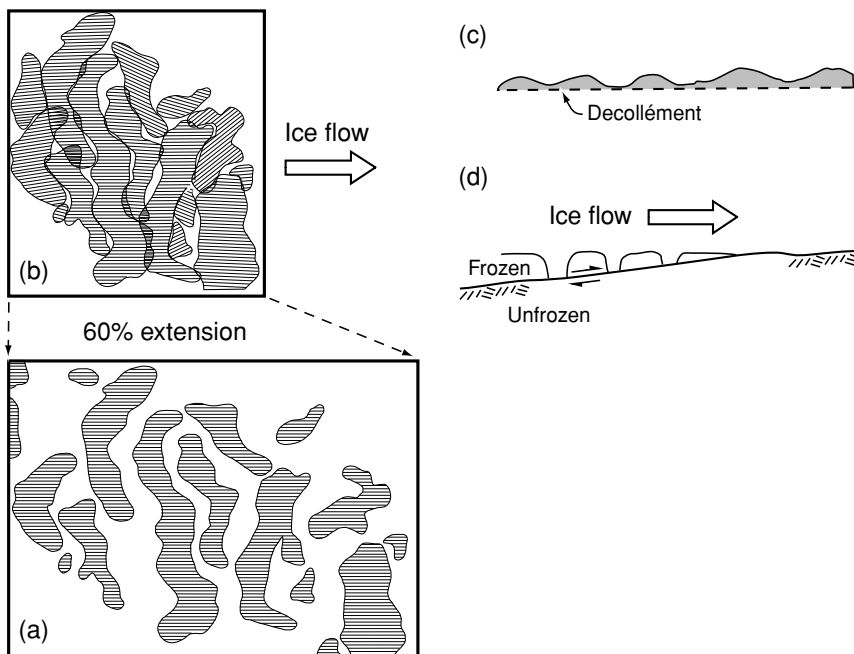


Figure 6.18. Formation of ribbed moraine. (a) Map of ribbed moraine ridges near Lake Rogen in west-central Sweden. The line pattern on the ridges shows the direction of faint fluting. (b) Inferred original relative positions of ridges. Areas of overlap are attributed to streamlining after the ridges were pulled apart. (c) Schematic cross section through a series of ridges showing thickness of material above decollément. (d) Schematic diagram showing how a layer of frozen soil overlying thawed material could be pulled apart by extensional flow in the ice. ((a) and (b) from Hättestrand and Kleman, 1999. Reproduced with permission of the authors and Elsevier Science.)

flux. If calculations suggest that the bed is at the pressure melting point, the temperature gradient is adjusted to ensure that calculated basal temperatures do not exceed the melting point.

By using appropriate simplifications, we studied solutions to the energy balance equation for the situation at an ice divide, for the situation near the glacier surface but some distance from the divide, and for a column of ice extending through an ice sheet some distance from the divide. Two key assumptions in the latter, the so-called Column model, are that w decreases linearly with depth and that longitudinal advection can be approximated by assuming a warming rate at depth that equals that at the surface. Both of these lead to basal temperatures that are too cold, and the second may result in physically impossible temperature distributions in areas where surface temperatures are changing rapidly in the longitudinal direction. With suitable caution, however, we found that the

Column model was useful for illustrating how various physical processes that affect the temperature distribution were reflected in calculated temperatures along a flowline of the Laurentide Ice Sheet. Comparison of basal temperatures beneath the Antarctic ice sheet calculated by using the Column model and with a state-of-the-art numerical model served to emphasize both the value and the limitations of the former.

Finally, we discussed some geomorphic features formed at boundaries between zones of thawed and frozen bed, and noted that these could be used to constrain numerical models of ice sheets.

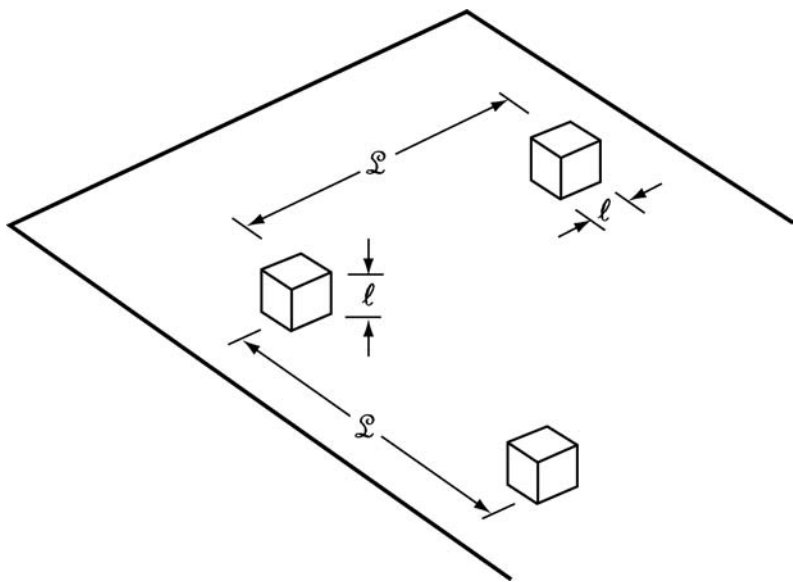
Chapter 7

The coupling between a glacier and its bed

In Chapter 4 we found that the rate of deformation of ice, $\dot{\varepsilon}_e$, could be related to the applied stress, σ_e , by: $\dot{\varepsilon}_e = (\sigma_e/B)^n$ (Equation (4.5)). The rigorous basis for this flow law will not be developed until Chapter 9, but some indications of the complexities involved in applying it have already been mentioned. Despite these complexities, calculations using it are reasonably accurate. Computed deformation profiles are an example. This is, in large part, because ice is a crystalline solid with relatively uniform properties. The principal causes of inaccuracy in such calculations are a consequence of impurities in the ice, including water, of anisotropy associated with the development of preferred orientations of crystals, and of incomplete knowledge of the temperature and boundary conditions.

As mentioned briefly in Chapter 5 (Figure 5.5), glaciers also move over their beds readily when the basal temperature is at the pressure melting point. However, the rate at which this movement occurs is far more difficult to analyze. This is again, in part, because the boundary conditions, principally the water pressure and the morphology of the bed, are not known. However, a more fundamental problem is the fact that granular rock debris is usually present, either in the ice or between the ice and the bed, or both. There is considerable uncertainty surrounding the processes involved in the deformation of such material and the appropriate constitutive relations describing its deformation and that of ice containing it. Furthermore, unlike the situation with pure ice, the properties of the rock debris vary, not only from glacier to glacier, but also from point to point beneath a single glacier.

Figure 7.1. Bed geometry used in Weertman's (1964) analysis of basal sliding.



Although it may be impossible to know the boundary conditions well enough to predict accurately the rate of movement of a glacier over its bed, it is nevertheless important to understand the processes in order to place limits on the rate. Thus, a significant effort has been made to analyze these processes, using judicious assumptions where necessary as a substitute for detailed data. This analysis has led to relations between the rate of movement and measurable quantities such as water pressure and driving stress that can be tested with field data.

We start this discussion by looking at the movement of clean ice over an irregular hard rigid bed – the traditional sliding problem. Some of the principal shortcomings of the analysis are then discussed. Finally we take up the problem of deformation of the granular materials over which many glaciers move.

Sliding

The basic processes by which ice moves past an obstacle on a rigid bed, regelation and plastic flow, were first discussed by Deeley and Parr (1914) and later quantified by Weertman (1957a, 1964). *Regelation* involves melting of ice in the region of high pressure on the upglacier or stoss side of the obstacle and refreezing of that water in the region of lower pressure on its lee face. *Plastic flow* is simply deformation of ice in a three-dimensional flow field around the obstacle. In his analysis, Weertman used a simplified model of the bed geometry, sometimes called the tombstone model, consisting of uniformly spaced rectangular blocks on a flat surface (Figure 7.1). This model has been roundly criticized as being

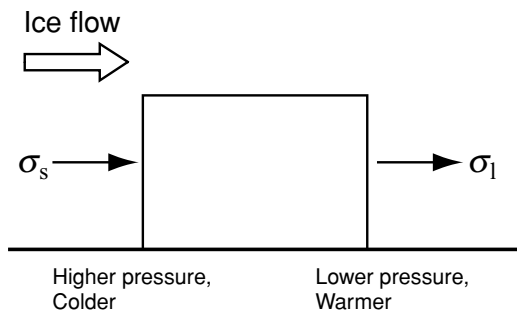


Figure 7.2. Pressure and temperature on stoss and lee sides of a rectangular bump on a glacier bed.

unrealistic, and inappropriately defended by arguing that fudge factors can be inserted to make it applicable to real situations. The real value of the model is that the physical principles involved in the sliding process are illustrated without resorting to sophisticated mathematical techniques.

Consider the bed shown in Figure 7.1. For simplicity we will use cubical obstacles with sides of length, ℓ , instead of Weertman's rectangular ones. The mean spacing between obstacles is \mathcal{L} , and we therefore define $r = \ell/\mathcal{L}$ as the roughness of the bed. The mean drag on the bed is τ . As the ice is separated from the bed by a thin film of water, we assume that faces parallel to the flow cannot support a shear stress. Thus the entire drag over an area \mathcal{L}^2 must be supported by one obstacle. The total force on the obstacle is then $F = \tau \mathcal{L}^2$, so the stress difference across the obstacle, $\sigma_s - \sigma_l$, is:

$$\sigma_s - \sigma_l = \frac{\tau \mathcal{L}^2}{\ell^2} = \frac{\tau}{r^2} \quad (7.1)$$

where the subscripts, s and l, refer to stoss and lee, respectively.

Regelation

Let us deal with regelation first. The average temperature at the bed is constrained to be at the pressure melting point determined by the average pressure in the water layer. The average pressure is a function of the local glacier thickness. The pressure in the water film on the stoss face of the obstacle is higher than the average, and the pressure on the lee face is lower (Figure 7.2). We denote the pressure difference across the obstacle, $\sigma_s - \sigma_l$, by ΔP . This pressure difference results in a temperature difference, $\Delta T = \mathbf{C} \Delta P$, where \mathbf{C} is the change in melting temperature with pressure (Equation (2.2)).

The temperature difference across the obstacle, from Equation (7.1), is thus:

$$\Delta T = \mathbf{C} \left(\frac{\tau}{r^2} \right) \quad (7.2)$$

and the temperature gradient through it is $\Delta T/\ell$. The heat flow through the obstacle is thus:

$$Q = \frac{\Delta T}{\ell} K_r \ell^2 = \Delta T K_r \ell \quad (7.3)$$

where ℓ^2 is the cross-sectional area of the obstacle and K_r is the thermal conductivity of rock. K_r has the dimensions $J \text{ m}^{-2} \text{ s}^{-1} (\text{K}/\text{m})^{-1}$, or $\text{J} \text{ m}^{-1} \text{ s}^{-1} \text{ K}^{-1}$. A typical value for rock or ice is 2.2. Q has the dimensions J s^{-1} .

This heat flow can melt ice at a rate $Q/H\rho$, where H is the heat of fusion, $3.3 \times 10^5 \text{ J kg}^{-1}$, and ρ is the density of ice, $\sim 900 \text{ kg m}^{-3}$. Thus, the melt rate is expressed in $\text{m}^3 \text{ s}^{-1}$. Dividing this rate by the cross-sectional area of the obstacle, ℓ^2 , gives the speed with which ice can move past the obstacle by regelation, S_r . Thus, using Equations (7.2) and (7.3):

$$S_r = \frac{Q}{\ell^2 H \rho} = \frac{\mathbf{C} \tau K_r}{\ell H \rho r^2} \quad (7.4)$$

In reality, some heat also flows from the low-pressure region to the high pressure region through the ice above the obstacle and through the rock beneath it, so this relation slightly underestimates S_r .

The water formed by melting in the high-pressure area on the stoss side of the obstacle flows either upglacier or downglacier to areas of lower pressure. The area of low pressure in the lee of the obstacle that we have been analyzing is one such sink. Because heat is conducted away from this area by the temperature gradient through the obstacle, this water refreezes. Thus, to complete the regelation cycle, the water flux to the lee of the obstacle must equal the melt on the stoss side. We will examine the consequences of a failure of this condition later, and consider plastic flow next.

Plastic flow

Plastic flow (or creep) of ice around an obstacle clearly must contribute to flow of a glacier past the obstacle. Weertman suggested that this plastic flow is enhanced owing to the high stresses on the obstacle. He thus assumes that the speed with which ice moves past the obstacle by this process, S_p , is proportional to ℓ and to the creep rate obtained by using the stress difference from Equation (7.1) in the flow law:

$$S_p = b \dot{\varepsilon} \ell = b \left(\frac{\tau}{B r^2} \right)^n \ell \quad (7.5)$$

where b is a dimensionless constant of proportionality. Note that dimensionally $\dot{\varepsilon} \ell$ is a speed.

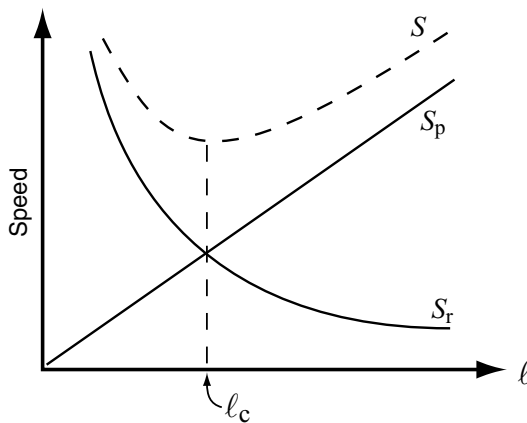


Figure 7.3. Relation between sliding speed and obstacle size for regelation, S_r , plastic flow, S_p , and their sum, S .

Sliding speed

Comparing Equations (7.4) and (7.5), you will note that as ℓ increases, S_r decreases but S_p increases (Figure 7.3). S_r decreases because the path that heat follows back through the obstacle increases with ℓ , so the temperature gradient decreases, thus decreasing the heat flow. The physical reasons for the increase in S_p are less obvious; dimensionally, it results from the fact that to obtain a speed from a strain rate, one must multiply by a length scale, and the obvious length scale in the present situation is ℓ .

The total sliding speed, S , is generally considered to be the sum of the contributions from regelation and plastic flow (Figure. 7.3), thus:

$$S = S_r + S_p = A_r \frac{\tau}{\ell r^2} + A_p \left(\frac{\tau}{r^2} \right)^n \ell \quad (7.6)$$

where, for simplicity, the factors that are physical constants for any given situation have been lumped into the parameters A_r and A_p . We, also, will consider the contributions to be additive, but note that Nye (1969, pp. 455–456) finds that this is not strictly correct on real beds consisting of roughness elements of many different sizes. This is because the pressure distribution resulting from regelation is then not the same as that resulting from plastic deformation.

Let us seek the obstacle size, ℓ_c , for which, as shown in Figure 7.3, S is a minimum. To do this we take the derivative of S with respect to ℓ , thus:

$$\frac{dS}{d\ell} = -A_r \frac{\tau}{\ell^2 r^2} + A_p \left(\frac{\tau}{r^2} \right)^n \ell \quad (7.7)$$

set the result to 0, and solve for ℓ_c :

$$\ell_c = \sqrt{\frac{A_r}{A_p}} \left(\frac{\tau}{r^2} \right)^{\frac{1-n}{2}} \quad (7.8)$$

Inserting this back into the expressions for S_r and S_p (Equations (7.4) and (7.5)) yields:

$$S_r = \sqrt{A_r A_p} \left(\frac{\tau}{r^2} \right)^{\frac{n+1}{2}} \quad \text{and} \quad S_p = \sqrt{A_r A_p} \left(\frac{\tau}{r^2} \right)^{\frac{n+1}{2}} \quad (7.9)$$

Thus when S is a minimum, $S_r = S_p$ and $S = 2S_r = 2S_p$.

A glacier bed has irregularities of many sizes, but the sliding speed in any one area of the bed must be the same for all of them. Suppose that r is also the same for all obstacle sizes in this area. Then, in the size range where plastic flow dominates, it is clear from Equation (7.5) (or Figure 7.3) that the drag exerted on the base of the glacier by obstacles of size ℓ_c will be greater than the drag exerted by larger obstacles. (With S_p , b , B , and r all constant, τ varies inversely with ℓ .) Similarly, in the size range where regelation dominates, the drag exerted by obstacles of size ℓ_c will also be greater than that exerted by smaller obstacles. In other words, obstacles of size ℓ_c exert more drag on the base of the glacier than do obstacles of any other discrete size, and this has thus come to be called the *controlling obstacle size*. As implied by $S_r = S_p$, regelation and plastic flow contribute equally to motion of ice past roughness elements of size ℓ_c .

When one considers a bed composed of a continuous spectrum of obstacles sizes, and particularly of roughnesses, on the other hand, the concept of a controlling size is no longer as relevant (Nye, 1969, p. 459). Nevertheless, an obstacle size for which $S_r = S_p$ normally appears when bed geometry is simplified in order to make theoretical studies of sliding mathematically tractable. The name *controlling obstacle size* for this size is probably irrevocably ingrained in the literature.

Making use of the fact that $S = S_r + S_p$ and the relations in Equation (7.9), assuming that $n = 3$, and combining the constant factors into a single constant, A , yields:

$$S = A \frac{\tau^2}{r^4} \quad (7.10)$$

This is true only for beds composed of uniform obstacles of size ℓ_c or for beds with a homogeneous distribution of roughness elements – so-called white roughness. For beds composed of much smaller obstacles, $S \rightarrow A_r \tau / (\ell r^2)$ (Equation (7.4)) whereas for beds of much larger obstacles, $S \rightarrow A_p \ell \tau^3 / r^6$ (Equation (7.5)). Of particular interest in Equation (7.10) is the quadratic dependence of S on τ , and the strong inverse dependence on r .

Nye (1969) and Kamb (1970) have analyzed sliding of glaciers over a bed with a more realistic geometry consisting of superimposed sine waves. As in Weertman's development, the two processes by which ice moved past roughness elements on the bed were regelation and plastic

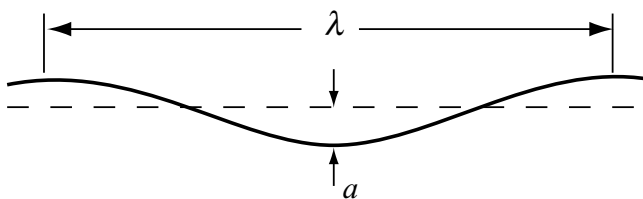


Figure 7.4. Wavelength and amplitude of a sinusoidal wave on a glacier bed.

flow. The mathematical techniques that Nye and Kamb employ are elegant (and beyond the scope of this book). A price paid for this realism was that to obtain exact solutions, both Nye and Kamb had to assume a linear rheology ($n = 1$) for ice. Kamb also obtained an approximate solution for a nonlinear rheology. Both Kamb (Equation (45)) and Nye (Equation (34)) concluded that $S \propto \tau/r^2$ in the linear theory. This is consistent with our Equation (7.9) with $n = 1$. In Kamb's (Equation (79)) nonlinear theory, the dependence of τ on ℓ_c (see Equation (7.8) above) also leads to $S \propto \tau^2$, at least for certain roughness spectra; this is of interest in the light of some laboratory and field studies discussed below. The dependence of S on r in Kamb's nonlinear theory is more complicated owing to the way in which roughness is defined. Let us now examine this in more detail.

Roughness in the Nye–Kamb theory

A different definition of bed roughness is needed in the Nye–Kamb models in which the bed topography is modeled by superimposed sine waves. Thus, Kamb introduces a relative roughness parameter, $\varsigma = a/\lambda$, where a and λ are the amplitude and length of a sine wave (Figure 7.4). Note that ς is not so much a measure of the heights of bumps, a , but rather of the steepness of the adverse slope that they present to the glacier. As before, we can define a controlling wavelength, λ_c , for which $S_r = S_p$.

Lliboutry (1975) has suggested a modification of the Kamb–Nye approach. Let x be the direction of flow and let $z(x,y)$ describe the elevation of the bed above some reference plane. Then let $z_*(x,y)$ weight the contribution of various roughness elements to the total roughness in such a way that wavelengths bigger and smaller than the controlling size contribute less resistance to flow. The roughness is then defined by:

$$r = \frac{1}{A} \int_{-\infty}^{\infty} \int_{-\infty}^{\infty} \left(\frac{\partial z_*}{\partial x} \right)^2 dx dy$$

where A is the area of the bed. Thus, the roughness is considered to be related to the square of the bed slope in the direction of flow, averaged over the bed and weighted as just described.

When ζ is constant for all wavelengths, the spectrum is called *white*. This is one of the spectra for which $S \propto \tau^2$ in Kamb's nonlinear theory. From casual observations of glacier beds, however, it is quickly clear that ζ is not constant; there is commonly a distinct absence of short wavelengths. In his studies, Kamb found almost no obstacles with wavelengths less than 0.5 m in the direction of flow. He further observed that ζ was commonly ~ 0.05 . On bedrock exposed in front of Glacier de Saint-Sorlin in France, on the other hand, roughness elements with wavelengths shorter than 0.5 m are common (Benoist, 1979).

The frequent absence of short wavelengths is usually attributed to preferential abrasion of these features by regelating ice. As noted, regelation is most effective over small obstacles. During regelation, any rock particles that become incorporated into the regelation layer, say by entrainment during refreezing in the lee of a previous obstacle, are forced into strong contact with the next obstacle upon the stoss side of which this ice melts. Thus small obstacles are abraded away whereas larger ones, accommodated principally by plastic flow, are not.

Tests of sliding theories

The only sliding theory that can be reasonably tested with field data is Kamb's approximate nonlinear one. The sliding speed and other data used for the test were collected on Blue and Athabasca Glaciers, using boreholes to the bed and tunnels along the bed. In neither of these techniques was a large enough area of the bed exposed to permit direct measurement of the roughness. Thus, instead, Kamb calculated ζ and λ_c from the measured sliding speeds and known glacier geometry (Table 7.1).

When Kamb used a full white roughness spectrum in his calculations, the values of ζ were about one-third those in the table. Thus, in accord with his observations, he assumed that obstacles with short wavelengths had been abraded away, and instead of the full white roughness spectrum he used a truncated spectrum that did not have obstacles with those wavelengths. This yielded values of ζ (Table 7.1) that are consistent with observations on exposed bedrock outcrops, thus providing support for the theory. (It is noteworthy that in the absence of these shorter wavelengths, $S \propto \tau^3$ (our Equation (7.5); Kamb's Equation (90)).)

Another test of the theory comes from observations of the thickness of the regelation layer at the base of a glacier. Regelation ice can be

Table 7.1. *Measured sliding speeds and corresponding calculated roughnesses and controlling wavelengths (from Kamb, 1970)*

Location	Measured $S, \text{ m a}^{-1}$	Calculated ζ	Calculated $\lambda_c, \text{ m}$
Blue Glacier			
Borehole K	22	0.05	0.32–0.45
Borehole V	4	0.09	0.47–0.67
Western ice fall	6	0.02–0.04	0.62–1.12
Central ice fall			
On ridge	128	0.03	0.15–0.28
In trough	4	0.13	0.37–0.53
Athabasca Glacier			
Hole 1B	41	0.02	0.50–0.70
Hole 1A	42	0.02	0.33–0.47
Hole 209	3	0.06	0.59–0.84
Means		0.054	0.53

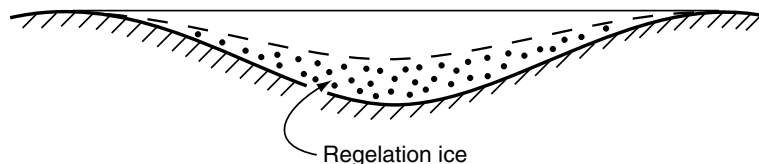


Figure 7.5. In the lee of a bump of the controlling size, regelation ice should fill the lower half of the space between bumps.

distinguished from more highly deformed ice by grain size and crystal orientation. Thin sections of the ice viewed through crossed polarizers are used for this purpose. Kamb and LaChapelle (1964) measured thicknesses of the regelation layer in ice tunnels beneath Blue Glacier. They judged the average thickness to be about 5 mm while the maximum was 29 mm. These values can be compared with those calculated from Kamb's theory. The calculation is based on the fact that the thickness of the regelation layer in a depression in the lee of a bump is proportional to the degree to which the bump was accommodated by regelation. For example, for obstacles of the controlling size, accommodated half by regelation and half by plastic flow, regelation ice should half fill the depression between bumps (Figure 7.5). The predicted thicknesses were 1–10 mm. The fact that these thicknesses were less than those observed suggests that regelation may be more important than predicted by the theory.

Weaknesses of present sliding theory

There are a number of processes involved in sliding of ice over a hard bed that are not adequately described in the above theoretical models. An obvious example is the failure to consider frictional forces between rock particles in the basal ice and the underlying bedrock. To study this effect, Iverson *et al.* (2003) conducted an experiment at the Svartisen Subglacial Laboratory in Norway. The laboratory is situated in a tunnel system in the bedrock beneath Engabreen (the Enga Glacier), an outlet glacier from the Svartisen Ice Cap. The tunnels were excavated for a hydroelectric power project. One inclined tunnel, excavated specifically for scientific studies, leads upward to the base of the glacier, giving access to the bed beneath 210 m of sliding temperate ice. Using this inclined tunnel, Iverson and his colleagues placed an instrumented panel at the base of the glacier. The upper surface of the panel consisted of a 0.09 m² smooth granite tablet. Debris-laden ice slid across the tablet and the shear traction on it was recorded along with sliding speed, water pressure, and temperatures in the panel. Shear tractions on the panel varied from 60 to 110 kPa, and at one point rose to 200 kPa. The spatially averaged driving stress is estimated to be between 150 and 300 kPa, so the measured shear tractions on the panel were a significant fraction of the total drag. As the tablet was smooth and mounted flush with the fixed edges of the panel, shear tractions on it would presumably have been negligible if the ice had been free of sediment.

Let us explore the reason for the high frictional forces between the panel and the dirty ice. Ice is relatively soft, so one might imagine that a particle imbedded in basal ice would simply be pushed up into the ice rather than exert a sustained high contact force against the bed. However, in a temperate glacier, ice at the bed is melting and some or all of the meltwater may drain away. To replace this loss, ice must flow past the particle toward the bed. As first recognized by Hallet (1979a), it is this flow that drives particles toward the bed and maintains high contact forces between the particles and the bed. This is why glacier beds are striated. As with flow of ice past obstacles on the bed, flow of ice past particles *toward* the bed can be analyzed in terms of regelation and plastic flow. And as with bumps on the bed, particles of a certain size, ~0.1 m, are forced against the bed more vigorously than smaller or larger particles. The ice moves more readily past smaller particles by regelation and past larger particles by plastic flow.

“Frictional” drag may also occur in areas where ice becomes temporarily frozen to the bed. Robin (1976) proposed two mechanisms for forming such *cold patches*. In the first, which he termed the “heat pump effect” (Figure 7.6a), water that is formed in the zone of high pressure

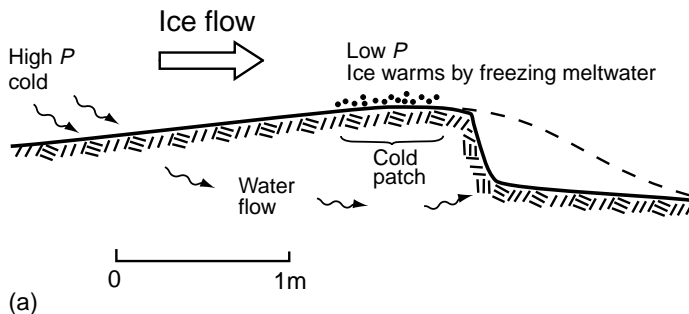
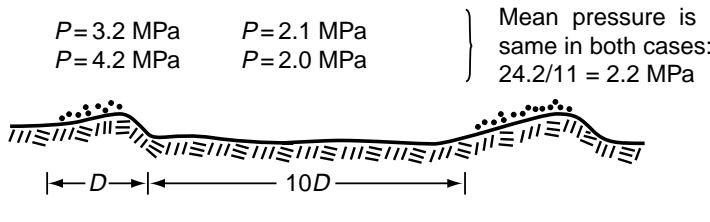


Figure 7.6. Formation of cold patches (after Robin, 1976). (a) Water that is squeezed out of the ice on the stoss side of an obstacle may drain away and thus not be available to refreeze in the low pressure zone at the top of the obstacle. (b) Small changes in pressure between obstacles result in large changes on tops of obstacles.



on the stoss side of a bump, where the melting point is depressed, is squeezed out of the ice through veins formed where three ice crystals abut one another (see Figure 8.1). When this “cold” ice is transported to the top of the bump, where the pressure is less, any water remaining in the ice and along the ice–rock interface refreezes, releasing the heat of fusion and thus warming the ice. The water within the ice is likely to freeze first, followed by that at the interface. If the amount of water present is sufficient, enough heat will be released to warm the ice to the new pressure melting point without freezing all of the water at the interface. However, if some of the melt water escaped around the bump as shown in Figure 7.6a, *all* of the water at the interface may freeze, thus cementing the glacier to the bed.

The second mechanism discussed by Robin involves local increases in water pressure in areas between bumps. Because the weight of the glacier is constant, any such increase will decrease the pressure on stoss sides of bumps, where the pressure is already higher than average. In the example shown in Figure 7.6b, the area between bumps is 10 times the area of the bumps. Thus a 0.1 MPa increase in pressure between bumps reduces the pressure over the bumps by 1 MPa, resulting in a $\sim 0.7^\circ\text{C}$ increase in the pressure melting point. The ice, being at the pressure melting point, was colder while the pressure was high. Thus, the decrease in pressure leads to freezing of any water present, potentially including any at the ice–rock interface.

In addition to increasing the drag between the glacier and the bed, such cold patches may be an effective erosional mechanism. Rock fragments that have been loosened from the bed but do not project appreciably above it are separated from the ice by a melt film. As long as the melt film exists, they may be held in the bed by rock-to-rock frictional forces that exceed the drag exerted by the ice through the film. However, such fragments may be entrained if the melt film becomes frozen.

There are also a number of problems surrounding the use of the simple regelation theory presented above. Nye (1973a) notes, for example, that at any point on an obstacle, the melt rate (or freezing rate) required for movement of ice past that obstacle by regelation is completely determined by the geometry of the obstacle, and in particular by the inclination of the face to the direction of motion. The melt rate determines the heat sources and sinks, so the temperature distribution is known, and hence also the pressure distribution. The melting and freezing rates also determine the water fluxes required. The awkward fact is that for normal bed geometries, the pressure distribution predicted by the simple theory commonly does not provide pressure gradients in the melt film that are consistent with the water fluxes required. To resolve this discrepancy, one has to take into consideration spatial variations in the thickness of the melt film and temperature gradients across it.

Impurities provide a second problem for regelation theory. Water moving in a melt film over an obstacle on the bed may absorb ions from the bed or from rock flour between the bed and the ice. Such impurities lower the freezing point. Thus, the temperature in the lee of the obstacle is lower than would be the case with pure water, and the temperature gradient through the obstacle is correspondingly reduced (see Figure 7.2). This reduces the heat flux through the obstacle, and thus reduces S_r .

When impurities collect in the freezing water film in the lee of a bump, fractionation occurs; some of the impurities are carried away by the ice that forms, while the rest remain in the melt film. The steady-state situation is one in which the concentration of impurities in the film is such that the rate of removal of ions from the lee side during freezing equals the influx of ions in water coming from the stoss side of the bump. The impure ice thus formed will melt on the next suitable bump downglacier around which regelation is occurring, and the resulting impure melt water will acquire more impurities. After several such cycles, the concentration of ions in water on the lee sides of obstacles becomes high enough to induce precipitation. The most common such precipitates are CaCO_3 , but Fe/Mn coatings are also observed. Hallet (1976a, 1979b), Hallet *et al.* (1978), and Ng and Hallet (2002) have made detailed studies of the calcium carbonate precipitates, and Hallet (1976b) has calculated the degree to which basal sliding over a hypothetical bed composed of sinusoidal waves of a single wavelength would be

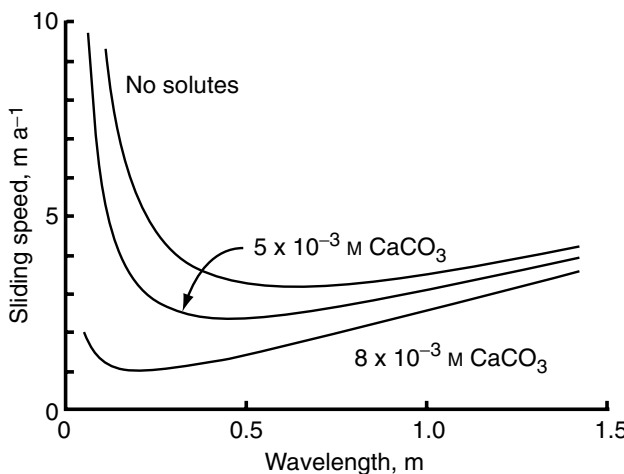


Figure 7.7. Effect of solutes on speed of sliding over a sinusoidal bump. (After Hallet, 1976b. Reproduced with permission of the author and the International Glaciological Society.)

reduced by various concentrations of CaCO_3 in the melt film (Figure 7.7). Note, in Figure 7.7, that the wavelength for which S is a minimum, that is λ_c , is reduced from 0.6 m for the case of no solutes to 0.2 m for the highest solute concentration. This is because solutes reduce the efficacy of the regelation process, effectively shifting the S_r curve in Figure 7.3 downward.

A further effect of solutes has been observed in regelation experiments with wires (Drake and Shreve, 1973). As the stress driving the regelation increases, the pressure in the lee of the wire decreases, and may reach the triple point pressure. At this point a vapor pocket forms and the temperature cannot be raised further. Because the temperature on the stoss side can continue to decrease as the pressure increases, the mean temperature around the wire is less than the far-field temperature, and heat will flow from the surroundings toward the wire. This increases the rate of melting, but also means that some of the melt water formed on the high-pressure side of the wire will not refreeze on the lee side. This water collects in pockets that are then left behind in the ice, resembling a wake, as the wire advances. Such a process might occur beneath glaciers in areas of relatively high basal shear traction.

Finally, the rheology of basal ice may be somewhat different from that of ice well above the bed, thus altering the role of plastic flow, and cavities may form in the lee of obstacles. These effects are discussed next.

Rheology of basal ice

In comparison with ice higher in a glacier, basal ice may have fewer bubbles, a different solute content, and more sediment. In addition, it is quite likely to have more interstitial water because strain heating is

significant here, and there is no way to remove this heat other than by melting ice. Finally, the constant changes in stress field as the ice flows around successive bumps may result in zones of transient creep as the crystal structure adjusts to the changes.

In a unique experiment to study these effects, Cohen (2000) utilized the facilities of the Svartisen Subglacial Laboratory described above. He placed an instrumented flat-topped conical obstacle at the base of the glacier under 210 m of ice. The obstacle was 0.15 m high, and was 0.05 m in diameter at its top and 0.25 m at its base. Cohen measured forces on the obstacle, temperatures at many places in it, and the speed with which ice flowed past it. He then modeled the flow with the use of a fully three-dimensional numerical model employing the finite-element method (Chapter 11). Assuming $n = 3$, he found that the observed forces and ice speeds could be reproduced in the model with values of B ranging from 0.06 to 0.13 MPa $a^{1/3}$. A normal value for temperate ice with little or no interstitial water would be slightly more than 0.2 MPa $a^{1/3}$ (Figure 4.18). Because $n \approx 3$, the 2- to 4-fold reduction in B results in an 8- to 64-fold increase in $\dot{\epsilon}$.

Cohen (1998, 2000) also studied the structure and texture of the basal ice at the site of the experiment. The ice contained sediment-bearing lamellae, several millimeters thick, interlaminated with clean ice. This is very typical of basal ice from both temperate and polar glaciers. Debris concentrations in the sediment-rich layers at the level of the obstacle were about 20% by volume. The cross-sectional area of the crystals averaged $\sim 7 \text{ mm}^2$ compared with $\sim 50 \text{ mm}^2$ in the overlying clean ice. There was no preferred orientation of c -axes, so this could not explain the low value of B . Cohen also measured the water content of the basal ice and found that it was $\sim 2\%$. A nonlinear extrapolation of the data in Figure 4.18 suggests that even this high a water content cannot explain the low viscosity. Instead, Cohen suggested that unbound water at the interface between the ice and the sediment particles acts as a lubricant, enhancing sliding between the sediment-rich layers and the lamellae of clean ice. Such interfacial water layers are nanometers in thickness.

Echelmeyer and Wang (1987) also found that ice in the basal zone of Urumqi Glacier No. 1 in western China deformed much more readily than clean ice. In this case, the material involved was ice-cemented drift with an ice content of $\sim 31\%$ by weight. The temperature was -2°C . The measured deformation rate would correspond to a value of B of $\sim 0.04 \text{ MPa } a^{1/3}$. They, too, attributed the softness of the drift to liquid-like interfacial water layers.

At lower temperatures, dirt appears to strengthen ice, presumably because the amount of unbound water decreases. In a series of

experiments at -9.1°C , Hooke *et al.* (1972) found that B was $\sim 85\%$ higher in ice with 20 volume percent dispersed fine sand than it was in clear ice. They also found that B increased approximately linearly with sand content. They concluded that sand particles inhibited movement of dislocations, and attributed the strengthening of the ice to development of dislocation tangles in the vicinity of the particles.

The role of normal pressure

Another effect that is overlooked in the sliding theories discussed above is that of normal stresses. Budd *et al.* (1979) carried out some laboratory experiments in which ice blocks upon which a normal load, N , had been placed, were dragged across rough rock surfaces. Temperature control was achieved by immersing the ice and rock surfaces in an ice-water bath. They found that $S \propto \tau^3/N$. The cubic dependence on τ might suggest that plastic flow was the dominant sliding process, and this may very well have been the case as it was possible for melt water formed at the interface to escape to the surrounding bath. Thus, heat released by refreezing of this melt water in the lee of the obstacle might not have been available. In that case, the only heat available for melting would be frictional heat and heat conducted from the bath to the interface. (The interface would be colder than the bath owing to depression of the melting point.)

More puzzling is the inverse dependence on N ; this is what one expects in a purely frictional system, such as would be provided by a rock being dragged across a bedrock surface. To the extent that the ice–rock interface in the experiments was perfectly lubricated by a melt film, however, we would presume that no tractions could have been supported parallel to the surface. In this case, the sliding speed should have been independent of the normal pressure. However, some erosion of the rock surface occurred during the experiments, and the erosion rate was proportional to $N^{2/3}$. Rock particles entrained in the basal ice and in contact with the bed would have increased the drag. It seems doubtful, however, that the small amount of rock debris involved could account for a significant reduction in sliding speed.

Budd *et al.* suggested that in studies of real glaciers, N should be replaced by the effective normal pressure, N_e , or the normal pressure minus the water pressure, a factor first vigorously emphasized by Lliboutry (1968 and earlier). The importance of water pressure on sliding speed is now widely recognized (see, for example, Figure 7.8), but, as we will discuss next, some of the mechanisms involved are not frictional as first suggested.

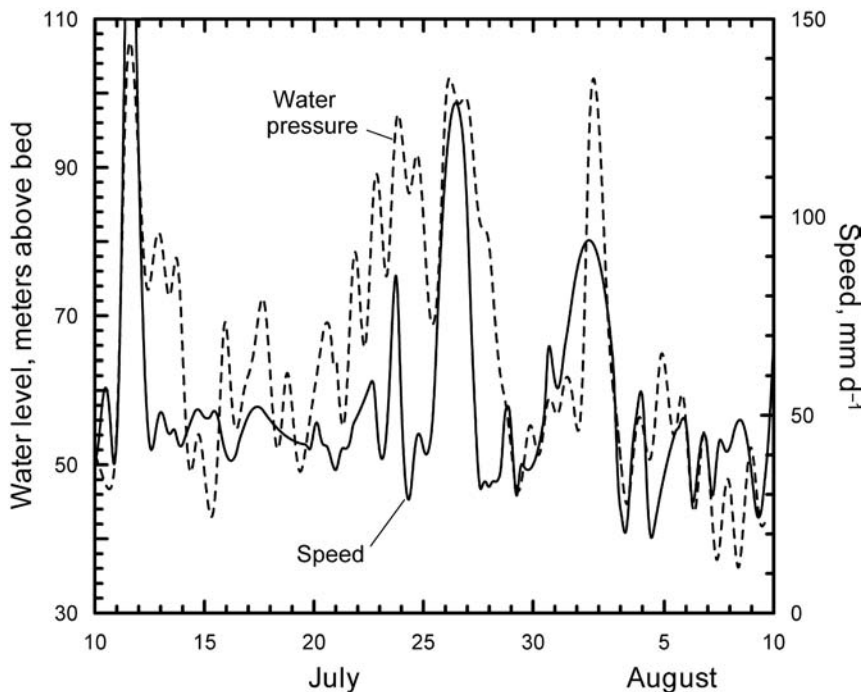


Figure 7.8. Diurnal variations in surface speed on Storglaciären, Sweden, measured with the use of a computer-controlled laser distance meter. The distance from a point off the glacier to a stake on the glacier was determined every 10 min. The dashed line shows corresponding water pressures measured in nearby boreholes. Only the major peaks in speed are clearly related to water pressure peaks. (Modified from Hanson *et al.*, 1998. Reproduced with permission of the author and the International Glaciological Society.)

Cavities and the effect of water pressure

Elevated water pressures increase the sliding speed in two ways: (1) by increasing the degree of separation of ice from the bed, thereby increasing the shear traction on parts of the bed still in contact with the ice; and (2) by exerting a net downglacier force on ice that bridges cavities. In addition, they weaken any deforming subglacial till over which the glacier is moving, thus increasing u_d (Figure 5.5). Here, we consider the first two of these. The third will be addressed in connection with our discussion of subglacial till deformation.

The degree of separation of ice from the bed in the lee of obstacles is increased when water pressures remain elevated for periods of a few days or weeks. Let us briefly examine the conditions required for such separation in an idealized situation. The pressure at the bed is:

$$P(x, y) = \sigma_o + P_o(x, y)$$

where σ_o is the ice overburden pressure and $P_o(x, y)$ is a fluctuating contribution that is positive on the stoss sides of bumps and negative on lee sides (Iken and Bindschadler, 1986). The basal drag due to this effect can be expressed in terms of P_o , thus:

$$\tau_b = \frac{1}{A_r} \int_{A_r} P_o(x, y) \frac{\partial z}{\partial x} dx dy \quad (7.11)$$

Here, the x -axis is directed downglacier and z is normal to the mean bed and positive upward, so a positive $\partial z / \partial x$ is a slope opposing flow, while negative values indicate downglacier-sloping surfaces. A_r is an area of the bed large enough to be representative of average conditions.

If we consider a sinusoidal bed of amplitude a and wavelength λ , P_o will vary sinusoidally; Iken and Bindschadler (1986) find that its maximum amplitude is:

$$|P_o|_{\max} = \sqrt{2} \langle P_o^2 \rangle^{1/2} = \frac{\lambda \tau_b}{a \pi} \quad (7.12)$$

where $\langle P_o^2 \rangle$ is the root mean square of P_o . The minimum pressure will occur at inflection points on the downglacier faces of the undulations, and is:

$$P_{\min} = \sigma_o - \frac{\lambda \tau_b}{a \pi} \quad (7.13)$$

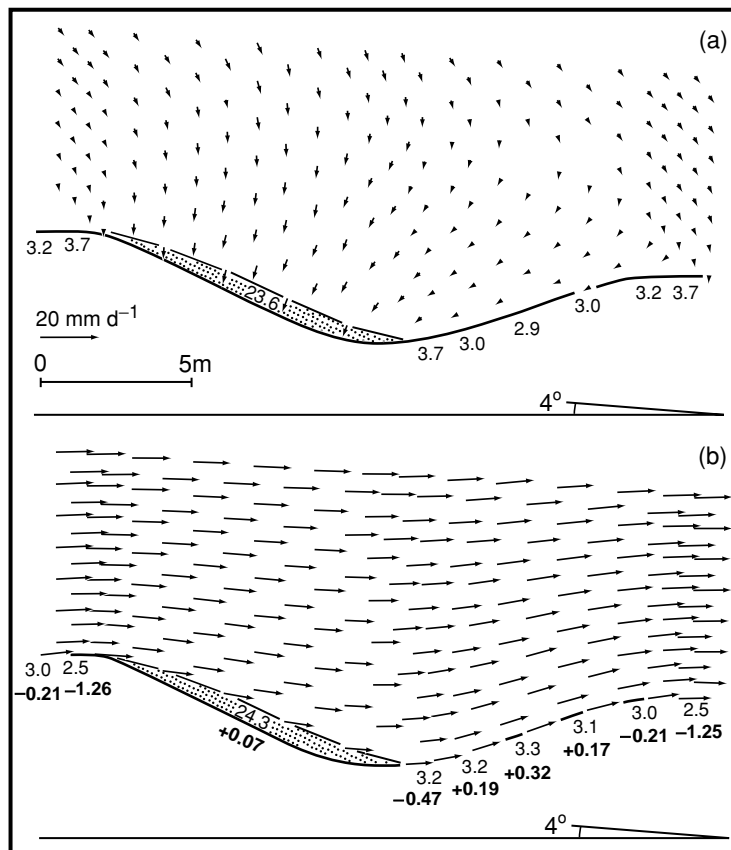
Note that P_{\min} decreases as τ_b increases, and hence as the sliding speed increases. If the water pressure exceeds this minimum value, separation occurs and cavities will grow to a size determined by the degree to which the water pressure exceeds P_{\min} . Roughness elements on the bed that are bridged by such cavities no longer exert any drag on the ice. The task of balancing the driving force, $\rho g h \alpha$, is thus shifted to places where the ice is still in contact with the bed. S increases, and this results in the necessary increase in shear traction on these surfaces. (Note that S is the independent variable in this situation, while τ_b is dependent. This is a subtle but important distinction.)

The second mechanism by which elevated water pressures lead to acceleration of a glacier is a type of hydraulic jacking. If the subglacial drainage system is reasonably well connected to cavities on the lee sides of bumps, increasing water pressures in the drainage system result in increased water pressures in the cavities. (Pressures in the water film on the stoss sides of the bumps are always in excess of the overburden pressure, and thus are not affected appreciably by changes in the (lower) pressure in the cavities.) The water in the cavity thus pushes upglacier against the bedrock and downglacier against ice. The result is a downglacier force that is added to the downglacier component of the body force. Drag forces on the bed must then increase to balance this

Figure 7.9. Flow around a subglacial cavity in the lee of a sinusoidal bump based on a numerical model using the finite element method.

(a) The water pressure in the cavity, 2.36 MPa, is too low, so the cavity is shrinking. (b) The water pressure in the cavity is too large, so the cavity is expanding.

Light-faced numbers show pressure at bed. Bold numbers show change in pressure following a 0.07 MPa change in water pressure in the cavity. The basal drag was 0.103 MPa in both experiments, and the mean pressure at the bed was 2.72 MPa. The cavity would be stable at a pressure of 2.41 MPa. (After Röthlisberger and Iken, 1981, Figure 3. Reproduced with permission of the authors and the International Glaciological Society.)



additional downglacier force. Again, an increase in sliding speed results in this increase in drag.

Over time spans of the order of hours, cavity sizes cannot change appreciably because such changes require ice flow. Thus, on bedrock beds, diurnal changes in speed resulting from input of meltwater or from storms (Figure 7.8) must be a result, principally, of hydraulic jacking. Of course, cavity size increases during hydraulic jacking as a result of the increased flow rate, so if high speeds are sustained the degree of separation will increase sufficiently to result in a significant further increase in speed.

The effect of changing water pressures in a lee-side cavity is nicely illustrated by a numerical modeling study conducted by Röthlisberger and Iken (1981) (Figure 7.9). When the pressure in the model cavity was 0.05 MPa lower than the 2.41 MPa necessary to support it, velocity vectors were toward the cavity (Figure 7.9a), tending to close it. An increase in pressure of only 0.07 MPa was sufficient to start enlarging the

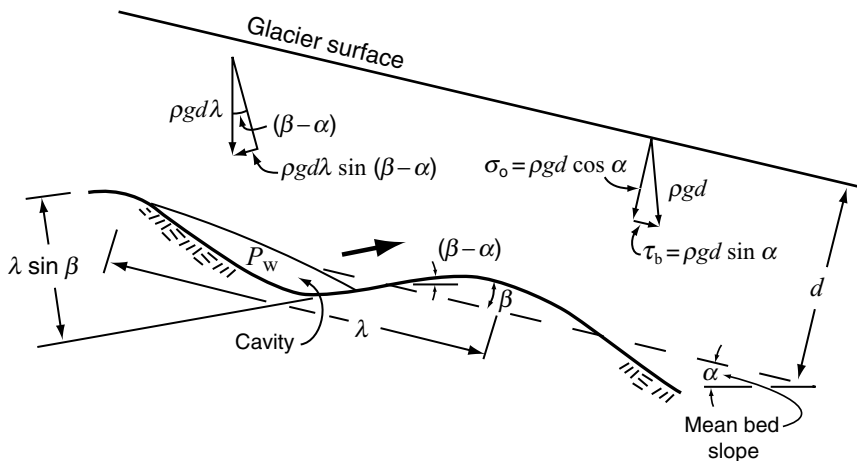


Figure 7.10. Diagram illustrating calculation of P_{crit} .

cavity at a rate of about 10 mm d^{-1} (Figure 7.9b). Note, in particular, the substantial reductions in normal pressure, indicated by the bold numbers in Figure 7.9b; the decrease of over 1.2 MPa at the crest of the bump could easily have resulted in freezing there in a real situation, as suggested by Robin (Figure 7.6b).

Iken (1981) notes that for a given adverse bed slope, β , measured with respect to the average slope of the bed, there is a critical pressure, P_{crit} , above which the glacier may accelerate without bound. Such acceleration would occur if (Figure 7.10):

$$P_w \lambda \sin \beta > \rho g d \lambda \sin(\beta - \alpha) \quad (7.14)$$

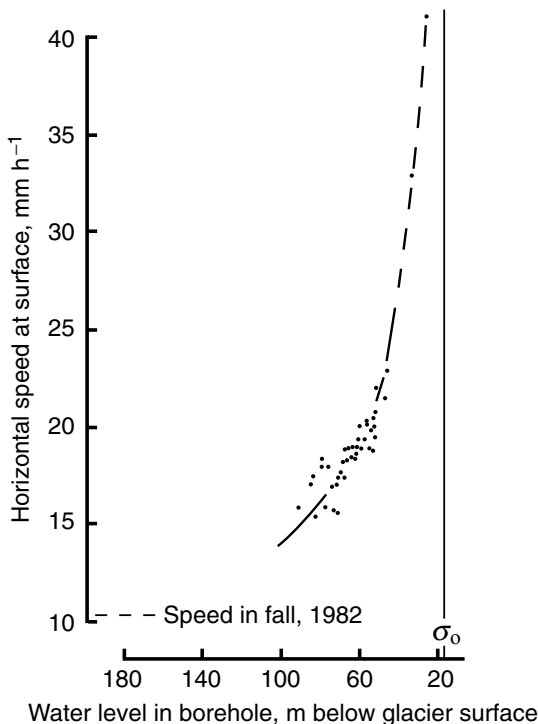
Here, P_w is the pressure in the cavity and $\lambda \sin \beta$ is the projected area of the cavity face, normal to the back slope of the bump, against which P_w acts. Thus, this is the force trying to push the glacier up the back slope of the bump. The right-hand side of the equation is the component of the body force acting parallel to the back slope of the bump and in the upglacier direction. Using the expressions for σ_o and τ_b shown in Figure 7.10 and the trigonometric identity $\sin(\beta - \alpha) = \sin \beta \cos \alpha - \cos \beta \sin \alpha$, we obtain:

$$P_{\text{crit}} = \sigma_o - \frac{\tau_b}{\tan \beta} \quad (7.15)$$

On an actual glacier bed consisting of a variety of sizes and shapes of obstacles, P_{crit} would not be exceeded everywhere simultaneously. Thus, for most situations, $P_{\text{crit}} \approx \sigma_o$ is probably more realistic.

Working on Findelengletscher (Findelen glacier), Iken and Bindschadler (1986) have collected an outstanding set of field data on the

Figure 7.11. Speed of a stake on the surface of Findelengletscher as a function of water pressure, here represented by the water level in a borehole. Were the water level to rise to 18 m below the surface, the glacier would float. (After Iken and Bindschadler, 1986, Figure 6. Reproduced with permission of the authors and the International Glaciological Society.)



relation between water pressure and surface speed (Figure 7.11). Here, the expected exponential increase in speed with increased water pressure, with water pressure asymptotically approaching the limit σ_0 , is clearly demonstrated.

Iken and Bindschadler suppose that the character of the bed in front of Findelengletscher is similar to that beneath the glacier, and thus are able to calculate sliding speeds using Kamb's (1970) theory. For wavelengths and roughnesses that they believe to be appropriate, the theory gives sliding speeds that are too large, compared with the surface speed, to be realistic. They attribute the discrepancy largely to failure of the theory to take rock-to-rock friction into consideration.

Jansson (1995) has studied the relation between effective pressure, N_e , and surface speed, u_s , on Findelengletscher and Storglaciären, using Iken and Bindschadler's (1986) data (Figure 7.11) for Findelengletscher, and finds that a relation of the form

$$u_s = CN_e^{-0.4} \quad (7.16)$$

fits the data well (Figure 7.12). Note that τ_b does not vary significantly within either of the two data sets, so its effect is incorporated into the

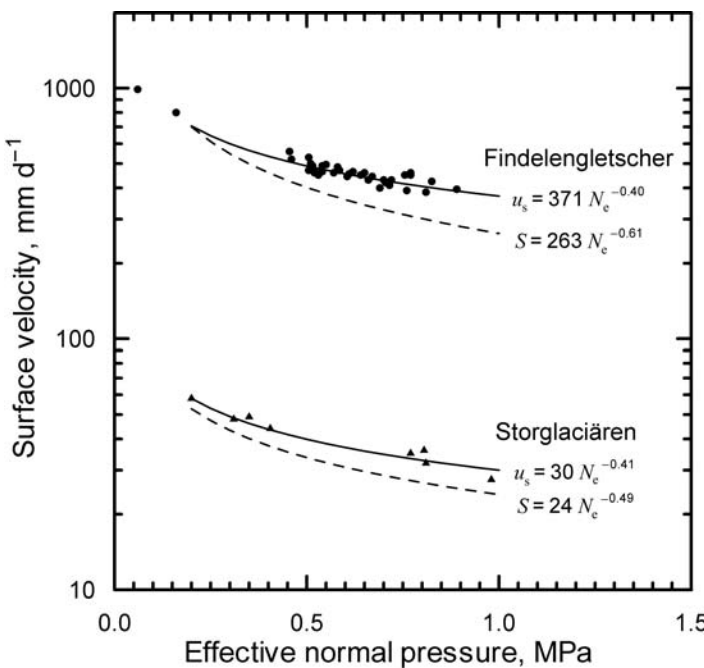


Figure 7.12. Relation between surface speed, u_s , sliding speed, S , and effective pressure, N_e , on Findelengletscher and Storglaciären. Dashed lines show sliding speed estimated by subtracting internal deformation from u_s . (After Jansson, 1995. Reproduced with permission of the author and the International Glaciological Society.)

constant factor, C , which is more than an order of magnitude higher on Findelengletscher (Figure 7.12). Even after subtracting the contribution of internal deformation, estimated with the use of Equation (5.16), Jansson found that Findelengletscher still seemed to be sliding more than ten times as fast as Storglaciären under comparable effective pressures. Such a difference in sliding speed would have resulted in a basal drag beneath Findelengletscher that was two to three times that beneath Storglaciären, but driving stresses (albeit uncorrected for longitudinal stress gradients; see Figure 12.7) at the sites of the measurements were nearly equal on the two glaciers.

More recent data from Findelengletscher (Iken and Truffer, 1997) serve only to further emphasize our lack of understanding of the effect of water pressure on sliding. By 1985, three years after the measurements shown in Figures 7.11 and 7.12, the surface speed had decreased 25% for comparable water pressures. By 1994 there had been an additional 35% decrease. There have not been any changes in the geometry of the glacier, and hence in driving stress, that could explain this deceleration. Iken and Truffer suggest that the basal water system was better connected in 1982, so that high water pressures reached more subglacial cavities. Thus, in effect, there may have been more subglacial hydraulic jacks urging the glacier forward in earlier years.

Deformation of subglacial till

We have known for decades that ice moving over granular subglacial materials can deform these materials. (Herein, the term “granular material” should be understood to include materials with significant amounts of clay, although a distinction between granular materials and clays is usually made in the soil mechanics literature.) Commonly, the granular material is till, either formed by erosion during the present glacial cycle, or left from a previous one. Recently it has become clear that a large fraction of the surface velocity of a glacier may be a result of deformation of such till (Figure 5.5).

Intense interest in the rheology of till dates from work on Whillans Ice Stream in Antarctica where studies of seismic velocities suggested that a layer with high porosity, saturated with water under high pressure, and 2–13 m thick was present beneath the ice (Blankenship *et al.*, 1986). The high porosity suggested active deformation, facilitated by the high water pressure. Thus, the high speed of the ice stream, about 450 m a^{-1} , was attributed to deformation of the till. Subsequent drilling revealed that the ice stream was, indeed, underlain by till, and also confirmed that the water pressure was close to the overburden pressure (Engelhardt *et al.*, 1990). A key question, then, is whether the till is deforming, or alternatively whether the high water pressures have simply decoupled the ice stream from the till. Experiments addressing this question will be described later in this chapter.

More recently, some scientists studying the Quaternary period have suggested that the large volumes of material found in till sheets in the midwestern United States and the large volumes of glacigenic material found in some submarine fans surrounding the Barents Sea could only have been transported to their present locations in deforming subglacial till layers (e.g. Alley, 1991; Hooke and Elverhøi, 1996). It is estimated that the amount of material that could be transported in basal ice or by subglacial melt streams is too low to account for the volumes of these deposits in the time inferred to be available for their formation. In the Barents Sea case, calculated basal melt rates are so high that little material is likely to have been entrained by basal ice, and yet they are too low to provide the water volumes required for significant fluvial transport.

Because glacial till is a granular material, its rheology is quite different from that of ice. Granular materials normally have a yield strength below which they deform only elastically. This yield strength, s , is related to two physical properties of the material, the cohesion, c , and the angle of internal friction, φ , by the classical Mohr–Coulomb relation:

$$s = c + N_e \tan \varphi \quad (7.17)$$

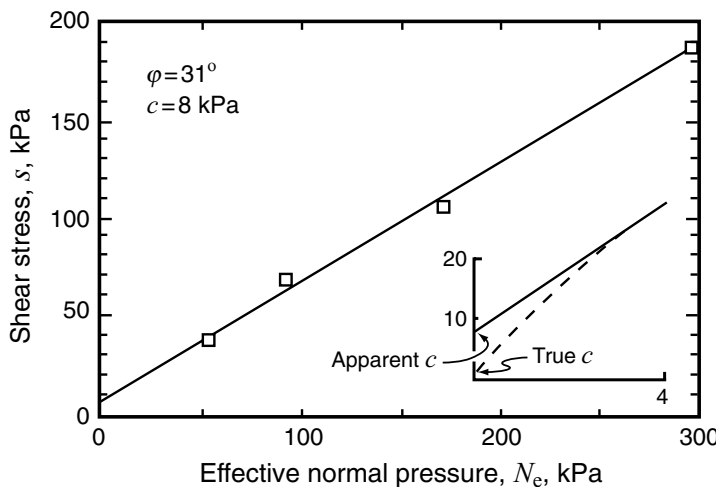


Figure 7.13. Relation between s and N_e obtained from a laboratory test on a sample of till from beneath Storglaciären (Iverson, unpublished data). Inset shows, schematically, how s may actually vary with N_e at low effective pressures.

where N_e is the effective normal pressure. To determine c and φ , laboratory tests are conducted in which the stress needed to initiate deformation of a material is measured at various effective normal pressures. When s varies linearly with N_e (Figure 7.13), the slope of the line is $\tan \varphi$, and the intercept is the apparent cohesion.

The term *apparent* cohesion is used because detailed measurements often show that the variation of s with N_e is not linear at low effective normal pressures, but rather is as shown by the dashed line in the inset in Figure 7.13. The true cohesion is the value of s at the intercept of this dashed line with the ordinate. Because the apparent cohesion varies directly with the true cohesion, however, we normally will not draw a distinction between the two quantities.

Let us now examine the physics involved in cohesion, and the physical significance of φ .

Cohesion

True cohesion in soils is a consequence of cementation, of electromagnetic forces between clay particles, and of electrostatic forces resulting from charge imbalances among ions absorbed on clay minerals (Mitchell, 1993, pp. 125, 373–374). Cementation is the major source of cohesion in subaerial soils, but would not be significant in continuously deforming subglacial tills. Thus, the magnitude of c in such tills is determined primarily by the amount and species of clay minerals present.

In situ deforming subglacial tills formed by erosion in the current cycle of glaciation do not seem to have much clay-sized material unless the glacier has moved over a bed containing such material. Furthermore,

most of the clay-sized particles that are present in such clay-poor tills are not clay minerals. Thus, c may be small in such tills. For example, records from tiltmeters emplaced in till beneath Storglaciären demonstrate that this till is deforming. However, only $\sim 5.4\%$ (by weight) of the particles in samples collected through boreholes are less than $2 \mu\text{m}$, and these particles are largely quartz and hornblende (Iverson, unpublished data). Laboratory tests yield $c = 8 \text{ kPa}$ for this till (Figure 7.13). Similar tests on till samples collected from beneath Whillans ice stream, containing $\sim 35\%$ clay, gave $c = 3 \pm 1.3 \text{ kPa}$ (Tulaczyk *et al.*, 2000a). (In this case, the clay-sized material, which does consist of clay minerals, is inferred to have been derived from Tertiary glaciomarine sediments (Tulaczyk *et al.*, 1998; Kamb, 2001).) For comparison, values for silty and clayey sands are typically between 20 and 75 kPa (Hausmann, 1990).

The absence of clay-sized material in deforming tills is likely to be largely a consequence of flushing by subglacial streams. In addition, however, it is noteworthy that the deviatoric stress required to fracture a grain increases as the particle size decreases, and that in the limit very fine grains deform plastically rather than fracture into still smaller particles (Kendall, 1978). That the clay-sized particles present in such tills tend not to be clay minerals is the result of the absence of subaerial weathering processes. Higher concentrations of clay-sized particles and of clay minerals in Pleistocene tills may be a consequence either of subaerial weathering after retreat of the ice, or of incorporation of previously weathered material over which the ice moved.

Cohesion is not increased by saturation by water unless clay minerals are present. The well-known fact that the walls of wet sand castles stand up better than dry ones is, rather, a result of surface tension. Surface tension effects are present when the sand is wet but pore spaces still contain air. This is because surface tension is a result of stresses associated with the air–water interface.

Consolidation

When a granular material accumulates gradually, it compacts under its own weight. Such a material is called *normally consolidated*. If an additional load, such as a shear stress, is then placed on the material, it becomes *overconsolidated*. The term overconsolidated is also used to describe a granular material which, after being normally consolidated, experiences a reduction in overburden pressure due to erosion or, perhaps, to melting of an overlying glacier. The highest past effective stress to which a sample has been subjected is called the *preconsolidation stress*.

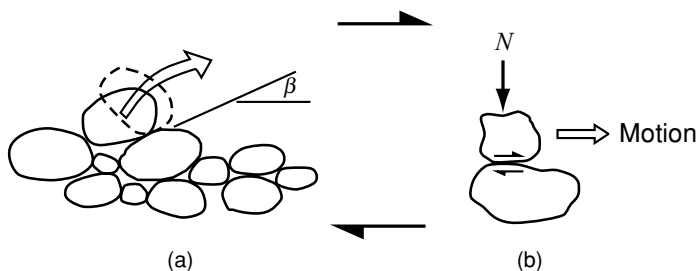


Figure 7.14. Deformation of a granular medium involves both (a) dilation as grains move apart in order to pass over one another; and (b) friction between grains that are constrained to slide past one another.

The state of consolidation is altered whenever a granular material is sheared. Thus, for example, if a subglacial till, previously consolidated by an effective pressure of 100 kPa, is later deformed at an effective pressure of 30 kPa, the preconsolidation stress is reset to the lower value (Tulaczyk *et al.*, 2001a).

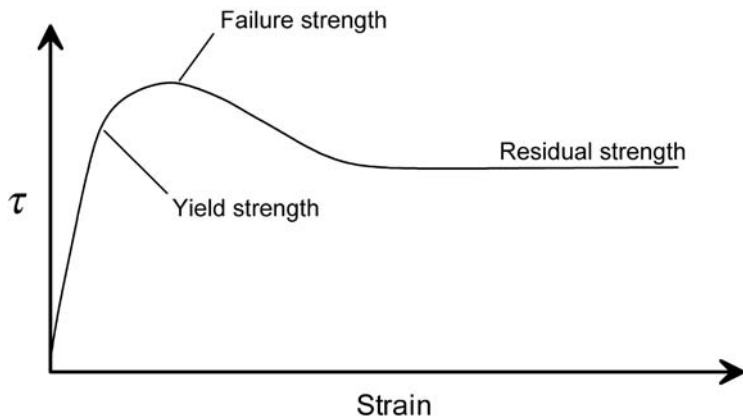
Angle of internal friction

When an overconsolidated granular material begins to deform under a shear stress, it must *dilate* so that individual grains can move over one another (Figure 7.14a). A normally consolidated material may either dilate or compact slightly, depending on the granulometry (size distribution of particles) and the conditions under which it accumulated. Dilatation increases pore space, which is why the high porosity of the till beneath Whillans Ice Stream suggests deformation.

Grains in such a deforming material must also *slide* past one another locally (Figure 7.14b). The forces resisting this sliding motion are frictional. Frictional forces are a consequence of the interlocking of microscopic asperities on the surfaces of the materials (Mitchell, 1993, p. 362). The maximum shearing stress that can be supported by friction between two surfaces, τ_p , is proportional to the effective normal pressure, N_e : $\tau_p = \mu N_e$. The constant of proportionality, μ , is called the coefficient of friction.

Let us define β as the angle, relative to the shear plane, that particles must ascend during dilation from an overconsolidated state (Figure 7.14a) and also define $\omega = \tan^{-1} \mu$. Then $\varphi = \beta + \omega$ (Iverson *et al.*, 1996). In granular materials that do not have much clay, ω is typically 20–25° and φ is typically between 25° and 40° (Mitchell, 1993, pp. 343, 366). Thus, more than half of the resistance to deformation of such a material is a consequence of frictional forces, while the remainder is due to processes such as dilation and crushing (Mitchell, 1993, p. 401).

Figure 7.15. Schematic illustration of the variation of mean shear stress with time (or displacement) in a granular medium that is sheared at a constant rate.



As a result of the dependence of φ on β , φ depends, also, on the granulometry of the material. For example, if spaces between particles in Figure 7.14a were filled with finer material, a particle could not settle down into the gap between subjacent particles, and thus would not have to rise so much to move over its neighbor. Then β would be lower, and hence so would φ . For example, φ is 31° in the sandy Storglaciären till (Figure 7.13) and 24° in the clay-rich till from beneath Whillans Ice Stream (Tulaczyk *et al.*, 2000a).

Normal pressures suppress dilation and also force particles into firmer contact, thus increasing τ_p . These two factors account for the dependence of s on N_e .

When a granular material is deformed at a constant strain rate (with the shear stress, τ , being measured as a function of time or displacement), τ first increases rapidly to a peak. The initial linear portion of the rise reflects elastic (recoverable) deformation. The point at which the rise begins to deviate from linearity is called the *yield strength* (Figure 7.15). Subsequent strain reflects irrecoverable visco-plastic deformation. The peak of the curve is the *failure strength*. If the material was initially overconsolidated, τ then declines slightly before reaching a constant value. The final value of τ , normally reached after a shear strain of the order of only 10%, is called the *residual* or *ultimate strength* (Skempton, 1985). The difference between the peak and the residual strength reflects the additional stress needed to induce dilation. The decrease from the peak to the residual strength reflects a decrease in β and hence in φ . Once dilated, the material remains dilated as long as N_e remains constant. Thus, the stress required for deformation remains constant. (In materials in which clay-sized particles are abundant ($>20\%$) and are predominantly clay minerals, a further decline in strength may occur as the platy clay particles become aligned parallel to the direction of shear.)

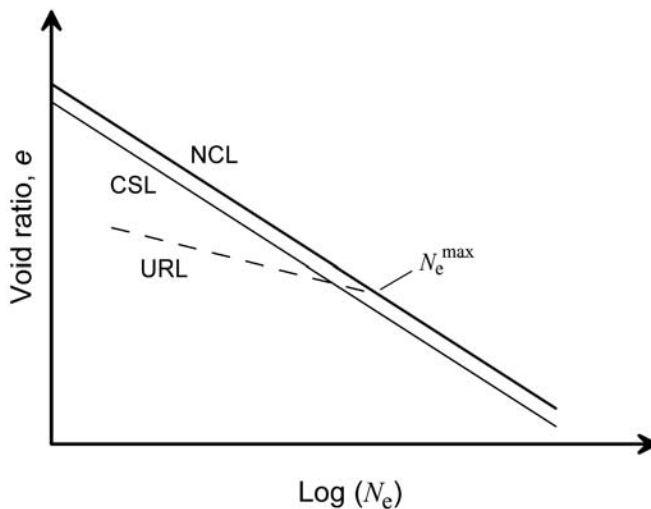


Figure 7.16. Schematic diagram showing variation of void ratio with effective normal pressure. See text for explanation.

Void ratio

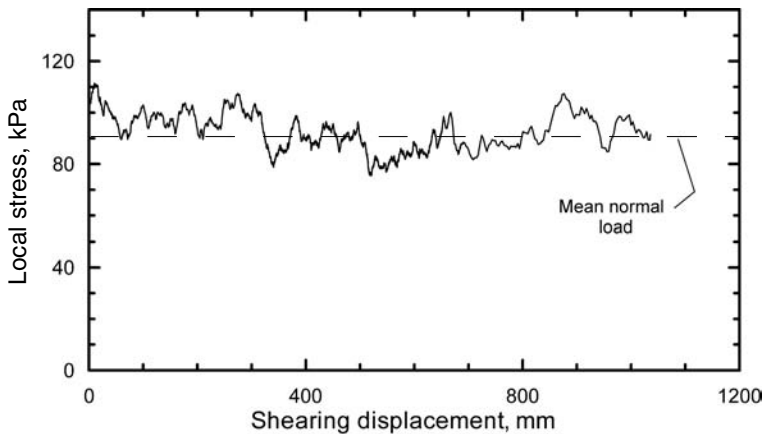
The void ratio, e , is the ratio of the volume of pores, V_p , to the volume of solids, V_s : $e = V_p/V_s$. (Note that this is not the same as porosity; porosity is the percentage of voids in the total volume.) The void ratio varies with N_e , thus:

$$e = e_o - C_p \log \frac{N_e}{N_{eo}} \quad (7.18)$$

where e_o is the void ratio at an effective normal pressure of N_{eo} , and C_p is a dimensionless coefficient of compressibility (e.g. Tulaczyk *et al.*, 2000a).

As a normally consolidated material accumulates, the void ratio will decrease as shown, schematically, by the line labeled NCL (*normal consolidation line*) in Figure 7.16. The slope of this line is $-C_p$. In an overconsolidated material, the void ratio will be below the NCL. If the material is sufficiently overconsolidated and is then sheared, resulting in dilation, the void ratio will increase initially and then reach a steady value shown by the line labeled CSL (*critical state line*) in Figure 7.16. Note that the CSL is below the NCL so if deformation stops, the material will not consolidate again unless N_e is increased by more than the amount indicated by the horizontal spacing between the two lines. If the load on a consolidated material is relaxed, the material will expand elastically along a path like the one labeled URL (*unloading-reloading line*) in Figure 7.16. Upon reloading, it will follow the same path back to its original position, and will then begin to consolidate further along the NCL line. By collecting an undisturbed sample in the field and subjecting it to a gradually increasing load in the laboratory, in what is called

Figure 7.17. Variation in local pressure with time in a granular medium, ~ 55 mm thick, as it is deformed in a ring shear experiment. (Data courtesy of N. R. Iverson and T. S. Hooyer.)



a *preconsolidation test*, this property can be exploited to determine the maximum effective normal pressure, N_e^{\max} , to which the sample has been subjected.

Hooyer and Iverson (2002) did such preconsolidation tests on several samples of till deposited by the Des Moines Lobe, a lobe of the Laurentide ice sheet that advanced out of North Dakota into Minnesota and Iowa about 13 800 radiocarbon years ago. Their values of N_e^{\max} ranged from 120 to 300 kPa. These values are quite low, considering the probable ice thickness, suggesting that pore water pressures beneath the lobe were high. This, in turn, implies that motion of the lobe could have been largely by a combination of sliding over the underlying till and deformation of that till, thus providing an explanation for the considerable extent of the lobe despite other evidence suggesting that driving stresses were quite low.

Grain fracture and the granulometry of deforming subglacial till

If a granular medium is sheared at a constant rate between moving platens, in one of which there is a pressure sensor that is many times the diameter of individual grains but much smaller than the platen itself, the pressure recorded by this sensor varies with time (Figure 7.17) (Mandl *et al.*, 1977; Iverson *et al.*, 1996). Sometimes it exceeds the mean normal load on the sample by as much as 25%, while at other times it is significantly less than the mean. One logical explanation for this is that grains in the medium become aligned to form bridges such as that shown in Figure 7.18a. When traced through a granular material of significant thickness, these bridges are much more complicated than suggested by the simple sketch in Figure 7.18a; high contact stresses are distributed

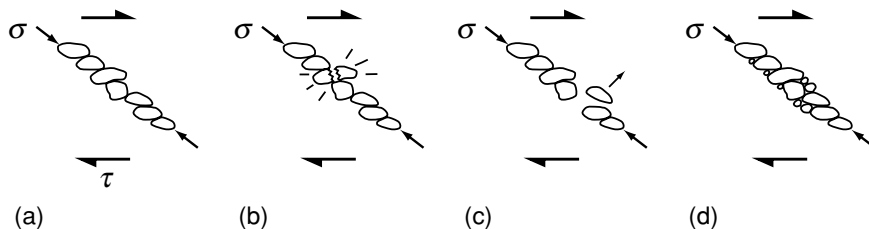


Figure 7.18. (a) A grain bridge, formed by nearly coaxial alignment of several grains in a deforming granular medium, may fail by: (b) fracture of a grain; or (c) slip between grains. (d) Stresses at contacts between grains are reduced when additional particles occupy pore space. Heavy arrows show the shear stress applied to material, τ , and the component of this stress along a grain bridge, σ . (Modified from Hooke and Iverson, 1995, Figure 1.)

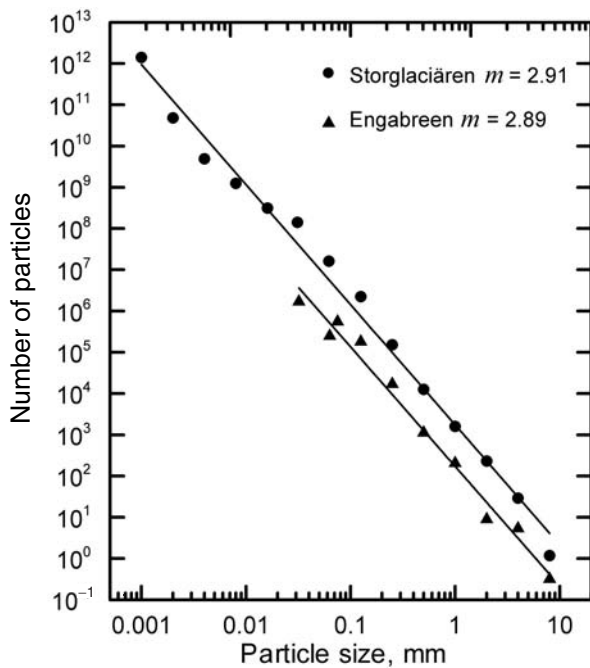


Figure 7.19. Grain bridges in a two-dimensional array of photoelastic disks under shear. (Adapted from Howell *et al.*, 1999.)

along a three-dimensional array of routes, forming what could be called a grain-bridge network (Iverson *et al.*, 1996). The complexity of a two-dimensional network can be studied by shearing an array of photoelastic disks and viewing them in transmitted polarized light (Figure 7.19). Changes in the optical properties of disks under stress makes them appear lighter. Thus, the bridges show up as chains of lighter disks in Figure 7.19.

For deformation to occur, grain bridges must fail. Failure may be a consequence either of fracture of a grain (Figure 7.18b) or of slippage between grains (Figure 7.18c). Fracture is most likely when two adjacent grains are of roughly equal size and when the space between them is not filled with smaller grains that absorb some of the stress. Slip between grains occurs when resolved stresses parallel to contacts between particles are greater than τ_p . Because the deviatoric stress required to fracture a grain varies with particle size, and because contacts between grains may have different orientations leading to different resolved stresses, there must be a wide range of bridge strengths.

Figure 7.20. Grain-size distributions in two subglacial tills that were deforming. Fractal dimension of each till is shown. (Modified from Hooke and Iverson, 1995, Figure 2.)



Grain fracture alters the granulometry of a material. Biegel *et al.* (1989) argue that the end product of this process is a granulometry that maximizes the support that each particle receives, and thus minimizes stress concentrations capable of causing fracture. For example, forces between particles in Figure 7.18d are distributed over several contact points, so local stresses are less likely to reach a level that will cause fracture. The granulometry that provides maximum support, according to Biegel *et al.*, is one in which no two particles of the same size are in contact. Such a material has a fractal particle-size distribution with a fractal dimension of ~ 2.6 . That is, if N_o is the number of particles of a reference size, d_o , then the number of particles of size d , $N(d)$, is:

$$N(d) = N_o \left(\frac{d}{d_o} \right)^{-m} \quad (7.19)$$

The fractal dimension is m . (As is evident from Equation (7.19), fractal size distributions appear to be the same at all scales. Thus, if there is one particle of unit size in a field of view, there will be 10^m particles that are $1/10$ this size, regardless of the units used in making the measurement.) Sammis *et al.* (1987) have shown that gouge from the Lopez Canyon Fault in California has such a particle-size distribution.

Deforming subglacial tills also have a fractal granulometry, with a fractal dimension close to 2.9 (Figure 7.20). This suggests that grain fracture may play an important role in till deformation. That the fractal

Table 7.2. Sliding speed, till thickness, and strain rate in the till beneath various glaciers

Glacier	Sliding speed, u_b , m a ⁻¹	Till thickness, h_t , m	$\dot{\varepsilon}_t = u_b h_t$, a ⁻¹	Reference
Blue Glacier ^a	4	0.1	40	Engelhardt <i>et al.</i> (1978)
Breidamerkurjökull	24	0.5	48	Boulton and Hindmarsh (1987)
Storglaciären ^a	10	0.2	50	Hooke <i>et al.</i> (1992)
Trapridge Glacier	33	0.5	66	Fischer and Clarke (1994)
Whillans Ice Stream	450	6 ^b	75	Alley <i>et al.</i> (1987a)
Whillans Ice Stream	360	2.5–0.5	144–720	Tulaczyk <i>et al.</i> (2001b)
Whillans Ice Stream	360	0.3–0.03	1200–12000	Engelhardt and Kamb (1998)
Columbia Glacier	1300	0.65	2000	Humphrey <i>et al.</i> (1993)

^a Values of $\dot{\varepsilon}_t$ for Blue Glacier and Storglaciären may be maximum estimates of the critical strain rate as the deformation is inferred to extend to the till/bedrock interface.

^b Thickness of deforming till layer beneath Ice Stream B is inferred on the basis of geophysical data, whereas other values of h_t are based on more direct measurements.

dimension is larger than the ideal of 2.6 is attributed to the production of fine material by abrasion, a process that would be inhibited by the higher effective normal pressures characteristic of deformation in active faults (Hooke and Iverson, 1995). However, more work is needed fully to understand the processes that give rise to fractal size distributions.

Strain rates in subglacial till

Estimates of strain rates in till based on field data all exceed 40 a⁻¹ (Table 7.2). Many of these may be minimum estimates as observations, discussed at greater length below, suggest that deformation is commonly concentrated in shear zones. The thickness of these shear zones may be limited by the length of grain-bridge networks. The length of a network may be limited if stress build up is slow and multiple small adjustments between particles relieve stresses. Thus, thicker shear zones may indicate higher rates of deformation.

Till rheology – the Coulomb plastic model

Our discussion thus far has focused on the strength of granular materials. There is a considerable volume of literature on this topic because of the interest in the conditions under which slopes fail, leading, for example,

to landslides or the collapse of highway embankments. In contrast, studies of the time-dependent behavior of deforming granular materials are less common. Furthermore, they often deal with materials containing an abundance of clay minerals, as clays are an important constituent of many slow-moving landslides.

As noted, failure occurs when the failure strength of a material is exceeded (Figure 7.15). We, however, are interested in the rate of steady deformation some time after failure. Thus, the relevant measure of strength for studies of rheology is the residual strength. More specifically, we need to know whether the residual strength increases with strain rate, other factors such as effective pressure, granulometry, mineralogy, and so forth, remaining constant (Kamb, 1991). If such an increase occurs, the strain rate may be a unique function of the applied stress, and a “flow law” for till may exist. If the residual strength does not increase with strain rate, till is a perfectly plastic substance; once the residual strength is reached, it will deform at whatever rate is necessary to prevent the applied stress from rising above that strength.

In Chapter 4 we discussed possible mechanisms that might control the rate of deformation of ice. Let us now do the same for till. The principal processes we have discussed are dilation and failure of grain bridges. Dilation occurs early in the deformation process, and once the medium is dilated it remains so. Thus, dilation should not be rate controlling, and in the absence of repeated formation of grain bridges, we might expect the material to deform steadily and homogeneously, once the failure strength is exceeded. Grain bridges do form, however, and deformation proceeds only when a bridge fails. This suggests that failure of grain bridges may be the rate-controlling process in till deformation. If this is the case, and if the formation of grain bridges is stochastic in time and space, then a mechanistic rheological model for till deformation should be based on these processes. Analysis should focus on the frequency of failure of grain bridges and on the amount of deformation resulting from each failure.

Studies of processes that are thermally activated, such as the creep of ice (Equation (4.6)), provide a conceptual framework for such a model. In thermally activated processes, the process operates or proceeds when a certain energy barrier is exceeded. In the creep of ice, the barrier is the energy needed to break an atomic bond, thus allowing movement of a kink in a dislocation (Figure 4.6). Fundamental to the theory of thermally activated processes is a premise, based on principles of statistical mechanics, that the probability distribution, $p(f)$, of energy levels, f , in atomic bonds is given by:

$$p(f) = Ae^{-\alpha f} \quad (7.20)$$

where A and α are constants (Glasstone *et al.*, 1941, p. 159). In containers filled with beads and subjected to a normal load, the distribution of force levels at intergranular contacts is, indeed, given by Equation (7.20) with f now defined as the force at such contacts (Liu *et al.*, 1995). Thus, it seems plausible that the theory of thermally activated processes can be adapted to the analysis of deformation of granular materials. Mitchell *et al.* (1968) and Mitchell (1993, pp. 349–361) have used this approach, and conclude that a relation of the form:

$$\dot{\varepsilon} = \Gamma e^{\gamma\tau} \quad (7.21)$$

should describe the steady strain rate in a granular material. Here, τ is a mean shear stress sufficient to cause deformation and thus maintain dilation, and Γ and γ are constants presumably dependent upon the strength and granulometry of the material.

A flow law for till that is of this form is:

$$\frac{\tau}{\tau_0} = 1 + b \ln \frac{\dot{\varepsilon}}{\dot{\varepsilon}_0} \quad (7.22)$$

(e.g. Mitchell, 1993, Figure 14.15). This relation is consistent with laboratory data. Here, τ_0 is normally taken to be the stress at a reference strain rate, $\dot{\varepsilon}_0$; τ_0 must be greater than s (Equation (7.17)) as the material is deforming. In other words, the Coulomb yield criterion must be met. Thus, for example, if we choose $\dot{\varepsilon}_0$ to be some constant low strain rate, independent of N_e , we can write $\tau_0 = s + \Delta s$ where Δs is the amount by which τ_0 must exceed s to yield that $\dot{\varepsilon}_0$. The reference stress, τ_0 , depends on N_e ; an increase in N_e increases τ_0 and therefore decreases $\dot{\varepsilon}$ as expected.

In engineering tests on sandy materials preconsolidated to 392 kPa, $b \approx 0.013$ (Nakase and Kamei, 1986, Figure 14), whereas for materials with significant quantities of clay, it is ~ 0.043 (Mitchell, 1993, Figure 14.15). Tests on till from beneath Whillans Ice Stream yielded values that ranged from 0.10 for samples preconsolidated at 35 kPa to 0.002 for samples preconsolidated at 343 kPa (Figure 7.21) (S. Tulaczyk, written communication, 8/03). Nakase and Kamei's value is broadly consistent with the latter (Figure 7.21). Tulaczyk *et al.* (2001a) found that the preconsolidation stresses of samples from beneath Whillans Ice Stream were typically 10–20 kPa, so a value of b of ~ 0.1 is probably appropriate, at least for these fine-grained tills.

Treating $\dot{\varepsilon}_0$ as a constant, Equation (7.22) may be written:

$$\dot{\varepsilon} = k_1 e^{\frac{\tau}{b\tau_0}} \quad (7.23)$$

where $k_1 = \dot{\varepsilon}_0 e^{-1/b}$. Comparing this with Equation (7.21) we see that $k_1 = \Gamma$ and $1/b\tau_0 = \gamma$. Based on the experimental values of b , it is clear

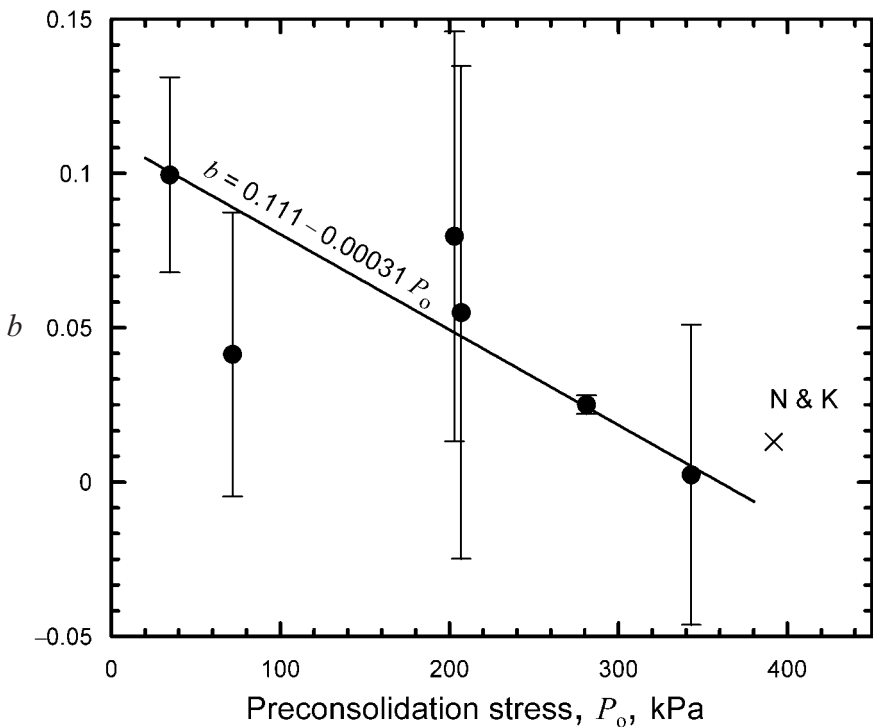


Figure 7.21. Effect of preconsolidation stress on b . Data are based on undrained triaxial tests on samples of till from beneath Whillans Ice Stream (Tulaczyk *et al.*, 2000a). Values of b were kindly calculated by Tulaczyk (written communication, 8/03). Error bars are estimated from plots supplied by Tulaczyk. Line is drawn by eye, ignoring points with largest uncertainties. Point labeled N&K is from Nakase and Kamei (1986).

that strain rates should increase substantially with only a small increase in τ , as Kamb (1991) recognized.

Such a dependence of $\dot{\epsilon}$ on τ in till is also consistent with field measurements on Storglaciären (Hooke *et al.*, 1997). The measurements were made by inserting instruments into till beneath ~ 120 m of ice, using boreholes through the glacier to gain access to the till. One instrument consisted of a cylinder with conical ends (the “fish”) that was dragged through the till by a wire connected to a load cell. The force required to drag the fish varied between about 407.4 N and 408.6 N during a period of several days when the speed of the glacier varied diurnally (Figure 7.22). The variations were basically in phase with those in N_e , which is consistent with Equation (7.17). However, the force was not related to the surface speed. As the speed with which the fish was pulled through the till should have varied in phase with the surface speed and the

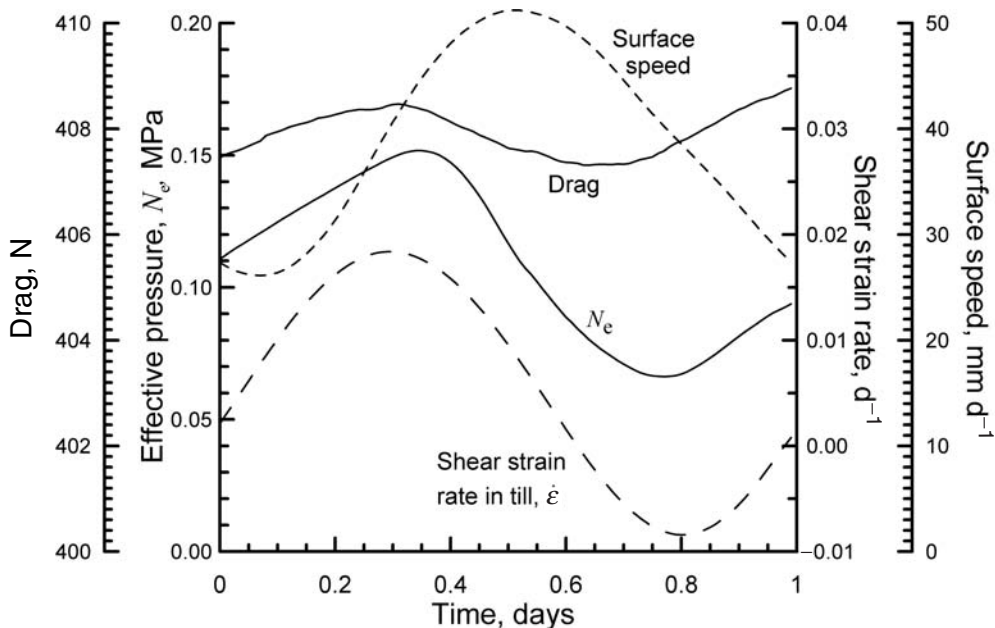


Figure 7.22. Relation among drag on a cylinder pulled through subglacial till beneath about 120 m of ice, surface speed, water pressure in a nearby borehole, and shear strain rate in the till. Data are from a period of about 10 d in August, 1992, at a time when all parameters were varying diurnally, and are “stacked” by averaging values obtained at the same time of day each day. (After Hooke *et al.*, 1997. Reproduced with permission of the International Glaciological Society.)

variations should have been of similar amplitude, it appears that the force on the fish did not depend significantly on its speed through the till, and hence did not depend on the strain rate in the till immediately adjacent to it. This is consistent with a constitutive relation of the form of Equation (7.23).

If till is a Coulomb-plastic material (Equations (7.17) and (7.23)) one would also expect that increases in N_e would strengthen the material and thus decrease the strain rate, and conversely. This may be seen in many of the small diurnal variations shown in Figure 7.23 (see especially July 28–August 1 and August 7–10). (Because changes in pressure in a borehole take time to penetrate into the subglacial till, $\dot{\varepsilon}$ lags N_e slightly in these diurnal signals.)

The alert reader may have noticed that the variations in N_e and $\dot{\varepsilon}$ in Figure 7.22 are in phase, contrary to what one would expect in a Coulomb-plastic material. The reason for this seemingly contradictory behavior becomes apparent if one notes that N_e averages ~ 0.1 MPa in Figure 7.22, but is > 0.4 MPa during the diurnal fluctuations in

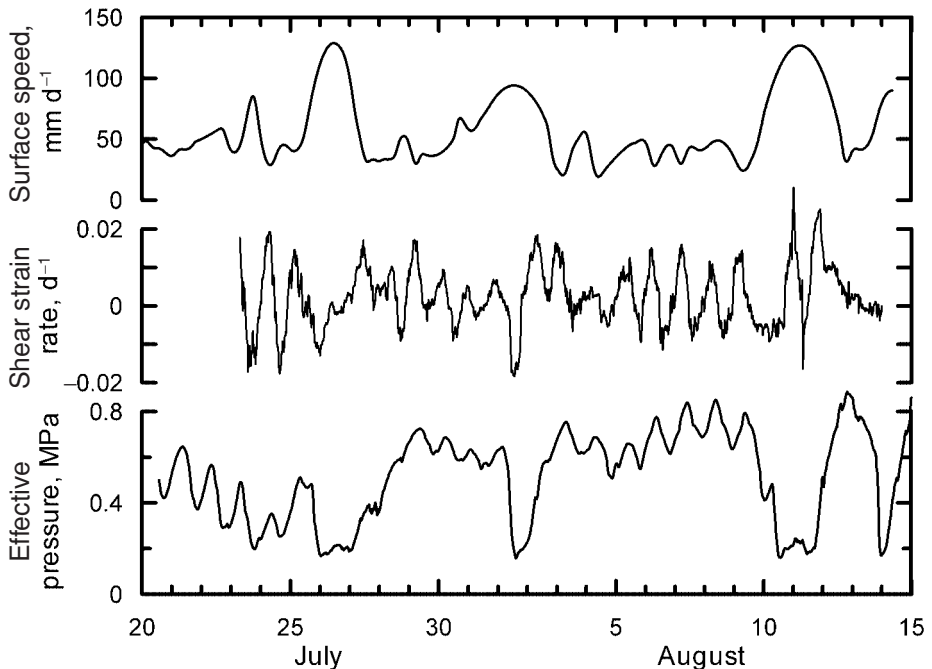


Figure 7.23. Relation among shear strain rate in till beneath Storglaciären, water pressure in a nearby borehole, and surface velocity. (Modified from Iverson *et al.*, 1995.)

Figure 7.23. Low values of N_e correspond to high water pressures, and at high enough water pressures the coupling between the glacier and the bed may be reduced, thus decreasing the shear stress applied to the till by the ice, and hence $\dot{\varepsilon}$ in the till. The in-phase variations of $\dot{\varepsilon}$ with N_e in Figure 7.22 are attributed to such partial decoupling. The physics of coupling is discussed further below.

Because the strength of granular materials appears to increase slightly with strain rate, it is pseudo-plastic rather than perfectly plastic. However, the rate of increase is so small that referring to such materials as Coulomb-plastic is justified.

Tulaczyk *et al.* (2000a) have suggested that the increase in strength with increased strain rate is the result of a process called *dilatant hardening*. Dilatant hardening occurs when a sample dilates but the water content cannot vary; the dilation then reduces the pore pressure, resulting in an increase in N_e , and hence in strength (Equation (7.17)) (Lambe and Whitman, 1969, p. 445). In their tests of till samples from beneath Whillans Ice Stream, Tulaczyk *et al.* used *undrained* tests (in which the water content does remain constant) and found that the pore pressure did indeed decrease when the strain rate was increased. They attributed this to dilation and dilatant hardening.

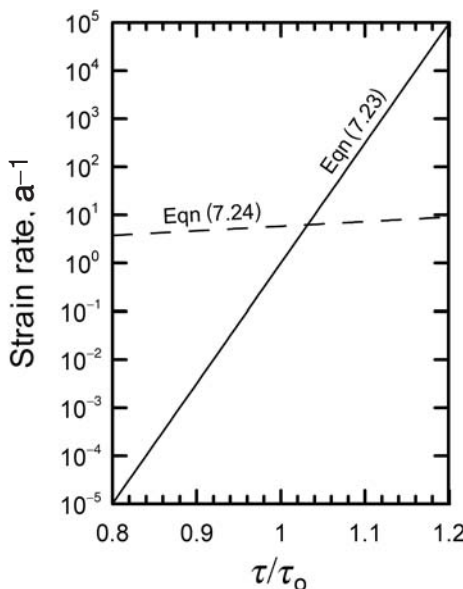


Figure 7.24. Experimentally determined relation between stress and strain rate in granular media (solid line) compared with a commonly used viscous constitutive relation for till rheology (dashed line).

Alternatively, one could attribute the increase in strength to the physical nature of frictional processes. As noted above, friction results from interlocking of asperities on two surfaces that are in contact with one another. Failure of a contact between two interlocked asperities may occur by fracture or by dislocation creep within the asperities. In the latter case, a frictional interface that initially appears to be stable may, in time, slip. Thus, if the stress builds up slowly on such a contact, it may eventually fail at a stress that could be sustained, at least briefly, if the stress increased rapidly.

Till rheology – the viscous model

In a number of papers (see, for example, Alley *et al.*, 1987b; Boulton and Hindmarsh, 1987; MacAyeal, 1989), a constitutive relation of the form:

$$\dot{\varepsilon} = k_2 \frac{(\tau - \tau_c)^m}{N_e^p} \quad (7.24)$$

has been used to describe till rheology. Here, k_2 is a constant and τ_c is a critical shear stress below which no deformation occurs. Some authors assume that $\tau_c = 0$, and others let $\tau_c = s$ (Equation (7.17)). This relation is entirely intuitive; there are no reliable field or laboratory data that support it.

In Equation (7.24), it is normally assumed that $1 < m < 2$, so the sensitivity of $\dot{\varepsilon}$ to τ is far less than suggested by Equation (7.23). This is illustrated in Figure 7.24. The other major difference between

Equations (7.23) and (7.24) is in the way in which the effective pressure is incorporated. As τ_o (Equation (7.23)) must be greater than s by an amount sufficient to deform the material at a rate $\dot{\varepsilon}_o$, τ_o must vary directly with N_e , albeit in a poorly constrained and perhaps nonlinear way. Thus, lower effective pressures increase $\dot{\varepsilon}$. In Equation (7.24), lower effective pressures also increase $\dot{\varepsilon}$, but in this case the influence is through both the explicit effect in the denominator and the implicit effect on τ_c in the numerator.

Viscosity is defined as $\tau / \dot{\varepsilon}$ (Equation (2.17)) implying a linear dependence of strain rate on stress. Equation (7.24) implies a linear ($m = 1$) or mildly nonlinear ($1 < m \leq 2$) dependence of $\dot{\varepsilon}$ on τ , and thus is generally referred to as the viscous model of till deformation.

Sliding of ice over till

At sufficiently high water pressures, or low effective pressures, a glacier on a deformable bed may become partially decoupled from the underlying till. This may result in a decrease in $\dot{\varepsilon}$ despite the decrease in N_e (which should weaken the till). As discussed above, this appears to be what happened during the experiment shown in Figure 7.22. Partial decoupling also appears to have occurred during the three periods of low effective pressure on about July 26, August 3, and August 12 in Figure 7.23. Other examples are discussed by Iverson *et al.* (1995) and Hooke *et al.* (1989, 1997).

The process of decoupling is rather complicated. As the water pressure rises, it seems likely that a glacier will begin to slide over the till in some places whereas in others, clasts that are gripped in the ice and project down into the till will continue to plough through it, causing local bed deformation. Evidence for such ploughing is occasionally preserved in tills in deglaciated areas (Clark and Hansel, 1989). Because of the extent of the local bed deformation, the stress exerted on a clast by the ice, τ_c , must be ~ 5 times the shear strength of the till, s , in order for ploughing to occur. Thus, if f_c is the fractional area of the interface covered by ploughing clasts, τ_i is the strength of the interface between the ice and the till, and τ_{ic} is the strength contributed by ploughing clasts, we have:

$$\tau_{ic} = f_c k_c \tau_c$$

where $k_c \approx 5$, as noted (Tulaczyk, 1999).

The total strength of the interface must include any traction, τ_{im} , between the ice and macroscopically flat parts of the boundary, thus:

$$\tau_{im} = (1 - f_c) k_{im} s$$

where $0 < k_{im} < 1.0$. Physically, $k_{im} \rightarrow 1$ as the roughness of the ice–till interface approaches the roughness of the failure planes in the till, and $k_{im} \rightarrow 0$ as the ice–till interface becomes smooth. Thus, in this idealized model the total strength of the interface is (Tulaczyk, 1999):

$$\tau_i = (1 - f_c)k_{im}s + f_c k_c \tau_c \quad (7.25)$$

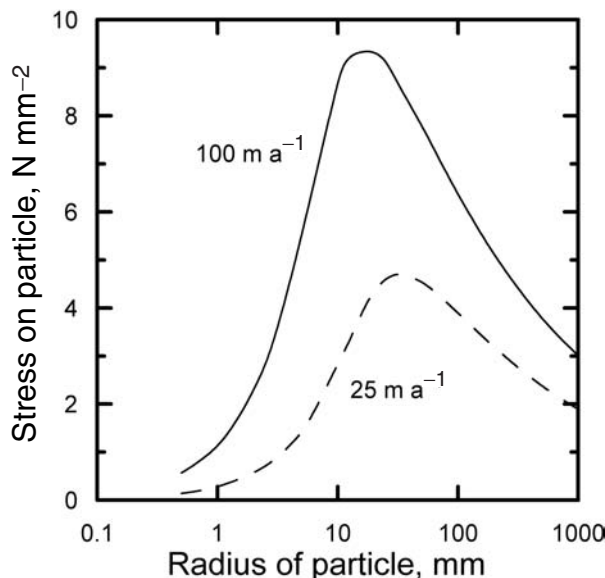
Two factors that affect k_{im} need to be considered at this point. First, where melting is occurring, there will be a water film between the base of the glacier and the till. The thicker the water film, the lower the value of k_{im} . Secondly, under high effective pressures, ice can regelate into pore spaces in the till (Iverson, 1993). Thus, at high effective pressures the ice base will conform to the till surface better than at low effective pressures, so k_{im} will be higher at high effective pressures. This infiltration of ice into till is inhibited, however, by surface tension between water and sediment grains in capillary spaces. Such surface tension effects are particularly important in fine-grained tills with small pore spaces, so k_{im} will be lower for such tills.

In summary, Equation (7.25) shows that the strength of the interface, τ_i , will be higher when the till is coarse as f_c is then larger and ice will be able to penetrate into pore spaces more readily, increasing k_{im} . The strength will also be higher when the effective pressure is higher and the water film thinner. Tulaczyk has shown that τ_i is likely to be less than s in fine-grained tills like those underlying Whillans Ice Stream but greater than s in coarse-grained tills like those common to most valley glaciers. Thus, the preferred mode of basal motion is likely to be sliding with ploughing in the former, and coupling with more pervasive till deformation in the latter. Extensive sliding would limit sediment transfer in deforming till sheets, so this again raises the question of how the large volumes of till deposited by the Pleistocene ice sheets were moved. Deformation concentrated in shear zones at depth in the till, discussed below, may provide an answer.

Ploughing

The ploughing process has been studied by Brown *et al.* (1987). They considered spherical clasts of radius R , embedded half in the ice and half in the till, and suggested that the force required to push such a clast through the till scales with the cross-sectional area of the clast; that is, with R^2 . As this force must be provided by the ice, and as the ice is at the pressure melting point, regelation and plastic flow must be occurring around the clast. As with obstacles on a glacier bed, the stress that the ice exerts on the clast will be low for both small clasts

Figure 7.25. Stress exerted by ice on a spherical clast half embedded in till. Curves are for ice sliding at 25 and 100 m a^{-1} and were calculated with the use of Equation (2) of Brown *et al.* (1987).



accommodated largely by regelation and for large clasts accommodated largely by plastic deformation (Figure 7.25). Whether a clast ploughs or not will be dependent upon the strength of the till, which is controlled by the effective pressure. However, based on Figure 7.25, it appears that clasts in the 20–40 mm size range will be the first to move.

Depth of deformation in a subglacial till

Let us now address two questions, to which there are currently no firm answers: (1) what controls the thickness of the layer of subglacial till that can be mobilized by an overriding glacier; and (2) what is the shape of the velocity profile through this layer?

Evidence for thick layers of deforming till is ambiguous. As noted, Alley (1991) and Hooke and Elverhøi (1996) have suggested that, during the Pleistocene, huge amounts of sediment must have been moved long distances in deforming subglacial layers of till. This would seem to require layers at least a few meters thick. However, studies of cores of subglacial till obtained through boreholes that penetrated the kilometer-thick Whillans Ice Stream revealed little evidence for deformation (Tulaczky *et al.*, 1998; Kamb, 2001, p. 172). Clasts were not striated and there were no distinct shears or other visible macroscopic or microscopic fabrics or textures suggestive of deformation. On the other hand, diatoms of different ages were mixed together, requiring some sort of deep deformation process.

Analysis of the variation of τ and N_e with depth provides a basis for calculating the thicknesses of deforming layers and velocity profiles in them. Beneath a glacier of thickness h with surface slope α and a horizontal bed:

$$\begin{aligned}\tau &= \rho_i g h \alpha + \rho_t g z \alpha = \tau_b + \rho_t g z \alpha \\ N_e &= N_{eb} + (\rho_t - \rho_w) g z\end{aligned}\quad (7.26)$$

Here ρ_i , ρ_t and ρ_w are the density of ice, the bulk density of the till, and the density of water, respectively, subscript b refers to the conditions at the ice–till interface, and z is measured downward from the interface. Alley (1989b) refers to the second of Equations (7.26) as a *hydrostatic* variation of N_e with depth because the pressure in the water increases as $\rho_w g z$. Assuming $\rho_t \approx 2000 \text{ kg m}^{-3}$, and taking derivatives with respect to z yields:

$$\begin{aligned}\frac{d\tau}{dz} &= \rho_t g \alpha \approx 20 \alpha \text{ kPa m}^{-1} \\ \frac{dN_e}{dz} &= (\rho_t - \rho_w) g \approx 10 \text{ kPa m}^{-1}\end{aligned}\quad (7.27)$$

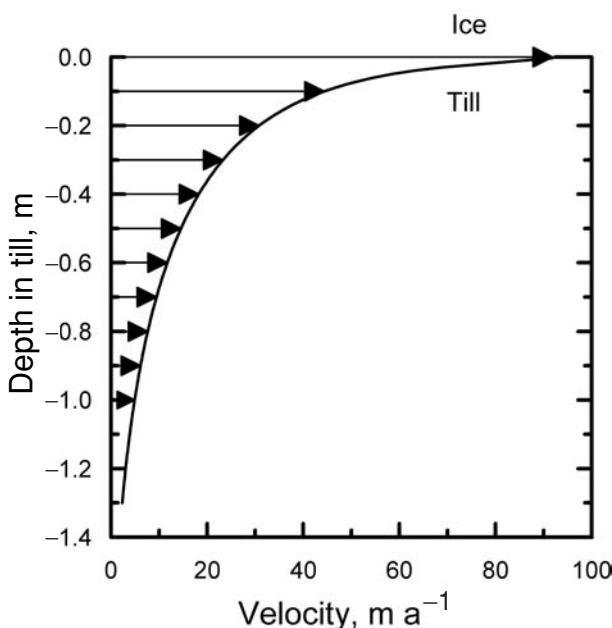
For typical surface slopes, the rate of increase of N_e with depth clearly exceeds that of τ , so the strength of the till should increase faster than the applied stress. Thus, the decrease in $\dot{\varepsilon}$ in the till is likely to be nonlinear, and deformation will cease at the depth at which s exceeds τ .

Elaborating on this approach, Iverson and Iverson (2001) calculated the velocity profile shown in Figure 7.26. In their model, displacements are assumed to occur across shear zones several millimeters thick when grain bridges fail. Their analysis is based on the assumptions that: (1) the deforming part of the till can be viewed as consisting of a stack of shear zones, (2) slip on any given shear zone occurs intermittently, (3) the frequency of slip is the same on all shear zones, and (4) the amount of slip on a shear zone during a given event decreases with depth owing to the relative rates of change of N_e and τ with depth. By varying some of their less well-constrained parameters within reasonable limits, they were able to match a profile measured in a coarse-grained till quite well.

In situations in which water is produced by melting at the ice–till interface and is lost downward by flow through a permeable substrate, the hydraulic head must decrease downward through the till. Then dN_e/dz will be higher than in the purely hydrostatic case represented by the second of Equations (7.27), and the deforming layer should be thinner than otherwise (Alley, 1989b).

On the other hand, Tulaczyk *et al.* (2001a) found that in sediment cores, up to 3 m long, obtained from beneath Whillans Ice Stream the

Figure 7.26. Velocity profile in a deforming subglacial till calculated by Iverson and Iverson (2001). See text for explanation. (Modified from Iverson and Iverson, 2001, Figure 3. Reproduced with permission of the authors and the International Glaciological Society.)



void ratio did not vary with depth. This suggests that $dN_e/dz = 0$ (Figure 7.16). Alley (1989b) refers to this as a *lithostatic* variation of N_e with depth because the pressure in the water increases as $\rho_w g z$. Such a situation would seem to be possible only in situations in which the permeability of the till was quite low and the till was at least occasionally deforming to depths of at least 3 m.

To actually measure the ratio of till deformation to sliding at an ice–till interface, Engelhardt and Kamb (1998) implanted stakes in the till, again through boreholes drilled for the purpose. As the ice moved away from a stake, a wire attached to the stake was pulled off of a spool anchored in the basal ice and the rate of rotation of the spool was measured. In such a “tethered-stake” experiment on Whillans Ice Stream, the top of the stake was believed to be about 30 mm below the base of the ice, and the rate of relative motion between the spool and the stake was $\sim 1.0 \text{ m d}^{-1}$, or 83% of the surface speed. Thus, sliding and deformation in the top 30 mm of the till accounted for most of the ice movement. The remaining 17% could have been either internal deformation of the ice or deformation deeper in the till layer.

In a similar tethered-stake experiment on Bindschadler Ice Stream, however, the sliding speed, including deformation in the upper 0.34 m of the till, was only 10%–20% of the 1 m d^{-1} surface speed (Kamb, 2001). As the driving stress was too low to cause significant internal ice deformation, Kamb attributed the remaining 80%–90%

of the motion to deformation below the level of emplacement of the stake.

In another experiment, observations in a tunnel beneath the glacier Breidamerkurjokull in Iceland demonstrated that within about 0.5 m of the glacier sole deformation of the till was pervasive, while at greater depths it was localized in shear zones (Boulton and Hindmarsh, 1987). Such shear zones are characteristic of virtually all laboratory experiments on granular materials, and similar zones are a well known characteristic of granular materials that have been overridden by glaciers (Brown *et al.*, 1987; Menzies and Shilts, 1996, pp. 48–49).

Evidence for still deeper deformation comes from an experiment on Black Rapids Glacier in Alaska. Truffer *et al.* (2000) emplaced tiltmeters at depths of ~0.1, 1, and 2 m in a 7-m thick till layer beneath the glacier. The tiltmeters recorded little deformation of the till in 410 days, despite the fact that the base of the glacier and the 2 m of till containing the tiltmeters moved 35–45 m during that time interval. They concluded that the motion must be along one or more shear zones at greater depths in the till.

Iverson *et al.* (1998) have proposed a mechanism for distributing deformation through a significant thickness of till as observed in the upper 0.5 m of till at Breidamerkurjokull. They suggest that deformation starts in a thin shear zone which then dilates. Dilatant hardening then strengthens the zone, causing the locus of deformation to shift. The process is facilitated by frequent water-pressure fluctuations because a dilated zone will begin to consolidate back to its original porosity when the water pressure drops (Figure 7.16), so the next episode of deformation may initiate a shear zone in a quite different place.

Tulaczyk (1999) has suggested two possible physical explanations for concentration of deformation in a single shear zone at depth, as inferred from the Black Rapids data.

- (1) If the basal water pressure fluctuates, alternating waves of high and low pressure will penetrate into the till much as seasonal temperature waves penetrate into the surface of a glacier (see Figure 6.8). The rate at which these waves penetrate depends on the hydraulic diffusivity of the till. If we presume that the till is homogeneous and that deformation occurs in a relatively narrow shear zone at the weakest point in it – namely the point where the water pressure is highest – then this shear zone will migrate downward through the till with the pressure wave. According to the calculations of Tulaczyk *et al.* (2000a), diurnal pressure fluctuations could distribute shear through ~0.07 m of till like that from the bed of Whillans Ice Stream and through over a meter of a coarser till typical of valley glaciers.

- (2) Alternatively, because the peak strength of a non-deforming till is greater than the residual strength (Figure 7.15), shear zones may not migrate readily. In this case, the strength of the till may be determined by the maximum effective pressure that the material experiences during a water pressure cycle. A shear zone could develop and persist at the depth at which this maximum pressure was lowest. Till above this level would move as a plug without significant internal deformation.

In the case of Black Rapids Glacier, calculations suggested that the lowest maximum effective pressure in an annual cycle would be between 3.5 and 4.6 m below the ice–till interface (Truffer *et al.*, 2000). Thus, Tulaczyk’s second explanation could explain the lack of deformation in the uppermost 2 m of this till.

In summary, first-order models suggest that layers of deforming till should be relatively thin, particularly in fine-grained tills, and some measurements support this interpretation. However, other observations suggest that layers may be meters thick in certain situations, and more sophisticated models are emerging that explain such layers. The seemingly contradictory evidence from till from beneath Whillans Ice Stream, in which diatoms of different ages were mixed but few deformation structures were found, may be explained by the cushioning effect of soft clay minerals, which comprise ~35% of the matrix of this till. Cushioning would inhibit formation of striations and other deformation structures.

Stability of ice streams

As we have noted previously, the driving stress in ice streams is typically only 10–20 kPa, but the strength of the subglacial till layer is significantly lower so only 20%–50% of the driving stress is supported by the bed (Raymond *et al.*, 2001). Because the stress supported by the bed is so small, one might expect that the stability of ice streams would be sensitive to conditions in the bed. Tulaczyk *et al.* (2000b) and Raymond (2000) have studied this question. They focus on the melt rate, \dot{m} , at the bed, which is given by:

$$\dot{m} = \frac{\tau_b u_b + G - K\beta_o}{L\rho_i} \quad (7.28)$$

Here τ_b is the basal drag (which equals the strength of the till), u_b is the sliding speed, $\tau_b u_b$ is the frictional heat production (see Equation 6.37), G is the geothermal heat flux, and $K\beta_o$ is the heat conducted away from the interface upward into the ice. G and $K\beta_o$ are constant for any given location, and as τ_b is a function of u_b , \dot{m} can be plotted against τ_b . This is done in Figure 7.27 for three possible values of G . It turns out that $\tau_b u_b$ has a maximum at $\tau_b = (1/4)\tau_d$, where τ_d is the driving stress.

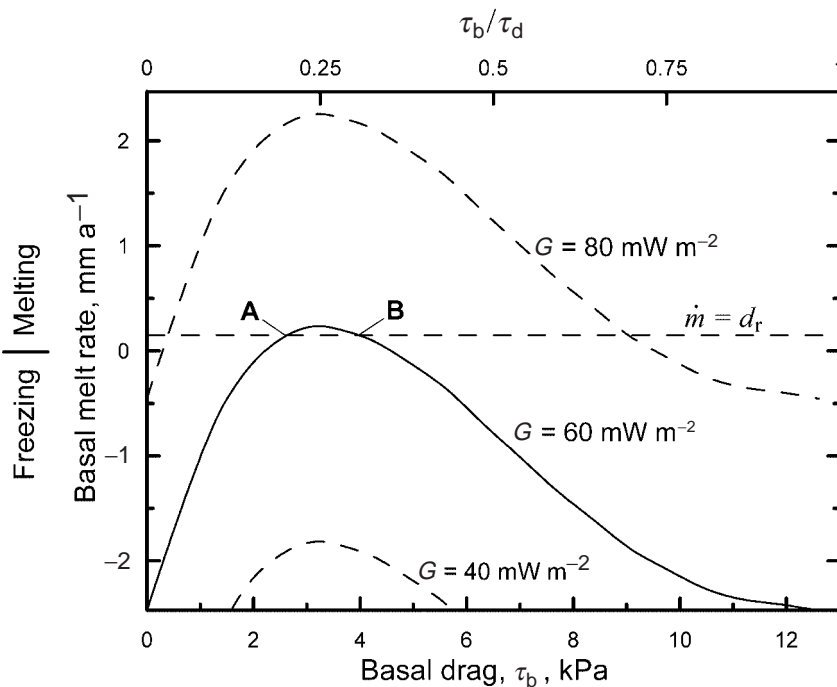


Figure 7.27. Variation of basal melt rate with shear stress and geothermal flux for a cross section of Whillans Ice Stream. (Modified from Tulaczyk *et al.*, 2000b, Figure 6. Reproduced with permission of the author and the International Glaciological Society.)

Tulaczyk *et al.* (2000b) obtained this result by partitioning the driving stress between the ice stream margins and the bed, and considering the internal deformation that would result from the drag exerted by both the margins and the bed.

A steady state water balance exists when $\dot{m} = d_r$, where d_r is the rate of loss of meltwater either by drainage along the bed or by advection in the deforming till layer. Let this state be represented by the horizontal dashed line in Figure 7.27. In this state, any decrease in void ratio, e , would increase τ_b and decrease u_b , and conversely. When the steady state is one in which $\tau_b < (1/4)\tau_d$, as at **A** in Figure 7.27, it turns out that the increase in τ_b exceeds the decrease in u_b and more meltwater is formed, thus increasing e and restoring the steady state (Table 7.3, Case 1). Similarly, an increase in e decreases $\tau_b u_b$ and hence \dot{m} , once again restoring the balance (Case 2). Thus **A** is a stable steady state. In contrast, if the steady state is one in which $\tau_b > (1/4)\tau_d$, as at **B** in Figure 7.27, an increase in e results in an increase in $\tau_b u_b$ because u_b increases faster than τ_b decreases. Thus, in this case \dot{m} increases and e then increases

Table 7.3. Effect of changes in void ratio, e on \dot{m} in Figure 7.27

Stable: $\tau_b < (\frac{1}{4}) \tau_d$
(1) $\downarrow e \rightarrow \uparrow \tau_b > \downarrow u_b \rightarrow \uparrow \tau_b u_b \rightarrow \uparrow \dot{m} \rightarrow \uparrow e$
(2) $\uparrow e \rightarrow \downarrow \tau_b > \uparrow u_b \rightarrow \downarrow \tau_b u_b \rightarrow \downarrow \dot{m} \rightarrow \downarrow e$
Unstable: $\tau_b > (\frac{1}{4}) \tau_d$
(3) $\uparrow e \rightarrow \downarrow \tau_b < \uparrow u_b \rightarrow \uparrow \tau_b u_b \rightarrow \uparrow \dot{m} \rightarrow \uparrow e \rightarrow \tau_b < (\frac{1}{4}) \tau_d$
(4) $\downarrow e \rightarrow \uparrow \tau_b < \downarrow u_b \rightarrow \downarrow \tau_b u_b \rightarrow \downarrow \dot{m} \rightarrow \downarrow e \rightarrow \text{frozen bed}$

Up and down arrows represent increases or decreases.

Horizontal arrows may be read as “leads to” or “results in”.

further, driving the system back toward **A** (Case 3). Similarly, a decrease in e decreases $\tau_b u_b$, thus decreasing \dot{m} and driving the system to a frozen bed condition (Case 4). In other words, there appear to be two stable states, one in which the bed is frozen and one in which it is at the melting point, $\dot{m} = d_r$, and $\tau_b < (\frac{1}{4})\tau_d$.

Raymond (2000) has considered an alternative situation in which a change in \dot{m} changes d_r by changing the thickness of the water layer, δ , separating the ice from the till. An increase in \dot{m} increases δ and hence d_r . He defines two possible states. In the first, an increase in δ increases u_b more than it decreases τ_b , so \dot{m} increases, and conversely. He refers to this state as *drainage limited* because if the rate of increase in drainage exceeds that in \dot{m} the situation is stable; otherwise it is unstable. In the second state, the increase in δ decreases τ_b more than it increases u_b , so \dot{m} decreases. He refers to this as *production limited*. This state is always stable.

Also meriting consideration are the relative magnitudes of $\tau_b u_b$, G , and $K\beta_o$. If the heat produced by straining, $\tau_b u_b$, is greater than the heat loss to the overlying ice, $K\beta_o$, no geothermal heat is necessary to maintain pressure melting conditions at the bed. This appears to be the case beneath Bindschadler, Kamb, and MacAyeal Ice Streams (Raymond, 2000). However, if $\tau_b u_b < K\beta_o$, geothermal heat is required to maintain sliding. This seems to be the case beneath Whillans Ice Stream. Indeed, at the lower end of Whillans Ice Stream the required value of G is close to the measured value, suggesting that freezing may be occurring there. This could account for the deceleration of this part of the ice stream documented by Bindschadler and Vornberger (1998).

In some cases, water input from upglacier may be crucial for maintaining a stable state. Consider a unit area of the bed, say 1 km^2 . Clearly, $d_r = q_{\text{out}} - q_{\text{in}}$, where q_{out} and q_{in} are the water fluxes into the control area on its upglacier side and out of it on its downglacier side. If q_{in} decreases

without a corresponding decrease in q_{out} , e (or δ) will decrease, thus increasing τ_b . For small increases in τ_b , $\tau_b u_b$ will increase (Case 1), thus increasing \dot{m} to compensate for the decrease in q_{in} . However, if the decrease in q_{in} is large enough, the increase in \dot{m} may not be sufficient to compensate for it. In this case, τ_b would rise above its unstable equilibrium value at **B** and the ice stream would shut down. Thus, Retzlaff and Bentley's (1993) speculation that the shut down of Kamb Ice Stream might be the result of changes in subglacial drainage in the area where Kamb and Whillans Ice Streams are close together (Figure 5.20) seems well founded.

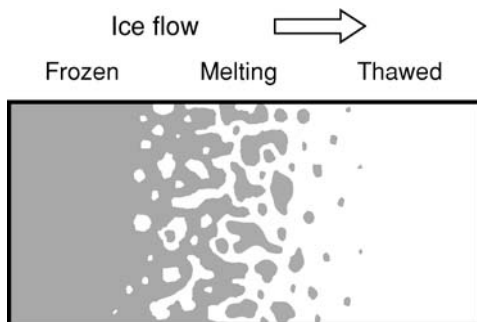
The dashed curves in Figure 7.27 illustrate the sensitivity of the ice streams to the geothermal flux. If the flux were slightly lower the ice streams would not exist, while if it were higher, they might be even more common.

The extreme sensitivity of ice streams to external conditions is illustrated by a recent experiment at the mouth of Whillans Ice Stream. Bindschadler *et al.* (2003) used Geographical Positioning Systems (GPS) units to measure the movement of the ice stream at 5-min intervals. They discovered that movement occurred in pulses lasting 10–30 minutes separated by periods of quiescence lasting 6–18 h. The pulses were in phase with the diurnal ocean tidal cycle (one high tide per day) often occurring just after high tide and just before low tide. The event just after high tide is attributed to strain accumulated over about 18 h since the last event. The event just before low tide is attributed to reduced back pressure from the sea. Clearly, very small variations in stress can cause failure, either of the ice–till interface or of the till itself.

Effect of a frozen bed

When the temperature at the base of a glacier is below the pressure melting temperature and the ice is frozen to the bed, it is usually assumed that sliding cannot take place. For most purposes, this is a reasonable assumption. However, Shreve (1984) showed that a liquid-like layer, present at interfaces between ice and foreign particles (including a glacier bed), could result in regelation of ice past bumps on the bed at subfreezing temperatures. The presence of the liquid-like layer is commonly attributed to a change in chemical potential of water adjacent to the foreign surface, much as molecules of a solute change the chemical potential of the water in which they are dissolved (Gilpin, 1979). For a driving stress of 0.1 MPa and a bed roughness spectrum measured by Nye (1970, pp. 386–387), Shreve calculated sliding rates ranging from 3.5 mm a^{-1} at -20°C to 35 mm a^{-1} at -5°C . Echelmeyer and Wang (1987) measured a sliding speed of 180 mm a^{-1} at -4.6°C under Urumqi Glacier No. 1 in

Figure 7.28. Hypothetical distribution of frozen and thawed areas within a transition zone from a region of frozen bed to one of thawed bed. (Modified from Hughes, 1992, Figure 14.)



western China. After adjusting for differences in driving stress and bed roughness, this speed was consistent with Shreve's theory. These sliding speeds are too low to be of significance glaciologically. However, over a period of years they could result in striations, a possibility which should give nightmares to glacial geologists who commonly interpret striations as evidence of a thawed bed.

As ice moves from a region of frozen bed to one of thawed bed, the sliding speed increases, resulting in geomorphic features like the transverse till scarps (Figure 6.17) and ribbed moraine (Figure 6.18) described in Chapter 6. However, as suggested in Chapter 6, the transition from frozen to thawed bed occurs in a broad zone, not along a single line. Within the transition zone, hill tops and areas underlain by materials with lower thermal conductivity may remain frozen while intervening areas reach the pressure melting point. Thus, there is a gradual transition from completely frozen to completely thawed (Figure 7.28). As the fraction of the bed that is wet increases, the sliding speed increases, but the increase is nonlinear. Even when 85% of the bed is thawed, u_b is still only 25% of the speed when the bed is completely thawed, $u_{b\max}$ (Figure 7.29). However, as the fraction of the bed that is frozen decreases, frictional heating from high shear tractions on the remaining frozen areas should raise temperatures fairly rapidly.

Summary

In this chapter we have explored the coupling between glaciers and both rigid and deformable beds. In the former, the dominant processes by which ice moves past irregularities on the bed are regelation and plastic flow. As small obstacles are accommodated more readily by regelation and larger obstacles by plastic flow, there are, theoretically, obstacles of intermediate size that exert more drag on a glacier than do larger or smaller ones, at least if the roughness is constant. This intermediate size has come to be called the controlling obstacle size, although on a glacier

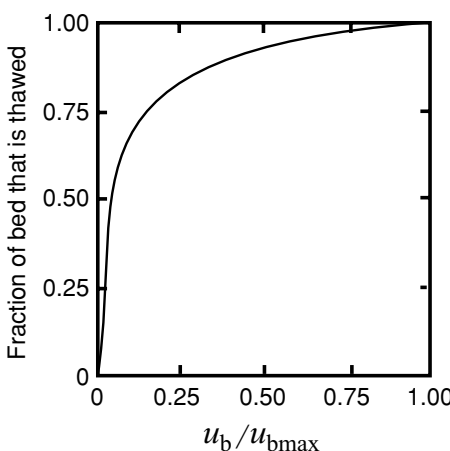


Figure 7.29. Relation between fraction of the bed that is thawed and normalized sliding speed. (From Hughes, 1992, Figure 13. Reproduced with the permission of the author and Elsevier Science Publishers. Original calculations by J. Fastook.)

bed with a continuum of obstacle sizes and roughnesses, the concept of a “controlling” size becomes less relevant.

Theoretically, the speed with which ice moves past obstacles by regelation is proportional to τ_b , whereas for plastic flow it is proportional to τ_b^3 . When both processes are involved, $S \propto \tau_b^2$.

The theory of sliding over rigid beds is imperfect because it does not take into account friction resulting from rock fragments entrained in the basal ice and dragged over the bed, local freezing of the ice to the bed, certain complications in the regelation theory for obstacles of irregular geometry, impurities in the melt water formed during regelation, and effects of changing water pressure. A good deal of recent research effort has been focused on the last of these effects. Increases in water pressure can increase sliding speed by hydraulic jacking and, over somewhat longer time spans, by increasing the degree of separation of the glacier from the bed.

Our understanding of movement of glaciers over soft beds is still modest. It is well known that the strength of granular materials depends on cohesion, on friction between individual grains, and on the need for such materials to dilate before appreciable deformation can occur. Once the strength is exceeded, however, we wish to know the relation between the stress and the strain rate. Theoretical considerations, geotechnical studies, and field measurements suggest that $\dot{\epsilon} \propto e^{\gamma\tau}$, although an alternative relation in which $\dot{\epsilon}$ is far less sensitive to τ has often been used. Equally crucial, however, is developing an understanding of the conditions under which a glacier becomes decoupled from such a soft bed so that it glides over it without deforming it significantly.

Factors controlling the velocity profile in deforming subglacial till and the depth to which deformation extends are still elusive. This has

significance for our understanding of the time scales for accumulation of Pleistocene moraines and till sheets.

Intricate feedbacks among the sliding speed, till strength, basal melt rate, void ratio, and thickness of the subglacial water layer appear to result in two stable states. In one, the ice is frozen to the bed. In the other, the shear strength of the till is a small fraction of the driving stress, basal melting occurs, and ice stream flow is possible. These states are consistent with observations of ice streams on the Siple Coast in Antarctica. Ice stream flow appears to require a subglacial source of fine-grained material and may not occur if the geothermal flux is too low. Transitions between states may occur if subglacial drainage conditions change.

Chapter 8

Water flow in and under glaciers: geomorphic implications

A great deal has been learned about water flow through glaciers in the past three decades. Much of the progress has been theoretical, as experimental techniques for studying the englacial and subglacial hydraulic systems are few and not yet fully exploited, and observational evidence is difficult to obtain for obvious reasons. An added benefit of the recent progress is that we have gained a much better understanding of glacial erosional processes and of the origin of certain glacial landforms that owe their existence to the interaction between water and ice.

We begin this chapter with a discussion of the development and geometry of englacial water conduits in temperate glaciers. Then, the subglacial part of the system is examined. Finally, we consider geomorphic implications of some of the recent research.

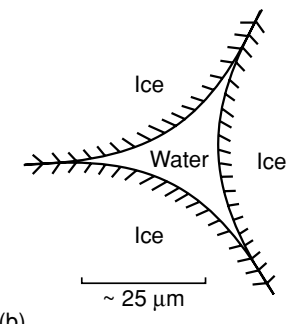
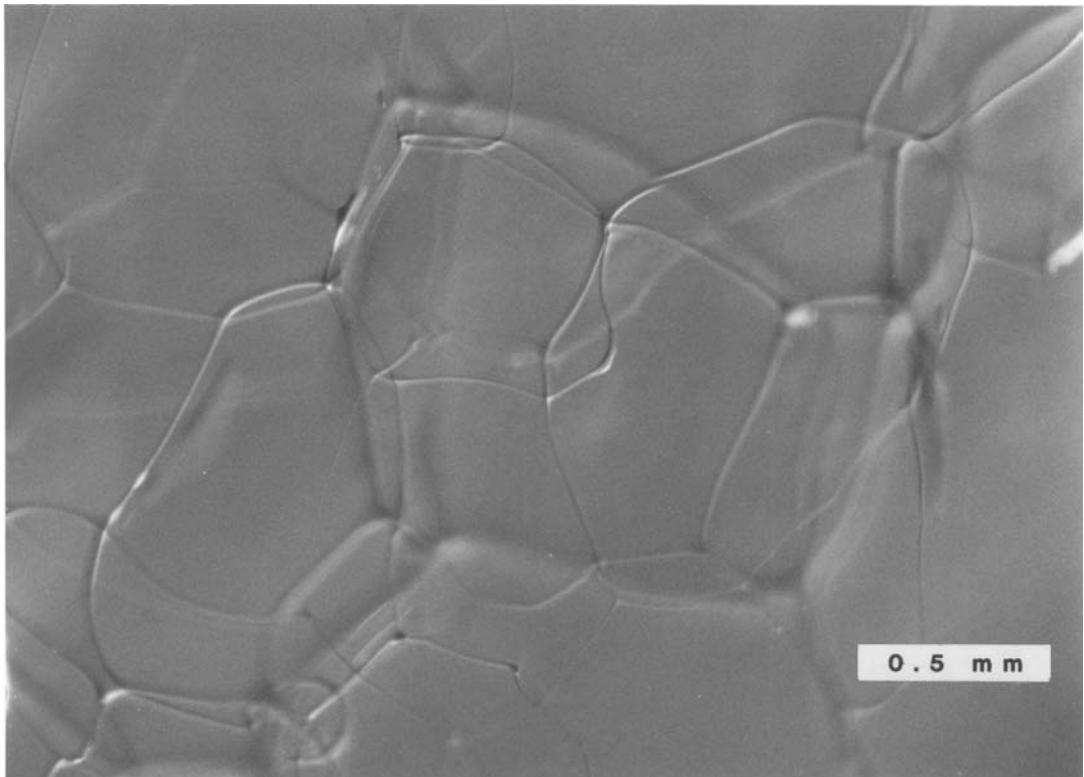
The upper part of the englacial hydraulic system

Veins and the initial development of passages

Nye and Frank (1973) argued that veins should be present along boundaries where three ice crystals meet, and that at four-grain intersections these veins should join to form a network of capillary-sized tubes through which water can move. They thus concluded that temperate ice should be permeable.

Such capillary passages have been observed in ice cores obtained from depths of up to 60 m on Blue Glacier, Washington (Figure 8.1a) (Raymond and Harrison, 1975). The veins are triangular in shape (Figure 8.1b) and roughly 25 μm across.

(a)

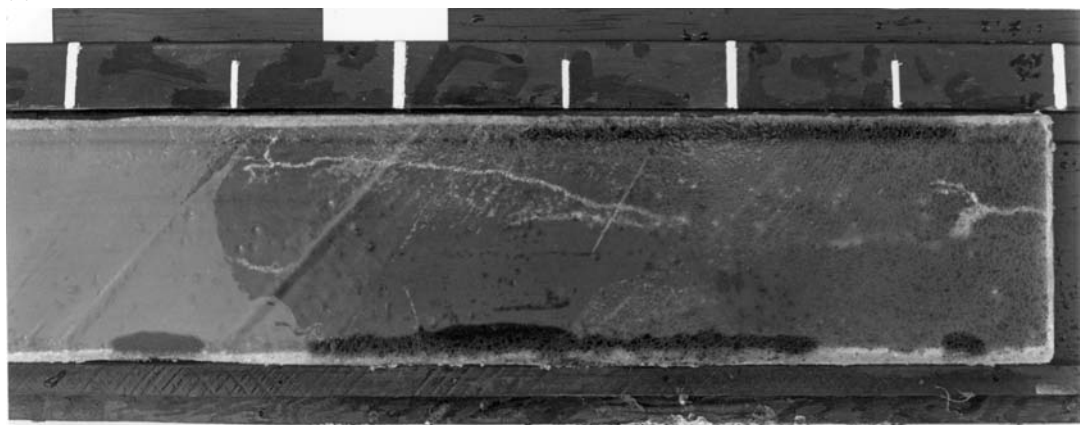


(b)

Figure 8.1. (a) Veins in ice from Blue Glacier. (b) Cross section of a vein with approximate scale. (c) Millimeter-sized tubes from a depth of 20 m in Blue Glacier. ((a) and (c) from Raymond and Harrison, 1975. Reproduced with permission of the authors and the International Glaciological Society.)

Estimates of the permeability of glacier ice resulting from this vein system vary widely. Expressed in terms of the thickness of a water layer that would be transmitted downward into the ice, values range from $\sim 1 \text{ mm a}^{-1}$ in coarse-grained ice with relatively few crystal boundaries per unit volume (Raymond and Harrison, 1975) to 1 m a^{-1} in fine-grained

(c)

**Figure 8.1.** (cont.)

ice (Nye and Frank, 1973). Lliboutry (1971) noted that the existence of supraglacial streams precludes the possibility of significantly higher permeabilities. He further argued that, at permeabilities near the upper end of this range, the potential energy released by the descending water would rapidly enlarge the conduits to the point of completely melting the glacier.

Lliboutry (1971) concluded that deformation and recrystallization of ice must constrict the veins, rendering the ice essentially impermeable. Alternatively, air bubbles located along the veins might block water movement. Lliboutry considered and rejected the latter idea, but Raymond and Harrison thought that it might have merit in coarse ice with few veins.

When water moves through such a vein system, viscous energy is dissipated in the form of heat. The amount of heat produced is proportional to the water flux. To a first approximation, the ice is already isothermal and at the pressure melting point. Thus, the heat cannot be conducted away from the veins, but instead must be consumed by melting ice. In this way, passages are enlarged. Shreve (1972) and Röthlisberger (1972) argued that when two such passages of unequal size separate and rejoin, the larger passage carries more flow per unit of wall area and is thus enlarged at the expense of the smaller passage. They suspected that some of the capillary passages would thus become enlarged to millimeter-scale tubes a short distance below the surface.

Raymond and Harrison confirmed the existence of such tubes in a slab of ice cut from a core from a depth of 20 m in Blue Glacier (Figure 8.1c). The tubes formed an upward-branching arborescent network, as expected. Because the Shreve–Röthlisberger argument applies equally well to larger anastomosing passages, we may imagine that at greater

depths, the arborescent network continues to evolve, with ever larger conduits developing. These conduits drain water produced by strain heating in the deforming ice in addition to that from the surface.

Connections to the surface

In the accumulation area, one can visualize continuous connections between the vein system and the overlying porous firn. As the veins do not necessarily transmit downward all of the percolating meltwater, a local water table commonly forms in the firn (Vallon *et al.*, 1976; Fountain, 1989). Measurements of the slope of this water table in the vicinity of crevasses demonstrate that the latter are actually the principal conduits for movement of water deeper into the glacier (Fountain, 1989).

In the ablation area there may be a surface layer of cold ice, several meters in thickness, in which the veins are frozen. This cold layer forms on glaciers in more continental climates where snow fall is low enough to allow appreciable cooling of the ice by conduction during the winter (Hooke *et al.*, 1983). It is less likely to form in maritime climates where larger snow falls form an effective insulating layer. When present, it is likely to persist well into the melt season, if not entirely through it, and thus forms an effective barrier to penetration of surface meltwater. Because of this cold layer, and because the vein system, even on glaciers without such a cold layer, is relatively ineffective in transmitting water downward, it is, again, principally by way of crevasses that surface water in the ablation area is able to reach the interior of the glacier.

When a crevasse first forms, it may fill with water and overflow. In larger crevasses, however, this situation normally does not persist for long. It seems probable that once a crevasse penetrates deep enough to intersect the millimeter-scale conduit system, increasing the water supply to these conduits dramatically, the conduits are quickly enlarged until they can transmit all of the incoming water downward into the glacier.

Crevasses may close as they are moved into areas or are rotated into orientations with lower tensile stresses. However, where melt streams in the ablation area pour into such a crevasse, the viscous energy dissipated maintains a connection to the englacial conduit system. The hole thus formed in the glacier surface is called a *moulin*.

When a crevasse opens across a melt stream upglacier from a moulin, it cuts off the water supply to the moulin. In the absence of further dissipation of viscous heat, the moulin's connection to the deeper drainage system is then constricted by inward flow of ice, and during the winter the upper part of the moulin fills with snow. In due course, the snow becomes saturated with water which eventually freezes. These processes result in distinctive structures in the ice.

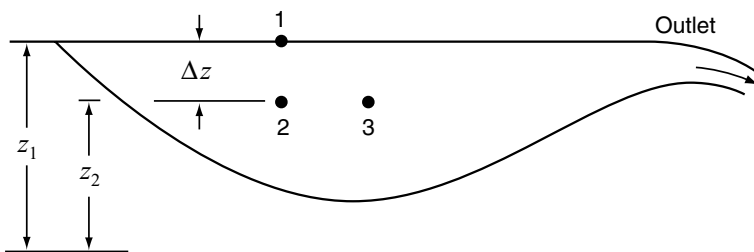


Figure 8.2. Illustration of difference between pressure field and potential field.

Over a period of several years Holmlund (1988) carefully mapped such structures on Storglaciären as ablation exposed ever deeper levels in the glacier. He also descended into some of the moulin during the winter. He found that moulin are typically 30–40 m deep, although deeper ones occur on other glaciers, that channels leading from the bottoms of moulin are typically meandering and trend in the direction of the initiating crevasse, and that after some distance the meandering channel ends in a vertical conduit leading deeper into the glacier.

Shreve (1972) has compared the drainage system we have just described with one developed in a permeable limestone in which karst has developed. The anastomosing vein system provides the basic permeability, while the moulin and larger arborescent network of conduits are the analog of the karst system. Our task now is to consider the geometry of the system of larger conduits deeper in the glacier, below the level of Holmlund's mapping. One possibility is that these conduits are not vertical, but rather slope steeply downglacier, normal to equipotential surfaces in the glacier. We develop the theory behind this idea next, following closely the analysis of Shreve (1972).

Equipotential surfaces in a glacier

In a permeable porous medium, water flows in the direction of the negative of the maximum gradient of the potential, Φ , where Φ is defined by:

$$\Phi = \Phi_0 + P_w + \rho_w g z \quad (8.1)$$

Here, Φ_0 is a reference potential, P_w is the pressure in the water, ρ_w is the density of water, g is the acceleration of gravity, and z is the elevation above some datum level such as sea level.

To gain some appreciation for this concept, consider the situation in a lake (Figure 8.2). Let $\Phi = \Phi_1$ at point 1 on the lake surface. Moving down a distance Δz to point 2 increases P_w by $\rho_w g \Delta z$ but decreases the third term on the right in Equation (8.1) by the same amount. Therefore $\Phi_2 = \Phi_1$ and there is no flow between points 1 and 2. However, if the lake

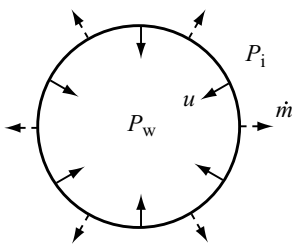


Figure 8.3. In a steady state, closure of a cylindrical conduit, u , is balanced by melt, \dot{m} .

surface slopes gently towards the outlet, moving horizontally at constant $z = z_2$ from point 2 to point 3 will result in a decrease in P_w , and hence in Φ . Flow will then be toward the position of lower P_w , which also is a position of lower Φ . In other words, it is not the gradient in P_w that controls the direction of flow, but the gradient in Φ .

To determine the potential field in a glacier from Equation (8.1), we must determine P_w everywhere. P_w is not hydrostatic because the water is moving, and most of it is a long way from the surface through many small passages.

In general, the pressure in the ice, P_i , is different from that in the water, and the ice deforms as a result of this pressure difference. P_w rarely exceeds P_i significantly, but it can be much less than P_i . Passages may thus increase in size slightly at very high water pressures, and they decrease in size rapidly at low pressures. In addition, as noted, heat generated by viscous dissipation melts conduit walls, enlarging passages (Figure 8.3). In a steady state, the rate of closure of passages by creep of ice, u , is equal to the melt rate, \dot{m} , so the net rate of increase in size of the passages, $\dot{r} = \dot{m} - u$, is 0. (Although mathematically untidy, note that we have defined positive u as being inward, while positive \dot{m} is outward. This simplifies some of the later equations.)

Let us assume that the flow of ice can be represented by $\dot{\varepsilon}_e = (\sigma_e / B)^n$, that ice is incompressible and isotropic, and that the passages are circular in cross section. We further define the pressure causing creep closure, P_c , by:

$$P_c = P_i - P_w \quad (8.2)$$

(Figure 8.3). To a good approximation, $P_i = \rho_i g(H - z)$, where H is the elevation of the ice surface above the datum level (Figure 8.4). Then:

$$\frac{u}{r} = \left(\frac{P_c}{nB} \right)^{\frac{1}{n}} \quad (8.3)$$

(Nye, 1953). This relation will be derived in Chapter 12 (Equation (12.22)). In the derivation it is assumed that $\sigma_e = (1/\sqrt{2})\sigma'_{rr}$, where σ'_{rr} is the radial stress deviator. In other words, other components of the deviatoric stress tensor, and hence of the strain rate tensor, are assumed to be negligible (see Equation (2.10)). Thus, there can be no deformation of the ice other than that resulting from the presence of the passage. In the present application, in which this assumption is clearly violated, we add a multiplying factor, K , which is approximately 1. K equals 1 if $\sigma_e = (1/\sqrt{2})\sigma'_{rr}$. Rearranging and substituting for P_c and P_i , we can rewrite Equation (8.2) as:

$$P_w = \rho_i g(H - z) - KnB \left(\frac{u}{r} \right)^{\frac{1}{n}} \quad u \geq 0 \quad (8.4)$$

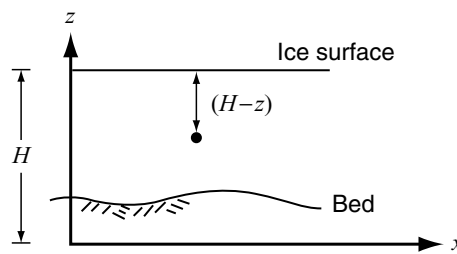


Figure 8.4. Coordinate axes used in discussion of conduit closure.

(If $u < 0$, implying that the passage is opening as a result of water pressures in excess of the ice pressure, $|u|$ must be used, and the sign of the second term adjusted accordingly, but $u < 0$ is rare in nature.) In excess of a couple of kilometers from the glacier terminus, parameters in the last term on the right change relatively little along a tunnel. Thus, combining Equations (8.1) and (8.4) and taking the derivative with respect to an arbitrary direction, s , yields:

$$\frac{\partial \Phi}{\partial s} = \rho_i g \frac{\partial(H - z)}{\partial s} + \rho_w g \frac{\partial z}{\partial s} \quad (8.5)$$

To determine the orientations of equipotential planes in the glacier, we make use of the fact that if s lies in such a plane, $\partial \Phi / \partial s = 0$, so:

$$-(\rho_w - \rho_i) \frac{\partial z}{\partial s} = \rho_i \frac{\partial H}{\partial s} \quad (8.6)$$

Our objective is to define the dip of this plane, β . The dip in some horizontal direction, x , will be dz/dx because z is the vertical coordinate of the plane (Figure 8.5). Therefore, multiply Equation (8.6) by $\partial s / \partial x$ and rearrange, thus:

$$\frac{\partial z}{\partial s} \frac{\partial s}{\partial x} = -\frac{\rho_i}{\rho_w - \rho_i} \frac{\partial H}{\partial s} \frac{\partial s}{\partial x}$$

or, inserting numerical values for the respective densities, letting $\alpha = dH/dx$, the slope of the glacier surface, and noting that $\tan \beta = dz/dx$:

$$\beta \approx -\tan^{-1}(11\alpha) \quad (8.7)$$

Thus, the equipotential planes dip upglacier (note the minus sign) with a slope of about 11 times the slope of the glacier surface (Figure 8.6), a result first obtained by Shreve (1972), and water entering the glacier through a moulin should reach the bed of the glacier some distance downglacier from the entry point. In support of this, Iken and Bindschadler (1986) found that pressure fluctuations in boreholes drilled to the bed of Findelengletscher, just below the firn edge, did not correlate with marked variations in stream flow entering nearby moulin. Rather, the pressure fluctuations seemed to reflect a slower delayed input of water through the snow cover above the firn edge.

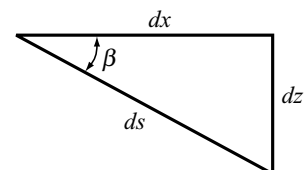


Figure 8.5. Sloping conduit showing how ds and β are defined.

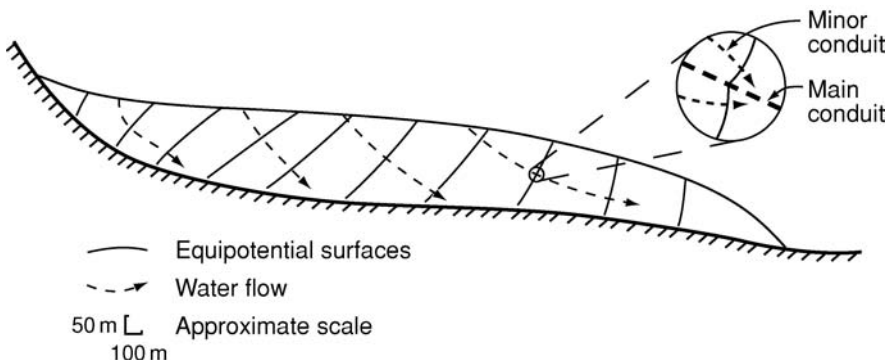


Figure 8.6. Longitudinal section of a glacier showing upglacier-dipping equipotential surfaces and the theoretical directions of englacial water flow. Inset shows dimpling of an equipotential surface and consequent diversion of flow in smaller passages toward the main conduit. (After Hooke, 1989, Figure 1.)

Rigorously, the equipotential surfaces are defined only within the water passages, but with suitable caution, they can be treated as though they were defined throughout the glacier. Because $P_w < P_i$ under normal conditions, Φ is slightly lower in the conduit than in the surrounding ice. Thus, the equipotential surfaces are dimpled in the vicinity of the conduits. As Φ decreases downglacier, the dimples point upglacier as shown in Figure 8.6. With the use of the theory presented below, it can be shown that the difference between P_i and P_w increases with increasing conduit size, so dimples around larger conduits are larger. Thus, water in smaller conduits flowing normal to equipotential surfaces will be deflected toward the larger ones. This strengthens the tendency of the conduit system to evolve toward an arborescent pattern.

Alternative derivation of equipotential-plane dip

Consider the situation in Figure 8.7. There is a conduit along the bed between points 1 and 2. We wish to determine under what conditions the upglacier slope of the hill will be parallel to an equipotential plane so that water in the conduit will not flow. The ice pressure at (1) is $P_{i1} = \rho_i g(h_1 + h_2 + \Delta h)$, and that at (2) is $P_{i2} = \rho_i g h_2$. In the absence of water flow and conduit closure, the pressure in the water at (1), P_w , would be the sum of P_{i1} plus the hydrostatic head in the conduit, $\rho_w g h_1$. If $P_{i1} > P_w$, the conduit will begin to close and water will be forced out over the hill. Thus, the condition we seek is $P_{i1} = P_w$, or:

$$\rho_i g(h_1 + h_2 + \Delta h) = \rho_i g h_2 + \rho_w g h_1 \quad (8.8)$$

Solving this for h_1 , dividing by Δx , noting that $\alpha = -\Delta h/\Delta x$ and $\tan \beta = h_1/\Delta x$, and inserting numerical values for the densities leads directly to Equation (8.7) Q.E.D.

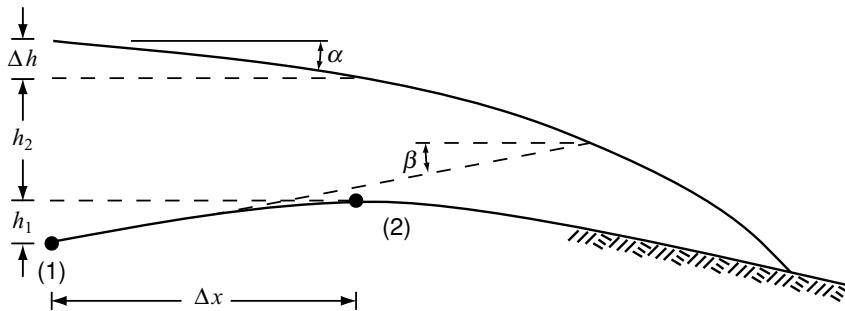


Figure 8.7. Sketch illustrating alternative derivation of dip of equipotential planes in a glacier.

Melt rates in conduits

Let us now consider the rate of melting of conduit walls, following Shreve (1972). The total amount of energy available per unit length of conduit, Δs , per unit time is:

$$\frac{Q}{\Delta s} = \frac{\partial \Phi}{\partial s} \quad (8.9)$$

$$\frac{\text{m}^3}{\text{s}} \quad \frac{\text{N/m}^2}{\text{m}} \quad \text{m} = \frac{\text{N} - \text{m}}{\text{s}} = \frac{\text{J}}{\text{s}}$$

Some of this energy must be used to warm the water to keep it at the pressure melting point as ice thins in the downglacier direction. The rest is available to melt ice, thus:

$$\dot{m} \Delta s (2\pi r \rho_i L) + \rho_w C_w \mathbf{C} \frac{\partial(H-z)}{\partial s} \rho_i g \Delta s Q = Q \frac{\partial \Phi}{\partial s} \Delta s \quad (8.10)$$

$$\frac{\text{m}}{\text{s}} \quad \frac{\text{m}}{\text{m}} \quad \frac{\text{kg}}{\text{m}^3} \quad \frac{\text{J}}{\text{kg}} \quad \frac{\text{kg}}{\text{m}^3} \quad \frac{\text{J}}{\text{kgK}} \quad \frac{\text{K}}{\text{N/m}^2} \quad \frac{\text{m}}{\text{m}} \quad \frac{\text{kg}}{\text{m}^3} \quad \frac{\text{m}}{\text{s}^2} \quad \frac{\text{m}}{\text{s}} \quad \frac{\text{m}^3}{\text{s}}$$

Here, r is the radius of the conduit, L is the latent heat of fusion, C_w is the heat capacity of water, and \mathbf{C} is the change in the melting point per unit of pressure (see Equation (2.2)). As you will see from inspection of the terms and the dimensions of the various quantities in them, the first term on the left is the energy used to melt tunnel walls, and the second is the energy needed to warm the water to keep it at the pressure melting point. Here, we have implicitly taken the positive s -direction to be upglacier, in the direction opposite to that of the water flow. Thus, both $\partial \Phi / \partial s$ and $\partial(H-z) / \partial s$ are positive.

It is common to define $k = \rho_w C_w \mathbf{C}$. Inserting numerical values ($\rho_w = 1000 \text{ kg m}^{-3}$, $C_w = 4180 \text{ J kg}^{-1}\text{K}^{-1}$, and $\mathbf{C} = 0.074 \times 10^{-6} \text{ K Pa}^{-1}$) we find that $k = 0.309$ and that it is dimensionless. If we assume that the water is saturated with air, and adjust \mathbf{C} accordingly, $k = 0.410$.

Then, using Equation (8.5) and dividing by Δs yields:

$$\dot{m}(2\pi r\rho_i L) + k \left(\frac{\partial \Phi}{\partial s} - \rho_w g \frac{\partial z}{\partial s} \right) Q = Q \frac{\partial \Phi}{\partial s} \quad (8.11)$$

or solving for \dot{m} :

$$\dot{m} = \frac{Q \left[(1-k) \frac{\partial \Phi}{\partial s} + k \rho_w g \frac{\partial z}{\partial s} \right]}{2\pi r \rho_i L} \quad (8.12)$$

It is interesting to insert some numbers into this equation to get a sense of the magnitude of \dot{m} . Consider a horizontal tunnel so $\partial z/\partial s = 0$. Suppose the tunnel has a diameter of 0.5 m and that it is under a glacier with a surface slope of 0.01. We now need a relation between Q and the tunnel roughness. The Gaukler–Manning–Strickler equation is one of two that are commonly used for such calculations. It is:

$$\bar{v} = \frac{Q}{\pi r^2} = \frac{R^{2/3} S^{1/2}}{n'} \quad (8.13)$$

Here, \bar{v} is the mean velocity over the tunnel cross section, R is the hydraulic radius of the tunnel, or the cross-sectional area divided by the perimeter (so $R = r/2$ in circular tunnels), S is the nondimensional headloss:

$$S = \frac{1}{\rho_w g} \frac{\partial \Phi}{\partial s} \quad (8.14)$$

which is approximately equal to the glacier surface slope, and n' is known as the Manning roughness coefficient. For smooth channels, n' may be as low as $0.005 \text{ m}^{-1/3} \text{ s}$, but studies of floods, called *jökulhlaups*, resulting from drainage of ice-dammed lakes through subglacial conduits yield values ranging from 0.08 to $0.12 \text{ m}^{-1/3} \text{ s}$ (Björnsson, 1992). A still higher value was obtained from dye-trace experiments on Storglaciären; flow velocities there suggested $n' \approx 0.2 \text{ m}^{-1/3} \text{ s}$ (Seaberg *et al.*, 1988; Hock and Hooke, 1993). Where roughness elements on the tunnel walls and floor are large in comparison with the tunnel size, n' will be higher; this is probably responsible for the relatively high value from Storglaciären. Choosing an intermediate value of $0.1 \text{ m}^{-1/3} \text{ s}$, Equation (8.13) gives a mean velocity of about 0.25 m s^{-1} , or $Q \approx 0.05 \text{ m}^3 \text{ s}^{-1}$, and Equation (8.14) gives $\partial \Phi / \partial s \approx 98 \text{ N m}^{-3}$. Whence $\dot{m} \approx 0.22 \text{ m a}^{-1}$. This may not seem like a lot but, volumetrically, the amount of ice melted in a year is 2.6 times the size of the original conduit.

A consequence of this melting and the resulting inward flow of ice towards the conduit is that structures such as foliation in the ice are also bent inward. A beautiful example of this is shown in Figure 8.8.

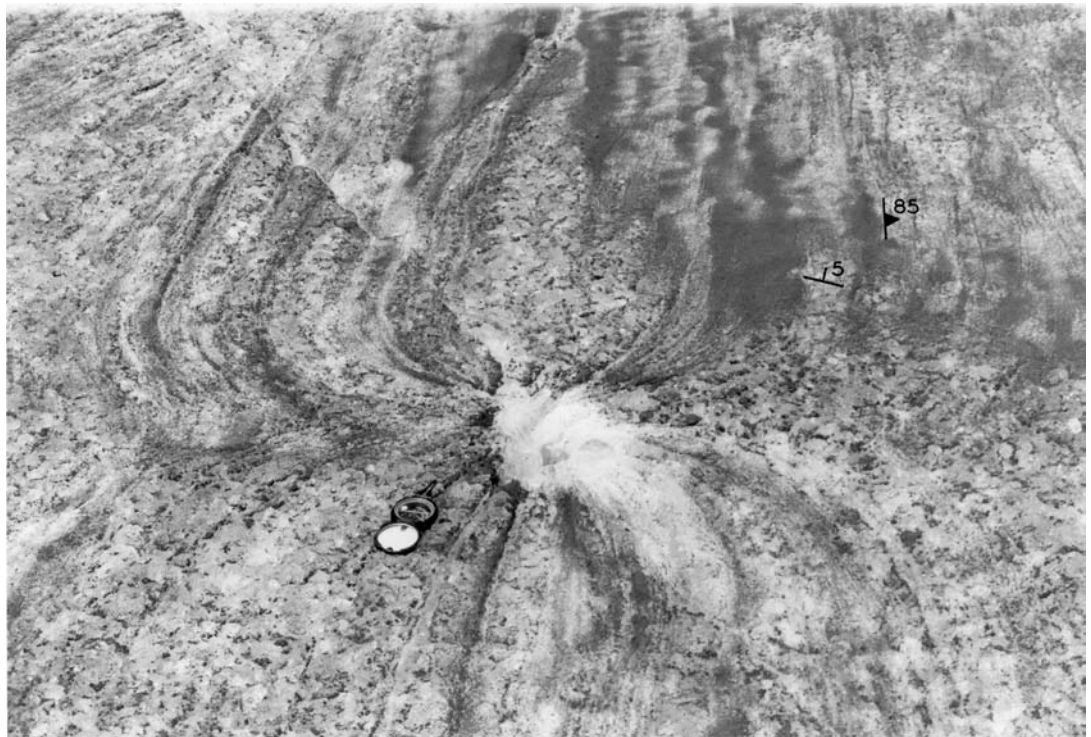


Figure 8.8. Foliation deflected into a conduit by inward flow of ice in response to melting of conduit walls. (From Taylor, 1963, Figure 11. Reproduced with permission of the author and the International Glaciological Society.)

Some heat may also be advected into the glacier in water originating at the glacier surface and entering the englacial conduit system by way of moulin. The melt rate from such water, \dot{m}_s , is:

$$\dot{m}_s = \frac{Q\rho_w C_w (\partial\theta/\partial s)}{2\pi r_i L} \quad (8.15)$$

(Shreve, 1972). Here, $\partial\theta/\partial s$ is the rate at which the water cools as it flows through the conduit. If we assume that $\partial\theta/\partial s \approx 0.1 \text{ K km}^{-1}$ and use the discharge in the previous example, $\dot{m}_s \approx 0.08 \text{ m a}^{-1}$. Thus, this is a heat source that cannot be neglected. A possible mitigating factor, however, is that ice crystals are often carried in streams on a glacier surface. Thus, some of the heat would be used to melt these crystals rather than the conduit walls. It is not clear how the energy will be partitioned in this situation. One would also expect most of this heat to be consumed in the moulin itself or in the first few hundred meters of flow in an englacial passage.

Water pressures in subglacial conduits on hard beds

Our next task is to determine the water pressure in conduits. Our discussion focuses on subglacial conduits on hard beds, but much of the development is equally applicable to englacial ones that are deep enough that P_w is greater than atmospheric pressure. The water pressure in subglacial conduits is of considerable interest owing to its effect on the sliding speed.

Qualitatively, we expect P_w to increase upglacier because the ice thickness increases, and P_c must remain relatively constant so that $u = \dot{m}$. The increase in P_w , or more rigorously in Φ , provides the potential gradient that drives water toward the terminus. Less obvious is the way in which P_w should vary with Q , yet this is quite important because if P_w decreases as Q increases, water will be drawn from smaller conduits toward larger ones, leading to the development of an arborescent drainage network. Conversely, if P_w increases as Q increases, the conduit system will tend to remain braided or *distributed*. In the type of system that we have been discussing, consisting of conduits that may vary in size but not in shape in the longitudinal direction, it turns out that P_w decreases as Q increases. However, in subglacial drainage systems in which conduits locally lie in the lee of bedrock steps, so that conduit geometry is controlled by the steps, the reverse may be true. Qualitative explanations of these phenomena are difficult because the result depends upon the details of the way in which conduit size changes with discharge and in which u and \dot{m} change with conduit size. We thus turn to a quantitative analysis, following closely the work of Röthlisberger (1972). Initially, we will focus on circular conduits.

We start with the steady-state condition, $u = \dot{m}$, and obtain an expression representing this condition by combining Equations (8.3) and (8.12), thus:

$$r \left(\frac{P_c}{nB} \right)^n = \frac{Q \left[(1-k) \frac{\partial \Phi}{\partial s} + k \rho_w g \frac{\partial z}{\partial s} \right]}{2\pi r \rho_i L} \quad (8.16)$$

Noting that $R = r/2$ in circular conduits and solving Equations (8.13) and (8.14) for r yields:

$$r^2 = \frac{2^{\frac{1}{2}} n'^{\frac{3}{4}} Q^{\frac{3}{4}} (\rho_w g)^{\frac{3}{8}}}{\pi^{\frac{3}{4}} \left(\frac{\partial \Phi}{\partial s} \right)^{\frac{3}{8}}} \quad (8.17)$$

Combining Equations (8.16) and (8.17) to eliminate r , letting:

$$D = 2^{\frac{3}{2}} \pi^{\frac{1}{4}} (\rho_w g)^{\frac{3}{8}} \rho_i L = 3.63 \times 10^{10} \left(\frac{N}{m^2} \right)^{\frac{11}{8}} m^{-\frac{3}{8}}$$

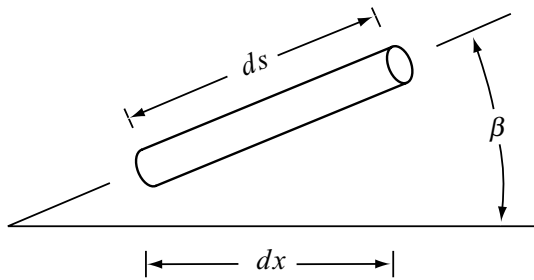


Figure 8.9. Definition of ds in terms of β and dx .

and simplifying, we obtain:

$$\left(\frac{\partial \Phi}{\partial s}\right)^{\frac{11}{8}} + \frac{k}{1-k} \rho_w g \frac{\partial z}{\partial s} \left(\frac{\partial \Phi}{\partial s}\right)^{\frac{3}{8}} = \frac{Dn'^{\frac{3}{4}} P_c^n}{(1-k)Q^{1/4}(nB)^n} \quad (8.18)$$

We now need to relate $\partial \Phi / \partial s$ to P_w and to the geometry of the tunnel system. Differentiating Equation (8.1) with respect to s yields:

$$\frac{\partial \Phi}{\partial s} = \frac{\partial P_w}{\partial s} + \rho_w g \frac{\partial z}{\partial s} \quad (8.19)$$

Referring to Figure 8.9, we see that:

$$ds = \frac{dx}{\cos \beta} \quad (8.20)$$

so, noting again that $dz/dx = \tan \beta$, Equation (8.19) becomes:

$$\frac{\partial \Phi}{\partial s} = \left[\frac{dP_w}{dx} + \rho_w g \tan \beta \right] \cos \beta \quad (8.21)$$

Letting:

$$G = \left[\frac{dP_w}{dx} + \rho_w g \tan \beta \right] \quad (8.22)$$

and using Equations (8.21) and (8.22) in Equation (8.18) yields:

$$G^{\frac{11}{8}} - kG^{\frac{11}{8}} + k \left(G - \frac{dP_w}{dx} \right) G^{\frac{3}{8}} = \frac{Dn'^{\frac{3}{4}} P_c^n}{Q^{1/4}(nB)^n \cos^{11/8} \beta} \quad (8.23)$$

Canceling the two terms in $kG^{11/8}$ and replacing P_c and G by their equivalents from Equations (8.2) and (8.22) results in the relation we have been seeking:

$$\left[\frac{dP_w}{dx} + \rho_w g \tan \beta \right]^{\frac{11}{8}} - k \left[\frac{dP_w}{dx} + \rho_w g \tan \beta \right]^{\frac{3}{8}} \frac{dP_w}{dx} = \frac{Dn'^{\frac{3}{4}} (P_i - P_w)^n}{Q^{1/4}(nB)^n \cos^{11/8} \beta} \quad (8.24)$$

Equation (8.24) is a nonlinear differential equation that can be integrated numerically to obtain the water pressure, P_w , in a conduit as a function of distance from the terminus, $x = 0$, subject to the boundary condition that $P_w = 0$ at the terminus. If the conduit is not full of water

at the terminus, the boundary condition applies some distance upglacier from the terminus, where the conduit first becomes full, and the integration must start at this point. (Atmospheric pressure is ignored, as it is uniform over the area.) To carry out the integration, one uses the surface and bed topography along the course of the conduit to calculate P_i and β at each step, dx .

In the derivation of Equation (8.24), we assumed that the conduit was circular. If, instead, we were to assume that it was semicircular, a more rational assumption for a conduit on a hard bed, and modified Equations (8.12) and (8.13) accordingly, we would find that the form of Equation (8.24) was unchanged. However, D would be 2.00×10^{10} (N m^{-2}) $^{11/8}\text{m}^{-3/8}$. We would then be assuming, implicitly, that Equation (8.3) still applied. These assumptions will be discussed further in the [next section](#).

Equation (8.24) is clearly quite complicated, but we can gain insight into the general behavior of the water pressure field by studying some idealized cases. Consider, for example, a circular tunnel at the base of a slab of ice, 250 m thick, resting on a horizontal bed. Then, $\beta = 0$ and $P_i = \text{constant}$. Röthlisberger presented some solutions for this case. They are shown in Figure 8.10, in which the water pressure is represented on the ordinate by the height to which water would rise in a vertical borehole that intersects the tunnel, or the *piezometric head*. A line connecting these water levels in a series of boreholes along a tunnel is called the *hydraulic grade line* or *energy grade line*, and its slope is $\partial\Phi/\partial s$. The *water equivalent line* in Figure 8.10 is the piezometric head at which the glacier would float. The values of n' and B used in the calculations are shown.

Aside from the obvious increase in P_w in the upglacier direction, thus providing the hydraulic head necessary to drive the flow on a horizontal bed, there are two characteristics of the patterns in Figure 8.10 that merit comment.

1. Water pressures increase as B decreases (compare curves (1), (2) and (3)). This is because lower values of B imply softer ice and hence higher tunnel closure rates. Thus, higher pressures are necessary to reduce the closure rate so that $u = \dot{m}$.
2. Water pressures increase as Q decreases (curves (3), (3a), and (3b)). Although obvious from inspection of Equation (8.24), this is somewhat counterintuitive. Consider the consequences of halving Q , holding, for the moment, P_w and hence $\partial\Phi/\partial s$ constant. \dot{m} will thus be halved (Equation (8.12)). Clearly, halving Q will require a decrease in the cross-sectional area of the conduit, A . Now A varies as r^2 but

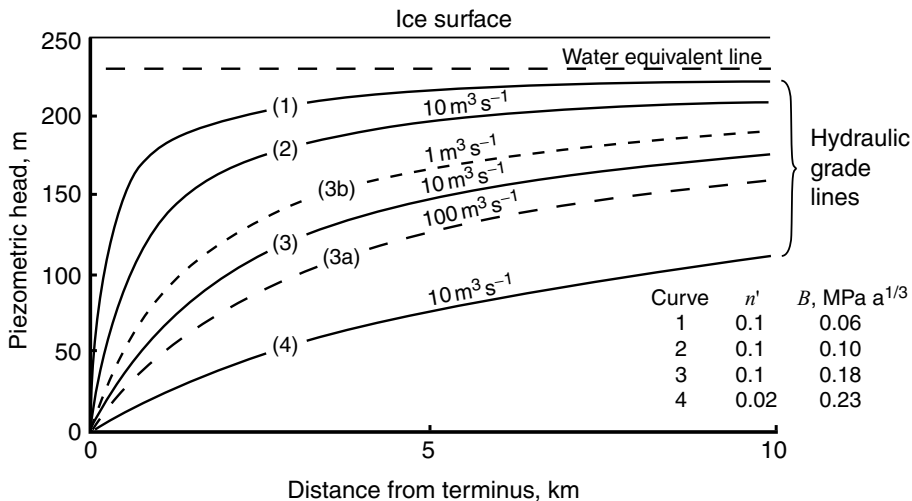


Figure 8.10. Hydraulic grade lines for a horizontal circular conduit under a slab of ice 250 m thick. (Modified from Röthlisberger, 1972, Figure 2. Reproduced with permission of the International Glaciological Society.)

the conduit closure rate, u , varies as r (Equation (8.3)). Thus, by the time r has decreased enough to halve u and hence match the new \dot{m} , A would have decreased so much that P_w would be forced to increase to continue to drive the flow.

A simple numerical calculation may be useful. If subscripts “o” refer to the conditions before the change and subscripts “1” after the change, we find from Equation (8.17) that $r_1 = 0.77 r_o$ and, because $u \propto r$ (from Equation (8.3)), $u_1 = 0.77 u_o$. Now when $\partial\Phi/\partial s$ is constant, Equation (8.12) can be written as $\dot{m}r = \Gamma Q$, where Γ is a constant. Therefore, $\dot{m}_1 r_1 = \frac{1}{2} \dot{m}_o r_o$. So, $\dot{m}_1 = \frac{1}{2} \dot{m}_o r_o / r_1 = 0.65 \dot{m}_o$. Thus, \dot{m} is reduced 35% while u is reduced only 23%, and they are now unequal. The tunnel will thus close, constricting the flow and raising the pressure.

Röthlisberger also presented some solutions for other idealized situations, and three of these are shown in Figure 8.11. Three interesting points merit discussion.

1. The negative P_w in Figure 8.11b implies that for $u = \dot{m}$, there must be suction. In other words, the u provided by the pressure of the overlying ice, alone, is not adequate to match \dot{m} , even with $P_w = 0$. Suction is necessary to increase u . Actually, the natural result is more likely to be that air will enter the channel from the terminus, resulting in open channel flow.

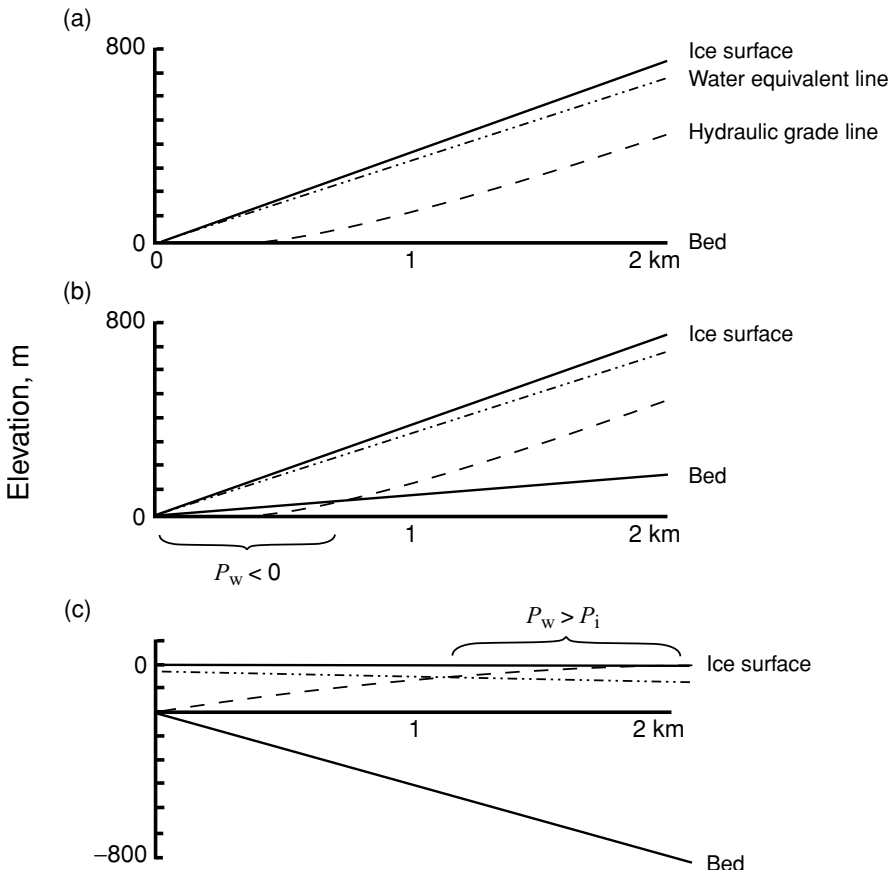


Figure 8.11. Hydraulic grade lines for some idealized situations with constant discharge of $10 \text{ m}^3 \text{s}^{-1}$. (Modified from Röthlisberger, 1972, Figure 5. Reproduced with permission of the International Glaciological Society.)

In this case, u is low because the ice is thin, and \dot{m} is high because the bed slopes downward in the direction of flow, thus increasing the contribution of the second term on the right in Equation (8.5) to the energy dissipation. In fact, it is easy to show that unless the ice is more than a couple of hundred meters thick, even slight positive bed slopes will increase the energy dissipation sufficiently to lead to open channel flow in circular or semicircular conduits (Hooke, 1984). The energy available to melt ice is then easily calculated from the decrease in potential energy, mgh .

2. In Figure 8.11c, $P_w > P_i$ some distance from the terminus. In this situation, the tunnel would be expanding, if it existed, and the tunnel size would be maintained by freezing of ice to the walls. Actually, in

these situations it is more likely that water leaks out along the bed and the glacier, in effect, floats.

This condition arises when, as in Figure 8.11c, the bed has an adverse slope that is so steep that water flowing up it does not dissipate enough energy to remain warmed to the pressure melting point. Mathematically, the second term on the left in Equation (8.10) exceeds the term on the right, forcing \dot{m} to become negative. Physically, the water becomes supercooled, leading to freezing. The latent heat released warms the rest of the water to keep it at the pressure melting point. We will discuss this further later, in connection with the origin and shape of overdeepenings in glacier beds.

3. Finally, it will be noted that with increasing distance from the terminus, the hydraulic grade lines in both Figures 8.10 and 8.11 become nearly parallel to the water equivalent line. As the slope of the water equivalent line represents the gradient in ice pressure at the bed, this means that $(P_i - P_w)$, and hence also u/r , are nearly constant (see Equations (8.2) and (8.3)). This justifies ignoring the $KnB(u/r)^{1/n}$ term in Equation (8.4) when differentiating to obtain $\partial\Phi/\partial s$ (Equation (8.5)).

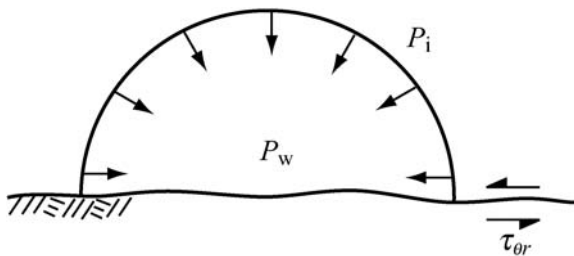
Shapes of subglacial conduits

Equation (8.24) makes specific predictions about basal water pressures. These predictions have been tested in the field, and the agreement with theory is not good. Water pressures are significantly higher than expected. Röthlisberger (1972) and Iken and Bindschadler (1986) found that in order to obtain agreement between measurement and theory they had to use values of B of ~ 0.1 and ~ 0.03 MPa $a^{1/3}$ respectively. In earlier discussions of this problem, these values seemed low compared with typical values of ~ 0.2 MPa $a^{1/3}$ for temperate ice. However, Cohen's (2000) study of basal ice in Engabreen, discussed in Chapter 7, suggests that at least Röthlisberger's value may not be unreasonably low.

On the other hand, there are three potential problems with application of Equation (8.24) to subglacial conduits. First, as noted, it was derived for conduits with circular cross sections. Clearly, tunnels at the bed of a glacier are not circular. Thus, it is appropriate to see whether agreement can be improved by assuming some other tunnel shape. Secondly, stresses and the resulting strain rates parallel to the conduit axis are ignored in the derivation. Thirdly, sinuosity of the conduit is not included.

Let us deal first with the question of tunnel shape. Unfortunately, Equation (8.3) is only valid when the conduit is circular, whereas a semicircular shape would be a more reasonable first approximation for

Figure 8.12. Some of the stresses around a semicircular subglacial tunnel.



a conduit at the bed. In a semicircular conduit, Equation (8.3) should closely approximate the true closure rate if $\tau_{\theta r}$ (Figure 8.12) is vanishingly small. However, when the value of D for semicircular conduits is used in Equation (8.24), the agreement of theory with field measurements is only marginally improved.

On an irregular bed $\tau_{\theta r}$ is not likely to be negligible. In addition, when a significant fraction of the water is derived from the glacier surface, water fluxes vary diurnally. During periods of low flow, the water may not fill the tunnel, in which case melting will be concentrated low on the walls. As $\tau_{\theta r}$ also inhibits closure there, one might expect the tunnel to become broad and low. Closure of a broad, low conduit will be faster than that of a semicircular one with the same cross sectional area. This is because the conduit roof receives much less support from the walls.

Faster closure rates can be simulated by multiplying the right-hand side of Equation (8.24) by a factor, $\Omega > 1$, and rather good agreement of theory with field measurements can be obtained in this way (Figure 8.13). However, Ω can be interpreted as reflecting either softening of the ice by unbound water as suggested by Cohen (2000) or weakening of the tunnel arch by widening. The result shown in Figure 8.13 was obtained with $\Omega = 150$, which corresponds to $B \approx 0.03 \text{ MPa } a^{1/3}$. Numerical modeling using the finite-element method suggests, alternatively, that this value of Ω would correspond to a tunnel that was $\sim 6 \text{ m}$ wide and 0.03 m high (Hooke *et al.*, 1990). Neither seems reasonable alone, so a combination of the two effects may be involved. However, in other cases studied Ω was as low as 4, corresponding to $B \approx 1.0 \text{ MPa } a^{1/3}$ or to a width-to-height ratio of ~ 12 , both of which are within the realm of possibility.

Equation (8.24) also ignores the effect that stresses parallel to the conduit axis have on the closure rate. As noted previously (Equation (2.10)), such stresses increase the rate of tunnel closure even though they do not act in the direction of the closure. However, it turns out that the additional stresses are normally small compared with P_c so including them has a negligible effect on σ_e .

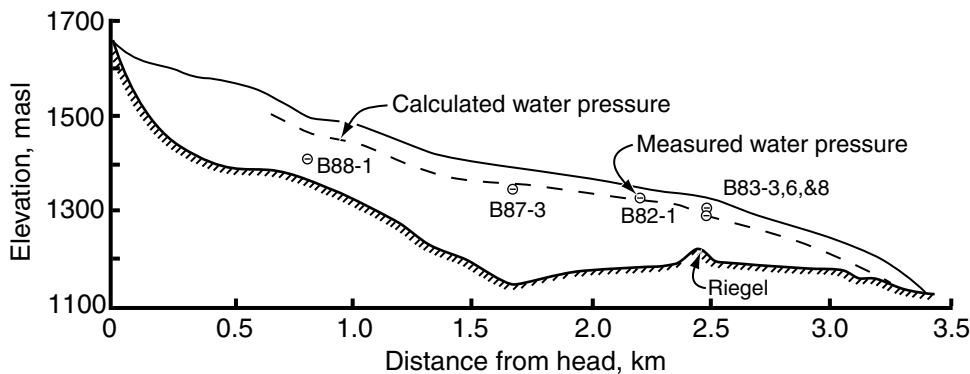


Figure 8.13. Longitudinal section of Storglaciären showing locations of boreholes, mean winter water levels in holes, and calculated hydraulic grade line. For several reasons, the water level in hole B88-1 is not thought to be representative of winter conditions. (From Hooke *et al.*, 1990, Figure 3. Reproduced with permission of the International Glaciological Society.)

Finally, because dP/dx is calculated along a flow path, the more sinuous the flow path the higher the pressure at a point a given straight line distance from a glacier margin. However, to achieve the agreement between measured and calculated pressures shown in Figure 8.13, the flow path would have to be ~ 30 times the straight line distance (Hooke *et al.*, 1990). This seems extreme, but some sinuosity of the flow path is likely and this may be partially responsible for the high observed water pressures.

In conclusion, where drainage along a glacier bed is in well-defined tunnels, the tunnels are likely to be broad and low. This is because melting may be concentrated low on tunnel walls, and closure is inhibited there. In addition, the conduits are likely to be at least slightly sinuous. Finally, unbound water along interfaces between entrained sediment particles and ice is likely to make basal ice softer than clean ice higher in a glacier. Observed water pressures in glaciers can be modeled well with the use of Equation (8.24) either by assuming that conduits are broad and low or by adopting a lower value of B . In all likelihood, high observed water pressures are a consequence of a combination of these two factors with some additional contribution from sinuosity.

Types of subglacial drainage system

Hitherto in our discussion of subglacial drainage, we have been dealing, implicitly if not explicitly, with systems composed of relatively straight channels cut upward into the ice and resting on hard beds. Such

channels are commonly called *Röthlisberger channels*, or simply *R channels*. Nye (1973b) suggested, alternatively, that channels might be incised into the bed of a glacier, and such channels, frequently called *Nye* or *N channels*, have been described (Walder and Hallet, 1979; Hallet and Anderson, 1980). They are typically 0.1–0.2 m deep and 0.2–0.5 m wide, although some reach widths and depths of several meters. Nye channels are not common, perhaps because changes in ice surface profile, movement of the ice, and melting of the conduit walls can all displace the flow laterally, so streams do not stay in one place long enough.

Two other types of drainage system on hard beds have also been suggested: the linked-cavity system and the multi-branched arborescent system. In addition, there are drainage systems on soft beds. These are described in the next three sections.

The linked-cavity system

In some experiments on Variegated Glacier, Alaska, it was found that despite a water discharge, Q , of $5 \text{ m}^3 \text{ s}^{-1}$, dye moved through the subglacial drainage system with a speed, v , of only 0.025 m s^{-1} . Because $Q = vA$, where A is the cross-sectional area of the conduit, A must have been $\sim 200 \text{ m}^2$. If the flow were in a single conduit, this would present a problem because, for any reasonable conduit roughness, n' , Equation (8.13) would then predict velocities that were one to two orders of magnitude higher than those observed.

Kamb (1987) suggested that the flow, rather than being in a single conduit, was in a network of linked cavities (Figure 8.14a). The cavities are believed to form in the lee of steps in the bed (Figure 8.14b), and indeed precipitates and the lack of striations in such locations on deglaciated bedrock surfaces argue strongly for their existence. The cavities are linked together by orifices that are much smaller in cross-sectional area than the cavities (Figure 8.14b). The cavities provide the large A required, and the orifices throttle the flow, reducing the velocity.

A cavity or orifice formed in the lee of a step is shown in Figure 8.15. Panel (a) shows the geometry under certain basal-water-pressure and sliding-velocity conditions. Panel (b) illustrates the geometry when heat released by viscous dissipation in the flowing water enlarges the orifice by melting its roof. Note that the cavity or orifice becomes both longer and more arched in this case. In the case of an orifice, Kamb assumes that all of the heat is used to melt ice in the orifice in which the heat is produced. As some of the heat will be advected into the next cavity, this will overestimate the orifice size. He also assumes that deformation of ice can be represented by a Newtonian flow law ($n = 1$)

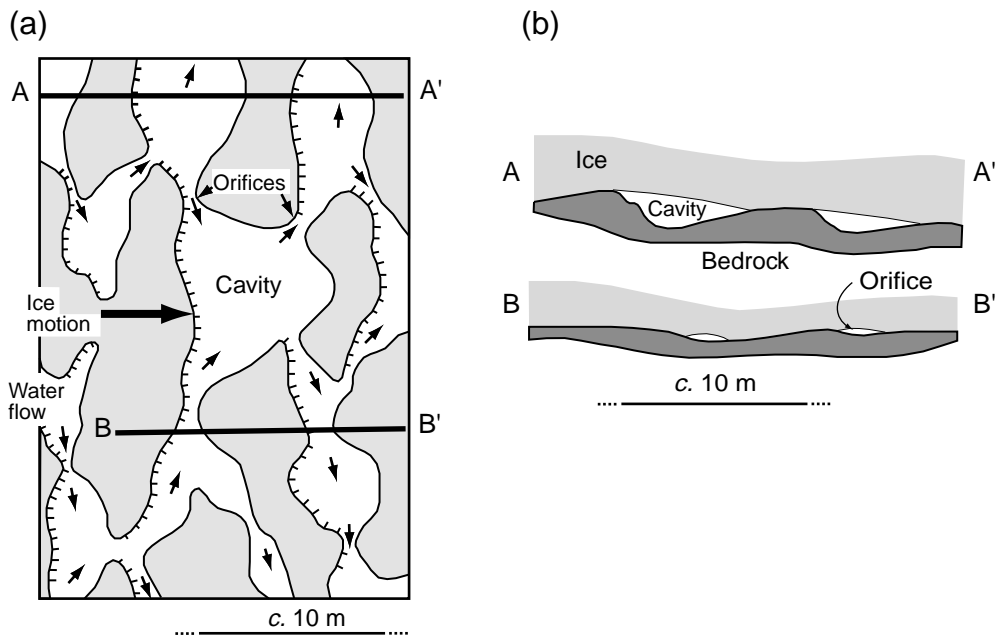
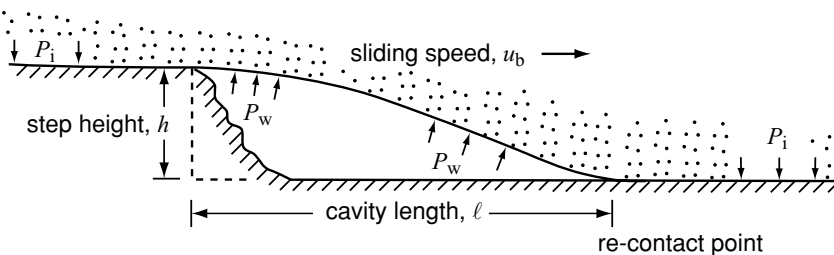


Figure 8.14. (a) Schematic map of a linked-cavity basal water system. (b) Cross sections through the linked-cavity system of (a). (After Kamb, 1987, Figures 1 and 2.)

(a) Without roof melting



(b) With roof melting

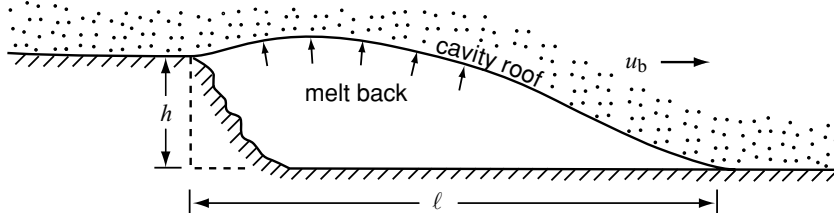


Figure 8.15. Geometry of ideal cavity or orifice in lee of a step in the bed: (a) without roof melting, (b) with roof melting. (Modified from Kamb, 1987, Figure 5.)

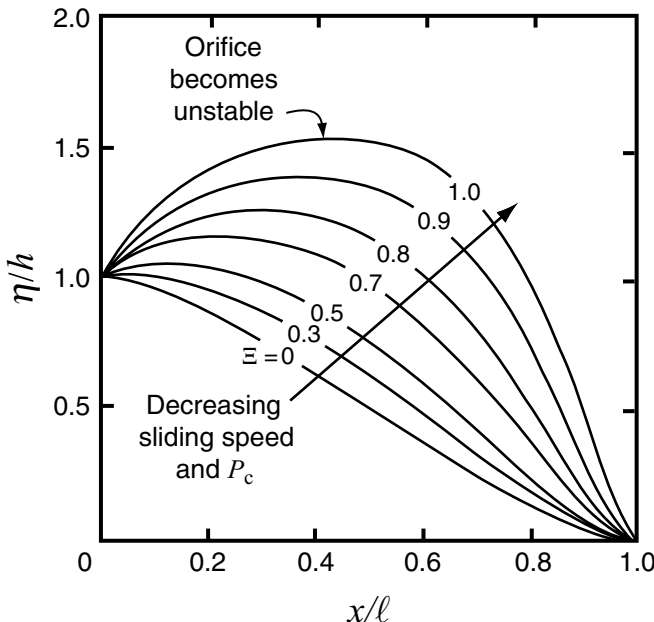


Figure 8.16. Steady-state configuration of an orifice roof. (After Kamb, 1987, Figure 8. Reproduced with permission of the author. Copyright by the American Geophysical Union.)

if the viscosity is chosen appropriately. (This assumption is commonly made when the problem is otherwise mathematically intractable.)

A critical parameter in Kamb's theoretical development is the orifice stability parameter, Ξ . For an orifice in the lee of a step of height h , Ξ is given by:

$$\Xi = \frac{2^{\frac{1}{3}} S^{\frac{1}{2}}}{\sqrt{\pi} \Lambda n'} \left(\frac{\mu}{u_b(P_i - P_w)} \right) h^{\frac{7}{6}} \quad (8.25)$$

where Λ is a constant factor involving the latent heat of fusion, μ is the equivalent Newtonian viscosity, u_b is the sliding speed, and the other parameters are as defined previously. The hydraulic head, S , contains a correction for the sinuosity of the flow.

The cross-sectional shape of the orifice is governed by Ξ (Figure 8.16). In this figure, η is the height of the orifice, so the ordinate, η/h is the height of the orifice scaled to the height of the step. With increasing Ξ , the orifice becomes increasingly arched until a point of instability is reached at $\Xi \approx 1.0$. The orifice also becomes longer by about a factor of 3 as ξ increases from 0 to 1.0, but this is not shown because the ordinate is scaled to the final length, ℓ , in each case.

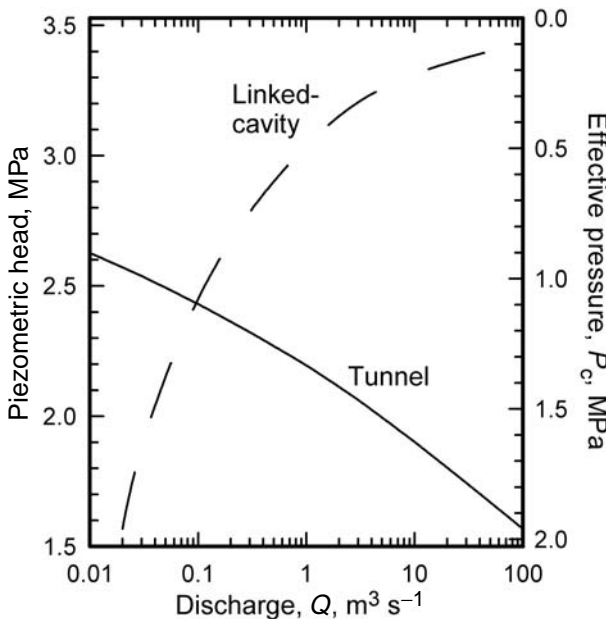


Figure 8.17. Relation between Q and P_c for tunnel and linked-cavity systems. (After Kamb, 1987, Figure 12. Reproduced with permission of the author. Copyright by the American Geophysical Union.)

Note that the orifice roof is less arched when u_b is high. This is because higher sliding speeds replenish the melting ice more quickly. Conversely, it is more arched when P_w is large (P_c small) because closure rates are then reduced.

The instability at $\Xi \approx 1$ is of considerable interest. Actually, the instability shown is of a mathematical nature only. It does not have a direct physical interpretation. However, it is a manifestation of a physical instability that Kamb has investigated further. He finds that if ξ is high enough, say about 0.8, and that if P_w is increased enough to decrease P_c by about 20%, the length of the orifice, ℓ in Figure 8.15, will increase without bound. This may be the point at which a linked-cavity system is transformed into a tunnel system.

The way in which P_w changes with Q in a linked-cavity system is also of interest. We noted that decreasing Q in a tunnel system resulted in an increase in the steady-state pressure in the system (Figure 8.17). However, in a linked-cavity system, decreasing Q has a relatively small effect on ξ and an even smaller effect on the cross-sectional area of the orifices. This is because the orifice is, in effect, propped open by the step (Figure 8.15). As a result, the lower discharge can be driven with a decreased head gradient (represented in Figure 8.17 by the piezometric head on the left ordinate).

As noted, a consequence of the direct dependence of Q on P_w in the linked-cavity system is that a stable system of many interconnected

cavities can exist. In a tunnel system, in contrast, the larger tunnels have lower pressures and thus capture the flow of the smaller ones.

Another important feature of Figure 8.17 is that for discharges in excess of $\sim 0.1 \text{ m}^3 \text{ s}^{-1}$ and with orifices generated by step heights less than $\sim 0.1 \text{ m}$, a much higher pressure is required to drive the flow in a linked-cavity system. This is because high pressures are required to open and maintain the orifices. High water pressures, of course, increase the speed of a glacier (Chapter 7).

Transitions between conduit and linked-cavity systems

Tunnels are commonly observed emerging from the margins of glaciers, and the rapidity with which dye poured into moulin often appears in outlet streams at the terminus (see Hock and Hooke, 1993; Seaberg *et al.*, 1988; among others) argues strongly for tunnel flow. However, as long as part of a glacier's movement is by sliding, linked cavities are certainly present, as ice must separate from the bed in the lee of at least some obstacles, and striations or joints in the rock will provide connections between resulting cavities. We thus need to investigate the conditions for stability of tunnels in the presence of cavities.

Fowler (1987) and Raymond (unpublished, cited by Fowler, 1987) have studied this problem. Their approach is to consider the consequences of a small increase in pressure in, for example, the tunnel part of the system. This will lead to flow of water from the tunnels to linked cavities, thus necessitating an increase in volume of the cavities, and hence of the pressure in the cavities. If the increase in cavity pressure thus required is greater than the initial increase in pressure in the tunnels, the pressures will eventually equilibrate and the combined system will be stable. However, if the required increase in cavity pressure is less than the initial increase in tunnel pressure, the cavities will grow larger than required, sucking water out of the tunnel system and leading, possibly, to its collapse.

Whether the change in pressure in the cavities satisfies the requirement for stability depends upon the sliding speed, bed geometry, water pressure, and water discharge in the conduits. Lower sliding speeds and lower water pressures tend to favor stability, whereas lower discharges favor collapse of the tunnels, with only the linked-cavity part of the system surviving.

Both the Kamb (1987) and the Fowler (1987) theories suggest that the limit of stability of the tunnel system is approached in winter when discharges are low, tunnels are thus shrinking, and water pressures are increasing. Locally, the tunnel system may collapse entirely, especially under thicker glaciers. More commonly, however, remnants of the

previous year's tunnel system, maintained by the small winter discharge provided by subglacial melt, are likely to survive. These conduits will increase in size rapidly as water inputs increase in the spring. This is because the water backs up in the undersized conduit system, resulting in high potential gradients and hence high melt rates on conduit walls, and also high pressures that inhibit closure. If such remnant tunnels do not exist, or if they do not enlarge rapidly enough, the water pressure may rise to the level where Kamb's stability limit for the linked cavity system is exceeded. New tunnels may then form by growth and coalescence of links. In either case, water pressures drop abruptly as the tunnel system is reestablished. Measurements of seasonal variations in water pressure (Hooke *et al.*, 1989), of dye dispersion (Seaberg *et al.*, 1988; Hock and Hooke, 1993), and of surface velocity (Hodge, 1974; Hooke *et al.*, 1989) lend strong support to this model.

A reasonable supposition is that the linked-cavity and tunnel models represent end members of a continuum of drainage types. The drainage system beneath fast-moving glaciers, including those that are surging (discussed below), may be near the linked-cavity end member in this continuum. Conversely, ice sheets that are nearing stagnation, and thus beneath which there is little separation and cavity formation, may have drainage systems approximating the tunnel end member.

Multi-branched arborescent system

A conduit system that has some of the characteristics of both the tunnel and the linked-cavity systems is one that consists of an arborescent network of broad, low conduits, each of which is individually braided (Figure 8.18). Hock and Hooke (1993) called this a multi-branched arborescent system. They envisaged subglacial streams flowing in tunnels that are, in comparison with the linked-cavity system, relatively straight and uniform in size. As in the linked-cavity system, it is specifically recognized that no part of the glacier bed should be far from a conduit.

Hock and Hooke developed the idea of the multi-branched arborescent system from tracer studies on Storglaciären. Dye was injected into a moulin about a kilometer from the terminus, and its arrival in one of the two streams draining the glacier, Sydjåkk (Figure 8.18a), was recorded. As is commonly observed in tracer studies, the water velocities obtained from these tests were too low to be consistent with the existence of a single large tunnel from the moulin to the terminus. However, the velocities could be modeled rather well by assuming that the drainage system bifurcated several times between the terminus and the moulin, so that each of the highest tributaries of the system carries an average of

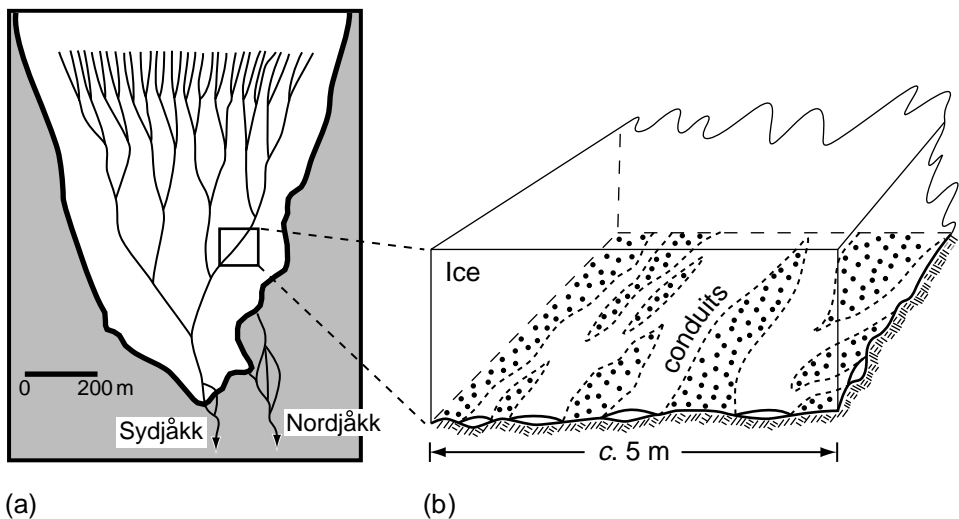


Figure 8.18. Schematic sketches (a) of the multi-branched arborescent conduit system postulated to exist beneath Storglaciären, and (b) of an individual braided channel in the system. (After Hock and Hooke, 1993, Figures 4 and 6.)

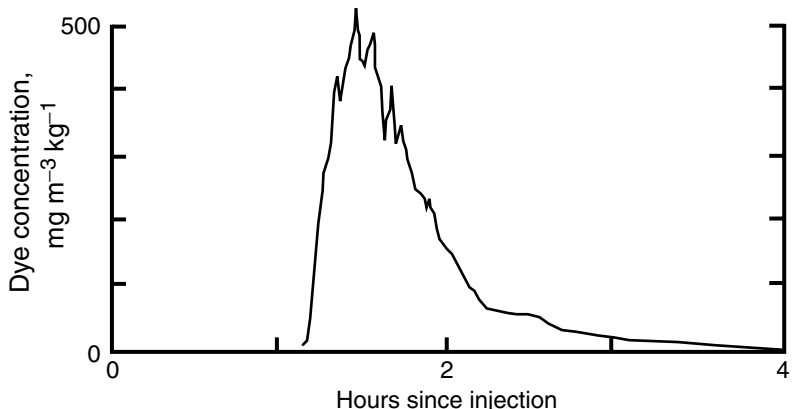


Figure 8.19. Typical dye-return curve from a test on Storglaciären. Ordinate is milligrams of dye per cubic meter of water and kilogram of dye injected. (From Hock and Hooke, 1993, Figure 3.)

only $\sim 3\%$ of the discharge at the terminus (Figure 8.18a). This model is also consistent with the observation that there are many small streams and moulin at this location on the glacier, implying many sources.

That the individual channels are braided (Figure 8.18b) is suggested by multiple peaks in some of the dye-return curves (Figure 8.19). Such peaks occur when dye following one anabranch of a braided system moves more slowly than that in another anabranch. The two packages of dye then reach the terminus at different times.

The multi-branched arborescent model is consistent with two basic observations: (1) that measured water velocities are much lower than they would be in a single conduit; and (2) that water pressures are relatively uniform over the bed, as observed by Iken and Bindschadler (1986) on Findelengletscher. The uniform drainage for all parts of the glacier bed provided by the multi-branched arborescent system should result in such relatively uniform water pressures. It is likely, however, that many of the smaller tributaries providing this uniform drainage are actually linked cavities.

As noted (Figure 8.13), winter water pressures beneath Storglaciären have been modeled rather well with the use of Röthlisberger's theory modified to reflect, approximately, the wide shallow geometry of the channels. Thus, in contrast to the situation in a linked-cavity system, it seems likely that steady-state water pressures in the wide shallow channels that characterize the multi-branched arborescent system decrease with increasing discharge.

Even within the framework of the multi-branched arborescent model, however, there can be appreciable differences among nearby glaciers. Iken and Bindschadler (1986, p. 110), for example, used electrical conductivity measurements in proglacial streams and other observations to study the differences between the subglacial drainage of Findelengletscher and Gornergletscher. These two glaciers are both near Zermatt in the Swiss Alps and are of comparable size. They concluded that the drainage of Gornergletscher was in a few large tunnels, whereas that of Findelengletscher was in a larger number of smaller conduits. They did not propose an explanation for this difference.

Conduits on deforming till

Hitherto, our discussion of subglacial conduits has focused on situations in which the bed was comparatively rigid. Many glaciers, however, move over beds of deformable till. In Chapter 7 we found that the deformability of till and the nature of the coupling between it and the glacier sole are both strongly dependent upon the effective pressure, $P_i - P_w$. In turn, the effective pressure depends, through P_w , on the nature of the drainage system at the ice–till interface. As P_w at such an interface is clearly of prime importance in the development of ice streams and also in surging by a mechanism proposed by Truffer *et al.* (2000), a quantitative understanding of conduits on deformable substrates is clearly needed.

As with a conduit at an ice–rock interface, the roof of a conduit at an ice–till interface also tends to close when $P_w < P_i$, and in the steady state this tendency is balanced by melting. In addition, however, creep of till into the conduit may tend to constrict it, and in the steady state any such

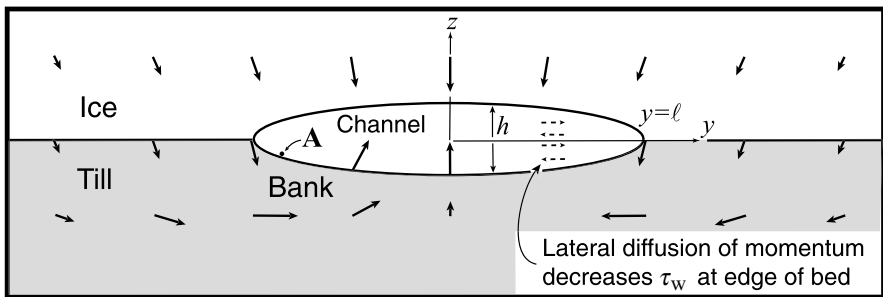


Figure 8.20. Possible geometry of a subglacial conduit incised into till. Vectors are based on Ng (2000b, Figure 9) and show approximate transverse velocity distribution in the ice and in the till for a situation in which the effective viscosity of the till is substantially less than that of the ice (see text). Some vectors on the right are omitted for clarity.

flow must be balanced by erosion of the till by the flowing water (Alley, 1989a; Walder and Fowler, 1994; Ng, 2000a, b). The physics of the latter processes are still poorly understood, as neither the rheology of till nor the mechanics of sediment transport are known well enough.

Nevertheless, we can make some predictions about the nature of the drainage system. Consider the channel shown in Figure 8.20. If any sediment on the sloping “bank” of the channel, as at A in Figure 8.20, can be moved downstream by the current, gravitational forces will tend to move it, also, toward the middle of the channel. Consequently, channels should become wider and shallower until the velocity and shear stress on the banks are too low to move sediment. Parker (1979) has proposed that in the transition zone between the bed and the bank, lateral diffusion of downstream momentum results in a gradual outward decrease in the shear stress, τ_w , exerted by the water on the bed, so that movement of bed material actually decreases gradually toward the banks rather than ceasing abruptly at some particular threshold depth. Although Parker’s model was developed for subaerial gravel-bedded rivers, there is no obvious reason why it should not also apply to subglacial conduits in noncohesive till, even if the till is fine grained, so long as there is an inward-sloping bank region. Channels in till are thus likely to be wide and shallow, as illustrated in Figure 8.20, a conclusion shared by Engelhardt and Kamb (1997), Walder and Fowler (1994), and Ng (2000a, b).

Ng (1999) has suggested that in such a conduit, the vertical closure rate, w , due to flow of ice should be given approximately by:

$$w(y) = \left(\frac{P_c}{2B} \right)^n \sqrt{\ell^2 - y^2} \quad (8.26)$$

where ℓ is the half width of the conduit, y is the distance from its center, and the appropriate value for B is $\sim 0.16 \text{ MPa a}^{1/3}$. Thus, w is highest in the middle of the channel, at $y = 0$, and decreases toward the bank, $y = \ell$. ($w \neq 0$ at $y = \ell$ for reasons described below.) This would be consistent with the suggestion (Shreve, 1985a) that melt rates should be higher where the water is deeper and the energy dissipation thus greater. Ng also proposes a similar relation for creep of till into the conduit, with $(P_c/2B)^n$ in Equation (8.26) replaced with an appropriate relation for till.

In Figure 8.20, $w \neq 0$ at $y = \ell$ because the till layer is of finite thickness and removal of sediment creeping into the conduit results in thinning of the till layer adjacent to the conduit. Thus, the ice–till boundary adjacent to the channel sinks, and vectors in the till are nearly horizontal. In addition, the vectors in Figure 8.20 reflect a situation in which the effective viscosity of the till is substantially less than that of the ice. If the effective viscosities are roughly equal, flow of the till is much slower, owing in part to the limited thickness of the till (Ng, 2000b).

Let us now consider the water pressure in such a conduit. Walder and Fowler (1994) note that a low water pressure will promote flow of ice toward a conduit but strengthen till. Under these conditions, they argue that the channel bed may be relatively flat, and the conduit will be melted upward into the ice. Conversely, a high water pressure will promote flow of till into a conduit but inhibit inward flow of ice. In this case, the channel may tend to be cut downward into the till. Their analysis suggests that the transition between these two regimes should occur at an effective pressure of $\sim 0.8 \text{ MPa}$, but the uncertainty in this figure is quite large.

Ice sheets tend to have relatively low surface slopes. Potential gradients are thus low, so \dot{m} is low (Equation (8.12)). The conduit system must then adjust to provide a high P_w , thus inhibiting closure by ice flow. This may enhance deformation of till into conduits. Conversely, valley glaciers normally have higher surface slopes, so \dot{m} will be higher and P_w lower, perhaps leading to conduit geometries controlled by the inward flux of ice.

We have seen that in circular or semicircular conduits, P_w decreases as Q increases so water is diverted from smaller conduits to larger ones, leading to an arborescent drainage network. Of interest, then, is the question of whether this relation between P_w and Q also holds for conduits on deforming till.

Let us leave this question for the moment to describe an elegant analysis by Ng (2000a) in which he derived three coupled ordinary differential equations that could be solved numerically for the discharge, Q , and sediment discharge, Q_s , in a conduit, and the effective pressure, P_c , all as functions of distance along a conduit from its source. The

principal independent variables in the analysis are the fluxes of water and sediment into the conduit. The water flux is from basal melting over some distance on either side of the conduit, and the sediment flux is from small tributaries along the conduit. The coupling among these variables occurs because P_c is a measure of: (1) the flux of ice toward the conduit, and thus of the contributions of melting of the conduit roof to Q , and (2) the strength of the till and hence of the flux of till into the bottom of the conduit. Knowing these three parameters, Ng calculates ℓ , τ_w , \dot{m} , $d\Phi/ds$, conduit height, h (Figure 8.20), mean water velocity, \bar{u} , and mean sediment concentration, \bar{c} , subject to the constraints, expressed as equations, that:

- $\bar{c} = Q_s/Q$;
- \bar{c} is related to τ_w and h because they determine the intensity of turbulence;
- τ_w is related to \bar{u} and the hydraulic roughness of the conduit;
- \bar{u} times the cross-sectional area of the conduit must equal Q ;
- w , integrated across the conduit, must equal $\dot{m}\ell$;
- $d\Phi/ds$ is related to the slope of the ice surface and to dP_c/ds (Equation (8.5)); and
- \dot{m} is related to $d\Phi/ds$ and Q (Equation (8.12)).

Thus, there are seven equations and seven unknowns. Closure of the conduit by ice flow is assumed to be given by Equation (8.26) and closure by flow of till by a similar equation. Taken as constant in the solution are sediment grain size, conduit roughness, and the slope of the ice surface. In addition, energy used to keep the water at the pressure melting point (Equation (8.10)) is neglected, so rigorously the solution applies only to an ice sheet of uniform thickness. Particularly noteworthy in this solution is the fact that conduit size and shape and the rate of erosion of the bed are all determined solely by the independent variables – the water and the sediment fluxes from basal melting and small tributaries – together with some parameters like grain size that are specified and held constant.

In an illustrative calculation based on this model, Ng assumed that a small amount of water was seeping through the till and along the ice–till interface upstream from the head of the conduit. This water entered the conduit without transporting any sediment, so $Q > 0$ but $Q_s = 0$ here. P_c was taken to be 0.1 MPa at the head, well below the hypothesized transition at ~ 0.8 MPa. Along the conduit, basal melting was presumed to supply water at a constant rate of $0.01 \text{ m}^3 \text{ s}^{-1} \text{ km}^{-1}$, and the sediment flux from tributaries was taken to be $265 \text{ g s}^{-1} \text{ km}^{-1}$.

Downstream changes in several key variables are shown in Figure 8.21. At the upstream end of the conduit there is a boundary zone about 30 km long in which $dP_c/ds \neq 0$ (Figure 8.21b), and ℓ and h vary somewhat erratically (Figure 8.21d); downstream from this zone,

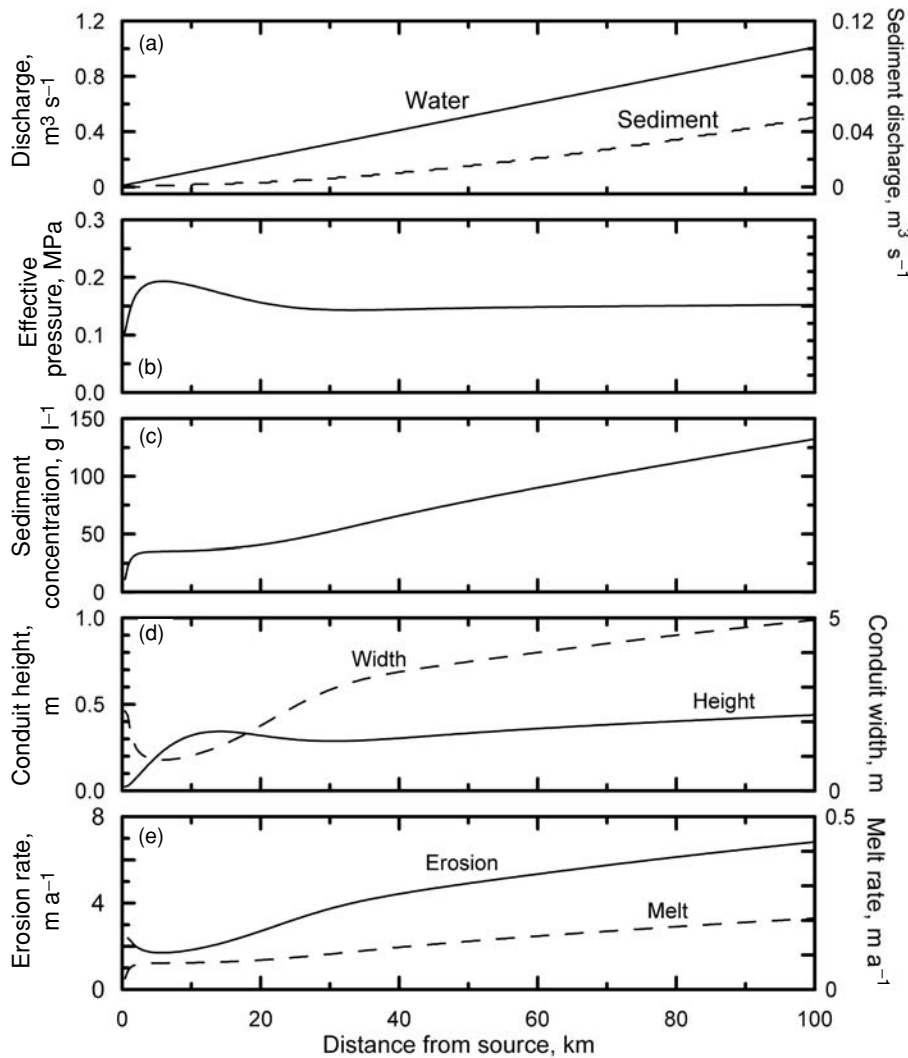


Figure 8.21. (a) Discharge and sediment load in a stream 100 km long beneath an ice sheet of uniform thickness. (b) Effective pressure and (c) sediment concentration in the stream, (d) width and height of the conduit, and (e) melt rate on the conduit roof and sediment flux into conduit by till creep. (Plotted from data kindly supplied by Felix Ng, some of which were used in his 2000a paper.)

$P_c \propto Q_s^{1/2} Q^{-5/6}$ which turns out to be essentially constant. The contribution of roof melting (Figure 8.21e) to Q is negligible in comparison with the total Q so the discharge increases nearly linearly (Figure 8.21a). On the other hand, Q_s increases nonlinearly (Figure 8.21a). This is because \bar{c} also increases (Figure 8.21c), and $Q_s = \bar{c}Q$. The increase in \bar{c} is a consequence of increases in both \bar{u} and τ_w in response to the

increase in h (Figure 8.21d). As deduced earlier, $h \ll \ell$ (Figure 8.21e) so the conduit is wide and low. Generally, dQ_s/ds is substantially more than the $265 \text{ g s}^{-1} \text{ km}^{-1}$ supplied by tributaries. For example, 70 km from the head of the conduit $dQ_s/ds \approx 1800 \text{ g s}^{-1} \text{ km}^{-1}$. Thus the bulk of the sediment load is supplied by erosion of till creeping into the conduit. Indeed, the rate of erosion of the conduit floor ranges from ~ 2 to nearly 7 m a^{-1} (Figure 8.21e). This is substantially higher than the melt rate of $\sim 0.17 \text{ m a}^{-1}$ on the conduit roof.

In the foregoing analysis, the fact that $P_c \propto Q^{-5/6}$ is particularly important because this means that P_w increases as Q increases and a distributed drainage system with many wide low conduits like the one in Figure 8.20 is to be expected. Field evidence also suggests that the drainage is distributed when water pressures are high (or P_c is low). On Storglaciären, Hooke and Pohjola (1994) found that in an area where water pressures were uniformly high, neither dye-trace experiments nor water pressure records gave any indication of channelized drainage along the bed. Indeed, both the dye-trace studies and video observations of the bed suggested a drainage system in which low conduits with high aspect ratios were frequently opened and closed, resulting in episodic movement of water from one pocket to another. Flow velocities were of order 10^{-2} m s^{-1} . These observations were made in an overdeepened basin in which much of the viscous energy may have been needed to keep the water at the pressure melting point. However, they are consistent with observations in boreholes in West Antarctic ice streams (Engelhardt and Kamb, 1997; Kamb, 2001). The holes were drilled with the use of a hot water drill. During drilling, the water level in a hole is at the ice–firn transition, but upon breakthrough to the bed, it falls rapidly until the pressure exerted by the column of water in the hole equals the pressure in the local subglacial hydraulic system. By measuring the rates at which water levels fell, Engelhardt and Kamb calculated that a gap between the ice and the bed that was only $\sim 2 \text{ mm}$ high would be sufficient to account for the observed rate of fall. Analysis of oscillations in water pressure in nearby holes, interpreted as indicating seiche-like flow back and forth between the holes when the second hole reached the bed, also suggested a gap of this size (Kamb, 2001, p. 187).

Engelhardt and Kamb made other observations that provide insight into the nature of the drainage system beneath ice streams. In some holes, water levels dropped more slowly or, rarely, not at all. This suggests that the hole reached the ice–till interface at a place where gaps were smaller or where there was no gap at or near the hole bottom. They also observed that, upon breakthrough, the falling water level resulted in a pressure pulse in other nearby holes on some occasions but not on others. Over time spans of several months they noted that water levels fluctuated

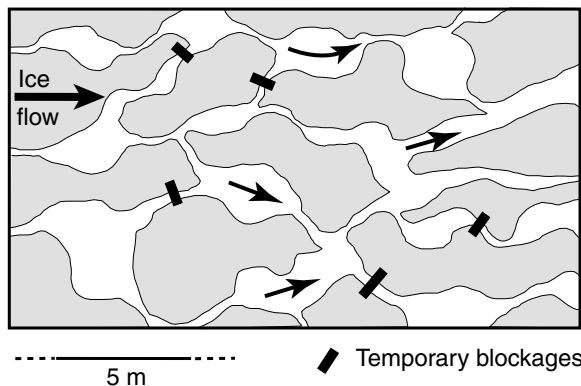


Figure 8.22. Possible geometry of a linked-water-pocket drainage system on till at the base of an ice sheet.

and that the fluctuations in some holes were well correlated, while those in others showed no correlation whatsoever. Indeed, holes that showed good correlation over some time periods showed no correlation over other time periods. Finally, while water levels in holes within $\sim 10^2$ m of one another were often, but not always comparable, levels in more distant holes commonly differed by several meters. Pressures in some holes even rose above the estimated overburden pressure on occasion.

A distributed drainage system consisting of wide shallow linked water pockets (Figure 8.22) with links periodically blocked by deformation of till or ice, would be compatible with all of these observations. Individual pockets might be meters across and millimeters to tens of millimeters deep and links might be centimeters wide. In such a system, one can readily imagine that some holes might bottom in areas between pockets and have difficulty forcing a connection to one, that a pressure wave initiated at one borehole might have to travel a long distance down one tortuous waterway and then up another in order to reach a nearby hole, that when a conduit became blocked the water pressure in it might rise temporarily and be out of phase with pressure variations in other holes, and even that pressures might rise above the overburden pressure in waterways that were blocked downstream but remained connected upstream. Also conducive to development of a distributed drainage system is the fact that the water source, basal melting, is distributed.

In summary, there is good theoretical and observational evidence supporting the conclusion that conduits on till beneath ice sheets are probably wide and shallow and that they form a distributed drainage network. Beneath steeper valley glaciers, conduits may be narrower and deeper, and may form an arborescent drainage system. Consistent with a distributed drainage system on till beneath ice sheets is the observation that landforms characteristic of dendritic drainage networks, such as eskers (see below), are much less common in areas where the ice sheet

moved over a thick till unit (Clark and Walder, 1994). Instead, gravel lenses, some of which are known to be ribbon-like, elongated in the direction of ice flow, are common in till deposited by continental ice sheets. These are interpreted to be the beds of wide shallow subglacial conduits (Eyles *et al.*, 1982; Brown *et al.*, 1987).

Temporal and spatial distribution of drainage system types

Although we have been treating drainage systems on hard beds and soft beds separately, most glaciers rest on bedrock in some areas and on loose material in others. The character of the loose material is also quite variable. Till beneath valley glaciers commonly contains substantial amounts of sand and gravel, while that beneath Antarctic ice streams and that overridden by the Laurentide Ice Sheet in the midwestern United States is much finer. This is probably largely a consequence of the nature of the bedrock supplying the debris: resistant mountain ranges on the one hand and large areas of weak sedimentary rock on the other. The granulometry of the till affects the angle of internal friction and thus its strength (Chapter 7). Also affecting till strength is the effective pressure, which is typically higher beneath valley glaciers and lower beneath ice sheets. These two factors combined make till deformation more likely beneath ice sheets. From the point of view of a valley glacier, coarse till that is not deforming may look very much like rough bedrock and the drainage system developed on it may thus have characteristics of a system on a hard bed.

Thus, the nature of the drainage system must vary from place to place beneath a glacier and from one glacier to another. Where basal melting occurs, the melting is distributed, so some parts of any subglacial drainage system must be distributed. Some systems may be entirely distributed, while others may have an arborescent component. On short time scales, both types of system are likely to be altered or disrupted by flow of the ice, though the linked cavity system, stabilized by the location of cavities on the lee sides of bedrock obstacles, is less subject to such change. On longer time scales, the drainage system at a particular place must vary as the glacier profile changes, the bed is eroded, and subglacial materials are rearranged. The challenge, therefore, is to determine not what type of conduit system is present beneath a particular glacier, but rather the spatial distribution of the different types of system.

Surges

A surge is a rapid advance of a glacier, lasting from a few months to a couple of years, that is unrelated to changes in mass balance. During a

surge, the terminus may advance as much as a few kilometers at speeds of $10^1\text{--}10^2 \text{ m d}^{-1}$, and relatively stagnant ice in the terminus region may be overridden. As a result of the high strain rates, surges are accompanied by dramatic crevassing.

During a surge, a large amount of ice is transferred from a *reservoir area*, which is usually, though not always, in the accumulation area, to a *receiving area* in the terminus region. Accordingly, the surface elevation in the reservoir area is drawn down and the receiving area thickens. Changes in thickness of tens of meters are common.

Surges are followed by a period of quiescence, lasting on the order of decades. During quiescence ice speeds are less than the balance velocity so the glacier thickens in the reservoir area and thins in the receiving area, thus becoming steeper. Before the resulting increase in driving stress can raise speeds to equal the balance velocity, however, another surge occurs. Thus, the process is periodic.

Surges may occur on glaciers resting on either hard beds composed mainly of bedrock, or on soft beds composed of till. Surges may also occur on glaciers that are, at least in part, frozen to their beds. Any complete theory of surging must accommodate all of these possibilities. While such a theory does not yet exist, it is likely that high basal water pressures play a role in all surges.

In the case of temperate glaciers on hard beds, the increase in thickness and speed during build up to a surge means that water pressures must rise higher before the limits of stability of the linked-cavity system are exceeded (Figure 8.16) and the transition to a tunnel system thus initiated. Surging may begin on the upper thicker part of the glacier when this stability limit is not reached as water pressures rise in the late winter or spring (Kamb, 1987). The resulting increase in sliding speed decreases the size of orifices (Figure 8.16), thus further increasing P_w and hence u_b in a positive feedback process. According to this model, surging occurs when the glacier geometry is such that the linked-cavity system can persist for several weeks or months beneath the upper part of the glacier, the destabilizing effect of increases in water pressure being exceeded by the stabilizing effect of the increase in sliding speed. As the surge front moves downglacier, the tunnel system beneath the lower part of the glacier is transformed into a linked-cavity system behind the front (Humphrey and Raymond, 1994). Eventually, however, owing either to further increases in water pressure or to changes in glacier geometry or both, the tunnel system is finally re-established under the bulk of the glacier and the surge ends.

This model is consistent with observations leading up to and during the 1982–1983 surge of Variegated Glacier, Alaska, one of the best studied examples of a surging glacier in the world (Kamb *et al.*, 1985;

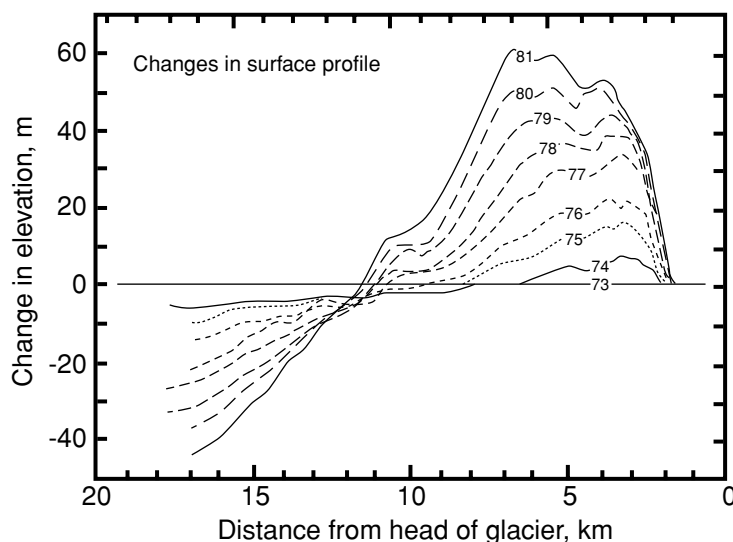
Kamb, 1987). During the decade leading up to the surge, the glacier became thicker and steeper and the surface speed during the winter on the upper part of the glacier increased (Figure 8.23a, b) (Raymond and Harrison, 1988). Calculated and measured rates of internal deformation indicate that the increase in u_s was largely a result of an increase in u_b . The acceleration to surge speeds started in the early winter on the upper part of the glacier (Fig. 8.23c) when decreasing water input is likely to have led to increasing water pressures, and the high sliding speed may have resulted in destruction of a tunnel system. Dye-trace data, mentioned earlier (p. 216), suggest that the drainage system consisted largely of linked cavities at this time. The dye moved slowly and emerged at a number of points across the width of the glacier terminus, and the water was extremely turbid. The speed gradually increased, presumably in the positive feedback process mentioned above. Eventually, large floods of dirty water emerged at the terminus, the glacier surface dropped abruptly, indicating that the water had been in subglacial storage reservoirs, and the surge ended. A dye trace following the surge suggested that the drainage system had reverted to a tunnel configuration. The dye moved quickly and appeared in only one stream, and the sediment concentration was lower. Measurements of water pressure in a borehole confirm that P_w was within 0.5 MPa of the overburden pressure during the surge, with frequent fluctuations to within 0.15 MPa of overburden, and occasionally above it. Before and after the surge it was typically 0.8–1.6 MPa below the overburden pressure, which was 3.6 MPa at the site of the hole.

Presenting a contrary view, Truffer *et al.* (2000) suggest that if a glacier is underlain by till, surges could be initiated when water pressures and shear stresses become large enough to mobilize the till. Any efficient tunnel drainage would be disrupted when the till is mobilized, and would be replaced by an inefficient distributed drainage. A substantial amount of water can be stored in such a drainage system, and water pressures will be high, thus sustaining the fast motion. A sudden release of the stored water would end the surge, as commonly observed.

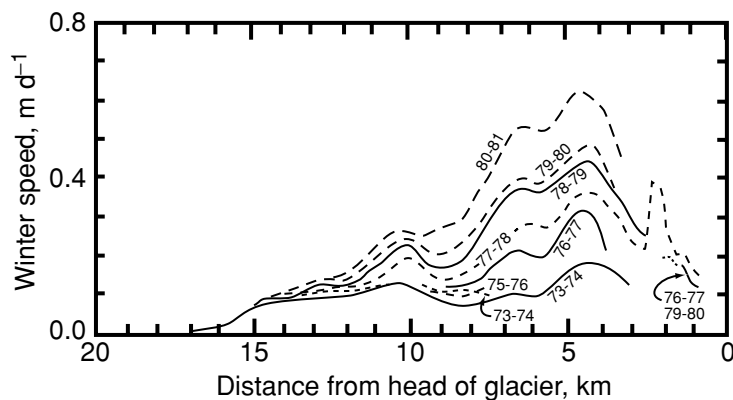
Subglacial drainage paths and the formation of eskers

Traces of subglacial drainage paths are often preserved in the landscape. Eskers are one of the more common geomorphological features that define these paths. Eskers are sinuous ridges of gravel deposited by streams flowing in subglacial tunnels. They typically have undulating crests. They are largest and best developed in areas that were covered

(a)



(b)



(c)

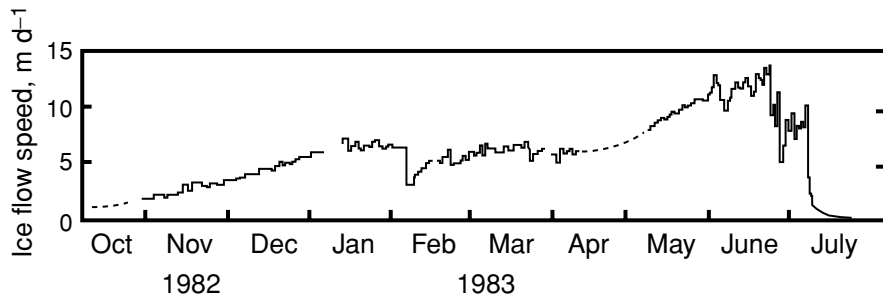


Figure 8.23. Evolution of the: (a) surface profile, and (b) speed of Variegated Glacier during its build up to a surge. (c) Surface speed of the upper part of Variegated Glacier during its surge in 1982–1983. ((a) and (b) from Raymond and Harrison, 1988, Figures 4 and 5b; (c) from Kamb *et al.*, 1985, Figure 2b. Reproduced with permission of the authors, the International Glaciological Society, and the American Association for the Advancement of Science.)

by continental ice sheets during the late Pleistocene. Some are tens of meters in height and tens or hundreds of kilometers in length.

Eskers often appear to follow bizarre paths when viewed from the perspective of people accustomed to the courses of subaerial streams. Eskers may climb hills, trend diagonally down valley sides, and run along valley sides instead of in valley bottoms. Shreve (1972, 1985a, 1985b) has shown that these characteristics can be readily understood from consideration of the hydraulic potential field beneath an ice sheet.

We have noted (Figure 8.6) that englacial water is expected to move in directions that are normal to equipotential planes in a glacier. Similarly, along the bed of a glacier water flow should be normal to the intersections of these equipotential planes with the bed. This is equivalent to saying that water flow down a hillslope should be normal to topographic contours, as topographic contours are the intersections of surfaces that are a constant height above sea level (\equiv equipotential surfaces) with the topography.

Let us consider a couple of examples of this. The solid lines on the map in Figure 8.24a are topographic contours. They depict a gentle slope leading down to a valley that drains to the south. East of the valley there is a ridge that varies in elevation. Now, visualize the situation when an ice sheet covered the landscape, as shown in Figure 8.24b. The surface of the glacier sloped to the east, so the equipotential planes dipped westward. The dashed contours show the intersections of these planes with the landscape. These intersections are precisely analogous to the outcrop pattern that would be formed on the landscape by a westward-dipping sedimentary rock unit.

Under subaerial conditions, creeks would run down the gentle slope on the west side of the map, and then turn south. However, when ice covered the area, subglacial water would not have turned south. Instead, flowing normal to the contours of equipotential, it would have been deflected toward the low point in the ridge. If such a subglacial stream could not carry all of the sediment delivered to it, we might now find an esker crossing the ridge at its lowest point. This is commonly observed in situations in which ridges cross the paths of eskers.

The equipotential planes in the vicinity of the ridge are distorted. This is because the ice is flowing and the pressure is thus higher on the stoss side of the ridge than on the lee. To understand why the planes are distorted as shown, remember that in a situation in which z is constant, the decrease in potential from A to C is the result of a decrease in pressure, P_w (Equation (8.1)). Thus, if some distance away from the ridge a potential drop of 10 units occurs over the horizontal distance \overline{AB} , nearer the stoss side of the ridge a longer distance, \overline{BC} , is required for the same drop because the pressure at C is elevated. In the lee of the ridge, the distortion is in the opposite sense.

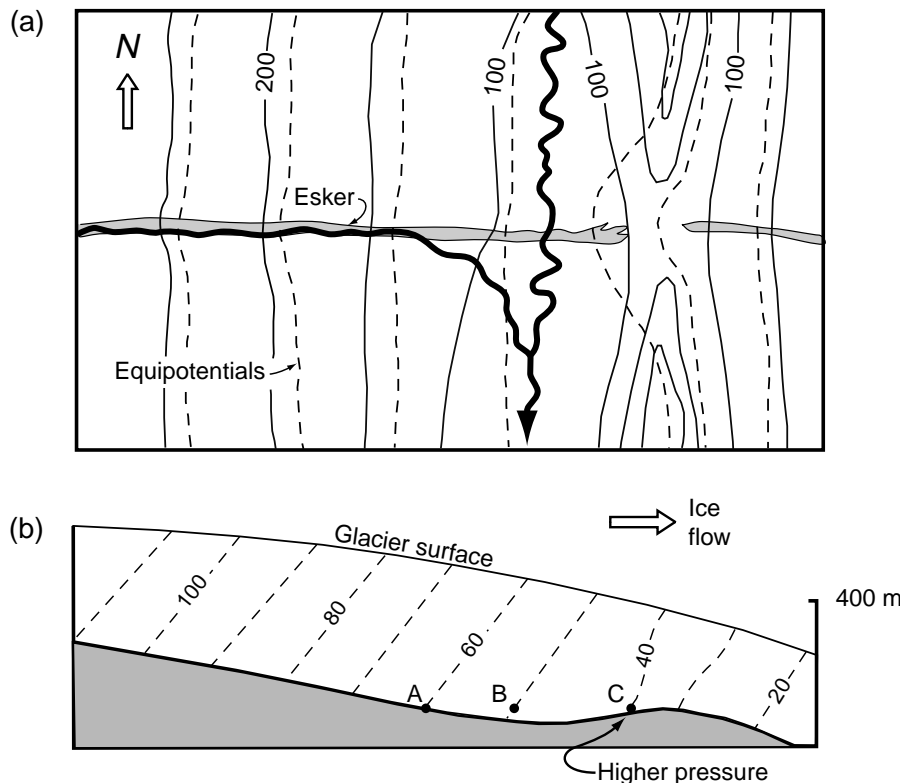
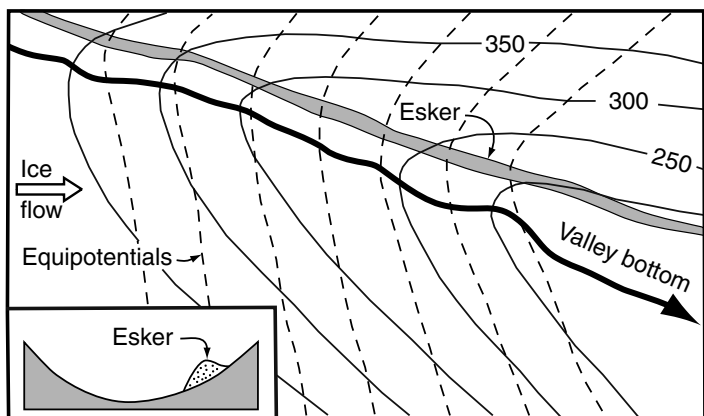


Figure 8.24. (a) Contour map of a landscape on which are superimposed contours (dashed) of equipotential from a time when an ice sheet covered the landscape. (b) Topographic cross section from a time when ice was present, showing the equipotential surfaces in the ice sheet.

Because the velocity of water in the tunnel is proportional to $\partial\Phi/\partial s$ (Equations (8.13) and (8.14)), this distortion of the potential field affects the velocity. In particular, where $\partial\Phi/\partial s$ is higher over the crest of the ridge, the velocity would be higher. This is consistent with the observation that eskers are commonly discontinuous across the crests of such ridges; the higher velocity flow there presumably inhibits deposition.

Another hypothetical situation is shown in Figure 8.25. Here, a topographic valley drains southeastward, diagonally across the direction of glacier flow. As a result, the trough in the equipotential contours is on the valley side rather than in the valley bottom, and this is where an esker would be found if conditions were otherwise suitable for its formation. Again, eskers are commonly found in such positions under these circumstances.

Figure 8.25. Topographic map of a valley trending diagonally across the direction of ice flow, showing how an esker formed in such a situation would be on the side of the valley.



With an understanding of the physical processes that determine the locations of eskers in situations such as those in Figures 8.24 and 8.25, it is sometimes possible to determine the surface slope of the glacier beneath which the esker formed. As an example of this, consider the section of the Katahdin esker near the town of Medway in Maine shown in Figure 8.26a. Ice flow was roughly from north to south in this area. In the northern part of the map, the two branches of the esker follow respective branches of the Penobscot River, but are slightly offset from the river, up onto the valley sides, in the downglacier direction. However, south of the junction between the two branches, the esker departs from the valley of the Penobscot to run *up* the valley of a small tributary and then across the divide between this tributary and another small southward-flowing creek. To clarify the reasons for this, Shreve (1985a) constructed a series of maps of the potential field in the Medway area for different possible ice surface slopes. The one that best explained the course of the esker (Figure 8.26b) utilized a surface slope of 0.0048.

By determining ice-surface slopes in this way at a number of locations along a single esker system, one might be able to reconstruct the surface profile of an ice sheet, and from this calculate the basal shear stress. For such a reconstruction, however, the entire esker system must have been active simultaneously. In situations in which contemporaneity can be demonstrated, this is one of the few techniques available for determining surface profiles of vanished ice masses.

Sediment supply to eskers

Eskers form where the sediment load delivered to a subglacial stream exceeds the transport capacity of the stream. The debris-laden basal ice

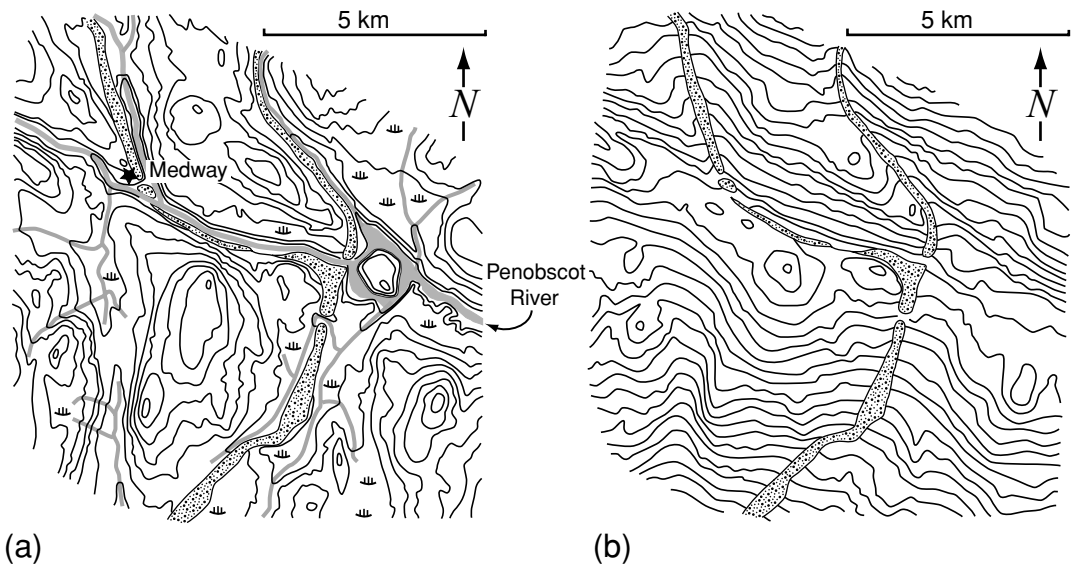


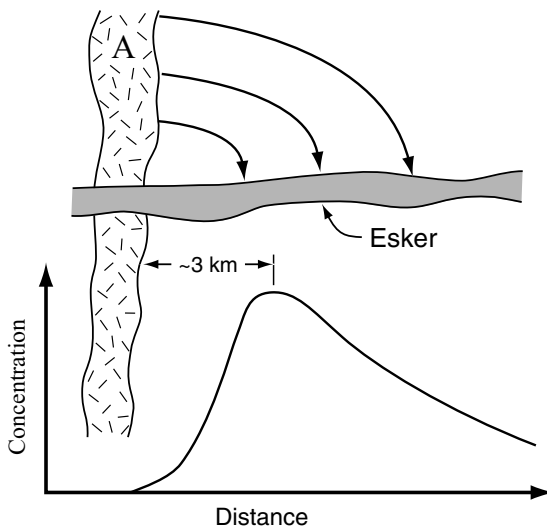
Figure 8.26. (a) Map of the Penobscot River and a section of the Katahdin esker near Medway, Maine. Near the middle of the map, the esker leaves the valley of the river and trends south-southwestward up a small tributary valley. (b) Map of equipotential contours beneath a glacier with a southward surface slope of 0.0048. The esker generally follows a trough in the potential surface. (After Shreve, 1985a. Reproduced with permission of the author and the Geological Society of America.)

of the glacier is one source of such sediment. As the energy dissipated by the flowing water melts this ice, debris is released and an inward flow of ice toward the tunnel is induced.

A nice demonstration of this process is provided by lithologic pebble counts from the Great Pond section of the Katahdin esker, down-flow from a point where the esker crosses bedrock units of distinctive lithology (Van Beaver, 1971). The concentration of pebbles of these lithologies in the esker reaches a maximum about 3 km down-flow from the point where the esker crosses the units (Figure 8.27). Had the stream been acquiring the pebbles directly from the bedrock, a difficult task at best once the esker began to develop on top of the rock, the concentration should have peaked at the down-flow edge of the unit. Rather, we infer that it was the glacier that eroded the pebbles from the bed and carried them along arcuate paths, as shown, until they were released into the stream (Shreve, 1985a).

Calculations suggest that this source of sediment is quite adequate to overload a subglacial stream, leading to deposition. For example, suppose the median (by weight) grain size in an esker is 0.03 m, and that

Figure 8.27. Schematic sketch showing variation in concentration of lithology A in an esker down-flow from the point where the esker crosses the outcrop of this lithology. Rocks eroded by the glacier are carried along arcuate paths downglacier and inward toward the tunnel.



the esker is forming in a tunnel beneath a glacier with a surface slope of 0.005. Then, based on equations for sediment transport in gravel-bedded streams (Parker, 1979), a conduit ~ 0.7 m high with a discharge of $1.0 \text{ m}^3 \text{ s}^{-1}$ per meter of conduit width would be required to transport this material, and the sediment load would be about $0.04 \text{ m}^3 \text{ d}^{-1}$ per meter width. Under these conditions, the energy available for melting would be $\sim 50 \text{ J m}^{-2} \text{ s}^{-1}$, and the melt rate on the conduit roof would be $\sim 0.014 \text{ m d}^{-1}$ (Equations (8.9) and (8.12)). If the basal ice contained 10% debris by volume, the debris released by this melting would overload the stream after it flowed along the conduit for only 30 m ($0.014 \times 0.10 \times 30 = 0.04 \text{ m}^3 \text{ d}^{-1}$ per meter width).

In some eskers, however, some of the water and sediment load may have been derived from the glacier surface by way of moulin. For example, Mooers (1990a) found eskers in central Minnesota that headed in conical hills of glaciofluvial gravel. He inferred that the hills were formed by sediment-laden supraglacial streams that reached the glacier bed through moulin and deposited a significant fraction of their load there before continuing to the margin through the subglacial conduits in which the esker formed.

Size and location of water conduits on eskers

It is natural to assume, as a first approximation, that the tunnel within which an esker formed was comparable in size to the esker (Figure 8.28a). This is consistent with the observation that some eskers are composed of coarse gravel with a dearth of sedimentary structures. However, this

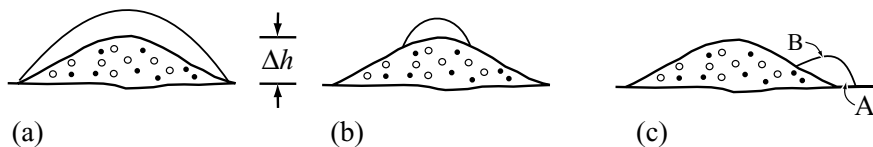


Figure 8.28. Esker of height Δh with: (a) conduit comparable in size to esker; (b) small conduit on top of esker; and (c) small conduit low on side of esker.

may be a poor assumption in many instances, as the flux of water implied by a tunnel of this size would be horrendous. As basal melt rates are relatively low, such high fluxes would require either collection of water from a very large area of the bed or a surficial source. In some areas the former is improbable as the drainage area between the heads of eskers and inferred ice divides is insufficient. Likewise, surficial sources many tens of kilometers from the glacier margin are problematical, as near-surface ice temperatures are likely to be well below 0°C at these elevations, and it is not clear how moulin could develop through a thick cold surface layer.

An alternative is that the tunnel was comparatively small (Figure 8.28b). This might further suggest that the esker formed slowly over a period of many years.

If the tunnel is small compared with the size of the esker, it is also of interest to determine whether it is on top of the esker or low on the side (Figure 8.28c). The intersections of upglacier-dipping equipotential planes with an esker will be convex down-flow, as in a ridge, and streams are not noted for flowing along ridge crests. This suggests that the conduits should be low on the side of the esker. However, one might then expect eskers to be broad-crested and low rather than sharp-crested and high, as is commonly the case.

Shreve (1985a) suggests that debris washed from the crest of the esker down the flank, together with that released from ice near the bed, which has a higher debris content, will accumulate on the lower side of the conduit, at A in Figure 8.28c. Melting will then be concentrated at B and the conduit will migrate back to the top of the esker. He visualizes a situation in which the conduit spends most of the time on top of the esker, but periodically slips down one flank or another and then migrates back to the top. However, the steepest potential gradient would still be away from the esker so it is not clear why the conduit would migrate back up onto the esker rather than laterally away from it, leaving a sheet of gravel in its wake.

Alternatively, this problem can be addressed using the following argument, adapted from (Lliboutry, 1983). If the height of the esker is Δh

(Figure 8.28), and there are two channels that are connected hydraulically, one on top of the esker and one on the side, then:

$$\begin{aligned} P_w^{\text{side}} &= P_w^{\text{top}} + \rho_w g \Delta h \\ P_i^{\text{side}} &= P_i^{\text{top}} + \rho_i g \Delta h \end{aligned} \quad (8.26)$$

The pressure causing tunnel closure is $P_c = P_i - P_w$, so subtracting the first of Equations (8.26) from the second:

$$P_c^{\text{side}} = P_c^{\text{top}} - (\rho_w - \rho_i)g \Delta h$$

Now, from Equation (8.18), holding all other factors constant and using $n = 3$, we find that $Q \propto P_c^{12}$. Thus:

$$\frac{Q^{\text{top}}}{Q^{\text{side}}} = \left[\frac{P_c^{\text{top}}}{P_c^{\text{side}}} \right]^{12} = \left[\frac{P_c^{\text{side}} + (\rho_w - \rho_i)g \Delta h}{P_c^{\text{side}}} \right]^{12} \quad (8.27)$$

Thus, $Q^{\text{top}} > Q^{\text{side}}$ so the conduit on top of the esker will expand at the expense of that on the side. Phrased differently, owing to the nonlinearity of the flow law, the increase in potential closure rate as one moves down off the esker is not offset by the increase in P_w , so closure rates are higher in the conduit on the side, and water in it is forced up onto the top of the esker.

The model of Figure 8.28b is consistent with the observation that sedimentary stratification in eskers is commonly discontinuous, both laterally and longitudinally. The stratification, defined by variations in grain size, could be produced by transverse variations in conduit height combined with lateral migration of the conduit even if flow through the conduit were steady. Pseudoanticlinal bedding is also commonly observed, with beds mimicking the transverse profile of the esker. Such a form would be likely if the conduit periodically slipped down the flank and then migrated back to the crest as Shreve suggested.

In summary, although questions remain, the shape and stratigraphy of sharp-crested eskers suggest that some combination of the processes Shreve identified and those summarized by Equations (8.26) probably result in a tendency for conduits to be on tops of eskers, despite the potential gradient favoring positions on the flanks.

Ramp structures and esker nets

The analysis leading to Equation (8.27) is valid as long as $u = \dot{m}$. However, near the terminus of a glacier where the ice is thin, \dot{m} may exceed u as we discussed in connection with Figure 8.11b. In this situation, the flow may slip off the side of the esker and build daughter eskers parallel to the parent, forming an *esker net*. Alternatively, the conduit may expand leading to deposition of coarser sediment in a

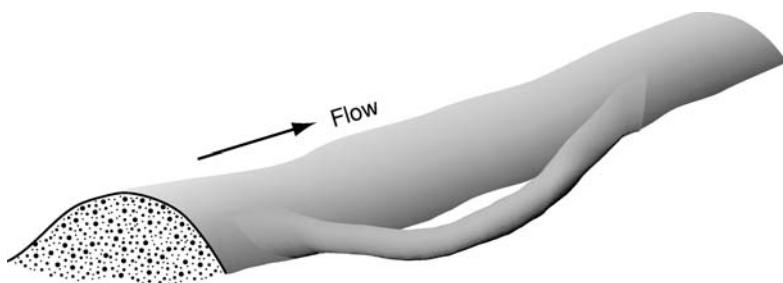


Figure 8.29. Sketch of small daughter esker diverging from and later rejoining parent esker. This may occur near the margin where the ice is thin and conduit closure rates are low. (Bruce Hooke assisted with artwork.)

massive wedge-shaped deposit that increases in height downstream. Steep distal slopes mark the downstream ends of these wedges, which I call *ramp structures*.

Esker nets were apparently first described by Stone (1899), who called them reticulate eskers. A particularly good example is found in a valley called Atnedalen in Norway. Following the esker down-flow, one first encounters several situations in which a small esker drops down off the side of the parent, parallels it for a short distance, and then climbs back up onto it again (Figure 8.29). This is probably because the ice thickness required to keep the conduit on top of the esker was becoming marginal. Closer to the ice margin, where the ice was still thinner, these daughter eskers grow to nearly the same size as the parent, forming an anastomosing pattern of ridges. Still further downstream, the ridge character becomes indistinct and the system merges into a kettled outwash plain.

Esker nets and ramps are characteristic of the Katahdin esker. A typical segment of the esker begins as a relatively small, sharp-crested ridge. Down flow, the ridge increases in size, at first rather gradually, but near the end more rapidly. Some segments end in ramps. Others end in esker nets or in a combination of the two forms (Figure 8.30). Downstream from ramps and esker nets there is commonly either a fan or a delta built into the sea in which the glacier terminated. These fans and deltas are composed of sand and fine gravel that was flushed through the enlarged conduit as coarser material was deposited. The transition from ramp to fan has been described well by Ashley *et al.* (1991, p. 112). The next segment down flow may develop from a continuation of one of the ridges in an esker net, may emerge from a fan or delta, or may pick up after a short gap.

Tunnel valleys

The margins of many ice lobes of the southern Laurentide Ice Sheet are marked by broad, relatively straight valleys, oriented normal to

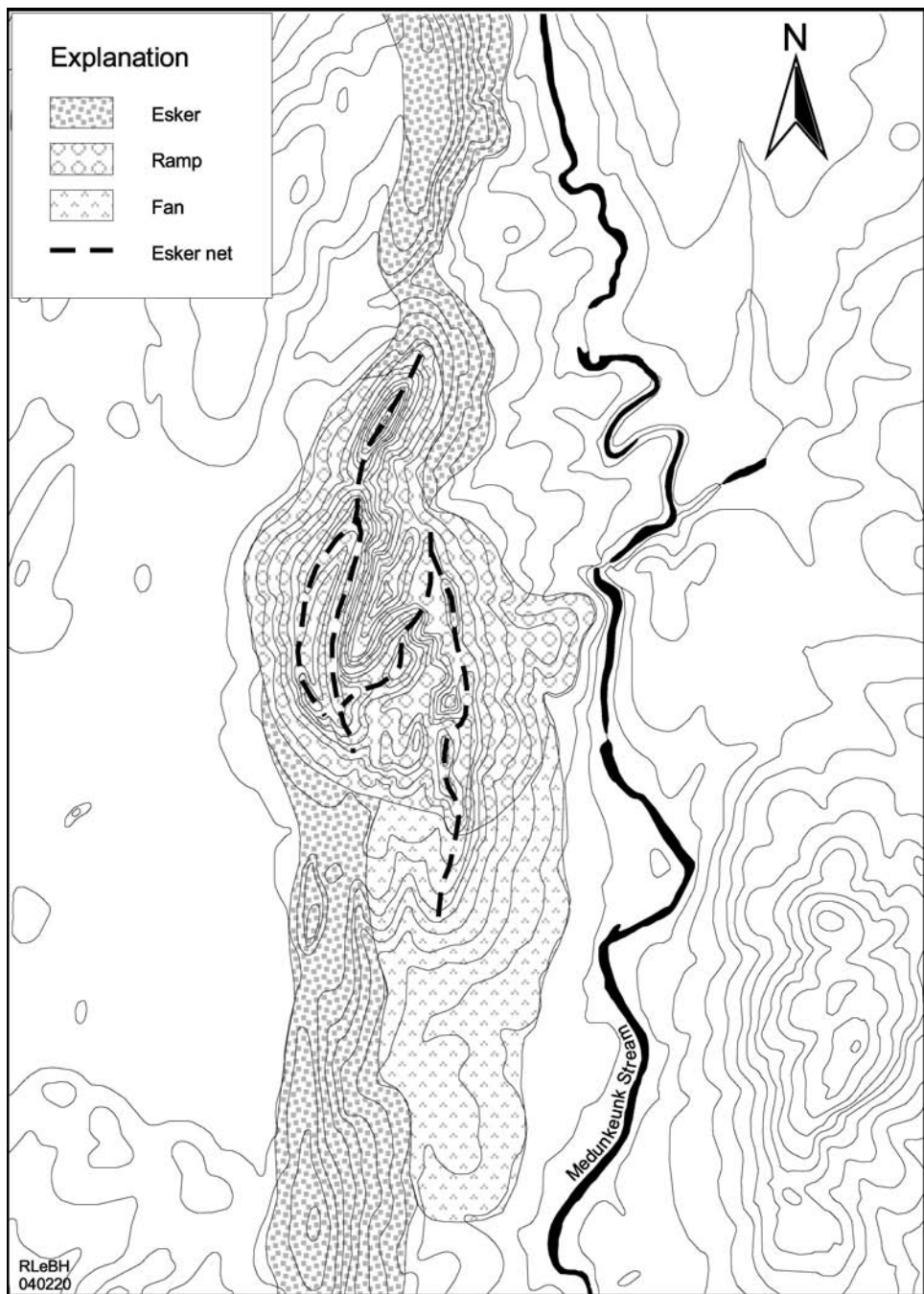


Figure 8.30. Map of a section of the Katahdin esker showing a ramp and esker net. There is a fan down-flow from the ramp. (The site is 4.5 km NNE of Lincoln Center, Maine.)

the former ice margin. These features, apparently first described by Ussing (1903) from Jylland in Denmark, are called *tunnel valleys*. They are typically 10–20 km long, although they may be shorter or longer; a few hundred meters wide; and ~10 m deep, though depths as great as 70 m have been reported (Wright, 1973) and the depth of any fill is generally not known. Small eskers are occasionally associated with the valleys (Johnson, 1999; Mooers 1989), and some valleys have tributaries or distributaries. The valleys end at former ice margins, where they debouch onto proglacial gravel fans. Thus, they must have been formed subglacially. The lack of evidence for modification by overriding ice implies that any subsequent ice movement was probably not very vigorous. Some tunnel valleys in Minnesota trend across the regional gradient and are cross cut by present stream courses (Wright, 1973). Others ascend adverse gradients near their termini (Cutler *et al.*, 2002; Mooers, 1989). Both characteristics suggest that they were excavated by pressurized subglacial water. Mooers describes one situation in which a tunnel valley terminating at one recessional moraine is cross cut by a younger tunnel valley terminating at a younger recessional moraine. The process of formation thus must have been intermittent, with the earlier valley becoming completely closed, presumably by infilling with ice, before the later one formed. Tunnel valleys are rare or absent along the most southerly margin of the Laurentide Ice Sheet, suggesting that they may be characteristic of colder environments where frozen bed conditions were likely to have been present along the ice margin (Cutler *et al.*, 2000). This, however, is controversial.

The origin of the water and the nature of the flows that cut the tunnel valleys are actively debated. Was the water from basal melt alone, or was there a contribution from the surface? Was the water flow continuous over a period of decades or centuries, or was the water released catastrophically? Wright argued for a catastrophic release of subglacial water because he thought that a number of tunnel valleys were carved simultaneously and that the ice was cold enough to preclude drainage from the surface. Cutler *et al.* found that some fans at the ends of tunnel valleys consisted of tens of meters of sand and gravel overlain by a bed, 3–5 m thick, containing boulders up to 2 m in diameter. They thought the gravel might have been deposited by superglacial melt-water reaching the bed through moulin near the margin. The boulder bed, however, seemed to require a water flux greater than could be supplied by superglacial water or by steady-state basal melt. Accordingly, they suggested that it was deposited by subglacial water that was released when a seal was breached. They believed that the seal was a marginal zone in which the ice was frozen to the bed. Relict permafrost features,

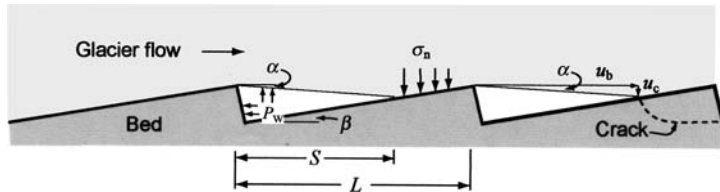


Figure 8.31. Bed geometry and parameters used in Hallet's (1996) analysis of glacier quarrying.

pollen evidence, and numerical modeling all suggest that a wedge of frozen ground might well have extended several kilometers in under the ice sheet at this time (as in the left diagram in Figure 6.16). Patterson (2002) thinks that sapping, driven by the high gradient in hydraulic head across a marginal seal, may be an important process in initiating an outburst.

Water pressure and glacier quarrying

Quarrying is an important process of glacier erosion. In quarrying, blocks of bedrock must first be loosened, either along preglacial joints or along fractures formed by subglacial processes. Then they must be entrained by the glacier. Because rock fragments that have been loosened but not removed are uncommon on deglaciated bedrock surfaces, Hallet (1996) argues that loosened blocks are readily entrained. He thus concludes that fracture must be the rate-limiting process.

To analyze the stresses causing fracture, Hallet considers an idealized bed consisting of steps as shown in Figure 8.31. The distance between steps is L . The treads slope upglacier at an angle β . The crests of the steps are at the same elevation, so the average bed slope is 0. Ice sliding over the crest of one step separates from the bed, forming a water-filled cavity under pressure P_w . The ice regains contact with the bed a distance S from the crest. The slope of the cavity roof is α . The glacier is supported in part by water in the cavity and in part by a vertical stress, σ_n , on the crest of the step, so summing forces:

$$P_i L = P_w S + \sigma_n(L - S) \quad (8.28)$$

The slopes α and β are related by:

$$S \tan \alpha = (L - S) \tan \beta \quad (8.29)$$

From Equation (8.28), noting that the effective pressure (or pressure causing closure of the cavity), P_c , is $P_i - P_w$, we obtain:

$$\sigma_n = P_i + P_c \frac{S}{L - S} \quad (8.30)$$

Now σ_n acts on the crest of a step, promoting fracture, but P_w supports the rock face, resisting fracture. Thus, the total stress causing fracture (the non-hydrostatic or deviatoric stress – see Chapter 2) is:

$$\sigma'_n = \sigma_n - P_w = P_c \left(\frac{L}{L - S} \right) \quad (8.31)$$

To determine σ'_n we need to know S .

Hallet assumes that the rate of closure of the cavity roof, u_c , can be approximated by a relation of the form of Equation (8.3), thus:

$$u_c = kSP_c^3 \quad (8.32)$$

where k is a constant involving, among other things, the ice viscosity parameter, B . If u_c is considered to be vertical and uniform over the cavity roof and u_b is the horizontal sliding speed, then:

$$\tan \alpha = \frac{u_c}{u_b} \quad (8.33)$$

Combining Equations (8.29), (8.32), and (8.33) then yields¹:

$$S^2 \frac{kP_c^3}{u_b} + S \tan \beta - L \tan \beta = 0 \quad (8.34)$$

Thus, for a given L , P_c , u_b , and β , Equation (8.34) can be solved for S and Equation (8.31) then gives σ'_n .

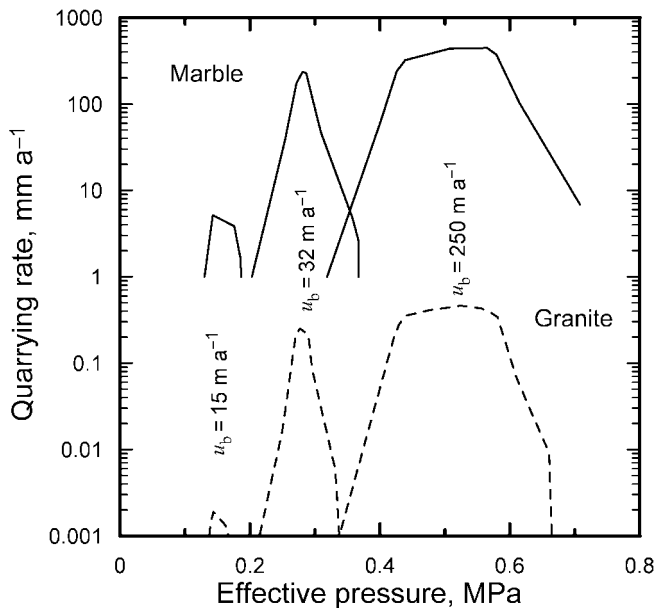
Hallet then uses principles of fracture mechanics (Chapter 4), into which we will not delve further here, to estimate the rate of crack growth. In his calculations, deviatoric stresses in the ice are constrained to be less than the tensile strength of ice. By assuming that the crack is initiated at a distance $(L - S)$ from the crest of the step (Figure 8.31), he then calculates the quarrying rate (Figure 8.32) for two rock types, a granite and a marble. The softer marble erodes 1000 times faster than the granite!

As expected, quarrying rates increase with sliding speed. In addition, as u_b increases maximum quarrying rates occur at higher effective pressures. To understand the latter, note in Equation (8.31) that as $S \rightarrow L$, the term in brackets increases without bound. An increase in S can result either from an increase in u_b or from a decrease in P_c . This is because both of these changes cause ice in the roof of the cavity to regain contact with the bed further from the crest of the preceding step. If an increase in S is a consequence of a decrease in P_c , σ'_n does not increase so much because the two effects offset one another in Equation (8.31) (note that $S = L$ when $P_c = 0$ because the glacier is then afloat). Thus, quarrying

¹ This differs from Hallet's analysis because he takes u_c to be normal to the cavity roof. Considering the approximations in Equation (8.32) and the simplifications achieved by using Equation (8.33), taking u_c to be vertical seems justified.

Figure 8.32. Theoretical rates of quarrying of marble (solid lines) and granite (dashed lines) on a bed like that shown in Figure 8.31.

Parameters used in the calculation were $L = 10$ m, $\beta = 11.5^\circ$, and $k = 5 \text{ a}^{-1} \text{ MPa}^{-3}$. (Based on Hallet, 1996, Figure 2. Reproduced with permission of the author and the International Glaciological Society.)



rates have maxima at some fairly low P_c (Figure 8.32). On the other hand, if the increase in S is a consequence of an increase in u_b , then the maxima in σ'_n and the quarrying rate can occur at a higher P_c . Also noteworthy in Figure 8.32 is the sensitivity of the quarrying rate to P_c ; under 450 m of ice, for example, P_c may vary from 0 to ~ 4 MPa, but significant erosion occurs over $< 10\%$ of that range.

Because stresses that can be generated in the rock in this way are limited by the tensile strength of ice, the maximum steady σ'_n that can be applied to a rock is about 10 MPa, while tensile strengths of strong crystalline rocks without macroscopic flaws generally range from 10 to 20 MPa (Hallet, 1996). Water-pressure fluctuations in cavities in the lee of a bump on a glacier bed provide a mechanism for fracturing this strong rock. They also accelerate propagation of fractures in weaker rocks or those with macroscopic flaws and play a role in the entrainment process (Röthlisberger and Iken, 1981; Iverson, 1989). Let us consider fracture first.

Water-pressure fluctuations are particularly rapid where moulin connections from the surface of a glacier to the bed. Water inputs from rain or melt can then cause subglacial cavities to fill and drain faster than they can adjust by flow of the ice. The resulting pressure fluctuations transfer the weight of the glacier first to and then from the tops of bumps. Under 250 m of ice, for example, the pressure could

vary from a relatively uniform 2.2 MPa on all faces of a bump to over 12 MPa, say, on the top, and nearly zero on the lee face.

All rocks contain microcracks, fractions of a millimeter to a few millimeters in length, and the stress variations resulting from these water pressure fluctuations can lead to propagation of tensile fractures at the tips of favorably oriented cracks (Griffith, 1924). This can occur even at stresses well below the experimentally determined tensile strength of the rock (Atkinson and Rawlings, 1981; Atkinson, 1984; Segall, 1984). The likelihood of crack growth increases when the water pressure within cracks remains elevated while that in an adjacent cavity drops, or when stress corrosion resulting from repeated pressure changes reduces the strength of the rock (Iverson, 1991). Even higher and more concentrated stress differences can result when a cobble or boulder is dragged over a bump by the ice. Thus, it now seems safe to conclude that even sound crystalline rocks can be fractured subglacially through the action of ice and water, despite the fact that the ice is weaker than the underlying rock.

Boulders with smooth stoss faces and plucked lee faces that are embedded in till, called *bullet boulders*, provide convincing field evidence for subglacial fracture (see, for example, Sharp, 1982). These boulders must have been transported by the ice and become lodged in the till as the basal ice melted. They would not have had their characteristic shape prior to lodgement, nor could they have been transported to their present location, intact, if they had pre-existing fractures. Thus their shape must have been produced by the overriding glacier after they became lodged.

Once a block of rock is isolated by fractures, bed-parallel forces tending to slide it out of position must exceed frictional forces tending to hold it in place in order for entrainment to occur (Iverson, 1989). Both the bed-parallel and the frictional forces are affected by fluctuations in water pressure. As noted earlier (Figure 7.6), pressure-release freezing may occur on tops of bumps when increases in water pressure in cavities transfer part of the weight of a glacier away from the bumps (Robin, 1976), and similar cold patches can also develop owing to simple flow of the ice from the stoss side of a bump to its crest. Both processes increase the drag exerted by the ice on the block. The latter process is more effective at higher sliding velocities, so increases in subglacial water pressure that cause increases in sliding speed should increase its effectiveness.

Frictional forces resisting dislodgement of loosened blocks are reduced as water pressures rise (Iverson, 1989). This is because the normal pressure that ice exerts on a bedrock surface upglacier from a

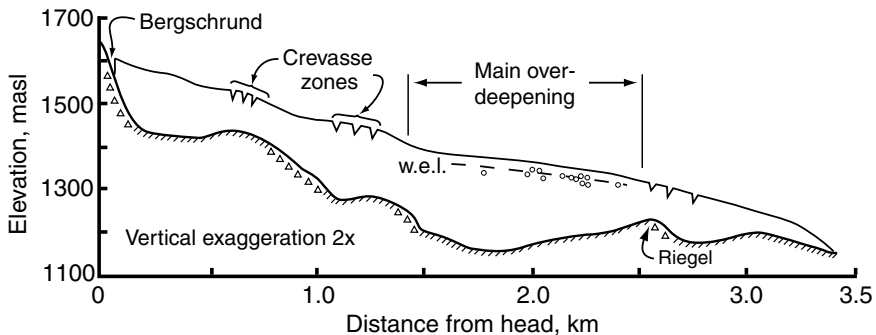


Figure 8.33. Longitudinal section of Storglaciären, Sweden, approximately along a flowline showing cirque, overdeepened basins, water-input points (crevasse zones and bergschrund), and inferred locations of quarrying (indicated by $\Delta\Delta$). Here w.e.l. = water equivalent line; circles (o) show heights of water in boreholes. (Modified from Hooke, 1991, Figure 2.)

cavity is reduced, thus decreasing the friction along fractures that bound loosened blocks. In addition, once fractures are well-developed and in hydraulic communication with cavities, increases in water pressure in the fractures themselves reduce the effective pressure across fracture surfaces.

In summary, it appears that steady flow and low effective pressures can fracture weaker rocks or rocks with macroscopic flaws. However, fluctuations in subglacial water pressure and associated transient changes in glacier sliding speed facilitate quarrying, particularly of more resistant lithologies. Abrupt reductions in water pressure promote subglacial fracture while increases, whether rapid or more gradual, promote the dislodgement of loosened blocks.

Origin of cirques and overdeepenings

Cirques and overdeepened basins in glacier beds, such as those in Figure 8.33, are similar in form. Both have steep headwalls and both tend to have beds with adverse slopes. We will discuss the headwalls first.

Headwalls have ragged surfaces, apparently resulting from fracture and removal of blocks of rock. This morphology suggests that they are eroded by glacial quarrying. As we have just discussed, quarrying appears to be a result of water-pressure fluctuations on time scales of hours to days. These fluctuations seem to be most pronounced close to areas of water input (Hooke, 1991). In the case of cirques, the water input is localized by the bergschrund, and in the case of overdeepenings, by crevasses that form over the convexities at their heads

(Figure 8.33). Thus, these water inputs and resulting pressure fluctuations occur at precisely the points where erosion is necessary to maintain the headwalls.

In the case of the headwall of an overdeepening, a positive-feedback process appears to be operating. Crevassing over a minor convexity in the bed, an initial perturbation, localizes water input and hence erosion. The erosion is concentrated on the downglacier side of the convexity. Thus, as the erosion progresses, the convexity is amplified, resulting in further crevassing.

The other defining characteristic of cirques and overdeepenings is the gentle adverse slope of their beds. The steepness of this slope may be limited by the ability of water to flow along the bed. For example, if $k = 0.309$ and $\rho = 916 \text{ kg m}^{-3}$ in Equation (8.12), it is easy to show (by using Equation (8.5)) that $\dot{m} = 0$ when $dz/ds = -1.7 dH/ds$. (This is left as an exercise for the reader. Note that the constant of proportionality is lower if the water is partially or completely saturated with air and a higher value of k is thus used.) In other words, when the adverse bed slope, dz/ds , is 1.7 times the surface slope, all of the energy dissipated in the flowing water is needed to warm the water to keep it at the pressure melting point as the ice thins in the downglacier direction, and none is available to melt more ice (see Equation (8.10) and discussion of Figure 8.11c). Where the adverse slope is steeper, Equation (8.12) predicts, mathematically, that \dot{m} should become negative, so water should freeze in the conduit, and Equation (8.24) then predicts that $P_w > P_i$. Indeed, measured water pressures in the main overdeepening of Storglaciären are quite close to the overburden pressure (Figure 8.33).

Actually, field data suggest that the water, rather than remaining in the conduit, spreads out in a maze of linked water pockets with flow velocities that are too low to move significant amounts of sediment (Figure 8.22). If the adverse slope is steep enough, *frazil ice* (platelets of ice that form in the flowing water) may form and further inhibit flow. Because the subglacial drainage system is thus disrupted in overdeepenings, water is forced to follow englacial conduits through them (Hooke and Pohjola, 1994).

Where subglacial streams are thus not available to flush out the products of erosion, a layer of till must accumulate. Substantial amounts of this sediment can be entrained if frazil ice forms and is eventually incorporated into the glacier sole (Lawson *et al.*, 1998). Continuity considerations suggest that the till layer will increase in thickness until the downglacier mass transfer by deformation within it and entrainment by frazil ice at its surface equals sediment production by erosion. Such a sediment layer would protect the bed throughout the downglacier reaches

of an overdeepening, thus concentrating erosion at its head. This is probably why overdeepenings exist, and why their longitudinal profiles are characteristically asymmetrical with the deepest point at their upglacier ends (Hooke, 1991).

Summary

In this chapter we have investigated the glacier hydraulic system, starting with the vein network along lines of intersection among three ice crystals and progressing through the englacial to the subglacial system. We found that theoretically water flow in the englacial system should be normal to equipotential surfaces that dip upglacier at an angle roughly 11 times the slope of the glacier surface. Along the bed, water flow is normal to the intersections of these equipotential surfaces with the bed.

Water moving through conduit systems in or beneath glaciers releases viscous energy. This energy melts ice on conduit walls. However, the pressure in the water is generally less than that in the surrounding ice, so the conduits close by creep. In the steady state, the water pressure is everywhere adjusted so that $u = \dot{m}$. Along the bed u is inhibited by drag. In addition, melting is concentrated low on the walls when tunnels are not full of water. Thus, the steady-state conduit shape is likely to be broad and low.

The water pressure in conduits increases upglacier, approximately in proportion to the increase in ice thickness over the conduit. In conduit systems consisting of tunnels, P_w decreases as Q increases, but in systems consisting of cavities in the lee of bedrock steps linked by orifices, P_w increases as Q increases. Thus, tunnel systems are believed to be arborescent, while linked-cavity systems are distributed. In all probability, these are end members of a continuum of drainage system types.

Tunnel systems are likely to collapse when discharges are low, tunnels are shrinking, and water pressures are increasing. If the tunnel system cannot regenerate when discharges increase again, water pressures may rise high enough to initiate a surge.

In conduits between a glacier and a deformable bed, the steady-state condition is one in which, in addition to $u = \dot{m}$, erosion of sediment by the flowing water must balance the flux of sediment into the conduit. Under these conditions, conduit systems are likely to be distributed. Analysis suggests that this condition is most likely when glacier surface slopes are low and water pressures high, as is commonly the case beneath ice sheets. Beneath valley glaciers, water pressures are typically lower, so bed deformation is not as likely.

In the last part of the chapter, we investigated three problems of geomorphic interest: the formation and courses of eskers, the origin of tunnel valleys, and the erosion of cirques and overdeepenings. Many esker characteristics can be understood in terms of gradients of hydraulic potential at the base of an ice sheet. The source of the water that carved tunnel valleys is unclear, but indications are that large discharges were involved at least occasionally. Erosion of hard bedrock by glaciers is greatly facilitated by fluctuations in water pressure at the bed.

Chapter 9

Stress and deformation

In this chapter we will derive general equations for calculating the force per unit area, or traction, on a plane that is not parallel to the coordinate axes, and then use these equations to determine the orientation of the plane on which tractions are a maximum. We will see how this leads to the concept of the *invariant* of a tensor, and show that this provides the fundamental basis for Glen's flow law. Then we derive the stress equilibrium equations.

In the second half of the chapter we derive expressions for strain rates in terms of velocity derivatives, and develop some relations based on these expressions and some other basic equations. This will set the stage for calculating stresses and velocities in a very simple ice sheet, consisting of a slab of ice of uniform thickness on a uniform slope (Chapter 10) and for investigating some more realistic problems (Chapter 12).

Stress

Although we have been referring to stresses and strain rates throughout the last few chapters, we will now enter into a much more detailed discussion, involving the tensor properties of these quantities. The reader may find it helpful, therefore, to review the section on stresses and strain rates in Chapter 2.

General equations for transformation of stress in two dimensions

Consider a domain in a slab of material of unit thickness (measured normal to the page) as shown in Figure 9.1. Stresses are uniformly

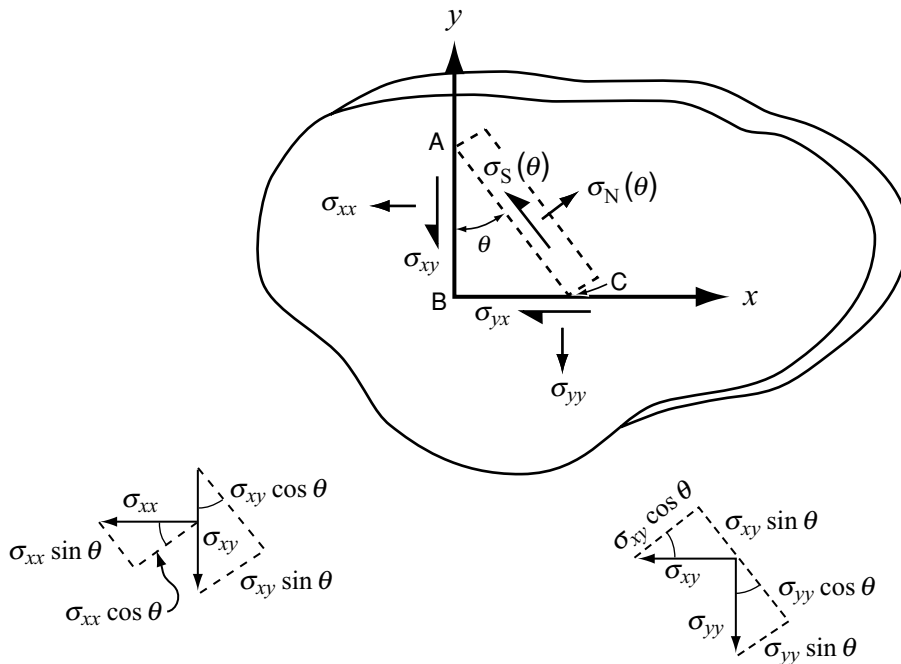


Figure 9.1. Stresses on a triangular prism of material isolated from a domain.

distributed over the domain; in terms of the $x-y$ coordinate system shown, they are σ_{xx} and σ_{xy} in the x -direction, and σ_{yy} and σ_{xy} in the y -direction. Shear forces on any small element of the domain of unit size in the x - and y -directions must be in equilibrium if there is to be no tendency for the element to rotate. Thus, $\sigma_{xy} = \sigma_{yx}$, so we will use σ_{xy} to represent both. Now cut the domain along plane \overline{AC} , which makes an angle θ with the y -axis. This plane has an area which we designate dA . As a consequence of the stress field in the slab, the edges of the cut will have a tendency to move with respect to one another. We will ignore the part of the domain to the right of the cut, and ask what forces must be applied on dA to balance this tendency. Specifically, we wish to find the stress vectors $\sigma_N(\theta)$ and $\sigma_S(\theta)$ on this plane, where the subscripts N and S refer to normal and shear respectively.

To do this, consider the prism ABC, and sum forces on it that act normal (F_N) and parallel (F_S) to dA , remembering that a force is a stress times an area, and set the sums equal to 0, the condition for static equilibrium. Note that surface \overline{AB} has area $dA \cos \theta$ and surface \overline{BC} has area $dA \sin \theta$. The force summation yields:

$$\begin{aligned}\sum F_N &= \sigma_N(\theta)dA - \sigma_{xx} \cos^2 \theta dA - \sigma_{xy} \sin \theta \cos \theta dA \\ &\quad - \sigma_{xy} \cos \theta \sin \theta dA - \sigma_{yy} \sin^2 \theta dA = 0\end{aligned}$$

and

$$\begin{aligned}\sum F_S &= \sigma_S(\theta)dA + \sigma_{xx} \sin \theta \cos \theta dA - \sigma_{xy} \cos^2 \theta dA \\ &\quad + \sigma_{xy} \sin^2 \theta dA - \sigma_{yy} \cos \theta \sin \theta dA = 0\end{aligned}$$

Simplifying results in:

$$\sigma_N = \sigma_{xx} \cos^2 \theta + \sigma_{yy} \sin^2 \theta + \sigma_{xy}(2 \sin \theta \cos \theta)$$

and

$$\sigma_S = -\frac{1}{2}(\sigma_{xx} - \sigma_{yy})(2 \sin \theta \cos \theta) + \sigma_{xy}(\cos^2 \theta - \sin^2 \theta)$$

These relations may be further simplified with the use of the trigonometric identities:

$$\sin 2\theta = 2 \sin \theta \cos \theta$$

and

$$\cos 2\theta = \cos^2 \theta - \sin^2 \theta = 2 \cos^2 \theta - 1 = 1 - 2 \sin^2 \theta$$

to yield:

$$\sigma_N = \sigma_{xx} \frac{(1 + \cos 2\theta)}{2} + \sigma_{yy} \frac{(1 - \cos 2\theta)}{2} + \sigma_{xy} \sin 2\theta$$

or

$$\sigma_N = \frac{\sigma_{xx} + \sigma_{yy}}{2} + \frac{\sigma_{xx} - \sigma_{yy}}{2} \cos 2\theta + \sigma_{xy} \sin 2\theta \quad (9.1)$$

and

$$\sigma_S = -\frac{\sigma_{xx} - \sigma_{yy}}{2} \sin 2\theta + \sigma_{xy} \cos 2\theta \quad (9.2)$$

These are the desired relations for $\sigma_N(\theta)$ and $\sigma_S(\theta)$.

Principal stresses

We now wish to find the orientation, θ , of the plane on which σ_N is either a maximum or minimum. Take the derivative of Equation (9.1) with respect to θ and set the result equal to 0, thus:

$$\frac{\partial \sigma_N}{\partial \theta} = -2 \frac{\sigma_{xx} - \sigma_{yy}}{2} \sin 2\theta + 2\sigma_{xy} \cos 2\theta = 0 \quad (9.3a)$$

or

$$\tan 2\theta = \frac{2\sigma_{xy}}{(\sigma_{xx} - \sigma_{yy})} \quad (9.3b)$$

This equation may be satisfied by either of two values of 2θ , 180° apart. Thus, there are two solutions for θ that are 90° apart. One is the plane of maximum σ_N and the other is the plane of minimum σ_N . We call the stresses acting in these directions the *principal stresses*. This is an important concept to understand, and we will return to it frequently.

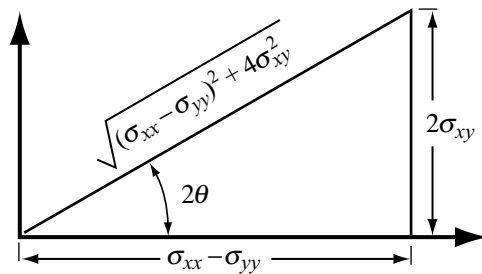


Figure 9.2. Illustration of relation among $(\sigma_{xx} - \sigma_{yy})$, σ_{xy} , and 2θ in Equation (9.3b).

The magnitude of the principal stresses is obtained by substituting for 2θ in Equation (9.1). Equation (9.3b) and the diagram in Figure 9.2 are used to get expressions for $\cos 2\theta$ and $\sin 2\theta$. The result is:

$$\begin{aligned}\sigma_{1,2} = & \frac{\sigma_{xx} + \sigma_{yy}}{2} + \frac{\sigma_{xx} - \sigma_{yy}}{2} \frac{\sigma_{xx} - \sigma_{yy}}{\sqrt{(\sigma_{xx} - \sigma_{yy})^2 + 4\sigma_{xy}^2}} \\ & + \sigma_{xy} \frac{2\sigma_{xy}}{\sqrt{(\sigma_{xx} - \sigma_{yy})^2 + 4\sigma_{xy}^2}}\end{aligned}$$

or

$$\sigma_{1,2} = \frac{\sigma_{xx} + \sigma_{yy}}{2} \pm \frac{1}{2} \sqrt{(\sigma_{xx} - \sigma_{yy})^2 + 4\sigma_{xy}^2} \quad (9.4)$$

σ_1 is $\sigma_{N\max}$ and σ_2 is $\sigma_{N\min}$. Thus, $(\sigma_1 + \sigma_2) = (\sigma_{xx} + \sigma_{yy})$.

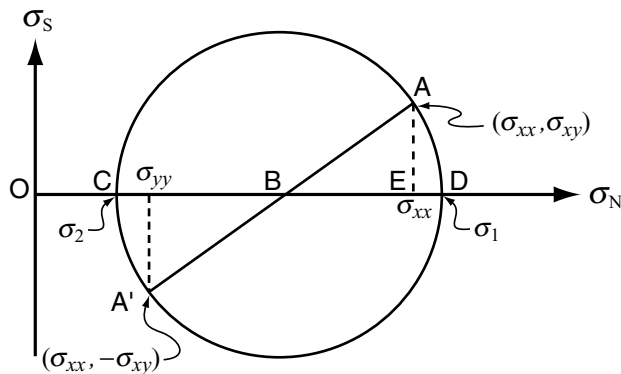
Comparing Equations (9.2) and (9.3a), it will be seen that $(\partial\sigma_N/\partial\theta) = 2\sigma_S$. Thus when $(\partial\sigma_N/\partial\theta) = 0$, $2\sigma_S = 0$. This is another important principle. *Shear stresses vanish on planes on which the normal stresses are a maximum or minimum.*

The orientations and magnitudes of the maximum shear stresses can be obtained in a similar manner. This is left as an exercise for the reader.

Mohr's circle

A convenient way to illustrate the dependence of σ_{xx} , σ_{yy} , and σ_{xy} on 2θ is to use a graphical construction known as Mohr's circle (Figure 9.3). To construct the figure do the following.

- (1) Draw a rectangular coordinate system with normal stresses (σ_N) on the abscissa and shear stresses (σ_S) on the ordinate, and plot points A and A' at $(\sigma_{xx}, \sigma_{xy})$ and $(\sigma_{yy}, -\sigma_{xy})$, respectively.
- (2) Connect points A and A' with a straight line, and draw a circle with B as the center and passing through A and A'.

Figure 9.3. Mohr's circle.

In this figure, $\overline{BE} = \frac{1}{2}(\sigma_{xx} - \sigma_{yy})$ so the radius of the circle is:

$$\sqrt{\left(\frac{1}{2}(\sigma_{xx} - \sigma_{yy})\right)^2 + \sigma_{xy}^2} = \frac{1}{2}\sqrt{(\sigma_{xx} - \sigma_{yy})^2 + 4\sigma_{xy}^2}$$

Thus, from Equation (9.4) the magnitudes of σ_1 and σ_2 are represented by the lengths of lines \overline{OD} and \overline{OC} respectively, and angle ABD is 2θ .

Invariants of a tensor

Regardless of the orientation of the axes in Figure 9.1, the magnitudes and orientations of σ_1 and σ_2 cannot change as long as the overall stress field does not change. This is because σ_1 and σ_2 are functions of the state of stress in the domain and not of θ . We now use this fact and Mohr's circle to illustrate another fundamental principle.

Because the magnitudes of σ_1 and σ_2 , as represented by \overline{OD} and \overline{OC} respectively, determine the size of the circle and its position on the σ_N -axis, the size and position do not change as θ varies. Thus:

$$\frac{1}{2}(\sigma_{xx} + \sigma_{yy}) \quad (9.5a)$$

and

$$\frac{1}{2}[(\sigma_{xx} - \sigma_{yy})^2 + 4\sigma_{xy}^2]^{1/2} \quad (9.5b)$$

(represented by \overline{OB} and the radius of the circle, respectively) remain constant. These two quantities are thus independent of the orientation of the axes, or θ ; they are known as the *invariants* of the tensor. On the other hand, σ_{xx} , σ_{yy} , and σ_{xy} do vary as θ varies. This variation is represented by movement of points A and A' around the circle.

Phrased in terms of Equation (9.4), σ_1 and σ_2 will remain constant and independent of θ only if the quantities $\frac{1}{2}(\sigma_{xx} + \sigma_{yy})$ and $\frac{1}{2}[(\sigma_{xx} - \sigma_{yy})^2 + 4\sigma_{xy}^2]^{1/2}$ are independent of θ . Thus, these two quantities must be invariant.

Extension to three dimensions and introduction of deviatoric stresses

It has been found empirically that, to a first approximation, deformation of ice subjected to a normal stress is independent of the hydrostatic pressure or mean stress, P (see discussion of Equation (4.9)). This might well be anticipated from the observation that ice is (nearly) incompressible. In three dimensions, the mean stress is given by:

$$P = \frac{1}{3}(\sigma_{xx} + \sigma_{yy} + \sigma_{zz}) \quad (9.6)$$

Because deformation is independent of P , we define a new set of stresses, denoted by primes, by $\sigma'_{xx} = \sigma_{xx} - P$, $\sigma'_{yy} = \sigma_{yy} - P$, and $\sigma'_{zz} = \sigma_{zz} - P$. These stresses are variously known as *deviatoric stresses*, *stress deviators*, or *non-hydrostatic stresses*. “Deviator” refers to the fact that they are deviations from the mean stress.

A more compact relation for the deviatoric stresses is:

$$\sigma'_{ij} = \sigma_{ij} - \frac{1}{3}\delta_{ij}\sigma_{kk} \quad i, j, k = x, y, z \quad (9.7)$$

Here, we have introduced the Kronecker δ ; δ_{ij} takes the values:

$$\begin{aligned} \delta_{ij} &= 1 & i = j \\ \delta_{ij} &= 0 & i \neq j \end{aligned}$$

We have also introduced the summation convention. Whenever two subscripts are repeated in the same term, as in σ_{kk} , that term is summed over all possible combinations of the subscripts. Equation (9.7), therefore, represents nine equations, of which three are identical owing to the symmetry of the tensor. Two of the nine are:

$$\begin{aligned} \sigma'_{xx} &= \sigma_{xx} - \frac{1}{3}(\sigma_{xx} + \sigma_{yy} + \sigma_{zz}) \\ \sigma'_{xy} &= \sigma_{xy} \end{aligned}$$

As you see, deviatoric shear stresses are identical to their non-deviatoric (or total) counterparts. Only the normal stresses are different. In general, deformation depends only on these non-hydrostatic components of the stress field.

If we were to go through a derivation similar to that above (Equations (9.1)–(9.5)) in three dimensions (Johnson and Mellor, 1962, pp. 23–25), we would find that there were three invariants having the form:

$$\begin{aligned} J_1 &= \sigma'_{xx} + \sigma'_{yy} + \sigma'_{zz} \\ J_2 &= \sigma'_{xy}^2 + \sigma'_{yz}^2 + \sigma'_{zx}^2 - \sigma'_{xx}\sigma'_{yy} - \sigma'_{yy}\sigma'_{zz} - \sigma'_{zz}\sigma'_{xx} \\ J_3 &= \sigma'_{xx}\sigma'_{yy}\sigma'_{zz} + 2\sigma'_{xy}\sigma'_{yz}\sigma'_{zx} - \sigma'_{xx}\sigma'_{yz}^2 - \sigma'_{yy}\sigma'_{xz}^2 - \sigma'_{zz}\sigma'_{xy}^2 \end{aligned} \quad (9.8a)$$

If total stresses were used instead of deviatoric stresses, the right-hand sides of Equations (9.8a) would be the same, except for the primes, but on the left, by convention, we would use I rather than J , thus:

$$\begin{aligned} I_1 &= \sigma_{xx} + \sigma_{yy} + \sigma_{zz} \\ I_2 &= \sigma_{xy}^2 + \sigma_{yz}^2 + \sigma_{zx}^2 - \sigma_{xx}\sigma_{yy} - \sigma_{yy}\sigma_{zz} - \sigma_{zz}\sigma_{xx} \\ I_3 &= \sigma_{xx}\sigma_{yy}\sigma_{zz} + 2\sigma_{xy}\sigma_{yz}\sigma_{zx} - \sigma_{xx}\sigma_{yz}^2 - \sigma_{yy}\sigma_{xz}^2 - \sigma_{zz}\sigma_{xy}^2 \end{aligned} \quad (9.8b)$$

It is easy to show that J_1 is 0. Just use Equation (9.7) to express the deviatoric stresses in terms of their total counterparts, and simplify. Note also that:

$$\frac{1}{3}I_1 = P \quad (9.9)$$

Let us now derive an alternative expression for J_2 . To do this, square the first of Equations (9.8a), thus:

$$J_1^2 = \sigma_{xx}^{\prime 2} + \sigma_{yy}^{\prime 2} + \sigma_{zz}^{\prime 2} + 2(\sigma'_{xx}\sigma'_{yy} + \sigma'_{yy}\sigma'_{zz} + \sigma'_{zz}\sigma'_{xx}) = 0$$

This expression equals zero because $J_1 = 0$, so we have:

$$\sigma_{xx}^{\prime 2} + \sigma_{yy}^{\prime 2} + \sigma_{zz}^{\prime 2} = -2(\sigma'_{xx}\sigma'_{yy} + \sigma'_{yy}\sigma'_{zz} + \sigma'_{zz}\sigma'_{xx})$$

Substituting this into the expression for J_2 yields:

$$2J_2 = \sigma_{xx}^{\prime 2} + \sigma_{yy}^{\prime 2} + \sigma_{zz}^{\prime 2} + 2\sigma_{xy}^{\prime 2} + 2\sigma_{yz}^{\prime 2} + 2\sigma_{zx}^{\prime 2} \quad (9.10)$$

or, using the summation convention:

$$J_2 = \frac{1}{2}\sigma'_{ij}\sigma'_{ij}$$

The reader will recognize the right-hand side of Equation (9.10) as $2\sigma_e^2$ (Equation (2.10)). Thus, the effective shear stress that we have mentioned several times previously is, in fact, the square root of the second invariant of the stress tensor: $\sigma_e = \sqrt{J_2} = [\frac{1}{2}\sigma'_{ij}\sigma'_{ij}]^{1/2}$.

Using the summation convention, the effective strain rate Equation (2.11) can also be written more compactly as $\dot{\epsilon}_e = [\frac{1}{2}\dot{\epsilon}_{ij}\dot{\epsilon}_{ij}]^{1/2}$.

A yield criterion

A yield criterion is a statement of the conditions under which deformation will occur. If the condition is not met, there is no deformation, and conversely. The simplest imaginable yield criterion is that of Tresca (1864):

$$|\sigma_\ell - \sigma_m| \geq k \quad \ell, m = 1, 2, 3$$

or when the difference between any two principal stresses exceeds a material constant, k (determined experimentally for any given material),

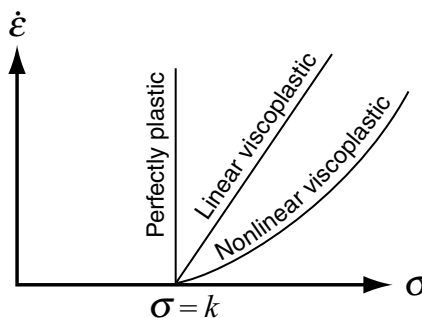


Figure 9.4. Variation of strain rate, $\dot{\epsilon}$, with applied stress, σ , in perfectly plastic and viscoplastic materials.

yielding will occur. An alternative, the von Mises yield criterion, is:

$$(\sigma_1 - \sigma_2)^2 + (\sigma_2 - \sigma_3)^2 + (\sigma_3 - \sigma_1)^2 \geq k$$

In this case, each of the three principal stresses contributes.

Let us investigate the relation between the von Mises criterion and J_2 . After some manipulation we can obtain:

$$(\sigma_1 - \sigma_2)^2 + (\sigma_2 - \sigma_3)^2 + (\sigma_3 - \sigma_1)^2 = 2(\sigma'_1^2 + \sigma'_2^2 + \sigma'_3^2) + 2J_2 \quad (9.11)$$

where the primes denote deviatoric stresses as before. Note that we started with total stresses on the left side. Had we started with deviatoric stresses, we would have obtained the same result, as P drops out. Thus, *the yield criterion is unchanged if we use deviatoric stress instead of total stress*. From Equation (9.10), noting that the shear stresses vanish because we are here dealing with principal stresses, we find that the term in brackets on the right-hand side of Equation (9.11) is equal to $2J_2$. Thus, the von Mises yield criterion reduces to $6J_2 \geq k$, or since $J_2 = \sigma_e^2$, we have $\sigma_e \geq \sqrt{k/6}$. In other words, when σ_e equals or exceeds $\sqrt{k/6}$, yielding will occur.

Yield criteria are often associated with perfect plasticity. A perfectly plastic material does not deform at stresses below its yield strength, k . However, once the applied stress reaches k , the material begins to deform, and it deforms at a rate such that the stress does not exceed k (Figure 9.4). In terms of Glen's flow law, a perfectly plastic material would be represented by $n \rightarrow \infty$ so there would be no strain until σ_e equaled B , where B would be the equivalent of $\sqrt{k/6}$. Viscoplastic or Bingham materials also exhibit a yield stress, but once the yield stress is reached, the material deforms at a rate that depends on the amount by which the applied stress exceeds the yield stress (Figure 9.4). Inasmuch as there may, indeed, be a stress below which ice does not deform, it resembles a nonlinear viscoplastic material. Glen's flow law does not recognize this yield stress, however, but approximates it by predicting very small strain rates at low stresses.

Thus, by using σ_e in the flow law, we are not incorporating a yield stress per se. Rather, we are simply saying that the strain rate in any given direction is likely to be a function of all of the stresses acting on the material, not just the stresses in that direction. For example, the flow law states that ice will shear faster under a stress σ_{xy} if there is also a deviatoric normal stress, σ'_{xx} , on it. Experiments by Li *et al.* (1996) firmly support this concept.

The invariants in plane strain

Let us now examine the relation between the invariants in plane strain (Equations (9.5)) and those in Equations (9.8). By *plane strain* we mean that there is no deformation in one of the coordinate directions, in this case the z -direction. As deformation is caused by deviatoric stresses, this implies that σ'_{zz} , σ'_{xz} , and σ'_{yz} are all 0. From Equation (9.7) we thus have:

$$\sigma'_{zz} = \sigma_{zz} - P = 0 \quad (9.12)$$

so $\sigma_{zz} = P$, and then from Equation (9.6):

$$P = \frac{1}{2}(\sigma_{xx} + \sigma_{yy}) \quad (9.13)$$

(Note that since $\sigma_{zz} = P$, σ_{zz} does *not* equal 0 even though σ'_{zz} does.) With $\sigma'_{zz} = 0$, $J_1 = (\sigma'_{xx} + \sigma'_{yy})$. By using Equations (9.7) and (9.13), it is then easy to show that, as in three dimensions, J_1 also equals 0 in plane strain.

Then from Equation (9.10), adding and subtracting $2\sigma'_{xx}\sigma'_{yy}$ to complete the square:

$$J_2 = \frac{1}{2}(\sigma'^2_{xx} + 2\sigma'^2_{xy} + \sigma'^2_{yy} + 2\sigma'_{xx}\sigma'_{yy} - 2\sigma'_{xx}\sigma'_{yy})$$

So:

$$J_2 = \frac{1}{2}[(\sigma'_{xx} - \sigma'_{yy})^2 + 2\sigma'^2_{xy} + 2\sigma'_{xx}\sigma'_{yy}]$$

Changing to total stress by substituting Equation (9.7) then yields:

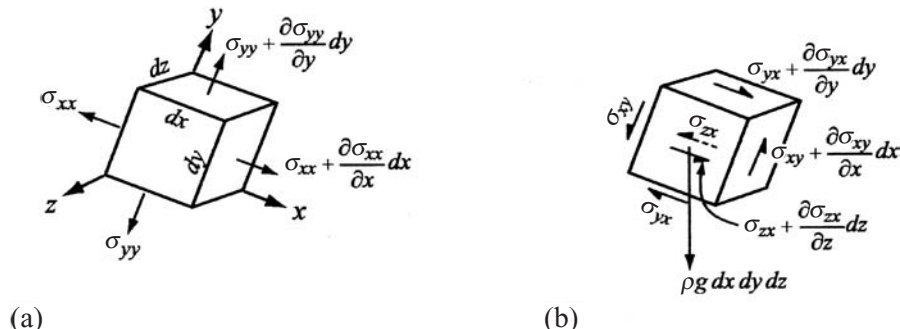
$$J_2 = \frac{1}{2}[(\sigma_{xx} - \sigma_{yy})^2 + 2\sigma^2_{xy} + 2(\sigma_{xx}\sigma_{yy} - \sigma_{xx}P - \sigma_{yy}P + P^2)]$$

After some manipulation using Equation (9.13), we then obtain:

$$J_2 = \left\{ \frac{1}{2}[(\sigma_{xx} - \sigma_{yy})^2 + 4\sigma^2_{xy}]^{1/2} \right\}^2 \quad (9.14)$$

(It can then be shown that the $J_3 = J_2$ in two dimensions, but we will not do this here.)

You will recognize the right-hand sides of Equations (9.13) and (9.14) as being the invariants in Equations (9.5a) and (9.5b), respectively. Using Equation (9.9) you will see that $\frac{1}{2}(\sigma_{xx} + \sigma_{yy}) = \frac{1}{3}I_1$ and



(a)

(b)

Figure 9.5. Stresses on a block of size $dx dy dz$. (a) Normal stresses. (b) Shear stresses (in the x -direction only).

from Equation (9.14) that $\frac{1}{2}[(\sigma_{xx} - \sigma_{yy})^2 + 4\sigma_{xy}^2]^{1/2} = \sqrt{J_2} = \sigma_e$. So the invariants we first identified in Equations (9.5) in two dimensions are functions of I_1 and J_2 .

The right-hand side of Equation (9.14) turns out to be the maximum shear stress in plane strain. You can show this by setting the derivative of Equation (9.2) equal to 0. If the axes were, in addition, chosen to be parallel to the principal stresses, σ_{xy} would vanish, leaving:

$$\sigma_e = \pm \frac{1}{2}(\sigma_1 - \sigma_2)$$

The directions of the maximum shear stresses would then be 45° and 135° to the principal axes. (To show this, determine the orientation of the planes on which σ_S is a maximum, using a procedure similar to that which we used to obtain Equations (9.3), and compare these planes with the orientations of the planes on which σ_N is a maximum.)

Momentum balance

The stress equilibrium equations are derived by balancing forces in the directions of the coordinate axes. Consider forces in the x -direction on a block of size $dx dy dz$ as shown in Figure 9.5:

$$\begin{aligned} \sum F_x &= -\sigma_{xx} dy dz + \left(\sigma_{xx} + \frac{\partial \sigma_{xx}}{\partial x} dx \right) dy dz - \sigma_{yx} dx dz + \left(\sigma_{yx} + \frac{\partial \sigma_{yx}}{\partial y} dy \right) dx dz \\ &\quad - \sigma_{zx} dx dy + \left(\sigma_{zx} + \frac{\partial \sigma_{zx}}{\partial z} dz \right) dx dy + \rho g_x dx dy dz = 0 \end{aligned}$$

The first two terms on the right are the normal forces on the faces of the block that are normal to the x -axis. Note that in each case, the stress (shown in Figure 9.5) is multiplied by the area of the face, in this case

$dy dz$, to obtain a force. The next four terms are the shear forces in the x -direction on faces normal to the y - and z -axes, respectively. The last term is the body force; g_x in this term represents the component of the gravitational acceleration that is parallel to the x -axis. Canceling like terms of opposite sign and dividing by $dx dy dz$ yields:

$$\frac{\partial \sigma_{xx}}{\partial x} + \frac{\partial \sigma_{yx}}{\partial y} + \frac{\partial \sigma_{zx}}{\partial z} + \rho g_x = 0$$

Similar expressions are readily obtained in the y - and z -directions. Using the summation convention, these become:

$$\frac{\partial \sigma_{ij}}{\partial x_i} + \rho g_j = 0 \quad (9.15)$$

As i is repeated in the first term, this represents three terms. However, j is not repeated, so we can write separate equations for $j = x, y$, and z . Thus Equation (9.15) represents three equations.

Because $F = ma = m(dv/dt) = (d/dt)(mv)$ where m is mass, a is acceleration, v is velocity, and mv is momentum, Equations (9.15) represent conservation (e.g. $d/dt = 0$) of linear momentum.

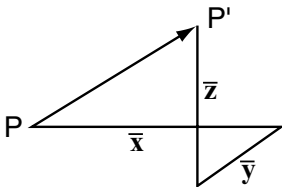


Figure 9.6. Components of a displacement from P to P' .

Deformation

Having applied a stress to a medium, we expect strain or deformation to occur. Suppose \bar{x} , \bar{y} , and \bar{z} (Figure 9.6) represent the displacement of a particle from P to P' in the directions of the coordinate axes, respectively. We will consider infinitesimal displacements so the time required for the deformation $\rightarrow 0$.

Normal strain in the x -direction at P is defined as:

$$\varepsilon_{xx} = \text{Lim}_{\ell \rightarrow 0} \frac{\Delta\ell}{\ell} \quad (9.16)$$

where ℓ is the length of a line drawn in the x -direction, and $\Delta\ell$ is the elongation of that line, so $\Delta\ell/\ell$ is the elongation of the line per unit length. Referring to Figure 9.7, if a line, initially of length ℓ , is translated such that its left end moves a distance \bar{x} in the x -direction, its right end moves a distance $\bar{x} + \ell(\partial\bar{x}/\partial x)$ in this direction, and the x -component of its new length is $\ell + \Delta\ell$, then substituting into Equation (9.16) yields:

$$\varepsilon_{xx} = \text{Lim}_{\ell \rightarrow 0} \frac{\bar{x} + \ell(\partial\bar{x}/\partial x) - \bar{x}}{\ell} = \frac{\partial\bar{x}}{\partial x} \quad (9.17)$$

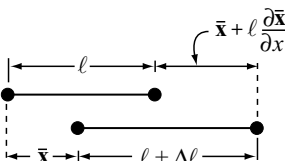


Figure 9.7. Elongation of a line during deformation.

By taking the limit as $\ell \rightarrow 0$ we eliminate the variation with x , thus obtaining ε_{xx} at point P . Similarly: $\varepsilon_{yy} = \partial\bar{y}/\partial y$ and $\varepsilon_{zz} = \partial\bar{z}/\partial z$.

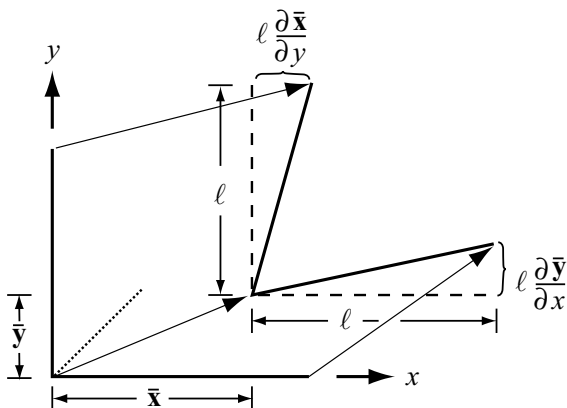


Figure 9.8. Change in a right angle during deformation.

Shear strain is defined as one half the decrease in an initially right angle. Referring to Figure 9.8, this can be expressed as:

$$\varepsilon_{xy} = \frac{\Delta\theta}{2} = \frac{1}{2} \text{Lim}_{\ell \rightarrow 0} \left[\tan^{-1} \frac{\ell(\partial\bar{x}/\partial y)}{\ell} + \tan^{-1} \frac{\ell(\partial\bar{y}/\partial x)}{\ell} \right]$$

For infinitesimal changes, $\theta \approx \tan \theta$ so:

$$\varepsilon_{xy} = \frac{1}{2} \left(\frac{\partial\bar{x}}{\partial y} + \frac{\partial\bar{y}}{\partial x} \right) \quad (9.18a)$$

and similarly

$$\varepsilon_{yz} = \frac{1}{2} \left(\frac{\partial\bar{z}}{\partial y} + \frac{\partial\bar{y}}{\partial z} \right) \quad (9.18b)$$

and

$$\varepsilon_{zx} = \frac{1}{2} \left(\frac{\partial\bar{x}}{\partial z} + \frac{\partial\bar{z}}{\partial x} \right) \quad (9.18c)$$

As before (Chapter 2), there are nine components of strain. Thus, this is another second rank tensor, the *strain tensor*. It, too, is symmetric because $\varepsilon_{xy} = \varepsilon_{yx}$ and so forth.

In general, shear results in rotation as well as distortion. For example, if $\partial\bar{x}/\partial y \neq \partial\bar{y}/\partial x$ in Figure 9.8, the dotted line inclined at 45° to the x -axis will be rotated through an angle:

$$\omega_{xy} = \frac{1}{2} \left(\frac{\partial\bar{x}}{\partial y} - \frac{\partial\bar{y}}{\partial x} \right)$$

Similar expressions may be written for other rotations.

To obtain rates, which are normally of greater interest in a deforming ice mass, we differentiate with respect to time. Thus, the normal strain rate in the x -direction, $\dot{\varepsilon}_{xx}$, is:

$$\dot{\varepsilon}_{xx} = \frac{d\varepsilon_{xx}}{dt} = \frac{d}{dt} \frac{\partial\bar{x}}{\partial x}$$

Velocity is defined as a change in distance with time, or if u is the velocity in the x -direction, $u = d\bar{x}/dt$. Thus, we obtain:

$$\dot{\varepsilon}_{xx} = \frac{\partial u}{\partial x} \quad (9.19)$$

Similarly, shear strain rates become:

$$\dot{\varepsilon}_{xy} = \frac{1}{2} \left(\frac{\partial u}{\partial y} + \frac{\partial v}{\partial x} \right) \quad (9.20)$$

and so forth.

The symmetry of Equation (9.20) suggests the possibility of again using the summation convention to write expressions for the strain rates, thus:

$$\dot{\varepsilon}_{ij} = \frac{1}{2} \left(\frac{\partial u_i}{\partial x_j} + \frac{\partial u_j}{\partial x_i} \right) \quad (9.21)$$

If $i=j$ in this expression, it reduces to Equation (9.19), so this formulation represents both shear and normal strain rates.

Similarly, the *rotation rate tensor* is:

$$\dot{\omega}_{ij} = \frac{1}{2} \left(\frac{\partial u_i}{\partial x_j} - \frac{\partial u_j}{\partial x_i} \right) \quad (9.22)$$

The rotation rate tensor is antisymmetric because $\dot{\omega}_{ij} = -\dot{\omega}_{ji}$. Note also that $\dot{\omega}_{ij} = 0$ when $i=j$. In other words, pure stretching does not result in rotation. If $\dot{\omega}_{ij} = 0$ for all i,j the flow is said to be *irrotational*. Rotations do not change the size or shape of an element, so they do not require the application of a stress.

As implied by the notation $\partial u_i / \partial x_j$ ($i,j = x,y,z$), the velocity vector has three components, and each of them can vary in each of the three coordinate directions. Thus there are nine velocity derivatives.

$$\begin{array}{ccc} \frac{\partial u}{\partial x} & \frac{\partial u}{\partial y} & \frac{\partial u}{\partial z} \\ \frac{\partial v}{\partial x} & \frac{\partial v}{\partial y} & \frac{\partial v}{\partial z} \\ \frac{\partial w}{\partial x} & \frac{\partial w}{\partial y} & \frac{\partial w}{\partial z} \end{array}$$

This is sometimes called the *velocity derivative tensor*. The velocity derivative tensor is not symmetric, as $\partial u_i / \partial x_j \neq \partial u_j / \partial x_i$ in general. Therefore, it can be decomposed into symmetric and antisymmetric parts. The symmetric part is represented by Equation (9.21), and the anti-symmetric part by Equation (9.22).

Logarithmic strain

In Equation (9.16) we defined strain by:

$$\varepsilon = \text{Lim}_{\ell \rightarrow 0} \frac{\Delta\ell}{\ell}$$

where ℓ is the initial length of a line and $\Delta\ell$ is the elongation of that line. This definition is suitable for small (infinitesimal) strains. However, when calculating strains or strain rates from measurements, the total strain is normally not infinitesimal. This is, in part, because deformations must be large enough to exceed the uncertainty in the measurement method.

If strains are infinitesimal, we can replace $\Delta\ell$ with $d\ell$. The total strain is then the sum of the infinitesimal strains, or:

$$\varepsilon = \sum_{\ell=\ell_0}^{\ell=\ell_1} \frac{d\ell}{\ell} = \int_{\ell_0}^{\ell_1} \frac{d\ell}{\ell}$$

where ℓ_0 is the initial length of the line and ℓ_1 is its final length. Integrating yields:

$$\varepsilon = \ln \frac{\ell_1}{\ell_0} \quad (9.23)$$

or in terms of rates:

$$\dot{\varepsilon} = \frac{1}{\Delta t} \ln \frac{\ell_1}{\ell_0} \quad (9.24)$$

where Δt is the time interval between measurements. This is known as logarithmic strain.

General equations for transformation of strain in two dimensions

Our next objective is to develop an expression for the strain rate in an arbitrary direction, θ . To simplify the equations, we restrict the analysis to the case of plane strain. We will then take the derivative of this expression and set it equal to zero to find the directions in which $\dot{\varepsilon}(\theta)$ is maximum and minimum (the *principal strain rates*). Finally we will look at the implications of this in terms of the flow law.

Let us examine the elongation of line \overline{OP} in Figure 9.9a. The line has an initial length ℓ and makes an angle θ with the x -axis. The line is stretched to a final length $\overline{OP'}$ through a displacement with components \bar{x} and \bar{y} in the x - and y -directions, respectively. The elongation is given by (Figure 9.9a):

$$\Delta\ell = \bar{x} \cos \theta + \bar{y} \sin \theta \quad (9.25)$$

The displacement \bar{x} is a consequence of strain parallel to the x -axis and a shear strain which results in tilting of any line that is initially normal

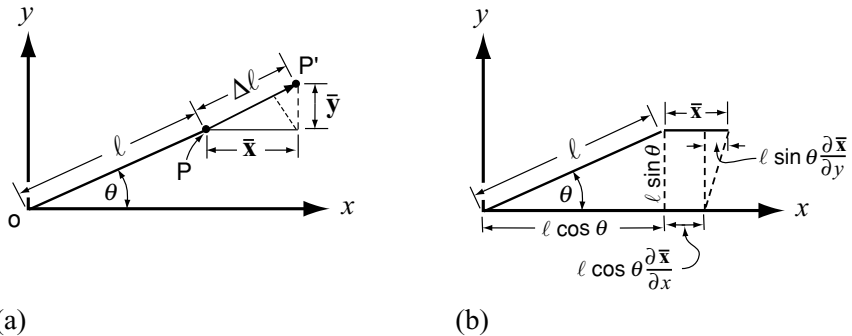


Figure 9.9. (a) Components of strain of a line of initial length $\ell = \overline{OP}$ and final length $\ell\overline{OP}$, and (b) details of the shear component of the strain.

to the x -axis (Figure 9.9b), thus:

$$\bar{x} = \ell \cos \theta \frac{\partial \bar{x}}{\partial x} + \ell \sin \theta \frac{\partial \bar{x}}{\partial y} \quad (9.26a)$$

The origin of the two terms on the right-hand side may be clarified by reference to Figures 9.7 and 9.8, respectively. Similarly:

$$\bar{y} = \ell \sin \theta \frac{\partial \bar{y}}{\partial y} + \ell \cos \theta \frac{\partial \bar{y}}{\partial x} \quad (9.26b)$$

Substituting Equations (9.26) into Equation (9.25) yields:

$$\Delta \ell = \ell \cos^2 \theta \frac{\partial \bar{x}}{\partial x} + \ell \sin^2 \theta \frac{\partial \bar{y}}{\partial y} + \ell \left(\frac{\partial \bar{x}}{\partial y} + \frac{\partial \bar{y}}{\partial x} \right) \cos \theta \sin \theta$$

Finally, dividing by ℓ ; noting that $\text{Lim}_{\ell \rightarrow 0} (\Delta \ell / \ell) = \varepsilon(\theta)$, the strain along the length of line \overline{OP} ; and using Equations (9.17) and (9.18a) to express the derivatives in terms of strains yields:

$$\varepsilon(\theta) = \varepsilon_{xx} \cos^2 \theta + \varepsilon_{yy} \sin^2 \theta + 2\varepsilon_{xy} \cos \theta \sin \theta$$

With the trigonometric identities used earlier (p. 254), this becomes:

$$\varepsilon(\theta) = \frac{\varepsilon_{xx} + \varepsilon_{yy}}{2} + \frac{\varepsilon_{xx} - \varepsilon_{yy}}{2} \cos 2\theta + \varepsilon_{xy} \sin 2\theta \quad (9.27)$$

Strain rates can be obtained by taking the derivative with respect to time. Equation (9.27) is a useful relation for obtaining normal strains or strain rates in an arbitrary direction, θ , when values in the coordinate directions x, y are known.

To obtain the maximum and minimum values of $\varepsilon(\theta)$, the principal strain rates, we proceed as before (Equations (9.3)) to take the derivative with respect to θ , set it to zero, and solve for θ , thus:

$$\tan 2\theta_{sr} = \frac{2\dot{\varepsilon}_{xy}}{\dot{\varepsilon}_{xx} - \dot{\varepsilon}_{yy}} \quad (9.28)$$

The two solutions for θ are the directions in which the strain rate is a maximum and minimum. The magnitudes of the principal strain rates can be obtained as we did for the principal stresses (Equation (9.4)).

Condition that principal axes of stress and strain rate coincide

In calculating the stress and velocity fields in a glacier in Chapter 10, we will need to assume that the principal axes of stress and strain rate coincide. Let us explore the consequences of this condition.

We found earlier (Equation (9.3b)) that the angle which the principal stresses make with the x -coordinate may be obtained from:

$$\tan 2\theta_{\text{stress}} = \frac{2\sigma_{xy}}{\sigma_{xx} - \sigma_{yy}} = \frac{2\sigma'_{xy}}{\sigma'_{xx} - \sigma'_{yy}}$$

Note that it does not matter whether we use deviatoric or total stresses here, as $\sigma'_{xy} = \sigma_{xy}$ and $\sigma'_{xx} - \sigma'_{yy} = \sigma_{xx} - P - (\sigma_{yy} - P) = \sigma_{xx} - \sigma_{yy}$.

The condition that the principal axes of stress and strain rate coincide is $\theta_{\text{stress}} = \theta_{\text{sr}}$, or at any given point in the medium:

$$\frac{2\sigma'_{xy}}{\sigma'_{xx} - \sigma'_{yy}} = \frac{2\dot{\epsilon}_{xy}}{\dot{\epsilon}_{xx} - \dot{\epsilon}_{yy}}$$

The only way to satisfy this condition in the general case is to let:

$$\dot{\epsilon}_{xy} = \lambda\sigma'_{xy}; \quad \dot{\epsilon}_{xx} = \lambda\sigma'_{xx}; \quad \dot{\epsilon}_{yy} = \lambda\sigma'_{yy}$$

where λ is a scalar; that is, its value at the particular point in the medium is independent of the direction in which the stress is acting. However, λ may vary from one point to another in the medium, so $\lambda = \lambda(x, y, z)$.

The fact that λ is a scalar implies that the deforming material is isotropic and incompressible. Thus, under a given stress, it will deform at the same rate regardless of the direction in which the stress is applied. Obviously, this is an approximation in a material such as ice that first has an hexagonal crystal structure, and secondly can develop a fabric with a preferred orientation. [If the material were compressible, a compressive deviatoric stress in, say, the x -direction, σ'_{xx} , would cause more deformation than the corresponding tensile deviatoric stress in the y -direction (which must equal σ'_{yy} in magnitude in plane strain). Thus, λ would differ between the two directions.]

We generalize this assumption to three dimensions and formalize it by writing:

$$\dot{\epsilon}_{ij} = \lambda\sigma'_{ij} \tag{9.29}$$

remembering that

$$\dot{\epsilon}_{ij} = \frac{1}{2} \left(\frac{\partial u_i}{\partial x_j} + \frac{\partial u_j}{\partial x_i} \right) \quad (9.30)$$

and

$$\sigma'_{ij} = \sigma_{ij} - \frac{1}{3} \delta_{ij} \sigma_{kk}$$

Because the stress and strain rate in the flow law are defined in terms of either the effective or the octahedral stress and strain rate, we can write out the first few terms of the effective strain rate and substitute Equation (9.29) into the right-hand side, as follows:

$$\begin{aligned} \dot{\epsilon}_e^2 &= \frac{1}{2} (\dot{\epsilon}_{xx}^2 + \dot{\epsilon}_{xy}^2 + \dot{\epsilon}_{xz}^2 + \dots) \\ &= \frac{1}{2} (\lambda^2 \sigma_{xx}'^2 + \lambda^2 \sigma_{xy}'^2 + \lambda^2 \sigma_{xz}'^2 + \dots) \\ &= \frac{\lambda^2}{2} (\sigma_{xx}'^2 + \sigma_{xy}'^2 + \sigma_{xz}'^2 + \dots) \\ &= \lambda^2 \sigma_e^2 \end{aligned}$$

Dropping the subscript e for convenience (and also because the flow law can be written in terms of either the effective or the octahedral stress and strain rate), we obtain:

$$\dot{\epsilon} = \lambda \sigma = f(\sigma) \quad \text{so} \quad \lambda = \frac{f(\sigma)}{\sigma} \quad (9.31)$$

Here, $f(\sigma)$ is used to emphasize that in the general case, λ is a function of the applied stress.

A few examples will serve to illustrate the meaning of λ .

- Newtonian fluid: $\lambda = 1/\eta$, where η is the Newtonian viscosity so in this case λ is not a function of σ (see Equation (2.17)).
- Power-law fluid: $\lambda = \sigma^{n-1}/B^n$, so $\dot{\epsilon} = \lambda \sigma = (\sigma/B)^n$.
- Perfectly plastic material: as noted earlier (Figure 9.4), in a perfectly plastic material there is no deformation below a critical stress, $\sigma = k$, so $\lambda = 0$ for $\sigma < k$. When $\sigma = k$, the material deforms at a rate such that the stress does not exceed k . In other words, λ depends on $\dot{\epsilon} : \lambda = f_1(\dot{\epsilon})$.

In the case of the power-law fluid, λ varies with σ and B , and because B is a function of temperature, density, crystal size and orientation, and perhaps other factors, λ varies with these properties as well.

Combining Equations (9.29), (9.30), and (9.31), writing $\dot{\epsilon}$ in terms of velocity derivatives, and using the summation convention, we now

have the following relation between individual components of the stress and strain rate tensors:

$$\frac{1}{2} \left(\frac{\partial u_i}{\partial x_j} + \frac{\partial u_j}{\partial x_i} \right) = \frac{f(\sigma)}{\sigma} \sigma'_{ij} \quad (9.32a)$$

This represents nine equations, only six of which are independent. Together with Equation (9.15):

$$\frac{\partial \sigma_{ij}}{\partial x_i} + \rho g_j = 0 \quad (9.32b)$$

which represents an additional three equations, we have nine independent equations which can be solved for the three normal stresses, three shear stresses, and three velocities. Our objective in Chapter 10 will be to do this, but to simplify the problem, we will confine our attention to plane strain.

Summary

In this chapter, we have reviewed some elementary principles of continuum mechanics with a particular focus on those principles needed to understand much of the classical as well as the modern literature on glacier flow.

In the first part of the chapter, we defined stress and showed that if we know the stresses in one coordinate system, we can calculate them in another system rotated with respect to the first. This allowed us to calculate the direction and magnitude of the maximum and minimum normal stresses, the *principal stresses*. We did the calculation in two dimensions, but the extension to three dimensions is straightforward, though tedious. We found that shear stresses vanish in coordinate systems chosen with axes aligned parallel to the principal stresses.

The orientation and magnitude of the principal stresses is a property of the stress field and not of the orientation of the axes. Thus, there are certain combinations of the stresses that must be independent of the orientation of the axes: the *invariants* of the stress tensor. Glen's flow law for ice is based on the second of these invariants. This is logical because it is invariant, and also because the von Mises yield criterion can be expressed in terms of this invariant. Recent experimental data have validated this approach.

In the second part of the chapter, we derived the stress equilibrium or momentum balance equations.

In the third part, we defined strain and derived equations for calculating strains or strain rates in coordinate systems rotated with respect to one another. These equations are similar to those for transformation

of stress. As with stresses, we introduced the concept of *principal strain rates*.

Finally, we showed that if a material is isotropic and incompressible, the principal axes of stress and strain rate coincide. Ice is clearly not isotropic and incompressible, but this approximation has proven to be a convenient starting point for calculations of glacier flow.

Chapter 10

Stress and velocity distribution in an idealized glacier

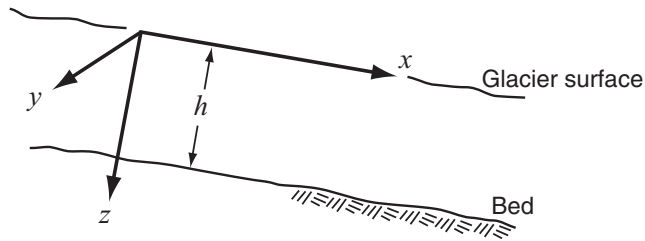
Let us now use Equations (9.32) to calculate stresses and velocities in an idealized glacier consisting of a slab of ice of infinite horizontal extent resting on a bed with a uniform slope. By appropriate choice of the coordinate system, the problem is thus reduced to two dimensions, or plane strain. The ice is assumed to be isotropic and incompressible. We will consider first the case of a perfectly plastic rheology. Then a more realistic nonlinear flow law is used. Our discussion is based on papers of Nye (1951, 1957), which are classics in glaciology.

Although glaciers consisting of such slabs are uncommon, to say the least, there are several reasons for undertaking this calculation. First, it provides an opportunity to apply some of the material discussed in the [previous chapter](#). Secondly, the stress distributions are representative of those which we expect to find in glaciers, and are commonly used approximations when the required assumptions can be justified by the geometry of a problem. Thirdly, the calculations demonstrate the limitations of analytical methods in situations in which boundary conditions are complex. For calculations involving glaciers with realistic shapes, numerical models are required for all but the simplest situations. Finally, the effect of longitudinal stresses on velocity profiles is elucidated.

Solutions for stresses and velocities in plane strain

The coordinate system to be used for the calculation is shown in Figure 10.1: x is parallel to the glacier surface in the direction of flow and z is directed downward normal to the surface. The origin is on the surface

Figure 10.1. Coordinate system used in calculating stresses and velocities in plane strain.



of the slab, which has a thickness h . The velocities are u , v , and w in the x -, y -, and z -directions, respectively.

In our discussion of plane strain in Chapter 9, we took $\dot{\varepsilon}_{zz}$ to be 0, but here our choice of coordinate axes makes $\dot{\varepsilon}_{yy} = 0$, so $\sigma'_{yy} = 0$. Therefore, as in Equations (9.12) and (9.13):

$$\sigma_{yy} = P = \frac{1}{2}(\sigma_{xx} + \sigma_{zz}) \quad (10.1)$$

Also:

$$\begin{aligned}\sigma_{xy} &= 0 \\ \sigma_{zy} &= 0 \\ v &= 0\end{aligned} \quad (10.2)$$

Equations (10.1) and (10.2) are four of the equations needed to solve for the three normal stresses, three shear stresses, and three velocities, so we need five more from Equations (9.32). These are:

$$\frac{\partial \sigma_{xx}}{\partial x} + \frac{\partial \sigma_{zx}}{\partial z} + \rho g_x = 0 \quad (10.3)$$

$$\frac{\partial \sigma_{zx}}{\partial x} + \frac{\partial \sigma_{zz}}{\partial z} + \rho g_z = 0 \quad (10.4)$$

$$\frac{\partial u}{\partial x} = \lambda \sigma'_{xx} = \lambda(\sigma_{xx} - P) = \lambda \left[\sigma_{xx} - \frac{1}{2}(\sigma_{xx} + \sigma_{zz}) \right] = \frac{\lambda}{2}(\sigma_{xx} - \sigma_{zz}) \quad (10.5)$$

and similarly

$$\frac{\partial w}{\partial z} = -\frac{\lambda}{2}(\sigma_{xx} - \sigma_{zz}) \quad (10.6)$$

and

$$\frac{1}{2} \left(\frac{\partial u}{\partial z} + \frac{\partial w}{\partial x} \right) = \lambda \sigma_{zx} \quad (10.7)$$

Note that $\partial u / \partial x = -\partial w / \partial z$ as required by the incompressibility condition in plane strain (Equation (2.5)).

Because $\lambda = f(\sigma)/\sigma$, we have to introduce an expression for σ , namely:

$$\sigma^2 = \frac{1}{4}(\sigma_{xx} - \sigma_{zz})^2 + \sigma_{zx}^2 \quad (10.8)$$

(see discussion following Equation (9.14)) which, as we have seen, can be derived from the von Mises yield criterion in plane strain, and is, in fact, the effective stress in plane strain. Still needed is an expression for $f(\sigma)$; this will be based on the specific flow law chosen for any given solution.

Stress solutions in a perfectly plastic medium

Suppose our slab is composed of perfectly plastic “ice”. Suppose, further, that accumulation and ablation are occurring on the surface of the slab, but that it is in a steady state so the profile does not change. Thus, it must be deforming to accommodate the addition or loss of mass. In order to avoid a discontinuity at depth, the deformation must extend throughout the slab. Furthermore, in a deforming perfectly plastic material, the stress must reach but cannot exceed the yield stress, k (Chapter 9). Therefore, $\sigma = k$ everywhere.

Near the bed, although a small uniform longitudinal strain rate is present, deformation is principally by simple shear. Because any tendency toward an increase in stress above k is absorbed by more rapid deformation in a perfectly plastic material, $\dot{\epsilon}_{zx} \rightarrow \infty$ at the bed. Thus, $\dot{\epsilon}_{zx}$ is the dominant term in $\dot{\epsilon}$, so σ_{zx} is the dominant term in σ (Equation (10.8)), and σ_{zx} must approach $\sigma (= k)$ at the bed. Therefore, we adopt the following boundary conditions:

$$\begin{aligned}\sigma_{zx} &= -k \text{ on } z = h \text{ (bed)} \\ \sigma_{zx} &= 0, \sigma_{zz} = 0 \text{ on } z = 0 \text{ (surface)}\end{aligned}$$

Here σ_{zz} and σ_{zx} are 0 at the surface because atmospheric pressure is a hydrostatic pressure that can be neglected and because there can be no traction on a free surface, respectively. Note that σ_{zx} is set equal to $-k$ on the bed because the drag exerted on the ice by the bed is in the negative x -direction. Because σ_{zx} is independent of x on the bed, we will seek a solution in which σ_{zx} is independent of x everywhere.

The following solution, previously unpublished, is contained in a manuscript by J. F. Nye that he kindly provided to the present author, and is used with his permission. We take the derivative of Equation (10.3) with respect to z and of Equation (10.4) with respect to x , thus:

$$\begin{aligned}\frac{\partial^2 \sigma_{xx}}{\partial z \partial x} + \frac{\partial^2 \sigma_{zx}}{\partial z^2} &= 0 \\ \frac{\partial^2 \sigma_{zz}}{\partial x \partial z} + \frac{\partial^2 \sigma_{zx}}{\partial x^2} &= 0\end{aligned}\tag{10.9}$$

As σ_{xx} and σ_{zz} are continuous functions, the order of differentiation can be reversed in the first of these equations. Subtracting then yields:

$$\frac{\partial^2}{\partial x \partial z} (\sigma_{xx} - \sigma_{zz}) = \left(\frac{\partial^2 \sigma_{zx}}{\partial x^2} - \frac{\partial^2 \sigma_{zx}}{\partial z^2} \right)\tag{10.10}$$

Substituting for $\sigma_{xx} - \sigma_{zz}$ from Equation (10.8) and setting $\sigma = k$ as noted above, we find:

$$\pm \frac{\partial^2}{\partial x \partial z} \left(2\sqrt{k^2 - \sigma_{zx}^2} \right) = \left(\frac{\partial^2 \sigma_{zx}}{\partial x^2} - \frac{\partial^2 \sigma_{zx}}{\partial z^2} \right) \quad (10.11)$$

Making use of the condition that σ_{zx} is independent of x allows us to simplify this to:

$$\frac{\partial^2 \sigma_{zx}}{\partial z^2} = 0 \quad (10.12)$$

which has the solution:

$$\sigma_{zx} = c_1 z + c_2 \quad (10.13)$$

To satisfy the boundary condition $\sigma_{zx} = 0$ on $z = 0$, we find that $c_2 = 0$. The boundary condition $\sigma_{zx} = -k$ on $z = h$ then yields $c_1 = -k/h$. Thus the solution for σ_{zx} becomes:

$$\sigma_{zx} = -\frac{kz}{h} \quad (10.14)$$

In other words, the shear stress varies linearly with depth.

Using this solution for σ_{zx} in Equations (10.3) and (10.4) yields:

$$\begin{aligned} \frac{\partial \sigma_{xx}}{\partial x} &= \frac{k}{h} - \rho g_x \\ \frac{\partial \sigma_{zz}}{\partial z} &= -\rho g_z \end{aligned}$$

which integrate to:

$$\begin{aligned} \sigma_{xx} &= \frac{kx}{h} - \rho g_x x + f_1(z) \\ \sigma_{zz} &= -\rho g_z z + f_2(x) \end{aligned} \quad (10.15)$$

where $f_1(z)$ and $f_2(x)$ are functions that are dependent only upon z and x , respectively, so that $\partial f_1(z)/\partial x = 0$ and $\partial f_2(x)/\partial z = 0$. They are analogous to the constants of integration in Equation (10.13), and must be evaluated with the use of the boundary conditions. Substituting these solutions for σ_{xx} , σ_{zz} and σ_{zx} back into Equation (10.8), the yield criterion, we obtain:

$$\frac{kx}{h} - \rho g_x x + f_1(z) + \rho g_z z - f_2(x) = \pm 2\sqrt{k^2 - \frac{k^2 z^2}{h^2}}$$

which is true for all x and z because, as noted, the yield criterion must be met throughout the slab. Thus, collecting the terms in x on the left-hand side and those in z on the right results in:

$$\frac{kx}{h} - \rho g_x x - f_2(x) = -\rho g_z z \pm 2k\sqrt{1 - \left(\frac{z}{h}\right)^2} - f_1(z) = c \quad (10.16)$$

Because the left-hand side is a function of x alone and the right-hand side is a function of z alone, the two sides can be equal to each other in the general case only if each, individually, is equal to the same constant, c , as shown. We can thus solve Equation (10.16) for $f_2(x)$ in terms of c , and for $f_1(z)$ in terms of c . These solutions are then inserted in Equations (10.15) to yield:

$$\begin{aligned}\sigma_{xx} &= \frac{kx}{h} - \rho g_x x - \rho g_z z \pm 2k\sqrt{1 - \left(\frac{z}{h}\right)^2} - c \\ \sigma_{zz} &= -\rho g_z z + \frac{kx}{h} - \rho g_x x - c\end{aligned}\quad (10.17)$$

Making use of the boundary condition $\sigma_{zz} = 0$ on $z = 0$ in the second of Equations (10.17) gives:

$$c = \frac{kx}{h} - \rho g_x x = x \left(\frac{k}{h} - \rho g_x \right)$$

As this must hold for all x , it is clear that $k/h - \rho g_x$ must equal 0, and therefore c must also be 0. Thus:

$$\frac{k}{h} = \rho g_x$$

This implies that the block must have some critical thickness, $h = k/\rho g_x$. Using these results in Equations (10.17), and repeating Equation (10.14), allows us to write the complete stress solutions thus:

$$\begin{aligned}\sigma_{xx} &= -\rho g_z z \pm 2k\sqrt{1 - \left(\frac{z}{h}\right)^2} \\ \sigma_{zz} &= -\rho g_z z \\ \sigma_{zx} &= -\frac{kz}{h}\end{aligned}\quad (10.18)$$

As a check on these solutions, they may be substituted back into the yield criterion, Equation (10.8), to show that $\sigma = k$.

A plot (Figure 10.2) will serve to illustrate the solutions. Scaling σ_{zz} by k ($= \rho g_x h$) results in:

$$\frac{\sigma_{zz}}{k} = -\frac{z}{h} \frac{\cos \alpha}{\sin \alpha}$$

σ_{zz} is 0 at the surface and it decreases linearly with depth. With $\tan \alpha = 1/5$, we find that $\sigma_{zz} = -5k$ on $z = h$ (Figure 10.2). Similarly, $\sigma_{xx} = \pm 2k$ on $z = 0$ and since $\sigma_{xx} = \sigma_{zz}$ on the bed $\sigma_{xx} = -5k$ there. In this case, however, the distribution with depth is elliptic. Finally, σ_{zx} also decreases linearly with depth to $-k$ on the bed.

The deviatoric stresses can also be calculated. Noting that:

$$P = \frac{1}{2} (\sigma_{xx} + \sigma_{zz}) = -\rho g_z z \pm k\sqrt{1 - \left(\frac{z}{h}\right)^2}$$

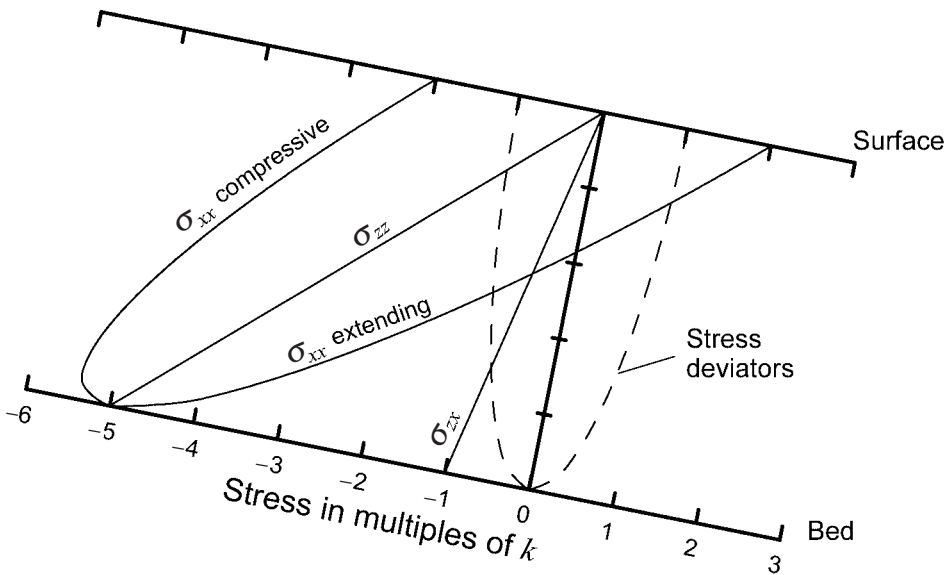


Figure 10.2. Depth variation of stress in a deforming slab of material with a perfectly plastic rheology. The slab is of uniform thickness and density, and is resting on a bed with a uniform slope. (Modified from Nye, 1951, Figure 2c. Reproduced with permission of the author and the Royal Society of London.)

we find that:

$$\begin{aligned}\sigma'_{xx} &= \sigma_{xx} - P = \pm k \sqrt{1 - \left(\frac{z}{h}\right)^2} \\ \sigma'_{zz} &= \sigma_{zz} - P = \mp k \sqrt{1 - \left(\frac{z}{h}\right)^2}\end{aligned}\quad (10.19)$$

so σ'_{xx} is $\pm k$ at the surface and decreases to 0 at the bed, as shown by the dashed lines describing a semi-ellipse in Figure 10.2. As required by continuity, $\sigma'_{zz} = -\sigma'_{xx}$; that is, if our medium is homogeneous, isotropic, and incompressible, as assumed, a deformation in the x -direction, $\dot{\epsilon}_{xx}$, caused by a stress σ'_{xx} must be accompanied by an equal deformation of opposite sign, $\dot{\epsilon}_{zz}$, in the z -direction, and this requires a stress equal to σ'_{xx} , but in the opposite direction.

Negative or compressive deviatoric stresses in the x -direction result in longitudinal compression, and this flow regime is thus referred to as *compressive flow*. Similarly, positive deviatoric stresses in the x -direction result in what is called *extending flow*. The former is characteristic of ablation zones of glaciers, where melt must be replaced by upward flow of ice, and the latter is characteristic of accumulation zones.

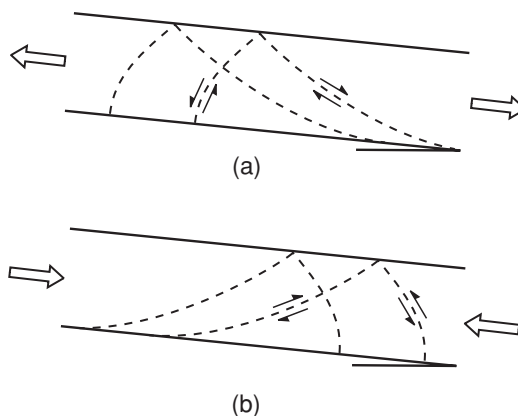


Figure 10.3. Slip line fields in a deforming slab of material with a perfectly plastic rheology. (a) Extending flow, and (b) compressive flow. (Modified from Nye, 1951, Figure 5.)

It is also of interest to examine the orientation of the principal stresses and of the maximum shear stresses. In Chapter 9 (Equation (9.3b)) we found that:

$$\tan 2\theta = \frac{2\sigma_{zx}}{(\sigma_{xx} - \sigma_{zz})}$$

so:

$$\theta = \frac{1}{2} \tan^{-1} \frac{-2kz/h}{\pm 2k \sqrt{1 - \left(\frac{z}{h}\right)^2}} = \frac{1}{2} \tan^{-1} \left(\mp \frac{z}{\sqrt{h^2 - z^2}} \right)$$

On $z = 0$, $\theta = 0^\circ$ or 90° and on $z = h$, $\theta = 45^\circ$ or 135° . Thus at the surface, the principal stresses are parallel and normal to the surface, and at the bed, they make an angle of 45° or 135° with the bed. The former could also be deduced from the fact that there is no shear traction on a free surface, so the stresses parallel and normal to this surface are principal stresses. The orientation of the planes of maximum shear stress may be found by differentiating Equation (9.2) with respect to θ (replacing y by z) and setting the result equal to 0, thus:

$$\theta_{ss} = \frac{1}{2} \tan^{-1} \left(\pm \frac{\sqrt{h^2 - z^2}}{z} \right)$$

In this case, $\theta_{ss} = \pm 45^\circ$ at the surface and 0° or 90° at the bed. (Thus, the planes of maximum shear stress make an angle of 45° with respect to the principal stresses.) At any intermediate depth there are two solutions for θ_{ss} that are 90° apart. Thus, the loci of the zones of maximum shear stress are as shown in Figure 10.3. This is what is known as the *slip line field* for the particular stress configuration.

Velocity solutions in a perfectly plastic medium

We now use the stress solutions, Equations (10.18), to obtain solutions for the velocities from Equations (10.5) through (10.7). From Equations (10.5) and (10.6) we obtain:

$$\begin{aligned}\frac{\partial u}{\partial x} &= -\frac{\partial w}{\partial z} = \frac{\lambda}{2} (\sigma_{xx} - \sigma_{zz}) \\ &= \pm \lambda k \sqrt{1 - \left(\frac{z}{h}\right)^2}\end{aligned}\quad (10.20)$$

and from Equation (10.7):

$$\frac{\partial u}{\partial z} + \frac{\partial w}{\partial x} = 2\lambda\sigma_{xz} = -2\lambda \frac{kz}{h} \quad (10.21)$$

Let us first examine the applicable boundary conditions. The stress solutions are valid only for the thickness $h = k/\rho g_x$. Therefore, we seek a velocity solution that will maintain this thickness. Because there is accumulation, b_n (or ablation, $-b_n$) at the surface, we know that:

$$\begin{aligned}w &= b_n \quad \text{on } z = 0 \\ w &= 0 \quad \text{on } z = h\end{aligned}$$

We will now show that $\partial w/\partial x = 0$. The stresses are independent of x , and the material is the limiting case of a purely viscous material in which stresses determine strain rates. Therefore, the strain rates must be independent of x . In particular, $\partial w/\partial z$ is independent of x , so:

$$\frac{\partial}{\partial x} \left(\frac{\partial w}{\partial z} \right) = 0$$

or, as w must be continuous in x and z :

$$\frac{\partial}{\partial z} \left(\frac{\partial w}{\partial x} \right) = 0$$

Therefore, $\partial w/\partial x = \text{const}$, independent of z . Then, because $\partial w/\partial x = 0$ on the upper and lower boundaries from the boundary conditions, $\partial w/\partial x = 0$ everywhere.

Equation (10.21) now becomes:

$$\frac{\partial u}{\partial z} = -2\lambda \frac{kz}{h} \quad (10.22)$$

Combining Equations (10.20) and (10.22) to eliminate λ yields:

$$\begin{aligned}\frac{\partial u}{\partial z} &= \pm \frac{2(kz/h)}{k\sqrt{1-(z/h)^2}} \frac{\partial w}{\partial z} \\ &= \pm \frac{2z}{\sqrt{h^2-z^2}} \frac{\partial w}{\partial z}\end{aligned}\quad (10.23)$$

Differentiating with respect to x and again making use of the fact that w is continuous in x and z gives:

$$\begin{aligned}\frac{\partial^2 u}{\partial x \partial z} &= \pm \frac{2z}{\sqrt{h^2 - z^2}} \frac{\partial w}{\partial x \partial z} \\ &= \pm \frac{2z}{\sqrt{h^2 - z^2}} \frac{\partial}{\partial z} \left(\frac{\partial w}{\partial x} \right) \\ &= 0\end{aligned}$$

where the last equality results from the fact that $\partial w / \partial x = 0$. Thus from Equation (10.20), differentiating with respect to z , we obtain:

$$\frac{\partial^2 u}{\partial z \partial x} = -\frac{\partial^2 w}{\partial z^2} = 0 \quad (10.24)$$

which has the solution:

$$w = c_1 z + c_2$$

Using the first boundary condition, $w = b_n$ on $z = 0$, yields $c_2 = b_n$, whereupon the second boundary condition, $w = 0$ on $z = h$, yields $0 = c_1 h + b_n$. The solution for the velocity in the z direction thus becomes:

$$w = b_n \left(1 - \frac{z}{h} \right) \quad (10.25)$$

Note that w varies linearly with depth. We discussed this in Chapter 5 (pp. 87–90) and will analyze it in greater detail later.

Using this solution for w in Equation (10.20) we obtain:

$$\frac{\partial u}{\partial x} = -\frac{\partial w}{\partial z} = \frac{b_n}{h} \quad (10.26)$$

and from Equation (10.23):

$$\frac{\partial u}{\partial z} = \mp \frac{2z}{\sqrt{h^2 - z^2}} \frac{b_n}{h} \quad (10.27)$$

In the coordinate system we have chosen, σ_{zx} is negative for positive z . Therefore $\dot{\varepsilon}_{zx}$, and hence in Equation (10.27), $\partial u / \partial z$, must be negative so that a negative stress produces a negative strain rate. (In other words, the horizontal velocity must decrease with depth.) Thus, when b_n is positive in Equation (10.27) we use the upper sign, and conversely. Equation (10.27) thus becomes:

$$\frac{\partial u}{\partial z} = -2 \frac{|b_n|}{h} \frac{z}{\sqrt{h^2 - z^2}} \quad (10.28)$$

Integrating Equation (10.26) yields:

$$u = \frac{b_n x}{h} + f(z)$$

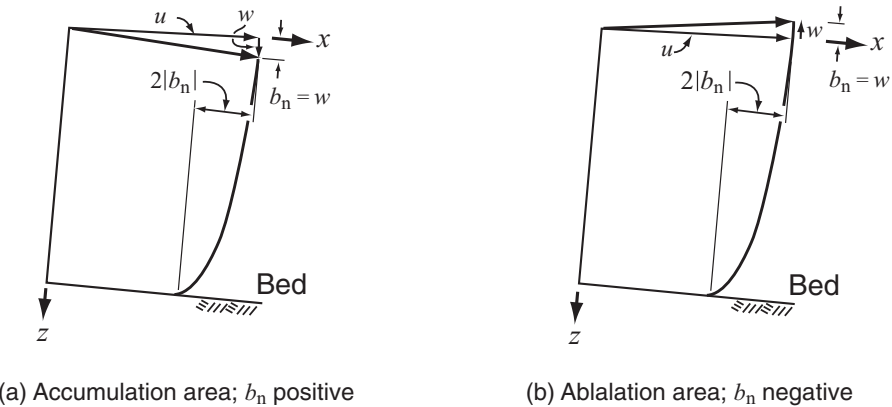
(a) Accumulation area; b_n positive(b) Ablation area; b_n negative

Figure 10.4. Velocity solutions for a deforming slab of material with a perfectly plastic rheology.

where, as in Equation (10.15), $f(z)$ represents some function of z alone. Taking the derivative of this with respect to z , substituting the result into Equation (10.28), and integrating gives:

$$f(z) = 2 \frac{|b_n|}{h} \sqrt{h^2 - z^2} + c$$

Thus, the solution for the velocity in the x -direction is:

$$u = \frac{b_n x}{h} + 2 \frac{|b_n|}{h} \sqrt{h^2 - z^2} + c \quad (10.29)$$

These velocity solutions are illustrated in Figure 10.4. On $z = 0$, $u = (b_n x / h) + 2 |b_n| + c$ and $w = b_n$, while on $z = h$, $u = (b_n x / h) + c$ and $w = 0$. Thus evidently $(b_n x / h) + c$ is the “sliding” speed. Note that Equation (10.29) implies that the ice must be free to slide on the bed at a speed determined by b_n , and independent of σ_{zx} and bed roughness.

If, on the contrary, the sliding speed were presumed to be a function of σ_{zx} and bed roughness, the distribution of stress and hence of w could not be independent of x , and the ice mass would not remain a uniform slab. A reasonable presumption is that the sliding speed would not increase sufficiently rapidly with x , and that conservation of mass would then require that the ice thickness increase upglacier, leading to a convex surface profile. Depending on the degree of convexity and the consequent change in ice thickness, such a profile would offer the potential for increasing σ_{zx} downglacier. This would provide the required increase in mass flux.

If the boundary conditions were selected such that $u = 0$ at $x = 0$, $z = h$, then c would be 0, but the original differential equations are

not necessarily valid at the ends of the slab. Note also that between any two vertical sections, x_1 and $x_1 + \Delta x$, u increases by $b_n \Delta x / h$, which would be the increase in mean velocity required to transmit the additional flux, $b_n \Delta x$, downglacier – the balance velocity that we discussed in Chapter 5.

If there is no accumulation or ablation, $b_n = 0$, and thus $u = c$ and $w = 0$ throughout the block. In this case there is no internal deformation. All movement is confined to sliding. The yield criterion is then satisfied only at the bed and σ_{xx} can take any value between the limits shown in Figure 10.2.

Stress and velocity solutions for a nonlinear material

Let us now relax the assumption that the material with which we are dealing is perfectly plastic, and instead allow it to have a nonlinear rheology, as is the case with real ice. We will still consider a slab of infinite extent and uniform thickness resting on a bed with a uniform slope. The stress equations are not changed, so the solutions for the stresses (Equations (10.18)) remain basically the same. However, now σ does not have a limiting value, k , the yield stress, so some changes must be made.

As before (Equations (10.18)), we note that $\sigma_{xx} \approx \sigma_{zz}$ on the bed, as both are dominated by the hydrostatic pressure. As $\sigma \gg 0$ at the bed, it is clear from Equation (10.8) that $\sigma \approx \sigma_{zx} \gg (\sigma_{xx} - \sigma_{zz}) \approx 0$ there. Again, this emphasizes that deformation at the bed is largely by simple shear. Thus $\sigma_{zx} \rightarrow \sigma$ on the bed, so we replace k with σ in Equations (10.18). In other words, while we still require that σ and σ_{zx} be uniform (independent of x) on the bed, we do not require that they are necessarily equal to some specific value, as in a yield stress. In general, of course, σ_{zx} is likely to increase with the budget gradient (Figure 3.7), as flow rates must then be higher. In addition, we make use of the fact that $k/h = \rho g_x$ from the discussion following Equation (10.17). With these changes, the stress solutions become:

$$\begin{aligned}\sigma_{xx} &= -\rho g_z z \pm 2\sqrt{\sigma^2 - (\rho g_x z)^2} \\ \sigma_{zz} &= -\rho g_z z \\ \sigma_{zx} &= -\rho g_x z\end{aligned}\tag{10.30}$$

As before, the upper sign is for extending, and the lower for compressive flow.

In order to evaluate $\sigma_{xx}(z)$, we need to know how σ varies with depth, z . This will emerge in the course of obtaining the velocity solutions.

To solve for the velocities, we start by combining the stress solutions with Equations (10.5) through (10.7) to obtain:

$$\begin{aligned}\frac{\partial u}{\partial x} &= -\frac{\partial w}{\partial z} = \frac{\lambda}{2}(\sigma_{xx} - \sigma_{zz}) = \pm\lambda\sqrt{\sigma^2 - (\rho g_x z)^2} \\ \frac{1}{2}\left(\frac{\partial u}{\partial z} + \frac{\partial w}{\partial x}\right) &= \lambda\sigma_{xz} = -\lambda\rho g_x z\end{aligned}\quad (10.31)$$

As before (discussion preceding Equation (10.22)), because $w = 0$ on the lower boundary, and because w must thus be independent of x everywhere to avoid discontinuities, $\partial w / \partial x = 0$ everywhere. Thus, using the arguments outlined in Equations (10.22)–(10.24) we obtain, as before:

$$w = c_1 z + c_2 \quad (10.32)$$

The boundary conditions now are not as clear as they were earlier because the thickness may change with time. Thus $w \neq b_n$ on $z = 0$.

From Equations (10.31) and (10.32) we have:

$$\frac{\partial w}{\partial z} = c_1 = -\frac{\partial u}{\partial x} \quad (10.33)$$

Therefore, from the first of Equations (10.31):

$$c_1 = \mp\lambda\sqrt{\sigma^2 - (\rho g_x z)^2} \quad (10.34)$$

Using this to eliminate λ in the second of Equations (10.31) yields:

$$\frac{\partial u}{\partial z} = \pm 2\rho g_x z \frac{c_1}{\sqrt{\sigma^2 - (\rho g_x z)^2}} \quad (10.35)$$

As λ is defined by $\dot{\epsilon}_{ij} = \lambda\sigma'_{ij}$, it must be positive if positive stresses are to produce positive strain rates. To ensure that this is the case, we give c_1 the values $\mp r$ where r is a positive constant. From Equation (10.33) it is clear that r is the longitudinal strain rate. Equation (10.33) thus becomes:

$$\frac{\partial u}{\partial x} = \pm r$$

The solution for w now becomes:

$$w = \mp r z + c_2$$

Applying the boundary condition $w = 0$ on $z = h$, we get $c_2 = \pm rh$, so:

$$w = \mp r(z - h) = \pm rh\left(1 - \frac{z}{h}\right) \quad (10.36)$$

Note that w still varies linearly with depth as in the perfectly plastic case, despite the variation in σ with depth. This is implicit in the fact that the longitudinal strain rate is independent of depth, which in turn results from the fact that stresses must be independent of x in a

slab on a uniform slope (see discussion following Equation (10.21); $\partial u / \partial x = -\partial w / \partial z$ and by Equation (10.24), $\partial w / \partial z = \text{constant}$).

To obtain u , integrate Equation (10.35) (with Equation (10.34)), thus:

$$u = -2g_x \int_0^z \lambda \rho z dz + f(x) \quad (10.37)$$

Setting the derivative of this with respect to x equal to $\pm r$, and integrating gives $f(x) = \pm rx + c$. Combining this with Equation (10.37) and using the boundary condition $u = u_0$ at $x = z = 0$ yields:

$$u = \pm rx - 2g_x \int_0^z \lambda \rho z dz + u_0 \quad (10.38)$$

The velocity, u_s , at the surface ($z = 0$), is $\pm rx + u_0$. Here u_0 is the velocity at the origin, $x = 0$, and rx is the increase (or decrease) in velocity between the origin and the point in question as a result of longitudinal straining. In a real glacier, $r = r(x)$, so one would have to integrate over x to obtain u_s in this way. In practice, we would be more likely to simply take u_s as known. Accordingly, we will replace $\pm rx + u_0$ with u_s in Equation (10.38).

To proceed further, we must assume a flow law; as before, we use $\dot{\varepsilon} = \lambda \sigma = (\sigma/B)^n$ with B and n constant, independent of position. Hence,

$$\lambda = \frac{\sigma^{n-1}}{B^n} \quad (10.39)$$

and Equation (10.38) becomes (assuming that ρ is independent of depth):

$$u = u_s - \frac{2\rho g_x}{B^n} \int_0^z \sigma^{n-1} z dz \quad (10.40)$$

To integrate this, σ must be expressed in terms of z . From Equation (10.34) with $c_1 = \mp r$:

$$\lambda = \frac{r}{\sqrt{\sigma^2 - (\rho g_x z)^2}} = \frac{\sigma^{n-1}}{B^n}$$

Rearranging, this becomes:

$$z = \frac{\sqrt{\sigma^{2n} - r^2 B^{2n}}}{\rho g_x \sigma^{n-1}} \quad (10.41)$$

whence:

$$\begin{aligned} \frac{dz}{d\sigma} &= \frac{n\sigma^{2n-1}}{\rho g_x \sigma^{n-1} \sqrt{\sigma^{2n} - r^2 B^{2n}}} - (n-1) \frac{\sqrt{\sigma^{2n} - r^2 B^{2n}}}{\rho g_x \sigma^{2(n-1)}} \sigma^{n-2} \\ &= \frac{n\sigma^n}{\rho g_x \sqrt{\sigma^{2n} - r^2 B^{2n}}} - (n-1) \frac{\sqrt{\sigma^{2n} - r^2 B^{2n}}}{\rho g_x \sigma^n} \end{aligned}$$

When $z = 0$, $\sigma^{2n} = r^2 B^{2n}$, or $\sigma = r^{1/n} B$, so Equation (10.40) is to be integrated from $r^{1/n} B$ to σ . Equation (10.40) thus becomes:

$$\begin{aligned} u &= u_s - \frac{2\rho g_x}{B^n} \int_{r^{1/n} B}^{\sigma} \frac{\sqrt{\sigma^{2n} - r^2 B^{2n}}}{\rho g_x} \\ &\quad \times \left[\frac{n\sigma^n}{\rho g_x \sqrt{\sigma^{2n} - r^2 B^{2n}}} - (n-1) \frac{\sqrt{\sigma^{2n} - r^2 B^{2n}}}{\rho g_x \sigma^n} \right] d\sigma \\ &= u_s - \frac{2}{\rho g_x B^n} \int_{r^{1/n} B}^{\sigma} [n\sigma^n - (n-1)\sigma^n + (n-1)r^2 B^{2n}\sigma^{-n}] d\sigma \end{aligned}$$

Carrying out the integration yields:

$$u = u_s - \frac{2}{\rho g_x (n+1)} \left[\sigma \left(\frac{\sigma}{B} \right)^n - (n+1)r^2 B^n \sigma^{1-n} + n r^{1+\frac{1}{n}} B \right] \quad (10.42)$$

which, together with Equation (10.41), provides the desired solution for u in terms of z . Expressing u explicitly in terms of z is awkward. Rather, it is better to assume a value of σ , and to use it to calculate the depth z to that σ and the velocity at that depth.

When $r = 0$, these equations reduce to:

$$u = u_s - \frac{2}{\rho g_x (n+1)} \left[\sigma \left(\frac{\sigma}{B} \right)^n \right]$$

and

$$z = \frac{\sigma^n}{\rho g_x \sigma^{n-1}} = \frac{\sigma}{\rho g_x}$$

Thus:

$$u = u_s - \frac{2}{n+1} \left(\frac{\rho g_x}{B} \right)^n z^{n+1}$$

which is the same as Equation (5.6). A fundamental assumption made in the derivation of Equation (5.6) should now be more meaningful: namely that all strain rates other than shear strain parallel to the bed, $\dot{\epsilon}_{zx}$, were negligible. In deriving Equation (10.42) we added only one additional strain rate, $\dot{\epsilon}_{xx}$ ($= r$), yet the complexity of the solution increased significantly.

Now that we have an expression relating σ and z , we can plot stress distributions from Equations (10.30). This is done in Figure 10.5 for a glacier with a longitudinal strain rate of 0.1 a^{-1} resting on a bed with a slope of 0.1. As in the perfectly plastic case (Figure 10.2), σ_{zz} and σ_{zx} vary linearly with depth, while σ_{xx} varies nonlinearly and is also double valued. Furthermore, for any given depth σ is a function of n (Equation (10.41)). Thus, σ_{xx} varies with n . As n becomes large, the solution for σ_{xx} converges on the elliptic distribution obtained earlier (Figure 10.2). For $n = 1$, σ (Equation (10.41)) and hence σ_{xx} (first of Equations (10.30)) decrease linearly with depth. As $P (= \frac{1}{2}(\sigma_{xx} + \sigma_{zz}))$ also

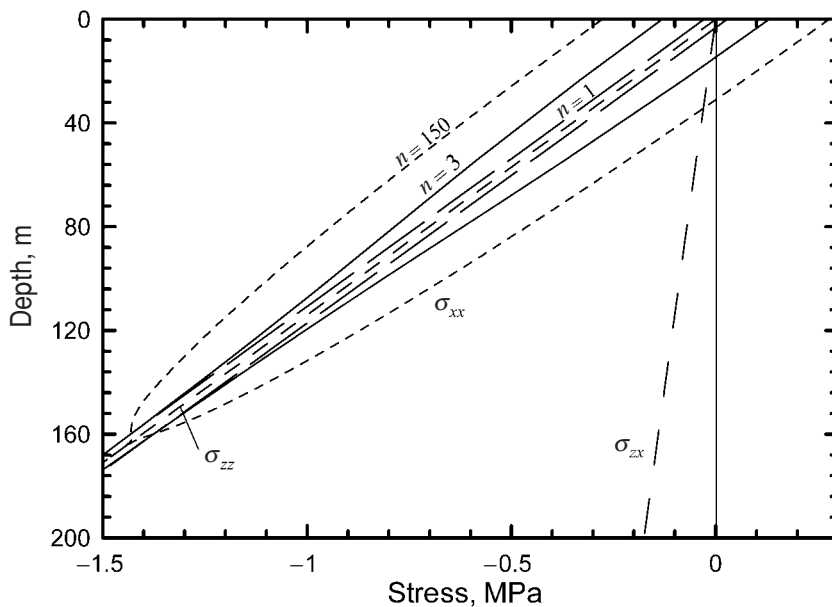


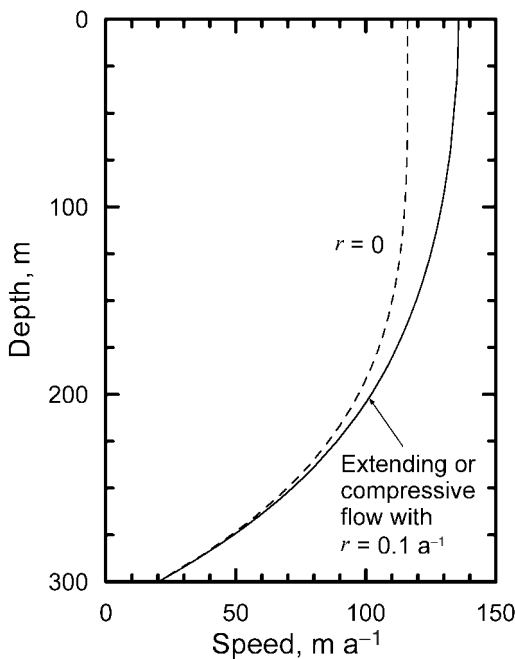
Figure 10.5. Depth variation of stress in an ice sheet with a power law rheology. The ice sheet consists of a slab of uniform thickness and density resting on a bed with a slope of 0.1. The distribution of σ_{xx} is given by the pairs of curves labeled with values of n . The distributions of σ_{zz} and σ_{zx} are the same for all n . Calculations use $n = 3$, $B = 0.141 \text{ MPa a}^{-1/n}$ and $r = 0.1 \text{ a}^{-1}$. As $n \rightarrow \infty$, the thickness of the ice sheet is limited to $h = B/\rho g_x$, which in this case is $\sim 160 \text{ m}$.

decreases linearly with depth with the same constant of proportionality, ρg_z , σ'_{xx} becomes independent of depth.

Further insight may be gained by considering the case when $\sigma = 0$. If $r \neq 0$, z becomes indefinite. This is because although $\sigma_{zx} = 0$ at the surface, $\sigma = \frac{1}{2}\sigma_{ij}\sigma_{ij} > 0$ there. Thus, when there is longitudinal strain, there is no place in the slab where $\sigma = 0$.

Two velocity profiles calculated from Equations (10.41) and (10.42) are shown in Figure 10.6. One profile is calculated with $r = 0$, and the other with $r = 0.1 \text{ a}^{-1}$. Note that u_s is adjusted to yield $u_b = 20 \text{ m a}^{-1}$ in both cases. One might initially think that the higher speed represented by the dashed profile in Figure 10.6 was a consequence of longitudinal stretching. However, r is a positive constant (so a negative value of r cannot be entered in Equation (10.42)) and $\partial u / \partial x = \pm r$. Thus, the dashed profile is applicable to compressive flow as well as extending flow. This is because the magnitude of the increase in σ , and hence in λ , resulting from the addition of a longitudinal stress, is independent of whether the longitudinal stress is compressive or extending. As λ increases so does $\dot{\varepsilon}_{ij}$ for any given σ_{ij} (Equation (9.29)). Specifically, $\dot{\varepsilon}_{zx}$ ($= \partial u / \partial z$) increases, regardless of whether σ_{xx} is positive or negative.

Figure 10.6. Velocity profiles, calculated from Equations (10.41) and (10.42), in a glacier consisting of an infinite slab of ice, 300 m thick, resting on a bed with a slope of 0.046 and sliding with a speed, u_b , of 20 m a^{-1} . Calculations use $n = 3$ and $B = 0.141 \text{ MPa a}^{-1/3}$, and two different values of r as shown.



Comparison with real glaciers

Real glaciers are not slabs of ice of uniform thickness, nor are they perfectly plastic. Thus, it is relevant to consider what aspects of the solutions we have obtained are applicable in reality.

Consider first the result that σ_{zz} and σ_{zx} vary linearly with depth. Such a linear variation is often assumed in studies of real glaciers and is a reasonable approximation in many situations.

In addition we found that, in general, flow is extending in accumulation areas and compressive in ablation areas. This is because r varies directly with b_n (if the glacier is not too far from a steady state), and σ varies directly with r for any given depth (Equation (10.41)). Thus, σ_{xx} varies directly with b_n , being positive when b_n is positive and conversely. In an actual glacier, however, longitudinal stresses also depend on factors such as the curvature of the longitudinal surface profile and the rate of change in thickness. Thus, it is not productive to try to calculate longitudinal stresses in a real glacier with the use of the theory presented here.

The physical processes by which the longitudinal strain rate is adjusted to balance b_n can be visualized qualitatively. If, in some location, r is too large so that thinning by extension exceeds thickening by accumulation, the profile will tend to become concave and this will have a tendency to decrease r .

Also relevant to real glaciers is the effect of longitudinal stress on velocities. Clearly, longitudinal compression should result in upward vertical velocities, and conversely. The linear decrease in w with depth, however, is an artifact of our slab model (see discussion following Equation (10.36)), although it is an approximation that is commonly used in calculations, as we noted in Chapter 5. With respect to vertical profiles of u , longitudinal stresses, whether extending or compressive, increase the effective stress, so they increase $\partial u / \partial z$ throughout the profile. This may be particularly evident near a glacier surface where σ_{zx} is small so $\dot{\varepsilon}_{zx}$ would be negligible were it not for the contribution of σ_{xx} to σ . We will find in Chapter 12, however, that certain peculiarities of measured deformation profiles cannot be explained in this way.

Summary

In this chapter, we have shown that Equations (9.32) can be solved for the three components of the velocity vector and nine components of the stress tensor in certain simple situations. Our solutions were for a slab of infinite horizontal extent resting on a bed with a uniform slope. We first obtained a solution for a perfectly plastic material, and found that the thickness of the slab was constrained by the yield strength of the material. We then obtained solutions for a nonlinear material which are more relevant to real glaciers.

We found that σ_{zz} and σ_{zx} vary linearly with depth, which is probably a reasonable approximation to the situation in many real glaciers. We also found that longitudinal stresses should be extending in accumulation areas and compressive in ablation areas, although the magnitude of the longitudinal stresses is not well constrained by our simple model.

Vertical velocities vary linearly with depth for the idealized situation that we studied, and this is commonly used as a first approximation in real glaciers (e.g. Equation 6.15). Horizontal velocities decrease nonlinearly with depth, as we found in Chapter 5. In this chapter, however, we were able to investigate the effect of longitudinal stresses on the velocity profile, and found that either longitudinal extension or longitudinal compression will increase $\partial u / \partial z$, leading to higher velocities.

Chapter 11

Numerical modeling

On several occasions when we encountered problems that could not be solved readily by analytical methods, we have referred to results from numerical models. In Chapters 5 and 10 we found, in fact, that analytical solutions to problems of glacier flow could be obtained only when the problems were quite simple. The two numerical methods that are most commonly used in modeling are the finite-difference and finite-element methods.

The analytical methods of calculus are based on taking the limit as intervals over which functions are evaluated are allowed to shrink toward zero. In finite-difference and finite-element models, in contrast, we let these intervals remain finite and assume that the functions describing the variation of parameters across them can be replaced by constants, by linear functions, or by low-order polynomials. The resulting equations turn out to be much simpler than the original differential equations, but because the domain of interest is now broken into many small intervals, one must do a large number of repetitive calculations to obtain a solution for the entire domain. Computers are thus used for all but the simplest numerical calculations. Moreover, the numerical solutions are not necessarily as accurate as analytical ones.

In this chapter, we first describe elementary numerical integration. This leads into some straightforward finite-difference calculations that can be carried out with the use of a spread sheet, a short computer program, or available mathematical software. The numerical details of more advanced finite-difference models and of finite-element models are beyond the scope of this book. However, we will discuss some of the

techniques used in these models, and then illustrate the use of models with a few examples.

Goals of modeling

“Solving” a mathematical problem analytically usually means finding values for one or more unknown quantities. This is true, also, of solutions using numerical models. In typical problems with several unknowns, for example, numerical models are commonly used to explore the universe of physically reasonable values of the unknowns, and thus determine which combinations give satisfactory agreement with observations. An example is a study of a temperature profile measured in a borehole that penetrated the Greenland Ice Sheet at Dye 3, where the ice is 2037 m thick (Dahl-Jensen and Johnsen, 1986). The three unknowns, or free variables, were the Pleistocene accumulation rate, Pleistocene surface temperature, and geothermal heat flux. It was found that these could be constrained to lie, respectively, between 33% and 75% of the present accumulation rate, -30 and -35 °C (12 °C below the present mean annual temperature), and 31 and 45 mW m $^{-2}$. If the model took all significant processes into consideration and did so accurately, these values are “solutions” for the three unknowns. More precise solutions are not possible because equally good matches to the observed temperature profile can be obtained with several combinations of these three parameters within the above limits.

The observations that one seeks to match need not necessarily be quantitative measurements. An exciting approach that is being used with increasing frequency and sophistication is the use of observations of the distribution of glacial landforms to constrain models of vanished ice sheets and, in turn, to support hypotheses regarding the origin of the landforms. Moraines obviously provide information on the extent of an ice sheet, and some glacial landforms, as we have discussed, appear to require a certain basal thermal regime. Combinations of model parameters that yield ice sheets of this size and with this basal temperature distribution are thus more likely to represent reality.

Numerical integration

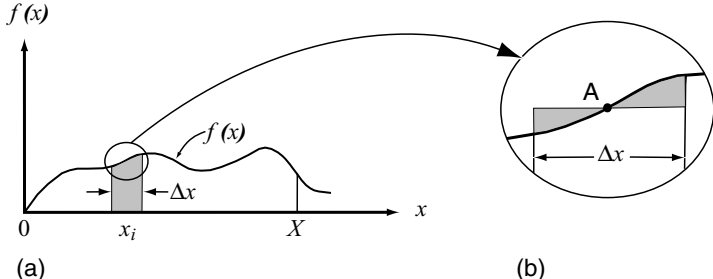
Consider a differential equation of the form:

$$\frac{d\varphi}{dx} = f(x)$$

with the solution:

$$\varphi = \int_0^X f(x) dx \quad (11.1)$$

Figure 11.1. (a) Illustration of a numerical integration to obtain the area under a curve. (b) Detail of the circled area in (a). See text for discussion.



If $f(x)$ is the curve shown in Figure 11.1a, for example, φ is the area under the curve between 0 and X . If the function $f(x)$ can be integrated analytically, φ is easily obtained. However, if $f(x)$ cannot be integrated analytically we can still carry out the integration numerically. (Numerical integration is sometimes called *quadrature*.) To do this, first divide the interval $0 \rightarrow X$ into n segments of equal length, Δx , and then evaluate the sum:

$$\varphi = \sum_{i=1}^n f(x_i) \Delta x \quad (11.2)$$

This sum can be obtained by evaluating $f(x)$ at the midpoint of every interval Δx , multiplying by Δx , and adding the results. The shaded area in Figure 11.1a would be one such product $f(x)\Delta x$. This procedure makes use of the fact that an integral is the limit as $\Delta x \rightarrow 0$ of the summation in Equation (11.2).

A common alternative to this is to evaluate $f(x)$ at the beginning and end of every interval, Δx , and then multiply Δx by the average of these two values. Because this approximates the shaded area as a trapezoid, it is called *trapezoidal integration*.

Neither solution for φ is exact. To see why this is the case, consider Figure 11.1b, which is an enlargement of the circled area in Figure 11.1a. The point labeled “A” is $f(x)$ at the midpoint of the interval Δx . The product $f(x)\Delta x$ overestimates the area under the curve in the interval Δx by the size of the shaded area to the left of A and underestimates it by the size of the shaded area to the right of A. In this particular instance, the latter is larger, so the area under the curve is underestimated. The magnitude of the final error will depend upon the sum of these individual errors. The smaller the intervals Δx , the closer the numerical solution will be to the exact solution.

More sophisticated techniques for numerical integration are also available. For example, the shape of a curve between two points may be approximated by a polynomial (Irons and Shrive, 1987, pp. 64–67). This technique, sometimes called *Gaussian quadrature*, produces highly

accurate results with fewer calculations, but the details are beyond the scope of this chapter.

Finite-difference models

Finite-difference modeling is basically an extension of numerical integration. The defining characteristic of the finite-difference method is that gradients in a parameter are approximated by obtaining values of the parameter at grid points and dividing by the distance between the grid points.

A simple example is the calculation of a temperature profile in the ablation area of a glacier. The relevant equation is:

$$\frac{d\theta}{dz} = \beta_o e^{\zeta^2 z^2} \quad (11.3)$$

(Equation (6.29)) which, again, cannot be integrated analytically. We start out, as before, by dividing the profile into n parts of equal height Δz . We then calculate $\beta_o e^{\zeta^2 z^2}$ at the midpoint of the interval, Δz , or alternatively at the end points and then average the two values. Either approach yields an approximation of the average temperature gradient through the interval Δz . Multiplying this by Δz gives an estimate of how much the temperature decreases over this interval. Subtracting the sum of these changes between this point and the bed from an assumed temperature at the bed gives an estimate of the temperature at the top of the interval Δz . Analytically, the equations for the second approach are:

$$\frac{\theta_{i+1} - \theta_i}{\Delta z} = \frac{\beta_o}{2} \left(e^{\zeta^2 z_{i+1}^2} - e^{\zeta^2 z_i^2} \right)$$

so

$$\theta_{i+1} = \theta_i + \Delta z \frac{\beta_o}{2} \left(e^{\zeta^2 z_{i+1}^2} - e^{\zeta^2 z_i^2} \right) \quad (11.4)$$

Note that $z = 0$ is at the bed (Figure 6.4), so β_o is the basal boundary condition.

Equation 11.4 is easy to solve repetitively, but it still incorporates the assumption that w varies linearly with depth (Equation (6.15)). Alternatively, one could start with Equation (6.14):

$$0 = \kappa \frac{d^2\theta}{dz^2} - w \frac{d\theta}{dz} \quad (11.5)$$

thus avoiding this assumption. Note that Equation (11.5) is one-dimensional inasmuch as θ and w vary only with z . It can be written as

$$\kappa \frac{d\beta}{dz} = w \frac{d\theta}{dz}$$

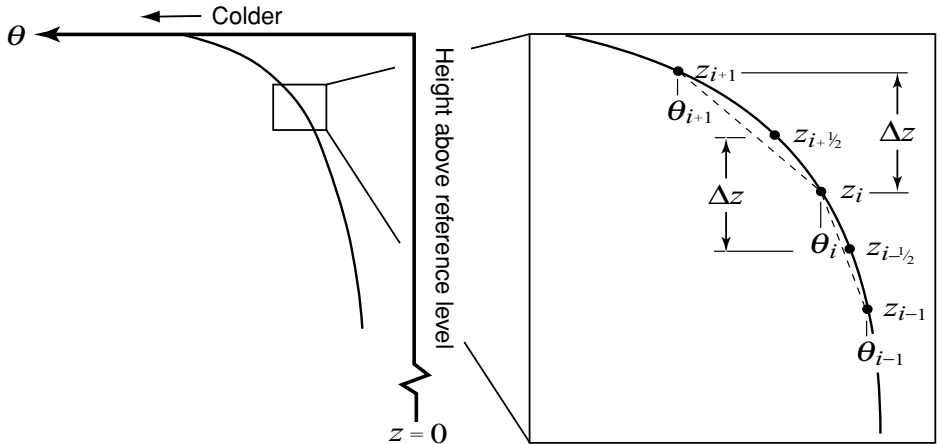


Figure 11.2. (a) The upper part of a temperature profile in the ablation area of a glacier. (b) Detail of area in (a) showing definitions of subscripts used in Equation (11.6). Light dashed lines show approximations to temperature gradients at $z_{i+1/2}$ and $z_{i-1/2}$.

and then in finite-difference form as

$$\kappa \left[\frac{\beta_{i+1/2} - \beta_{i-1/2}}{\Delta z} \right] = w_i \left[\frac{\theta_{i+1} - \theta_{i-1}}{2\Delta z} \right] \quad (11.6)$$

where $\beta_{i-1/2}$ and $\beta_{i+1/2}$ are, respectively, the average temperature gradients at depths $z_{i-1/2}$ and $z_{i+1/2}$, defined in Figure 11.2, and $\Delta z = z_{i+1/2} - z_{i-1/2}$. Note that the gradient in β is taken over Δz while that in θ is over $2\Delta z$. Because $\beta_{i-1/2} = (\theta_i - \theta_{i-1})/\Delta z$ and $\beta_{i+1/2} = (\theta_{i+1} - \theta_i)/\Delta z$, this becomes:

$$\kappa \left[\frac{1}{\Delta z} \left(\frac{\theta_{i+1} - \theta_i}{\Delta z} - \frac{\theta_i - \theta_{i-1}}{\Delta z} \right) \right] = w_i \left[\frac{\theta_{i+1} - \theta_{i-1}}{2\Delta z} \right]$$

or

$$\theta_i = \frac{1}{2} (\theta_{i+1} + \theta_{i-1}) - w_i \frac{\Delta z}{4\kappa} (\theta_{i+1} - \theta_{i-1}). \quad (11.7)$$

With Equation (11.7) one can use nonlinear variations in w with depth, such as Equations (5.24) or (5.25). However, when θ_i is being calculated, θ_{i+1} is not known so one must set up a system of simultaneous equations in order to solve the problem.

A rather similar problem is to calculate changes in a temperature profile through time as the climate, and hence the surface temperature changes. To simplify the problem, let us just consider seasonal changes so we can restrict the domain to the upper 20 or 30 m of the glacier, and

thus neglect advection and strain heating. The appropriate differential equation is then:

$$\kappa \frac{\partial^2 \theta}{\partial z^2} = \frac{\partial \theta}{\partial t} \quad (11.8)$$

(Equation (6.30)). This is now a two-dimensional problem in which θ varies with both depth and time. Proceeding as above, Equation (11.8) can be rewritten in finite-difference form as:

$$\kappa \left[\frac{\beta_{i+1/2} - \beta_{i-1/2}}{\Delta z} \right] \Delta t = \Delta \theta \quad (11.9a)$$

and then as

$$\kappa \left[\frac{1}{\Delta z} \left(\frac{\theta_{i+1} - \theta_i}{\Delta z} - \frac{\theta_i - \theta_{i-1}}{\Delta z} \right) \right] \Delta t = \Delta \theta \quad (11.9b)$$

To continue, we need a profile to serve as an initial condition at time $t = t_0$. From this profile we can get θ_{i-1} , θ_i , and θ_{i+1} and then solve Equation (11.9a) for $\Delta \theta$. This is the amount that the ice between $z_{i-1/2}$ and $z_{i+1/2}$ warmed or cooled during the time interval Δt . Once we have done this calculation for every depth interval, Δz , we will have the temperature profile at time $t_0 + \Delta t$, and a new calculation for the next time step can be initiated.

To clarify the physics involved, consider the profile in the inset of Figure 11.2 to be part of the temperature profile of interest. This profile may have been measured, calculated during an earlier time step, or assumed. The temperature gradient, $\Delta \theta / \Delta z$, at $z_{i+1/2}$ is larger than that at $z_{i-1/2}$, so more heat will be conducted out through the top of the volume of height Δz than is conducted in through the bottom. Thus the ice will become cooler during the time step. (With the coordinates shown in Figure 11.2, both $\beta_{i-1/2}$ and $\beta_{i+1/2}$ are negative, so since $\beta_{i+1/2}$ is larger, $\Delta \theta$ is negative (Equation (11.9a)).)

To model seasonal variations in the temperature profile, the boundary condition at the surface must be changed appropriately at the beginning of each time step. For example, if the initial profile was measured on January 1 and we choose a time step of 0.02 a (or 7.3 days), the boundary condition at the surface for the next iteration should be the temperature (measured or estimated) 7.3 days later. If the temperature variation at the surface is sinusoidal, the solution should closely approximate that given by Equation (6.31) after a number of iterations. However, the present solution has added versatility, inasmuch as accumulation or ablation can be simulated by adding or subtracting increments of thickness, Δz , at appropriate time steps.

Care must be taken in selecting Δt and Δz in such problems. The finite-difference solution is said to converge (or be stable) if it approaches

the exact solution as Δt and $\Delta z \rightarrow 0$. Our solution will converge if:

$$0 < \frac{\kappa \Delta t}{\Delta z^2} < \frac{1}{2} \quad (11.10)$$

(Irons and Shrive, 1987, p. 95; Carnahan *et al.*, 1969, p. 432). Thus, if $\Delta z = 1$ m, Δt would have to be less than about 1/75 of a year, or ~ 5 d. If the integration had to span centuries or millennia and Δz could not be increased, a very long calculation would be necessary.

Finite-difference techniques can also be used to integrate the momentum equation, but simplified versions of the momentum equation can be integrated analytically (e.g. Equations (5.6) and (10.42)), and versions including longitudinal stresses and varying ice thickness require more advanced techniques, outlined below. Thus, we have focused on the energy balance equation in these examples.

Because analytical solutions are not available for a large number of differential equations of importance in science and engineering, considerable effort has gone into refining the techniques we have just outlined, and study of these techniques is now a major subfield of applied mathematics. As might be anticipated, the primary goals of this effort have been to improve the stability and accuracy of the solutions without necessitating ever finer grid spacing. A few common approaches are outlined next.

Implicit methods

Equations like (11.9b) which use θ_{i-1} , θ_i , and θ_{i+1} from a temperature profile at time t_1 to calculate the profile at time t_2 are known as *explicit* forms of the finite-difference equation. One could also write Equation (11.9b) with θ_{i-1} , θ_i , and θ_{i+1} defined as being the temperatures at time t_2 which are, as yet, unknown. This is known as an *implicit* form. In this approach, equations must be written for all n points in the profile, and the equations then solved simultaneously for all the $\Delta\theta_i$. The temperatures at time t_2 are then obtained by adding these $\Delta\theta_i$ to the temperatures at the respective grid points at time t_1 . This approach has the advantage of being unconditionally stable so larger time steps can be used. Solution of the equations is actually not as daunting as it may seem, as most contain only three unknowns and those at the top and bottom, where the boundary conditions are applied, contain only two. The resulting equation matrix is a tridiagonal matrix with nonzero cells only on the diagonal and on the sub- and superdiagonals immediately adjacent to the diagonal. Efficient routines for solving such matrices are readily available.

A variation on this implicit method is the *Crank–Nicolson* method. In this approach, the gradients used in Equation (11.9a) are the averages of the gradients at times t_1 and t_2 . Because gradients at time t_2 are used, this is still an implicit method and requires solution of a system of equations. However, the equations are only slightly more complicated than those using just the gradients at time t_2 , and the increase in accuracy is substantial (Carnahan *et al.*, 1969, p. 451).

Alternating direction schemes

One way to avoid stability problems in explicit methods is to use alternating direction schemes. In such schemes, using the problem in Figure 11.2 as an example, one first calculates $\Delta\theta$ starting at the surface and progressing downward, and then calculates $\Delta\theta$ for the next time step, starting at the lower boundary and progressing upward. In the downward direction, $\beta_{i-1/2}$ for time t_2 is calculated from the temperatures from time t_1 , and $\beta_{i+1/2}$ is calculated from temperatures at time t_2 , thus:

$$\kappa \left[\frac{1}{\Delta z} \left(\frac{\theta_{i+1,t_2} - \theta_{i,t_2}}{\Delta z} - \frac{\theta_{i,t_1} - \theta_{i-1,t_1}}{\Delta z} \right) \right] \Delta t = \theta_{i,t_2} - \theta_{i,t_1} \quad (11.11a)$$

where the second subscript is the time step. This may be compared with equation (11.9b). Here, θ_{i+1,t_2} is known from the calculation at the previous depth so a simple algebraic transformation leads directly to a solution for θ_{i,t_2} . In the upward direction, calculating temperatures for time step t_3 , the appropriate equation is:

$$\kappa \left[\frac{1}{\Delta z} \left(\frac{\theta_{i+1,t_2} - \theta_{i,t_2}}{\Delta z} - \frac{\theta_{i,t_3} - \theta_{i-1,t_3}}{\Delta z} \right) \right] \Delta t = \theta_{i,t_3} - \theta_{i,t_2} \quad (11.11b)$$

Now, θ_{i,t_2} and θ_{i+1,t_2} are known from time step t_2 , and θ_{i-1,t_3} is known from the calculation at depth $i - 1$. This scheme, known as the Saul-yev alternating direction procedure (Carnahan *et al.*, 1969, p. 451), is explicit because calculations at any depth and time can be made using a single equation. It is also unconditionally stable.

The Saul-yev procedure was used to model several temperature profiles in Barnes Ice Cap (Hooke *et al.*, 1980). The study was motivated by temperature measurements in boreholes that suggested a recent warming at the surface and a systematic downglacier increase in the temperature gradient at the bed. To model these profiles, Equation (6.13) was simplified to two dimensions, thus:

$$\frac{\partial \theta}{\partial t} = \kappa \frac{\partial^2 \theta}{\partial z^2} - u \frac{\partial \theta}{\partial x} - w \frac{\partial \theta}{\partial z} + \frac{Q}{\rho C} \quad (11.12)$$

and then expressed in finite difference form. The modeling suggested that temperatures at the glacier surface had increased 0.1–0.5 K over

the past few decades, after a cooling in the early 1940s. The increase in gradient at the bed appeared to be a consequence of a warming of ~ 2 K about 250 years ago, near the end of the Little Ice Age. Use of an unconditionally stable finite-difference scheme greatly reduced the computer time needed for the calculations.

Other explicit unconditionally stable procedures, some of which also utilize alternating direction schemes, are available, as are implicit alternating-direction methods (Carnahan *et al.*, 1969, pp. 541–543). Some of these are readily extended to two and three dimensions.

Backward, forward, and centered differences

In some of the examples above, we estimated gradients from temperatures. If we know temperatures θ_{i-1} , θ_i , and θ_{i+1} and need the gradient β_i there are three possible approaches:

$$\begin{aligned}\frac{d\theta}{dz} &= \frac{\theta_i - \theta_{i-1}}{\Delta z} \\ \frac{d\theta}{dz} &= \frac{\theta_{i+1} - \theta_i}{\Delta z} \\ \frac{d\theta}{dz} &= \frac{\theta_{i+1} - \theta_{i-1}}{2\Delta z}\end{aligned}\tag{11.13}$$

These are known as backward, forward, and centered differences, respectively.

Non-dimensionalization

In writing computer code for finite-difference schemes, it should be evident from Equations (11.4) to (11.11) that the code will be much simpler if the units of *spatial discretization* (subdividing the domain into many small discrete units) are of equal size. Thus, Δz should not change with depth. If the problem at hand involves a substantial part of an ice sheet, say along a flowline that is broken into columns of width Δx , each of which is then subdivided into depth increments, Δz (Figure 11.3), it is clearly impossible to keep both the number of depth increments and their size, Δz , constant from one column to the next. To avoid problems of this type, modelers commonly normalize the depth by dividing by the thickness. Thus a point at a depth, z , of 600 m in an ice sheet that is $H = 1000$ m thick will be at a normalized depth, z^* , of 0.6. The columns then all have a non-dimensional thickness, H^* , of 1.0, and if they are each subdivided into 20 equal depth increments, all increments will have a non-dimensional thickness of $H^*/20$. Non-dimensionalization or *scaling* of lengths in this way generally requires scaling of the other parameters in the equations.

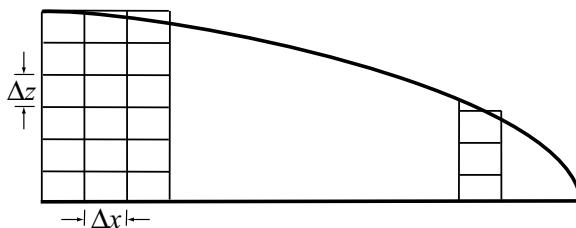


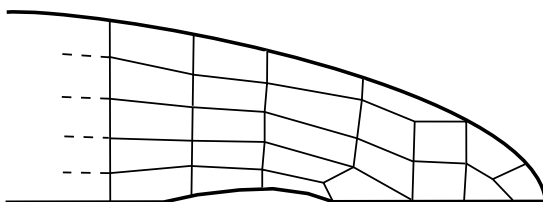
Figure 11.3. Illustration of problems encountered with a finite-difference discretization of an ice sheet along a flowline.

Such scaling greatly simplifies the mathematics in many situations. However, results from such computations have to be restated in dimensional form before most of us can derive useful physical insights from them. As our goal is to develop an appreciation for physical concepts, we will not delve further into this subject.

Shallow ice approximation

Most numerical models of ice sheets use what is known as the *shallow ice approximation*. While the shallow ice approximation was first introduced in glaciology by Fowler and Larson (1978) and in slightly different form by Hutter (1981), our discussion is based on Hutter (1983, p. 256ff). This approximation makes use of the fact that the horizontal extent of an ice sheet is large compared with its thickness. Longitudinal derivatives of stress, velocity, and temperature are thus small compared with vertical derivatives. If the wavelengths of major undulations in the surface and bed topography are relatively long, so the surface and bed elevations are slowly varying functions of x , the longitudinal coordinate can be scaled by using the relation $\xi = \mu x$, where μ is small. One logical possibility is to take μ as the ratio of the mean thickness to the horizontal extent of the ice sheet. The vertical coordinate is not changed. With this scaling, μ is introduced into the momentum balance, energy balance, and continuity equations, and into the boundary conditions. If all terms involving μ are then neglected and the resulting equations are solved, the solution is referred to as the zeroth-order solution. In this solution, the stress and velocity fields are calculated as if the ice sheet were a slab of uniform thickness, and the basal shear stress turns out to be $\rho g h \alpha$. Longitudinal stress gradients are thus not included. If terms involving μ^1 are included in the solution, the result is called a first-order solution. Longitudinal stress gradients are included in this solution, and a flow law that includes a linear term at low stresses is necessary to avoid a singularity in these stresses at the surface. This is the solution used in most existing finite-difference models of ice sheets. As might be expected from the above, a solution including terms in μ^2 is called a second-order solution. In

Figure 11.4. A possible finite-element discretization of a tapered glacier margin, showing the flexibility of the finite-element method to accommodate such geometries.



modeling ice shelves, longitudinal stress effects first appear in second-order solutions. Solutions including μ^2 or higher powers of μ are called *higher-order solutions*.

Finite-element models

The finite-element method is another way of obtaining an approximate solution to the governing equations. In both finite-element and finite-difference models, the domain of interest is broken up into a large number of small elements. In early applications of finite-element models to glaciological problems the elements were quadrilaterals, but commercial packages now in use commonly have higher-order element geometries. The corners of elements are called nodes. Unlike finite-difference models, in a finite-element model there is no advantage in making all of the elements rectangular and the same size.

As before, parameters are assumed to be constant over the elements or to vary in some simple way. In finite-element calculations, however, use is made of the fact that the relevant differential equations can be expressed in a form consisting of a sum of integrals. A solution method, called the method of weighted residuals, then guarantees that the resulting approximate solution will be the best possible solution mathematically obtainable with a given element configuration.

While initially more complicated to understand, finite-element formulations have been shown to be generally more stable, numerically, than finite-difference formulations (Strang and Fix, 1973). Furthermore, element shapes can be adjusted to conform to boundaries that would be awkward to model with rectangular elements (Figure 11.4). Finally, element size can be reduced in areas of high gradients and increased in areas of low gradients, thus increasing accuracy without increasing computation time. Complex, non-uniform, and variable boundary conditions are also easier to include in finite-element models.

Once a domain is discretized, stress or velocity conditions are specified at boundary nodes and equations are written relating stresses and velocities at interior nodes to each other, to the mean stress in the element, and to the stresses or velocities at the boundaries. As usual, the

basic equations being solved are those for conservation of momentum, mass, and energy (Equations (9.32b), (2.7), and (6.12a), respectively). Glen's flow law is normally used. For the simplest models utilized in two-dimensional plain strain calculations, this procedure yields approximately $2N + M$ equations where N is the number of nodes and M is the number of elements. Twenty-five years ago a problem with 200 elements and 300 nodes was considered large, but owing to advances in computer technology and in numerical methods for solving large systems of equations, a typical problem today may involve thousands of elements and nodes. The number of equations to be solved simultaneously is, thus, large, but the number of unknowns in each equation is small, so efficient routines for solving sparse matrices can be used. Owing to the nonlinearity of the flow law, the set of equations is nonlinear and an iterative solution is necessary. A trial solution is given initially, and this is corrected to obtain an improved solution at each iteration.

The two most common types of finite-element model are two-dimensional flow-band models and map-plane models. In flow-band models, the model domain extends along a flowline, which may be curvilinear, and is bounded at the top by the glacier surface and at the base by the bed or, in the case of some models that include temperature calculations, by a surface at some depth in the substrate. The domain is considered to be of unit thickness perpendicular to the flowline. Some models permit one to specify a transverse strain rate, and thus become quasi-three dimensional. A few are fully three dimensional (Hanson, 1995).

In map-plane models (Fastook and Chapman, 1989), the domain is bounded by the surface and the bed and by lateral boundaries which may be flowlines, a glacier margin, a divide, or an arbitrary transverse boundary in the glacier across which a mass flux is specified. Unlike flow-band models, map-plane models do not require prior knowledge of the direction of flow. Although many map-plane models are called three dimensional, they are actually quasi-three dimensional inasmuch as the basic elements are columns extending through the ice mass, and parameters such as velocity are averaged over the column. The models are thus said to be *vertically integrated*. In such models, some terms of the stress tensor are replaced by assumptions in the core of the model, and variations with depth are then obtained later by, for example, using equations like (5.16) and (5.18) to calculate $u(z)$ from \bar{u} .

Initial conditions and forcing

In earlier chapters we have found that it is necessary to specify conditions on the boundaries of a problem domain in order to obtain a solution for

parameters within the domain. Vertical velocities at the surface were specified in Chapter 5, temperatures and temperature gradients in Chapter 6, and stresses and velocities in Chapter 10. In all of these examples, the solutions we sought were steady-state solutions, so all time derivatives were 0.

In many modeling studies, time-dependent solutions are desired. Indeed one of the strengths of numerical modeling is that we can study the evolution of a complex system through time – a goal that is only rarely achievable with analytical solutions (Equation (6.31) is such an exception). In time-dependent models it is necessary to specify conditions at time $t = 0$, called *initial conditions*, and also, in most cases, the temporal evolution of some of these conditions, usually those at the surface. The latter is frequently referred to as the *forcing*. We have already encountered an example of an initial condition earlier in this chapter, in discussing the solution to Equation (11.8).

The choice of initial conditions depends on the extent of our knowledge of those conditions. If there is no well-defined condition from which to start the integration, it can be started with an unrealistic situation such as a temperature profile that varies linearly with depth or an ice sheet with a parabolic profile. This approach is particularly appropriate in problems involving cyclical changes, such as seasonal changes in temperature at the surface or changes in climate driven by variations in Earth’s orbit – the Milankovitch cycles. The model would then be run through several cycles until the solution at a given point in a cycle is essentially identical to that at the same point in the previous cycle. One can then conclude that the model has “forgotten” the unrealistic initial conditions. This procedure is commonly referred to as a *spin up* of the model. The final solution can then be saved for use as an initial condition in a subsequent run.

Alternatively, one can start with a known condition at sometime in the past. For example a model of cycles of ice sheet growth and decay could use a condition of no ice sheet as an initial condition, or a two-dimensional flowline model could use a profile measured 20 or 30 years ago. In the latter case, the model could be validated by comparing the final profile with one measured recently. The model might then be run into the future to predict the effects of various climate-change scenarios.

As just noted, forcing a time-dependent model usually involves varying the boundary conditions at the surface in some prescribed way. Boundary conditions at the bed or along an upstream or downstream boundary might also be varied by the modeler, but more frequently these will be calculated within the model as part of the solution. Relevant conditions at the surface are usually precipitation and temperature. These may be estimated from empirical relations, such as a relation between

mean annual temperature and the Milankovitch cycles, or may be calculated in another model, such as a global climate model (GCM). If the output from an ice-sheet model is used as input for a time step in a GCM, the output of which is then used for the next time step in the ice-sheet model, the models are said to be *coupled*.

Validation

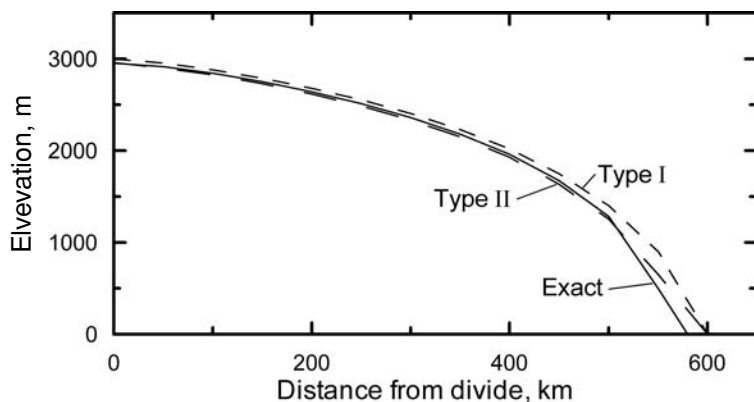
Once a model has been programmed and appears to be giving reasonable results, it must be *validated* to ensure that there are no subtle errors that affect the results significantly but not so much as to make them obviously unrealistic. A common way to initiate the validation process is to set parameters in the model in such a way that the model duplicates a situation for which there is an analytical solution. For example, if $\partial\theta/\partial t$, u , and Q are set to zero in Equation (11.12) and w is assumed to be downward and to decrease linearly with depth, the model should reproduce the Robin (1955) solution (Equation (6.24)). In flow models, the deformation of an infinite slab of ice on a uniform slope (Equation (10.42)) is a good choice. Of course, once these comparisons have been made, there is still the question of whether coding of some of the terms neglected in the test, such as $u(\partial\theta/\partial x)$ in Equation (11.12), is correct. The modeler will have to be more imaginative to find independent ways to test these algorithms. One possibility is to compare the output of similar models developed totally independently, as discussed next.

Intercomparison of models

Because of the large number of ice sheet models being developed, each employing slightly different approaches and each subject to inadvertent programming errors, a group of 16 modelers developed a set of tests for comparison of models (Huybrechts *et al.*, 1996; Payne *et al.*, 2000). One test, for example, utilizes a square domain, 1500 km on a side, with grid points at 50 km spacing. Initially there is no ice sheet in the domain. A radially symmetric mass balance pattern is specified as are the flow law constants n and B , and other relevant parameters such as ρ , g , and κ . Because the specified mass balance pattern is radially symmetric and constant with time, a model, when stepped through time, eventually produces a steady-state circular ice sheet.

An intercomparison of twelve finite-difference models done using this test found that most of the differences among them were inconsequential. The only significant difference was between so-called Type I and Type II models. Type I models used a mass flux parameterization that conserves mass but requires short time steps to achieve stability. Type II

Figure 11.5. Ice sheet profiles calculated using Type I and II finite-difference models compared with an exact solution. (After Huybrechts *et al.*, 1996, Figure 5a. Used with permission of the authors and the International Glaciological Society.)



models do not conserve mass, but have the advantage of allowing longer time steps. The means and standard deviations of the thicknesses of the model ice sheets at the divide were 2997 ± 7.4 m and 2959 ± 1.3 m for Types I and II models, respectively. An exact solution, obtained by integrating the mass balance function analytically, produced an ice sheet that was 20 km smaller in radius, and consequently somewhat thinner, but a model with a 50 km grid spacing cannot get closer. Surface profiles predicted by the two model types are compared with each other and with the exact solution in Figure 11.5.

The tests developed by these modelers, normally referred to as the EISMINT (*European Ice Sheet Modeling INiTiative*) benchmark tests, are an invaluable tool. Both new models that are developed and existing models that are being refined can be tested against these benchmarks to expose errors in reasoning or programming.

Sensitivity testing and tuning

Because the parameters used to define boundary conditions, initial conditions, and forcing are rarely known precisely, modelers normally test the sensitivity of their models by varying these parameters within reasonable limits. Suppose, for example, that the most likely temperature boundary condition for a particular model is -5°C , and suppose further that it is unlikely that the correct boundary temperature is lower than -7°C or higher than -1°C . The modeler then might run the model with all three temperatures to see if the conclusions changed when the extreme temperatures are used. If the conclusions are unchanged, the model is said to be *robust* against a reasonable range of temperature boundary conditions. Such tests are called *sensitivity tests*.

If there are N parameters that are only known approximately and if the maximum likely, minimum likely, and most probable values of all combinations of the parameters is to be tested, the total number of tests will be 3^N . If $N > 3$, such a task becomes daunting.

In a similar vein, models are often *tuned* so that they reproduce observed characteristics of a glacier. For example, in the model of the Barnes Ice Cap temperature profiles discussed above (Equation (11.12)), the surface temperature, θ_s , under which the profiles were presumed to have developed prior to the most recent warming, and the longitudinal gradient, $\partial\theta/\partial x$ were only loosely constrained by field measurements. Thus, the model was tuned by adjusting these parameters until the model profiles matched the lower parts of the measured profiles well. Then step increases of various sizes in θ_s were tested until the upper parts of the profiles were modeled reasonably well. Tuning can be viewed either as: (1) a way of solving for unknowns that cannot be evaluated analytically as mentioned earlier (p. 289), or (2) a necessary step if the model is going to be used to explore the consequences of future changes.

Coupling thermal and mechanical models

Because the viscosity parameter, B , is dependent on temperature and, conversely, the temperature distribution depends on the flow field through the advective terms in the energy balance equation, a complete model of a polar glacier or ice sheet must include calculations of both the flow field and the temperature distribution. It is not practical to combine these two calculations, so they must be done iteratively. First a flow field is determined, given an assumed or previously calculated temperature field. Then the temperature distribution is modeled and used as input to the next flow calculation. Time stands still during this iterative procedure. Once convergence is achieved, so the difference between successive solutions from one iteration to the next is within prescribed limits, the surface profile can be updated by multiplying the calculated surface velocities and prescribed mass balance rate by the time step. An updated temperature boundary condition at the surface can then be specified, and a new calculation started.

When energy balance and momentum balance models are coupled in this way, the result is commonly called a *thermomechanical model*.

Results from ten thermomechanical models were compared in a second phase of the EISMINT study (Payne *et al.*, 2000). The ice sheet modeled was again circular, and all models predicted a central zone in which the ice sheet was frozen to the bed surrounded by an outer zone in which the base was at the pressure melting point. This time, however,

results of the comparison were somewhat less consistent, inasmuch as the area of the inner cold zone varied among the models from 13% to 42% of the total area. Furthermore, when the surface temperature at the center of the ice sheet was -50°C , an instability appeared in all but one of the models. This instability is believed to be related to the positive feedback from velocity to frictional heat generation and thence to temperature. The models were otherwise consistent in their predictions of the area, volume, thickness at the divide, and basal temperature at the divide.

Examples

Let us now examine a few modeling projects that have been undertaken. The examples chosen utilize different types of models with differing objectives. They are intended to be illustrative only, and by no means an overview of the literature.

Calving

As we discussed in Chapter 3, a great deal of ice is lost from the Greenland and Antarctic Ice Sheets and from tidewater glaciers by calving. However, the calving process is poorly understood. In the case of tidewater glaciers, extending longitudinal strain in the last several kilometers of the glacier usually results in extensive crevassing, so the ice arrives at the calving face in a weakened condition. At the calving face, blocks ranging in size from fractions of a cubic meter to 10^4 m^3 break off and fall into the water. Other blocks break off below the water surface and float upward. Finally, there is a rain of smaller fragments, most of which are probably released by melting along grain boundaries. In Antarctica, in contrast, glaciers reaching the sea tend to form floating ice shelves. Any crevasses that were present near the grounding line are largely healed. Calving from ice shelves commonly involves blocks from 10^5 to 10^{11} m^3 . While the processes of calving from grounded tidewater glaciers and floating ice shelves both involve propagation of fractures (Chapter 4), it seems likely that the origin of the stresses is substantively different in the two cases.

It is widely believed that the demise of the Late Pleistocene ice sheets was facilitated by loss of ice in calving bays that formed at the ends of ice streams and migrated rapidly headward. Such calving would resemble that in grounded tidewater glaciers. For this reason, the process of calving of such glaciers has attracted considerable interest over the past decade. One of the first efforts to tackle this problem was by Brown *et al.* (1982). Using the method described in Chapter 3 (Equation 3.14), they found

that calving speeds, \bar{u}_c , were proportional to mean water depth, \bar{h}_w , thus:

$$\bar{u}_c = c\bar{h}_w \quad (11.14)$$

However, as we noted, the physical reasons for this relation are unclear. Analytical efforts to describe the static stress distribution in a calving ice tongue, involving both longitudinal stresses and torques due to the imbalance between hydrostatic stresses in the ice and in the water at the calving face, failed to detect any stresses that might vary with water depth and hence be responsible for an empirical relation like Equation (11.14).

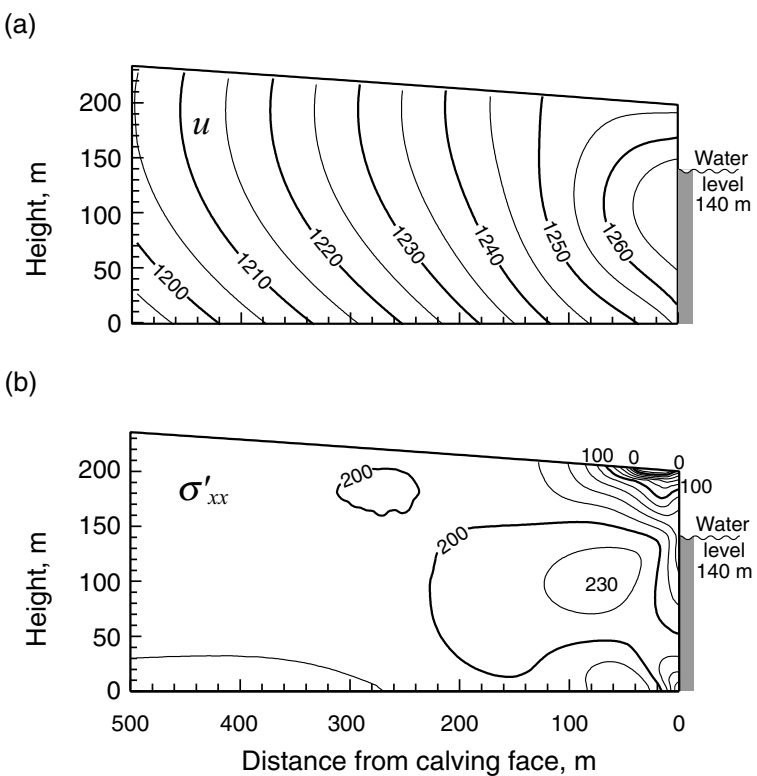
To study this problem further, Hanson and Hooke (2000) resorted to a plain-strain steady-state finite-element model. The model domain was 2000 m long in order to buffer the area of interest, the last ~ 500 m, from a poorly constrained ice flux into the upglacier end. The reference model had a calving face 200 m high and contained 16 000 elements and 16 440 nodes. (This necessitated solution of 48 440 simultaneous equations!) The lower 140 m of the face were submerged, so the subaerial part was 60 m high, a typical average height (Brown *et al.*, 1982). Sliding was allowed along the bed.

Figure 11.6 shows calculated distributions of horizontal velocity, u , and longitudinal stress deviator, σ'_{xx} , in the reference model. A zone of high u and σ'_{xx} is present just below the water line near the calving face. We hypothesized that this would tend to produce an overhang in the face, and that this might facilitate calving. As a measure of the rate of overhang development, we calculated the velocity gradient, du/dz , between this point of maximum velocity and the bed (where the glacier was sliding). Comparison of models with total calving-face heights ranging from 100 to 300 m, all of which had subaerial heights of 60 m, suggested that, in nature, du/dz probably increases nearly linearly with water depth (Figure 11.7). In addition, the rate of stretching along the bed just upglacier from the calving face, σ'_{xx} bed, increases with water depth (Figure 11.7). The latter may facilitate the formation of bottom crevasses, and hence submarine calving. The two effects, combined, provide a plausible physical explanation for the empirical relation, Equation (11.14).

Role of permafrost in ice sheet dynamics and landform evolution

For decades, glacial geologists have speculated on the effects that bed conditions have on ice sheet profiles and dynamics (see, for example, Matthews, 1974; Fisher *et al.*, 1985) and on the relation between basal

Figure 11.6. Contours of (a) horizontal velocity and (b) σ'_{xx} in a glacier 200 m thick at the calving face, calculated with the use of a finite-element model. (Reproduced from Hanson and Hooke, 2000. Used with permission of the authors and the International Glaciological Society.)



thermal conditions and glacial landforms (see, for example, Moran *et al.*, 1980; Mooers, 1990b; Attig *et al.*, 1989). Models of increasing sophistication have been used to study these effects. Here we discuss a recent time-dependent modeling effort by Cutler *et al.* (2000), using a flow-band finite-element model.

The modeled domain was a ~ 1700 km flow band extending from James Bay in Canada across the eastern end of Lake Superior and down the axis of the Green Bay lobe in Wisconsin to a Late Glacial Maximum terminal moraine and beyond. This flow band was chosen because ice-wedge casts and similar features demonstrate that permafrost was present along the margin in Wisconsin, and the modeling team wanted to estimate the thickness and horizontal extent, measured along a flowline extending upglacier from the margin, of the submarginal permafrost zone. Their ultimate goal was to investigate the role that permafrost may have played in the development of certain landforms.

The model domain was broken into ~ 100 columns with 50 nodes in the ice and 75 nodes in the substrate – a total of nearly 9000 nodes when the ice sheet extended to the terminal moraine. The particular model

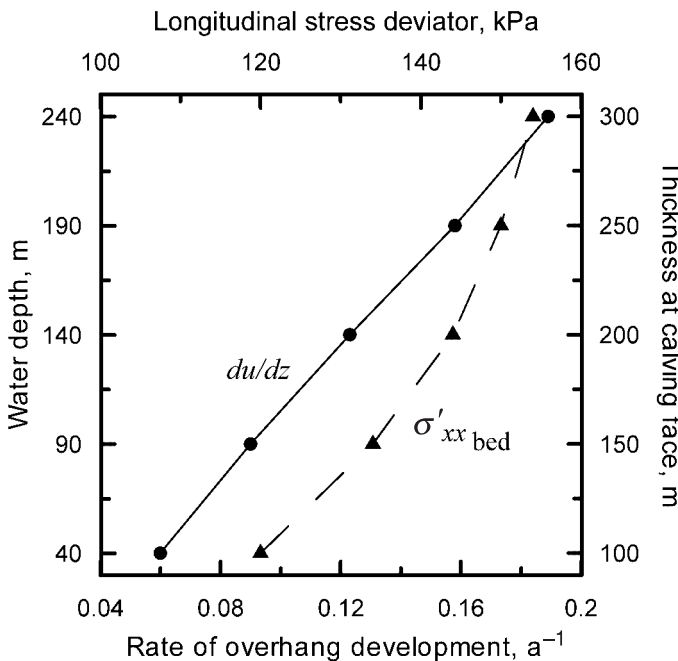


Figure 11.7. Variation of the rate of overhang development and of σ'_{xx} at bed with water depth. Subaerial part of calving face was 60 m high in all simulations. (Reproduced from Hanson and Hooke, 2000. Used with permission of the authors and the International Glaciological Society.)

run discussed here began at 55 ka, with ice already covering the first 275 km of the flowline, and ran to 21 ka, the Late Glacial Maximum. Time steps were 25 years. The model was forced with a mass balance pattern that depended on mean annual temperature and precipitation, and on the daily temperature range. The latter was essential to ensure melting when the mean daily temperature was still a few degrees below 0 °C. Temperature and precipitation were specified at the margin and were assumed to decrease in specified ways with increasing elevation and latitude along the ice sheet surface. The variation in margin temperature with time was based on well-dated paleoclimate studies (Figure 11.8a). Included in the model is a routine for keeping track of the amount of meltwater produced by subglacial melt and lost by flow through subglacial aquifers. The viscous energy dissipated by this groundwater flow was added to the geothermal flux. Divergence of the ice flow was *not* included.

Results of the model run are shown in Figure 11.8b–e. Figure 11.8b shows profiles of the ice sheet at eight times between 48 and 21 ka, and Figure 11.8c shows the ice extent as a function of time. The abrupt decrease in thickness of the ice sheet at distances greater than about 900 km from the divide (Figure 11.8b) is a consequence of the transition in the bed from crystalline rocks to a deformable substrate at ~30 ka

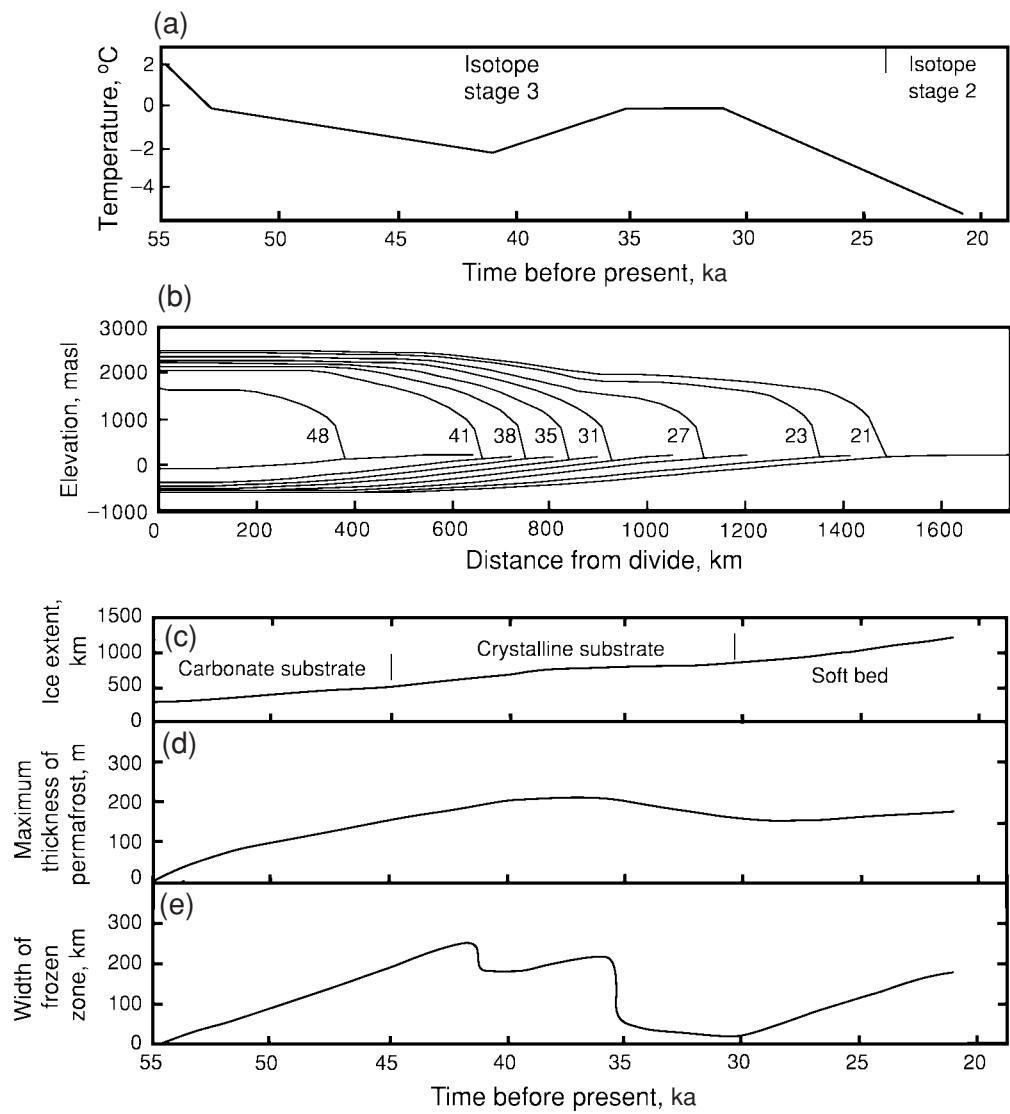


Figure 11.8. Model of a flowline down the axis of the Green Bay lobe of the Laurentide Ice Sheet. (a) Temperature specified at the margin from 55 to 20 ka. (b) Profiles of the ice sheet at eight times between 48 and 21 ka (numbers to left of curves). (c) Location of margin as a function of time. (d) Maximum thickness of permafrost. (e) Width of submarginal frozen zone measured upglacier from margin along the flowline. (Redrawn from Cutler *et al.*, 2000, Figures 3, 9, and 11. Used with permission of the authors and the International Glaciological Society.)

(Figure 11.8c). Basal sliding was allowed only over the latter and only when the bed was at the pressure melting point. With sliding, the balance velocity (Equation (5.1)) is reached with thinner ice and a lower driving stress ($\rho gh\alpha$). Note the progressive isostatic depression of the bed as the ice advances (Figure 11.8b) and the acceleration of the advance over the soft deformable bed (Figure 11.8c). Figures 11.8d and 11.8e show the maximum thickness of the permafrost and the width (measured along the flowline) of the submarginal frozen zone (see Figure 6.16). The permafrost is thickest when the glacier margin first reaches a given place on the landscape, and then thins as the ice cover thickens and insulates the site from the climate. The initial increase in maximum thickness is a response to the cooling climate (Figure 11.8a). The subsequent decrease from about 35 to 30 ka (Figure 11.8d) is a delayed reaction to the climatic amelioration that began at 40 ka. The width of the subglacial frozen zone reflects a balance between the rate of increase in width as the ice sheet advances over permafrost and the rate of decrease in width as the upglacier edge of the permafrost thaws. Changes in width thus result from a combination of changes in rate of advance and changes in climate: the decrease in rate of advance at ~ 38 ka (Figure 11.8c) results in a decrease in width (Figure 11.8e), and the increase in rate of advance at ~ 30 ka results in an increase in width. The abrupt ~ 70 km decrease in width at ~ 42 ka is puzzling, but both it and the abruptness of the decrease at 35 ka suggest that at the upglacier edge there was a wide zone of relatively thin permafrost that disappeared nearly simultaneously.

Cutler *et al.* (2000) reach three basic conclusions from this study.

- Permafrost persists for time spans of order 10^2 – 10^3 years beneath an advancing ice margin.
- The maximum width of the submarginal permafrost zone is of order 10^2 km.
- Submarginal permafrost severely inhibits drainage of basal meltwater, leading to high subglacial water pressures.

Although the dimensions of the permafrost layer (as well as many other model results) are sensitive to the values of the parameters used to define the climate, substrate characteristics, and sliding speed, these results appear to be robust; the modeled Late Glacial Maximum (LGM) ice sheet had a wide, persistent frozen toe with all tested values of the parameters. A caveat is that in their sensitivity studies Cutler *et al.* varied only one input parameter at a time. Their conclusion would be stronger if they had varied two or more parameters simultaneously in a direction to minimize the width of the frozen zone.

The probable existence of such a frozen margin during the LGM has several geomorphic implications.

- As the width of the frozen margin decreases, rather abrupt releases of stored subglacial water are likely. This supports the authors' hypothesis that tunnel valleys found along the LGM margin in Wisconsin were formed by such drainage.
- High subglacial water pressures are likely, so landforms associated with deforming beds are to be expected. Bands of drumlins upglacier from the presumed zone of frozen bed in Wisconsin (Attig *et al.*, 1989) are consistent with this, inasmuch as a mobile substrate appears to be an essential requirement for drumlin formation (Patterson and Hooke, 1995).
- Thrust features formed by the mechanism discussed in Chapter 6 (Figure 6.16) might be expected but somewhat surprisingly are not found in Wisconsin. Such features are present at comparable latitudes in neighboring states.
- Large proglacial lakes like those that formed between the advancing ice margin and the southern shores of Lakes Michigan and Erie would have inhibited formation of submarginal permafrost. This may explain, in part, why features such as drumlins, thrust features, and tunnel valleys are rare or absent south of these lakes, but higher marginal temperatures would also be a factor. It may also explain why ice lobes that filled these lakes extended further south.

While glacial geologists had speculated that permafrost might persist for some time under the margins of advancing continental ice sheets (see, for example, Mickelson, 1987), numerical modeling such as that carried out by Cutler *et al.* provides a much firmer theoretical basis for this speculation.

Three-dimensional models of ice sheets

Recently, glaciologists have put considerable effort into modeling entire ice sheets like those in Greenland and Antarctica. The results of some of these models have already been presented in Figures 5.2, 6.14, and 6.15. Armed with models that closely reproduce the characteristics of these modern ice sheets, one can examine the conditions under which past ice sheets expanded to lower latitudes, or predict the behavior of present ice sheets under various scenarios for climate change in the future.

An interesting application of a three-dimensional thermomechanical finite-difference model of a continental ice sheet is that of Marshall *et al.* (2000), who studied the Laurentide Ice Sheet. The model run starts at 122 ka, and is forced by a paleoclimate scenario based on a global

climate model tuned with ice core records. With an enhancement factor (Equation (4.10)) of 6 and without basal sliding, the model simulates the modern Greenland Ice Sheet well, and is in close agreement with other EISMINT models of Greenland. However, when it is then used to model the Laurentide Ice Sheet, it produces an LGM ice mass with a volume of $36.3 \times 10^6 \text{ km}^3$, whereas studies of moraines, LGM sea level, and post-glacial isostatic recovery suggest that the actual volume was only $\sim 22.5 \times 10^6 \text{ km}^3$. To try to bring the calculated volume into better agreement with that observed, Marshall *et al.* first added a calving routine. With reasonable calving rates, this reduced the volume only modestly. Higher calving rates led to inconsistencies with the known ice sheet extent in Hudson Bay and Hudson Strait. They then added a sliding routine but did not retain the calving algorithm. This reduced the volume to $29.1 \times 10^6 \text{ km}^3$ and resulted in an ice sheet extent that was in reasonable agreement with observations of glacial geologists (Figure 11.9). A further reduction in calculated ice volume could have been achieved by increasing the enhancement factor or by reducing precipitation in the climate forcing, but these options were not explored quantitatively.

The enhancement factor that Marshall *et al.* used for Greenland probably reflects: (1) development of strong single-maximum crystal fabrics, and (2) sliding, which occurs in Greenland but is not allowed in their model. Paterson (1991) has argued that the former is facilitated by impurities because impurities inhibit grain-boundary migration, resulting in smaller crystals, and smaller crystals recrystallize readily, leading to strong preferred orientations. Pleistocene ice tends to have more impurities, smaller grain sizes, and higher strain rates. The softness of Pleistocene ice was apparently first recognized in borehole deformation studies on Barnes Ice Cap (Hooke, 1973b) and later in similar studies on Devon (Paterson, 1977) and Agassiz (Fisher and Koerner, 1986) Ice Caps and then in Greenland (Dahl-Jensen and Gundestrup, 1987). During the Holocene the basal layers of Pleistocene ice in these four ice masses have thinned, so they now have less influence on the profile than was likely to have been the case during the Wisconsinan in the Laurentide Ice Sheet. Thus, it is reasonable to expect that the appropriate enhancement factor for the Laurentide Ice Sheet would be higher than that for Greenland today. Other modelers have also found that relatively high enhancement factors were required to model the accepted volume of the Laurentide Ice Sheet (Huybrechts and T'Siobbel, 1995; Tarasov and Peltier, 1999).

In conclusion, the Laurentide Ice Sheet can be modeled successfully if algorithms for sliding and calving are included, if Pleistocene ice is

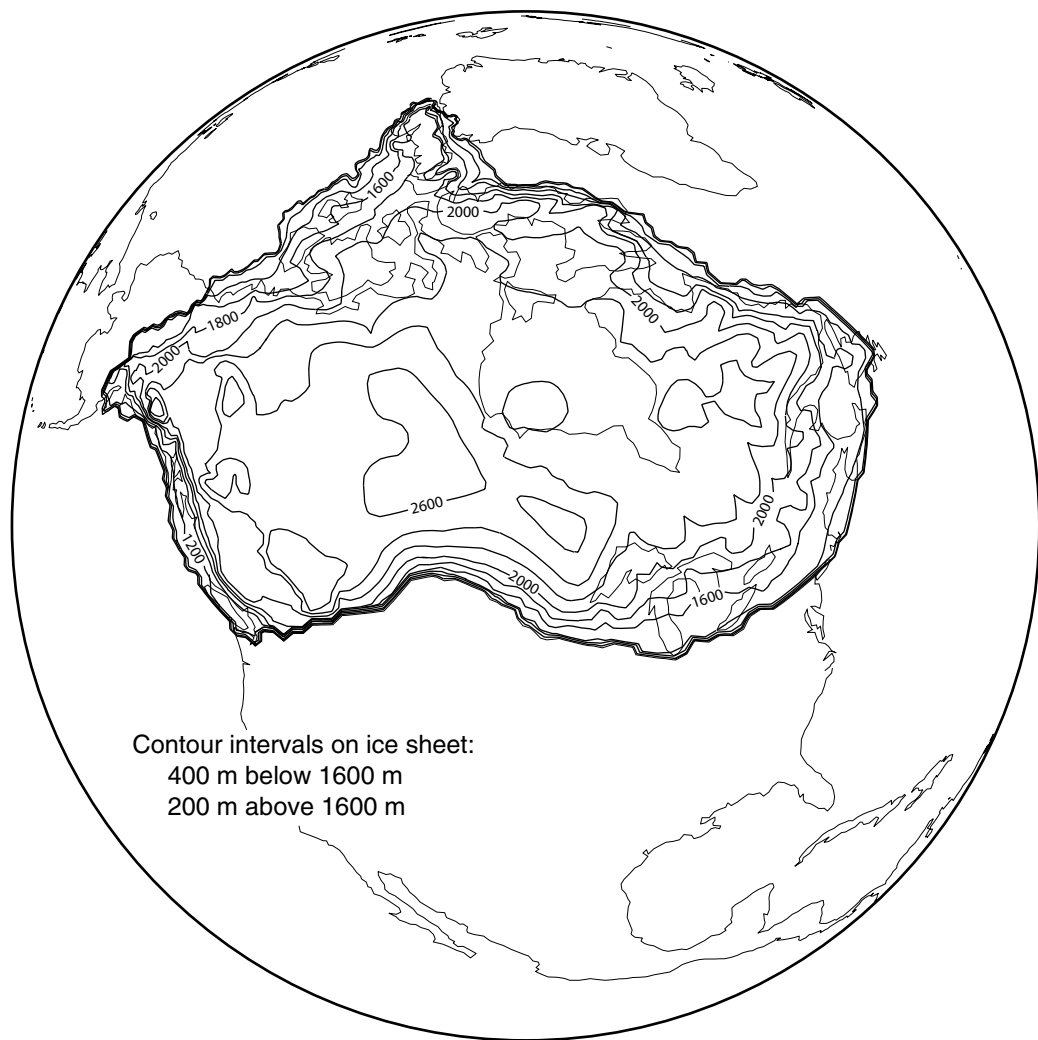


Figure 11.9. Surface topography of the Laurentide Ice Sheet at 20 ka calculated with a thermomechanical model that included a basal sliding routine. (Modified from Marshall *et al.*, 2000, Figure 9b. Used with permission of the authors and the Canadian Journal of Earth Sciences.)

assumed to have been softer than Holocene ice, and if the Pleistocene climate is assumed to have been somewhat drier than the Holocene climate. Marshall *et al.* (2000) do not pursue combinations of these effects, arguing sensibly that the physics of the calving and sliding processes are not known well enough. Sliding, for example, depends on pore water pressures in the substrate, and pore water pressures, in turn, depend

upon basal temperatures and the efficiency of the basal drainage system. Models of the basal drainage system are even more tenuous than those of calving and, as noted above, basal temperature distributions are not modeled consistently.

In short, we can choose between viewing the glass as half empty or half full. We have a long way to go to write calving and sliding algorithms that are well-supported by physics. On the other hand, the models seem to have already revealed important characteristics of the Laurentide Ice Sheet and of ice in it.

Summary

In this chapter we have reviewed the two main numerical modeling techniques commonly used in glaciology: the finite-difference and finite-element techniques. For simple problems, finite-difference approaches can be implemented with a spread sheet or simple computer program. Finite-element approaches and finite-difference solutions of more complex problems both require more sophisticated computer programs. While numerical details of these advanced techniques are beyond the scope of this book, we have introduced some of the vocabulary commonly associated with them.

Owing to their complexity, numerical models can easily have flaws that result in realistic but incorrect predictions. Parts of models can often be tested against analytical solutions before the model as a whole is applied to problems without such solutions. Output of models of entire ice sheets can be compared with the EISMINT benchmarks. The latter tests have shown that models generally do well at predicting the size and shape of an ice sheet, but relatively subtle differences among the models result in significant differences in solutions for basal temperature distribution, and in particular in the fraction of the bed that is at the pressure melting point.

In the last part of the chapter, we explored three applications of models to problems of glaciological and geomorphological significance. In the first, a finite-element model was used to study the stress distribution in a calving face in order to see if a physical explanation could be found for the commonly cited proportionality between water depth and calving rate. In the second, another finite-element model predicted that when an ice sheet advances over permafrost, a frozen margin of appreciable width is likely to develop and to persist for centuries or millennia. Certain landforms have been interpreted as being a consequence of such a frozen margin. Finally, we discussed a finite-difference model of the Laurentide Ice Sheet and found that with certain reasonable assumptions relatively

good agreement probably could be obtained between the size calculated by the model and that determined from moraines, sea level records, and isostatic rebound. The results point to the need for a better quantitative understanding of sliding, calving, and the development of basal drainage systems, and of climate history, while at the same time they constrain the ranges of these parameters that will yield agreement between model and probable reality.

Chapter 12

Applications of stress and deformation principles to classical problems

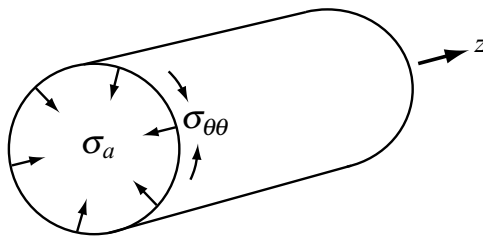
In this chapter, we will study some glaciologically significant problems for which an appreciation of the material presented in Chapters 9 and 10 is required. Our objective is not to provide a comprehensive overview of theoretical developments in glaciology, but rather to solidify the gains made in these preceding two chapters by applying the principles developed therein. In the course of this discussion, the student will be introduced to some definitive studies, frequently referenced in the glaciological literature.

Let us first consider the problem of closure of a cylindrical borehole, in part because this is relevant to our earlier discussion of glacier hydrology. Then we will investigate efforts to calculate basal shear stresses using a force balance model, followed by study of the creep of ice shelves. Finally, the problem of using borehole deformation experiments to obtain estimates of the values of the parameters in the flow law will round out the chapter.

Collapse of a cylindrical hole

The first problem we address is that of the closure of a cylindrical hole in ice. This problem was studied by Nye (1953) in the context of using closure rates of tunnels in ice to estimate the constants in Glen's flow law, and our development is based on Nye's paper. More recently, the theory has been used to analyze two problems in water flow at the base of a glacier: (1) the closure of a water conduit, and (2) leakage of water into or away from a subglacial conduit. We used the first of these analyses in Chapter 8 (Equation (8.3)).

Figure 12.1. Stresses on the wall of a cylindrical hole in a weightless medium.



Our approach is very similar to that used in Chapter 10 to obtain stresses and velocities in a “glacier” consisting of a slab of ice resting on a bed with a uniform slope. We first reduce the problem to one of plane strain by setting it up so that there is no deformation parallel to the axis of the hole. This reduces the number of unknowns from nine – the three components of the velocity vector and six components of the stress tensor – to five. Expressions for the stresses and strain rates are then obtained and inserted into the momentum and continuity equations. Finally, we use a constitutive relation between stress and stain rate, Glen’s flow law, to obtain the desired solution.

Consider, first, the closure of a hole of radius a in an infinite weightless medium (Figure 12.1). There is no strain parallel to its axis, the z -direction. Once the solution to this problem is obtained, we will modify it to apply to a real glacier. On the surface of the hole, at $r = a$, an internal tension, σ_a , is (somehow) applied. Eventually, this stress will be equated with that resulting from the difference between the pressure in the ice and that in the hole.

As there is no deformation in the z -direction, $\dot{\varepsilon}_{zz} = \lambda\sigma'_{zz} = 0$. Thus,

$$\sigma'_{zz} = 0 = \sigma_{zz} - \frac{1}{3}(\sigma_{rr} + \sigma_{\theta\theta} + \sigma_{zz})$$

or

$$\sigma_{zz} = \frac{1}{2}(\sigma_{rr} + \sigma_{\theta\theta}) \quad (12.1)$$

The mean stress thus becomes

$$P = \frac{1}{3}\sigma_{kk} = \frac{1}{3}\left[\frac{3}{2}(\sigma_{rr} + \sigma_{\theta\theta})\right]$$

so

$$\sigma'_{rr} = \frac{1}{2}(\sigma_{rr} - \sigma_{\theta\theta}) \quad (12.2)$$

and

$$\sigma'_{\theta\theta} = -\frac{1}{2}(\sigma_{rr} - \sigma_{\theta\theta}) \quad (12.3)$$

This gives us expressions for the three deviatoric stresses and the mean stress.

As stated, there is no deformation in the z -direction and, in addition, the hole wall cannot support shear tractions. Thus, in view of the radial symmetry, there can be no shear stresses in the θ - and z -directions in the medium away from the hole. Therefore, σ_{rr} , $\sigma_{\theta\theta}$, and σ_{zz} are principal stresses. The effective stress is then

$$\sigma^2 = \frac{1}{2} 2 \left[\frac{1}{4} (\sigma_{rr} - \sigma_{\theta\theta})^2 \right]$$

or

$$\sigma = \frac{1}{2} |\sigma_{rr} - \sigma_{\theta\theta}| \quad (12.4)$$

Let us now obtain another relation between σ_{rr} and σ by considering the condition for stress equilibrium. From Figure 12.2, we have

$$\sigma_{rr}(rd\theta) - \left(\sigma_{rr} + \frac{d\sigma_{rr}}{dr} dr \right) (r + dr) d\theta + 2\sigma_{\theta\theta} dr \frac{d\theta}{2} = 0$$

Canceling like terms of opposite sign, dividing by $dr d\theta$, and ignoring the term still containing a differential yields

$$r \frac{d\sigma_{rr}}{dr} + \sigma_{rr} - \sigma_{\theta\theta} = 0$$

or, by using Equation (12.4)

$$r \frac{d\sigma_{rr}}{dr} + \frac{2\sigma}{r} = 0 \quad (12.5)$$

At any radius $r \geq a$ the stress is σ_{rr} . At infinity $\sigma_{rr} = \theta$. Thus, Equation (12.5) may be integrated:

$$\int_{\sigma_{rr}}^0 d\sigma_{rr} = - \int_r^\infty \frac{2\sigma}{r} dr$$

or

$$\sigma_{rr} = \int_r^\infty \frac{2\sigma}{r} dr \quad (12.6)$$

In order to integrate Equation (12.6), we must express r in terms of σ . We will do this by determining the velocity field, and hence $\dot{\epsilon}$, and inserting a flow law. Let u be the velocity in the radial direction. Other velocities vanish owing to the radial symmetry and the absence of deformation in the z -direction. Conservation of mass requires that the mass flux through two concentric cylindrical surfaces with radii r and $r + dr$ (Figure 12.3) must be the same in an incompressible medium. Thus, we have

$$2u\pi r = 2 \left(u + \frac{du}{dr} dr \right) \pi(r + dr)$$

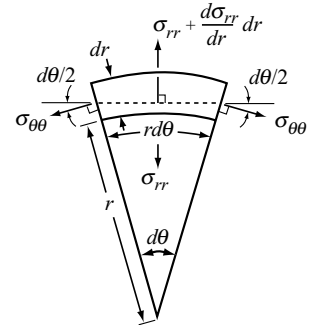
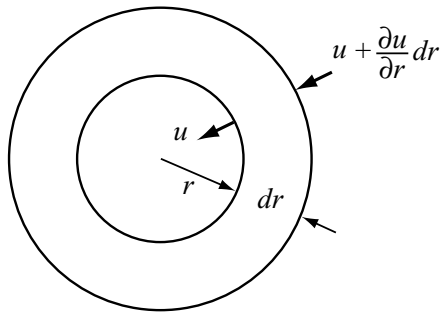


Figure 12.2. Stresses on a segment of the wall of a cylindrical hole.

Figure 12.3. Radial velocity field around a cylindrical hole.



which may be simplified, thus:

$$\frac{du}{dr} = -\frac{u}{r} \quad (12.7)$$

and integrated to yield

$$\ln u = -\ln r + \ln c$$

Because we obtained this without referring to the direction of u , a minus sign is now inserted to indicate that u is in the negative r -direction. Thus,

$$u = -\frac{c}{r}$$

So u is directed toward the hole and is a maximum on the hole wall, at $r = a$. It decreases to 0 at $r = \infty$.

From its definition in terms of velocity derivatives (Equations (9.21)), we see that $\dot{\epsilon}_{rr} = \partial u / \partial r$, so from Equation (12.7):

$$\dot{\epsilon}_{rr} = -\frac{u}{r}$$

and by continuity, since $\dot{\epsilon}_{zz} = 0$,

$$\dot{\epsilon}_{\theta\theta} = -\dot{\epsilon}_{rr} = \frac{u}{r}$$

The effective strain rate is thus:

$$\dot{\epsilon}^2 = \frac{1}{2} \dot{\epsilon}_{ij} \dot{\epsilon}_{ij} = \frac{1}{2} \left(2 \frac{u^2}{r^2} \right)$$

As $u = -c/r$, this becomes:

$$\dot{\epsilon} = \frac{c}{r^2} \quad (12.8)$$

We can retain the generality of the solution a little longer before inserting a flow law. Because $\dot{\epsilon} = f(\sigma)$, we have

$$f(\sigma) = \frac{c}{r^2} \quad (12.9)$$

To obtain r in terms of σ , note that (using Equation (12.9)):

$$\frac{df(\sigma)}{d\sigma} = \frac{df(\sigma)}{dr} \frac{dr}{d\sigma} = -\frac{2c}{r^3} \frac{dr}{d\sigma}$$

Again using Equation (12.9) to eliminate c :

$$\frac{df(\sigma)}{d\sigma} = -\frac{2}{r} f(\sigma) \frac{dr}{d\sigma}$$

so:

$$dr = -\frac{r}{2} \frac{df(\sigma)}{f(\sigma)}$$

Substituting this into Equation (12.6) yields

$$\sigma_{rr} = -\int \frac{2\sigma}{r} \frac{r}{2} \frac{df(\sigma)}{f(\sigma)} = -\int \frac{\sigma}{f(\sigma)} df(\sigma) \quad (12.10)$$

It is now necessary to make use of a flow law, specifically Glen's flow law, to obtain an analytical expression for the functional relation in Equation (12.9), thus:

$$\dot{\varepsilon} = f(\sigma) = \left(\frac{\sigma}{B}\right)^n = \frac{c}{r^2} \quad (12.11)$$

whence, differentiating:

$$df(\sigma) = \frac{n\sigma^{n-1}}{B^n} d\sigma$$

With the use of these last two relations, Equation (12.10) becomes

$$\sigma_{rr} = \int_0^\sigma \frac{\sigma}{(\sigma/B)^n} \frac{n\sigma^{n-1}}{B^n} d\sigma = \int_0^\sigma n d\sigma$$

so,

$$\sigma_{rr} = n\sigma \quad (12.12)$$

In other words, the radial stress at any distance $r \geq a$ from the hole wall is simply n times the effective stress. One cannot help but be impressed by the simplicity and elegance of this result, considering the effort required to obtain it. Unfortunately, real life is rarely so conveniently uncomplicated. Furthermore, we still have some way to go before obtaining relations that can be applied to real glaciers.

In preparation for relaxing the assumption that the medium is weightless, let us now scale this solution to the normal stress, σ_a , on the hole wall. Using the last equality in Equation (12.11) to obtain an expression for σ , σ_{rr} and σ_a become:

$$\sigma_{rr} = nB \left(\frac{c}{r^2}\right)^{1/n} \quad \text{and} \quad \sigma_a = nB \left(\frac{c}{a^2}\right)^{1/n}$$

whence:

$$\frac{\sigma_{rr}}{\sigma_a} = \left(\frac{a}{r}\right)^{2/n} \quad (12.13)$$

Solutions for the remaining stresses can now be written similarly, as follows. From Equations (12.4) and (12.12):

$$\sigma = \frac{1}{2} (\sigma_{rr} - \sigma_{\theta\theta}) = \frac{1}{2} (n\sigma - \sigma_{\theta\theta})$$

whence, transposing and again using the last equality in Equation (12.11):

$$\sigma_{\theta\theta} = (n - 2)\sigma = (n - 2)B \left(\frac{c}{r^2}\right)^{1/n}$$

so:

$$\frac{\sigma_{\theta\theta}}{\sigma_a} = \frac{n-2}{n} \left(\frac{a}{r}\right)^{2/n} \quad (12.14a)$$

Then, from Equations (12.1), (12.13), and (12.14a):

$$\begin{aligned} \frac{\sigma_{zz}}{\sigma_a} &= \frac{1}{2} \left(\frac{\sigma_{rr}}{\sigma_a} + \frac{\sigma_{\theta\theta}}{\sigma_a} \right) = \frac{1}{2} \left[\left(\frac{a}{r}\right)^{2/n} + \frac{n-2}{n} \left(\frac{a}{r}\right)^{2/n} \right] \\ &= \frac{1}{2} \left[\left(\frac{a}{r}\right)^{2/n} \left(1 + \frac{n-2}{n}\right) \right] \end{aligned}$$

so

$$\frac{\sigma_{zz}}{\sigma_a} = \frac{n-1}{n} \left(\frac{a}{r}\right)^{2/n} \quad (12.15)$$

Finally, from Equations (12.4), (12.13), and (12.14a):

$$\frac{\sigma}{\sigma_a} = \frac{1}{2} \left(\frac{\sigma_{rr}}{\sigma_a} - \frac{\sigma_{\theta\theta}}{\sigma_a} \right) = \frac{1}{2} \left[\left(\frac{a}{r}\right)^{2/n} - \frac{n-2}{n} \left(\frac{a}{r}\right)^{2/n} \right]$$

Thus,

$$\frac{\sigma}{\sigma_a} = \frac{1}{n} \left(\frac{a}{r}\right)^{2/n} \quad (12.16)$$

We can now relax the assumption that the medium is weightless. Suppose we have a horizontal hole at atmospheric pressure at a depth h_o in a real glacier. The hydrostatic pressure in the glacier is $\mathcal{P} = \rho gh$, and around the hole it is $\mathcal{P} = \rho gh_o$. Note that \mathcal{P} is not equal to the mean stress, $P (= \frac{1}{3}\sigma_{kk})$. If $h_o \gg a$, \mathcal{P} will be nearly uniform around the hole. We have not previously specified the magnitude of σ_a , so let us now solve Equations (12.13) through (12.16) for σ_{ii} ($i = r, \theta, z$) with $\sigma_a = \mathcal{P}$. Furthermore, because \mathcal{P} is hydrostatic, let us add a compressive stress, $-\mathcal{P}$, to the solutions. This is valid because a hydrostatic pressure influences all of the stresses equally, and therefore does not affect the local differences among the stresses given by Equations (12.13)

through (12.16). The resulting equations are:

$$\sigma_{rr} = \mathcal{P} \left(\frac{a}{r} \right)^{2/n} - \mathcal{P} = \mathcal{P} \left[\left(\frac{a}{r} \right)^{2/n} - 1 \right] \quad (12.17a)$$

$$\sigma_{\theta\theta} = \mathcal{P} \frac{n-2}{n} \left(\frac{a}{r} \right)^{2/n} - \mathcal{P} = \mathcal{P} \left[\frac{n-2}{n} \left(\frac{a}{r} \right)^{2/n} - 1 \right] \quad (12.17b)$$

$$\sigma_{zz} = \mathcal{P} \frac{n-1}{n} \left(\frac{a}{r} \right)^{2/n} - \mathcal{P} = \mathcal{P} \left[\frac{n-1}{n} \left(\frac{a}{r} \right)^{2/n} - 1 \right] \quad (12.17c)$$

$$\sigma = \frac{1}{2} (\sigma_{rr} - \sigma_{\theta\theta}) = \frac{\mathcal{P}}{n} \left(\frac{a}{r} \right)^{2/n} \quad (12.17d)$$

and the mean stress is

$$\begin{aligned} \frac{1}{3} \sigma_{kk} &= \frac{\mathcal{P}}{3} \left[\left(\frac{a}{r} \right)^{2/n} - 1 + \frac{n-2}{n} \left(\frac{a}{r} \right)^{2/n} - 1 + \frac{n-1}{n} \left(\frac{a}{r} \right)^{2/n} - 1 \right] \\ &= \mathcal{P} \left[\frac{n-1}{n} \left(\frac{a}{r} \right)^{2/n} - 1 \right] \end{aligned} \quad (12.18)$$

Now, the stress causing closure is no longer a hypothetical traction on the inside of the hole, σ_a . Rather it is the real hydrostatic stress in the medium. Note that all of the stresses decrease to $-\mathcal{P}$ (i.e. compressive) at large distances from the hole.

It is easy to show that the corresponding deviatoric stresses are:

$$\sigma'_{rr} = -\sigma'_{\theta\theta} = \frac{\mathcal{P}}{n} \left(\frac{a}{r} \right)^{2/n} \quad (12.19a)$$

$$\sigma'_{zz} = 0 \quad (12.19b)$$

That $\sigma'_{rr} = -\sigma'_{\theta\theta}$ and $\sigma'_{zz} = 0$ are a consequence of our assumption of plane strain.

Setting $r = a$ in Equations (12.17) we obtain the stresses on the hole wall:

$$\begin{aligned} \sigma_{rr} &= 0 \\ \sigma_{\theta\theta} &= -\frac{2\mathcal{P}}{n} \\ \sigma_{zz} &= -\frac{\mathcal{P}}{n} \\ \sigma &= \frac{\mathcal{P}}{n} \end{aligned} \quad (12.20)$$

Tunnel and borehole closure

These relations have been used to determine values of the constants n and B in the flow law with the use of measurements of the rate of closure of a tunnel or borehole. To do this, it is necessary to incorporate

the relations into the flow law. Deviatoric stresses are thus required. Because we are interested in closure, only $\sigma'_{rr(r=a)}$ is needed. Thus, using Equation (12.19a) with $r = a$, noting that $\sigma_{r=a} = \mathcal{P}/n$, and remembering Equations (9.29) and (10.39):

$$\dot{\varepsilon}_{rr(r=a)} = \frac{\sigma^{n-1}}{B^n} \sigma'_{rr(r=a)} = \frac{(\mathcal{P}/n)^{n-1}}{B^n} \frac{\mathcal{P}}{n} \quad (12.21)$$

Because $\dot{\varepsilon}_{rr(r=a)} = -u_a/a$, where u_a is the closure rate, we obtain

$$-\frac{u_a}{a} = \left(\frac{\mathcal{P}}{nB} \right)^n \quad (12.22)$$

To use Equation (12.22) to estimate the constants in the flow law, one needs values of u_a , a , and \mathcal{P} at two or more places. Inserting values for two such places in Equation (12.22) would yield two equations with two unknowns (n and B). With three or more sets of data, it is useful to plot $\log \dot{\varepsilon}$ against $\log \mathcal{P}$ as is done for some tunnel-closure experiments in Figure 12.4.

Some caution is required, however. In tunnel-closure studies, for example, pegs are normally inserted in the tunnel walls and closure is measured by determining the change in distance between the heads of pegs on opposite sides of the tunnel. In this case, particularly in temperate glaciers, the point where the pegs are actually gripped by the ice may be some distance back in the wall. Furthermore, such tunnels are rarely if ever circular in cross section. Thus the correct value of a must be guessed.

In borehole-closure studies, closure rates are measured with calipers, so determining the appropriate value of a is not a problem. However, the time interval between measurements is often fairly large, and a substantial amount of closure may occur between measurements. In this case, approximating u_a by $\Delta a/\Delta t$ is likely to yield a poor estimate (Paterson, 1977). The correct procedure is to use the temporal mean value of u_a/a , which is, by the definition of a mean:

$$\bar{\dot{\varepsilon}}_a = -\frac{1}{\Delta t} \int_{t_1}^{t_2} \frac{u_a}{a} dt$$

Noting that $u_a = da/dt$, this becomes:

$$\bar{\dot{\varepsilon}}_a = -\frac{1}{\Delta t} \int_{t_1}^{t_2} \frac{1}{a} \frac{da}{dt} dt = -\frac{1}{\Delta t} \ln \frac{a_2}{a_1}$$

Some results from four borehole closure studies are presented in Figure 12.5 (open circles) along with data on the variation of B with temperature from a large number of other laboratory and field experiments.

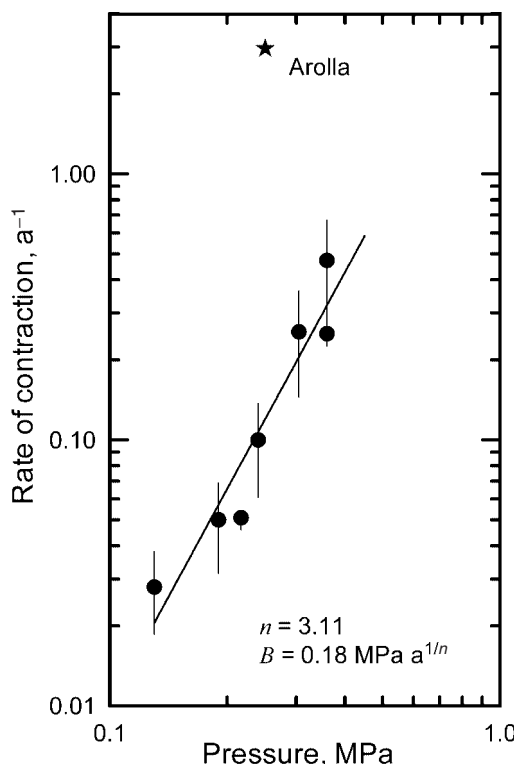


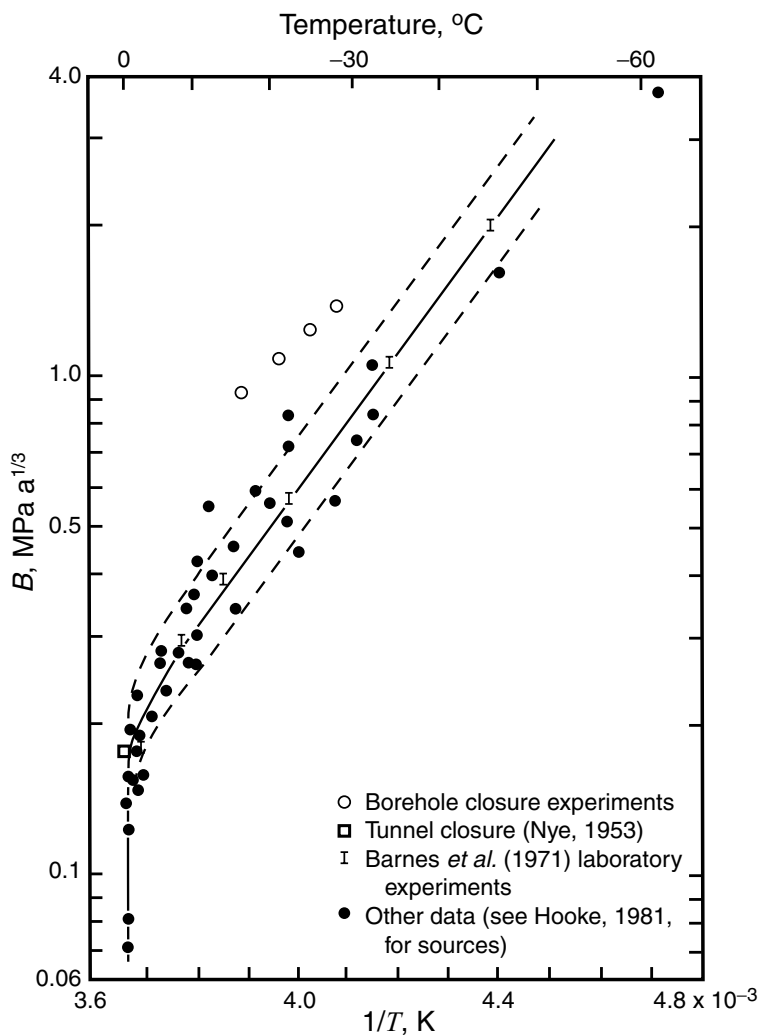
Figure 12.4. Rate of contraction, u_a , of tunnel sections plotted against overburden pressure, P (Replotted from Nye, 1953, Figure 1. Reproduced with permission of the author and The Royal Society of London.)

It is instructive to look at the results in Figures 12.4 and 12.5 in somewhat greater detail. In Figure 12.4, it will be noted that several of the sets of tunnel closure data fall along a line with $n = 3.11$ and $B = 0.18 \text{ MPa } a^{1/n}$. This value of B is plotted as the open square in Figure 12.5; it is quite consistent with other data from temperate ice. However, the point representing data from the Arolla ice tunnel falls well above the line in Figure 12.4. The Arolla tunnel is at the base of an ice fall. Owing to the contribution of longitudinal stresses, σ may be significantly higher than P/n here, and, as observed, one would thus expect the actual closure rate to be higher than that calculated using $(P/n)^{n-1}$ to approximate σ^{n-1} in Equation (12.21).

The problem with the borehole-closure rates, which seem to be too low and therefore yield values of B that appear to be too high in Figure 12.5, is different. Here, we speculate that the crystallographic fabric in the ice is adjusted to a stress regime in which the dominant deviatoric stress is simple shear normal to the axis of the hole. Such a fabric may have inhibited closure.

Figure 12.5. Values of B from various experiments in which the minimum strain rate was measured or estimated.

Octahedral stresses and strain rates were used in calculating B . Straight part of solid line is based on data from Barnes *et al.* (1971). Dashed lines are values of B that would give strain rates half or double those on solid line. (After Hooke, 1981, Figure 2).



Subglacial water conduits

In Chapter 8 we applied Equation (12.22) to closure of subglacial water conduits. As noted there, problems arise when one attempts to estimate closure rates of semicircular conduits, owing to drag on the bed. Even more profound difficulties arise in attempting to estimate closure rates of broad low conduits, as stresses in the ice are no longer symmetrically distributed about the conduit.

Here, we look into another problem of interest: the normal stresses on the bed at the boundaries of a semicircular conduit, and in particular, the gradient in these stresses outward from the conduit (Figure 12.6). This problem was first studied by Weertman (1972). If pressures are

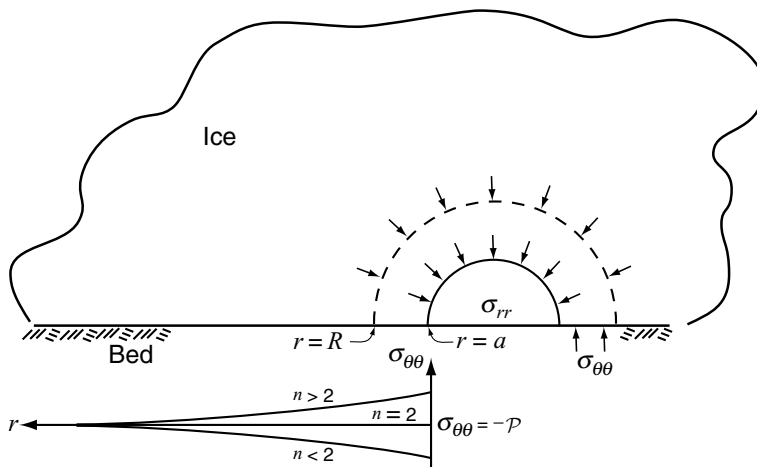


Figure 12.6. Stresses around a semicircular conduit: σ_{rr} is extending and $\sigma_{\theta\theta}$ is compressive (hence the minus sign on P). The variation in $\sigma_{\theta\theta}$ away from the tunnel is shown schematically. For $n > 2$, $\sigma_{\theta\theta}$ is less compressive than P , and conversely.

higher adjacent to the conduit, water in a film at the ice–bed interface will be forced away from the conduit, and conversely.

The significance of this problem lies in its application to water flow beneath polar ice sheets. Several authors have suggested that for conduits to exist beneath such ice masses in the absence of water inputs from the glacier surface, there must be an influx of water from adjacent parts of the bed (Alley, 1989a; Walder, 1982; Weertman and Birchfield, 1983; Ng, 2000a). The problem of the existence of such conduits is fundamental; where they are present, subglacial water pressures are probably appreciably lower than otherwise. Thus, any attempt to explain, for example, the fast flow of ice streams hinges upon an understanding of the nature of the water flow system.

The relevant stress in this problem is $\sigma_{\theta\theta}$. Thus, let us start with the expression for $\sigma_{\theta\theta}$ in Equation (12.14a). Note that in so doing, we tacitly assume that the bed is flat and slippery so that shear stresses do not impede movement of ice inward toward the tunnel. The appropriate value for σ_a is now the difference between the pressure in the ice and that in the water in the conduit, ΔP . As before, we add a pressure, $-P$, everywhere to account for the weight of the ice. With a little rearranging, Equation (12.14a) thus becomes:

$$\sigma_{\theta\theta} = \frac{n-2}{n} \Delta P a^{\frac{2}{n}} r^{-\frac{2}{n}} - P \quad (12.14b)$$

Note that $\sigma_{\theta\theta}$ is negative, or compressive, as P always exceeds the first term on the right.

It may appear from Equation (12.14b) that $\sigma_{\theta\theta}$ will not support the weight of the glacier when $n > 2$, as then $\sigma_{\theta\theta} \rightarrow -P$ as $r \rightarrow \infty$ but

$\sigma_{\theta\theta} > -\mathcal{P}$ near the conduit. In other words, $\sigma_{\theta\theta}$ is sufficiently compressive to support the glacier far from the conduit but not near or beneath it. However, $\sigma_{(rr=R)}$ is more compressive than $\sigma_{(rr=a)}$ (Equation (12.17a)), and this provides the additional support. In other words, referring to Figure 12.6, the vertical force acting on the surface at radius R balances that on the bed, which is: $2 \int_0^a (\Delta\mathcal{P} - \mathcal{P}) dr + 2 \int_a^R (\sigma_{\theta\theta} - \mathcal{P}) dr$.

Let us now consider a semicircular conduit at a depth h_0 on a horizontal bed beneath an ice sheet of uniform thickness and infinite horizontal extent. Taking the derivative of $\sigma_{\theta\theta}$ with respect to r along the bed yields

$$\frac{d\sigma_{\theta\theta}}{dr} = -\frac{2}{n} \left(\frac{n-2}{n} \right) \Delta\mathcal{P} a^{\frac{2}{n}} r^{-\left(\frac{2}{n}+1\right)} \quad (12.23)$$

If $n > 2$, as might be expected, $d\sigma_{\theta\theta}/dr$ is negative. Thus $\sigma_{\theta\theta}$ decreases, or becomes more negative, or more compressive, away from the tunnel (Figure 12.6). In this case, water in a film will be forced toward the conduit, enhancing discharge in it. However, when one considers coupling of stresses, particularly where there is a shear stress on the bed parallel to the conduit, the situation is not so simple. It appears that in this case water flow may be away from the tunnel (Weertman, 1972, pp. 299–300).

The physical reason for the change in behavior of $d\sigma_{\theta\theta}/dr$ with n is not obvious. We might expect that if a cavity is introduced at the base of a glacier, compressive stresses adjacent to the cavity would increase in order to support that part of the weight of the glacier that is no longer supported by the bed under the cavity. However, toward the tunnel u , and hence $\dot{\varepsilon}_{rr}$, increase and this requires an increase in σ'_{rr} . The way in which the stress field is modified to satisfy this requirement, and hence the way in which the pressure on the bed is redistributed, depends upon n . A more intuitive explanation of this effect is elusive.

Calculating basal shear stresses using a force balance

To a first approximation, the basal drag can be estimated from $\tau_b = \rho g h \alpha$ (or $\tau_b = S_f \rho g h \alpha$ in a valley glacier). However, if longitudinal forces are unbalanced, τ_b may be either greater or less than $\rho g h \alpha$. For example, in Figure 12.7, the body force, $\rho g h$, has a downslope component, $\rho g h \alpha$. In addition, there are longitudinal forces F_u and F_d . If $F_u > F_d$, as suggested by the lengths of the arrows in the figure, τ_b will clearly have to be greater than $\rho g h \alpha$ in order to balance forces parallel to the bed, and conversely. We now explore this effect in greater detail. The first part of the development is a three-dimensional generalization of an approach suggested by B. Hanson (Hooke and Hanson, 1986, p. 268).

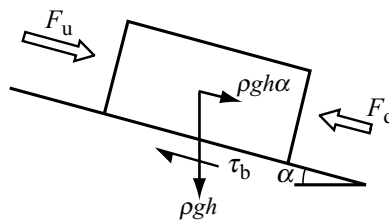


Figure 12.7. Longitudinal forces on a segment of a glacier on a sloping bed. If $F_u > F_d$ the basal drag will be greater than $\rho gh\alpha$, and conversely.

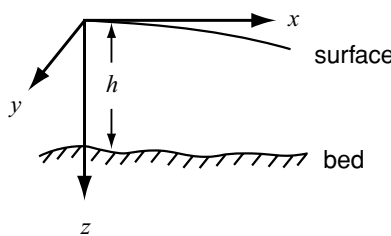


Figure 12.8. Coordinate system used in force balance analysis.

Because our goal is to calculate the drag exerted on the glacier by the bed, the momentum balance equations (Equations (9.32b)) are the obvious starting point for the analysis. The coordinate system to be used is shown in Figure 12.8. The x -axis is horizontal and in the direction of flow, and the z -axis is vertical. Writing out the momentum balance equations in the x - and z -directions, remembering that $\sigma_{ij}' = \sigma_{ij} - \delta_{ij}P$, leads to:

$$\frac{\partial \sigma'_{xx}}{\partial x} + \frac{\partial \sigma_{yx}}{\partial y} + \frac{\partial \sigma_{zx}}{\partial z} + \frac{\partial P}{\partial x} = 0 \quad (12.24a)$$

and

$$\frac{\partial \sigma_{xz}}{\partial x} + \frac{\partial \sigma_{yz}}{\partial y} + \frac{\partial \sigma'_{zz}}{\partial z} + \frac{\partial P}{\partial z} = -\rho g \quad (12.24b)$$

The procedure now will be to solve Equation (12.24b) for P , substitute the result into Equation (12.24a), and integrate over the depth to obtain $\sigma_{zx}(z=h) (= \tau_b)$.

To solve Equation (12.24b) for P , separate variables and integrate over depth z :

$$\int_0^z dP = - \int_0^z \frac{\partial \sigma_{xz}}{\partial x} dz - \int_0^z \frac{\partial \sigma_{yz}}{\partial y} dz - \int_0^z d\sigma'_{zz} - \int_0^z \rho g dz$$

or, noting that $P = 0$ at the surface:

$$P = - \int_0^z \frac{\partial \sigma_{xz}}{\partial x} dz - \int_0^z \frac{\partial \sigma_{yz}}{\partial y} dz - \sigma'_{zz} + \sigma'_{zz}|_{z=0} - \rho g z$$

Now take the horizontal derivative, assuming that $\partial\sigma_{zz}'/\partial x|_{z=0}$ is negligible and noting that $dz/dx = \alpha$, and substitute the result into Equation (12.24a), thus:

$$\frac{\partial\sigma'_{xx}}{\partial x} + \frac{\partial\sigma'_{yx}}{\partial y} + \frac{\partial\sigma_{zx}}{\partial z} - \int_0^z \frac{\partial^2\sigma_{xz}}{\partial x^2} dz - \int_0^z \frac{\partial^2\sigma_{yz}}{\partial x \partial y} dz - \frac{\partial\sigma'_{zz}}{\partial x} - \rho g \alpha = 0 \quad (12.25)$$

Equation (12.25) is in terms of stresses at any given level, z , in the glacier, whereas we are interested in summing the stresses over depth to obtain τ_b . Thus, as just noted, we integrate over depth:

$$\begin{aligned} & \int_0^h \left(\frac{\partial\sigma'_{xx}}{\partial x} - \frac{\partial\sigma'_{zz}}{\partial x} \right) dz + \int_0^h \frac{\partial\sigma_{yx}}{\partial y} dz + \int_0^h d\sigma_{zx} \\ & - \int_0^h \int_0^z \left(\frac{\partial^2\sigma_{xz}}{\partial x^2} + \frac{\partial^2\sigma_{yz}}{\partial x \partial y} \right) dz dz - \rho g h \alpha = 0 \end{aligned} \quad (12.26)$$

Clearly, $\sigma_{zx}(z=h)$ ($= \tau_b$) will be obtained from integrating the third term, and the last term is the familiar $\rho g h \alpha$. Some simplification is obviously desirable, however.

The double integral term in Equation (12.26), also sometimes referred to as the T-term, is difficult to interpret physically. In two dimensions, Budd (1969, p. 116) has shown that it can be approximated by:

$$\int_0^h \int_0^z \frac{\partial^2\sigma_{xz}}{\partial x^2} dz dz \cong \frac{1}{6} \left[\rho g \frac{\partial^2}{\partial x^2} (\alpha h^3) \right] \quad (12.27)$$

Van der Veen and Whillans (1989) argue that this term is related to “bridging” effects, in which the pressure on the bed varies spatially owing to the influence of bed irregularities and, particularly, cavity formation. Because ice is “soft”, they suggest that these bridging effects should be small compared with the average normal pressure. Thus, they neglect the T-term in force-balance calculations, and we shall follow their lead in this respect. They acknowledge, however, that the “physical implications” of doing so are “not conceptually straightforward”.

Turning to the first term in Equation (12.26), σ'_{zz} can be eliminated by noting that, owing to the proportionality between deviatoric stress and strain rate, the incompressibility condition, $\dot{\epsilon}_{xx} + \dot{\epsilon}_{yy} + \dot{\epsilon}_{zz} = 0$, leads to $\sigma'_{xx} + \sigma'_{yy} + \sigma'_{zz} = 0$. In addition, because σ_{zx} would be zero on a free horizontal surface, and is only slightly different from zero on the gently sloping glacier surface, the third term in Equation (12.26) is the desired basal drag, τ_b , as just noted. With these modifications, Equation (12.26)

becomes:

$$\int_0^h \frac{\partial}{\partial x} (2\sigma'_{xx} + \sigma'_{yy}) dz + \int_0^h \frac{\partial \sigma_{yx}}{\partial y} dz + \tau_b - \rho gh\alpha = 0 \quad (12.28)$$

To get an intuitive sense for this relation, consider a situation in which σ'_{xx} and σ_{yx} are independent of depth and σ'_{yy} is negligible. Then Equation (12.28) reduces to:

$$\rho gh\alpha - \tau_b = 2 \frac{\partial \sigma'_{xx}}{\partial x} h + \frac{\partial \sigma_{yx}}{\partial y} h \quad (12.28a)$$

In two dimensions ($\sigma_{yx} = 0$), this equation says that if the driving stress, $\rho gh\alpha$, exceeds the drag provided by the bed, τ_b , the stretching rate ($\dot{\varepsilon}_{xx} \propto \sigma'_{xx}$) will increase downglacier ($\partial \sigma'_{xx}/\partial x > 0$), and conversely. The second term on the right takes shear stresses on the valley sides into consideration. (Adjusting for the fact we have neglected bridging effects and have taken the z -direction to be positive downward, Equation (12.28) is identical to Van der Veen and Whillans' (1989) Equation (12.25). The rest of our development follows theirs.)

Our objective now is to express Equation (12.28) in a form that will allow evaluation of τ_b from strain rate measurements at the glacier surface. To this end, we note that because

$$\sigma^{n-1} = (\dot{\varepsilon}^{\frac{1}{n}} B)^{n-1}$$

the flow law can be written:

$$\dot{\varepsilon}_{ij} = \frac{\sigma^{n-1}}{B^n} \sigma'_{ij} = \frac{\dot{\varepsilon}^{\frac{n-1}{n}}}{B} \sigma'_{ij}$$

Inserting this in Equation (12.28), reversing the order of differentiation and integration, and rearranging terms yields:

$$\tau_b = \rho gh\alpha - \frac{\partial}{\partial x} \int_0^h \frac{B}{\dot{\varepsilon}^{\frac{n-1}{n}}} (2\dot{\varepsilon}_{xx} + \dot{\varepsilon}_{yy}) dz - \frac{\partial}{\partial y} \int_0^h \frac{B}{\dot{\varepsilon}^{\frac{n-1}{n}}} \dot{\varepsilon}_{yx} dz \quad (12.29)$$

Van der Veen and Whillans (1989) developed a numerical procedure to carry out the integration over depth, z . However, for simple applications we assume that strain rates are independent of depth, and express Equation (12.29) in finite-difference form, thus:

$$\begin{aligned} \tau_b = \rho gh\alpha - B \dot{\varepsilon}^{\frac{1-n}{n}} & \left[\frac{(2\dot{\varepsilon}_{xx} + \dot{\varepsilon}_{yy})h|_{\text{dwn}} - (2\dot{\varepsilon}_{xx} + \dot{\varepsilon}_{yy})h|_{\text{up}}}{\Delta x} \right] \\ & - B \dot{\varepsilon}^{\frac{1-n}{n}} \left[\frac{\dot{\varepsilon}_{yx}h|_{\text{rgt}} - \dot{\varepsilon}_{yx}h|_{\text{lft}}}{\Delta y} \right] \end{aligned} \quad (12.30)$$

Here, the symbols $|_{\text{dwn}}$, $|_{\text{up}}$, $|_{\text{rgt}}$, and $|_{\text{lft}}$ refer, respectively, to the downglacier and upglacier ends, and to the left and right sides (looking downglacier), of a “block” of the glacier of length Δx and width Δy .

Table 12.1. Force balance calculations

Time	$\dot{\varepsilon}_{xx}$ (up), a^{-1}	$\dot{\varepsilon}_{xx}$ (dwn), a^{-1}	Term 2*, kPa	Term 3*, kPa	τ_b , kPa	$\Delta\tau_b$, %
Block A						
Winter	-0.016	-0.004	1	-34	-82	—
July 1983	0.001	-0.005	-25	-38	-52	-37
July 1983	-0.006	-0.011	-17	-36	-62	-24
May 1984	-0.008	-0.018	-19	-38	-58	-29
June 1984	0.001	-0.002	-26	-40	-49	-40
June 1985	-0.010	-0.007	-7	-38	-69	-16
Block B						
Winter	0.006	-0.008	-28	-25	-92	—
July 1983	Data incomplete					
July 1983	Data incomplete					
May 1984	0.000	-0.053	-23	-31	-91	-1
June 1984	-0.002	0.037	40	-15	-170	+84
June 1985	-0.002	-0.002	9	-25	-129	+40

The values of $\rho gh\alpha$ were 115 kPa beneath block **A** and 145 kPa beneath block **B**.

*Terms 2 and 3 are the second and third terms on the right-hand side of Equation (12.30), the longitudinal and transverse terms, respectively.

The second term on the right represents the contribution to τ_b of an imbalance in forces on the ends of the block, while the third represents the contribution of forces on the sides.

An example of an application of this procedure is provided by an experiment conducted on Storglaciären, Sweden (Hooke *et al.*, 1989). Some stakes on the glacier surface (Figure 12.9) were surveyed frequently between 1982 and 1985 to determine velocities (Figure 12.10). The pattern of stakes was such that longitudinal and transverse strain rates could be calculated at the upglacier and downglacier ends of the “blocks” labeled **A** and **B** in Figure 12.9, and shear strain rates could be calculated along the sides. Results of the calculations for six time periods are shown in Table 12.1. One time period represents mean winter conditions; τ_b was then -82 kPa beneath block **A** and -92 kPa beneath block **B**. The other five time periods were those during which high velocity events occurred (Figure 12.10). During these events, τ_b was reduced an average of nearly 30% beneath block **A**. Beneath block **B** the change in τ_b was more variable, but significant increases occurred during two events.

Study of the patterns of changes suggests that acceleration of block **A** was, in every case, accompanied by an increase in magnitude of

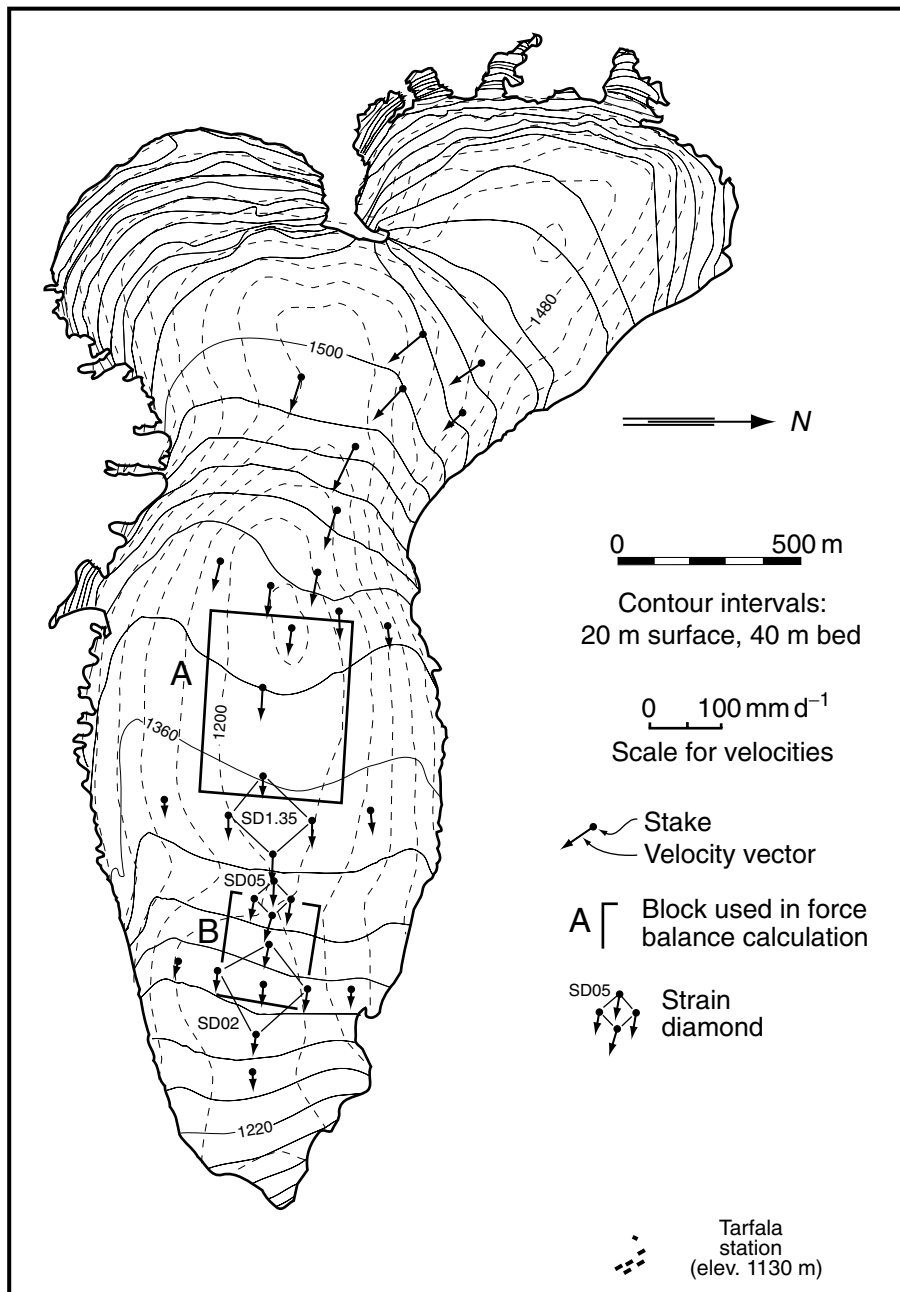


Figure 12.9. Map of Storglaciären showing generalized surface and bed topography (solid and dashed contours, respectively), locations of stakes used for velocity measurements, velocities, and blocks used in force balance calculations. (Data from Hooke *et al.*, 1989, Figure 1a. Base map courtesy of Peter Jansson.)

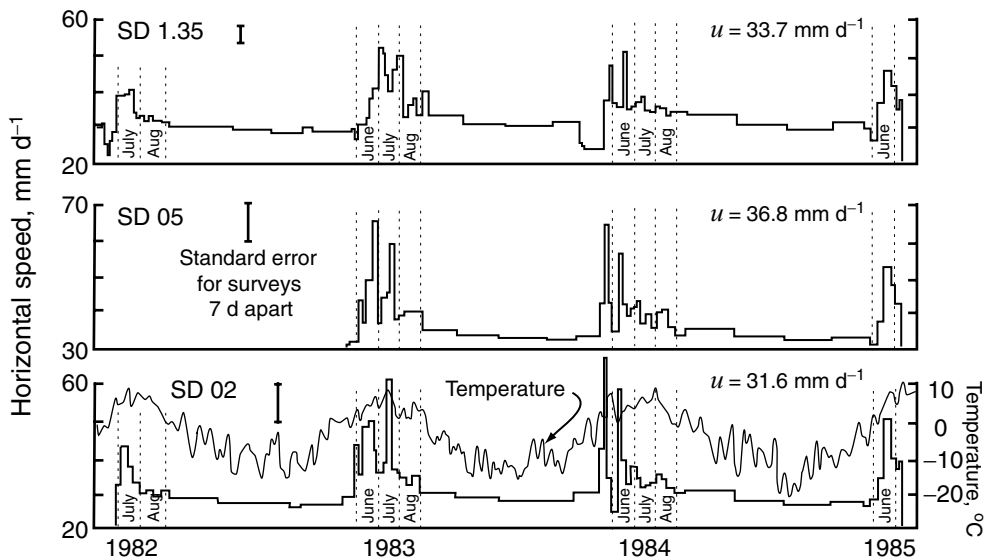


Figure 12.10. Time series of mean horizontal velocities of the three strain diamonds (SD) shown in Figure 12.9. Velocities are averages of those of the four (or five) stakes in each diamond. Mean daily temperature, smoothed using a five-day running mean, is shown in the bottom panel. (Modified from Hooke *et al.*, 1989, Figure 3a. Reproduced with permission of the International Glaciological Society.)

Term 2 (the second term on the right in Equation (12.30)). From the strain rate data, it can be seen that at the upglacier end of the block $\dot{\varepsilon}_{xx}$ became less compressive, and in two cases, even extending, while at the downglacier end it became more compressive in all but one case. Thus, the accelerations were not due to either push from upglacier or pull from downglacier. The clear implication is that they were a result of a reduction in resistive drag at the bed, presumably induced by increases in water pressure.

In the case of block **B**, the strain rate data indicate that the marked change in Term 2 reflects push from upglacier and, in the case of the June 1984 event, pull from downglacier. This combination of push and pull resulted in higher strain rates in the basal ice, and hence, owing to the proportionality between stress and strain rate, in higher basal drag.

Because we assumed that strain rates are uniform over the sides and ends of the blocks, and also owing to other uncertainties in the calculations, the values of τ_b obtained are only estimates. However, as the errors are probably of comparable magnitude and sign in all calculations, the direction and approximate magnitude of the *changes* in τ_b are probably reliable. These calculations thus help us understand the mechanisms

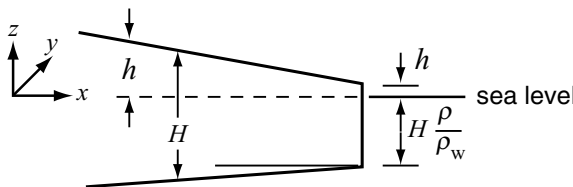


Figure 12.11. Coordinate system used in discussion of floating ice shelves.

by which the accelerations took place in these instances. Through such analyses, we can gain insight into spatial and temporal variations in factors controlling the velocity of a glacier.

Creep of floating ice shelves

Ice shelves around Antarctica play an important environmental role, as they act as dams, restraining the flow of ice from the interior of the continent. Were they to break up, ice levels in the interior would decrease rapidly over a period of a few centuries, and sea level would rise accordingly. Break up of ice shelves in northeastern North America may have contributed to the collapse of the Laurentide Ice Sheet at the end of the Wisconsinan. Thus, understanding the flow of ice shelves is a problem of both academic and environmental significance.

The problem of ice shelf flow is unique because τ_b is likely to be quite low where the shelf is grounded, and goes to zero in the limiting case when the shelf is afloat. Herein, we consider only the latter case. Weertman (1957b) was the first modern glaciologist to study this problem, and our approach follows his initially, but then incorporates some important modifications introduced by Thomas (1973a).

The coordinate system to be used is shown in Figure 12.11. The origin is at sea level, but is within the ice mass. The \$z\$-axis is vertical and positive upward. \$H\$ is the thickness of the shelf, and \$h\$ is the height of the surface above sea level. Inland, the surface rises gradually and the base drops further below sea level, so \$H\$ and \$h\$ both increase. As long as the ice shelf does not become grounded, however, we assume that hydrostatic equilibrium is maintained; therefore, assuming a constant density and thus ignoring the low density snow and firn at the surface, $(H - h)\rho_w = H\rho_i$, where \$\rho_w\$ and \$\rho_i\$ are the densities of water and ice, respectively.

At the risk of being repetitive, it is convenient, once again, to write out the momentum balance equation in the \$z\$-direction:

$$\frac{\partial \sigma_{xz}}{\partial x} + \frac{\partial \sigma_{yz}}{\partial y} + \frac{\partial \sigma_{zz}}{\partial z} + \rho_i g = 0 \quad (12.31)$$

Our objective is to obtain an expression for \$\sigma'_{xx}\$, and then to use the flow law to solve for \$\dot{\varepsilon}_{xx}\$.

Because shear stresses are zero at the bed and surface, it is reasonable to assume that $\sigma_{xz} = \sigma_{zx} = \sigma_{yz} = \sigma_{zy} = 0$. This means that velocities and strain rates are independent of z . Equation (12.31) can thus be integrated:

$$\int_{\sigma_{zz}}^0 d\sigma_{zz} = -\rho_i g \int_z^h dz$$

to yield:

$$\sigma_{zz} = \rho_i g(h - z) \quad (12.32)$$

Thus, σ_{zz} is simply the hydrostatic pressure at depth $(h - z)$.

Suppose that field measurements at some point give:

$$\dot{\varepsilon}_{yy} = \eta \dot{\varepsilon}_{xx} \quad \text{and} \quad \dot{\varepsilon}_{xy} = v \dot{\varepsilon}_{xx} \quad (12.33)$$

Then, from the incompressibility condition:

$$\dot{\varepsilon}_{zz} = -(1 + \eta) \dot{\varepsilon}_{xx} \quad (12.34)$$

Both η and v are functions of horizontal position, but because strain rates are independent of z , η and v are also independent of z . Then because we assume that ice is isotropic, we have $\dot{\varepsilon}_{ij} = \lambda \sigma'_{ij}$, where, as before, $\lambda = \sigma^{n-1}/B^n$. Thus,

$$\sigma'_{yy} = \eta \sigma'_{xx}, \quad \sigma'_{xy} = v \sigma'_{xx}, \quad \text{and} \quad \sigma'_{zz} = -(1 + \eta) \sigma'_{xx}$$

From the last of these expressions, converting to total stresses, we obtain

$$\sigma'_{xx} - \sigma'_{zz} = \sigma'_{xx} + (1 + \eta) \sigma'_{xx} = (\sigma_{xx} - P) - (\sigma_{zz} - P)$$

or:

$$\sigma'_{xx} = \frac{\sigma_{xx} - \sigma_{zz}}{2 + \eta} \quad (12.35)$$

When $\eta = 0$, this expression reduces to one that often appears in analyses in plane strain. It can be derived, for example, from Equations (10.18) and (10.19).

It is interesting to consider the implications of this relation: σ_{zz} varies linearly with depth (Equation (12.32)) but $\dot{\varepsilon}_{xx}$ is independent of depth. However, because the temperature of an ice shelf is normally well below 0 °C at the surface and close to the pressure melting point at the base, B , and hence σ'_{xx} , also vary strongly with depth (Figure 12.5). Thus, σ_{xx} varies with depth in a way that is not intuitively obvious. We will avoid this problem by seeking an expression for $\dot{\varepsilon}_{xx}$ in terms of the depth-integrated values of B and σ_{xx} .

Let us proceed by determining the total force per unit width. To do this, integrate Equation (12.35) from the base, b , to the surface, s :

$$\begin{aligned} \int_b^s \sigma'_{xx} dz &= \frac{1}{2+\eta} \int_{-(H-h)}^h [\sigma_{xx} - \rho_i g(z-h)] dz \\ &= \frac{1}{2+\eta} \left[\int_b^s \sigma_{xx} dz - \rho_i g \left(\frac{z^2}{2} - hz \Big|_{-(H-h)}^h \right) \right] \\ &= \frac{1}{2+\eta} \left[\int_b^s \sigma_{xx} dz - \rho_i g \left(-\frac{h^2}{2} - \frac{(h-H)^2}{2} + h(h-H) \right) \right] \\ &= \frac{1}{2+\eta} \left[\int_b^s \sigma_{xx} dz + \rho_i g \frac{H^2}{2} \right] \end{aligned}$$

or defining:

$$F = - \int_b^s \sigma_{xx} dz$$

we obtain

$$\int_b^s \sigma'_{xx} dz = \frac{1}{2+\eta} \left[\rho_i g \frac{H^2}{2} - F \right] \quad (12.36)$$

F is the total force opposing movement of a vertical section, of unit width normal to the flow direction, of the ice shelf.

We now need to use the flow law to express the left-hand side of Equation (12.36) in terms of strain rates. First, the effective stress is

$$\begin{aligned} \sigma &= \left[\frac{1}{2} \sigma_{ij} \sigma_{ij} \right]^{1/2} \\ &= \left[\frac{1}{2} (\sigma'_{xx}^2 + \sigma'_{yy}^2 + \sigma'_{zz}^2 + 2\sigma'_{xy}^2) \right]^{1/2} \\ &= \left[\frac{1}{2} (1 + \eta^2 + 1 + 2\eta + \eta^2 + 2\nu^2) \sigma'_{xx}^2 \right]^{1/2} \\ &= (1 + \eta + \eta^2 + \nu^2)^{1/2} |\sigma'_{xx}| \end{aligned}$$

Thus, from the flow law:

$$|\dot{\varepsilon}_{xx}| = \frac{(1 + \eta + \eta^2 + \nu^2)^{\frac{n-1}{2}}}{B^n} |\sigma'_{xx}|^n$$

If $n = 3$, we can drop the absolute value signs, which we now do. Thus, rearranging:

$$\sigma'_{xx} = \frac{\dot{\varepsilon}_{xx}^{1/n}}{(1 + \eta + \eta^2 + \nu^2)^{(n-1)/2n}} B$$

As strain rates are assumed to be independent of z , Equation (12.36) now becomes

$$\int_b^s \sigma'_{xx} dz = \frac{\dot{\varepsilon}_{xx}^{1/n}}{(1 + \eta + \eta^2 + v^2)^{(n-1)/2n}} \int_b^s B dz = \frac{1}{2 + \eta} \left[\rho_i g \frac{H^2}{2} - F \right]$$

Because B varies with depth, we define a depth-averaged B by

$$\bar{B} = \frac{1}{H} \int_b^s B dz$$

We also define θ by

$$\theta = \frac{(1 + \eta + \eta^2 + v^2)^{(n-1)/2}}{(2 + \eta)^n}$$

Solving for $\dot{\varepsilon}_{xx}$ now yields

$$\dot{\varepsilon}_{xx} = \frac{\theta}{\bar{B}^n} \left[\rho_i g \frac{H}{2} - \frac{F}{H} \right]^n \quad (12.37)$$

To proceed further, we need to evaluate F , the force per unit width opposing motion. We do this for two special situations. In the first, the ice shelf is free to expand in both the x - and y -directions, and movement is restrained by seawater pressure only. Then, $\eta = 1$ and

$$F_w = - \int_{-(H-h)}^0 \rho_w g z dz = \rho_w g \frac{(H-h)^2}{2}$$

Making use of the condition of hydrostatic equilibrium, $\rho_w(H-h) = \rho_i H$, yields

$$F_w = \frac{1}{2} \rho_w g \left(\frac{\rho_i}{\rho_w} \right)^2 H^2 = \frac{1}{2} \rho_i g \left(\frac{\rho_i}{\rho_w} \right) H^2$$

and Equation (12.37) becomes:

$$\dot{\varepsilon}_{xx} = \frac{\theta}{\bar{B}^n} \left[\frac{1}{2} \rho_i g \left(H - H \frac{\rho_i}{\rho_w} \right) \right]^n$$

The term in the inner brackets on the right-hand side is simply h so this becomes

$$\dot{\varepsilon}_{xx} = \theta \left[\frac{\rho_i g h}{2 \bar{B}} \right]^n \quad (12.38)$$

As this expression is always positive, strain rates will always be extending. Note that the surface slope does not appear in this solution; thus, even an iceberg with a horizontal surface will deform. This solution does not apply very near a calving face where bending moments are present.

It is instructive to compare this expression with that developed in Chapter 5 (Equation (5.3) with (5.2c)) for $\dot{\varepsilon}_{zx}$ at the bed of a land-based

glacier in the absence of significant longitudinal strain:

$$\dot{\varepsilon}_{zx} = \left[\frac{\rho_i g H \alpha}{B} \right]^n$$

Assuming that $n = 3$ and noting that $h = (1 - \rho_i/\rho_w)H \approx 0.1 H$, and that $\theta = 1/9$ when $\eta = 1$, $\nu = 0$, Equation (12.38) becomes:

$$\dot{\varepsilon}_{xx} = \left[\frac{0.024 \rho_i g H}{B} \right]^3 \quad (12.39)$$

Thus, the driving stress ($\rho_i g h$) in an ice shelf is comparable to that in a land-based glacier of the same thickness with a surface slope of ≈ 0.024 . However, because B increases with decreasing temperature, strain rates in ice shelves are normally less than those in land-based glaciers of comparable thickness.

The second example is that of an ice shelf between approximately parallel valley walls. In this case, $F = F_w + F_s$, where F_s is the shear force on the valley sides. Utilizing the expression for F_w just obtained, $\dot{\varepsilon}_{xx}$ becomes

$$\dot{\varepsilon}_{xx} = \theta \left[\frac{\rho_i g h}{2B} - \frac{F_s}{H B} \right]^n \quad (12.40)$$

Here, $\dot{\varepsilon}_{xx}$ can be negative, or compressive, if F_s is sufficiently large.

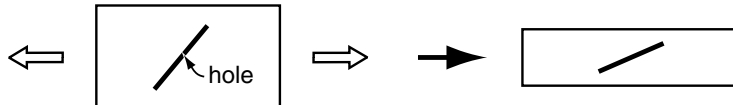
F_s merits further comment. Suppose that a is the distance from the centerline of an ice shelf to the valley wall. Suppose further that the depth-averaged drag on a valley wall is $\bar{\tau}_s$. Then $\bar{\tau}_s H$ is the force on the valley wall per unit length along the direction of flow. This force must balance forces acting in the direction of flow over the half-width of the ice shelf. In the absence of basal drag, it is reasonable to assume that any vertical slice of unit width extending through the ice shelf and parallel to the direction of flow will be restrained equally by this side drag. Thus, any such slice will experience a drag of $\bar{\tau}_s H/a$ per unit length along the direction of flow. Noting that $\bar{\tau}_s$ is a negative quantity, as it is directed in the upflow direction (Figure 12.11), the resisting force per unit width is

$$F_s = - \int_x^L \bar{\tau}_s \frac{H}{a} dx \quad (12.41)$$

Here, x is the coordinate position where the calculation is being made, and L is the x -coordinate of the edge of the shelf. Note that, consistent with being a force per unit width, F_s has the dimensions $N m^{-1}$.

Equation (12.41) says that F_s increases as the distance to the edge of the shelf increases. Thus, from Equation (12.40), $\dot{\varepsilon}_{xx}$ may change from extending nearer the shelf edge to compressive farther inland. This is the reverse of the normal situation in a grounded glacier, in which compressive flow is the rule in the ablation area and extending flow

Figure 12.12. Effect of longitudinal extension on an inclined borehole.



in the accumulation area. The implications of this are fascinating. With extending flow nearer the shelf edge, a positive emergence velocity would occur only if the product of the velocity times the surface slope were high enough to offset any downward vertical velocity resulting from the extension. In the absence of such conditions, a steady state can exist only if the mass balance is positive, as, in fact, is typically the case. This means that ice shelves with ablation (= melt) zones near the shelf edge should be uncommon. Furthermore, if the mass balance near the shelf edge is positive, it must also be positive at higher elevations further inland. Thus, if F_s ever became large enough to make $\dot{\varepsilon}_{xx}$ compressive, the ice shelf would increase in thickness unstably until it became grounded.

Analysis of borehole-deformation data

Our next example is drawn from the work of Shreve and Sharp (1970) and deals with the analysis of inclinometry data collected in boreholes that are undergoing deformation. In the simplest case, we might assume that at depth d , $\sigma_{zx} = S_f \rho g d \alpha$, and that successive measurements of the inclination of a borehole would give $\partial u / \partial z$. Then $\dot{\varepsilon}_{zx} = \frac{1}{2} (\partial u / \partial z + \partial w / \partial x)$ and, if the deformation is entirely simple shear, $\partial w / \partial x = 0$. Thus, measurements of the change in inclination at several depths would permit a (double log) plot of σ_{zx} versus $\dot{\varepsilon}_{zx}$ and, if other stresses and strain rates were negligible, the slope and intercept of the resulting line could be used to obtain n and B , respectively. Such an approach would be valid if the borehole were in a slab of ice of uniform thickness and infinite horizontal extent. In other cases, non-zero vertical velocities and (or) longitudinal strain rates could result in errors.

Figure 12.12 illustrates the effect of the longitudinal strain rate on a borehole. In a zone of longitudinal extension, the inclination of a hole that is inclined with respect to the direction of extension will increase, even if there is no shear strain. Nye (1957) realized this and made a correction for this effect in his reanalysis of the Jungfraufirn borehole experiment. However, it was Shreve (Shreve and Sharp, 1970) who undertook the first complete study of the problem.

We start by looking at the difference in velocity between two points in a borehole from the point of view of motion of the ice. This is what we want to determine from the inclinometry measurements. The axes are as shown in Figure 12.13. Direction cosines describing the orientation of

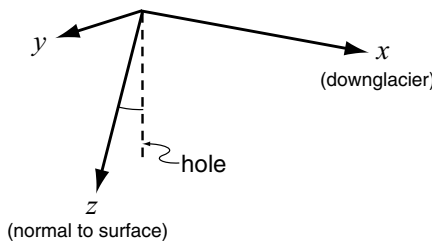


Figure 12.13. Coordinate system for analysis of borehole deformation.

the borehole are ℓ_i ($i = x, y, z$), and $d\lambda$ is an increment of length along the hole. Two points in the hole a distance $d\lambda$ apart will be separated from one another by distances $\ell_i d\lambda$ in the i -direction (Figure 12.14). The difference in the u_i velocity at depth $(d + \ell_z d\lambda)$ and that at depth d is du_i^λ . This is given by

$$du_i^\lambda = \ell_x \frac{\partial u_i}{\partial x} d\lambda + \ell_y \frac{\partial u_i}{\partial y} d\lambda + \ell_z \frac{\partial u_i}{\partial z} d\lambda$$

The first term on the right is the change in u_i as a result of moving a distance $\ell_x d\lambda$ in the x -direction, and so forth. Using the summation convention, this can be written:

$$du_i^\lambda = \ell_j \frac{\partial u_i}{\partial x_j} d\lambda \quad (12.42)$$

In terms of motion of the borehole casing (holes are often cased to provide a smoother and more reliable path for the inclinometer), we again consider the difference in velocity between points a distance $d\lambda$ apart (Figure 12.15). A point at depth d moves a distance ΔX , and a point at depth $(d + \ell_z d\lambda)$ moves a distance $\underline{\Delta x}$, both in time Δt . The inclinometry measurements, when combined with an accurate survey of the motion of the hole top, provide us with these distances. If Δu^λ is the difference in velocity between the two points, we have:

$$\Delta u^\lambda \Delta t = \Delta X - \underline{\Delta x} = u_{(d)} \Delta t - [u_{(d)} \Delta t + \ell_x d\lambda_{t=t_1} - \ell_x d\lambda_{t=0}]$$

where $u = u_x$, the x -component of the velocity, and $u_{(d)}$ is the value of u at depth d . The quantity in brackets represents the length $\underline{\Delta x}$; that is, it is the length ΔX plus the displacement, in the x -direction, of the upper point with respect to the lower one at time $t = t_1$ minus this displacement at time $t = 0$. Including the changes in $\ell_x d\lambda$ in the y - and z -directions, allowing for a change in $\ell_x d\lambda$ with time (unsteady flow), and expressing the result in differential form yields

$$\Delta u^\lambda \Delta t = \frac{\partial \ell_x d\lambda}{\partial x} u \Delta t + \frac{\partial \ell_x d\lambda}{\partial y} v \Delta t + \frac{\partial \ell_x d\lambda}{\partial z} w \Delta t + \frac{\partial \ell_x d\lambda}{\partial t} \Delta t$$

Here, the derivative with respect to x in the first term on the right gives the rate of change of $\ell_x d\lambda$ in the x -direction, and $u \Delta t$ gives the distance

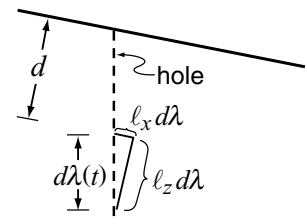
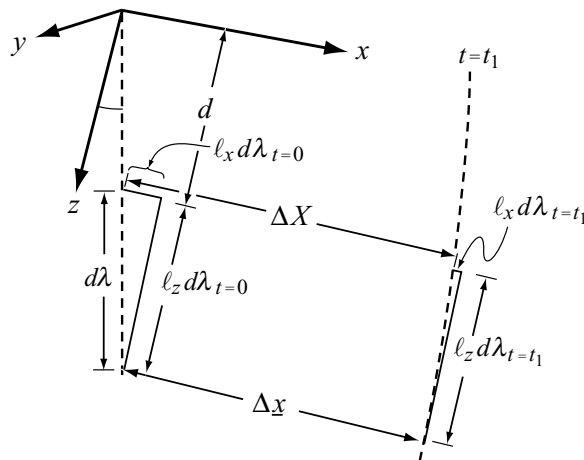


Figure 12.14. Distance between two points in a borehole expressed in terms of the direction cosines of the hole.

Figure 12.15. Deformation of a borehole casing through time.



moved in the x -direction, and so forth. Dividing by Δt and using the summation convention, we obtain

$$du_i^\lambda = u_j \frac{\partial \ell_i d\lambda}{\partial x_j} + \frac{\partial \ell_i d\lambda}{\partial t} = \frac{D}{Dt}(\ell_i d\lambda) \quad (12.43)$$

where D/Dt is the substantial or Lagrangian derivative (see Equation (6.12b)).

Equations (12.42) and (12.43) are both expressions for du_i^λ , the difference in velocity between two points a distance $d\lambda$ apart along the hole, so equating them yields

$$\ell_j \frac{\partial u_i}{\partial x_j} d\lambda = \frac{D}{Dt}(\ell_i d\lambda) = \ell_i \frac{D}{Dt} d\lambda + \frac{D\ell_i}{Dt} d\lambda \quad (12.44)$$

We would like to divide by $d\lambda$ to eliminate it from the first and last terms, but first we need an expression for $D(d\lambda)/Dt$. To obtain this, multiply both sides by ℓ_i :

$$\ell_i \ell_j \frac{\partial u_i}{\partial x_j} d\lambda = \ell_i \ell_i \frac{D}{Dt} d\lambda + \ell_i \frac{D\ell_i}{Dt} d\lambda$$

Because the sum of the squares of the direction cosines is unity, $\ell_i \ell_i = 1$. Similarly,

$$2\ell_i \frac{D\ell_i}{Dt} = \frac{D}{Dt}(\ell_i \ell_i) = \frac{D}{Dt}(1) = 0$$

Thus,

$$\frac{D}{Dt} d\lambda = \ell_i \ell_j \frac{\partial u_i}{\partial x_j} d\lambda \quad (12.45)$$

Equations (12.44) and (12.45) can be combined to yield the desired expression. However, we need to be careful of the subscripts when doing

this. Expanding Equation (12.44) for $i = x$ and dividing by $d\lambda$ yields

$$\ell_x \frac{\partial u}{\partial x} + \ell_y \frac{\partial u}{\partial y} + \ell_z \frac{\partial u}{\partial z} = \frac{1}{d\lambda} \ell_x \frac{D}{Dt} d\lambda + u \frac{\partial \ell_x}{\partial x} + v \frac{\partial \ell_x}{\partial y} + w \frac{\partial \ell_x}{\partial z} + \frac{\partial \ell_x}{\partial t} \quad (12.46)$$

Because the inclination of the casing is a function of z alone, $\partial \ell_x / \partial x = 0$ and $\partial \ell_x / \partial y = 0$. Expanding the right-hand side of Equation (12.45), using the result to replace the term involving $D(d\lambda)/Dt$ in Equation (12.46), and rearranging terms, we obtain:

$$\begin{aligned} \ell_x \frac{\partial u}{\partial x} + \ell_y \frac{\partial u}{\partial y} + \ell_z \frac{\partial u}{\partial z} &= -\ell_x \ell_x \ell_x \frac{\partial u}{\partial x} - \ell_x \ell_x \ell_y \frac{\partial u}{\partial y} - \ell_x \ell_x \ell_z \frac{\partial u}{\partial z} \\ &\quad - \ell_x \ell_y \ell_x \frac{\partial v}{\partial x} - \ell_x \ell_y \ell_y \frac{\partial v}{\partial y} - \ell_x \ell_y \ell_z \frac{\partial v}{\partial z} \\ &\quad - \ell_x \ell_z \ell_x \frac{\partial w}{\partial x} - \ell_x \ell_z \ell_y \frac{\partial w}{\partial y} - \ell_x \ell_z \ell_z \frac{\partial w}{\partial z} = w \frac{\partial \ell_x}{\partial z} + \frac{\partial \ell_x}{\partial t} \end{aligned} \quad (12.47)$$

Using the summation convention, this can be written as

$$\ell_k \frac{\partial u_i}{\partial x_k} - \ell_i \ell_j \ell_k \frac{\partial u_j}{\partial x_k} = w \frac{\partial \ell_i}{\partial z} + \frac{\partial \ell_i}{\partial t}$$

or even more compactly as

$$(\delta_{ij} - \ell_i \ell_j) \ell_k \frac{\partial u_j}{\partial x_k} = w \frac{\partial \ell_i}{\partial z} + \frac{\partial \ell_i}{\partial t} \quad (12.48)$$

Because i is not repeated in any of the terms in Equation (12.48), this equation represents three separate equations (for $i = x, y, z$). However, only two of these equations are independent because only two of the direction cosines are independent.

If the inclination of a borehole is known at two separate times, and if seven of the nine velocity derivatives in Equation (12.47) can be measured or estimated, Equations (12.48) can be solved for the two remaining velocity derivatives. Equations (12.48) are exact, but approximations have to be made in calculating the ℓ_i , $\partial \ell_i / \partial t$, and $\partial \ell_i / \partial z$ from observational data that are obtained at discrete points in time and space.

Two alternative approaches taken to this problem in two separate field experiments on Barnes Ice Cap (Hooke, 1973b; Hooke and Hanson, 1986) are outlined in Table 12.2. Strain nets were placed around the tops of the boreholes, so that some of the velocity derivatives could be measured directly at the surface. Assumptions were then made about how they varied with depth. In the first experiment, the boreholes were closely spaced so $\partial u / \partial x$ could be determined, as a function of depth, from the successive borehole profiles. As can be seen from Table 12.2, the two velocity derivatives that were calculated were $\partial u / \partial z$ and $\partial v / \partial z$. One might expect that measurements of the rate of tilting of the borehole would give these velocity derivatives directly, but this is not the case. Yet,

Table 12.2. Calculation of velocity derivatives in borehole deformation studies of Hooke (1973b) and Hooke and Hanson (1986)

Derivative	1973	1986
$\partial u / \partial x$	Two boreholes	We assumed that this decreased with depth in proportion to the decrease in u with depth
$\partial u / \partial y$	0 (assumed)	This was obtained from the measured u at the surface and the radius of curvature of the flow line
$\partial v / \partial x$	0 (assumed)	$\dot{\varepsilon}_{xy}$ was measured at the surface and assumed to decrease with depth in proportion to the decrease in u with depth. Then, from Equation (9.21): $\partial v / \partial x = 2\dot{\varepsilon}_{xy} - \partial u / \partial y$
$\partial v / \partial y$	This was measured at the surface, and we assumed that it decreased with depth in proportion to the decrease in $\partial u / \partial x$	
$\partial w / \partial z$	$= -\partial u / \partial x - \partial v / \partial y$ by continuity $\partial w / \partial z$ was then integrated over depth to obtain w as a function of depth, using either a no slip boundary condition at the bed where temperatures are well below the melting point, or the measured w at the surface	Same as 1973
$\partial w / \partial x$	Two boreholes	This was measured at the surface; we assumed that it decreased with depth in proportion to the decrease in w with depth
$\partial w / \partial y$	We set $\dot{\varepsilon}_{yz} = \frac{1}{2} \left(\frac{\partial v}{\partial z} + \frac{\partial w}{\partial y} \right)$ at the surface, and let $\partial w / \partial y$ decrease linearly with depth. $\partial v / \partial z$ was calculated (see below), so an iterative procedure was required	Same as $\partial w / \partial x$
$\partial u / \partial z$, $\partial v / \partial z$	These derivatives were then calculated from Equations (12.48)	Same as 1973

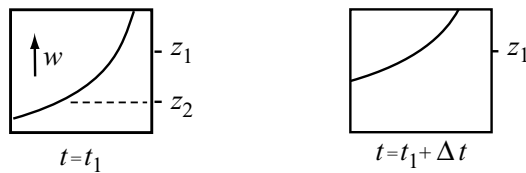


Figure 12.16. Effect of vertical advection on borehole inclination.

as one would expect and as implied by our opening discussion, $\partial u / \partial z$ is one of the most important velocity derivatives.

Sensitivity studies suggest that the solutions obtained in these two Barnes Ice Cap experiments do not depend strongly on the assumptions. The most important term is $\partial \ell_i / \partial t$. In instances where the casing bends abruptly, as at joints, $w \partial \ell_i / \partial z$ also becomes important. In experiments on other glaciers, the results might be more sensitive to some of the other velocity derivatives, and hence to any assumptions made in obtaining them.

Further insight into Equation (12.48) can be achieved by considering the situation in plane strain. Assuming incompressible flow and a uniform longitudinal strain rate, r , we then have $\partial u / \partial x = -\partial w / \partial z = r$, $\partial w / \partial x = 0$, $\ell_x = \sin \theta$, $\ell_z = \cos \theta$, and $\ell_y = 0$, where θ is the inclination of the borehole from the vertical. Equation (12.48) then reduces to

$$\frac{\partial u}{\partial z} = \frac{\partial}{\partial t} \tan \theta - 2r \tan \theta + w \frac{\partial}{\partial z} \tan \theta \quad (12.49)$$

The first term on the right is the obvious one, involving a change in inclination of the borehole with time. The second is the one illustrated in Figure 12.12 and discussed earlier. The third is an advection effect. In an area of non-zero vertical velocity, a section of a borehole at depth z_2 , measured with respect to some constant datum, and with inclination $\ell_i(z_2)$ will, at the end of a time interval Δt , be at, say, depth z_1 (Figure 12.16). If the initial inclination of the borehole at depth z_1 was different from $\ell_i(z_2)$, our measurements would show that the inclination at depth z_1 had changed, and this would be true even if $\partial u / \partial z$ were 0. This is why $w \partial \ell_i / \partial z$ becomes important near some joints, as just mentioned.

The results of the borehole deformation experiment reported by Hooke and Hanson (1986) will be used to illustrate an application of this analysis. Four boreholes, located approximately along a flowline on Barnes Ice Cap (Figure 12.17), were drilled and cased and inclinometry data were obtained from them over a period of up to four years. Figure 12.18a shows the deformation profiles, and Figure 12.18b shows values of $\partial u / \partial z$ calculated from Equations (12.48).

The deformation profiles in most of the holes end at the top of a zone of white ice (Figure 12.18a). Oxygen isotope data demonstrate that this ice is of Pleistocene age (Hooke and Clausen, 1982). The ice is white

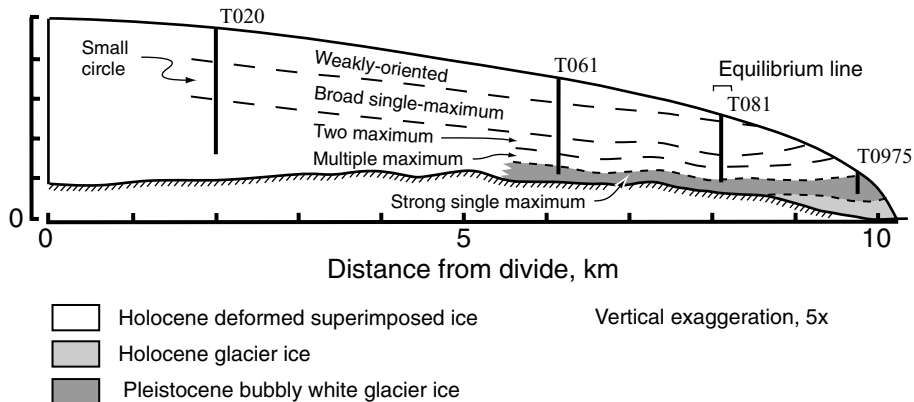


Figure 12.17. Longitudinal section along a flowline on Barnes Ice Cap showing types of ice encountered in boreholes. The deformed superimposed ice near the margin was overridden during an advance of the glacier (see Figure 5.17). (After Hooke and Hanson, 1986, Figure 2. Reproduced with the kind permission of Elsevier Science.)

because it contains a lot of air bubbles. As a result of these bubbles, the density of this ice is only 870 kg m^{-3} , compared with a density of 920 kg m^{-3} in the overlying blue ice. We presume that the high concentration of air bubbles is a result of two processes.

1. When the climate warmed at the end of the Pleistocene, meltwater percolation increased, and ice lenses formed. These lenses trapped air in the underlying porous firn.
2. As basal meltwater escaped into the underlying permeable bedrock, air may have been left behind in a sort of physical fractionation process.

As noted in Chapter 11 (p. 311), it is commonly found that such Pleistocene ice is softer than Holocene ice, apparently because impurities lead to smaller grain sizes that then develop strong single-maximum fabrics (Paterson, 1991). The high strain rates implied by the dotted extrapolations of the deformation profiles for holes T061 and T081 in Figure 12.18a are indicative of this weakening. The value of B obtained for this ice from the deformation profile in hole T0975 is $0.1 \text{ MPa a}^{1/3}$ (at -10.1°C), which is much lower than those ranging from 0.23 to $0.30 \text{ MPa a}^{1/3}$ in the overlying blue Holocene ice in holes T061 and T020 (Table 12.3) and also much lower than other experimental values at this temperature (Figure 12.5).

Also of interest are the values of the parameter Λ , defined by (see Equation (9.29))

$$2\Lambda = \frac{1}{\lambda} = \frac{\sigma'_{zx}}{\dot{\varepsilon}_{zx}} = \frac{B}{\dot{\varepsilon}^{\frac{n-1}{n}}} \quad (12.50)$$

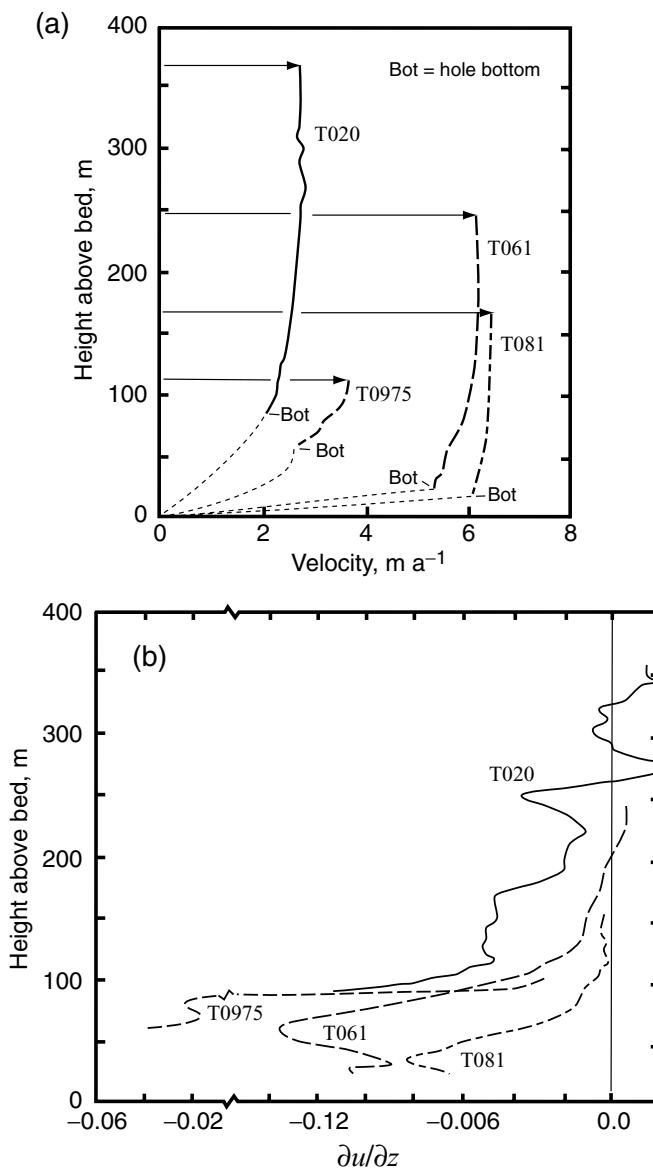


Figure 12.18. (a) Velocity profiles in boreholes; and (b) $\partial u / \partial z$ as a function of depth. (After Hooke and Hanson, 1986, Figure 3. Reproduced with the kind permission of Elsevier Science.)

$\dot{\varepsilon}_{zx}$ is obtained from the velocity derivatives (Table 12.2) using Equation (9.21), while σ_{zx} is estimated with the use of

$$\sigma_{zx} = -\rho g h \alpha - \frac{\partial}{\partial x} \int_0^z \frac{B}{\dot{\varepsilon}^{\frac{n-1}{n}}} (2\dot{\varepsilon}_{xx} + \dot{\varepsilon}_{yy}) dz - T \quad (12.51)$$

which is derived from Equation (12.26) in much the same way that we derived Equation (12.29) except that we now retain the T term and also assume that changes in the transverse direction are negligible in an

Table 12.3. Values of B in MPa $a^{-1/3}$ for different ice types^a

Borehole	T0975	T081	T061	T020
Ice type				
Weakly oriented	—	—	0.23 (−10.2)	—
Broad single maximum ^b	—	0.46 (−9.0) ^c	0.26 (−8.4)	0.30 (−7.4)
Two maxima	—	0.44 (−8.6)	0.24 (−7.5)	0.26 (−6.5)
Three or four maxima	—	0.50 (−8.3)	0.30 (−6.8)	—
White ice (clean)	0.10 (−10.1)	0.18 ^d (−7.8)	0.10 ^d (−6.4)	—
		0.18 ^e (−7.8)		
White ice (dirty)	0.13 (−9.8)			

^a Values given are for zones in which fabric is well developed, and thus exclude transition regions.

^b Equivalent fabric in T020 is small circle.

^c Numbers in brackets are mean temperatures in °C.

^d Velocity profile calculated by assuming no slip on the bed.

^e Measured over two weeks, starting three weeks after completion of hole in 1977. No smoothing used in calculation.

ice cap. Equation (12.27) was used to evaluate the T term. If B and n are constant, as might be expected, Λ should vary inversely with $\dot{\varepsilon}$. The awkward fact is that near the surface where $\dot{\varepsilon}_{zx}$ is low, this does not appear to be the case. Figure 12.19a shows that Λ is effectively independent of $\dot{\varepsilon}$. Even the direction of change of Λ with depth is not consistent from one hole to the next, as indicated by the arrows on the curves in Figure 12.19a. This problem is not unique to Barnes Ice Cap; Raymond (1973) also found that Λ was independent of $\dot{\varepsilon}$ near the surface of Athabasca Glacier.

Somewhat deeper in the glacier the situation improves, and Λ decreases steadily with increasing $\dot{\varepsilon}$ (Figure 12.19b). Here, the slope and intercept of the $\log \Lambda - \log \dot{\varepsilon}$ line can be used to determine B and n (Equation (12.50)). In the present case, however, Hooke and Hanson (1986) chose, instead, to assume that $n = 3$; they then calculated B as a function of depth, and related changes in B to changes in crystallographic fabric. The results are shown in Table 12.3. Although there was quite a lot of noise in the record, it appears that B is slightly lower in fabrics containing only two maxima, and increases in fabrics with three or four maxima. This stiffening can be seen at the bottoms of the deformation profiles in Figure 12.18a. It is consistent with expectation, as it is the third and fourth maxima in these multiple-maximum fabrics that are inclined to the direction of shear (Figure 4.14f). In other words, the basal planes of crystals with these orientations dip either up- or downglacier,

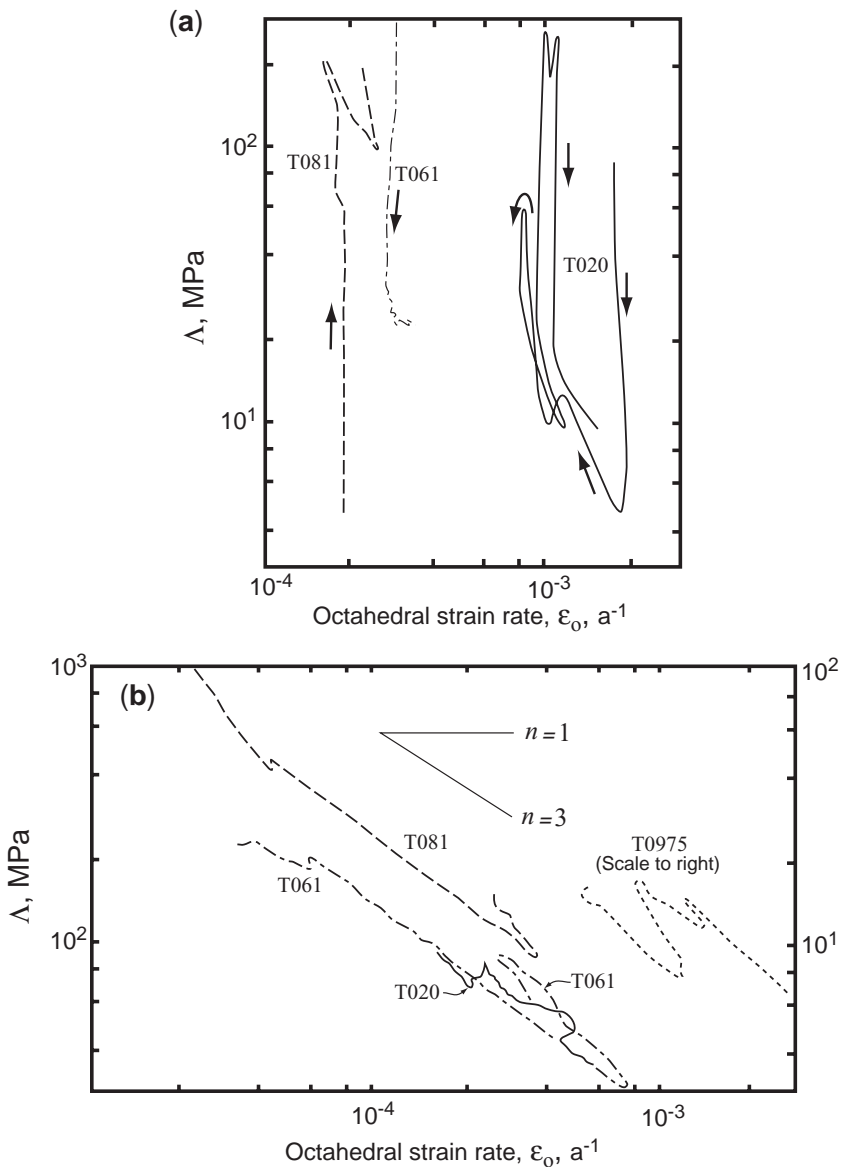


Figure 12.19. Octahedral shear strain rate, ε_o , plotted against Λ . (a) The upper 50 m of holes T061 and T081, and the upper 150 m of hole T020. Arrows show direction of increasing depth. (b) The lower parts of the holes. Depth increases from upper left, following lines of points. Reversals in trends reflect hardening of ice in zones where fabric is changing. (After Hooke and Hanson, 1986, Figure 4. Reproduced with the kind permission of Elsevier Science.)

whereas the basal planes in the first two maxima that form dip in the transverse direction (Figure 4.14e).

Values of B in hole T081 are nearly double those in the other holes. Hooke and Hanson assumed that this was because stresses at this location on the glacier were overestimated. However, they were unable to isolate the apparently erroneous assumption that led to this error, even though they undertook calculations with a finite-element model.

Summary

In this chapter we have studied four classical problems in glacier mechanics: closure of cylindrical holes, calculation of force balances, creep of ice shelves, and deformation of boreholes. As examples of applications of the theory presented, we discussed problems such as the flow of water to, from, and in subglacial conduits, the mechanics of glacier accelerations, the stability of ice shelves, and the extraction of flow-law parameters from borehole deformation data. From these examples, we gained insights into the dynamic and kinematic behavior of glaciers. These, however, were secondary objectives.

The primary objective of the chapter was to help students develop facility with the mathematics of stress and deformation as applied to problems in glacier mechanics. Such analyses are complicated because multiple stresses, strains, and strain rates are involved, and even more so because the strains in which we are interested are a consequence of deviatoric, not total stresses. In many cases, once the physics of a problem have been formulated, prescribed mathematical procedures must be followed before a result with clear physical significance reappears. Students who have mastered the material in this chapter will be able to understand many papers in the glaciological literature that would otherwise be impenetrable.

Chapter 13

Finite strain and the origin of foliation

Suppose one were to drop a deformable sphere into the accumulation area of a glacier. As the sphere became buried deeper and deeper in the glacier, it would be deformed by the flow. Because the accumulation area is normally an area of longitudinal extension and vertical compression, it would become an ellipsoid, elongated in the direction of flow and compressed vertically. If there were also significant transverse compression it would become a prolate ellipsoid, whereas if there were transverse extension, it would become oblate. Figure 13.1 illustrates schematically, in two dimensions, how the shape of a cross section through the sphere would change as the sphere passed through the glacier.

Our objective in this chapter is to discuss the cumulative deformation experienced by ice as it is advected through a glacier, and to show the relation between this deformation and the banded structure, called *foliation*, that is characteristic of glaciers.

The strain ellipse

The ellipsoid we have just discussed is called the strain ellipsoid or, in two dimensions, the strain ellipse. Following normal convention, we will denote the greatest, intermediate, and shortest principal semi-axes of the ellipsoid by subscripts 1, 2, and 3, and the directions of these axes by X , Y , and Z , respectively. These axes will rotate with respect to our fixed x , y , z coordinate system as the strain ellipsoid rotates (Figure 13.2). The lengths of the axes of the ellipsoid are a measure of the strain it has experienced. As in Equation (9.16) we define the strain by:

$$e = \frac{\ell - \ell_o}{\ell_o} = \frac{\ell}{\ell_o} - 1 \quad (13.1)$$

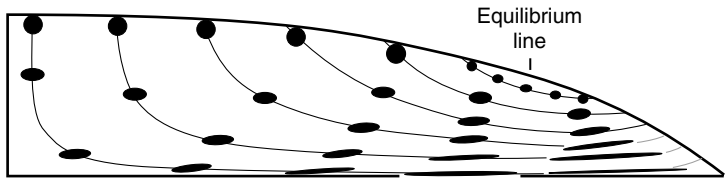
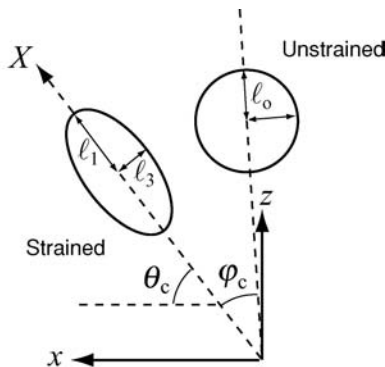


Figure 13.1. Schematic illustration of the deformation that would be experienced by an object that is initially spherical (or circular in two dimensions) as it moves through a glacier from the accumulation zone to the ablation zone. (From Hooke and Hudleston, 1978, Figure 3B. Reproduced with permission of the International Glaciological Society.)

Figure 13.2. Sketch showing parameters used to describe, in two dimensions, the cumulative strain experienced by an initially circular object. (Modified from Hooke and Hudleston, 1980, Figure 8C.)



φ_c Rotation of line that becomes the greatest principal axis in the strained state

θ_c Orientation of greatest principal axis

$$\gamma_{oc} = \frac{\sqrt{6}}{3} \ln \frac{\ell_1}{\ell_3}$$

If ℓ_0 , the radius of the initial sphere, is taken as 1, then $\ell_i = 1 + e_i$ is the length of the i th semi-axis of the ellipsoid (Figure 13.2). From Equation (9.23) the logarithmic strain is then:

$$\varepsilon_i = \ln \frac{\ell_i}{\ell_0} = \ln(1 + e_i) \quad (13.2)$$

Let us now take ℓ_i / ℓ_j ($i, j = 1, 2, 3$ and $i \neq j$) as a measure of the strain in the i, j plane. Then

$$\varepsilon_i - \varepsilon_j = \ln \frac{\ell_i}{\ell_j} \quad (13.3)$$

A useful measure of the magnitude of the *total strain* experienced by the ellipsoid is then:

$$\bar{\gamma}_{oc} = \frac{2}{3}[(\varepsilon_1 - \varepsilon_2)^2 + (\varepsilon_2 - \varepsilon_3)^2 + (\varepsilon_3 - \varepsilon_1)^2]^{1/2} \quad (13.4)$$

$\bar{\gamma}_o$ is called the natural octahedral unit shear (Nadai, 1950, p. 115) and the additional subscript c denotes cumulative. (“Natural” in this context is a reference to the appearance of the natural logarithm in the expressions for ε_i , not to a contrast with some “artificial” counterpart.) The expression on the right-hand side of Equation (13.4) is twice the root mean square of the strains in the three mutually perpendicular planes of our coordinate system.

In plane strain with $\varepsilon_2 = 0$ and $\varepsilon_1 = -\varepsilon_3$, the intermediate or Y-axis of the ellipsoid will be transverse to the flow and thus parallel to the y-axis of the fixed coordinate system. Equation (13.4) can then be simplified and combined with Equation (13.2) to yield:

$$\bar{\gamma}_{oc} = \frac{2\sqrt{6}}{3}\varepsilon_1 = \frac{2\sqrt{6}}{3} \ln \frac{\ell_1}{\ell_o} \quad (13.5)$$

or using Equation (13.2) to eliminate ℓ_o :

$$\bar{\gamma}_{oc} = \frac{\sqrt{6}}{3} \ln \frac{\ell_1}{\ell_3} \quad (13.6)$$

Simple and pure shear

As we have discussed previously (Figure 4.14), when a two-dimensional object is deformed by a compressive stress parallel to the z-axis and an extensional stress parallel to the x-axis, the deformation is known as *pure shear* (Figure 13.3a), whereas if it is deformed by a shear stress, σ_{zx} , parallel to the x-axis, the deformation is known as *simple shear* (Figure 13.3b). In Figure 13.3a the axis of maximum shortening is clearly parallel to the z-axis and the axis of maximum extension is parallel to the x-axis. This is also true of the *instantaneous stretching axes*, or axes along which the maximum and minimum normal strain *rates* occur during any infinitesimal strain. *Material lines* (lines of physical points in the deforming material) that are initially parallel to the instantaneous stretching axes remain parallel to these axes. The strain is thus *irrotational*, and the deformation is said to accumulate *coaxially*.

In contrast, in simple shear the instantaneous stretching axes are always at $\pm 45^\circ$ to the direction of shear ($\theta_{in} = 45^\circ$, where the subscript “in” refers to instantaneous or infinitesimal; see Figure 13.3b). However, the axis of maximum extension will be at 45° only after the first infinitesimal increment of strain. In the next increment, the initial axis

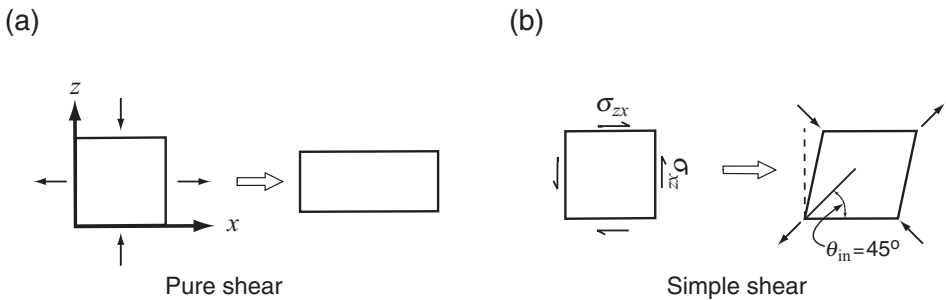


Figure 13.3. Sketches illustrating (a) pure and (b) simple shear.

of maximum extension will be rotated slightly. This axis is parallel to a material line that started at an angle greater than 45° to the x -axis and that has been rotated through the 45° position to an angle less than 45° . This is most easily visualized if one considers very large strains, as in the lower right part of Figure 13.1. The material line that became the nearly horizontal axis of maximum extension in this case started off nearly vertical. Because material lines rotate through the axes of instantaneous stretching (which are *non-material lines*) the deformation in simple shear is *rotational* and *non-coaxial*.

In either simple or pure shear there are always two lines that are initially perpendicular and that are still perpendicular after deformation. These lines coincide with the directions of maximum extension (or elongation) and shortening in the deformed state. They are called the *principal axes of strain*.

Parameters describing cumulative deformation

Although $\bar{\gamma}_{oc}$ describes the deformation of the original sphere, it does not describe either its rotation or its final orientation. For that we need two additional parameters, θ and φ (Figure 13.2); φ_c is *the angle through which the material line that becomes a principal axis in the strained state has rotated*, and θ_c is *the angle that the greatest principal axis makes with the x -axis*. Again, the subscript c denotes cumulative.

In the pure shear of Figure 13.3a, the axis of maximum elongation, the X -axis of the ellipsoid, is horizontal, both for infinitesimal strains and for cumulative strain over a long period of time. Thus, θ_c is 0, and because the X -axis does not rotate, φ_c is also 0. In contrast, in simple shear as in Figure 13.3b, the X -axis is at 45° to the shear direction for any infinitesimal increment of strain. However, during any such increment, the line that became the X -axis will have rotated slightly from its original orientation, so φ_c is slightly greater than 0 and θ_c slightly less than 45° .

Divide

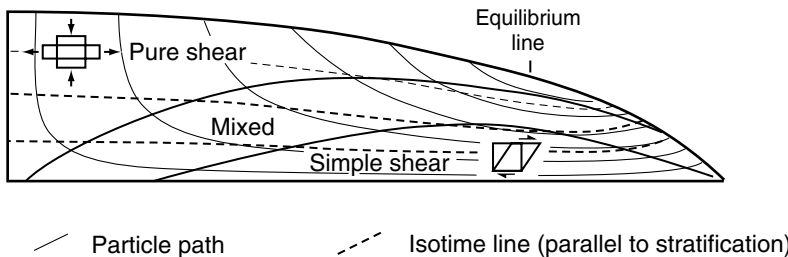


Figure 13.4. Schematic illustration of the strain fields in an ice sheet. The fields are for small increments of strain only. The horizontal component of the pure shear field is extensional above the equilibrium line and compressive below. (From Hooke and Hudleston, 1978, Figure 3A. Reproduced with permission of the International Glaciological Society.)

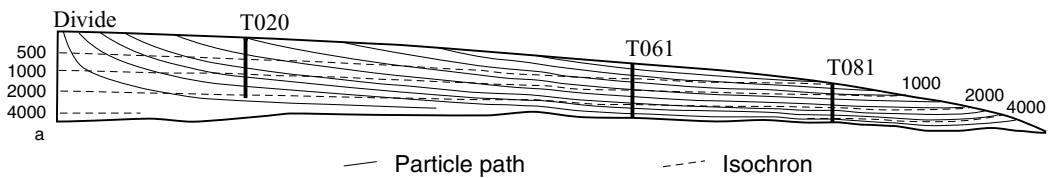
As the strain accumulates, φ_c will increase toward 90° (but it will never actually become 90°) and θ_c will approach 0° . The reader may wonder why $\varphi_c \rightarrow 90^\circ$ when the X -axis after the first increment of strain was inclined at 45° . The answer lies in the phrase “. . . the rotation of the line that *becomes* the principal axis . . .”. After very large shear strains, the line that becomes the X -axis will be the one that started out nearly vertical.

As one would expect from consideration of velocity profiles like those in Figure 10.6, pure shear dominates near the glacier surface where $\partial u / \partial x$ and $\partial w / \partial z$ are large compared with $\partial u / \partial z$, and conversely, simple shear dominates near the bed where $\partial u / \partial z$ becomes large compared with $\partial u / \partial x$ and $\partial w / \partial z$ (Figure 13.4). Immediately beneath the divide, $\partial u / \partial z = 0$ at all depths, so the pure shear field extends all the way to the bed. Near the equilibrium line, the vertical velocity decreases and the flow gradually changes from extending to compressive so both $\partial w / \partial z$ and $\partial u / \partial x$ decrease. Thus the ratio of simple shear to pure shear increases, so despite the small $\partial u / \partial z$ in the upper part of the glacier the thickness of the pure shear field decreases.

Calculating cumulative strain

In order to calculate the cumulative strain in a glacier, one first must know the velocity field. One then calculates the path that a particle of ice would follow through the glacier and velocity derivatives at discrete points along the path. To obtain the incremental strain as the ice moves from one point to the next, strain rates are then calculated from the velocity derivatives and multiplied by the time needed for this movement

(a) Particle paths and isochrons



(b) Direction of maximum cumulative extension

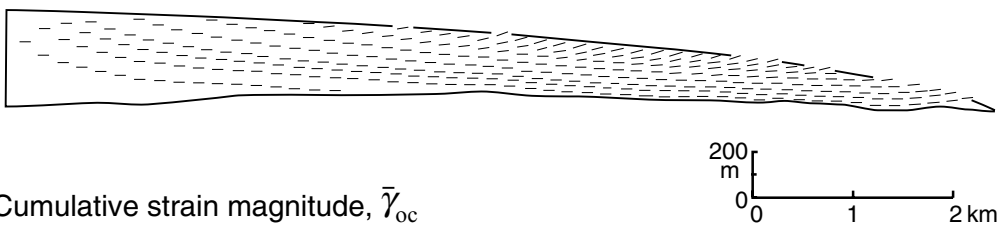
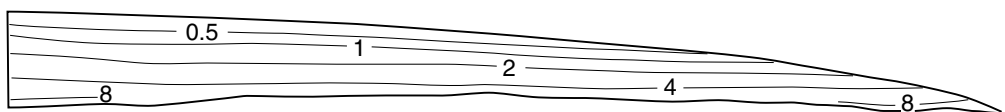
(c) Cumulative strain magnitude, $\bar{\gamma}_{oc}$ 

Figure 13.5. (a) Particle paths calculated from the velocity field described in the text. Ages of isochrons are shown in years. (b) Orientation of maximum cumulative extension direction shown by bars at 200 m intervals along the particle paths in (a). (c) Contours of $\bar{\gamma}_{oc}$. (From Hudleston and Hooke, 1980, Figures 6 and 7. Reproduced with permission of Elsevier Scientific Publishing.)

(Ramsay and Graham, 1970, Equations 7–10). Finally, these incremental strains are added to get the cumulative strain.

Hudleston (Hooke and Hudleston, 1980; Hudleston and Hooke, 1980) made such a calculation using a comprehensive set of data on velocities and mass balance along the flow line on Barnes Ice Cap illustrated in Figure 13.5a (see also Figure 12.17). To estimate horizontal velocities at depth, he used measured surface velocities and adjusted the value of B in Equation (5.7) to get zero velocity on the bed, where the temperature is well below the melting point. Rather than use measured vertical velocities, he used the mass balance data to estimate the long-term steady-state vertical velocity at the surface and assumed that it decreased linearly with depth. Transverse strain rates are small, so he assumed that they could be neglected.

The results of his calculations are shown in Figures 13.5 and 13.6. By following particles starting at nine points in the accumulation area, he first mapped nine flowlines (Figure 13.5a). He then calculated the

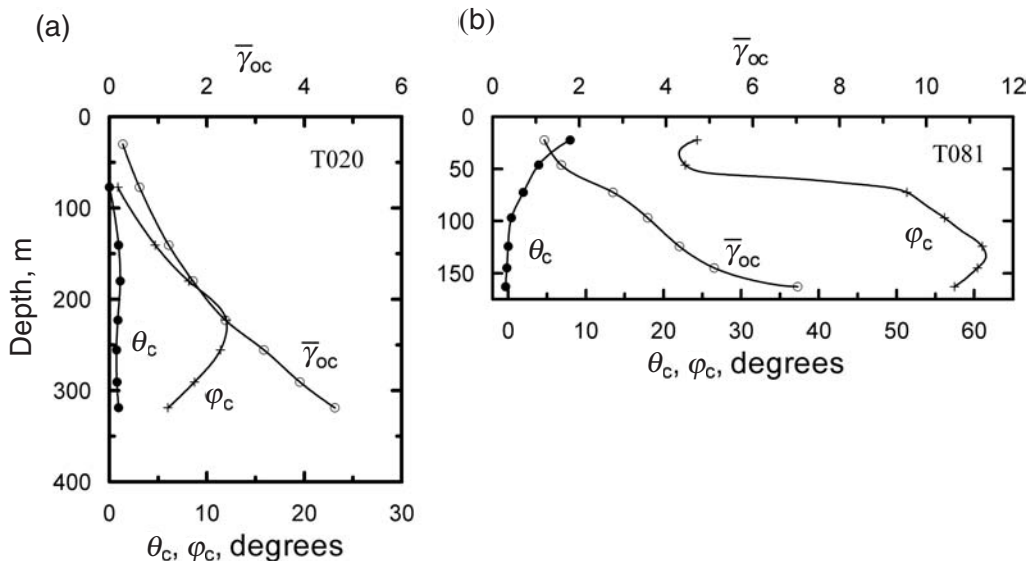


Figure 13.6. Calculated variation of $\bar{\gamma}_{oc}$, $y_i\theta_c$, and φ_c with depth at locations of Barnes Ice Cap boreholes (a) T020 and (b) T081. Locations of boreholes are shown in Figure 13.5. (From Hooke and Hudleston, 1980, Figures 8a and 9a. Reproduced with permission of the International Glaciological Society.)

orientations of the axes of maximum cumulative extension (X -axes: Figure 13.5b). Noteworthy in this figure is the fact that these axes are nearly parallel to the bed throughout most of the glacier. The increased upglacier dip at the surface near and downglacier from borehole T061 is a consequence of the increase in the ratio of simple shear to pure shear as the equilibrium line is approached. As just noted, in simple shear the axis of maximum elongation dips 45° initially; with increasing deformation it is gradually rotated toward parallelism with the plane of the shear.

The cumulative strain magnitude, $\bar{\gamma}_{oc}$, is shown in Figure 13.5c. These numbers do not appear significant until one realizes that $\bar{\gamma}_{oc}$ is proportional to the natural logarithm of the axial ratio of the strain ellipse. Thus, $\bar{\gamma}_{oc} = 8$, found in the most basal ice, corresponds to an elongation of $\sim 18\,000:1$. A 1 m cube would be stretched into a 1-m wide ribbon 134 m long and 7.5 mm thick!

Figure 13.6 shows the variation of $\bar{\gamma}_{oc}$, θ_c , and φ_c with depth in boreholes T020 and T081 (Figure 13.5a). Because the dominant strain pattern at T020, particularly in the upper part of the glacier, is nearly pure shear with vertical compression and longitudinal extension, the axis of maximum cumulative extension is nearly horizontal. Thus, θ_c remains close to 0. On the other hand, φ_c is 0 at the surface and initially increases

gradually with depth as $\partial u / \partial z$ increases. However, with increasing depth in the glacier, the ice arriving at T020 has passed through a larger and larger region dominated by pure shear (Figure 13.4). Thus, φ_c reaches a maximum ($\sim 12^\circ$) at a depth of ~ 240 m and then decreases at greater depth.

The pattern at the site of borehole T081 is different in several respects. Because this hole is in the upper part of the ablation area, ice at the surface accumulated some strain as it moved from higher in the glacier. Thus, $\bar{\gamma}_{oc} > 0$ at the surface. With increasing depth, the ice has traveled a greater distance and accumulated more strain so $\bar{\gamma}_{oc}$ increases to about 7, representing an axial ratio of over 5000. Because ice near the surface has experienced a modest amount of mixed simple and pure shear (Figure 13.4), $\theta_c \approx 10^\circ$ and $\varphi_c \approx 25^\circ$ here. With increasing depth, φ_c first increases, reaching a maximum at a depth of ~ 120 m and then decreases, reflecting the early history of pure shear that this deeper ice experienced.

To further quantify the influence of the early history of pure shear, Hudleston calculated φ_c for a particle of ice that experienced a total strain, $\bar{\gamma}_{oc}$, of 3.75 entirely by simple shear (Hooke and Hudleston, 1980). In this case, φ_c is 80° and increases toward 90° as $\bar{\gamma}_{oc}$ increases further. For comparison, in holes T020 and T081 the actual rotations at this strain magnitude are 9° and 57° , respectively.

Let us now use our understanding of cumulative strain to study the origin of foliation.

Components of foliation

The pronounced banded character of glaciers (see, for example, Figures 5.18 and 8.8) has led to considerable confusion. Banding is most prominent in the ablation area once the winter snow has melted. However, banding may also be seen in crevasse walls in the accumulation area, although it has a very different appearance there and most people would, correctly, refer to it as annual layering or sedimentary stratification. The banding is normally subparallel to the nearest bounding surface, be it the bed, the surface, or the valley walls. However, in the lower part of the ablation area it typically dips gently to steeply upglacier (Figure 13.7b). The banding is penetrative; that is, the bands are cross sections of layers in the ice.

On close inspection, one finds that the banded appearance most commonly results from variations in bubble or dirt content. The latter, coupled with the suggestive upglacier dip of the bands near the margin, has given rise to the mistaken impression that the banding is a reflection of shear planes in the ice along which debris was (somehow) carried to the

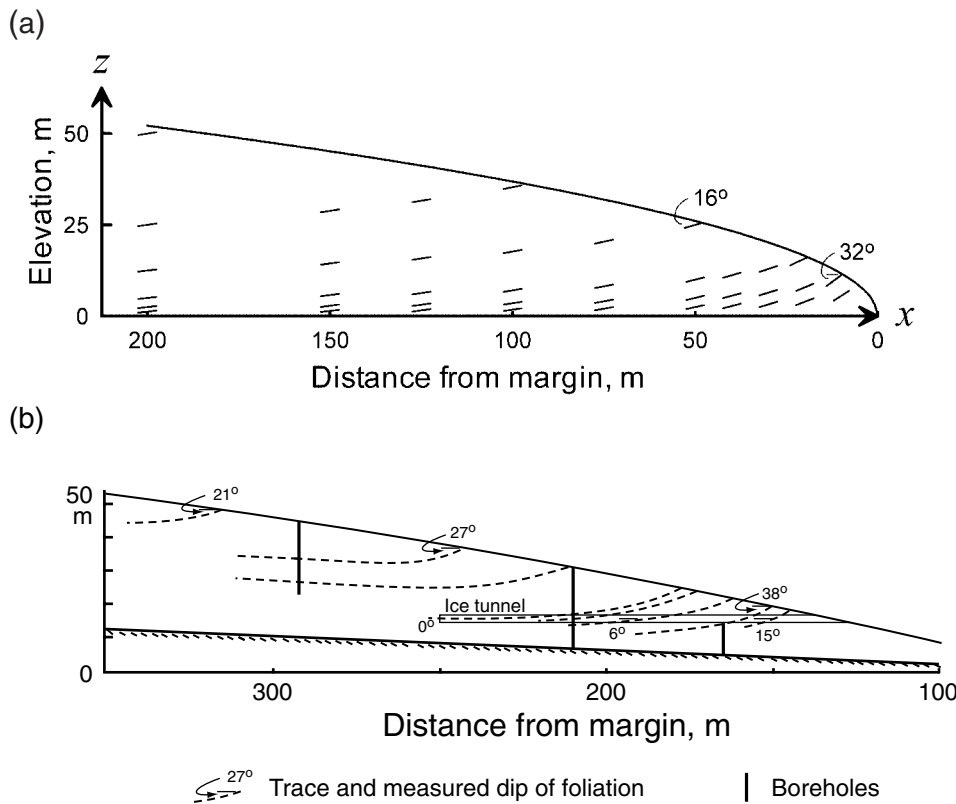


Figure 13.7. (a) Foliation attitudes in the margin of an idealized perfectly plastic glacier with a parabolic surface profile. See text for explanation. (b) Cross section of the margin of Barnes Ice Cap showing dips of foliation planes measured on the ice surface and in a tunnel excavated in the margin. Dashed lines show traces of foliation planes inferred from measured dips and core stratigraphy.

surface. This is rarely the case. Elongate bubbles and, in some instances, elongate crystals may contribute to the banded appearance.

Foliation is the end product of subjecting inhomogeneities of any origin to cumulative stretching and shearing by strains such as those discussed in the first part of this chapter. After such treatment, the origin of the initial inhomogeneity is not likely to be obvious. Suppose, for example, that the 1 m cube we mentioned earlier were a Michelangelo sculpture in a material with a rheology similar to that of ice. Would we recognize it after it had become a ribbon 135 m long and 7.5 mm thick? Perhaps we could identify the material, but certainly not the original handsome shape.

So what are the inhomogeneities that result in foliation? The most obvious is the sedimentary stratification that one sees in crevasse walls in the accumulation area. This stratification is defined by variations in grain size, particularly near the base of an annual layer where depth hoar forms. Wind-blown dust picked up from snow-free ground during the melt season commonly discolors the surface of annual layers, and percolating meltwater may spread out and refreeze along horizons defined by variations in snow density, forming relatively bubble-free lenses. Both contribute to the stratified appearance. Gland-shaped bodies of ice may also form from refreezing of percolating meltwater (p. 20). From the pattern of elongation directions shown in Figure 13.5b, it is clear that these inhomogeneities will be stretched longitudinally and compressed vertically. Thus, the deformation accentuates the original layering. By the time the inhomogeneities reappear low in the ablation area, they will bear little resemblance to the original sedimentary stratification or glandular structures. Once such inhomogeneities have been deformed beyond ready recognition, the structure is properly called foliation.

Another major component of foliation is crevasse fillings. Snow blows into crevasses during the winter and meltwater may saturate this snow during the summer. When the crevasse gets moved into a location, or rotated into an orientation, such that stresses across it are compressional, it closes and this filling gets squashed. A band is thus formed that cross cuts either sedimentary layering or foliation derived from such layering. Initially, this cross-cutting relation is obvious and the filling can be properly identified as what it is, even if it cross cuts foliation the origin of which cannot be identified. However, once the filling has been squashed further, rotated to near parallelism with other foliation, and stretched, its origin will be less obvious. Careful observers, however, may still be able to detect the cross-cutting relation.

Another prominent component of foliation in basal ice is debris. As we have discussed, there are various mechanisms by which debris may become entrained in basal ice – the refreezing part of the regelation cycle, freeze-on by the mechanisms discussed by Robin (Figure 7.6) or in areas where temperature gradients in basal ice lead to local refreezing (Figure 6.12), entrainment in frazil ice in overdeepenings (Figure 8.33), and so forth. In all situations, the resulting layers are parallel to the bed or valley walls and are in areas subject to high rates of simple shear. The precise origin of the layers is hard to determine before they become deformed, and after shearing the task is usually hopeless, although chemical and isotopic signatures may help (Souchez and Lorrain, 1978).

Foliation in the marginal zone

We noted above that foliation in glacier margins has often been mistaken for so called “shear planes” that would presumably be parallel to planes of maximum shear stress. Here, we demonstrate that the upglacier dip of the foliation at a glacier surface bears little relation to directions of maximum shear stress.

As in the case of Figures 13.5 and 13.6, the first task is to determine the velocity field. Then we use that velocity field to see how foliation that is nearly parallel to the bed some distance from the margin will be deformed as it is passively advected to the margin.

We adopt a coordinate system in which the origin is at the margin, the x -axis is horizontal and directed upglacier along the bed, and the z -axis is vertical and positive upward (Figure 13.7a). We assume that: (1) the profile of the ice surface in the marginal zone can be approximated by $h = \sqrt{cx}$, where h is the surface elevation, x is the distance from the margin and c is a constant¹; (2) the ablation rate, b_n (a negative number), is uniform over the area of interest; (3) the profile is a steady-state profile with $b_n = -w_s + u_s \tan \alpha$ (Equation (5.26)); (4) the horizontal velocity, \bar{u} , is independent of depth; (5) the strain is two dimensional (plane strain); and (6) ice is incompressible. The amount of ice lost by ablation downglacier from a position x is then $b_n x$ and this must equal the mass flux past x , or $\bar{u}h$. Thus,

$$\bar{u} = \frac{b_n x}{\sqrt{cx}} = \Omega x^{1/2} \quad (13.7)$$

where $\Omega = b_n c^{1/2}$. (As b_n is negative, Ω is negative. This is consistent with u being in the negative x -direction.) The assumption of incompressibility may be represented by:

$$\frac{\partial u}{\partial x} + \frac{\partial w}{\partial z} = 0 \quad (13.8)$$

Differentiating Equation (13.7) and using the result to integrate Equation (13.8) yields:

$$w = -\frac{1}{2} \Omega x^{-1/2} z \quad (13.9)$$

We now determine the coordinates of an element of ice as a function of time. The element starts at position (x_0, z_0) at time $t = 0$. As $\bar{u} = dx/dt$, Equation (13.7) can be integrated to obtain:

$$x = (x_0^{1/2} + \frac{1}{2} \Omega t)^2 \quad (13.10)$$

¹ This equation, first derived by Nye (1951), can be obtained by integrating Equation (5.2c) with $\alpha = dh/dx$. The reader will then find that $c = \sqrt{2\sigma_{zx}/\rho g}$.

Then combining Equations (13.9) and (13.10) to eliminate x , noting that $w = dz/dt$, and integrating we obtain:

$$z = z_0 \left(\frac{x_0}{x} \right)^{1/2} \quad (13.11)$$

where z is the height of the element of ice after it has traveled a distance $(x_0 - x)$ from (x_0, z_0) . The position of the element at time t_1 can be determined by selecting a time $t_1 > 0$ and solving Equation (13.10) for x and then Equation (13.11) for z . A plot of x versus z defines the path of the element. By setting $z = \sqrt{cx}$ in Equation (13.11) and solving for x we can determine the x -coordinate of the point where the element reaches the glacier surface.

Now consider a foliation plane in this element of ice. At (x_0, z_0) the plane has an upglacier dip, β_0 , with respect to the particle path, and we wish to compute its dip when the element reaches the glacier surface. (Because θ_c is always greater than 0 under steady-state conditions, the foliation plane will dip more steeply than the particle path. The consequences of a non-steady-state situation will be discussed further below.) The element is subjected to longitudinal compression and vertical extension which will change the inclination of any line that is not parallel to the direction of compression or extension (Figure 12.12). In addition, at any given height above the bed, w increases toward the margin as h decreases (Equation (13.9), noting that $\Omega x^{1/2} = b_n/h$). Therefore, the shear strain $\partial w/\partial x$ will also increase the upglacier inclination of the plane. The problem thus strongly resembles the deformation of a bore-hole (Chapter 12) except that now the “hole” is nearly horizontal, not vertical, and the primary shear to which it is subjected is $\partial w/\partial x$, not $\partial u/\partial z$. Consequently, Equation (12.49) is applicable in the form:

$$\frac{\partial \beta}{\partial t} = \frac{\partial w}{\partial x} + 2\beta \frac{\partial w}{\partial z} - u \frac{\partial \beta}{\partial x} \quad (13.12)$$

To express β in terms of x alone, we obtain $\partial w/\partial x$ and $\partial w/\partial z$ from Equation (13.9) and use the chain rule:

$$\frac{d\beta}{dt} = \frac{d\beta}{dx} \frac{dx}{dt}$$

to evaluate the term on the left. Noting that $dx/dt = \bar{u}$ and using Equation (13.11), we end up with a first-order linear ordinary differential equation:

$$\frac{d\beta}{dx} + \frac{\beta}{2x} - \frac{z_0 x_0^{1/2}}{8x^{5/2}} = 0 \quad (13.13)$$

which can be solved by setting $\beta = a(x)b(x)$, where a and b are functions of x to be determined (Sokolnikoff and Redheffer, 1958, pp. 23–24). The result is:

$$\beta = \sqrt{\frac{x_0}{x}} \left[\beta_0 + \frac{z_0}{8} \left(\frac{1}{x_0} - \frac{1}{x} \right) \right] \quad (13.14)$$

β_o is negative in our coordinate system, indicating an upglacier dip. As $x_o > x$ in this system, β is also negative.

Dips of foliation planes at different positions in the margin of such an idealized perfectly plastic glacier, calculated with Equation (13.14), are plotted in Figure 13.7a. In the calculation the surface profile was taken to be $h = (13.6x)^{1/2}$. This is equivalent to a uniform basal drag of 0.06 kPa, a good approximation for Barnes Ice Cap. The initial positions of six elements of ice were taken to be $x_o = 1250$ m and $z_o = 0.5, 1, 2, 5, 10$, and 20 m. Here β_o was upglacier and 2.5° steeper than the flow paths. These elements were assumed to follow paths defined by Equations (13.10) and (13.11), and the dips of foliation planes contained in the elements were determined at various points along the way. The balance rate, b_n , was taken to be -0.5 m a $^{-1}$, but this only affects the speed of the element and not the orientation of the foliation plane in it. A rapid increase in dip of foliation near the surface is clearly shown. This is consistent with foliation attitudes measured on the surface and in an ice tunnel in the margin of Barnes Ice Cap (Figure 13.7b).

Foliation attitudes calculated from Equation (13.14) are sensitive to the choice of β_o as well as other parameters, so detailed comparison between the calculated and observed attitudes is not warranted. The important point is that passive deformation of foliation that is nearly parallel to the bed some distance from the margin can account for observed dips at the surface near the margin. Furthermore, because shear stresses vanish on a free surface, the planes of maximum shear stress dip 45° up- and downglacier relative to the surface (Figure 10.3). Observed foliation attitudes (Figure 13.7; see Allen *et al.*, 1960, and Hooke, 1970, among others) bear no such consistent relation to planes of $\sigma_{S\max}$.

Recumbent folds in basal ice

Foliation in basal ice is sometimes deformed into recumbent folds (Figure 13.8). Hudleston (1976) studied some such folds in the marginal zone of Barnes Ice Cap, and hypothesized that they might have formed when foliation that had developed over a period of many years under a stable flow regime was subjected to a new regime. Some distance from the margin the initial foliation would be nearly parallel to the bed (Figure 13.5b), and thus nearly parallel to particle paths in the ice (Figure 13.5a). If there were a bump in the bed, Hudleston speculated, a change in flow regime might alter the particle paths enough to generate a fold.

To explore this possibility, he developed a numerical model of the flow. As the flow is nearly two dimensional, he assumed that the variation in u with depth was adequately described by Equation (5.6) with the



Figure 13.8. Recumbent fold in foliation in basal ice of Barnes Ice Cap.

surface slope averaged over a distance equal to the local ice thickness. Because the thickness decreases downglacier, u at any specific height above the bed also decreases. This compressive strain can then be used to calculate the variation in the vertical velocity with depth. Reasonably satisfactory agreement with measured velocities was obtained with $B = 0.6 \text{ MPa } a^{1/n}$ and $n = 1.6$. These values are consistent with values determined from borehole deformation experiments in the marginal zone of Barnes Ice Cap (Hooke, 1973b). Using this velocity field, he then calculated particle paths and, as mentioned above, assumed that a steady state had obtained for a long enough period of time that foliation had become essentially parallel to those particle paths.

An advance or retreat of the glacier changes the velocity vector at any given point because the ice thickness and surface slope change. If the change in the velocity field is such that a velocity vector becomes inclined upward with respect to the previous particle path, as shown in Figure 13.9a, a point on a foliation plane will be moved upward with respect to more distal points on that plane. As $\partial u / \partial z$ is high near the base, the point will move to a level of higher u and will gradually overtake the more distal parts of the foliation plane. If the distance to the margin is sufficient, this will result in a fold (Figure 13.9c–e). Note that while the folds are seeded over the bump in the bed, they do not become apparent until the ice has moved some distance toward the margin. Folds developed in higher foliation planes reach the margin first, and are somewhat more open. After a sufficiently long time without further changes in regime, all folds will melt out and this record of the regime change will vanish.

While Hudleston's model ignores effects of longitudinal strain on the velocity profile and uses surface slopes that are averaged over relatively short distances, it is robust inasmuch as "... a more sophisticated

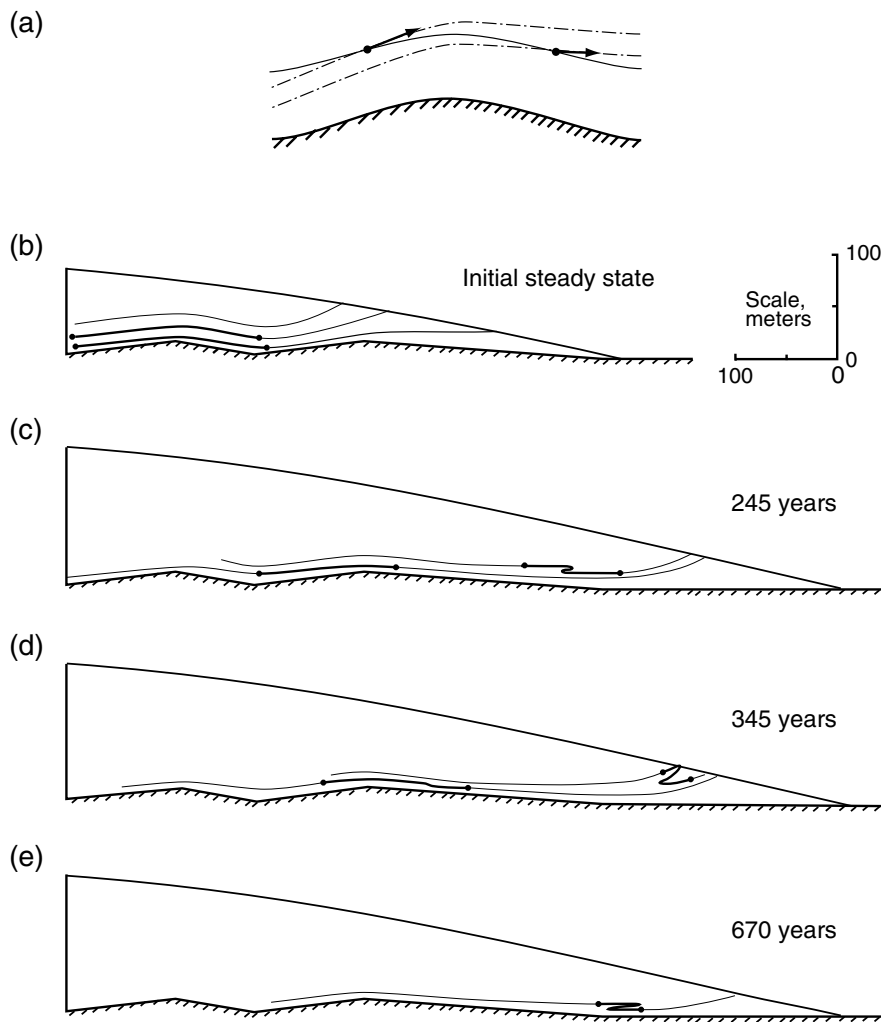


Figure 13.9. Generation of recumbent folds as a result of an advance of a glacier. (a) Sketch showing one of several possible changes in velocity vectors that would result in a fold. (b) Initial steady-state geometry. Foliation is assumed to have developed parallel to the three particle paths shown. Heavier parts of paths, between dots, are followed downflow in panels (c) through (e). (c) Situation after a ~200 m advance lasting 30 model years followed by a new steady state lasting 245 model years. (d) and (e) Situation 345 and 670 model years after establishment of the new steady state. (Compiled from Hudleston, 1976, Figures 7 and 8. Reproduced with the permission of the author and the Geological Society of America.)

model would still predict the formation of folds in the manner described, although details of the process would be somewhat different” (Hudleston, 1976, p. 1691).

Because glaciers advance and retreat, and because they rest on irregular beds, folding in basal ice is likely to be common. Indeed, oxygen isotope profiles from the 3000 m GRIP and GISP 2 cores through the Greenland Ice Sheet are quite similar to a depth of 2750 m, but below that depth the correlation breaks down (Grootes *et al.*, 1993). Similar discrepancies were found in the lowest 10 m of two 299 m cores, taken 27 m apart, from Devon Ice Cap (Paterson *et al.*, 1977), and in the lowest 12 m of three cores, within 2 km of each other, from Agassiz Ice Cap (Fisher, 1987). A likely explanation for the lack of correlation in deeper ice in these cores is folding, although boudinage or shearing is also possible.

Summary

In this chapter, we have reviewed the fundamentals of finite strain and showed that three quantities are needed to describe the cumulative change in shape and orientation of a hypothetical sphere of ice as it is squeezed and stretched while being advected through a glacier or ice sheet. These are a measure of the total strain, the natural octahedral unit shear, $\bar{\gamma}_{oc}$; the orientation of the X -axis of the strain ellipse with respect to the x -axis of the coordinate system, θ_c ; and the rotation of the line that eventually becomes the X -axis in the strained state, φ_c . With increased deformation, $\bar{\gamma}_{oc}$ increases and θ_c approaches 0 as the X -axis approaches parallelism with particle paths or flow lines. However, φ_c may remain substantially less than 90° if the ice experiences a long early history of nearly pure shear.

Inhomogeneities in the ice such as sedimentary stratification, crevasse fillings, meltwater glands and lenses, and debris-rich layers become buried, stretched longitudinally, and squeezed vertically during flow in the accumulation zone. By the time these features are re-exposed in the ablation area, their origin is likely to be difficult or impossible to determine. The result is then properly called foliation. Once a foliation has developed, it may be enhanced with further strain and then deformed as it is passively advected toward the margin. If the flow regime changes, foliation may become folded.

Chapter 14

Response of glaciers to changes in mass balance

As we discussed in Chapter 3, climatic change may involve changes in precipitation, in temperature, in radiation balance, or most likely in all three of these variables. From the perspective of a glacier, however, the net effect is to change the amount and the spatial distribution of accumulation and melt. This leads to discrepancies between the specific net balance and the local emergence or submergence velocity, and hence to changes in glacier geometry (see pp. 90–92).

Were the climate of a region to remain constant for a long time, several decades or even centuries, the geometry of non-surging glaciers in that region would adjust so that the specific net balance was everywhere equal to the local emergence or submergence velocity, and in addition (or as a consequence) the integral of the specific net balance over the glacier, $B_n = \int b_n dA$, would be zero. The glacier would then be said to be in a steady state, an ideal that may occasionally be approached but rarely, if ever, reached.

The principal adjustment that takes place is, of course, a change in length or size. A positive mass balance, maintained over a period of years, will result in an advance. As the glacier expands to lower elevations or more southerly latitudes, the summer balance becomes more negative until it becomes equal (in magnitude) to the winter balance, and the net balance returns to zero, and conversely.

The goal of this chapter is to study the details of the adjustment process. In particular, we will see that changes in mass balance lead to changes in thickness which influence the speed of the glacier, and hence the rate at which ice is transferred from the accumulation area to the ablation area. The changes in thickness propagate and diffuse down the

glacier. Thus, the propagation and diffusion processes control the way in which the profile adjusts to the new mass balance conditions. In addition, the total time required for the adjustment depends on the volume of ice that must be gained or lost in order to reach a new steady state. Thus, years can elapse before the terminus gets the message that something has happened higher on the glacier, and decades may pass before it adjusts to the changes.

Positive feedback processes

Before proceeding, it is appropriate to mention some feedback processes that can influence the way in which a polar glacier adjusts to climatic change, but which we will not consider in detail. One process, discussed by Lliboutry (1970), results from the fact that a change in temperature has not only an immediate effect on the mass balance, but also a delayed effect on the flow, owing to the temperature dependence of the flow law. For example, an increase in temperature may increase ablation and thus decrease the annual net balance. The decrease in net balance causes the glacier to thin. Then, as the temperature change gradually penetrates into the glacier, the flow rate increases. As this increases the mass flux to the terminus relative to the input of ice upglacier, this results in further thinning. The decrease in thickness, a combined effect of the changes in mass balance and temperature, leads to further warming of the glacier surface, the boundary condition, owing to the increase in temperature with decreasing elevation.

It is well to keep in mind, however, that if the climate is sufficiently cold, increases in temperature may actually increase the winter balance, as the atmosphere is then able to hold more moisture in the vapor state. For example, studies of the volume of air in bubbles in a core from Byrd Station on the West Antarctic Ice Sheet suggest that as the Pleistocene gave way to the Holocene, the ice sheet there became ~ 250 m thicker (Raynaud and Whillans, 1982). This change is inferred to have been a result of an increase in precipitation as the climate warmed. Eventually, however, as the warm wave penetrated deeper and the flow rate increased, the ice sheet began to thin (Alley and Whillans, 1991). Thus in this case, the processes did not reinforce one another. Measurements of strain rate and mass balance along a 160 km strain network upglacier from Byrd Station suggest that the thinning is continuing today (Whillans, 1977).

Superimposed on these positive feedback loops in large ice masses is yet another delayed response, that of the Earth's crust to the additional ice load. As the crust is depressed isostatically, the surface elevation of the ice sheet is lowered resulting in warming and possibly initiating a positive feedback as just discussed. In some areas the bed may become

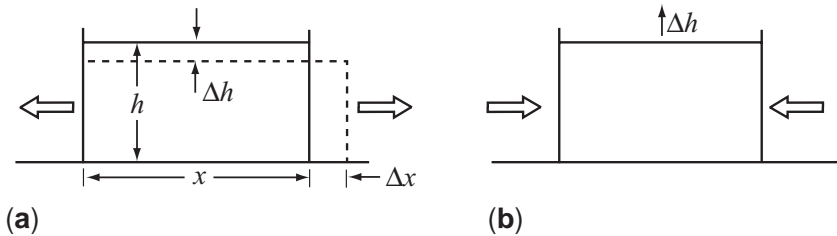


Figure 14.1. Sketch illustrating why adjustment toward a new steady state is:
(a) stable where flow is extending, and (b) unstable where flow is compressive.

depressed below sea level. Then any thinning of the ice sheet, or climatic warming that results in a rise in sea level, is likely to lead to buoyant forces at the bed that greatly increase flow speeds, potentially leading to collapse of the ice sheet. Numerical models of ice sheets are used to study the possibility that such collapses occurred in the past, and that the West Antarctic Ice Sheet might collapse in the future in response to greenhouse warming. MacAyeal (1993a, b), among others, has also considered the possibility that several layers of ice-raftered sediment that have been detected in cores across the North Atlantic Ocean, the *Heinrich* layers, reflect repeated collapses of the Laurentide Ice Sheet.

Response of a temperate glacier

Let us now consider, qualitatively, how a temperate glacier should respond to a change in mass balance. Suppose b increases, becoming more positive in the accumulation area and less negative in the ablation area. Initially, this leads to an increase in thickness. Suppose further that the longitudinal strain rate is extending in the accumulation area, as is normally the case. Over the course of a year, this extension, operating on a block of ice of thickness h , results in thinning by an amount Δh (Figure 14.1a). For a constant rate of extension, Δh is proportional to h . (For example, in the figure, conservation of mass requires that $\Delta h \propto (h - \Delta h) \Delta x$ or, ignoring second-order terms, $\Delta h \propto h(\Delta x/x)$.) Thus, as the glacier grows thicker, the amount of thinning, Δh , resulting from the stretching, increases each year. After many years, Δh becomes large enough to absorb most of the increased accumulation and the glacier gradually approaches a new steady state. As we shall see, however, the time required for full adjustment is theoretically infinite.

The situation is quite different if the longitudinal strain rate is compressive, as is normally the case in ablation areas. Δh is still proportional to h , but now, because both the longitudinal strain rate and the change in mass balance cause the glacier to become thicker (Figure 14.1b), Δh

increases each year, unstably. Thus, in the absence of some mitigating effect, a new steady state would never be reached. This contrast in behavior between the accumulation and ablation areas, however, leads to kinematic waves which restore stability.

As Nye (1960) emphasizes, kinematic waves are not dynamic waves like waves on a water body, and indeed kinematic waves need not have a wave form. Dynamic waves are a consequence of inertial forces. Because velocities are low in glaciers, inertial forces are negligible in comparison with gravitational and viscous forces. Kinematic waves, on the other hand, are a consequence of a conservation law. On a glacier, it is mass (or volume at constant density) that is conserved, and the type of kinematic wave in which we are interested is a wave of constant ice flux. Kinematic waves move through a medium at a speed that is different from the speed of the medium itself.

Kinematic waves on glaciers arise from the fact that if the ice flux into an element of a glacier of length dx is greater than the flux out of it, the glacier becomes thicker there. Because both the ice velocity and the ice flux in the thicker ice are greater than in the thinner ice on either side of it, the resulting wave moves faster than the ice.

Numerical modeling experiments suggest that kinematic waves on glaciers are likely to be long and low, and that the increases in velocity and thickness associated with them should rarely exceed about 10% of the unperturbed values (van de Wal and Oerlemans, 1995). Thus, they will be difficult to detect in the field. Larger waves have been observed in the field, but these are probably a consequence of changes in other factors, such as sliding speed. Of course, changes in sliding speed can be induced by perturbations in mass balance.

(For comparison, waves of denser traffic on a highway are also a form of kinematic wave. In this case, cars catching up to a wave from behind are forced to slow down, while those finally making their way through the wave can accelerate again. Thus, in this case, the wave speed is less than the speed of the individual cars.)

Elementary kinematic wave theory

Let us now develop these ideas analytically. In this development, following an analysis by Nye (1960), we consider a slab of ice on a slope, $\beta(x)$, with thickness, $h(x, t)$, and surface slope, $\alpha(x, t)$ (Figure 14.2). We assume that $\partial h / \partial x$ is small and that the slab is of infinite extent in the horizontal direction normal to the x -axis. The surface slope is related to the bed slope by:

$$\alpha = \beta - \frac{\partial h}{\partial x} \quad (14.1)$$

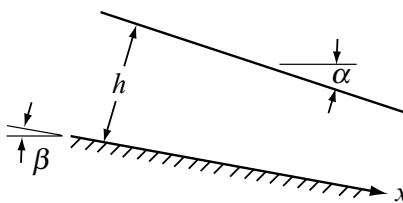


Figure 14.2. Relation among surface slope, α , bed slope, β , and thickness, h .

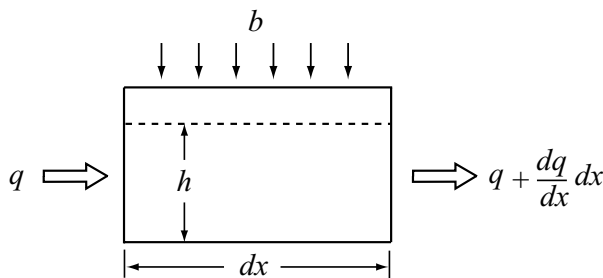


Figure 14.3. Contributions to change in mass in an element of a glacier of length dx .

Note that if h decreases downglacier, $\partial h / \partial x$ is negative so $\alpha > \beta$.

Consider conservation of mass in an element of a glacier of length dx (Figure 14.3). For convenience, we will express mass fluxes in terms of the equivalent volumes of ice, based on a standard density. Ice flows into the element at a rate, $q(x, h, \alpha, t)$, and out of it at a rate, $q + (\partial q / \partial x) dx$. Here, q is the flux per unit of glacier width, and thus has the dimensions $\text{m}^3 \text{a}^{-1} \text{m}^{-1}$. In addition, there is accumulation at a rate $b dx$. If more ice flows into, or accumulates in, the element than leaves it, the glacier increases in thickness at a rate $(\partial h / \partial t)$, so the increase in volume of ice in the element is $(\partial h / \partial t) dx$. Thus:

$$q - \left(q + \frac{\partial q}{\partial x} dx \right) + b dx = \frac{\partial h}{\partial t} dx$$

or, simplifying:

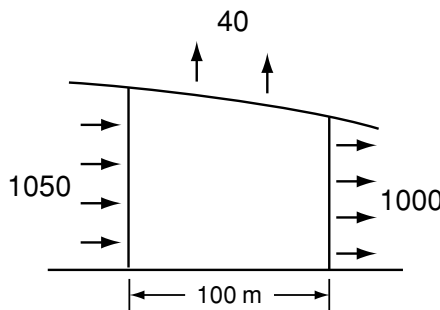
$$\frac{\partial q}{\partial x} + \frac{\partial h}{\partial t} = b \quad (14.2)$$

Because q is a function of h and x , the functional dependence expressed by Equation (14.2) leads to a general class of motions in flow systems known as kinematic waves (Lighthill and Whitham, 1955). Our objective next is to gain some appreciation for the nature of such waves on glaciers.

Let us begin by considering the wave speed. Suppose we multiply both sides of Equation (14.2) by $(\partial q / \partial h)_x = c$, where c is the change in flux resulting from a change in thickness at point x , thus:

$$c \frac{\partial q}{\partial x} + \frac{\partial q}{\partial h} \frac{\partial h}{\partial t} = bc \quad \text{or} \quad c \frac{\partial q}{\partial x} + \frac{\partial q}{\partial t} = bc \quad (14.3)$$

Figure 14.4. Numerical interpretation of the terms in Equation (14.3).



Equation (14.3) is known as the kinematic wave equation; c has the dimensions $\text{m}^3\text{a}^{-1}\text{m}^{-1}/\text{m} = \text{m a}^{-1}$. Thus, it is a speed. In fact, it is the celerity (or speed) of the wave. (Because $q = \bar{u}h$, where \bar{u} is the mean (depth-averaged) speed, $\partial q/\partial h = \bar{u} + h(\partial \bar{u}/\partial h)$.)

To gain some appreciation for the implications of Equation (14.3), consider the situation in Figure 14.4. The ice flux into the element of the glacier is $1050 \text{ m}^3\text{a}^{-1}\text{m}^{-1}$, while that out is $1000 \text{ m}^3\text{a}^{-1}\text{m}^{-1}$. The element is in the ablation area and the ablation rate is -0.4 m a^{-1} , or $-40 \text{ m}^3\text{a}^{-1}\text{m}^{-1}$ over the length of the element. As a result of this positive balance, with more ice entering the element than leaving it, the glacier is increasing in thickness. With the use of Equation (14.3) we can calculate the rate of increase in mass flux, $\partial q/\partial t$, resulting from this increase in thickness as follows. The flux gradient, $\partial q/\partial x$, over the 100 m long element is $-50 \text{ m}^3\text{a}^{-1}\text{m}^{-1}/100 \text{ m}$ or -0.5 m a^{-1} . Suppose $c = 200 \text{ m a}^{-1}$. Then, $\partial q/\partial t$ is $20 \text{ m}^3\text{a}^{-1}\text{m}^{-1}$. In other words, owing to the increase in thickness and the resulting increase in speed, the mass flux increases by $20 \text{ m}^3\text{a}^{-1}\text{m}^{-1}$.

The relationship among q , h , \bar{u} , and c is illustrated in Figure 14.5, in which q is plotted against h . Because of the nonlinearity of the flow law, we expect q to increase nonlinearly with h as shown. The mean speed, \bar{u} , of a glacier with a thickness and ice flux given by the values of q and h at point P in the figure is $\bar{u} = q/h$. This is represented by the slope of the dashed line connecting P with the origin. However, the speed, c , of a kinematic wave is $(\partial q/\partial h)_P$, which is the slope of a line drawn tangent to the $q-h$ curve at point P. In other words, as mentioned earlier, the speed of the kinematic wave is appreciably larger than the mean speed of the glacier.

To get a sense of how much faster the kinematic wave moves, consider the case of a glacier moving entirely by internal deformation such that (see Equation 5.19):

$$\bar{u} = \frac{2}{n+2} \left(\frac{S_f \rho g \alpha}{B} \right)^n h^{n+1} \quad (14.4)$$

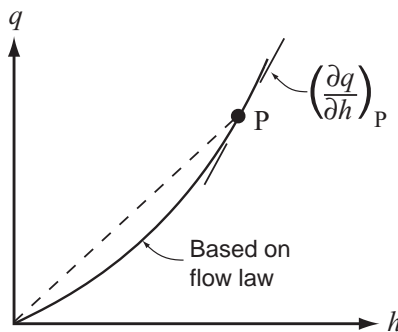


Figure 14.5. Relation between mean speed of a glacier and speed of a kinematic wave.

Noting that $q = \bar{u}h$, we have:

$$q = \frac{2}{n+2} \left(\frac{S_f \rho g \alpha}{B} \right)^n h^{n+2}$$

so:

$$c = \frac{\partial q}{\partial h} = 2 \left(\frac{S_f \rho g \alpha}{B} \right)^n h^{n+1} = (n+2)\bar{u} \quad (14.5)$$

or with $n \cong 3$:

$$c \cong 5\bar{u} \quad (14.6)$$

In other words, the kinematic wave moves with a speed that is roughly five times the depth-averaged velocity of the glacier. If there is basal sliding and the sliding speed varies as τ^2 (Equation (7.10)), the ratio is likely to be slightly less than 5. This relation applies, rigorously, only to infinitesimal waves. Waves of finite amplitude may have higher speeds.

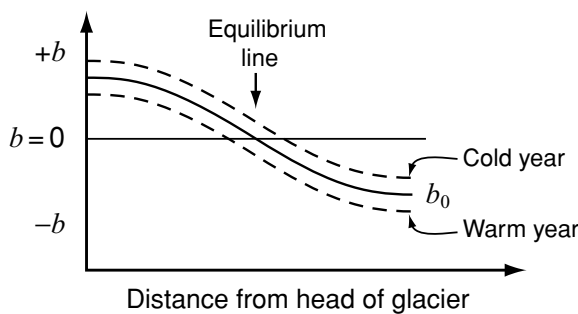
Analysis of the effect of a small change in mass balance using a perturbation approach

Let us now, following Nye (1960, pp. 561–562), use perturbation techniques to study the change in thickness with time after a small change in mass balance. Consider the situation in which the specific mass balance is shown by the solid line in Figure 14.6. We will refer to the situation represented by this solid line as the “0” or *datum* or *equilibrium* state, and analyze the effect of small perturbations from this state such as those represented by the dashed lines in the figure. For example, during a cold or unusually snowy year the mass balance may be increased everywhere by an amount $b_1(x, t)$ so we have:

$$b(x, t) = b_0(x) + b_1(x, t)$$

Note that b_0 is a function only of x ; it does not vary with time because the datum state is a steady state. Other properties of the datum state are

Figure 14.6. Perturbations in mass balance from an equilibrium state, b_0 .



$q_0(x, h, \alpha)$, $h_0(x)$, and $\alpha_0(x)$. In the perturbed state these become $q = q_0 + q_1$, $h = h_0 + h_1$, and $\alpha = \alpha_0 + \alpha_1$. Substituting these into the continuity equation (Equation (14.2)) yields:

$$\frac{\partial}{\partial x}(q_0 + q_1) + \frac{\partial}{\partial t}(h_0 + h_1) = b_0 + b_1 \quad (14.7)$$

We now write Equation (14.2) in terms of the datum state, thus:

$$\frac{\partial q_0}{\partial x} + \frac{\partial h_0}{\partial t} = b_0$$

and subtract this from Equation (14.7) to obtain:

$$\frac{\partial q_1}{\partial x} + \frac{\partial h_1}{\partial t} = b_1 \quad (14.8)$$

In passing, it is again worth noting that $\partial h_0 / \partial t = 0$ because h_0 is a property of the steady state.

At any position, x , q varies with h and α so we can write:

$$dq = \frac{\partial q}{\partial h} dh + \frac{\partial q}{\partial \alpha} d\alpha$$

or for small perturbations, $dq = q_1$, $dh = h_1$, and $d\alpha = \alpha_1$ so:

$$q_1 = \frac{\partial q}{\partial h} h_1 + \frac{\partial q}{\partial \alpha} \alpha_1 \quad (14.9)$$

Previously we identified $\partial q / \partial h$ with the celerity of a kinematic wave, c , or in the datum state: $(\partial q / \partial h)_0 = c_0$. Now we similarly define $D_0 = (\partial q / \partial \alpha)_0$, so in the datum state, Equation (14.9) becomes:

$$q_1 = c_0 h_1 + D_0 \alpha_1 \quad (14.10)$$

This relation is valid only for small perturbations. Were we interested in larger perturbations, terms involving h_1^2 , h_1^3 , ..., α_1^2 , α_1^3 , ... would have to be included. Thus, our approach is referred to as a *linearized* theory.

Equations (14.8) and (14.10) are a pair of simultaneous differential equations that can be solved for the change in ice flux and thickness

resulting from a perturbation in net balance. Let us first eliminate q_1 from the two equations, thus:

$$\frac{\partial c_0}{\partial x} h_1 + c_0 \frac{\partial h_1}{\partial x} + \frac{\partial D_0}{\partial x} \alpha_1 + D_0 \frac{\partial \alpha_1}{\partial x} + \frac{\partial h_1}{\partial t} = b_1 \quad (14.11)$$

Returning to Equation (14.1) we see that in the datum and perturbed states, respectively:

$$\alpha_0 = \beta - \frac{\partial h_0}{\partial x} \quad \text{and} \quad \alpha_0 + \alpha_1 = \beta - \frac{\partial h_0}{\partial x} - \frac{\partial h_1}{\partial x} \quad (14.12)$$

Thus, subtracting the first of these expressions from the second: $\alpha_1 = -\partial h_1 / \partial x$. This result can be substituted into Equation (14.11) to yield, after some rearranging:

$$\begin{array}{llll} \frac{\partial h_1}{\partial t} & = b_1 - \frac{\partial c_0}{\partial x} h_1 - \left(c_0 - \frac{\partial D_0}{\partial x} \right) \frac{\partial h_1}{\partial x} + D_0 \frac{\partial^2 h_1}{\partial x^2} \\ \text{(i)} & \text{(ii)} & \text{(iii)} & \text{(iv)} \end{array} \quad (14.13)$$

Equation (14.13) was first derived by Nye (1960, p. 562). As he noted, the terms in it have the following meanings.

- (i) h_1 increases at a rate given by the perturbation in accumulation.
- (ii) This term results in an exponential decrease or increase in the rate of change of h_1 as we shall show below.
- (iii) This represents a kinematic wave of constant h_1 . The speed of propagation of the wave is $c_0 - \partial D_0 / \partial x$ in the $+x$ direction. Note that both c_0 and $\partial D_0 / \partial x$ have dimensions $\ell \text{ t}^{-1}$.
- (iv) This represents diffusive damping of the perturbation h_1 , in accord with the diffusion equation, with diffusivity D_0 .

Our objective now is to solve Equation (14.13) for a simple case, neglecting diffusion. Then we will investigate the role of diffusion.

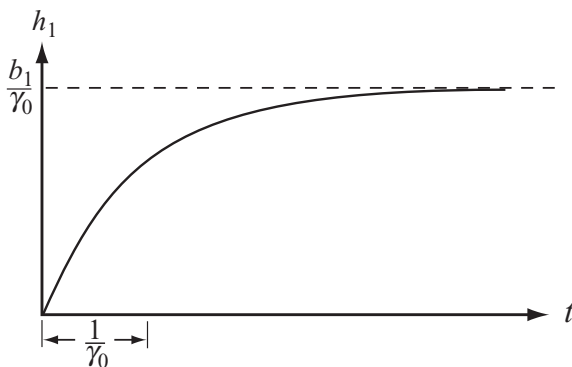
Solution for a small part of a glacier with uniform longitudinal strain rate and without diffusion

Consider a situation in which a glacier is initially in a steady state with an accumulation rate b_0 (Nye, 1960, p. 563). Then the accumulation rate increases abruptly by an amount b_1 to $b = b_0 + b_1$ and remains at this increased level indefinitely. Suppose $\partial c_0 / \partial x$ is independent of x on this glacier. From Equations (14.5) we see that:

$$\frac{\partial c_0}{\partial x} \cong (n + 2) \frac{\partial \bar{u}_0}{\partial x} \quad (14.14)$$

where $\partial \bar{u}_0 / \partial x$ is the longitudinal strain rate, r_0 . This, thus, corresponds to a situation in which the longitudinal strain rate is uniform in the x -direction. We seek a solution to Equation (14.13) such that h_1 is

Figure 14.7. Asymptotic adjustment of a glacier toward a new steady state, b_1/γ_0 , following a perturbation in accumulation rate, b_1 , in an area of extending flow. $1/\gamma_0$ is the response time.



independent of x so $\partial h_1 / \partial x = 0$. Thus, the increase in thickness is uniform over the glacier. We will let $\gamma_0 = \partial c_0 / \partial x$.

With these simplifications, Equation (14.13) becomes:

$$\frac{dh_1}{dt} = b_1 - \gamma_0 h_1 \quad (14.15)$$

Separating variables we obtain:

$$\int_0^{h_1} \frac{dh_1}{b_1 - \gamma_0 h_1} = \int_0^t dt$$

Integration yields:

$$h_1 = \frac{b_1}{\gamma_0} (1 - e^{-\gamma_0 t}) \quad (14.16)$$

If γ_0 is positive, corresponding to a positive longitudinal strain rate (Equation (14.14)) such as we expect in an accumulation area, h_1 asymptotically approaches the value b_1/γ_0 (Figure 14.7). In other words, after a very long time, the glacier will have increased in thickness by this amount. This is the situation described earlier and illustrated in Figure 14.1a.

The quantity $1/\gamma_0$, which has the dimensions of time, is known as the *time constant* for this change. This is sometimes associated with the “response time” of a glacier, or the length of time required for a glacier to respond to a change in climate. When $t = 1/\gamma_0$, $(1 - e^{-\gamma_0 t}) \cong 2/3$ so h_1 is $\sim 2/3$ of the way to the new equilibrium state. Mathematically (Equation (14.16)), it is clear that the new equilibrium state is never reached. Thus, it would be meaningless to try, instead, to define the response time as the total time required to attain a new steady state.

From Equation (14.14) we see that $1/\gamma_0 \cong 1/5r_0$. In other words, in this simple model the response time is inversely proportional to the longitudinal strain rate. For example, typical longitudinal strain rates for Storglaciären, Barnes Ice Cap, and the Antarctic Ice Sheet are 0.015 a^{-1} , 0.005 a^{-1} , and 0.00005 a^{-1} respectively. Thus, the response time of

Barnes Ice Cap might be expected to be three times as long as that of Storglaciären, and that of the Antarctic Ice Sheet, 100 times as long as Barnes Ice Cap. While these multiples are not unrealistic, it turns out that $1/5r_0$ seriously underestimates the actual response time. As we will see below, this is because diffusion has been neglected.

If γ_0 is negative, corresponding to longitudinal compression as would be typical in an ablation zone, there is an obvious problem. Equation (14.16) then predicts that h_1 will increase exponentially with time. Thus, a new steady state is never even approached. This is the situation which we discussed in connection with Figure 14.1b.

Clearly, it is not possible to have the upper part of a glacier increasing in thickness slowly and stably while the lower part is increasing rapidly and unstably. In the absence of diffusion, Nye (1960) suggests that the initial response in the ablation area would, indeed, be unstable. At any location, however, stability would be restored when a kinematic wave, initiated in the vicinity of the equilibrium line and propagating down glacier, reached that location. With diffusion, however, such an unstable response may never develop.

Effect of diffusion

Diffusion occurs whenever fluxes are proportional to gradients. In the present case, the flux, q , is proportional to the slope (or gradient), α . Where α is largest, on the downslope side of a wave, q is highest. Conversely, q is lowest on the upslope side of the wave. Thus, the flux into the wave is diminished and that out of it is enhanced. This tends to decrease the amplitude and increase the wavelength of a wave.

As in the case of c (or c_0) (Equation (14.5)), an analytical expression for D_0 can be obtained by differentiating q with respect to α , thus:

$$D_0 = \left(\frac{\partial q}{\partial \alpha} \right)_0 = n \left(\frac{2}{n+2} \right) \left(\frac{S_f \rho g}{B} \right)^n h^{n+2} \alpha^{n-1} = \frac{nq}{\alpha}$$

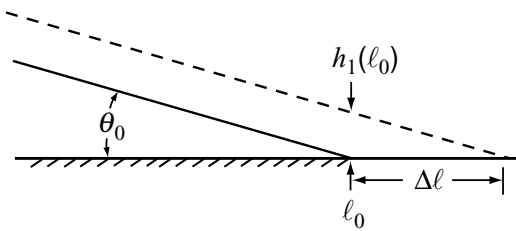
or with $n \cong 3$:

$$D_0 \cong \frac{3\bar{u}h}{\alpha} \quad (14.17)$$

In other words, diffusion will be most significant where the glacier is thick, the speed high, and the slope low.

Unfortunately, it is difficult to probe this dependence more thoroughly at the level of the treatment herein. However, Nye (1963a, pp. 442–445) has shown that diffusion decreases the rate of thickening, a result that is intuitively logical. As a result, the response time increases quite markedly. In one example, the response time increases by more than an order of magnitude (Nye, 1963a, Figure 4a). In addition, the

Figure 14.8. Geometry of the terminus region.



increase in thickness of the glacier near the equilibrium line is substantially greater when diffusion is taken into consideration.

The problem at the terminus

It is difficult to use Nye's kinematic wave theory to study the details of the advance and retreat of real glaciers. This is, in part, because the mass flux, q , cannot go to zero at the terminus if the glacier is to respond to an increase in accumulation by advancing. However, Equation (14.4) suggests that $u \rightarrow 0$ as $h \rightarrow 0$. To avoid this, Nye (1963b, p. 92) assumes that the glacier is sliding at the terminus so $q = u_{b0}(\ell_0)h$ where $u_{b0}(\ell_0)$ is the sliding speed, u_b , at the terminus, ℓ_0 , in the datum state. Here ℓ_0 is the length of the glacier, measured from the bergschrund. Then $c_0 = \partial q / \partial h = u_{b0}(\ell_0)$.

In addition, the amount of advance, $\Delta\ell$, is sensitive to the assumed geometry of the terminus. As shown in Figure 14.8:

$$\Delta\ell = \frac{h_1(\ell_0)}{\tan\theta_0} \quad (14.18)$$

where $h_1(\ell_0)$ is the perturbation in ice thickness at the terminus. Thus $\Delta\ell$ depends on θ_0 .

Further study of the response time

Jóhannesson *et al.* (1989) have studied the question of response times and of conditions at the terminus in greater detail. They identify three possible natural time scales that might be used in the analysis of glacier responses:

$$t_C = \frac{\ell_0}{c_0} \left[\frac{m}{ma^{-1}} \right] \quad (14.19a)$$

$$t_D = \frac{\ell_0^2}{\pi^2 D_0} \left[\frac{m^2}{m^2 a^{-1}} \right] \quad (14.19b)$$

$$t_V = \frac{V_1}{\overline{b}_1 \ell_0} \left[\frac{m^3 m^{-1}}{ma^{-1} m} \right] \quad (14.19c)$$

Here, t_C and t_D are time constants for propagation or diffusion* of a disturbance over the length of a glacier. In effect, they are measures of the time required to establish the general shape of the new thickness profile, $h_1(x, t)$. As the size of such a disturbance decreases with time, the rate of propagation or diffusion also decreases. Therefore, as with $1/\gamma_0$, t_C and t_D are measures of the time required for the processes to proceed about 2/3 of the way to completion. Similarly, as we shall show below, t_V is the time required for accumulation (or loss) of about 2/3 of the volume (per unit width), V_1 , required to re-establish an equilibrium geometry after a perturbation in mass balance that adds a volume of ice $\bar{b}_1\ell_0$ to the glacier every year.

Jóhannesson *et al.* find that t_V is usually appreciably longer than t_C or t_D . This means that perturbations in ice thickness are spread out over the glacier by propagation and diffusion rather quickly in comparison with the time needed for accumulation of the additional mass. Clearly, a glacier cannot be considered to have returned some specified fraction of the way to a new equilibrium state until the necessary additional mass has accumulated (or been lost).

In an extension of the Nye theory, t_V would be viewed approximately as follows: at any given time after a perturbation in mass balance, the mean perturbation in thickness, averaged over the length of the glacier, would equal the perturbation at the terminus, $h_1(\ell_0, t)$, multiplied by some function of the conditions in the datum state, of the magnitude of the perturbation, b_1 , and of time, thus:

$$\overline{h_1(x, t)} = f(c_0, D_0, b_1, t) \cdot h_1(\ell_0, t) \quad (14.20)$$

Remember that ℓ_0 is the position of the terminus in the datum state. Once a new equilibrium geometry has been attained, at $t = \infty$, the increase in volume of the glacier would be obtained by multiplying Equation (14.20) by the length of the glacier, thus:

$$V_1 = \overline{h_1}\ell_0 = f(t = \infty) \cdot h_1(\ell_0, \infty)\ell_0 \quad (14.21)$$

However, once a new steady state has been attained, the annual mass gain resulting from the perturbation, $\bar{b}_1\ell_0$, must equal the flux past the old terminus position, $u_{b0}(\ell_0) \cdot h_1$, thus:

$$\bar{b}_1\ell_0 = u_{b0}(\ell_0)h_1(\ell_0, \infty) \quad (14.22)$$

Eliminating h_1 from these two equations yields:

$$V_1 = \frac{f(t = \infty)\bar{b}_1\ell_0^2}{u_{b0}(\ell_0)} \quad (14.23)$$

* The π^2 term in Equation (14.19b) comes from the Fourier solution of the diffusion equation (T. Jóhannesson, written communications dated November 7 and 14, 1996).

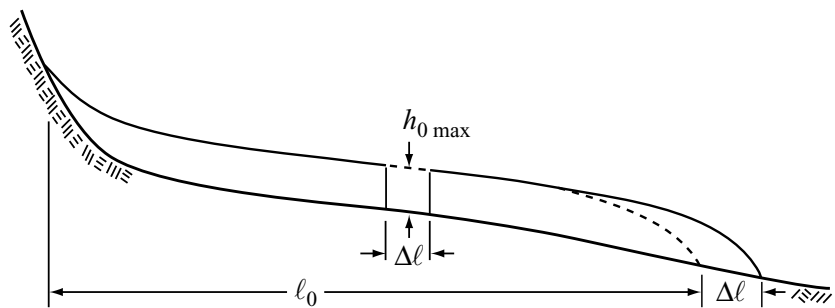


Figure 14.9. Geometrical argument for evaluating t_V . During an advance, $\Delta\ell$, the mass that must be added to a glacier is approximately $\Delta\ell \cdot h_{0\max}$.

Whence, from Equation (14.19c):

$$t_V = \frac{f(t = \infty)\ell_0}{u_{b0}(\ell_0)} \quad (14.24)$$

Thus, by this approach, t_V turns out to be sensitive to the unknown sliding speed at the terminus. In addition, the function, f , is highly sensitive to the details of the variations in c_0 and D_0 , especially near the terminus (Jóhannesson *et al.*, 1989, p. 364 and appendices).

Jóhannesson *et al.* have developed a much simpler geometrical argument to estimate t_V . Consider the situation in Figure 14.9 in which an advance of a glacier by an amount $\Delta\ell$ is illustrated graphically by cutting the glacier at its point of maximum thickness and sliding the lower part forward by $\Delta\ell$. Then, the increase in volume of the glacier is approximately $\Delta\ell \cdot h_{0\max}$. Detailed numerical modeling suggests that this is a good approximation to the response of a real glacier when the dynamical properties of the glacier are the same in the initial and final state, and thus influence the initial and final profiles in the same way. Now, rather than equate the annual mass gain resulting from the perturbation with the flux past the old terminus position, as in Equation (14.22), we equate it with the mass loss over the new part of the glacier, $\Delta\ell$, thus:

$$\bar{b}_1\ell_0 = |b_t| \Delta\ell \quad (14.25)$$

where b_t is the mean net balance rate over $\Delta\ell$ which may be approximated by $b(\ell_0)$, the net balance rate at the terminus (a negative quantity) if $\Delta\ell$ is small. Therefore:

$$V_1 = \Delta\ell h_{0\max} = \frac{h_{0\max} \bar{b}_1 \ell_0}{|b(\ell_0)|} \quad (14.26)$$

Whence, from Equation (14.19c):

$$t_V = \frac{h_{0\max}}{|b(\ell_0)|} \quad (14.27)$$

Thus, t_V can be estimated, quite easily, from knowledge of the thickness of the glacier and the net balance rate at the terminus.

We noted above that t_V is a time constant in the same sense that $1/\gamma_0$ is. Let us now demonstrate this. Immediately after a permanent change in balance rate, b_1 , the rate at which additional mass, V_1 , is acquired by the glacier, dV_1/dt , is $B_1 = \bar{b}_1 \ell_0$. However, as the glacier becomes longer (by an amount $\Delta\ell(t)$), some of the additional annual input is lost through ablation in the new part of the terminus region. Thus:

$$\frac{dV_1}{dt} = B_1 - |b_0(\ell_0)| \Delta\ell$$

Now from Equation (14.26) or Figure 14.9, $\Delta\ell \cong V_1/h_{0\max}$, so:

$$\frac{dV_1}{dt} = B_1 - \frac{|b_0(\ell_0)|}{h_{0\max}} V_1$$

Comparing this with Equation (14.15), it is clear that $h_{0\max}/|b(\ell_0)|$ is the analog of $1/\gamma_0$.

When calculating t_V in practice, the three-dimensional geometry of the glacier must be taken into consideration. Thus, in the case of a glacier like Storglaciären that has a number of overdeepened basins in its longitudinal profile, $h_{0\max}$ needs to be replaced by an appropriate longitudinally averaged thickness. In addition, the terminus of Storglaciären is constrained between bedrock and morainal highs so that its width is about half the average width of the glacier (Figure 12.9). Accordingly, Equations (14.25) to (14.27) need to be generalized to three dimensions. For example, if we write Equation (14.25) as:

$$\bar{b}_1 A_0 = |b(\ell_0)| W(\ell_0) \Delta\ell \quad (14.28)$$

where A_0 is the initial area of the glacier and $W(\ell_0)$ is the width of the terminus, Equation (14.19c) becomes:

$$t_V = \frac{V_1}{\bar{b}_1 A_0} \quad (14.29)$$

V_1 must now be estimated based on the glacier geometry. For instance, by analogy with Figure 14.9, one might consider that the new geometry could be approximated by (mentally) sliding forward the central part of the glacier of width $W(\ell_0)$. V_1 is then $\bar{h}_{0\max} W(\ell_0) \Delta\ell$, where $\bar{h}_{0\max}$ is a mean thickness over this central part. Inserting this in Equation (14.29) and using Equation (14.28) then yields:

$$t_V = \frac{\bar{h}_{0\max}}{|b(\ell_0)|} \quad (14.30)$$

Harrison *et al.* (2001) have pointed out that the formulation of t_V in Equation (14.19c) ignores the normal increase in b_n with elevation. Owing to this increase, perturbations that result in thickening or thinning

of a glacier are effectively amplified. This positive feedback, known as the *Böðvarsson effect* (Böðvarsson, 1955), can lead to significant underestimates of the response time. In extreme cases, it may lead to unstable (or runaway) growth or shrinkage of a glacier.

To include this effect, Harrison *et al.* suggest adding a term to Equation (14.27), thus:

$$t_{\text{VH}} = \frac{H}{|b_e| - G_e H} \quad (14.31)$$

H is now a thickness scale, not necessarily equal to $h_{0 \text{ max}}$, b_e is an *effective balance rate* at or just below the terminus, and G_e is the *effective budget gradient*. The subscript H is added to t_V to distinguish this time scale from that of Jóhannesson *et al.* (Readers should refer to Elsberg *et al.* (2001) and Harrison *et al.* (2001) for a rigorous derivation of Equation (14.31) and definitions of b_e , G_e , and H . Suffice it to say here that the theory is grounded in the reference-surface approach to mass balance discussed briefly in Chapter 3 (p. 25.) It will be readily seen that the added term has the desired effect. Both G_e and H are positive, so subtracting $G_e H$ from $|b_e|$ in the denominator increases t_{VH} and in extreme cases may make t_{VH} negative – the unstable response.

Unfortunately, b_e , G_e , and H are not easy to determine. To evaluate b_e one needs detailed balance rate data from the terminus that can be extrapolated into the area below the terminus and also a map showing bed elevations in the terminus area. In an application of their theory to South Cascade Glacier in the state of Washington (USA), Elsberg *et al.* (2001) found that setting $b_e \approx 0.75 b(\ell_0)$ yielded a good approximation to the true value. Likewise, rigorously $H = dV/dA$ and neither ΔV nor ΔA are measured routinely. Finally, an average value of G_e may not be appropriate; again Elsberg *et al.* (2001) found that setting G_e equal to 0.9 times the specific balance gradient half way between the terminus and the equilibrium line worked well on South Cascade Glacier, but they caution that these approximations may not be appropriate for other glaciers.

An important characteristic of Equation (14.31) appears if one notes that since b_e is a balance rate near the terminus, and $b_n = 0$ at the equilibrium line, then $b_e/\Delta z_{t \rightarrow e} \approx G_e$, where $\Delta z_{t \rightarrow e}$ is the elevation difference between the terminus and the equilibrium line. Then the ratio of the two terms in the denominator of Equation (14.31) is:

$$\frac{G_e H}{|b_e|} \approx \frac{H}{\Delta z_{t \rightarrow e}}$$

Clearly, t_{VH} becomes large as this ratio approaches unity, and the system is unstable if it exceeds unity. $\Delta z_{t \rightarrow e}$ will be smaller on glaciers that are relatively flat, and may approach H on such glaciers. Thus glaciers with

low slopes may be expected to have longer response times, a characteristic that does not appear in Jóhannesson *et al.*'s formulation.

For purposes of illustration, let us put some realistic numbers into some of these equations. The ablation rate on the lower part of the tongue of Storglaciären averages $\sim 1.3 \text{ m a}^{-1}$ and the mean thickness over the central region of the glacier is between 100 and 150 m, so t_V is ~ 100 years. Rigorous estimates of G_e and b_e probably could be obtained for Storglaciären, but as the necessary calculations have not been done let us use the approximations that Elsberg *et al.* found appropriate for South Cascade Glacier. Then, $b_e \approx -0.98 \text{ m a}^{-1}$ and $G_e \approx 0.003 \text{ a}^{-1}$ (Schytt, 1968, and unpublished data), so t_{VH} ranges from ~ 150 to ~ 300 years, depending on the value of H . For comparison, numerical modeling (Brugger, 1992) suggests a response time of ~ 80 years, while field measurements show that about 2/3 of Storglaciären's retreat from its Little Ice Age maximum position, which it reached in 1910, took place in ~ 45 years (Holmlund, 1987). The sizeable difference between t_V and t_{VH} probably reflects, in part, the fact that the denominator in Equation (14.31) is a small difference between two numbers that are large (compared with their difference) and that have large uncertainties. However, the result serves to emphasize the potential importance of the Böðvarsson effect. The more rapid response observed is likely to be a consequence of two factors: (1) $b(\ell_0)$ was probably higher (more negative) when the glacier extended to lower elevations, and (2) the change from Little Ice Age conditions was hardly a small perturbation. In any case, all of these times are substantially longer than the $1/5r_0$ (≈ 13 years) time scale mentioned above. This is in part because diffusion is neglected in the latter, as noted, and in part because the $1/5r_0$ time scale does not allow enough time to accumulate or lose the required mass, and thus violates conservation of mass.

Numerical modeling of glacier responses

In the absence of analytical solutions to Equation (14.13), glaciologists have resorted to numerical modeling. In such models one can, in addition, retain nonlinear effects which are neglected in linearized theories. Thus, the models are not restricted to infinitesimal perturbations. Furthermore, one can use glacier shapes and mass balance patterns that are specific to a particular glacier.

A good example is a model of Hintereisferner in the Austrian Alps by van de Wal and Oerlemans (1995). First the authors calculated a surface profile that would be in equilibrium with a certain mass balance rate, $b_0(x)$ (Figure 14.10a). Then they increased the mass balance rate by 0.5 m a^{-1} for one year. This could represent the situation

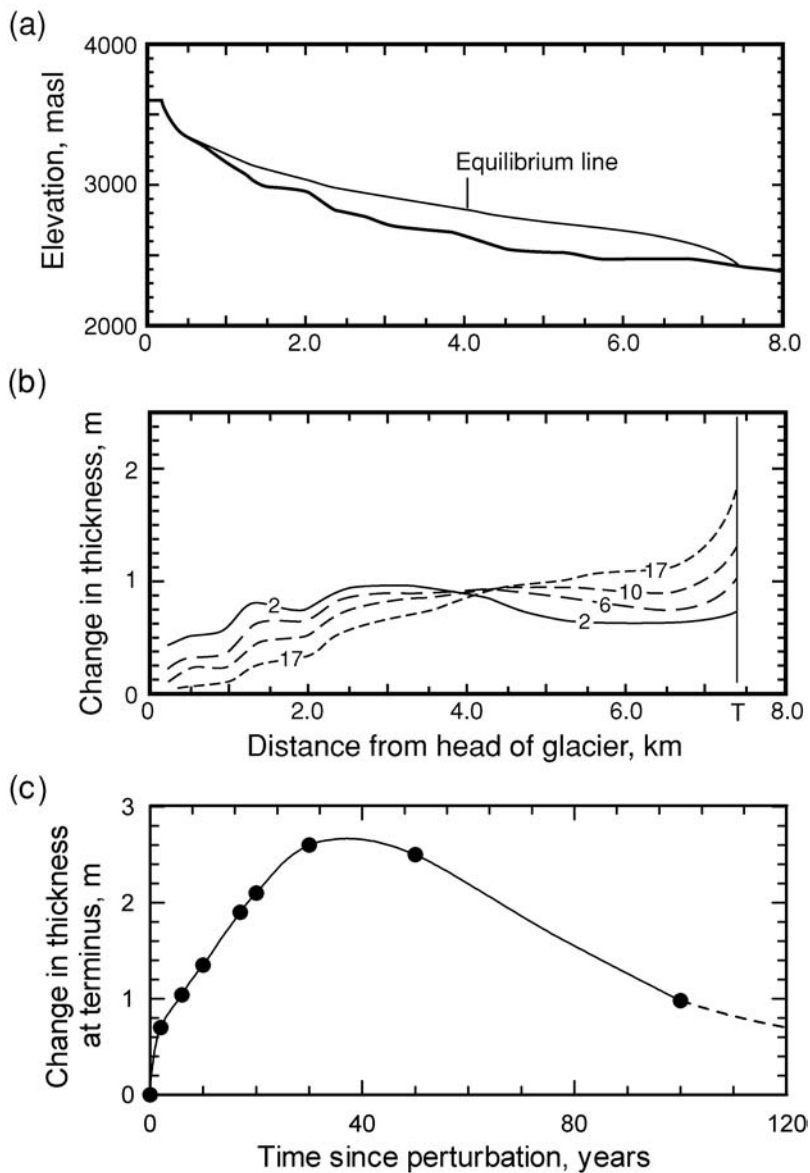


Figure 14.10. (a) Longitudinal profile of Hintereisferner in a stable state. (b) Changes in thickness of Hintereisferner resulting from a 0.5 m perturbation in mass balance, b_1 , at time $t = 0$. The increase in b_n lasted 1 year. Times are in years. Thickness changes are larger than 0.5 m because they include a contribution from the unperturbed mass balance, b_0 . T = terminus. (c) Change in thickness at the terminus of Hintereisferner as a function of time after the perturbation. (Both (a) and (b) are reproduced from van de Wal and Oerlemans, 1995, Figures 7a and 9b, with permission of the authors and the International Glaciological Society; (c) is calculated from data in Figures 9b and 9c of van de Wal and Oerlemans, 1995.)

during an unusually positive balance year (see the curve labeled “+” in Figure 3.5a or that labeled “Cold year” in Figure 14.6). The following year, the net budget was returned to its normal value. Figure 14.10b shows the increase in thickness as a function of distance from the head of the glacier at various times after the perturbation. After 2 years, a wave has formed with its crest ~ 3 km from the head, or about 1 km upglacier from the equilibrium line. By the sixth year, the crest is a little more than 4 km from the head, representing a wave speed of about 300 m a^{-1} . For comparison, the depth-averaged velocity over this part of the glacier is a little under 50 m a^{-1} . In addition, the wave has been damped and lengthened by diffusion. With time, diffusion continues to smooth the wave, the surface in the accumulation area sinks back towards its original level, and the surface in the ablation area, particularly at the terminus, rises sharply. In Figure 14.10c it will be seen that the terminus begins to collapse back to its original form after about 30 years, but that a significant thickening remains after 100 years.

The Hintereisferner modeling experiment serves to emphasize that kinematic waves on glaciers are likely to be long and low, as mentioned earlier. Thus, sophisticated survey techniques are required to detect them in the field. In addition, the modeling suggests that the wave speed is ≥ 6 times the depth-averaged velocity, \bar{u} , rather than $\leq 5\bar{u}$ as implied by Equation (14.6) and the following discussion. Van de Wal and Oerlemans think that this may be due to changes in the longitudinal strain rate which appear in the numerical model but which are not taken into consideration in the linear model. Such changes are likely to affect the $q-h$ relation. Finally, the response at the terminus is stable, as shown in Figure 14.10c.

Comparison with observation

Let us now discuss some actual examples of how glaciers have responded to climatic perturbations. We have already mentioned Storglaciären briefly, and noted that estimates of the response time based on Equation (14.30), on a numerical model, and on observation are reasonably consistent with each other, and suggest a time of decades to a century. As expected, t_{VH} is longer than t_V , but the magnitude of the difference between them is probably due, in part, to errors in estimating the parameters. In contrast, $1/\gamma_0$ is only ~ 13 years. Nisqually and South Cascade glaciers are two others that have been studied extensively.

Nisqually Glacier

Nisqually Glacier on Mt Rainier in Washington retreated several hundred meters during the first part of the twentieth century. A trimline



Figure 14.11. Nisqually Glacier, Mt Rainier, Washington, in September, 1964, showing distinct trimline. The glacier tongue is covered with debris.

on the valley side above and down glacier from the present terminus (Figure 14.11) shows the shape of the glacier at its nineteenth-century maximum position, a position that it occupied, more or less, from about 1840 to 1910 (Meier, 1965, p. 803). Thus, the difference in elevation between the present (debris-covered) glacier surface and the trimline represents the amount of thickening that would need to occur in order for the glacier to readvance to that maximum position. The amount of thickening increases rapidly toward and down-valley from the terminus.

The response of Nisqually Glacier to perturbations in mass balance is illustrated in Figures 14.12 and 14.13. The upper part of Figure 14.12 shows that the net budget was generally positive between 1942 and 1951. In fact, the retreat rate of many temperate alpine glaciers in the Northern Hemisphere decreased during this time period, and some actually advanced. Thus, this represents a major climatic event (Meier, 1965, p. 803). However, in the middle part of Figure 14.12 it will be seen that the terminus was still retreating during this time; it was responding to negative mass budgets of the early 20th century. The total retreat between 1918 and 1960 was ~ 1000 m.

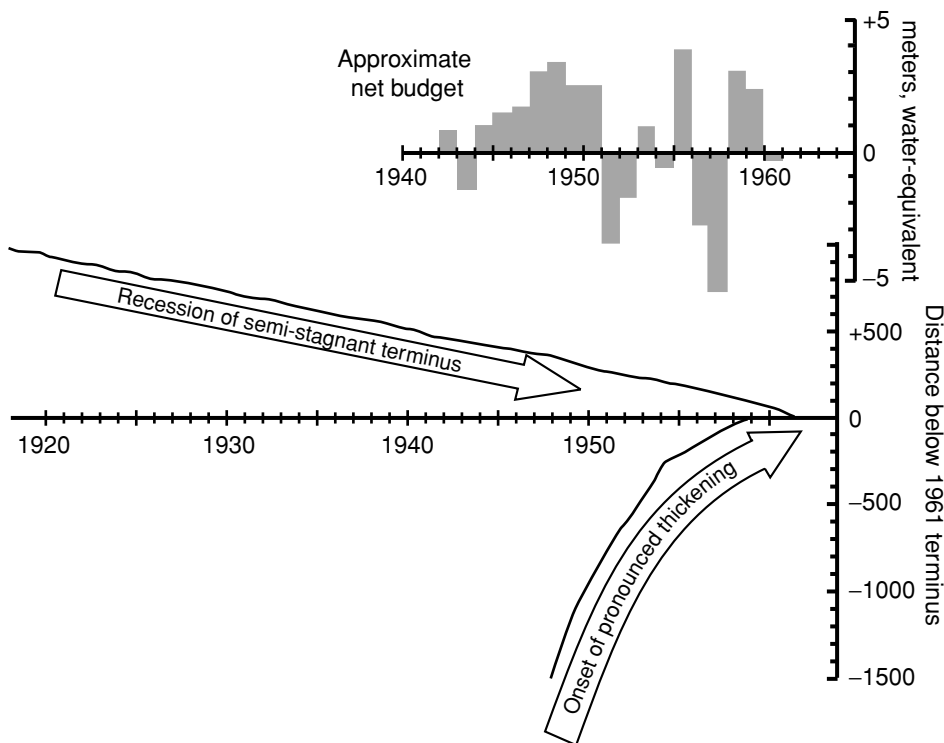


Figure 14.12. Recession of Nisqually Glacier between 1918 and 1961, together with the advance of a wave of pronounced thickening and the approximate net budget. (Reproduced from Meier, 1965, Figure 8, with permission of the author.)

In the mid 1940s, a wave of thickening was detected ~ 1500 m upglacier from the terminus, and this wave was tracked downglacier until it reached the terminus in about 1960 (lower part of Figure 14.12). This wave was presumably a response to the positive mass budgets of the 1940s. The progress of the wave is documented in Figure 14.13a, which is based on surveys, conducted almost every year, of the elevation of the glacier surface along three profiles across the glacier. The average elevation of the ice surface on each profile is shown as a function of time. At Profile 3, which is 2.7 km from the mid-twentieth-century terminus, thickening began in about 1945. Profile 2 is 1.6 km from the terminus; thickening began there in 1949. The wave reached Profile 1, 0.8 km from the terminus, in 1955. In Figure 14.13b the ice surface slope, surface elevation, and velocity are shown as functions of time at Profile 2. As noted earlier, this is probably not a pure kinematic wave as the changes in thickness and velocity are rather large. Thus, some

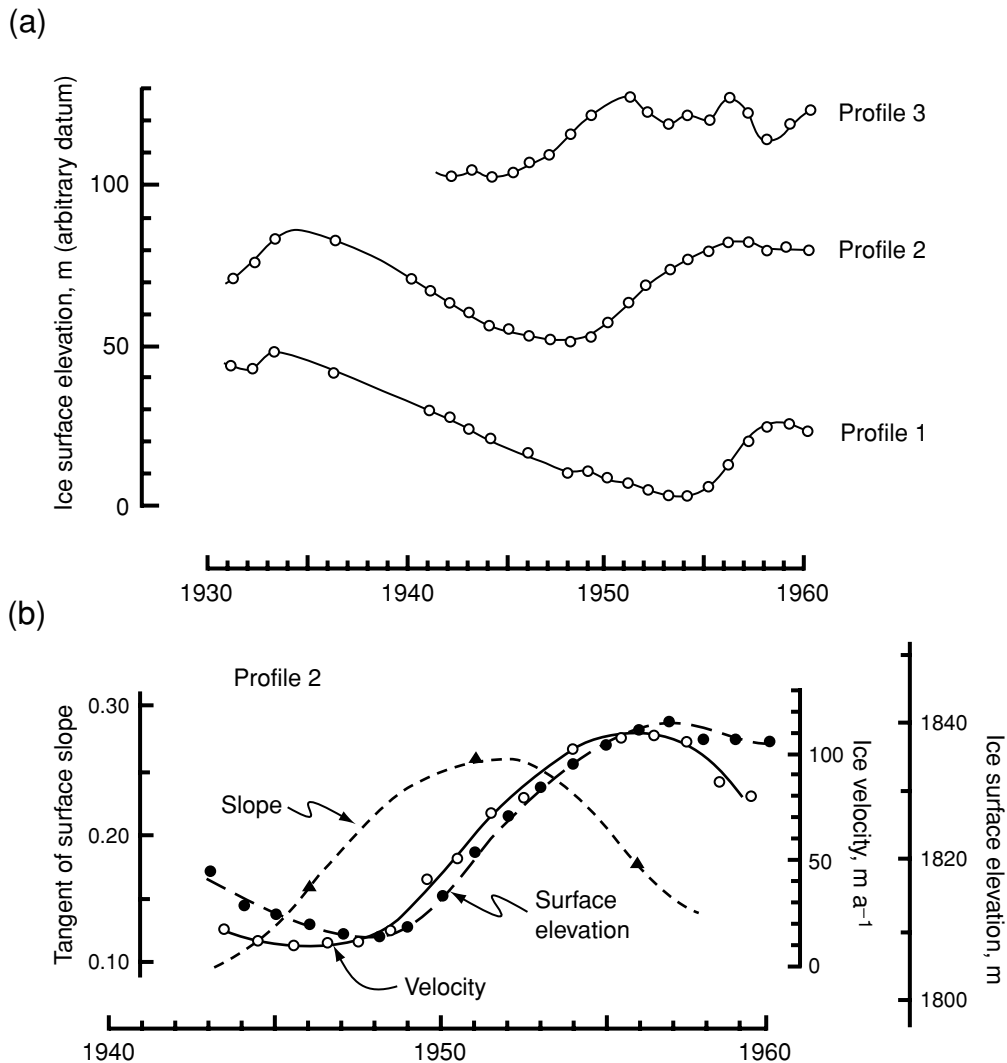


Figure 14.13. (a) Variation in ice surface elevation on three transverse profiles on Nisqually Glacier, 1931–1960. (b) Variations in ice surface elevation, velocity, and surface slope at Profile 2, 1943–1960. ((a) is from Johnson, 1960, Figure 2; (b) is from Meier, 1965, Figure 4; reproduced with permission of the authors.)

other mechanisms, such as an increase in sliding speed, were probably involved.

The reader may find it of interest to compare the change in velocity in Figure 14.13b with that predicted by Equation (5.7) with $u_b = 0$:

$$u_s = \frac{2}{n+1} \left(\frac{\rho g \alpha}{B} \right)^n h^{n+1} \quad (14.32)$$

To do this, take the differential of Equation (14.32) and divide the result by Equation (14.32) to yield:

$$\frac{du_s}{u_s} = n \frac{d\alpha}{\alpha} + (n+1) \frac{dh}{h} \quad (14.33)$$

To make this calculation you need the ice thickness, which is about 80 m at Profile 2. Despite the approximations inherent in Equations (14.32) and (14.33) and in estimating the values of the parameters in Equation (14.33) from the field data, the calculated du_s is surprisingly close to that observed. (The numerical computations are left as an exercise for the reader; see Problem 14.2.)

South Cascade Glacier

Owing to the availability of an impressive data base, South Cascade Glacier is another that has been analyzed in some detail. We have already mentioned Harrison *et al.*'s use of these data. In addition, Nye (1963b) used them to test the kinematic wave theory. To do this, he had to take into consideration the three-dimensional character of the glacier. Thus our Equations (14.8) and (14.10) become:

$$\frac{\partial Q_1}{\partial x} + w_0 \frac{\partial h_1}{\partial t} = w_0 b_1 \quad (14.34)$$

$$Q_1 = c_0 h_1 + D_0 \alpha_1$$

where $Q(x)$ is the ice flux through a cross section of the glacier at position x , and $w_0(x)$ is the width of the glacier as a function of x . In addition, c_0 and D_0 have to be redefined as:

$$c_0 = \frac{1}{w_0} \left(\frac{\partial Q}{\partial h} \right)_0 \quad \text{and} \quad D_0 = \frac{1}{w_0} \left(\frac{\partial Q}{\partial \alpha} \right)_0$$

As was the case with Equations (14.8) and (14.10), Equations (14.34) are a pair of simultaneous differential equations that can be solved for the changes in ice flux, $Q_1(x, t)$, and thickness, $h_1(x, t)$, resulting from a perturbation in mass balance, $b_1(x, t)$.

Previously (Equations (14.6) and (14.17)) we found that, in the absence of sliding, c_0 and D_0 could be related to certain measures of the speed and ice flux. Thus, if the geometry and velocity field of a glacier are known, reasonable estimates of $c_0(x)$ and $D_0(x)$ can be made. Nye calculated these parameters for South Cascade Glacier (Figure 14.14) and used the results to solve Equations (14.34) for the situation in which perturbations in b_1 varied sinusoidally with period, T , in years, or frequency, $\omega = 2\pi/T$. The solution is expressed in terms of series approximations, and detailed study of it is beyond the scope of this book. Numerical results are shown in Figure 14.15.

Figure 14.14. $w_0 c_0$ and $w_0 D_0$ as functions of x for South Cascade Glacier. (After Nye, 1963b, p. 104, Figure 7. Reproduced with permission of the author and the Royal Society, London.)

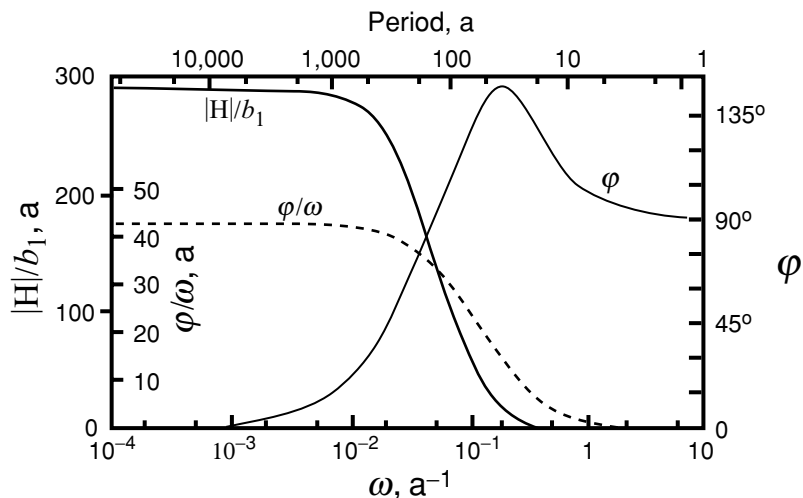
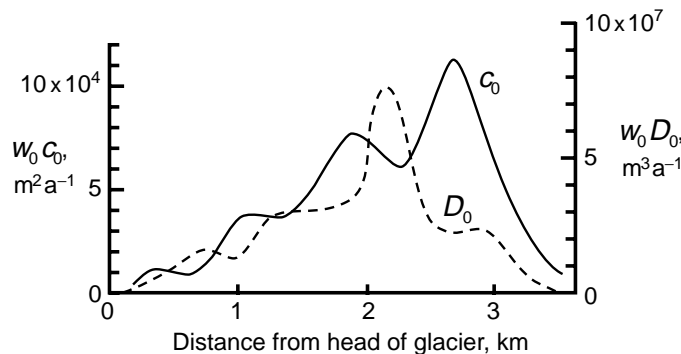


Figure 14.15. Theoretical response of the terminus of South Cascade Glacier to a sinusoidal perturbation of amplitude b_1 , period, T , and frequency, ω . Curves shown are the phase lag, φ , the time lag φ/ω , and the amplitude of the response $|H|/b_1$. (After Nye, 1963b, p. 107, Figure 9. Reproduced with permission of the author and the Royal Society, London.)

The curve of φ in Figure 14.15 is the phase lag between the variation in budget and the response of the terminus. For example, for an oscillation in mass balance that has a period of 100 years, the phase lag is approximately 110° . This means that the maximum thickness of the glacier at the terminus (and hence the maximum extent of the glacier) would occur $(110/360) \cdot 100 \cong 31$ years after the maximum in the mass balance. This latter number can be read from the curve of φ/ω , using the inner scale on the left side of the figure. Thus φ/ω is the time lag between the maximum accumulation rate and the maximum thickness. For variations in budget with very long periods, the phase lag decreases,

but the time lag does not change appreciably. For example, for an oscillation with a period of 1000 years, the time lag is ~ 43 years. Conversely, for oscillations with a period of only 1 year, which would represent the seasonal cycle from winter accumulation to summer melt, $\varphi = 90^\circ$ so the time lag is $\frac{1}{4}$ year. In other words, the maximum thickness does not occur when the rate of snow fall is a maximum, but rather at the end of the accumulation season when accumulation gives way to melt.

The curve of $|H|/b_1$ shows the change in thickness of the glacier at the terminus, expressed in terms of the perturbation in accumulation. For a perturbation with a period of 100 years, the increase in thickness here would be about 100 times the amplitude of the perturbation. Thus, a perturbation with an amplitude of 0.1 m would produce a change in thickness of ~ 10 m.

The ultimate objective of an analysis such as this might well be to solve the inverse problem, namely, given a history of advance and retreat of a glacier, to deduce the mass balance history and thus to learn something about the climatic changes that produced the fluctuations. Nye (1965b) did this for South Cascade Glacier and for Storglaciären with mixed results. He concluded that the records of terminus position of the two glaciers were not sufficiently well known to accurately deduce annual changes in net budget, but that coarser features of the records yield net balance figures that are in agreement with decadal means of recent observations.

It is of interest to use the data in Figure 14.14 to estimate the respective time scales from Equations (14.19). As South Cascade Glacier averages about 800 m in width, $t_C \cong 47$ years and $t_D \cong 33$ years. T. Jóhannesson (written communications dated November 7 and 14, 1996) suggests that time scales calculated in this way, however, are likely to be maximum estimates because many perturbations do not cover the entire glacier and thus are advected and diffused over the glacier more rapidly. Nevertheless, the relative magnitudes should be correct. Because $t_D < t_C$, disturbances should be damped by diffusion before a significant unstable response is generated. T. Jóhannesson (written communication dated December 23, 1995) finds that this is generally the case, and thus argues that diffusion cannot be neglected.

As with Storglaciären, it is difficult to estimate t_V for South Cascade Glacier because, again, there is a riegel beneath the middle of the ablation area. However, it appears that $100 < \overline{h}_{0\max} < 200$ m and $b(\ell_0) \cong 5 \text{ m a}^{-1}$, so $20 < t_V < 40$ years. Using detailed field data to evaluate b_e , G_e , and H , Harrison *et al.* (2001) obtained a value of t_{VH} of ~ 36 years. These values are reasonably consistent with those for t_C and t_D obtained above, particularly considering that the latter are likely to be maximum values. This is somewhat unusual, however, as Jóhannesson *et al.* (1989) find that t_V

is usually significantly longer than t_C or t_D , as noted earlier. The value of t_{VH} is also consistent with Nye's estimate of 43 years. For comparison, the $1/r_0$ time scale for South Cascade Glacier is about 15 years.

Summary

In this chapter, we have reviewed Nye's kinematic wave theory for predicting the response of a glacier to changes in mass balance, and have solved the resulting linearized equation (Equation (14.13)) for a simplified situation neglecting diffusion. Largely because it neglects diffusion, this solution predicts response times that are, in general, too short. The more complete approaches that Nye (1963a, b) used in his later papers, however, are sensitive to conditions at the terminus of the glacier, so although the linearized theory can yield reasonable estimates of the response time if these terminus conditions are well known, attempts to generalize from it have often led to times that are too long. Nevertheless, evidence from real glaciers is consistent with at least two of the conclusions from Nye's theory: that the most visible response is at the terminus, and that this response lags the perturbation by years, decades, or even centuries.

Jóhannesson *et al.* (1989) have suggested three alternative time scales for adjustment. Their time scales for propagation and diffusion of a disturbance over a glacier, t_C and t_D , provide measures of the time required for the glacier to adjust its shape (but not size) to changed conditions. Their volume time scale, t_V , on the other hand, utilizes a conservation of mass argument. That is, after a change in climate a glacier will be either too large or too small, and thus will not be in equilibrium with the changed conditions. It takes time for the surplus or deficit in mass balance to bring about the necessary change in volume. Thus, the volume time scale is more consistent with "response times" based on observation, and indeed with those based on numerical modeling. Harrison *et al.* (2001) have refined Jóhannesson *et al.*'s approach to include the Böðvarsson effect, an effect that lengthens the predicted response time, especially on relatively flat glaciers, and that can lead to an unstable response.

Numerical modeling suggests that kinematic waves such as those which Nye envisioned should form on glaciers, but they are likely to be long and low, and the increase in speed within them, small. Thus, they will be difficult to detect. Additional factors, such as major changes in conditions at the bed, are probably responsible for the impressive waves that have been documented by field observations. Because diffusive processes dampen kinematic waves relatively rapidly, unstable responses (Figure 12.1b) in areas of compressive flow are unlikely.

Appendix Problems

Chapter 3

- 3.1. Determine the changes in b_w , R , and T_a that would, if they occurred alone, result in a 100 m increase in equilibrium line altitude. Assume a 120 d melt season and a lapse rate of $-0.007 \text{ }^{\circ}\text{C m}^{-1}$.

Chapter 4

- 4.1. Determine the activation energy for creep for the following two sets of data.

Data set 1		Data set 2	
$\dot{\varepsilon}, \text{a}^{-1}$	$T, \text{ }^{\circ}\text{C}$	$\dot{\varepsilon}, \text{a}^{-1}$	$T, \text{ }^{\circ}\text{C}$
18.65	-5.5	1.33	-30.4
9.06	-9.9	0.0047	-61.0

All experiments were run at the same stress. Express the activation energy in kJ mol^{-1} .

- 4.2. (a) The temperature dependence of ice creep can be represented by an Arrhenius-type relation:

$$\dot{\varepsilon}_e = \left(\frac{\sigma_e}{B_0} \right)^n e^{-\frac{Q}{R\theta_K}}$$

By differentiating this with respect to θ_K and expressing the result in terms of differentials, determine the fractional change in $\dot{\varepsilon}$, $d\dot{\varepsilon}/\dot{\varepsilon}$, due to a change, $d\theta_K$, in θ_K .

- (b) In a laboratory experiment run at a temperature of $-15 \text{ }^{\circ}\text{C}$, what would be the approximate percentage variation in $\dot{\varepsilon}$ if the temperature were allowed to vary by $0.5 \text{ }^{\circ}\text{C}$? Use $Q = 79 \text{ kJ mol}^{-1}$.
- 4.3. Demonstrate analytically that the temperature dependence of ice creep can be reasonably approximated by:

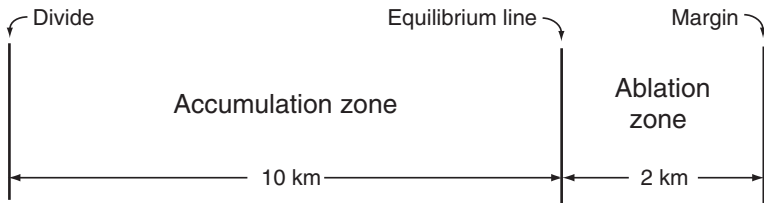
$$\dot{\varepsilon} = \dot{\varepsilon}_o e^{k\theta}$$

where θ is the temperature in degrees Celsius and $\dot{\varepsilon}_o$ is the strain rate at $0 \text{ }^{\circ}\text{C}$. What are reasonable values of k for different temperatures?

- 4.4. Calculate and plot the variation of crevasse depth with tensile stress up to a tensile stress of 0.2 MPa.

Chapter 5

- 5.1. Calculate the difference between the surface velocity and the bed velocity in a glacier 300 m thick with a surface slope of 0.046. Use $n = 3$ and $B = 0.141 \text{ MPa } a^{1/n}$. Use:
- the infinitely wide approximation,
 - an approximation based on Raymond's estimate of the appropriate shape factor for Athabasca Glacier (0.58), and
 - the semicircular approximation.
- Which result comes closest to the values measured by Raymond on Athabasca Glacier, and why?
- 5.2. At the equilibrium line on the Barnes Ice Cap Trilateration Net, the surface velocity is 6.7 m a^{-1} , the ice is 185 m thick, and the surface slope is 0.07. Using $B = 0.317 \text{ MPa } a^{1/n}$ (appropriate for ice at about -5°C) and $n = 3$, calculate and plot a velocity profile through the ice cap. What is the basal velocity. Is your result consistent with the above ice temperature?
- 5.3. An infinitely wide glacier has a velocity of 1 m a^{-1} at the surface and 0.7 m a^{-1} at a depth of 16 m. Determine the thickness of the glacier. Assume $u_b = 0$ and $n = 3$.
- 5.4. (a) An ice sheet has a surface profile given by $h = \sqrt{cx}$, where h is the height in meters and x is the distance from the margin, also in meters. Differentiate this to obtain an expression for the surface slope, S . By inserting this in the expression for the basal drag, $\tau = \rho ghS$, show that τ is independent of x . Obtain a numerical value for τ if $c = 16 \text{ m}$.
- (b) Let the ablation rate be $b_n \text{ m a}^{-1}$. By equating the discharge through any cross section to the volume of ice lost by melting downglacier from that cross section, show that the average horizontal velocity in the ablation zone is: $u = \Omega\sqrt{x}$ where $\Omega = b_n/\sqrt{c}$. (Note that Ω is negative because b_n is negative. Thus, u is negative, consistent with the fact that it is in the $-x$ -direction.)
- (c) At $x = 1500 \text{ m}$ the glacier flows over a bump in the bed, 0.5 m high, and quarries a cobble from the lee slope of the bump. The ice closes under the cobble, so at the start of its journey to the margin it is 0.5 m above the bed. Determine the x and z coordinates (z vertical) of the point where the cobble will melt out, and its time en route. Plot its path. Assume plug flow and incompressibility. Use $b_n = 0.6 \text{ m a}^{-1}$ and $c = 16 \text{ m}$, and assume the ablation zone is 2 km wide. Hint: use the incompressibility condition, $du/dx = -dw/dz$, and the result from Problem 5.4b to get $w(x)$. Then use the definition of velocity, $u = dx/dt$, and the initial condition, $x(t=0) = x_0$, to integrate the expression for u to get $x(t) = (x_0^{1/2} + \frac{1}{2}\Omega t)^2$. Then use $w = dz/dt$, and the initial condition, $z(0) = z_0$ to obtain $z(t) = z_0(x_0/x)^{1/2}$.
- (d) The accumulation zone in the above problem is 10 km wide (Figure P1). At the end of the Pleistocene a mammoth dies 500 m from the divide. Determine the x and z coordinates of the point where he melts out, and his

**Figure P1.**

time en route. Assume the glacier has had a balanced budget for the last 10 000 a, and that the ablation rate is 0.6 m a^{-1} over the 2 km wide ablation zone, as before. Plot the path. Hint: do as in Problems 5.4b and 5.4c, remembering that the horizontal velocity is now $u = -b_n(L - x)/\sqrt{cx}$, where L is the distance from the margin to the divide. You will encounter an integral $\int \sqrt{x}/(L - x) dx$ which may be transformed using $r = L - x$ and then evaluated using the tabulated integral:

$$\int \frac{\sqrt{L-r}}{r} dr = 2\sqrt{(L-r)} + L \left(\frac{1}{\sqrt{L}} \ln \frac{\sqrt{(L-r)} - \sqrt{L}}{\sqrt{(L-r)} + \sqrt{L}} \right)$$

- (e) If the mammoth was 3 m long and, when he died, he was lying down with his tail 3 m closer to the divide than his head, determine the time required for his body to pass completely beneath the equilibrium line, and his approximate length when he is at this point in his journey.

Chapter 6

- 6.1. Calculate and plot a temperature profile for an ice sheet that is 1368 m thick, assuming that $\theta_s = -24^\circ\text{C}$, $b_n = 0.35 \text{ m a}^{-1}$, $\kappa = 37.2 \text{ m}^2\text{a}^{-1}$, $\bar{u} = 0$, and $\beta_o = -0.0228^\circ\text{C m}^{-1}$. Obtain temperatures at least at 0, 200, 500, and 900 m above the bed.

- 6.2. (a) Determine the influence of strain heating on a temperature profile by integrating the energy balance equation, simplified with the use of the following assumptions:

- horizontal temperature gradients are negligible,
- $\kappa = \text{constant}$,
- steady state,
- zero accumulation (or $w_s = 0$), and
- $\dot{\epsilon} = (\sigma/B)^n$.

Note: this is easier if the z -axis points downward. If you retain a z -axis pointing upward, the sign of β_o below must be changed.

- (b) Plot the profile for a glacier that is 1000 m thick with:

$$\begin{aligned} \theta_s &= -35^\circ\text{C} & \rho &= 900 \text{ kg m}^{-3} & \alpha &= 0.01 \\ \beta_o &= 0.0228^\circ\text{C m}^{-1} & K &= 7.1 \times 10^7 \text{ J m}^{-1}\text{a}^{-1}^\circ\text{C}^{-1} & n &= 3 \\ B &= 0.397 \text{ MPa a}^{1/3} \end{aligned}$$

To see the effect, you will need to make calculations at about 25 m intervals between 900 and 1000 m depth, and you will need to use a long temperature axis.

- 6.3. Solve Problem 6.2 but with the additional assumption that strain heating is negligible, and calculate the temperature at the base of this same 1000 m thick glacier. How much does strain heating increase the basal temperature?
- 6.4. (a) To get a sense of the influence of longitudinal advection, calculate and plot a temperature profile for the glacier in Problem 6.1, assuming $\bar{u} = 15 \text{ m a}^{-1}$. Use the Column model with the values of θ_s , b_n , κ , H , and β_o given in Problem 6.1, the value of K in Problem 6.2, $\alpha = -0.01$, $\lambda = -0.01 \text{ }^{\circ}\text{C m}^{-1}$, and $w_b = 0 \text{ m a}^{-1}$.
 (b) Compare the result with that from Problem 6.1 in detail.
- 6.5. (a) Obtain an expression for the temperature gradient and the temperature distribution in a stagnant sheet of ice of infinite horizontal extent, and thickness H . Assume that the climate has been warming at a rate of $\dot{\theta}$, and that the interior of the glacier is warming at the same rate.
 (b) By examining the original differential equation after simplification, explain how the uniform warming rate is accomplished.

Chapter 8

- 8.1. Water flowing along a glacier bed must warm up as the ice thins and the pressure melting point increases. Water flowing up an adverse bed slope must warm up more rapidly, as the ice is thinning more rapidly. The energy needed to warm the water comes from viscous dissipation. Determine how steep the bed slope can get, relative to the surface slope, without exceeding the amount of viscous energy available. Obtain a numerical value for the constant of proportionality between the two slopes.
- 8.2. The discharge in a horizontal subglacial conduit with a circular cross section is $0.025 \text{ m}^3 \text{ s}^{-1}$. The water pressure in the conduit is 1.5 MPa and the hydrostatic pressure in the adjacent ice is 2.0 MPa. The Manning roughness of the conduit is $0.1 \text{ m}^{-1/3} \text{ s}$ and the viscosity parameter, B , is $0.16 \text{ MPa a}^{1/3}$. Determine the pressure gradient in the conduit, the radius of the conduit, the water velocity in the conduit, and the melt rate on the conduit walls (or closure rate).
- 8.3. An esker splits as shown in Figure P2. Stratigraphic relations suggest that the branch around the end of the ridge is younger. Explain why the esker changed course, and estimate the basal shear stress at the time of the change in course. Assume that the glacier had a parabolic profile, $h = \sqrt{cx}$. Assume further that water flow down the potential gradient could be maintained even though some water might be forced to refreeze to keep the temperature at the pressure melting point.
- 8.4. Consider a glacier with a parabolic profile, $h = \sqrt{16x}$, where x is the horizontal coordinate in meters and h is the surface elevation. Assume that the glacier is 2 km long and is on a horizontal bed. It is drained by a circular conduit at the bed. Calculate and plot the height of the hydraulic grade line as a function of distance from the terminus for discharges of $0.015 \text{ m}^3 \text{ s}^{-1}$, a winter

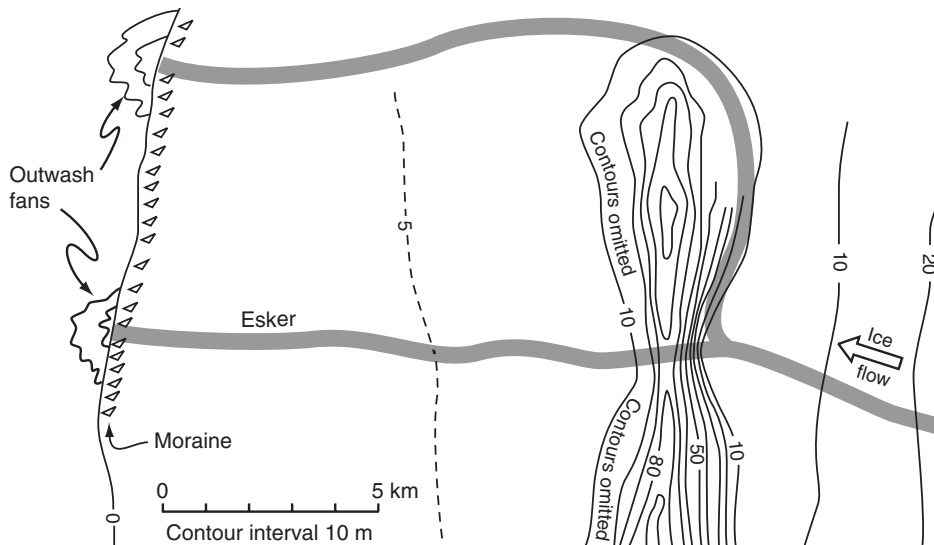


Figure P2.

discharge, and $1.0 \text{ m}^3 \text{s}^{-1}$, a summer discharge. Use a channel Manning roughness of $0.1 \text{ m}^{-1/3} \text{s}$ and ice viscosity parameter, $B = 0.06 \text{ MPa a}^{1/3}$.

Assume that the conduit is at atmospheric pressure within 50 m of the margin. (As the integration has to be carried out numerically, you might want to write a short program to do the calculations.)

Chapter 9

9.1. Use Equation (9.2.) for σ_S in terms of σ_{xx} , σ_{yy} , and θ to do the following.

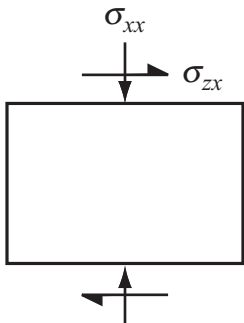
- Determine the angle θ of the planes on which σ_S is a maximum.
 - Determine the orientation of these planes relative to those on which σ_N is a maximum.
 - Determine the normal stress, σ_N , on the plane on which σ_S is a maximum.
 - Determine the magnitude of $\sigma_{S\max}$.
- Express all answers in terms of σ_{xx} , σ_{yy} , and σ_{xy} .

9.2. Show that J_1 and J_2 in three dimensions (Equations 9.8a) reduce to Equations (9.5) in two dimensions.

9.3. We have shown (Chapter 6) that $\frac{1}{2}\dot{\varepsilon}_{xz}\sigma_{xz} + \frac{1}{2}\dot{\varepsilon}_{zx}\sigma_{zx}$ is the total work done per unit time in a unit volume of ice subjected to simple shear. It is also true that $\frac{1}{2}\dot{\varepsilon}_{xx}\sigma'_{xx}$ is the work done by a normal stress. Thus the total work done is $W = \frac{1}{2}\dot{\varepsilon}_{ij}\sigma'_{ij}$. Show that because $\dot{\varepsilon}_{ij} = \lambda\sigma'_{ij}$, $W = \dot{\varepsilon}_e\sigma'_e$.

9.4. A laboratory ice deformation experiment is run using biaxial compression with applied stresses σ_1 and σ_2 on the faces of a cube. Stresses in the third direction are atmospheric. Strain rates are $\dot{\varepsilon}_1$ and $\dot{\varepsilon}_2$ in the σ_1 and σ_2 directions.

Determine the effective stress and the effective strain rate.

**Figure P3.**

- 9.5. An experimental system is designed to run tests in combined uniaxial compression and simple shear (Figure P3). Determine the effective stress and effective strain rate for this stress configuration.
- 9.6. The third invariant of the stress tensor, J_3 , can be interpreted in terms of the stress configuration. To do this, we define a stress configuration parameter, ξ , by $\xi = J_3^*$. Here, J_3^* is a normalized value of J_3 obtained by dividing all of the stresses by a constant factor, c , which you will derive below. The motivation for doing this is that it simplifies the expression for ξ . We proceed as follows.

The octahedral shear stress is defined by: $\sigma_o^2 = \frac{1}{3}\sigma'_{ij}\sigma'_{ij}$. Let us normalize σ_o by dividing all stresses by a constant factor, c , thus: $\sigma_o^{2*} = (1/3c^2)(\sigma'_{ij}\sigma'_{ij})$. (Here, the $*$ is used to indicate the normalized value.) Let us further select c such that $\sigma_o^* = 2^{1/6}$. Obtain an expression for c in terms of the second invariant of the stress tensor, J_2 . Because the normalized stresses must retain the sign of the original stresses, use $|c|$ where necessary.

Show the following.

- The deviatoric stresses in uniaxial compression under a compressive stress, σ_3 , are: $(-\sigma_3/3, -\sigma_3/3, 2\sigma_3/3)$, and (remembering that σ_3 is negative) that $\xi = -1$ for this case.
- The deviatoric stresses in pure shear under stresses $-\sigma_1, \sigma_3$, are: $(-\sigma_1, 0, \sigma_3)$, and that $\xi = 0$ for this case.
- For the stress configuration in Problem 9.5 above, obtain an expression for ξ in terms of σ_{xx} and σ_{xz} , and evaluate this for:

$$\sigma_{xx} = -0.1 \text{ MPa}, \sigma_{xz} = 0.1 \text{ MPa}, \text{ and}$$

$$\sigma_{xx} = -0.1 \text{ MPa}, \sigma_{xz} = 0 \text{ MPa}.$$

Chapter 10

- 10.1. Calculate and plot velocity profiles for an infinitely wide glacier that is 300 m thick with a surface slope of 0.046. Use $n = 3$ and $B = 0.141 \text{ MPa}^{1/n}$. Calculate one profile for $\dot{\epsilon}_{xx} = 0.0$ and one for $\dot{\epsilon}_{xx} = 0.1 \text{ a}^{-1}$. Assume a sliding velocity, u_b , of 20 m a^{-1} . Explain the difference between the profiles.

Chapter 11

- 11.1. Calculate a temperature profile in the ablation area of a glacier in a place where the ice is 500 m thick, the vertical velocity at the surface, w , is 0.25 m a^{-1} (upward), β_o is $-0.017 \text{ }^\circ\text{C m}^{-1}$, and the temperature at the surface is $-20 \text{ }^\circ\text{C}$. Assume that w decreases linearly with depth.
- 11.2. Using Equation (11.9b) and an initial condition in which $\theta = -20 \text{ }^\circ\text{C}$ at the surface, varies linearly to $-10 \text{ }^\circ\text{C}$ at a depth of 4 m, and is then independent of depth to a depth of 15 m, calculate a temperature profile for the end of June ($t = \frac{1}{2} \text{ year}$). Use $\kappa = 16 \text{ m}^2 \text{ a}^{-1}$ and a sinusoidal variation in temperature

with time at the surface, with $\theta_r = 18^\circ\text{C}$. The initial condition applies on January 1 ($t = 0$). Compare your solution to the analytical solution given by Equation (6.31).

Chapter 12

- 12.1. For comparison of borehole deformation rates, with shear stress σ_{zx} and shear strain rate $\dot{\epsilon}_{zx}$, with deformation rates in uniaxial compression, the stress in uniaxial compression must be multiplied by $1/\sqrt{3}$ and the strain rate by $\sqrt{3}/2$ (Nye, 1953). Show that this is true by calculating σ_e and $\dot{\epsilon}_e$ for the two stress configurations.
- 12.2. Starting with Equation (12.48), verify Equation (12.49). To do this it is necessary to use only one of Equations (12.48) (i.e. for $i = 1$).
- 12.3. Starting with $\dot{\epsilon} = (\sigma/B)^n$ and $\dot{\epsilon}_{ij} = \lambda\sigma'_{ij}$, show that the constants n and B in Glen's flow law can be evaluated if one can determine only one component of the stress tensor, the corresponding component of the strain rate tensor, and $\dot{\epsilon}$ at two or more places. Here n and B are determined either algebraically when there are only two points, or by plotting $1/\lambda$ against $\dot{\epsilon}$ and drawing a straight line through the points. Explain.
- 12.4. Determine n and B in MPa $\text{a}^{1/n}$ for the following two sets of velocity derivatives.

Depth	Velocity	x	y	z
9.4 m	u	-0.004 45	0.000 00	-0.014 17
	v	0.000 00	0.000 13	0.003 61
	w	0.000 99	-0.000 40	0.004 32
12.5 m	u	-0.004 14	0.000 00	-0.022 96
	v	0.000 00	0.000 12	0.003 93
	w	0.000 99	-0.004 68	0.004 02

The surface slope is 0.152. Depths are in meters and velocities in m a^{-1} . The y -axis is transverse and the z -axis is normal to the surface and directed downward. Data are from the Barnes Ice Cap boreholes.

- 12.5. Verify that the vertically downward forces on the top of the semi-cylinder of ice in Figure 12.6 balance the vertically upward forces on the bed when the pressure in the ice is P and the pressure in the conduit is ΔP .

Chapter 13

- 13.1. Verify Equation (13.5).
- 13.2. Calculate $\bar{\gamma}_{oc}$ for the mammoth in Problem 5.4e.
- 13.3. Verify that Equation (13.13) follows from Equation (13.12) and that Equation (13.14) is a solution to Equation (13.13).

Chapter 14

- 14.1. We found (Equation (5.7)) that one could obtain a first-order estimate of the surface velocity (assuming no sliding) from:

$$u_s = \frac{2}{n+1} \left(\frac{\rho g \sin \alpha}{B} \right)^n H^{n+1}$$

where H is the ice thickness and α is the surface slope. By expressing this in differential form and using the approximation $\alpha \cong \sin \alpha (\cong \tan \alpha)$, show that:

$$\frac{du_s}{u_s} = n \frac{d\alpha}{\alpha} + (n+1) \frac{dh}{h} \quad (\text{P14.1})$$

- 14.2. Use Figure 14.13 to do the following.

- (a) Compare the observed change in velocity of Nisqually Glacier from 1949 to 1951 with that calculated from Equation (P14.1) above. Use $h \approx 80$ m.
 - (b) Estimate the change in flux, Δq , and use Equation (P14.1) to estimate the fraction of the change that is due to the change in thickness and that due to the change in surface slope, respectively. Then calculate c_0 and D_0 from their definitions, expressed in finite difference form. (Note that q , c_0 , and D_0 are defined in terms of a unit width.)
- 14.3 Consider a perturbation, $b_l = 0.1$ m a^{-1} on Storglaciären, which is 2.8 km long and has a maximum velocity, $u_{0\max} \approx 35$ m a^{-1} . Calculate $\Delta\ell$ and the response time based only on the time needed to accumulate the additional mass. Use the Jóhannesson *et al.*'s model generalized to three dimensions. For this you will need to know the geometry of the glacier (Figures 8.13 and 12.9), and you will need:

glacier area = 3.03×10^6 m²

width at terminus, $W(\ell_o) = 400$ m

ablation rate at terminus = 1.3 m a^{-1} .

($W(\ell_o)$ is larger than shown in Figure 12.9 because the topography is such that the width would expand significantly as the glacier thickened here.) Assume that the average ice thickness over a cross section is $\sim \frac{1}{2}$ the thickness shown on the profile. (Remember that $\Delta V \neq \bar{h} \bar{W} \Delta\ell$ because $\bar{W} > W(\ell_o)$.)

References

- Allen, C. R., Kamb, W. B., Meier, M. F. and Sharp, R. P. (1960). Structure of lower Blue Glacier, Washington. *Journal of Geology*, **68**(6), 601–625.
- Alley, R. B. (1989a). Water pressure coupling of sliding and bed deformation: I. Water system. *Journal of Glaciology*, **35**(119), 108–118.
- (1989b). Water-pressure coupling of sliding and bed deformation: II. Velocity-depth profiles. *Journal of Glaciology*, **35**(119), 119–129.
- (1991). Deforming bed origin for the southern Laurentide till sheets? *Journal of Glaciology*, **37**(125), 67–76.
- (1992). Flow-law hypotheses for ice-sheet modeling. *Journal of Glaciology*, **38**(129), 245–256.
- Alley, R. B. and Whillans, I. M. (1991). Changes in the West Antarctic Ice Sheet. *Science*, **254**(5034), 259–263.
- Alley, R. B., Blankenship, D. D., Bentley, C. R. and Rooney, S. T. (1987a). Till beneath Ice Stream B 3. Till deformation: evidence and implications. *Journal of Geophysical Research*, **92**(B9), 8921–8929.
- Alley, R. B., Blankenship, D. D., Rooney, S. T. and Bentley, C. R. (1987b). Till beneath Ice Stream B 4. A coupled ice-till flow model. *Journal of Geophysical Research*, **92**(B9), 8931–8940.
- Alley, R. B. et al. (1993). Abrupt increase in Greenland snow accumulation at the end of the Younger Dryas event. *Nature*, **362**(6420), 527–529.
- Alley, R. B., Gow, A. J. and Messe, D. A. (1995). Mapping c-axis fabrics to study physical processes in ice. *Journal of Glaciology*, **41**(137), 197–203.
- Alley, R. B., Gow, A. J., Messe, D. A., Fitzpatrick, J. J., Waddington, E. D. and Bolzan, J. F. (1997). Grain-scale processes, folding, and stratigraphic disturbance in the GISP2 ice core. *Journal of Geophysical Research*, **102**(C12), 26, 819–826, 830.
- Anandakrishnan, S., Blankenship, D. D., Alley, R. B. and Stoffa, P. L. (1998). Influence of subglacial geology on the position of a West Antarctic ice stream from seismic observations. *Nature*, **394**, 62–65.
- Arendt, A. A., Echelmeyer, K. A., Harrison, W. D., Lingle, C. S. and Valentine, V. B. (2002). Rapid wastage of Alaska glaciers and their contribution to rising sea level. *Science*, **297**, 382–385.
- Ashley, G. M., Boothroyd, J. C. and Borns, H. W. Jr. (1991). Sedimentology of late Pleistocene (Laurentide) deglacial-phase deposits, eastern Maine; an example of a temperate marine grounded ice-sheet margin. *Geological Society of America Special Paper* 261, pp. 107–125.

- Atkinson, B. K. (1984). Subcritical crack growth in geological materials. *Journal of Geophysical Research*, **89**(B6), 4077–4144.
- Atkinson, B. K. and Rawlings, R. D. (1981). Acoustic emission during stress corrosion cracking in rocks. In Simpson, D. W. and Richards, P. G. (eds.) *Earthquake Prediction. An International Review* (Ewing Series, 4). Washington, D.C.: American Geophysical Union, pp. 605–619.
- Attig, J. W., Mickelson, D. M. and Clayton, L. (1989). Late Wisconsin landform distribution and glacier bed conditions in Wisconsin. *Sedimentary Geology*, **62**(3–4), 399–405.
- Baker, R. W. (1978). The influence of ice-crystal size on creep. *Journal of Glaciology*, **21**(85), 485–500.
- (1981). Textural and crystal-fabric anisotropies and the flow of ice masses. *Science*, **211**(4486), 1043–1044.
- (1982). A flow equation for anisotropic ice. *Cold Regions Science and Technology*, **6**(3), 141–148.
- Barnes, P., Tabor, D. and Walker, J. C. F. (1971). Friction and creep of polycrystalline ice. *Proceedings of the Royal Society, London*, **A324**(1557), 127–155.
- Bell, R. E., Blankenship, D. D., Finn, C. A., Morse, D. L., Scambos, T. A., Brozenal, J. M. and Hodge, S. M. (1998). Influence of subglacial geology on the onset of a West Antarctic ice stream from aerogeophysical observations. *Nature*, **394**, 58–62.
- Benoist, J.-P. (1979). The spectral power density and shadowing function of a glacial microrelief at the decimetre scale. *Journal of Glaciology*, **23**(89), 57–66.
- Benson, C. S. (1961). Stratigraphic studies in the snow and firn of the Greenland Ice Sheet. *Folia Geographica Danica*, **9**, 13–37.
- (1962). Stratigraphic studies in the snow and firn of the Greenland Ice Sheet. *U.S. Snow, Ice, and Permafrost Research Establishment Research Report 70*.
- Biegel, R. L., Sammis, C. G. and Dieterich, J. H. (1989). The frictional properties of simulated gouge having a fractal particle distribution. *Journal of Structural Geology*, **11**(7), 827–846.
- Bindschadler, R. A. and Scambos, T. A. (1991). Satellite-image-derived velocity field of an Antarctic ice stream. *Science*, **252**(5003), 242–246.
- Bindschadler, R. A. and Vornberger, P. (1998). Changes in the West Antarctic Ice Sheet since 1963 from declassified satellite photography. *Science*, **279**, 689–692.
- Bindschadler, R. A., King, M. A., Alley, R. B., Anandakrishnan, S. and Padman, L. (2003). Tidally controlled stick-slip discharge of a West Antarctic ice stream. *Science*, **301**, 1087–1089.
- Björnsson, H. (1992). Jökulhlaups in Iceland: prediction, characteristics, and simulation. *Annals of Glaciology*, **16**, 95–106.
- Blankenship, D. D., Bentley, C. R., Rooney, S. T. and Alley, R. B. (1986). Seismic measurements reveal a saturated, porous layer beneath an active Antarctic ice stream. *Nature*, **322**(6074), 54–57.
- Böðvarsson, G. (1955). On the flow of ice sheets and glaciers. *Jökull*, **5**, 1–8.
- Boulton, G. S. and Hindmarsh, R. C. A. (1987). Sediment deformation beneath glaciers: rheology and geological consequences. *Journal of Geophysical Research*, **92**(B9), 9059–9082.

- Broecker, W. S. (1994). Massive iceberg discharges as triggers for global climate change. *Nature*, **372**(6505), 421–424.
- Brown, C. S., Meier, M. F. and Post, A. (1982). Calving speed of Alaska tidewater glaciers, with application to Columbia Glacier. *U.S. Geological Survey Professional Paper* 1258-C, pp. C1–C13.
- Brown, N. L., Hallet, B. and Booth, D. B. (1987). Rapid soft-bed sliding of the Puget glacial lobe. *Journal of Geophysical Research*, **92**(B9), 8985–8997.
- Brugger, K. A. (1992). *A comparative study of the response of Rabots Glaciär and Storglaciären to recent climatic change*. Ph.D. thesis, University of Minnesota, 295 pages.
- Budd, W. F. (1969). The dynamics of ice masses. *Australian National Antarctic Expeditions Scientific Reports*, Series A (IV) Glaciology, Publication No. 108.
- Budd, W. F. and Jacka, T. H. (1989). A review of ice rheology for ice sheet modelling. *Cold Regions Science and Technology*, **16**(2), 107–144.
- Budd, W. F., Jensen, D. and Radok, U. (1971). Derived physical characteristics of the Antarctic Ice Sheet. *Australian National Antarctic Expeditions Interim Reports*, Series A (IV) Glaciology, Publication No. 120.
- Budd, W. F., Keage, P. L. and Bundy, N. A. (1979). Empirical studies of ice sliding. *Journal of Glaciology*, **23**(89), pp. 157–170.
- Butkovitch, T. R. (1954). The ultimate strength of ice. *Snow, Ice, and Permafrost Research Establishment Research Report* 11, 12 pages.
- Canals, M., Urgeles, R. and Calafat, A. M. (2000). Deep sea-floor evidence of past ice streams off the Antarctic Peninsula. *Geology*, **28**(1), 31–34.
- Carnahan, B., Luther, H. A. and Wilkes, J. O. (1969). *Applied Numerical Methods*. New York: John Wiley and Sons, Inc.
- Carslaw, H. S. and Jaeger, J. C. (1959). *Conduction of Heat in Solids*. Oxford Clarendon Press. 510 pages.
- Clark, C. D. and Stokes, C. R. (2001). Extent and basal characteristics of the Mc Clintock Channel Ice Stream. *Quaternary International*, **86**, 81–101.
- Clark, P. U. and Hansel, A. R. (1989). Clast ploughing, lodgement and glacier sliding over a soft glacier bed. *Boreas*, **18**(3), 201–207.
- Clark, P. U. and Walder, J. S. (1994). Subglacial drainage, eskers, and deforming beds beneath the Laurentide and Eurasian ice sheets. *Geological Society of America Bulletin*, **106**(2), 304–314.
- Clayton, L. and Cherry, J. A. (1967). Pleistocene superglacial and ice-walled lakes of west-central North America. In Clayton, L. and Freers, T. F. (eds.) *Glacial Geology of the Missouri Coteau and Adjacent Areas*. N. Dakota Geological Survey Miscellaneous Series 30, pp. 47–52.
- Clayton, L. and Freers, T. F. (1967). Roadlog. In Clayton, L. and Freers, T. F. (eds.) *Glacial Geology of the Missouri Coteau and Adjacent Areas*. N. Dakota Geological Survey Miscellaneous Series 30, pp. 1–24.
- Cohen, D. (1998). *Rheology of basal ice at Engabreen, Norway*. Ph.D. thesis, University of Minnesota, 166 pages.
- (2000). Rheology of ice at the bed of Engabreen, Norway. *Journal of Glaciology*, **46**(155), 611–621.

- Cook, E. R., D'Arrigo, R. D. and Briffa, K. R. (1998). A reconstruction of the North Atlantic Oscillation using tree-ring chronologies from North America and Europe. *The Holocene*, **8**, 9–17.
- Cullather, R. I., Bromwich, D. H. and Van Woert, M. L. (1996). Interannual variations in Antarctic precipitation related to El Niño-Southern Oscillation. *Journal of Geophysical Research*, **101**(D14), 19, 109–19, 118.
- Cutler, P. M., MacAyeal, D. R., Mickelson, D. M., Parizek, B. R. and Colgan, P. M. (2000). A numerical investigation of ice-lobe–permafrost interaction around the southern Laurentide ice sheet. *Journal of Glaciology*, **46**(153), 311–325.
- Cutler, P. M., Colgan, P. M. and Mickelson, D. M. (2002). Sedimentologic evidence for outburst floods from the Laurentide Ice Sheet margin in Wisconsin, USA: implications for tunnel-channel formation. *Quaternary International*, **90**, 23–40.
- Dahl-Jensen, D. and Gundestrup, N. S. (1987). Constitutive properties of ice at Dye 3, Greenland. *International Association of Hydrological Sciences Publication 170* (Symposium at Vancouver 1987 – *The physical basis for ice sheet modelling*), pp. 31–43.
- Dahl-Jensen, D. and Johnsen, S. J. (1986). Palaeotemperatures still exist in the Greenland ice sheet. *Nature*, **320**, 250–252.
- Dansgaard, W. and Oeschger, H. (1989). Past environmental long-term records from the Arctic. *The Environmental Record in Glaciers and Ice Sheets*. Oeschger, H. and Langway Jr., C. C. (eds.) New York: Wiley, pp. 287–318.
- Dansgaard, W., Johnsen, S. J., Clausen, H. B., Dahl-Jensen, D., Gundestrup, N. S., Hammer, C. U., Hvidberg, C. S., Steffensen, J. P., Sveinbjörnsdóttir, A. E., Jouzel, J. and Bond, G. (1993). Evidence for general instability of past climate from a 250-kyr ice-core record. *Nature*, **364**, 218–220.
- Deeley, R. M. and Parr, P. H. (1914). The Hintereis Glacier. *Philosophical Magazine*, **6**, 153–176.
- de La Chapelle, S., Duval, P. and Baudet, B. (1995). Compressive creep of polycrystalline ice containing a liquid phase. *Scripta Metallurgica et Materialia*, **33**(3), 447–450.
- Demorest, M. (1941). Glacier flow and its bearing on the classification of glaciers. *Geological Society of America Bulletin*, **52**(12), 2024–2025.
- (1942). Glacier regimens and ice movement within glaciers. *American Journal of Science*, **240**(1), 31–66.
- Drake, L. and Shreve, R. L. (1973). Pressure melting and regelation of ice by round wires. *Proceedings of the Royal Society, London*, **A332**(1588), 51–83.
- Duval, P. (1977). The role of water content on the creep rate of polycrystalline ice. In *Isotopes and impurities in snow and ice. Proceedings of the Grenoble Symposium*, Aug.–Sept. 1975, International Association of Scientific Hydrology Publication 118, pp. 29–33.
- Duval, P. (1978). Anelastic behavior of polycrystalline ice. *Journal of Glaciology*, **21**(85), 621–628.
- Duval, P. and Castelnau, O. (1995). Dynamic recrystallization of ice in polar ice sheets. *Journal de Physique IV*, Colloque C3, supplement to *Journal de Physique III*, **5**, C3-197–C3-205.

- Duval, P., Ashby, M. F. and Anderman, I. (1983). Rate-controlling processes in the creep of polycrystalline ice. *Journal of Physical Chemistry*, **87**(21), 4066–4074.
- Echelmeyer, K. and Wang, Z. (1987). Direct observation of basal sliding and deformation of basal drift at sub-freezing temperatures. *Journal of Glaciology*, **33**(113), 83–98.
- Elsberg, D. H., Harrison, W. D., Echelmeyer, K. A. and Krimmel, R. M. (2001). Quantifying the effects of climate and surface change on glacier mass balance. *Journal of Glaciology*, **47**(159), 649–658.
- Engelhardt, H. and Kamb, B. (1997). Basal hydraulic system of a West Antarctic ice stream: constraints from borehole observations. *Journal of Glaciology*, **43**(144), 207–230.
- (1998). Basal sliding of ice stream B, West Antarctica. *Journal of Glaciology*, **44**(147), 223–230.
- Engelhardt, H., Harrison, W. D. and Kamb, B. (1978). Basal sliding and conditions at the glacier bed as revealed by bore-hole photography. *Journal of Glaciology*, **20**(84), 469–508.
- Engelhardt, H., Humphrey, N., Kamb, B. and Fahnestock, M. (1990). Physical conditions at the base of a fast moving Antarctic ice stream. *Science*, **248**(4951), 57–59.
- Etchecopar, A. (1977). A plane kinematic model of progressive deformation in a polycrystalline aggregate. *Tectonophysics*, **39**, 121–139.
- Eyles, N., Salden, J. A. and Gilroy, S. (1982). A depositional model for stratigraphic complexes and facies superimposition in lodgement till. *Boreas*, **11**(4), 317–333.
- Fastook, J. L. and Chapman, J. E. (1989). A map-plane finite-element model: three modeling experiments. *Journal of Glaciology*, **35**(119), 48–52.
- Fastook, J. L. and Holmlund, P. (1994). A glaciological model of the Younger Dryas event in Scandinavia. *Journal of Glaciology*, **40**(134), 125–131.
- Fischer, U. H. and Clarke, G. K. C. (1994). Ploughing of subglacial sediment. *Journal of Glaciology*, **40**(134), 97–106.
- Fisher, D. A. (1987). Enhanced flow of Wisconsin ice related to solid conductivity through strain history and recrystallization. *International Association of Scientific Hydrology Publication* 170, pp. 45–51.
- Fisher, D. A. and Koerner, R. M. (1986). On the special rheological properties of ancient microparticle-laden Northern Hemisphere ice as derived from bore-hole and core measurements. *Journal of Glaciology*, **32**(112), 501–510.
- Fisher, D. A., Reeh, N. and Langley, K. (1985). Objective reconstructions of the late Wisconsinan Laurentide ice sheet and the significance of deformable beds. *Géographie Physique et Quaternaire*, **39**, 229–238.
- Fountain, A. G. (1989). The storage of water in, and hydraulic characteristics of, the firn of South Cascade Glacier, Washington State, U.S.A. *Annals of Glaciology*, **13**, 69–75.
- Fowler, A. C. (1987). Sliding with cavity formation. *Journal of Glaciology*, **33**(115), 255–267.

- Fowler, A. C. and Larson, D. A. (1978). On the flow of polythermal glaciers: II. Surface wave analysis. *Proceedings of the Royal Society, London, A370*, 155–171.
- Funk, M. and Röhlisberger, H. (1989). Forecasting the effects of a planned reservoir which will partially flood the tongue of Unteraargletscher in Switzerland. *Annals of Glaciology*, **13**, 76–81.
- Gilpin, R. R. (1979). A model of the “liquid-like” layer between ice and a substrate with applications to wire regelation and particle migration. *Journal of Colloid and Interface Science*, **68**(2), 235–251.
- Giovinetto, M. B. and Zwally, H. J. (2000). Spatial distribution of net surface accumulation on the Antarctic ice sheet. *Annals of Glaciology*, **31**, 171–178.
- Glasstone, S., Laidler, K. J. and Eyring, H. (1941). *The Theory of Rate Processes*. New York: McGraw-Hill.
- Glen, J. W. (1955). The creep of polycrystalline ice. *Proceedings of the Royal Society, London, A228* (1175), 519–538.
- (1958). The flow law of ice. A discussion of the assumptions made in glacier theory, their experimental foundations and consequences. *International Association of Scientific Hydrology*, **47**, 171–183.
- (1963). Contribution to the discussion. *International Association of Scientific Hydrology Bulletin*, **8**, 2, 68.
- Gogineni, S., Chuah, T., Allen, C., Jezek, K. and Moore, R. K. (1998). An improved coherent radar depth sounder. *Journal of Glaciology*, **44**(148), 659–669.
- Gold, L. W. (1958). Some observations on the dependence of strain on stress for ice. *Canadian Journal of Physics*, **36**(10), 1265–1275.
- Goldthwait, R. P. (1951). Development of end moraines in east-central Baffin Island. *Journal of Geology*, **59**(6), 567–577.
- Gow, A. J. and Williamson, T. (1976). Rheological implications of the internal structure and crystal fabrics of the West Antarctic ice sheet as revealed by deep core drilling at Byrd Station. *Geological Society of America Bulletin*, **87**, 1665–1677.
- Gravenor, C. P. (1955). The origin and significance of prairie mounds. *American Journal of Science*, **253**, 475–481.
- Gravenor, C. P. and Kupsch, W. O. (1959). Ice disintegration features in western Canada. *Journal of Geology*, **67**, 48–67.
- Griffith, A. A. (1924). Theory of rupture. *Proc. First International Congress Applied Mechanics*, Delft, 55–63.
- Grootes, P. M., Stuiver, M., White, J. W. C., Johnsen, S. and Jouzel, J. (1993). Comparison of oxygen isotope records from the GISP 2 and GRIP Greenland ice cores. *Nature*, **366**, 552–554.
- Grove, J. M. (1988). *The Little Ice Age*. London: Methuen.
- Haefeli, R. (1962). The ablation gradient and the retreat of a glacier tongue. In *Symposium of Obergurgl, International Association of Scientific Hydrology*, Publication 58, 49–59.
- Hallet, B. (1976a). Deposits formed by subglacial precipitation of CaCO₃. *Geological Society of America Bulletin*, **87**(7), 1003–1015.
- (1976b). The effect of subglacial chemical processes on sliding. *Journal of Glaciology*, **17**(76), 209–221.

- (1979a). A theoretical model of glacial abrasion. *Journal of Glaciology*, **23**(89), 39–50.
- (1979b). Subglacial regelation water film. *Journal of Glaciology*, **23**(89), 321–334.
- (1996). Glacial quarrying: a simple theoretical model. *Annals of Glaciology*, **22**, 1–8.
- Hallet, B. and Anderson, R. S. (1980). Detailed glacial geomorphology of a proglacial bedrock area at Castleguard Glacier, Alberta, Canada. *Zeitschrift für Gletscherkunde und Glazialgeologie*, **16**, 171–184.
- Hallet, B., Lorrain, R. D. and Souchez, R. A. (1978). The composition of basal ice from a glacier sliding over limestones. *Geological Society of America Bulletin*, **89**(2), 314–320.
- Hamilton, W. C. and Ibers, J. A. (1968). *Hydrogen Bonding in Solids; Methods of Molecular Structure Determination*. New York: W. A. Benjamin.
- Hanson, B. (1995). A fully three-dimensional finite-element model applied to velocities on Storglaciären, Sweden. *Journal of Glaciology*, **41**(137), 91–102.
- Hanson, B. and Hooke, R. LeB. (2000). A model study of the forces involved in glacier calving. *Journal of Glaciology*, **46**(153), 188–194.
- Hanson, B., Hooke, R. LeB. and Grace, E. M., Jr. (1998). Short-term velocity and water-pressure measurements down-glacier from a riegel, Storglaciären, Sweden. *Journal of Glaciology*, **44**(147), 359–367.
- Harper, J. T., Humphrey, N. F., Pfeffer, W. T., Huzurbazar, S. V., Bahr, D. B. and Welch, B. C. (2001). Spatial variability in the flow of a valley glacier: deformation of a large array of boreholes. *Journal of Geophysical Research*, **106**(B5), 8547–8562.
- Harrison, W. D. (1972). Temperature of a temperate glacier. *Journal of Glaciology*, **11**(61), 15–29.
- Harrison, W. D., Elsberg, D. H., Echelmeyer, K. A. and Krimmel, R. M. (2001). On the characterization of glacier response by a single time-scale. *Journal of Glaciology*, **47**(159), 659–664.
- Hättestrand, C. and Kleman, J. (1999). Ribbed moraine formation. *Quaternary Science Reviews*, **18**, 43–61.
- Hausmann, M. R. (1990). *Engineering Principles of Ground Modification*. New York: McGraw-Hill.
- Hays, J. D., Imbrie, J. and Shackleton, N. S. (1976). Variations in the Earth's orbit: Pacemaker of the ice ages. *Science*, **194**(4270), 1121–1132.
- Heinrich, H. (1988). Origin and consequences of ice rafting in the northeast Atlantic Ocean during the past 130,000 years. *Quaternary Research*, **29**, 141–152.
- Hobbs, P. V. (1974). *Ice Physics*. New York: Oxford Clarendon Press.
- Hock, R. and Hooke, R. LeB. (1993). Further tracer studies of internal drainage in the lower part of the ablation area of Storglaciären, Sweden. *Geological Society of America Bulletin*, **105**(4), 537–546.
- Hodge, S. M. (1974). Variations in sliding of a temperate glacier. *Journal of Glaciology*, **13**(69), 349–369.
- Hodge, S. M., Trabant, D. C., Krimmel, R. M., Heinrichs, T. A., March, R. S. and Joshberger, E. G. (1998). Climate variations and changes in mass balance of three glaciers in western North America. *Journal of Climate*, **11**, 2161–2179.

- Holmlund, P. (1987). Mass balance of Storglaciären during the 20th century. *Geografiska Annaler*, **69A**(3–4), 439–447.
- (1988). Internal geometry and evolution of moulins, Storglaciären, Sweden. *Journal of Glaciology*, **34**(117), 242–248.
- Hong, S., Candelone, J-P., Patterson, C. C. and Boutron, C. F. (1994). Greenland ice evidence of hemispheric lead pollution two millennia ago by Greek and Roman civilizations. *Science*, **265**, 1841–1843.
- Hooke, R. LeB. (1970). Morphology of the ice-sheet margin near Thule, Greenland. *Journal of Glaciology*, **9**(57), 303–324.
- (1973a). Flow near the margin of the Barnes Ice Cap and the development of ice-cored moraines. *Geological Society of America Bulletin*, **84**(12), 3929–3948.
- (1973b). Structure and flow in the margin of Barnes Ice Cap, Baffin Island, N. W. T., Canada. *Journal of Glaciology*, **12**(66), 423–438.
- (1976). Pleistocene ice at the base of the Barnes Ice Cap, Baffin Island, N. W. T., Canada. *Journal of Glaciology*, **17**(75), 49–60.
- (1977). Basal temperatures in polar ice sheets: a qualitative review. *Quaternary Research*, **7**(1), 1–13.
- (1981). Flow law for polycrystalline ice in glaciers: comparison of theoretical predictions, laboratory data, and field measurements. *Reviews of Geophysics and Space Physics*, **19**(4), 664–672.
- (1984). On the role of mechanical energy in maintaining subglacial conduits at atmospheric pressure. *Journal of Glaciology*, **30**(105), 180–187.
- (1989). Englacial and subglacial hydrology: a qualitative review. *Arctic and Alpine Research*, **21**(3), 221–233.
- (1991). Positive feedbacks associated with the erosion of glacial cirques and overdeepenings. *Geological Society of America Bulletin*, **103**(8), 1104–1108.
- Hooke, R. LeB. and Clausen, H. B. (1982). Wisconsin and Holocene $\delta^{18}\text{O}$ variations, Barnes Ice Cap, Canada. *Geological Society of America Bulletin*, **93**(8), 784–789.
- Hooke, R. LeB. and Elverhøi, A. (1996). Sediment flux from a fjord during glacial periods, Isfjorden, Spitsbergen. *Global and Planetary Change*, **12**, 237–249.
- Hooke, R. LeB. and Hanson, B. H. (1986). Borehole deformation experiments, Barnes Ice Cap, Canada. *Cold Regions Science and Technology*, **12**(3), 261–276.
- Hooke, R. LeB. and Hudleston, P. J. (1978). Origin of foliation in glaciers. *Journal of Glaciology*, **20**(83), 285–299.
- (1980). Ice fabrics in a vertical flowplane, Barnes Ice Cap, Canada. *Journal of Glaciology*, **25**(92), 195–214.
- (1981). Ice fabrics from a borehole at the top of the South Dome, Barnes Ice Cap, Baffin Island. *Geological Society of America Bulletin*, **92**(5), 274–281.
- Hooke, R. LeB. and Iverson, N. R. (1995). Grain size distribution in deforming subglacial tills: role of grain fracture. *Geology*, **23**(1), 57–60.
- Hooke, R. LeB. and Pohjola, A. (1994). Hydrology of a segment of a glacier situated in an overdeepening, Storglaciären, Sweden. *Journal of Glaciology*, **40**(134), 140–148.

- Hooke, R. LeB., Dahlin, B. B. and Kauper, M. T. (1972). Creep of ice containing dispersed fine sand. *Journal of Glaciology*, **11**(63), 327–336.
- Hooke, R. LeB., Alexander, E. C. Jr. and Gustafson, R. J. (1980). Temperature profiles in Barnes Ice Cap, Baffin Island, Canada, and heat flux from the subglacial terrane. *Canadian Journal of Earth Sciences*, **17**(9), 1174–1188.
- Hooke, R. LeB., Gould, J. E. and Brzozowski, J. (1983). Near-surface temperatures near and below the equilibrium line on polar and subpolar glaciers. *Zeitschrift für Gletscherkunde und Glazialgeologie*, **19**(1), 1–25.
- Hooke, R. LeB., Johnson, G. W., Brugger, K. A., Hanson, B. and Holdsworth, G. (1987). Changes in mass balance, velocity, and surface profile along a flow line on Barnes Ice Cap, 1970–1984. *Canadian Journal of Earth Sciences*, **24**(8), 1550–1561.
- Hooke, R. LeB., Calla, P., Holmlund, P., Nilsson, M. and Stroeven, A. (1989). A three-year record of seasonal variations in surface velocity, Storglaciären, Sweden. *Journal of Glaciology*, **35**(120), 235–247.
- Hooke, R. LeB., Laumann, T. and Kohler, J. (1990). Subglacial water pressures and the shape of subglacial conduits. *Journal of Glaciology*, **36**(122), 67–71.
- Hooke, R. LeB., Pohjola, V., Jansson, P. and Kohler, J. (1992). Intra-seasonal changes in deformation profiles revealed by borehole studies, Storglaciären, Sweden. *Journal of Glaciology*, **38**(130), 348–358.
- Hooke, R. LeB., Hanson, B., Iverson, N. R., Jansson, P. and Fischer, U. H. (1997). Rheology of till beneath Storglaciären, Sweden. *Journal of Glaciology*, **43**(143), 172–179.
- Hooyer, T. S. and Iverson, N. R. (2002). Flow mechanism of the Des Moines Lobe of the Laurentide ice sheet. *Journal of Glaciology*, **48**(163), 575–586.
- Houghton, J. T., et al. (2001). *Climate Change 2001: The Scientific Basis*. Report of the Intergovernmental Panel on Climate Change (IPCC), Cambridge University Press, 881 pages.
- Howell, D., Behringer, R. P. and Veje, C. (1999). Stress fluctuations in a 2D granular Couette experiment: a continuous transition. *Physical Review Letters*, **82**(96), 5241–5244.
- Huang, M., Ohtomo, M. and Wakahama, G. (1985). Transition in preferred orientation of polycrystalline ice from repeated recrystallization. *Annals of Glaciology*, **6**, 263–264.
- Hudleston, P. J. (1976). Recumbent folding in the base of the Barnes Ice Cap, Baffin Island, Northwest Territories, Canada. *Geological Society of America Bulletin*, **87**(12), 1678–1683.
- Hudleston, P. J. and Hooke, R. LeB. (1980). Cumulative deformation in the Barnes Ice Cap and implications for the development of foliation. *Tectonophysics*, **66**, 127–146.
- Hughes, T. (1987). Ice dynamics and deglaciation models when ice sheets collapsed, In Ruddiman, W. F. and Wright, H. E., Jr. (eds.) North American and adjacent oceans during the last deglaciation. *The Geology of North America* K-3. Boulder Colorado: Geological Society of America.
- (1992). Abrupt climate change related to unstable ice-sheet dynamics: toward a new paradigm. *Palaeogeography, Palaeoclimatology, Palaeoecology*, **97**, 203–234.

- Hulbe, C., Joughin, I., Morse, D. and Bindschadler, R. A. (2000). Tributaries to West Antarctic ice streams: characteristics deduced from numerical modelling of ice flow. *Annals of Glaciology*, **31**, 184–190.
- Hull, D. (1969). *Introduction to Dislocations*. New York: Pergamon Press.
- Humphrey, N. F. and Raymond, C. F. (1994). Hydrology, erosion and sediment production in a surging glacier: Variegated Glacier, Alaska, 1982–83. *Journal of Glaciology*, **40**(136), 539–552.
- Humphrey, N. F., Kamb, B., Fahnestock, M. and Engelhardt, H. (1993). Characteristics of the bed of the lower Columbia Glacier, Alaska: *Journal of Geophysical Research*, **98**(B1), 837–846.
- Hutter, K. (1981). The effect of longitudinal strain on the shear stress of an ice sheet. In defense of using stretched coordinates. *Journal of Glaciology*, **27**(95), 39–56.
- (1983). *Theoretical Glaciology*. Tokyo, Japan: D. Reidel Publishing, 510 pages.
- Huybrechts, Ph. (1990). A 3-D model for the Antarctic ice sheet: a sensitivity study on the glacial-interglacial contrast. *Climate Dynamics*, **5**, 79–92.
- (2002). Sea-level changes at the LGM from ice-dynamic reconstructions of the Greenland and Antarctic ice sheets during the glacial cycles. *Quaternary Science Reviews*, **21**(1–3), 203–231.
- Huybrechts, Ph. and T'Siobbel, S. (1995). Thermomechanical modeling of northern hemisphere ice sheets with a two-level mass balance parameterization. *Annals of Glaciology*, **21**, 111–117.
- Huybrechts, Ph., Payne, T. and The EISMINT Intercomparison Group. (1996). The EISMINT benchmarks for testing ice-sheet models. *Annals of Glaciology*, **23**, 1–12.
- Huybrechts, Ph., Steinhage, D., Wilhelms, F. and Bamber, J. (2000). Balance velocities and measured properties of the Antarctic ice sheet from a new compilation of gridded data for modelling. *Annals of Glaciology*, **30**, 52–60.
- Iken, A. (1981). The effect of subglacial water pressure on the sliding velocity of a glacier in an idealized numerical model. *Journal of Glaciology*, **27**(97), 407–421.
- Iken, A. and Bindschadler, R. A. (1986). Combined measurements of subglacial water pressure and surface velocity of Findelen-gletscher, Switzerland: conclusions about the drainage system and sliding mechanism. *Journal of Glaciology*, **32**(110), 101–119.
- Iken, A. and Truffer, M. (1997). The relationship between subglacial water pressure and velocity of Findelengletscher during its advance and retreat. *Journal of Glaciology*, **43**(144), 328–338.
- Irons, B. M. and Shrive, N. G. (1987). *Numerical Methods in Engineering and Applied Science: Numbers are Fun*. New York: John Wiley & Sons, 248 pages.
- Iverson, N. (1989). Theoretical and experimental analyses of glacial abrasion and quarrying. Ph.D. thesis, University of Minnesota, Minneapolis, 233 pages.
- (1991). Potential effects of subglacial water-pressure fluctuations on quarrying. *Journal of Glaciology*, **37**(125), 27–36.
- (1993). Regelation of ice through debris at glacier beds: Implications for sediment transport. *Geology*, **21**(6), 559–562.

- Iverson, N. and Iverson, R. M. (2001). Distributed shear of subglacial till due to Coulomb slip. *Journal of Glaciology*, **47**(158), 481–488.
- Iverson, N., Hanson, B., Hooke, R. LeB. and Jansson, P. (1995). Flow mechanics of glaciers on soft beds. *Science*, **267**(5194), 80–81.
- Iverson, N., Hooyer, T. S. and Hooke, R. LeB. (1996). A laboratory study of sediment deformation: stress heterogeneity and grain-size evolution. *Annals of Glaciology*, **22**, 167–175.
- Iverson, N., Hooyer, T. S. and Baker, R. W. (1998). Ring-shear studies of till deformation: Coulomb-plastic behavior and distributed strain in glacier beds. *Journal of Glaciology*, **44**(148), 634–642.
- Iverson, N., Cohen, D., Hooyer, T. S., Fischer, U. H., Jackson, M., Moore, P. L., Lappegård, G. and Kohler, J. (2003). Effects of basal debris on glacier flow. *Science*, **301**, 81–84.
- Jacka, T. H. (1984). Laboratory studies on the relationship between ice crystal size and flow rate. *Cold Regions Science and Technology*, **10**(1), 31–42.
- Jacka, T. H. and Maccagnan, M. (1984). Ice crystallographic and strain rate changes with strain in compression and extension. *Cold Regions Science and Technology*, **8**(3), 269–286.
- Jacobel, R. W., Scambos, T. A., Raymond, C. F. and Gades, A. M. (1996). Changes in the configuration of ice stream flow from the West Antarctic Ice Sheet. *Journal of Geophysical Research*, **101**(B3), 5499–5504.
- Jansson, E. P. (1995). Water pressure and basal sliding on Storglaciären, northern Sweden. *Journal of Glaciology*, **41**(138), 232–240.
- Jezek, K. C., Alley, R. B. and Thomas, R. H. (1985). Rheology of glacier ice. *Science*, **227**(4692), 1335–1337.
- Jóhannesson, T., Raymond, C. F. and Waddington, E. (1989). Time-scale for adjustment of glaciers to changes in mass balance. *Journal of Glaciology*, **35**(121), 355–369.
- Johnsen, S. J., Dansgaard, W., Clausen, H. B. and Langway, C. C., Jr. (1972). Oxygen isotope profiles through the Antarctic and Greenland ice sheets. *Nature*, **235**(5339), 429–434.
- Johnson, A. (1960). Variation in surface elevation of the Nisqually glacier Mt. Rainier, Washington. *International Association of Scientific Hydrology Bulletin*, **19**, 54–60.
- Johnson, M. D. (1999). Spooner Hills, northwest Wisconsin: High-relief hills carved by subglacial meltwater of the Superior Lobe. In Mickelson, D. M. and Attig, J. W. (eds.) *Glacial Processes Past and Present*. Boulder, Colorado, *Geological Society of America Special Paper* 337, 83–92.
- Johnson, W. and Mellor, P. B. (1962). *Plasticity for Mechanical Engineers*. London, Princeton: Van Nostrand, Ltd., 412 pages. (There is also a 1973 edition, in which the relevant pages are 44–49.)
- Jones, S. J. and Chew, H. A. M. (1983). Effect of sample and grain size on the compressive strength of ice. *Annals of Glaciology*, **4**, 129–132.
- Joughin, I., Gray, L., Bindschadler, R., Price, S., Morse, D., Hulbe, C., Mattar, K. and Werner, C. (1999). Tributaries of West Antarctic ice streams revealed by RADARSAT interferometry. *Science*, **286**, 283–286.

- Kamb, B. (1965). Structure of Ice VI. *Science*, **150**(3693), 205–209.
- (1970). Sliding motion of glaciers: theory and observation. *Reviews of Geophysics and Space Physics*, **8**(4), 673–728.
- (1972). Experimental recrystallization of ice under stress. In Heard, H. C., Borg, I. Y., Carter, N. L. and Raleigh, C. B. (eds.) *Flow and Fracture of Rocks*. American Geophysical Union Geophysical Monograph 16, 211–241.
- (1987). Glacier surge mechanism based on linked cavity configuration of the basal water conduit system. *Journal of Geophysical Research*, **92**(B9), 9083–9100.
- (1991). Rheological nonlinearity and flow instability in the deforming bed mechanism of ice stream motion. *Journal of Geophysical Research*, **96**(B10), 16, 585–16, 595.
- (2001). Basal zone of the West Antarctic ice streams and its role in lubrication of their rapid motion. In Alley, R. B. and Bindschadler, R. A. (eds.) *The West Antarctic ice sheet: behavior and environment*. *Antarctic Research Series*, **77**, 157–201.
- Kamb, B. and LaChapelle, E. (1964). Direct observation of the mechanism of glacier sliding over bedrock. *Journal of Glaciology*, **5**(38), 159–172.
- Kamb, B., Raymond, C. F., Harrison, W. D., Engelhardt, H., Echelmeyer, K. A., Humphrey, N., Brugman, M. M. and Pfeffer, T. (1985). Glacier surge mechanism: 1982–1983 surge of Variegated Glacier, Alaska. *Science*, **227**(4686), 469–479.
- Kanninen, M. F. and Popelar, C. H. (1985). *Advanced Fracture Mechanics*. New York: Oxford University Press. 563 pages.
- Kaspari, S., Mayewski, P. A., Dixon, D. A., Spikes, V. B., Snead, S. B., Handley, M. J. and Hamilton, G. S. (2004). Climate variability in West Antarctica derived from annual accumulation rate records from ITASE firn/ice cores. *Annals of Glaciology* (in press).
- Kell, G. S. (1967). Precise representation of volume properties of water at one atmosphere, *Journal of Chemical and Engineering Data*, **12**, 66–69.
- Kendall, K. (1978). The impossibility of comminuting small particles by compression. *Nature*, **272**, 710–711.
- Kenneally, J. (2003). *Crevassing and calving of glacial ice*. Ph.D. thesis, University of Maine, Orono. 145 pages.
- Ketcham, W. M. and Hobbs, P. V. (1969). An experimental determination of the surface energies of ice. *Philosophical Magazine*, 8th Series, **19**(162), 1161–1173.
- Kinosita, S. (1962). Transformation of snow into ice by plastic compression. *Low Temperature Science*, **A20**, 131–157.
- Kleman, J. and Borgström, I. (1994). Glacial landforms indicative of a partly frozen bed. *Journal of Glaciology*, **40**(135), 255–264.
- Kleman, J. and Häättestrand, C. (1999). Frozen-bed Fennoscandian and Laurentide ice sheets during the Last Glacial Maximum. *Nature*, **402**, 63–66.
- Krabill, W., Abdalati, W., Frederick, E., Manizade, S., Martin, C., Sonntag, J., Swift, R., Thomas, R., Wright, W. and Yungel, J. (2000). Greenland ice sheet: high-elevation balance and peripheral thinning. *Science* **289**, 428–430.

- Kuhn, M. (1981). Climate and glaciers. *International Association of Scientific Hydrology*, Publication 131, 3–20.
- (1989). The response of the equilibrium line altitude to climate fluctuations: Theory and observations. In Oerlemans, J. (ed.), *Glacier Fluctuations and Climatic Change*. Dordrecht: Kluwer Academic Publishers, pp. 407–417.
- Lambe, T. W. and Whitman, R. V. (1969). *Soil Mechanics*. New York: John Wiley, 553 pages.
- Lawn, B. (1993). *Fracture of Brittle Solids* 2nd edition. Cambridge: Cambridge University Press, 378 pages.
- Lawson, D. E., Strasser, J. C., Evenson, E. B., Alley, R. B., Larson, G. J. and Arcene, S. A. (1998). Glaciohydraulic supercooling: a freeze-on mechanism to create stratified, debris-rich basal ice: I. Field evidence. *Journal of Glaciology*, **44**(148), 547–562.
- Leonard, K. C. and Fountain, A. G. (2003). Map-based methods for estimating glacier equilibrium line altitudes. *Journal of Glaciology*, **49**(166), 329–336.
- Leonard, K. C., Bell, R. E. and Studinger, M. (2003). (Abstract.) The influence of subglacial topography on accumulation rates at Lake Vostok. *American Geophysical Union Annual Meeting*, December 7–12, 2003.
- Li, J., Jacka, T. H. and Budd, W. F. (1996). Deformation rates in combined compression and shear for ice which is initially isotropic and after the development of strong anisotropy. *Annals of Glaciology*, **23**, 247–252.
- Lighthill, M. J. and Whitham, G. B. (1955). On kinematic waves, I. Flood movement in long rivers. *Proceedings of the Royal Society, London*, **A229**(1178), 281–316.
- Liu, C.-H., Nagel, S. R., Schecter, D. A., Coppersmith, S. N., Majumdar, S., Narayan, O. and Witten, T. A. (1995). Force fluctuations in bead packs. *Science*, **269**(5223), 513–515.
- Liu, H., Jezek, K. C. and Li, B. (1999). Development of an Antarctic DEM database by integrating cartographic and remotely sensed data: a GIS approach. *Journal of Geophysical Research*, **104**(B10), 23 199–23 213.
- Lliboutry, L. (1964). *Traité de Glaciologie*, Vol. 1. Paris: Masson and Co.
- (1968). General theory of subglacial cavitation and sliding of temperate glaciers. *Journal of Glaciology*, **7**(49), 21–58.
- (1970). Ice flow law from ice sheet dynamics. Proceedings of the International Symposium on Antarctic Glaciological Exploration, Hanover, NH, 3–7 September, 1968; *International Association of Scientific Hydrology*, Publication 86, 216–228.
- (1971). Permeability, brine content, and temperature of temperate ice. *Journal of Glaciology*, **10**(58), 15–30.
- (1975). Loi de glissement d'un glacier sans cavitation. *Annals of Geophysics*, **31**(2), 207–226.
- (1976). Physical processes in temperate glaciers. *Journal of Glaciology*, **16**(74), 151–158.
- (1983). Modifications to the theory of intraglacial waterways for the case of subglacial ones. *Journal of Glaciology*, **29**(102), 216–226.

- Loewe, F. (1970). Screen temperatures and 10 m temperatures. *Journal of Glaciology*, **9**(56), 263–268.
- MacAyeal, D. R. (1989). Large scale ice flow over a viscous basal sediment: Theory and application to Ice Stream B, Antarctica. *Journal of Geophysical Research*, **94**(B4), 4071–4087.
- (1993a). A low-order model of the Heinrich event cycle. *Paleoceanography*, **8**(6), 767–773.
- (1993b). Binge/purge oscillations of the Laurentide Ice Sheet as a cause of the North Atlantic's Heinrich events. *Paleoceanography*, **8**(6), 775–784.
- Mandl, G., de Jong, L. N. J. and Maltha, A. 1977. Shear zones in granular material – an experimental study of their structure and mechanical genesis. *Rock Mechanics*, **9**(2–3), 95–144.
- Mantua, N. J. and Hare, S. R. (2002). The Pacific decadal oscillation. *Journal of Oceanography*, **58**, 35–44.
- Marshall, S. J., Tarasov, L., Clarke, G. K. C. and Peltier, W. R. (2000). Glaciological reconstruction of the Laurentide Ice Sheet: physical processes and modeling challenges. *Canadian Journal of Earth Sciences*, **37**, 769–793.
- Martinerie, P., Raynaud, D., Etheridge, D. M., Barnola, J. M. and Mazaudier, D. (1992). Physical and climatic parameters which influence the air content in polar ice. *Earth and Planetary Science Letters*, **112**(1/4), 1–13.
- Matsuda, M. and Wakahama, G. (1978). Crystallographic structure of polycrystalline ice. *Journal of Glaciology*, **21**(85), 607–620.
- Matthews, J. B. (1981). The seasonal circulation of Glacier Bay, Alaska fjord system. *Estuarine, Coastal, and Shelf Science*, **12**, 679–700.
- Matthews, W. H. (1974). Surface profiles of the Laurentide ice sheet in its marginal areas. *Journal of Glaciology*, **13**(67), 37–43.
- Maxwell, K. D. (2002). Pacific decadal oscillation and Arizona precipitation (available on-line from <http://www.wrhr.noaa.gov/wrhq/02TAs/0208/>).
- Meier, M. F. (1961). Mass budget of South Cascade Glacier. 1957–1960. U.S. Geological Survey Professional Paper 424-B, pp. 206–211.
- (1962). Proposed definitions for glacier mass balance terms. *Journal of Glaciology*, **4**(33), 252–263.
- (1965). Glaciers and climate. In Wright Jr., H. E. and Frey, D. G. (eds.). *The Quaternary of the United States*. Princeton: Princeton University Press, pp. 795–805.
- Meier, M. F., Rasmussen, L. A., Krimmel, R. M., Olsen, R. W. and Frank, D. (1985). Photogrammetric determination of surface altitude, terminus position, and ice velocity of Columbia Glacier, Alaska. U.S. Geological Survey Professional Paper 1258-F, pp. F1–F40.
- Meier, M. F., Lundstrom, S., Stone, D., Kamb, B., Engelhardt, H., Humphrey, N., Dunlap, W. W., Fahnestock, M., Krimmel, R. M. and Rasmussen, L. A. (1994). Mechanical and hydrologic basis for the rapid motion of a large tidewater glacier: 1. Observations. *Journal of Geophysical Research*, **99**(B8), 15, 219–215, 229.
- Mellor, M. and Testa, R. (1969). Effect of temperature on the creep of ice. *Journal of Glaciology*, **8**(52), 131–145.

- Menzies, J. and Shilts, W. W. (1996). Subglacial environments. In Menzies, J. (ed.) *Past Glacial Environments – Sediments, Forms, and Techniques. Glacial Environments*, Vol. 2. Oxford: Butterworth-Heinemann, pp. 15–136.
- Mickelson, D. M. (1987). Central Lowlands. In Graf, W. L., (ed.) *Geomorphic Systems of North America*. Boulder, CO: Geological Society of America, Centennial Special Volume 2, pp. 111–118.
- Mitchell, J. K. (1993). *Fundamentals of Soil Behavior* (2nd edition). New York: John Wiley.
- Mitchell, J. K., Campanella, R. G. and Singh, A. (1968). Soil creep as a rate process. *Journal of the Soil Mechanics and Foundations Division, American Society of Civil Engineers*, **94**(SM1), 231–253.
- Montagnat, M. and Duval, P. (2000). Rate controlling processes in the creep of polar ice, influence of grain boundary migration associated with recrystallization. *Earth and Planetary Science Letters*, **183**, 179–186.
- Mooers, H. D. (1989). On the formation of tunnel valleys of the Superior Lobe, Central Minnesota. *Quaternary Research*, **32**, 24–35.
- (1990a). A glacial-process model: the role of spatial and temporal variations in glacier thermal regime. *Geological Society of America Bulletin*, **102**(2), 243–251.
- (1990b). Ice marginal thrusting of drift and bedrock: thermal regime subglacial aquifers, and glacial surges. *Canadian Journal of Earth Sciences*, **27**(6), 849–862.
- Moran, S. R., Clayton, L., Hooke, R. LeB., Fenton, M. M. and Andriashuk, L. D. (1980). Glacier bed landforms of the prairie region of North America. *Journal of Glaciology*, **25**(93), 457–476.
- Morse, D. L., Waddington, E. D. and Steig, E. J. (1998). Ice age storm trajectories from radar stratigraphy at Taylor Dome, Antarctica. *Geophysical Research Letters*, **25**(17), 3383–3386.
- Müller, F. (1962). Zonation in the accumulation area of the glaciers of Axel Heiberg Island, N. W. T., Canada. *Journal of Glaciology*, **4**(33), 302–318.
- Murozumi, M., Chow, T. J. and Patterson, C. (1969). Chemical concentrations of pollutant lead aerosols, terrestrial dusts and sea salts in Greenland and Antarctic snow strata. *Geochimica et Cosmochimica Acta*, **33**, 1247–1294.
- Nadai, A. (1950). *Theory of Flow and Fracture of Solids*, Volume 1, 2nd edition. New York: McGraw Hill, 572 pages.
- Nakase, A. and Kamei, T. (1986). Influence of strain rate on undrained shear strength characteristics of K_0 -consolidated cohesive soils. *Soils and Foundations*, **26**, 85–95.
- Nereson, N. A., Raymond, C. F., Waddington, E. D. and Jacobel, R. W. (1998). Migration of the Siple Dome ice divide, West Antarctica. *Journal of Glaciology*, **44**(148), 643–652.
- Ng, F. S. L. (1999). A mathematical model of wide subglacial water drainage channels. In Wetzlaufer, J. S., Dash, J. G. and Untersteiner, N. (eds.) *Ice Physics and the Natural Environment*. NATO ASI Series I: Global Environmental Change 56. Berlin: Springer-Verlag, 325–327.

- (2000a). Canals under sediment-based ice sheets. *Annals of Glaciology*, **30**, 146–152.
- (2000b). Coupled ice–till deformation near subglacial channels and cavities. *Journal of Glaciology*, **46**(155), 580–598.
- Ng, F. S. L. and Hallet, B. (2002). Patterning mechanisms in subglacial carbonate dissolution and deposition. *Journal of Glaciology*, **48**(162), 386–400.
- NOAA (2003). <http://www.cpc.ncep.noaa.gov/products/winter.outlook/naoschem.both.gif>
- Nye, J. F. (1951). The flow of glaciers and ice sheets as a problem in plasticity. *Proceedings of the Royal Society, London*, **A207**(1091), 554–572.
- (1952a). Reply to Mr. Joel E. Fisher's comments. *Journal of Glaciology*, **2**(11), 52–53.
- (1952b). Mechanics of glacier flow. *Journal of Glaciology*, **2**(12), 82–93.
- (1953). The flow law of ice from measurements in glacier tunnels, laboratory experiments, and the Jungfraufirn borehole experiment. *Proceedings of the Royal Society, London*, **A219**(1139), 477–489.
- (1957). The distribution of stress and velocity in glaciers and ice sheets. *Proceedings of the Royal Society, London*, **A239**(1216), 113–133.
- (1960). The response of glaciers and ice sheets to seasonal and climatic changes. *Proceedings of the Royal Society, London*, **A256**(1287), 559–584.
- (1963a). On the theory of the advance and retreat of glaciers. *Geophysical Journal of the Royal Astronomical Society*, **7**(4), 432–456.
- (1963b). The response of glaciers to changes in the rate of nourishment and wastage. *Proceedings of the Royal Society, London*, **A257**(1360), 87–112.
- (1965a). The flow of a glacier in a channel of rectangular, elliptic, or parabolic cross section. *Journal of Glaciology*, **5**(41), 661–690.
- (1965b). A numerical method for inferring the budget history of a glacier from its advance and retreat. *Journal of Glaciology*, **5**(41), 589–607.
- (1969). The calculation of sliding of ice over a wavy surface using a Newtonian viscous approximation. *Proceedings of the Royal Society, London*, **A311**(1506), 445–467.
- (1973a). The motion of ice past obstacles. In Whalley, E., Jones, S. J. and Gold, L. W. (eds.), *The Physics and Chemistry of Ice*. Ottawa: Royal Society of Canada, pp. 387–394.
- (1973b). Water at the bed of a glacier. IUGG-AIHS Symposium on the Hydrology of Glaciers, Cambridge, September 7–13, 1969. *International Association of Scientific Hydrology*, Publication 95, pp. 189–194.
- Nye, J. F. and Frank, F. C. (1973). Hydrology of intergranular veins in a temperate glacier. IUGG-AIHS Symposium on the Hydrology of Glaciers, Cambridge, September 7–13, 1969. *International Association of Scientific Hydrology*, Publication 95, pp. 157–161.
- Nye, J. F. and Mae, S. (1972). The effect of non-hydrostatic stress on intergranular water veins and lenses in ice. *Journal of Glaciology*, **11**(61), 81–101.
- Parker, G. (1979). Hydraulic geometry of active gravel rivers. *Journal of the Hydraulics Division, American Society of Civil Engineers*, **105**(HY9), 1185–1201.

- Paterson, W. S. B. (1971). Temperature measurements in Athabasca Glacier, Alberta, Canada. *Journal of Glaciology*, **10**(60), 339–349.
- (1977). Secondary and tertiary creep of glacier ice as measured by borehole closure rates. *Reviews of Geophysics and Space Physics*, **15**(1), 47–55.
- (1991). Why ice-age ice is sometimes “soft”. *Cold Regions Science and Technology*, **20**, 75–98.
- (1994). *Physics of Glaciers* (3rd edition). New York: Pergamon Press.
- Paterson, W. S. B. *et al.* (1977). An oxygen-isotope climate record from Devon Island ice cap, arctic Canada, *Nature*, **266**, 508–511.
- Patterson, C. J. (1997). Southern Laurentide ice lobes were created by ice streams: Des Moines lobe in Minnesota, USA. *Sedimentary Geology*, **111**, 247–261.
- (2002). Toward a unified explanation for subglacial tunnel formation. *Geological Society of America Abstracts with Programs*, **36**(6), 59–3.
- Patterson, C. J. and Hooke, R. LeB. (1995). Physical environment of drumlin formation. *Journal of Glaciology*, **41**(137), 30–38.
- Payne, A. J., Huybrechts, P., Abe-Ouchi, A., Calov, R., Fastook, J. L., Greve, R., Marshall, S. J., Marsiat, I., Ritz, C., Tarasov, L. and Thomassen, M. P. A. (2000). Results from the EISMINT model intercomparison: the effects of thermomechanical coupling. *Journal of Glaciology*, **46**(153), 227–238.
- Philberth, K. and Federer, B. (1971). On the temperature profile and age profile in the central part of cold ice sheets. *Journal of Glaciology*, **10**(58), 3–14.
- Pimienta, P. and Duval, P. (1987). Rate controlling processes in the creep of polar glacier ice. *Journal de Physique*, **48**. Colloque C1, Supplement to no. 3, pp. C1-243–C1-248.
- Ramsay, J. G. and Graham, R. H. (1970). Strain variation in shear belts. *Canadian Journal of Earth Sciences*, **7**, 786–813.
- Rasmussen, E. M. (1984). El Niño: The ocean/atmosphere connection. *Oceanus*, **27**(2), 5–12.
- Rasmussen, L. A. and Meier, M. F. (1982). Continuity equation model of the predicted drastic retreat of Columbia Glacier, Alaska. *U.S. Geological Survey Professional Paper 1258-F*, pp. A1–A23.
- Ratcliffe, E. H. (1962). Thermal conductivity of ice: new data on the temperature coefficient. *Philosophical Magazine*, 8th Series, **7**, 1197–1203.
- Raymond, C. F. (1971). Flow in a transverse section of Athabasca Glacier, Alberta, Canada. *Journal of Glaciology*, **10**(58), 55–84.
- (1973). Inversion of flow measurements for stress and rheological parameters in a valley glacier. *Journal of Glaciology*, **12**(64), 19–44.
- (1983). Deformation in the vicinity of ice divides. *Journal of Glaciology*, **29**(103), 357–373.
- (2000). Energy balance of ice streams. *Journal of Glaciology*, **46**(155), 665–674.
- Raymond, C. F. and Harrison, W. D. (1975). Some observations on the behavior of liquid and gas phases in temperate glacier ice. *Journal of Glaciology*, **14**(71), 213–234.
- (1988). Evolution of Variegated Glacier, U.S.A., prior to its surge. *Journal of Glaciology*, **34**(117), 154–165.

- Raymond, C. F., Echelmeyer, K. A., Whillans, I. M., and Doake, C. S. M. (2001). Ice stream shear margins. In *The West Antarctic Ice Sheet: Behavior and Environment. Antarctic Research Series*, **77**, 137–155.
- Raynaud, D. and Whillans, I. M. (1982). Air content of the Byrd core and past changes in the West Antarctic Ice Sheet. *Annals of Glaciology*, **3**, 269–273.
- Raynaud, D., Jouzel, J., Barnola, J.-M., Chappellaz, J., Delmas, R. J. and Lorius, C. (1993). The ice core record of greenhouse gases. *Science*, **259**(5097), 926–934.
- Reeh, N. (1968). On the calving of ice from floating glaciers and ice shelves. *Journal of Glaciology*, **7**(50), 215–232.
- Retzlaff, R. and Bentley, C. R. (1993). Timing of stagnation of Ice Streams A, West Antarctica, from short-pulse radar studies of buried surface crevasses. *Journal of Glaciology*, **39**(133), 553–561.
- Retzlaff, R., Lord, N. and Bentley, C. R. (1993). Airborne-radar studies: Ice streams A, B and C, West Antarctica. *Journal of Glaciology*, **39**(133), 495–506.
- Rigsby, G. P. (1958). Effect of hydrostatic pressure on velocity of shear deformation of single ice crystals. *Journal of Glaciology*, **3**(24), 273–278.
- Rist, M. A., Sammonds, P. R., Murrell, S. A. F., Meredith, P. G., Doake, C. S. M., Oerter, H. and Matsuki, K. (1999). Experimental and theoretical fracture mechanics applied to Antarctic ice and surface crevassing. *Journal of Geophysical Research*, **104**(B2), 2973–2987.
- Robin, G. deQ. (1955). Ice movement and temperature distribution in glaciers and ice sheets. *Journal of Glaciology*, **2**(18), 523–532.
- (1970). Stability of ice sheets as deduced from deep temperature gradients. International Symposium on Antarctic Glaciological Exploration (ISAGE), Hanover, NH, September 3–7, 1968. *International Association of Scientific Hydrology*, Publication 86, pp. 141–151.
- (1976). Is the basal ice of a temperate glacier at the pressure melting point? *Journal of Glaciology*, **16**(74), 183–195.
- Röhlisberger, H. (1972). Water pressure in intra- and subglacial channels. *Journal of Glaciology*, **11**(62), 177–204.
- and Iken, A. (1981). Plucking as an effect of water-pressure variations at the glacier bed. *Annals of Glaciology*, **2**, 57–62.
- Russell-Head, D. S. and Budd, W. F. (1979). Ice-sheet flow properties derived from bore-hole shear measurements combined with ice-core studies. *Journal of Glaciology*, **24**(90), 117–130.
- Sammis, C. G., King, G. and Biegel, R. (1987). The kinematics of gouge deformation. *Pure and Applied Geophysics*, **125**(5), 777–812.
- Scambos, T. A., Hulbe, C., Fahnestock, M. and Bohlander, J. (2000). The link between climate warming and break-up of ice shelves in the Antarctic Peninsula. *Journal of Glaciology*, **46**(154), 516–530.
- Schytt, V. (1968). Notes on glaciological activities in Kebnekaise, Sweden during 1966 and 1967. *Geografiska Annaler*, **50**, 111–120.
- Seaberg, S. Z., Seaberg, J. Z., Hooke, R. LeB. and Wiberg, D. W. (1988). Character of the englacial and subglacial drainage system in the lower part of the ablation area of Storglaciären, Sweden, as revealed by dye-trace studies. *Journal of Glaciology*, **34**(117), 217–227.

- Segall, P. (1984). Rate-dependent extensional deformation resulting from crack growth in rock. *Journal of Geophysical Research*, **89**(B6), 4185–4195.
- Shabtaie, S. and Bentley, C. R. (1988). Ice-thickness map of the West Antarctic ice streams by radar sounding. *Annals of Glaciology*, **11**, 126–136.
- Sharp, M. (1982). Modification of clasts in lodgement tills by glacial erosion. *Journal of Glaciology*, **28**(100), 475–481.
- Shreve, R. L. (1972). Movement of water in glaciers. *Journal of Glaciology*, **11**(62), 205–214.
- (1984). Glacier sliding at subfreezing temperatures. *Journal of Glaciology*, **30**(106), 341–347.
- (1985a). Esker characteristics in terms of glacier physics, Katahdin esker system, Maine. *Geological Society of America Bulletin*, **96**(5), 639–646.
- (1985b). Late Wisconsin ice-surface profile calculated from esker paths and types, Katahdin esker system, Maine. *Quaternary Research*, **23**(1), 27–37.
- Shreve, R. L. and Sharp, R. P. (1970). Internal deformation and thermal anomalies in lower Blue Glacier, Mount Olympus, Washington, USA. *Journal of Glaciology*, **9**(55), 65–86.
- Shumskii, P. A. (1964). *Principles of Structural Glaciology*. New York: Dover.
- Sih, G. C. (1973). *Handbook of Stress-Intensity Factors; Stress-Intensity Factor Solutions and Formulas for Reference*. Bethlehem, PA: Institute of Fracture and Solid Mechanics, Leigh University.
- Skempton, A. W. (1985). Residual strength of clays in landslides, folded strata, and the laboratory. *Géotechnique*, **25**(1), 3–18.
- Sokolnikoff, I. S. and Redheffer, R. M. (1958). *Mathematics of Physics and Modern Engineering*. New York: McGraw Hill, 810 pages.
- Sommerfeld, R. and LaChapelle, E. (1970). The classification of snow metamorphism. *Journal of Glaciology*, **9**(55), 3–17.
- Souchez, R. A. and Lorrain, R. D. (1978). Origin of the basal ice layer from Alpine glaciers indicated by its chemistry. *Journal of Glaciology*, **20**(83), 319–328.
- Strang, G. and Fix, G. J. (1973). *An Analysis of the Finite-Element Method*. New York: Prentice Hall, 306 pages.
- Stone, G. H. (1899). *The Glacial Gravels of Maine and their Associated Deposits*. U.S. Geological Survey Monograph 34, 499 pages.
- Taylor, L. D. (1963). Structure and fabric on the Burroughs Glacier, south-east Alaska. *Journal of Glaciology*, **4**(36), 731–752.
- Tarasov, L. and Peltier, W. R. (1999). Impact of thermomechanical ice sheet coupling on a model of the 100 kyr ice age cycle. *Journal of Geophysical Research*, **105**(D4), 9517–9545.
- Thomas, R. H. (1973a). The creep of ice shelves: theory. *Journal of Glaciology*, **12**(64), 45–53.
- (1973b). The creep of ice shelves: Interpretation of observed behavior. *Journal of Glaciology*, **12**(64), 55–70.
- Thomas, R. H., Akins, T., Csatho, B., Fahnestock, M., Gogineni, P., Kim, C. and Sonntag, J. (2000). Mass balance of the Greenland ice sheet at high elevations. *Science*, **289**, 426–428.

- Thompson, L. G., Mosley-Thompson, E., Dansgaard, W. and Grootes, P. M. (1986). The Little Ice Age as recorded in the stratigraphy of the tropical Quelccaya Ice Cap. *Science*, **234**(4774), 361–364.
- Tresca, M. H. (1864). Mémoire sur l'écoulement des corps solides soumis à de fortes pressions. *Comptes Rendus des Séances de l'Academie des Sciences, Paris*, **59**, 754–758.
- Truffer, M., Harrison, W. D. and Echelmeyer, K. A. (2000). Glacier motion dominated by processes deep in underlying till. *Journal of Glaciology*, **46**(153), 213–221.
- Truffer, M., Echelmeyer, K. A. and Harrison, W. D. (2001). Implications of till deformation on glacier dynamics. *Journal of Glaciology*, **47**(156), 123–134.
- Tulaczyk, S. (1999). Ice sliding over weak, fine-grained tills: Dependence of ice-till interactions on till granulometry. In Mickelson, D. M. and Attig, J. W. (eds.) *Glacial Processes Past and Present*. Boulder, Colorado: Geological Society of America Special Paper 337, pp. 159–177.
- Tulaczyk, S., Kamb, B., Scherer, R. and Engelhardt, H. (1998). Sedimentary processes at the base of a West Antarctic ice stream: constraints from textural and compositional properties of subglacial debris. *Journal of Sedimentary Research*, **68**, 487–496.
- Tulaczyk, S., Kamb, W. B. and Engelhardt, H. F. (2000a). Basal mechanics of Ice Stream B, West Antarctica 1. Till mechanics. *Journal of Geophysical Research*, **105**(B1), 463–481.
- (2000b). Basal mechanics of Ice Stream B, West Antarctica 2. Undrained plastic bed model. *Journal of Geophysical Research*, **105**(B1), 483–494.
- (2001a). Estimates of effective stress beneath a modern West Antarctic ice stream from till preconsolidation and void ratio. *Boreas*, **30**, 101–114.
- Tulaczyk, S., Scherer, R. P. and Clark, C. D. (2001b). A ploughing model for the origin of weak tills beneath ice streams: a qualitative treatment. *Quaternary International*, **86**, 59–70.
- Ussing, N. V. (1903). On Jyllands hedesletter og teorierne om deres dannelse. [On Jyllands meltwater outwash plains and theories of their origin.] *Oversigt over det Kongelige Danske Videnskabernes Selskabs Forhandlinger*, **2**, 99–165.
- Vallon, M., Petit, J.-R. and Fabre, B. (1976). Study of an ice core to bedrock in the accumulation zone of an alpine glacier. *Journal of Glaciology*, **17**(75), 13–28.
- Van Beaver, H. G. (1971). *The significance of the distribution of clasts within the Great Pond esker and adjacent till*. MS thesis, University of Maine, Orono, 61 pages.
- Van der Veen, C. J. (1996). Tidewater calving. *Journal of Glaciology*, **42**(141), 375–385.
- (1998). Fracture mechanics approach to penetration of surface crevasses on glaciers. *Cold Regions Science and Technology*, **27**, 31–47.
- (2002). Calving glaciers. *Progress in Physical Geography*, **26**(1), 96–122.
- Van der Veen, C. J. and Whillans, I. M. (1989). Force budget: I. Theory and numerical methods. *Journal of Glaciology*, **35**(119), 53–60.

- (1994). Development of fabric in ice. *Cold Regions Science and Technology*, **22**, 171–195.
- van de Wal, R. S. W. and Oerlemans, J. (1995). Response of valley glaciers to climatic change and kinematic waves: a study with a numerical ice flow model. *Journal of Glaciology*, **41**(137), 142–152.
- Vaughan, D. G. (1993). Relating the occurrence of crevasses to surface strain rates. *Journal of Glaciology*, **39**(132), 255–266.
- Waite, A. H. and Schmidt, S. J. (1961). Gross errors in height indication from pulsed radar altimeters operating over thick ice or snow. *Institute of Radio Engineers International Convention Record*, **5**, 38–53.
- Walder, J. S. (1982). Stability of sheet flow of water beneath temperate glaciers and implications for glacier surging. *Journal of Glaciology*, **28**(99), 273–293.
- Walder, J. S. and Fowler, A. (1994). Channelized subglacial drainage over a deformable bed. *Journal of Glaciology*, **40**(134), 3–15.
- Walder, J. S. and Hallet, B. (1979). Geometry of former subglacial water channels and cavities. *Journal of Glaciology*, **23**(89), 335–346.
- Walters, R. and Meier, M. F. (1989). *Variability of Glacier Mass Balances in Western North America*. American Geophysical Union, Geophysical Monograph 55, pp. 365–374.
- Walters, R. A., Joshberger, E. G. and Driedger, C. L. (1988). Columbia Bay, Alaska: an “upside down” estuary. *Estuarine, Coastal, and Shelf Science*, **26**, 607–617.
- Warren, C. R., Glasser, N. F., Harrison, S., Winchester, V., Kerr, A. and Rivera, A. (1995). Characteristics of tide-water calving at Glaciar San Rafael, Chile. *Journal of Glaciology*, **41**(138), 273–289.
- Weertman, J. (1957a). On sliding of glaciers. *Journal of Glaciology*, **3**(21), 33–38.
- (1957b). Deformation of floating ice shelves. *Journal of Glaciology*, **3**(21), 38–42.
- (1964). Glacier sliding. *Journal of Glaciology*, **5**(39), 287–303.
- (1972). General theory of water flow at the base of a glacier or ice sheet. *Reviews of Geophysics and Space Physics*, **10**(1), 287–333.
- (1973). Can a water-filled crevasse reach the bottom surface of a glacier? *International Association of Scientific Hydrology Publication* 95, 139–145.
- (1983). Creep deformation of ice. *Annual Reviews of Earth and Planetary Science*, **11**, 215–240.
- Weertman, J. and Birchfield, G. E. (1983). Stability of sheet water flow under a glacier. *Journal of Glaciology*, **29**(103), 374–382.
- Whillans, I. M. (1977). The equation of continuity and its application to the ice sheet near “Byrd” Station, Antarctica. *Journal of Glaciology*, **18**(80), 359–371.
- Whillans, I. M. and Tseng, Y.-H. (1995). Automatic tracking of crevasses on satellite images. *Cold Regions Science and Technology*, **23**(2), 201–214.
- Whillans, I. M. and Van der Veen, C. J. 1993. New and improved determinations of velocity of Ice Streams B and C, West Antarctica. *Journal of Glaciology*, **39**(133), 483–490.
- WISC (2003). <http://uwamrc.ssec.wisc.edu/amrc/iceberg.html>

- Wright, H. E., Jr. (1973). Tunnel valleys, glacial surges and subglacial hydrology of the Superior Lobe, Minnesota. In Black, R. F., Goldthwait, R. P. and Willman, G. B. (eds.) *The Wisconsin Stage, Boulder, Colorado. Geological Society of America Memoir* 136, 251–276.
- Yarnal, B. (1984). Relationships between synoptic-scale atmospheric circulation and glacier mass balance in south-western Canada during the International Hydrological Decade. 1965–74. *Journal of Glaciology*, **30**(105), 188–198.
- Zwally, H. J. and Giovinetto, M. B. (2000). Spatial distribution of net surface mass balance on Greenland. *Annals of Glaciology*, **31**, 126–132.

Index

- ablation area 17
- accumulation area 17
- accumulation area ratio 31
- activation
 - energy xv, 49, 52, 67–68
 - enthalpy 68
 - volume 68
- Admundsen Sea 39
- Agassiz Ice Cap 311, 364
- Aleutian low 37, 39
- Antarctica
 - accumulation rate 35–36, 39
 - basal drag 138–139
 - basal temperature 138–142
 - basal temperature gradient 139
 - drifting (of snow) 99
 - ice shelves 333
 - ice streams in, *see* ice streams
 - mass balance 32
 - Pleistocene–Holocene transition 366
 - surface topography 138
- Arolla ice tunnel 323
- Athabasca Glacier 86–87, 95, 155
- Atnedalen, Norway 241
- axes
 - instantaneous stretching 351
 - principal, of strain 267, 352
 - principal, of strain rate 15
 - principal, of stress 254, 267
- B** 15, 66
 - effect of dirt on 160–161
 - effect of fabric on 69–70
 - effect of water content on 70
 - variation with temperature 67–68
- backward difference 296
- balance
 - net 23
 - specific 23
 - summer 23
- winter 23
- velocity 78–79
- Barnes Ice Cap
 - borehole deformation in 341–348
 - cumulative strain in 354–356
 - foliation in 361
 - ice fabrics in 62–63, 69–70
 - near surface temperature in 122
 - Pleistocene ice in 343–344
 - rheology of Pleistocene ice in 311
 - temperatures in 295–296
 - winter balance of 29
- basal, *see* bed
- basal ice, rheology of 159–160
- basal plane 43, 53
- bed
 - drag on 85–86, 163
 - freezing at 123–124, 136, 137
 - melting at 34, 123–124, 136
 - temperature at 135–137, 306
- Bindschadler Ice Stream 188–189,
 - 192
- Bingham material 259
- Bjerrum defects 44
- Black Rapids Glacier 189
- Blue Glacier 155, 177, 197, 199, 238
- Böðvarsson effect 379–381
- borehole
 - closure 321–323
 - deformation 338–341
 - problem near surface 346
 - use to determine n and B 346–348
- Boudinage 364
- Breidamerkurjokull 177, 189
- budget 23
 - gradient 29–31
- budget imbalance 24
- bulk modulus xv
- bullet boulders 247
- Burgers vector xv, 49

- Byrd Station
 debris in basal ice 137
 ice fabrics at 62
 thinning rate 131
 Pleistocene–Holocene transition 366
- c*-axis 44
- calving
 as a mode of ice loss 31–32
 numerical modeling of 304–305
 of ice shelves 36
 relation to water depth 33
 submarine 32–33
- Camp Century 137
- cavities, subglacial 162–167
- centered difference 296
- cirques 248–250
- Clausius Clapeyron slope 8
- clay, in till 169, 171–172
- climate
 continental 29, 31, 200
 maritime 29, 31, 200
- climatic change
 instabilities in response to 366–367
 isostatic response to 366–367
 modeling the response to 381–383
 response of glaciers 365–390
 analysis using perturbation theory 27–28, 371–373
 effect of diffusion 375–376
 effect of longitudinal strain rate 367–368
 observations of 383–384
 problem at terminus 376
 with uniform longitudinal strain rate 373–375
 response time–volume time scale 376–379
 thermal response to 366
- coaxial deformation 351
- cohesion 168, 169
 apparent 169
 role of clay 169
- cold patches 156–158
- Columbia Glacier 3, 34, 177
- compressive flow 276
- conduits
 englacial 197–201
 subglacial
 closure of 202, 324–326
 equilibrium size 202
 linked cavity 216–221
 multibranched arborescent 221–223
- Nye or N 216
 on eskers 238–240
 on till 223–230
 Röthlisberger or R 216
 shape of 213–215
 tunnel 215–216, 220–221
- conservation of mass 9–10, 78
- consolidation
 normal 170
 overconsolidated 170
- controlling obstacle size 152
- Crank–Nicolson 295
- creep
 Coble 64
 diffusional 63, 65–66
 Nabarro Herring 64
 power law 63
 primary 51
 secondary 51
 steady state 52
 tertiary 52
 transient 52
- crevasses
 formation of 73–74
 water flow in 200–201
- critical state line 173
- cross glide 47
- cross slip 52
- crystal size 65, 68–69
- cumulative strain
 calculating 353–354
 in Barnes Ice Cap 354–356
 parameters describing 346–348, 352
- cylindrical hole
 closure of 321–323
 strain rates around 317–318
 stresses around 316–321
- Dansgaard–Oeschger cycles 129
- Dawson’s integral 133
- debris entrainment, *see* erosion
- debris in basal ice 100, 137, 160
- debris-bearing ice
 rheology of 159–160, 161
- deformation, *see also* strain 262–264
 elastic 53, 54
 mechanism maps 63–66
 mechanisms 63–64
- Del operator 116

- density
 - bubble-free ice [xiv](#)
 - water [xiv](#)
- depth hoar [21](#)
- Devon Ice Cap [311, 364](#)
- Des Moines Lobe [174](#)
- diffusion
 - effect on response to climatic change [375–376](#)
- diffusional flow [63, 65–66](#)
- dihedral angle [xv](#)
- dilation, of till [171](#)
- disintegration ridges [103–105](#)
- dislocation
 - climb [50–52, 63](#)
 - cross slip [52](#)
 - density [49, 50](#)
 - edge [44](#)
 - formation of [46–47](#)
 - glide [63](#)
 - healing [66](#)
 - kinks in [47–48](#)
 - movement of [47–48](#)
 - recovery [50](#)
 - screw [44](#)
 - tangles [46, 50–52](#)
- dislocations [44–48](#)
- doughnuts [104](#)
- drag, basal, *see* bed
- drainage systems, subglacial
 - conduit [215–216](#)
 - linked cavity [216–220, 231](#)
 - multi-branched arborescent [221–223](#)
 - on till [223–230](#)
- drumlins [309–310](#)
- dry snow
 - line [20](#)
 - zone [20](#)
- effective normal pressure [161](#)
- electrical conductivity [65](#)
- electromagnetic forces, on clays [169](#)
- EISMINT [302](#)
- energy, specific surface
 - of grain boundary [xv](#)
 - of liquid–solid interface [xv, 7](#)
- energy balance [112–117](#)
 - advection effect [112–114](#)
 - conduction effect [114–115](#)
 - strain heating effect [115–116](#)
- energy grade line [210](#)
- Engabreen [156](#)
- enhancement factor [69–70, 311](#)
- ENSO [39–40](#)
- equilibrium line [17](#)
 - altitude [27–29](#)
- equipotential surfaces [201–204](#)
- erosion [142, 157–158](#)
 - thrust features [142](#)
- error function [121–122](#)
- eskers [232–241](#)
 - conduits on [238–240](#)
 - Katahdin [236, 241](#)
 - nets [240–241](#)
 - on valley sides [235](#)
 - over ridges [234–235](#)
 - ramp structures [240–241](#)
 - sediment supply to [236](#)
- Eulerian coordinate system [114, 117](#)
- extending flow [276](#)
- fabric [55](#)
 - conical [59](#)
 - development of [59](#)
 - effect on B [69–70](#)
 - measurement of [55–58](#)
 - multiple maximum [61–62, 65](#)
 - single maximum [61, 62](#)
 - small circle [60, 62](#)
 - variation with depth [62–63](#)
- facies [20](#)
- Findelengletscher [165–167, 203, 223](#)
- finite-difference modeling [291–298](#)
 - alternating direction schemes [295–296](#)
 - backward, forward and centered differences [296](#)
 - higher-order solutions [298](#)
 - implicit methods [294–295](#)
 - non-dimensionalization [296–297](#)
 - shallow ice approximation [297–298](#)
- finite-element modeling [298–299](#)
- firn [17](#)
- flow field [92–94](#)
- flow law [15–16, 66–70, 267–268](#)
 - effect of fabric [69–70](#)
 - effect of grain size [68–69](#)
 - effect of pressure [68](#)
 - effect of temperature [67–68](#)
- flowlines [92–93](#)
- flux, ice [87](#)

- foliation
 components of 356–358
 folds in 361–364
 in the marginal zone 359–361
- force balance 326–330
- forward difference 296
- fracture
 mechanics 70–74
 toughness *xvi*, 72
- Frank Reed sources 46
- frazil ice 249
- free energy 58, 59
- freezing at bed 123–124, 136, 137
- friction
 angle of internal 168, 171–172
 rock to rock 156, 171
- gas constant 49
- Gaukler Manning Strickler equation 206
- geothermal heat flux 119–120, 190
- glacier
 cirque 6
 classification 6–7
 mining near 3
 outlet 6
 polar 6–7
 polythermal 7
 sources of water 3
 subpolar 7
 temperate 7–8
 temperature of 6–8, 112–146
 tidewater 6
 valley 6
- Glen's flow law 15, 66
- global warming 3
- global positioning systems 77
- Gornergletscher 223
- grain boundary
 melting 65
 migration 52, 53, 58–59, 63, 65–66
 mobility 64
- grain bridges 174–175, 177, 178
- grain nucleation 58–59
- grain size (ice) 65, 68–69
- Greek lead smelting 2
- Greenland Ice Sheet
 dating ice in 21–22
 folds in 364
- lead in 2
- mass balance of 32, 41
- numerical model of 311
- hazards 2–3
- heat
 advection 112–114
 conduction 114–115
 sensible 26
- heat capacity 8
 air-free water *xiv*, 8
 air-saturated water 8
 ice *xiv*, 65
- heat flow unit 119
- heat of fusion *xiv*, 7, 124
- Heinrich layers 36, 110, 367
- Hill lake pair 142
- Hintereisferner 24, 381–383
- Hudson Bay 311
- Hudson Strait 36, 109, 311
- hydraulic grade line 210
- hydraulic jacking 163–165
- hydroelectric power 3, 156
- ice
 crystal structure of 43–44
 dating 21–23
 electrical conductivity of 22
 forms of 43–44
 Ic 43
 Ih 43–44
 as a metamorphic rock 2
 microparticles in 23
 Pleistocene 102, 311, 343–344
 water content of 70, 160
 volcanic ash in 23
- ice cap 6
- ice sheet 6
- ice shelves
 bottom melting of 36–37
 calving of 36
 creep of 333–338
 Larsen 36, 37–39, 74
 side drag on 337–338
 Ross 36
- ice streams 105–110
 erosional capabilities of 168
 in Pleistocene ice sheets 109–110
 speed of 168
 stability of 190–193

- temporal changes in
 - shear margins 108–109
 - speed 108
 - water pressure under 168
- ice-walled lake plains 105
- impurities
 - effect on ice rheology 65
 - effect on sliding 158–159
- incompressibility condition 9–10
- internal friction, angle of 168, 171–172
 - effect of granulometry on 171–172
 - frictional component of 171
- invariant, stress 256, 260–261
- irrotational deformation 264, 351
- isotropic 267
- Jokulhlaup 3, 206
- Kangerlussuaq 102
- Kamb Ice Stream 108, 192, 193
- kettled outwash plain 241
- kinematic waves
 - definition of 368
 - equation of 370
 - modeling 381–383
 - on Nisqually Glacier 386
 - speed of 369–370
 - theory 368–371
- kink pairs 47–48
- Kronecker delta 257
- Lagrangian coordinate system 114, 117
- Lake Vostok 99, 138
- lapse rate 31, 129
- Laurentide Ice Sheet
 - evidence of collapse 367
 - ice shelves 333
 - ice streams in 109
 - numerical models of 306–309, 310–313
 - temperature distribution in 135–137, 306
- Late Glacial Maximum (LGM) 306
- latent heat of fusion xiv, 7, 124
- linked cavity drainage system
 - orifice 216–219
 - stability of 218–219
 - transition to tunnel 219
- liquid–solid surface energy xv, 7
- Little Ice Age 2–3, 33
- longitudinal strain rate
 - depth variation 88–89
 - effect on transverse profiles 94–96
 - effect on longitudinal velocity profile 285
 - effect on glacier response to climatic change 367–368, 374–375
- role in balancing b_n 286
- role in calving 304
- role in borehole deformation 338
- MacAyeal Ice Stream 192
- Manning equation 206
- Manning roughness 206
- mass, conservation of 9–10, 78
- Mass balance, *see also* balance
 - causes of fluctuations 26–29
 - cumulative 25–26
 - global 40–41
 - of Alaskan glaciers 41
 - of polar ice sheets 34–36
 - effect of atmospheric circulation patterns on 36, 37–39
 - measurement of 23–24
 - principles 23–26
- material lines 351
- melting
 - at bed 124, 136
 - of conduit walls 205–207
- melting point depression xiv, 7–8
- meltwater, percolating 20, 122
- Mer de Glace 3
- microcracks 247
- Mohr’s circle 255–256
- Mohr–Coulomb relation 168
- momentum balance 261–262, 327, 333
- monocrystals 53
- moraines
 - ribbed 143, 194
 - stoss side moraines 143
 - Thule–Baffin 99
- moulin 200–201
- n 15, 49–54, 66
- non-dimensionalization 296
- North Atlantic Oscillation 40
- normal consolidation line 173
- Nisqually Glacier 383–387
- numerical integration 289–291
- numerical modeling 288–313
 - goals of 289
 - coupling 301, 303–304

- numerical modeling (*cont.*)
- finite-difference, *see* finite-difference modeling
 - finite-element 298–299
 - forcing 300–301
 - initial conditions 299–300
 - intercomparison of 301–302
 - sensitivity testing 302–303
 - thermomechanical 303
 - three-dimensional 310
 - tuning 303
 - validation 301
- numerical models of
- Antarctica 138
 - basal drag 138–139
 - basal temperatures 139–142
 - Laurentide Ice Sheet 310–313
- Nye channels 216
- octahedral plane 15
- orifice 216–219
- overdeepenings 248–250
- oxygen isotopes 22
- Pacific Decadal Oscillation 39–40
- paleoclimatology 2, 307
- Penobscot River 236
- percolation zone 20
- permafrost, role in glacier flow 305–310
- permeability of glacier ice 198–199, 201
- perturbation techniques
- applied to changes in ELA 27–28
 - applied to changes in profile 371–373
- Peyto Glacier 38
- piezometric head 210
- plane strain
- cylindrical hole 316–321
 - stresses in
 - nonlinear material 281, 284–285
 - perfectly plastic 273–277
- velocities in
- nonlinear material 281–285
 - perfectly plastic 278–281
- plasticity, perfect 259, 268
- Pleistocene ice, rheology of 343–344
- ploughing 185–186
- Poisson's ratio xv
- polygonization 58
- pore close off 19
- precipitates, subglacial 158
- precipitation gradient 30
- preconsolidation test 174
- pressure
- critical 165
 - effective 161
 - separation 163
- principal
- stresses 15
 - strain rates 15
- prismatic plane 52
- profiles, transverse surface 94–96
- pure shear 59, 351
- distribution of in an ice cap 353
- pyramidal plane 52
- quarrying 244–248
- quadrature 290
- Gaussian 290
- radar stratigraphy 96–98
- radiation 26, 28, 29
- radioactive waste 3–4
- ramp structures 240–241
- rate limiting processes
- in ice deformation 48–53
 - climb as 50–52
 - cross slip as 52
 - definition of 48
 - drag as 49–50
 - slip on pyramidal plane as 52, 53
 - in till deformation 178
- Raymond bump 98
- receiving area 231
- recrystallization 54–59
- dynamic 58, 64
 - by grain growth 58
 - by nucleation of new grains 58–59
 - by polygonization 58
- regelation 148, 156
- effect of impurities 158–159
 - into subglacial till 137
 - theory 149–150, 158
 - thickness of layer 154–155
 - unknown pressure field 158
- relict surfaces 142–143
- reservoir area 231
- response time 374, 376–379
- response to climatic change
- volume time scale 376–379
- rheology
- of Holocene ice 343–344
 - of Pleistocene ice 343–344
- Roman lead smelting 2

- Ross Ice Shelf 106, 108, 109
 rotation 263
 rotation rate 264
 Röthlisberger channels 216
 roughness of bed 149, 153–154
 truncated white 154
 white 152, 154
- sea level 109
 satellite interferometry 109
 Sentinel Glacier 38
 shallow ice approximation 297–298
 shape factor 84, 86–87
 shear
 pure 59, 351
 simple 61, 351–352
 shear modulus xv, 49
 shear stress
 basal 85–86
 calculation from force balance 326–330
 SI units 5
 simple shear 61, 351–352
 distribution of in an ice cap 353
 sintering 19
 Siple Coast 106, 107
 Siple Dome 97, 108
 Site 2 131
 sliding 148–159
 at subfreezing temperatures 193–194
 by plastic flow 148, 150
 by regelation 148
 effect of cavities 162, 163
 effect of impurities 158–159
 effect of rock–rock friction 156
 effect of water pressure 162–167
 over till 184–185
 regelation theory 149–150, 158
 role of normal pressure 161
 speed 151–153, 154, 177
 tests of theories 154–155
 weaknesses of theory 156–159
 slip line field 277
 snow drifting
 effect on budget gradient 30
 effect on velocity field 98–105
 snow
 line 20
 stratigraphy 20–21
 transformation to ice 20
 South Cascade Glacier 37, 387–390
 steady state 78–79, 91–93, 365
- Storglaciären
 basal shear stress 330–333
 conduit character 221–222, 228
 conduit roughness 206
 response time 381
 sliding speed 166–167
 till composition 170
 till rheology 177, 180–182
 water pressure in 249
- strain 262–264
 definition 12
 elastic 53, 54
 ellipse 349–351
 general theory of 262–264
 inhomogeneous 52–53
 logarithmic 13, 265
 notation 10–11
 plane, *see* plane strain
 principal axes of 267, 352
 rate 12, 263–264
 sign convention 10–11, 18
 transformation of 265
- strain heating 115–116
 boundary condition 132
- strain rate 12, 263–264
 effective 14–15, 258
 in monocrystals 53
 longitudinal, *see* longitudinal strain rate
 octahedral 14–15
 principal 15
 principal axes of 15
- stratigraphy, radar 96–98
 strength, crushing, of ice xvi, 32
 strength, of granular medium
 failure 172
 residual 172
 ultimate 172
 yield 172
- stress 252–261
 basal shear 79–81, 326–330
 comparison of theory with real glaciers 286–287
 definition 10
 deviatoric 13–14, 257, 276
 effective shear 14–15, 258
 equilibrium 261–262, 327, 333
 general theory of 252–261
 in a slab
 nonlinear material 281
 perfectly plastic material 273–277
 in plane strain 260, 272–277, 281, 284–285
 intensity factor 71, 72

- stress (*cont.*)
 internal 53–54
 invariants 256, 260–261
 longitudinal, effect on conduits 214, 326
 normal 10
 notation 10–11
 octahedral 14–15
 preconsolidation 170
 principal 15, 254–255
 principal axes of 254, 267
 shear 10, 255
 shear, depth variation 79–81
 sign convention 10–11, 18
 transformation of 252–254
 yield 13, 258–260
- striations, formation of 156
- structural geology 2
- summation convention 257
- superimposed ice 21
- superimposed ice zone 21
- surface, 500 mb 37
- surface elevation
 transverse profiles of 94–96
- surges 230–232
- Svartisen 156, 160
- Taylor Dome 98
- temperature
 homologous 63
 melting 7–8
 near surface 122–123
 mean annual 122–123, 127–129
 pressure melting 7–8
- temperature boundary conditions
 bed 119–120, 123–124
 surface 121–122
- temperature distribution along a flowline 135–137, 306
- temperature profile
 ablation area 127, 291–292
 accumulation area 133–134
 at a divide 117–123, 124–126
 column model 131–134, 139–142
 effect of sinusoidal oscillations at surface on 127–129
 error induced by assumed vertical velocity
 distribution 126–127
 near surface 127–131
 using to estimate thickening rate 130–131
 warming rate problem 137, 138
 with only conduction and warming 134–135
- tensor 11
 first rank 11
 invariants of 256, 260–261
 rotation rate 264
 second rank 11
 strain 263
 strain rate 263–264
 symmetric 12
 velocity derivative 264
- texture 54
- thermal conductivity
 ice xiv, 114, 150
 rock 150
 temperature dependence of 117
- thermal diffusivity xiv, 115
- thermal expansion coefficient
 ice xv
 water xv
- thrust features 142, 309–310
- Thule, Greenland 100
- Thule–Baffin moraines 99
- thin section 55
- tidewater glaciers 6
 cyclic behavior of 33–34
- till
 consolidation of 170–171
 decoupling of ice from 184–185
 deformation measurements in 180–182, 188–189, 190
 deformation of 168–184
 depth variation of 187
 rate controlling process in 178
 deforming, thickness of 186–190
- dilation of 171
- dilatant hardening of 182
 flow into subglacial conduits 223–224, 225
 fractal size distribution of 175–177
 grain bridges in 174–175, 177, 178
 grain fracture 170, 174–177
 granulometry of 174–177
 in overdeepenings 249–250
 ploughing of 185–186
 residual strength 172, 178
 rheology of 177–184
 strain rates in 177
 transport 186
 yield strength 172
- tiltmeters 181, 189
- time constant (for change in profile) 374
- Trapridge Glacier 177
- trimline 86

- transverse till scarps 143, 194
- trapezoidal integration 290
- triple point
 - pressure *xvi*, 159
 - temperature *xvi*, 7, 8
- tunnel closure 202, 321–323
- tunnel valleys 241–244, 309–310
- T* term 328, 345
- uniaxial compression 59
- units 5
- unloading–reloading line 173
- Urumqi Glacier No. 1 193
- Variegated Glacier
 - drainage system 216
 - surge of 231–232
- veins, water flow through 197–199
- velocity
 - balance 78–79
 - comparison of theory with field data 84, 86–87, 286–287
 - depth averaged 87–88
 - effect of drifting snow on 98–105
 - emergence 91–92, 365
 - flow field 92–94
 - in a slab of nonlinear material 282–284
 - in a slab of perfectly plastic material 278–280
 - in a valley glacier 83–87
 - in plane strain 278–285
 - measurement of 77–78
 - from satellite imagery 77–78
 - GPS 77
 - theodolite 77
 - submergence 91–92, 365
 - variation with depth
 - horizontal 81–82
 - vertical 88–90
 - vertical under divide 89–90
- viscoplastic 259
- viscous heating in
 - ice 115–116
 - water 199, 200, 202, 205–206
- void ratio 173–174
- water equivalent line 210
- water content of ice 70
- water flow
 - in englacial conduits 199–200
 - in subglacial conduits
 - on hard beds 208–223
 - on soft beds 223–230
 - in veins 197–199
 - up adverse bed slopes 213, 249
- water pressure
 - during surges 231–232
 - effect of *B* on 210
 - effect of bed slope on 211–213
 - in conduits 208–213
 - in conduits in till 225, 228
 - in pore water 142, 174, 312
- water table in glaciers 200
- waves, kinematic, *see* kinematic waves
- West Antarctic Ice Sheet
 - collapse of 367
 - ice streams in, *see* ice streams or ice stream name
- wet snow
 - line 20
 - zone 20
- Whillans Ice Stream
 - changes in drainage under 193
 - geothermal heat under 192
 - nature of bed under 107, 168
 - pulsed movement of 193
 - shear margins 108
 - speed of 107, 108
 - till composition 170
 - till deformation 177, 186
 - till void ratio 187
- Wolverine Glacier 37
- work hardening 50
- Worthington Glacier 94
- yield criterion 258–260
- yield strength 72
- yield stress 13
- Young's modulus *xv*, 63